Widely tunable and SI-traceable frequency-comb-stabilised mid-infrared quantum cascade laser : application to high precision spectroscopic measurements of polyatomic molecules

Dang Bao An Tran

UNIVERSITÉ PARIS 13 - SORBONNE PARIS CITÉ

LABORATOIRE DE PHYSIQUE DES LASERS

THÈSE DE DOCTORAT

pour obtenir le grade de

DOCTEUR DE L'UNIVERSITÉ PARIS 13

Discipline : PHYSIQUE

présentée et soutenue publiquement par

Dang Bao An Tran

Widely tunable and SI-traceable frequency-comb-stabilised mid-infrared quantum cascade laser : application to high precision spectroscopic measurements of polyatomic molecules

Soutenue le 15 Juillet 2019 devant le jury composé de :

Prof. **Anne Amy-Klein**	LPL	Directrice de thèse
Dr. **Alain Campargue**	LIPHY	Président
Dr. **Caroline Champenois**	PIIM	Rapporteuse
Dr. **Benoît Darquié**	LPL	Co-encadrant
Prof. **Laurent Hilico**	LKB	Rapporteur
Dr. **Rodolphe Le Targat**	LNE-SYRTE	Examinateur
Prof. **Gaël Mouret**	LPCA	Examinateur
Dr. **Gabriele Santambrogio**	LENS	Examinateur

L'équipe Métrologie, Molécules et Tests Fondamentaux (MMTF)
Laboratoire de Physique des Lasers
Université Paris 13, CNRS - UMR 7538
99 Avenue Jean Baptiste Clément,
93430 Villetaneuse, France

Acknowledgement

My work has been performed at the Metrology, Molecules, and Fundamental Tests (MMTF) group, Laboratoire de Physique des Lasers (LPL), CNRS, Université Paris 13.

First of all, I am deeply grateful to my supervisors Prof. Anne Amy-Klein and Dr. Benoît Darquié. To Anne, thank you both for your guidance and encouragement during four years of work. To Benoît, thank you all for your support, and boundless patience. I wouldn't got anything done without your continuous presence in laboratory. I am proud to have studied under the two of you. On top of that, I gratefully acknowledge this opportunity to work with you.

I would like to thank Prof. Laurent Hilico and Dr. Caroline Champenois for reviewing my thesis. I also thank other members of my board of examiners, Dr. Alain Campargue, Prof. Gaël Mouret, Dr. Rodolphe Le Targat, and Dr. Gabriele Santambrogio.

I would also like to thank Dr. Olivier Lopez for continual support for electronic control. The experience and the knowledge I got from him is invaluable and will help my further teaching greatly at HCMC University of Education, Vietnam. To Dr. Sean Tokunaga, thanks for your support for programming and optical alignment.

A special thanks to Dr. Rosa Santagata with whom we tried to develop the experiment together. Many of the results presented in this thesis resulted from working with her. To Dr. Anne Cournol and Dr. Mathieu Manceau, thank you for all your advice about the experiment, also to Matthieu Pierens and Louis Lecordier for interesting discussions. From Paris, I would like to thank Dr. Thomas Wall for the precious opportunity to understand the experimental setups at the Centre for Cold Matter, Imperial College London.

To researchers at LNE-SYRTE, thank you a lot for the best reference signal. I wouldn't have finished my work without the collaboration between LPL and LNE-SYRTE. I would also like to thank all the members of the MMTF group. To Prof. Frédéric Du Burck, Dr. Vincent Roncin, Amine Chaouche Ramdane, Karim Manamanni, thanks all for your discussions and working together in the same laboratory in the first three years. To Dr. Christophe Daussy and Dr. Moufarej Elias, thanks for sharing optical components, and to the other members for your valuable support.

To Dr. Ha Tran, Laboratoire de Météorologie Dynamique, Sorbonne Université and Dr. Ba-Tong Nguyen, Laboratoire de Physico-Chimie de l'Atmosphére, Université du Littoral Côte d'Opale, thank you all for discussions about molecular spectroscopy.

I would also like to thank to Olivier Gorceix, former director of LPL, for welcoming me in such a great working environment. I also thank all supports from administrative group: Carole Grangier, Maryse Médina, Sylvie Spielmann, and Solen Guezennec, from the

mechanics workshop: Albert Kaladjian and his colleagues, from the electronic workshop: Fabrice Wiotte and his colleagues, from the optics workshop: Thierry Billeton, and from IT technicians: Marc Barbier and Stéphane Simonazzi.

I gratefully acknowledge the Ministry of Education and Training, Vietnam (Program 911) for financial support during four years and L'école Doctorale Sciences, Technologies Santé - Galilée, Université Paris 13 for additional financial support. I would also like thank to my colleagues at Faculty of Physics, HCMC University of Education, Vietnam who have shared the teaching work during this course.

Finally, I would like to thank my family in Vietnam and my Vietnamese friends in France, especially, family of Dr. Van-Tuan Nguyen, a postdoc at Institut Pasteur, Paris and Thanh-Tuan Nguyen, a PhD student at Université de Toulon.

Contents

Acknowledgement iii

Introduction 1

1 Spectroscopic studies with molecules: principle and applications 5
1.1 Molecular spectroscopy . . . 5
1.1.1 Rovibrational spectrum . . . 6
1.1.2 Linear absorption spectroscopy . . . 8
1.1.3 Saturated absorption spectroscopy . . . 9
1.2 Tools for frequency control, high resolution spectroscopy, and metrology . 12
1.2.1 Frequency standards . . . 12
1.2.2 Ultra-stable signal . . . 17
1.2.3 The optical frequency comb . . . 18
1.2.4 Optical frequency dissemination . . . 21
1.3 Mid-infrared laser stabilization . . . 23
1.3.1 The need for mid-infared laser stabilization . . . 23
1.3.2 Methods for the frequency stabilization of mid-infrared lasers . . . 23
1.4 Previous precise molecular spectroscopic measurement at LPL . . . 25
1.5 Parity violation observation . . . 27
1.5.1 Parity violation in chiral molecules . . . 28
1.5.2 Proposed experimental approaches of the parity violation observation in chiral molecules . . . 29
1.5.3 Searching new chiral molecules . . . 30
1.5.4 New experimental setup under development . . . 31
1.6 Concluding remarks . . . 33

2 Tunable and SI-traceable optical frequency comb stabilized to a remote optical frequency reference signal 35
2.1 Introduction . . . 35
2.2 Reference signals from LNE-SYRTE . . . 36
2.2.1 Primary microwave reference signal . . . 36
2.2.2 Ultra-stable near-IR frequency reference from LNE-SYRTE . . . 38
2.2.3 Calibration of the US laser frequency to the primary standards . . . 43
2.3 Transfer of a stabilized frequency reference between LNE-SYRTE and LPL 44
2.3.1 Principle of fiber based optical frequency transfer . . . 44
2.3.2 Optical frequency transfer between LNE-SYRTE and LPL . . . 45
2.4 Local radio frequency references . . . 51
2.5 Widely tunable and ultra-stable optical local oscillator at 1.54 μm . . . 52

2.5.1 Experimental setup . . . 52
2.5.2 Low-phase noise microwave synthesizer without phase jumps . . . 54
2.6 The optical frequency comb at LPL . . . 55
2.6.1 The OFC at LPL: introduction and modules . . . 55
2.6.2 Free-running optical frequency comb . . . 61
2.7 Frequency stabilization of the OFC repetition rate onto the OLO . . . 63
2.7.1 Experimental setup . . . 63
2.7.2 Performances of the stabilization of the repetition rate of the OFC 65
2.7.3 Upgrading the experimental setup . . . 68
2.8 OFC repetition rate tuning performances . . . 70
2.9 Conclusion . . . 71

3 Development of a quantum cascade laser based widely tunable ultra-high resolution spectrometer 73
3.1 Introduction . . . 73
3.2 Quantum cascade laser . . . 75
3.2.1 What is a quantum cascade laser? . . . 75
3.2.2 The LPL mid-infrared quantum cascade laser . . . 77
3.3 Frequency stabilization of a quantum cascade laser to an optical frequency comb . . . 84
3.3.1 Sum frequency generation . . . 84
3.3.2 Locking the quantum cascade laser to the optical frequency comb . 89
3.3.3 Performances of the QCL frequency stabilization . . . 95
3.4 The QCL frequency control: summary and SI-traceability . . . 99
3.4.1 Summary . . . 99
3.4.2 SI-traceability of the QCL frequency . . . 102
3.4.3 Determination of the QCL absolute frequency . . . 103
3.5 Quantum cascade laser frequency tuning . . . 105
3.5.1 Wide frequency tuning of the stabilized QCL using the step motor 105
3.5.2 Using neighbouring modes . . . 109
3.5.3 Using a radio-frequency-stabilized OFC . . . 109
3.5.4 Perspective . . . 109
3.6 Conclusion . . . 109

4 High-precision mid-infrared spectrometer: application to the spectroscopy of methanol 111
4.1 The high-precision widely tunable SI-tracable QCL-based mid-infrared spectrometer . . . 112
4.1.1 Optical setup . . . 112
4.1.2 Vacuum setup . . . 116
4.1.3 Frequency modulation setup for saturated absorption spectroscopy 116
4.2 Rovibrational spectrum of methanol: an overview . . . 119
4.2.1 Methanol: a molecule with a variety of interests . . . 119
4.2.2 Structure of rovibrational energy levels and notation . . . 120
4.2.3 K-doublet . . . 123
4.2.4 High resolution spectroscopy of methanol in the literature . . . 124
4.3 Doppler-limited spectroscopy . . . 124
4.3.1 Spectrum acquisition . . . 124

4.3.2 Data processing and results . . . 125
4.4 Precise spectroscopy of methanol . . . 128
4.4.1 Spectrum acquisition . . . 128
4.4.2 Analysis of experimental data . . . 132
4.5 Spectroscopic measurements . . . 138
4.5.1 Power-induced frequency shift . . . 138
4.5.2 Pressure-induced frequency shift . . . 139
4.5.3 Power- and pressure-induced broadening effects . . . 140
4.5.4 Estimation of the transition dipole moment . . . 143
4.6 Absolute frequency measurement of rovibrational transitions of methanol 143
4.6.1 Absolute frequency measurement of the $P(E,\mathrm{co},0,2,33)$ methanol transition . . . 143
4.6.2 Absolute frequency determination of other methanol transitions . . 151
4.6.3 Summary . . . 160
4.7 Asymmetry K-doublets for A-symmetry transitions . . . 162
4.7.1 Resolved K-doublets . . . 163
4.7.2 Un-resolved K-doublet . . . 169
4.7.3 Summary . . . 169
4.8 Tunability and spectral coverage . . . 172
4.8.1 Wide tunability . . . 172
4.8.2 Spectral coverage . . . 177
4.9 Conclusion . . . 178

5 High-resolution spectroscopy of trioxane and ammonia 181
5.1 Introduction . . . 181
5.2 High-precision spectroscopy of trioxane . . . 182
5.2.1 Introduction . . . 182
5.2.2 Direct absorption spectrum of the ν_5 vibrational mode of trioxane 184
5.2.3 Saturated absorption spectroscopy in the ν_5 vibrational mode of trioxane . . . 185
5.2.4 Broadband saturated absorption spectra of trioxane . . . 190
5.2.5 Spectroscopic constants of trioxane . . . 198
5.2.6 Summary . . . 200
5.3 Hyperfine structure in ammonia . . . 200
5.3.1 Introduction . . . 200
5.3.2 The hyperfine structure in ammonia . . . 200
5.3.3 Saturated absorption spectroscopy of the ν_2 vibrational mode $asR(1,1)$ ammonia transition . . . 205
5.3.4 Hyperfine structure analysis and spectroscopic parameters . . . 205
5.3.5 Summary . . . 209

General conclusion and perspectives 210

A K+K counter 215

B Technical protocol for the sum frequency generation process 217
B.1 Creating a free space SFG signal . . . 217
B.2 Coupling SFG signal in a fiber . . . 217

C OsO_4-stabilized CO_2 laser **219**
C.1 Introduction 219
C.2 Operating principle 219
C.3 Performances 220

D Means and errors of the frequency measurement **223**

E List of line-center frequencies of methanol recorded by direct absorption spectra **225**

F Saturated absorption spectra of non-resolved K-doublets **231**

G Line-center frequencies and uncertainties of rovibrational lines of trioxane **235**

Introduction

Precision spectroscopic experiments on atoms can nowadays reach a fractional accuracy of a few part in 10^{18} level [1] have brought striking results: measurement of fundamental constants [2, 3] and their possible variation in time [4–9], clocks of highest accuracy [10, 11] or probes of general relativity and physics beyond the standard model [12].

Compared to atoms, molecules have a complex internal structure (i.e. rotational, and vibrational states) and strong intra-molecular fields, making their manipulation and control more complicated than for atoms. However, accurate spectroscopic studies of molecules give insight into many exciting advances in physical chemistry and fundamental physics, although the best spectroscopic precisions achieved with molecules is worse by more than three orders of magnitude than with atoms.

Accurate spectroscopic models are indeed required for improving our knowledge in atmospheric physics but also for environmental monitoring, and remote sensing greenhouse gases for example [13, 14]. More than 200 molecules have been detected in interstellar and circumstellar clouds, and they are excellent probes of the physical conditions and the history of their environments [15]. A better understanding of the spectra of those species would benefit astrophysics. In addition, molecular spectroscopy is being used in many applications including industrial monitoring, trace gas detection, and medical diagnosis.

Moreover, precise studies on molecules, whether it be neutral species or molecular ions, can play an important role to test fundamental physics, and in particular fundamental symmetries. Several groups are attempting to measure the electron's electric dipole moments (EDM), a signature of the violation of a combination of the time and parity symmetry, which is predicted to be very small but non-zero by theories beyond the Standard Model [16]. Diatomic and light radicals have already made a sizeable impact. For instance, recent experiment using heavy molecules (i.e. YbF [17], ThO [18] , HfH+ [19]) yield the best limits on the size of the EDM of the electron ($d_e| < 1.1 \times 10^{-29}$), outperforming the limit set by measurements on atoms. Molecular systems can also be used to test the parity symmetry, by measuring, for instance, parity violation (PV) signatures in the spectrum of chiral molecules [20–23]. Due to the parity violation inherent in the weak nuclear interaction, levels of the enantiomers of a chiral molecule are expected to have a tiny energy difference (see section 1.5 of this manuscript) and in turn their spectrum should exhibit small frequency differences. The latter may be however detectable by the most sensitive experiments.

Molecules are also being used to measure physical and fundamental constants. For instance, the Boltzmann constant k_B, that plays an important role in the recent redefinition of the Kelvin, has been precisely determined by molecular spectroscopic measurement.

This technique called Doppler broadening thermometry (DBT) consists in measuring accurately the Doppler-broadened absorption spectrum of a molecule to determine the Doppler width and extract k_B [24–26]. The first DBT experiment was performed at Laboratoire de Physique des Lasers on the NH_3 molecule probed with an ultra-stable CO_2 laser [27]. Precise measurements of the electron-to-proton mass ratio (m_e/m_p), a fundamental constant, is also currently being pursued by carrying out high-resolution spectroscopy of H_2, H_2+ and their isotopologue [28, 29, 29–32]. Such measurements also provide stringent tests of quantum electrodynamics and allow one to look for fifth forces or extra dimensions at the molecular scale. Precise molecular spectroscopy has also been and is currently being used to search for physics beyond the standard model by measuring possible variations of fundamental constants [33]. For instance, a fractional temporal variation of the proton-to-electron mass ratio of $(-3.8 \pm 5.6) \times 10^{-14} yr^{-1}$ was reported at LPL by comparing the frequency of a rovibrational transition of SF_6 molecule with the fundamental hyperfine transition in Cs over a two-year period [34]. Such variation can also be looked for by comparing precise spectroscopic measurements carried out in the laboratory to astronomical observation using several molecules (i.e. H_2, CH_3OH) [35,36].

All of these high-precision experiments on molecules described above are high-precision spectroscopic measurements and are often in the mid-infrared (mid-IR) spectral window, the so-called molecular fingerprint region which hosts many intense and narrow vibrational signatures of a considerable number of species. For this reason, ultra-stable, accurate and wide-tunable laser sources in this regions are highly desirable.

Available in the whole mid-IR region (3-25 μm), continuous wave quantum cascade lasers (QCLs) offer broad and continuous tuning over several hundred gigahertz at milliwatt to watt-level powers, but show substantial free-running frequency fluctuations. For the most precise frequency measurements considered here, it is thus required to address both the frequency stabilization of such sources as well as their traceability to a frequency standard [37–46].

As demonstrated in [40], this can be achieved by phase-locking to the secondary frequency standard of this spectral region, a CO_2 laser stabilized on a molecular saturated absorption line [47, 48]. Very few such standards are however available around 10 μm, and their stability and accuracy are a few orders of magnitude worse than the state-of-the-art performances offered by the optical clocks working in the visible domain (i.e., at a frequency of a few hundred of THz) and primary atomic standards working in the microwave domain (i.e., at a frequency of a few GHz)). These are available in national metrological institutes (NMI) where some of the most stable near-infrared (near-IR) references [49] are calibrated against some of the most accurate frequency standards, such as Cs fountain clocks, or optical atomic clocks. Using these as frequency references provides the state-of-the-art stabilities and accuracies, but those references have to be made available to remote user laboratories. This is achieved by using an optical fiber link that allows ultra-stable frequency references to be disseminated [50].

Moreover, optical frequency combs (OFCs) have proven to be essential for filling the gap between the near-IR and any region of the mid-IR region. First demonstrations of the transfer of the spectral purity of a remote near-IR frequency reference to a QCL have been recently reported by two collaborations one of them including Laboratoire de Physique des Lasers [45, 46].

My work in the field of optical frequency measurement and high-resolution spec-

troscopy is carried out in the Metrology, Molecules and Fundamental Test (MMTF) group at Laboratoire de Physique des Lasers (LPL). At LPL, several precise molecular spectroscopic setups have been developed for many applications such as tests of fundamental physics, molecular spectroscopic analysis, and metrology. Our group is currently developing a new molecular spectrometer using a buffer-gas-cooled molecular beam source, and ultra-stable and precise accurate mid-IR lasers. This setup will allow rovibrational transitions of molecules to be probed at the highest levels resolution and at ultimate accuracies using Ramsey interferometry. It will be used in the first place to measure parity-violating rovibrational frequency differences between enantiomers of a chiral molecule.

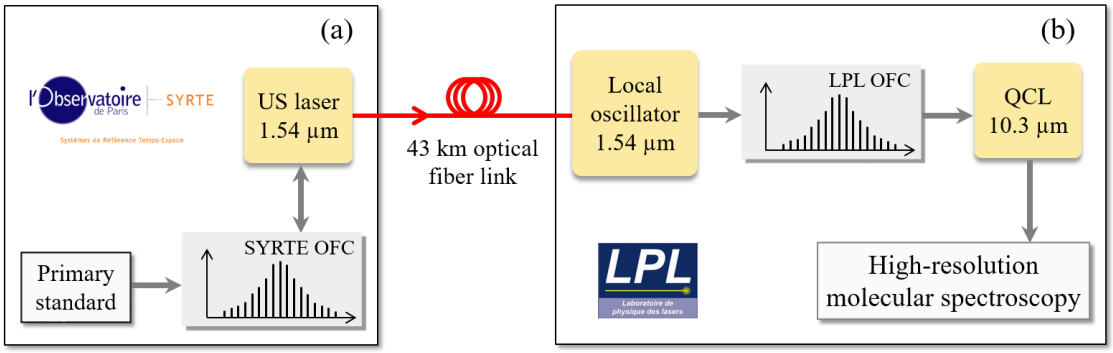

Figure 1 – Experimental setup. (a) The frequency of an ultra-stable (US) laser at 1.54 μm is monitored against primary frequency standard using an OFC at LNE-SYRTE. The signal of the laser is transferred from LNE-SYRTE to LPL via a 43 km-long fiber link with compensation of noise added by the link to the signal. (b) At LPL, a QCL at 10.3 μm is stabilized onto an OFC, that is locked onto an optical local oscillator at 1.54 μm itself referenced to the signal arriving from LNE-SYRTE. A spectrometer based on this stabilized QCL is developed to measure high resolution spectra of several polyatomic molecules. OFC: optical frequency comb and QCL: quantum cascade laser.

In the present manuscript, I report the development of a quantum cascade laser (QCL) based spectrometer that provides a unique combination of precision and tunability of any mid-IR spectrometer to date. Such a QCL-based spectrometer is crucial for our ongoing efforts to make the first observation of parity violation in chiral molecules, but opens also perspectives for many other precise spectroscopic measurements such as those listed above. An overview of the experimental setup and the work described in the manuscript is illustrated in Figure 1. In our experiments, we choose to use the best reference from LNE-SYRTE, the French NMI for time-frequency, for stabilizing mid-IR QCLs. This reference is generated by a 1.54 μm cavity-stabilized laser developed at LNE-SYRTE, the frequency of which is continuously monitored against primary frequency standards and potentially optical clocks in the future [45, 51]. This ultra-stable reference signal is transferred by a 43-km long noise-compensated optical fiber link from LNE-SYRTE to LPL without any degradation of its stability and accuracy. At LPL, we have build a high-precision mid-IR spectrometer based on a QCL at 10.3 μm that is phase-locked to the incoming reference by using an optical frequency comb at 1.55 μm.

My contribution to this work has mainly consisted and optimising the spectroscopic set-up of saturated absorption using a multipass cell, performing the precise spectroscopic measurements, including the stabilization of the comb and QCL, the fine alignment of the

QCL stabilization setup and analysing the data, including the test of different lineshape models.

This manuscript includes five chapters:

In chapter 1, we present the basics concepts underlying rovibrational molecular spectroscopy, list the tools needed for frequency control, high-resolution spectroscopy, and metrology, and discuss how to stabilize mid-IR lasers. Finally, we present the experimental setup under construction that will be dedicated to test the parity symmetry in cold chiral molecules using vibrational spectroscopy.

Chapter 2 describes the stabilization of an OFC at LPL onto the remote near-IR reference signal. To this end, we first present the accurate and ultra-stable reference signal at 1.54 μm developed at LNE-SYRTE from a cavity-stabilized laser. Then, we explain how this reference is distributed to LPL via a 43-km phase-noise-compensated optical fiber link. At LPL, a 1.54 μm stabilized tunable signal is generated by an optical local oscillator (OLO) locked to the remote near-IR reference and precisely tuned over 10 GHz using a home-built microwave oscillator. Finally, we report the stabilization of the comb to this OLO and the wide frequency tuning capabilities of the comb.

In chapter 3, we describe the stabilization of a QCL around 10 μm to the comb repetition rate, itself locked to the remote near-IR reference. This includes a description of a non-linear process between the QCL light and an additional comb output at 1.85 μm in an $AgGaSe_2$ crystal, a main component of the setup. Then we demonstrate the stabilization of the QCL frequency with a fractional frequency stability below 0.06 Hz (a relative value $< 2 \times 10^{-15}$). We also report the wide and continuous frequency tunability of the QCL obtained by scanning the OLO frequency, a crucial step greatly extending the flexibility of high-resolution spectroscopy and frequency metrology in the mid-IR region.

We present in chapter 4 the development of a saturated absorption spectroscopy setup based on the stabilized QCL and a multi-pass absorption cell. We then present metrological studies of rovibrational transitions of methanol, including measurement of line-center frequencies, pressure- and power-induced frequency shifts, broadenings at the sub-10-kHz level. Moreover, we were able to resolve subtle structures unresolved so far such as several so-called K-doublets in the methanol spectrum that result from the slight asymmetry of the molecules. The splittings observed are unusually large and reveal the existence of energy level crossings between the vibratrionally excited state probed and another underlying vibrational mode.

In chapter 5, we use the instrument to carry out precise spectroscopic measurements of a few other molecules, including trioxane and ammonia. We use the know-how gain in chapter 4 to determine uncertainties on the spectroscopic parameters.

At the end of the thesis, we give conclusions and perspectives.

CHAPTER 1

Spectroscopic studies with molecules: principle and applications

Contents

1.1 Molecular spectroscopy 5
1.1.1 Rovibrational spectrum 6
1.1.2 Linear absorption spectroscopy 8
1.1.3 Saturated absorption spectroscopy 9
1.2 Tools for frequency control, high resolution spectroscopy, and metrology 12
1.2.1 Frequency standards 12
1.2.2 Ultra-stable signal 17
1.2.3 The optical frequency comb 18
1.2.4 Optical frequency dissemination 21
1.3 Mid-infrared laser stabilization 23
1.3.1 The need for mid-infared laser stabilization 23
1.3.2 Methods for the frequency stabilization of mid-infrared lasers . 23
1.4 Previous precise molecular spectroscopic measurement at LPL 25
1.5 Parity violation observation 27
1.5.1 Parity violation in chiral molecules 28
1.5.2 Proposed experimental approaches of the parity violation observation in chiral molecules 29
1.5.3 Searching new chiral molecules 30
1.5.4 New experimental setup under development 31
1.6 Concluding remarks 33

1.1 Molecular spectroscopy

Molecular spectroscopy studies the interaction between molecules and light radiation in different spectral regions. Our aim is to develop an ultra-precise mid-IR spectrometer for molecular rovibrational frequency measurements. In this section, we review some basic knowledge about rovibrational spectra of molecules, direct absorption spectroscopy, and saturated absorption spectroscopy.

1.1.1 Rovibrational spectrum

A quantum mechanical treatment of molecules is often based on the Born-Oppenheimer approximation in which the vibrations of nuclei and the rotation of the molecule are treated separately from the motion of electrons. The Hamiltonian H of a molecule can be written as

$$H = H_e + H_{vib} + H_{rot} \tag{1.1}$$

in which H_e, H_{vib}, and H_{rot} correspond to the electronic, vibrational, and rotational contribution to the Hamiltonian. In the Born-Oppenheimer approximation, these terms can be considered independently. Electronic transitions are in the visible and ultraviolet region, rotational transitions are in microwave domain, and rovibrational transitions are in the near-IR and mid-IR regions. The main subject of the thesis is the development of a precise and high-resolution spectrometer in the mid-IR domain, we thus restrict our description to the rotation and the vibration.

In the frame of the rigid rotator model, the rotational energy levels of a diatomic molecule are given by the following equation [52]

$$F(J) = BJ(J+1), \tag{1.2}$$

in which J is the total rotational angular momentum on the molecular symmetry axis and B is the rotational constant, $B = h/(8\pi^2 Ic)$ with I the moment of inertia of the molecule, c the speed of light, and h the Planck constant. For pure rotational transition the selection rule is $\Delta J = \pm 1$. When it rotates, centrifugal forces make the molecule's bond length between two atoms to be stretched, leading to variation of the inertia moment. Therefore, the centrifugal effect must be taken into account by adding a centrifugal term to the rigid rotor model of Equation 1.2

$$F(J) = BJ(J+1) - DJ^2(J+1)^2, \tag{1.3}$$

in which D is the centrifugal distortion constant. $DJ^2(J+1)^2$ is the first term of the quartic expansion of centrifugal distortion.

For molecules composed of more than two atoms, the principal inertia moments I_a, I_b and I_c about the three molecular axes (a, b, and c) are different $I_c \geq I_b \geq I_a$, making rotational energy patterns of the molecules more complicated than for diatomic molecules. Symmetric top molecules, for instance, have two of their three principle moments of inertia equal. For the prolate rotor [1] with $I_c = I_b > I_a$, the rotational term is given by [52]

$$\begin{aligned} F(J,K) = {} & BJ(J+1) + (A-B)K^2 - D_J J^2(J+1)^2 \\ & - D_{JK} J(J+1)K^2 - D_K K^4 \end{aligned} \tag{1.4}$$

in which K is the quantum number associated with the projection of the total rotational angular momentum on the molecular symmetry axis, A and B are the rotational constants ($A = h/(8\pi^2 I_a c)$ and $B = h/(8\pi^2 I_b c)$), and D_J, D_{JK}, and D_K are the quartic centrifugal distortion constants. Methanol, the main molecule studied in this work, is an asymmetric top molecule. However, it can been modelled as a set of independent symmetric tops. Its energy level will be detailed in chapter 4.

1. For the oblate rotor, see Equation 5.13 in chapter 5.

Assuming that the vibrational motion of the diatomic molecule acts as a harmonic oscillator, the quantized vibrational energy levels can be determined by solving the Schrödinger equation with an harmonic potential and are given by [52]

$$G^{vib}(v) = h\nu_{vib}\left(v + \frac{1}{2}\right), \tag{1.5}$$

where ν_{vib} is the vibrational frequency, v is the vibrational quantum number, and h is the Planck constant. The selection rule for the most intense vibrational features is $\Delta v = \pm 1$ while overtone transitions with much lower intensities are obtained with $\Delta v = \pm 2$, 3, ...

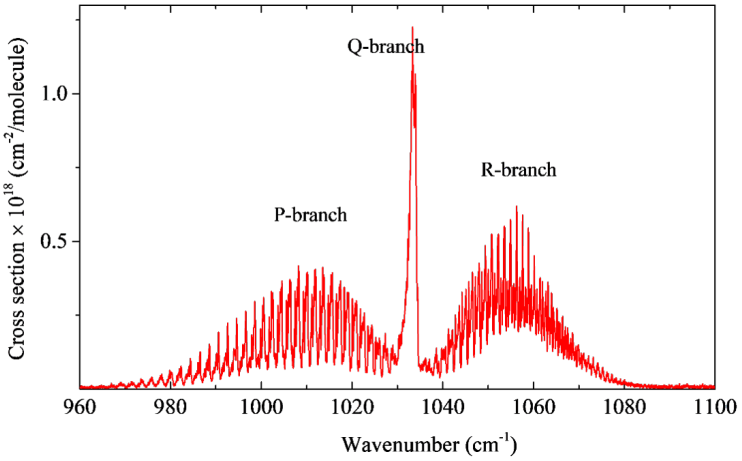

Figure 1.1 – Methanol absorption cross-section spectrum around 1030 cm^{-1} at a temperature of 273.1 K and gas pressure of 369.7 Torr. P, Q, and R branches correspond to rovibrational transitions with ΔJ = -1, 0, and 1, respectively. This spectrum is taken from [53, 54].

For a molecule both vibrationally and rotationally excited, energy of rovibrational levels is given by the sum of the rotational term $F_v^{vib}(J, K)$ and vibrational term $G^{vib}(v)$

$$E(J, K, v) = F_v^{vib}(J, K) + G^{vib}(v). \tag{1.6}$$

It is noted that the spectral constants in the rotational term depend on the vibrational states, as indicated by the subscript v on the term $F_v(J, K)$.

Frequencies of rovibrational transitions between the ground state $E(J", K", v = 0)$ and the first excited rovibrational state $E(J', K', v = 1)$ is given by

$$\nu(J", K") = \frac{E(J', K', 1) - E(J", K", 0)}{h}. \tag{1.7}$$

These transitions follow the selection rules $\Delta K = 0, \pm 1$ and $\Delta J = 0, \pm 1$. The spectrum of a molecule exhibits different kinds of transitions. The group of transitions with $\Delta J = -1$ creates the so-called P-branch while the transitions with $\Delta J = +1$ are responsible for the R-branch and of $\Delta J = 0$ transitions create the Q-branch. For instance, a spectrum around 1000 cm^{-1} of the C-O stretching vibrational mode of methanol is shown in Figure 1.1.

1.1.2 Linear absorption spectroscopy

1.1.2.1 Beer-Lambert's law

We now consider a molecular transition at an angular frequency ω_0. The intensity I of a laser beam, passing in the z-direction through an absorbing homogenous medium, decreases along the distance dz

$$dI = -k(\omega)I(\omega)dz = -n\sigma(\omega)I(\omega)dz, \tag{1.8}$$

where $k(\omega)$ denotes the absorption coefficient, $\sigma(\omega)$ represents the absorption cross-section, n is the molecular density of the species, and $I(\omega)$ is the laser transmitted intensity. Integrating Equation 1.8 gives an exponential reduction of the intensity with an absorption path-length L, known as Beer-Lambert's law

$$I(\omega) = I_0 \exp\left[-k(\omega)L\right] = I_0 \exp\left[-\alpha(\omega)\right], \tag{1.9}$$

in which I_0 represents the incident intensity and $\alpha(\omega)$ is the absorbance. For an ideal gas, the absorbance $\alpha(\nu)$ can be expressed as

$$\alpha(\omega) = nLS_0\phi(\omega - \omega_0) = \frac{P}{k_B T}LS_0\phi(\omega - \omega_0), \tag{1.10}$$

where S_0 denotes the line strength of the transition at ω_0, P refers to the gas pressure, k_B is the Boltzmann constant, T represents the temperature of the molecular sample, and $\phi(\omega - \omega_0)$ is the line shape profile. It is noted that all profiles presented in this thesis are normalized in such a way that their integral equals unity.

1.1.2.2 Line shape and linewidth

The absorption spectrum of molecules in the gas phase is typically broadened due to various mechanisms including homogeneous mechanisms (e.g. natural lifetime, collisions between molecules, and saturation power effect) and inhomogeneous mechanism (Doppler effect). In the case of linear absorption spectroscopy, resolution is limited by two major mechanisms: Doppler broadening related to the motion of molecules and pressure broadening associated to the collision-induced interruption of the coherent interaction of molecules with the laser, leading to the perturbation of population and transition dipole relaxation, and transition dipole dephasing. Contributions of natural lifetime and saturation power effect to the broadening are negligible in Doppler-limited spectrum (see next subsection for their descriptions). The Voigt profile, a convolution of a Gaussian profile modelling the Doppler broadening and a Lorentz profile modelling the pressure broadening, is typically used to model the direct absorption signal. The normalized Voigt line shape is given by

$$\Phi_V(\omega - \omega_0, \Delta\omega_D, \gamma_L) = \frac{\sqrt{\ln 2}}{\Delta\omega_D}\sqrt{\pi}\frac{a}{\pi}\int_{-\infty}^{\infty}\frac{e^{-y^2}}{(x-y)^2 + a^2}dy \tag{1.11}$$

with

$$a = \sqrt{2}\frac{\gamma_L}{\Delta\omega_D}, \tag{1.12}$$

$$x = \sqrt{\ln 2}\frac{\omega - \omega_0}{\Delta\omega_D}. \tag{1.13}$$

where $\Delta\omega_D$ and γ_L are the half-width-at-half-maximum (HWHM) linewidths of the Gaussian and Lorentz profiles respectively (see below). The HWHM linewidth of the Voigt profile is approximately given by the following equation [55]

$$\gamma_V = 1.0692\gamma_L + \sqrt{0.8664\gamma_L^2 + \Delta\omega_D^2}. \tag{1.14}$$

At low pressure where the collisions-induced broadening is not significant, the resolution of a direct absorption spectrum is mainly limited by the Doppler effect. The spectral line shape is thus given by a Gaussian profile that can be obtained by considering the Maxwell velocity distribution of molecules. The Gaussian profile is written as

$$\Phi_D(\omega - \omega_0, \Delta\omega_D) = \sqrt{\frac{2}{\pi}}\frac{1}{\Delta\omega_D}e^{-\ln 2\left(\frac{\omega-\omega_0}{\Delta\omega_D}\right)^2}, \tag{1.15}$$

where $\omega_0/2\pi$ is the central frequency of the resonance and $\Delta\omega_D$ is the Doppler HWHM width, given by

$$\Delta\omega_D = \frac{\omega_0}{c}\sqrt{\frac{2k_BT\ln 2}{m}} = \frac{\sqrt{\ln 2}}{c}\omega_0 u, \tag{1.16}$$

where m is the mass and $u = (2k_BT/m)^{1/2}$ is the most probable velocity of the molecule under investigation.

At high pressure, the rovibrational molecular transition is mainly broaden by molecular collisions that usually produces a Lorentz line shape profile

$$\Phi_L(\omega - \omega_0, \gamma_L) = \frac{1}{\pi}\frac{\gamma_L}{(\omega - \omega_0)^2 + \gamma_L^2}, \tag{1.17}$$

in which γ_L represents the HWHM pressure broadening and is given by

$$\gamma_L = B_p \times p, \tag{1.18}$$

where P represents the gas pressure and B_p is the pressure-broadening coefficient that can be experimentally determined by measuring the spectral linewidth at different pressures.

1.1.3 Saturated absorption spectroscopy

As written above, the resolution of the direct absorption spectroscopy at low pressure is mainly limited by the Doppler broadening. Various spectroscopic techniques can be implemented for increasing the resolution. Nonlinear spectroscopy techniques such as saturated absorption spectroscopy and two-photon spectroscopy allow one to remove the Doppler inhomogeneous spectral broadening and to reach spectral line widths few orders of magnitude narrower than the Doppler broadening. We now briefly present the principle of saturated absorption spectroscopy and also the broadening mechanisms contributing to its spectral linewidth.

1.1.3.1 Principle of saturated absorption spectroscopy

In a typical experimental setup of saturated absorption (or sub-Doppler) spectroscopy shown is Figure 1.2(a), a laser beam is split into pump and probe beams using a beam

splitter. These beams propagate through a gas-phase molecular sample in opposite direction. The saturated absorption signal is detected in the probe beam absorption signal.

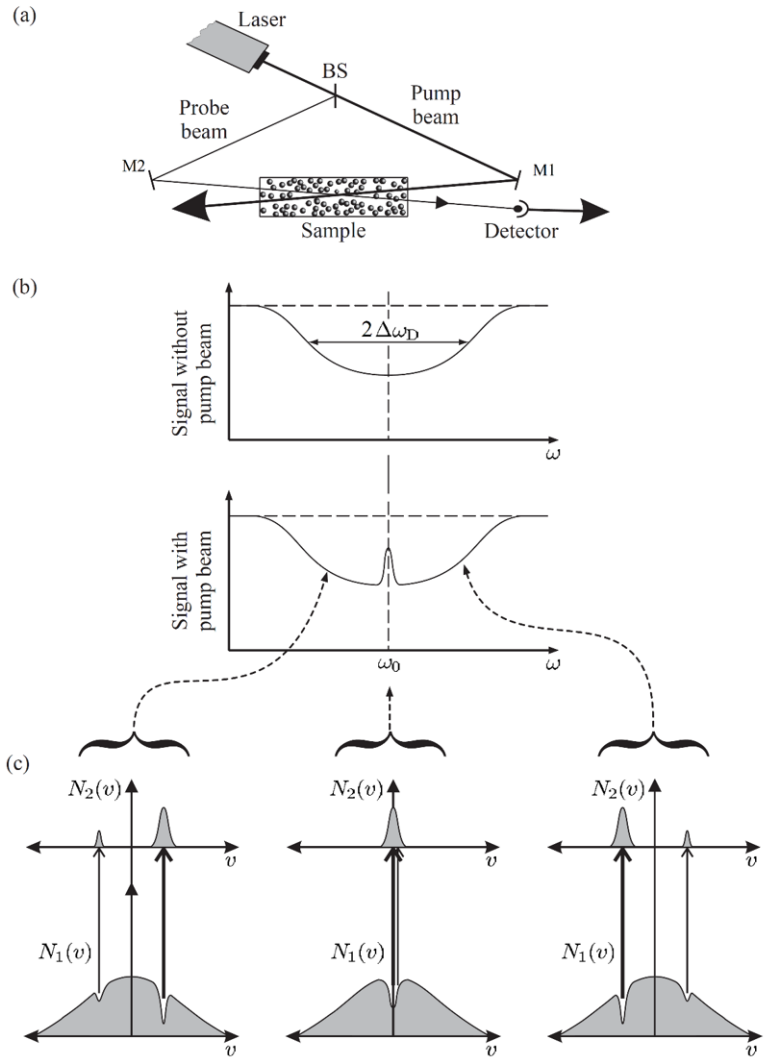

Figure 1.2 – (a) Experimental setup of the saturated absorption spectroscopy. M1 and M2: mirrors, BS: beam splitter. (b) Transmitted intensity of the probe beam as a function of the angular frequency ω. When the pump beam is blocked, the absorption spectrum at low pressure (top) has a Doppler-broadening linewidth at FWHM, $\Delta\omega_D$. Otherwise, a narrow peak appears at the center of the direct absorption spectrum (bottom). (c) Plots of the molecular population densities of the two levels $N_1(\nu)$ and $N_2(\nu)$ as a function of velocity v in three cases: laser frequency below, equal to, and above the resonant frequency. Taken from [56].

Due to the Doppler effect, the laser angular frequency ω_L in the laboratory frame is different from the angular frequency ω_{mov} seen in the particle frame moving at velocity $\vec{v}$. The relationship between these frequencies is given by

$$\omega_{mov} = \omega_L - \vec{k} \cdot \vec{v}, \tag{1.19}$$

where $\vec{k}$ denotes the light wave vector. We consider the case when pump beam propagates along the $+z$ axis and probe beam in the opposite direction. Molecules which have a velocity component v_z along the z axis will be resonant only when the laser frequency is closely tuned to

$$\omega_{pump} = \omega_0 + kv_z \tag{1.20}$$

for the pump beam and

$$\omega_{probe} = \omega_0 - kv_z \tag{1.21}$$

for the probe beam, where ω_0 is the molecular absorption angular frequency. When the pump beam is blocked, a direct absorption signal at low pressure with a Gaussian profile is obtained on the detector, as shown on the top of Figure 1.2(b). Under the effects of the pump-probe configuration, the population densities of the ground and excited states $N_1(\nu)$ and $N_2(\nu)$ will be changed depending on the velocity. Figure 1.2(c) shows the effects for three different laser frequencies: below, equal and above the resonant frequency. When the laser frequency is different from ω_0, the pump beam interacts with a group of molecules with a velocity of v_z while the probe beam interacts with a velocity of $-v_z$. Therefore, the pump beam interaction does not affect the probe beam interaction. When the laser frequency is exactly tuned to ω_0, both the pump and probe beams interact with the same group of molecules with $v_z \sim 0$. The depletion of the molecular density in the ground state due to the pump beam leads to a reduced absorption of the probe beam at the center ω_0 of the direct absorption profile (a sub-Doppler dip), as shown in the bottom of Figure 1.2(b).

1.1.3.2 Line width and line shape

We now consider the main broadening mechanisms of saturated absorption spectroscopy.

The first mechanism is the natural broadening related to the finite lifetimes of rovibrational energy levels. The estimated spectral profile is usually a Lorentzian profile. For a transition between lower and upper levels i and j, the natural linewidth (HWHM) γ_{nat} is equal to A_{ij} the Einstein-A coefficient of this transition [55].

The second mechanism is the transit-time [1] broadening caused by the finite transit time of the molecule through the laser beam. The line shape of the transition is complex [58]. The transit time HWHM width [2] is given by [58]

$$\gamma_t \simeq 2\pi \frac{u}{8w_0}, \tag{1.22}$$

where w_0 is the waist of the laser beam and u is the most probable velocity.

The third mechanism is the pressure broadening due to collisions between molecules that is given by Equation 1.18, as mentioned above. Its line shape is a Lorentzian. A typical value of B_p is around 100 kHz/Pa. Increasing the gas pressure not only leads to spectral broadening but also shifts the center frequencies of the molecular transitions, around 1 kHz/Pa. Note that the saturated absorption line shape will be more complicated than a Lorentzian when transit time is not negligible compared to the collisional broadening.

1. This contribution does not have to be taken into account in linear absorption spectroscopy of an isotropic medium such as a gas cell because it is already included in the Doppler broadening [57].
2. There is another expression of transit time $\gamma_t = 0.58u/w_0$ [59].

Finally, power broadening and shift become significant when the laser intensity exceeds a saturation intensity I_{sat}. Value of I_{sat} is typically deduced by observing variations of spectral line shape and line-center frequency of molecular transitions. Following V.S. Letokhov [59], when the absorption is saturated by a standing wave (pump and probe beams having the same power) the line shape can be modelled with a Lorentzian of power-broadened linewidth given by

$$\gamma = \gamma_0 \sqrt{1 + \frac{I}{I_{sat}}}, \tag{1.23}$$

in which I refers to the intensity of the pump and probe beams and γ_0 is the homogeneous FWHM linewidth of the transition combining all contributions including natural broadening, transit time, and collision broadening. In the case of a weak-probe beam, the power-broadened linewdith is given by

$$\gamma = \frac{\gamma_0}{2}\left(1 + \sqrt{1 + \frac{I}{I_{sat}}}\right). \tag{1.24}$$

Moreover, in the case of frequency modulation spectroscopy, allowing signal-to-noise ratio of saturated absorption spectrum to be improved, the spectral linewidth can be broadened by the frequency modulation excursion. In addition, the spectral line shape might be distorted due to the modulation and is likely to deviate from the Lorentzian profile. That will be described in chapters 4 and 5.

1.2 Tools for frequency control, high resolution spectroscopy, and metrology

In this section, we briefly introduce frequency standards, including principle of a basic standard, concepts of accuracy, frequency noise and frequency stability, primary and secondary frequency standards, and optical clocks. Then, we present important tools for high-precision spectroscopic measurements and metrology applications, such as optical frequency comb and their applications, how an ultra-stable signal is generated and dissemination of this signal between distant laboratories.

1.2.1 Frequency standards

1.2.1.1 What is a frequency standard?

A frequency standard is an accurate oscillator whose output signal is referenced to the SI definition of the frequency unit or to an oscillator itself referenced to the SI unit. Many frequency standards have been developed with various realizations varying from the radio-frequency and microwave to the optical frequency domain.

A standard is typically based on an oscillating source emitting at microwave or optical frequency which is locked to an atomic or molecular transition. Figure 1.3 illustrates the basic principle of a standard consisting of an atomic or molecular clock. The oscillator output passes through a cell containing an atomic/molecular sample and probes an atomic/molecular transition of frequency ν_0. Usually the sample excited fraction is quantified as a function of the oscillator frequency ν. An anti-symmetric error signal $S(\nu)$ can be derived from this to generate a correction signal acting on the oscillator to

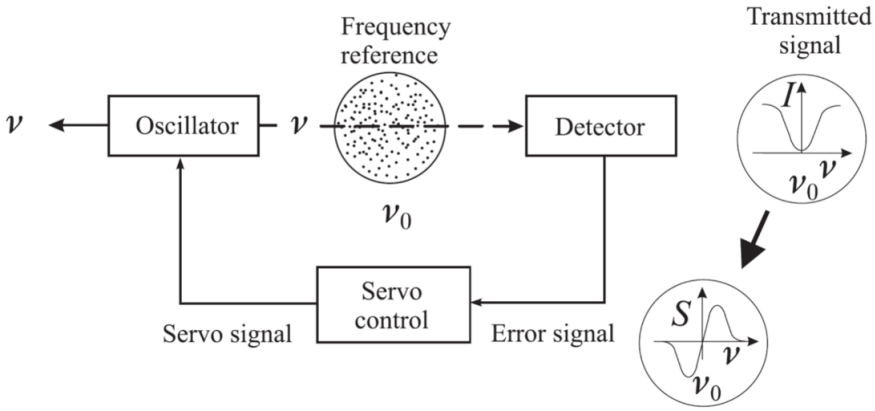

Figure 1.3 – Principle of an atomic/molecular clock. Taken from [60].

keep the frequency ν of the oscillator as close as possible to the frequency ν_0. When the servo loop is closed, this device can be used as a frequency standard provided that the atomic/molecular response is adequately known and stable.

1.2.1.2 Stability and accuracy of an oscillating source

Phase/frequency instability

Oscillators are usually found to be unstable in frequency. This can be described as a phase noise $\phi(t)$,

$$V(t) = V_0 \cos\left[2\pi\nu_0 t + \phi(t)\right]. \tag{1.25}$$

The instantaneous frequency of $V(t)$ is given as

$$\nu(t) = \frac{1}{2\pi}\frac{d}{dt}(2\pi\nu_0 t + \phi(t)) = \nu_0 + \frac{1}{2\pi}\dot{\phi}(t). \tag{1.26}$$

The frequency noise is defined as

$$\Delta\nu(t) = \nu(t) - \nu_0 = \frac{1}{2\pi}\dot{\phi}(t). \tag{1.27}$$

The fractional frequency fluctuation $y(t)$ of the oscillators (i.e. the instantaneous frequency fluctuation normalized to the carrier frequency ν_0) is defined as

$$y(t) = \frac{\Delta\nu(t)}{\nu_0} = \frac{\dot{\phi}(t)}{2\pi\nu_0} = \frac{dx(t)}{dt}. \tag{1.28}$$

in which $x(t) = \phi(t)/2\pi\nu_0$ is the phase-time fluctuation (i.e. the random phase fluctuation $\phi(t)$ converted into time).

In order to characterize the frequency fluctuation (instability) of an oscillator, there are two kinds of parameters meeting requirements for different applications: (i) spectral parameters related to the spread of signal energy in the Fourier frequency spectrum (i.e. phase noise power spectrum density (PSD), frequency noise PSD,...) and (ii) time parameters (i.e. Allan variance, modified Allan variance,...) allowing assessment of the stability over a given averaging time [61].

Phase/frequency noise power spectrum density

In the Fourier frequency domain, the phase-time fluctuation $x(t)$ is frequently characterized by the one-sided PSD of the phase-time fluctuation $S_x(f)$, defined only for $f > 0$. It is formally defined as the Fourier transform of the autocorrelation function $R_x(\tau)$ of $x(t)$ [62]

$$S_x(f) = 2\int_{-\infty}^{\infty} R_x(\tau)\exp[-2\pi i f\tau]d\tau \tag{1.29}$$

and

$$R_x(\tau) = \lim_{T\to\infty}\frac{1}{T}\int_{-T/2}^{T/2} x(t)x(t+\tau)dt. \tag{1.30}$$

where f is the Fourier frequency. The one-sided PSD is equal to two times the two-sided PSD when $f > 0$ and 0 when $f < 0$. The physical dimensions of $S_x(f)$ is s^2/Hz. Three quantities are commonly also used to analyze the phase/frequency noise, the PSD phase noise $S_\phi(f)$, the frequency noise PSD $S_{\Delta\nu}(f)$, and the normalized frequency noise $S_y(f)$, given by [62]

$$S_\phi(f) = (2\pi\nu_0)^2 S_x(f), \tag{1.31}$$

$$S_{\Delta\nu}(f) = f^2 S_\phi(f), \tag{1.32}$$

and

$$S_y(f) = \frac{f^2}{\nu_0^2}S_\phi(f). \tag{1.33}$$

The physical dimensions of $S_\phi(f)$, $S_{\Delta\nu}(f)$, and $S_y(f)$ are rad^2/Hz, Hz^2/Hz and Hz^{-1}, respectively.

The normalized frequency noise PSD $S_y(f)$ is usually modelled as a superposition of independent noise processes obeying power laws of α, with α an integer,

$$S_y(f) = \sum h_\alpha f^\alpha. \tag{1.34}$$

Most models include only five terms with $-2 \le \alpha \le 2$, denoted as random walk ($\alpha = +2$), Flicker ($\alpha = +1$), and white frequency noise ($\alpha = 0$), and Flicker ($\alpha = -1$) and white ($\alpha = -2$) phase noise (see below).

Frequency stability: Allan variance

The frequency instability of an oscillator in the time domain is assessed by a stream of sampled values $\bar{\nu}_i(t)$ of the frequency $\nu(t)$ that is measured by a frequency counter. Each sampled value $\bar{\nu}_i$ is obtained over a gate time (averaging time) τ_0 of the counter. It is converted into the sampled fractional frequency $\bar{y}_i = \dfrac{\bar{\nu}_i - \nu_0}{\nu_0}$. There are several tools for characterizing the frequency stability of an oscillator including the original Allan variance, the overlapping Allan variance, and the modified Allan variance.

The original non-overlapping or two-sample Allan variance is the standard time domain measure of frequency stability and is defined as [63]

$$\sigma_y^2(\tau) = \frac{1}{2(M-1)}\sum_{i=1}^{M-1}[\bar{y}_{i+1}(\tau) - \bar{y}_i(\tau)]^2, \tag{1.35}$$

where $\bar{y}_i(\tau)$ is the i^{th} of M (non-overlapped) fractional frequency values that are averaged

over the time τ, where $\tau = m\tau_0$ with m an integer.

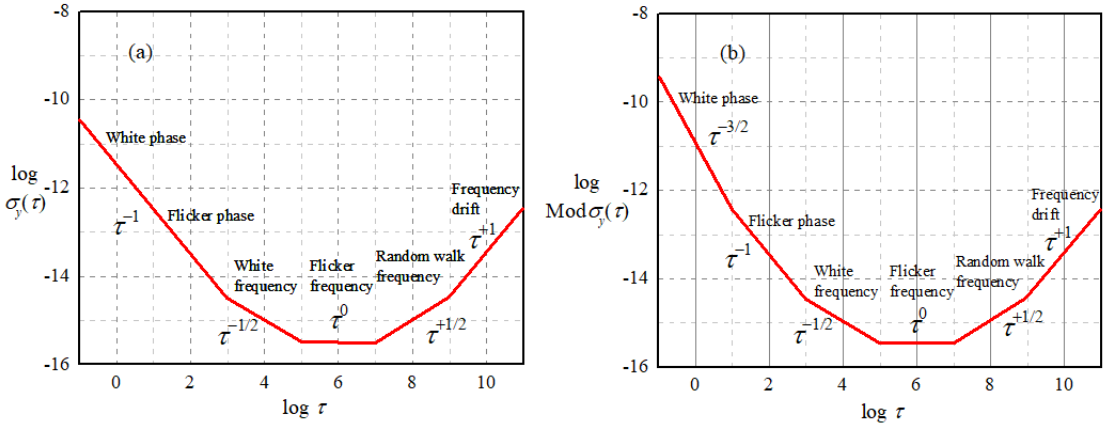

Figure 1.4 – Different types of an oscillator's noise with (a) the overlapping Allan deviation and (b) the modified Allan deviation. The latter allows to discriminate the white phase noise $\tau^{-3/2}$ and the Flicker phase noise τ^{-1}. Adapted from [63].

In order to improve the confidence interval of the Allan variance and increase the period of analysis, the overlapping Allan variance with samples $\bar{y}_{i+1}(\tau)$ and $\bar{y}_i(\tau)$ partially overlapping is typically used. This type of Allan variance is the most common measure of frequency stability. It is written as [63]

$$\sigma_y^2(\tau) = \frac{1}{2m^2(N-2m+1)} \sum_{j=1}^{N-2m+1} \left[\sum_{i=j}^{j+m-1} [\bar{y}_{i+m} - \bar{y}_i]^2 \right], \tag{1.36}$$

where $\tau = m\tau_0$ is the averaging time with m the averaging factor, τ_0 the gate time, and N the number of sampled frequency $\bar{y}_i$ (over the gate time τ_0). The square root of $\sigma_y^2(\tau)$ is the Allan deviation (ADEV) $\sigma_y(\tau)$.

The temporal variation of $\sigma_y(\tau)$ depends on the noise affecting the oscillator. As shown in Figure 1.4(a), the Allan deviation (ADEV) varies as τ^n with a slope n (in log-log scale) typical of each noise. However, it has the same temporal dependence of τ^{-1} for white phase noise and Flicker phase noise. In order to distinguish these noises, one can use the modified Allan variance that is defined as [63]

$$\text{Mod}\sigma_y^2(\tau) = \frac{1}{2m^4(M-3m+2)} \sum_{k=1}^{M-3m+2} \left(\sum_{j=1}^{M-2m+1} \left[\sum_{i=j}^{j+m-1} [\bar{y}_{i+m}(\tau) - \bar{y}_i(\tau)]^2 \right] \right). \tag{1.37}$$

The modified Allan deviation (MDEV) Mod$\sigma_y(\tau)$ is given by the square root of Mod$\sigma_y^2(\tau)$. As shown in Figure 1.4(b), the modified Allan deviation exhibits a $\tau^{-3/2}$ dependence for white phase noise and a τ^{-1} dependence for Flicker phase noise.

Accuracy versus stability

Accuracy is defined as the degree of conformity of a measured or calculated value to its definition [60]. In the time and frequency community, accuracy refers to the time offset or frequency offset of a device. Frequency offset is the difference between a measured frequency and a nominal frequency with zero uncertainty.

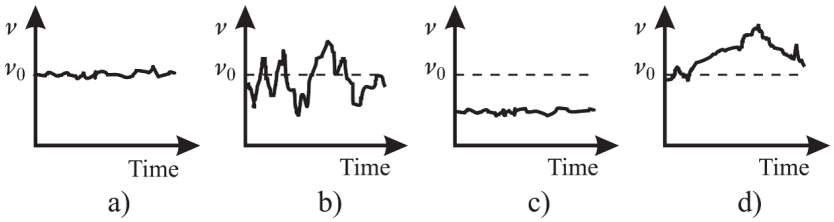

Figure 1.5 – Frequency of an oscillator is (a) accurate and stable, (b) accurate but not stable, (c) stable but not accurate, and (d) not accurate and not stable. Taken from [60].

Accuracy and stability are two distinct qualities of an oscillator that can resonate at a wrong frequency but still be stable or work on the nominal frequency but be unstable. The difference between accuracy and stability is illustrated in Figure 1.5.

Repeatability and reproducibility

There are two other concepts that have been used not only for charactering the quantity of a frequency standard but also for statistical analysis in metrological field: repeatability and reproducibility. The repeatability is expressed by the interval containing the spread of measured values when the experiments is repeated a number of times. Reproducibility can be understood as the spread of values of a replicated experiment that is done by different operators in different locations but using a close copy of all the relevant parts [62].

1.2.1.3 The primary frequency standard: microwave atomic fountain clocks

The present definition of the second unit is based on the $F = 3 \rightarrow F = 4$ hyperfine transition of the cesium ^{133}Cs atom in the electronic ground state at a temperature of 0 K which has been fixed to 9 192 631 770 Hz. The second is the duration of 9 192 631 770 periods of the radiation corresponding to the transition. An oscillator realizing the *mise en pratique* of this definition is a primary frequency standard. The best *mise en pratique* of this unit is performed with Cs fountain clocks. The first fountain clock was developed at Observatoire de Paris and its design became a standard for almost all subsequently constructed fountain clocks [64].

In a Cs fountain clock, the atoms are first cooled in a magneto-optic trap (MOT) and/or an optical molasses. They are then launched vertically and pass through an interrogating zone where the atoms interact with an ultra-stable microwave signal, for example generated by a reference source combined from an H-maser and a cryogenic sapphire oscillator (CSO) [65]. They then start a phase of free evolution, flying up and down, like in a fountain, before crossing the interrogation zone a second time to realise a Ramsey interferometer. They finally cross a detection zone where the atomic population is detected via the fluorescence light of the atoms. This signal depends on the microwave frequency and leads to a fringe pattern as a function of the microwave detuning with the central fringe corresponding to the atomic transition. The microwave signal is locked onto the atomic transition. This signal is very stable and accurate. The best stabilities obtained for the Cs fountain clocks are of about $2 \times 10^{-14}\ \tau^{-1/2}$ with τ the integration time and the best accuracies are of the order of 10^{-16} [66]. Besides, frequency standards based on rubidium (Rb) fountains have been developed [67–69] with performances similar

to those based on Cs atoms. These atomic fountain frequency standards are complicated and require a large as well as thermally/mechanically well controlled environment. They are thus developed only in metrological institutes.

In addition, commercial Cs atomic clocks exist. However, performances of these standards are not as good as the modern atomic fountain clocks. They generate reference signals with stabilities of the order of 10^{-11} and relative accuracies of 10^{-12} [60].

1.2.1.4 Secondary frequency standard

As mentioned above, primary frequency standards provide the best accurate reference signals, however not all laboratories can access these signals. A variety of atomic and molecular absorption lines has been recommended as secondary references by BIPM (Bureau International des Poids et Measures) [70], as for instance C_2H_2 at 1.54 μm, CH_4 at 3.39 μm, and OsO_4 at 10.3 μm in the infrared spectral region. One can obtain a secondary frequency standard by locking the frequency of a continuous-wave laser to an absorption resonance of one of these secondary references. Absolute frequencies of secondary standards have been calibrated against the primary standard first using optical frequency chains and more recently using optical frequency combs, allowing performances of the secondary standards to be evaluated [71–75]. The relative uncertainty of their absolute frequencies is in the range from 10^{-10} to a few 10^{-16}.

1.2.1.5 Optical clocks

Let us consider optical clocks based on optical transitions of cold ions/atoms. In an optical clock (see Refs. [76,77] for instance), an optical transition, either of an ion stored in an ion trap or of a large number of atoms stored in an optical lattice, is first detected by ultra-high precision spectroscopy. The frequency of the narrow-linewidth laser, used for carrying out spectroscopy, is then stabilized to the line-centre of this transition via a servo loop.

These clocks have a great potential for measuring time and frequency beyond the performances of the state-of-the-art primary standards with the best accuracy. The best estimated uncertainties of optical clocks have been reported in the 10^{-18} level, for example a $^{171}Yb^+$ single ion clock [77] or a ^{87}Sr optical lattice clock [10,78,79]. A number of frequency measurements for direct comparisons between optical clocks and Cs fountain primary frequency standards using optical frequency combs (see subsection 1.2.3) have been demonstrated with uncertainties fully limited by the microwave clock. Moreover, an increasing number of optical frequency ratios between optical clocks has been measured with much smaller uncertainties than when microwave clocks are involved, for example $^{40}Ca^+/^{87}Sr$ [80], $^{27}Yb^+(E3)/^{171}Yb^+(E2)$ [5], $^{199}Hg/^{87}Sr$ [81,82], and $^{171}Yb/^{87}Sr$ [11,83].

These optical clocks have better performances than Cs fountain clocks so that a new definition of the SI second based on them could be considered in the future.

1.2.2 Ultra-stable signal

Ultra-stable lasers are the core not only of optical clocks but also of the ultra-high precision spectroscopic measurements. The world's best ultra-stable signals are now generated by near-IR lasers locked to ultra-stable high-finesse cavities (see subsection 1.3.2). Their stability can reach levels below 10^{-16} at averaging times between 1 and 100 s [49, 84, 85]. However, these cavity-stabilized lasers lack precise knowledge of their ab-

solute frequency. Therefore their absolute frequency is typically measured or controlled to frequency standards (primary frequency standards and optical clocks) via optical frequency combs to provide reference signals that have both ultra-low noise and an excellent uncertainty on their absolute frequency (see subsection 2.2.3).

1.2.3 The optical frequency comb

1.2.3.1 Principle of optical frequency combs

Optical frequency combs (OFCs) have resulted in significant advances in optical frequency metrology and found wide applications in precise physical measurements and molecular finger printing [1, 86–88]. The development of the optical frequency comb technique ultimately led to the Nobel Prize in Physics for John L. Hall and Theodor W. Hänsch in 2005.

In the time-domain, short optical pulses are generated by a mode-locked laser. The pulses are separated by a time

$$\tau = \frac{L}{v_g}, \tag{1.38}$$

where L denotes the cavity length and v_g refers to the group velocity of the pulse's envelop (see Figure 1.6). The inverse of τ is called the repetition rate $f_{rep} = 1/\tau$. The dispersion in the cavity due to the wavelength dependence of the refractive index makes the phase and group velocity not equal. This results in a phase shift $\Delta\varphi$ of the carrier oscillation with respect to the pulse envelope after a round-trip inside the cavity, as shown in Figure 1.6. This pulse-to-pulse phase shift is given by

$$\Delta\varphi = (\frac{1}{v_g} - \frac{1}{v_p})L\omega_c, \tag{1.39}$$

in which v_p denotes the intra-cavity phase velocity and ω_c represents the carrier frequency.

In the frequency-domain, the spectrum of the OFC consists of a comb of frequencies whose spacing is determined by f_{rep}. It is easily obtained by using the Fourier transform of a series of pulses over time. The electric field of the train of pulses is written as [89]

$$E(t) = \sum_p A(t - p\tau)e^{i(\omega_c(t-p\tau)+p\Delta\varphi+\phi_0)}, \tag{1.40}$$

where p is an integer, $A(t)$ is the envelop and ϕ_0 refers to an overall phase offset. The Fourier transform of $E(t)$ is given by

$$\begin{aligned}
\tilde{E}(\omega) &= \int \sum_p A(t - p\tau)e^{i[\omega_c t - p(\omega_c\tau - \Delta\varphi)+\phi_0]}e^{-i\omega t}dt \\
&= \sum_p e^{i[p(\Delta\varphi - \omega_c\tau)+\phi_0]} \int A(t - p\tau)e^{-i(\omega-\omega_c)t}dt \\
&= \sum_p e^{i[p(\Delta\varphi - \omega_c\tau)+\phi_0]} \int A(u)e^{-i(\omega-\omega_c)(u+p\tau)}du \\
&= e^{i\phi_0} \sum_p e^{ip(\Delta\varphi - \omega\tau)} \tilde{A}(\omega - \omega_c)
\end{aligned} \tag{1.41}$$

where $\tilde{A}(\omega - \omega_c)$ is the Fourier transform of the envelop. The significant components in the spectrum are those for which the exponentials in the sum add coherently such that

the phase shift between the p and $p+1$ exponential is a multiple of 2π, equivalently

$$\omega\tau - \Delta\varphi = 2m\pi \tag{1.42}$$

with m an integer. This yields the comb spectrum of the laser and the m^{th} comb mode frequency is given by

$$\nu_m = \frac{\omega}{2\pi} = m f_{rep} + \frac{f_{rep}\Delta\varphi}{2\pi}. \tag{1.43}$$

We see that each comb mode is offset by a frequency $f_{ceo} = \frac{f_{rep}\Delta\varphi}{2\pi}$, known as the carrier envelop offset frequency of the comb. Figure 1.6(b) schematically shows the comb spectrum of the mode-locked laser with frequencies

$$\nu_m = m\, f_{rep} + f_{ceo}. \tag{1.44}$$

In our experiment, we have used an Erbium doped fiber OFC from MenloSystems (FC 1500) whose repetition rate is about 250 MHz. A detailed explanation of its structure and operational principle will be presented in section 2.6.

Following Equation 1.44, we see that each optical comb mode depends only on two radio frequencies: f_{rep} and f_{ceo}. Controlling these frequencies enables us to control all the comb mode frequencies in the optical domain. An OFC can thus be employed as a bridge between the radio-frequency and optical domains as well as between different optical domains (see below).

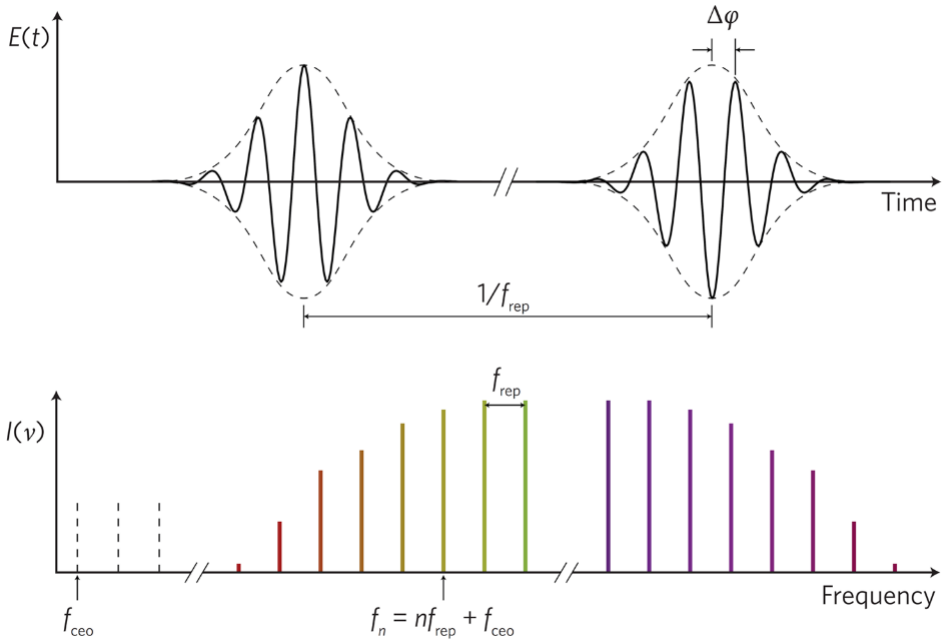

Figure 1.6 – The time-domain representation (top) of an optical frequency comb together with the frequency-domain representation (bottom). In the time-domain, the relative phase difference between the carrier (blue line) and the envelop (red line) changes by $\Delta\varphi$ from pulse to pulse. In the frequency-domain, the comb mode frequencies are separated by the repetition rate, f_{rep} and have a envelop-carrier offset frequency $f_{ceo} = f_{rep}\Delta\varphi/2\pi$. Taken from [89].

1.2.3.2 Applications of the optical frequency comb

We now describe in this section several applications of the OFCs. As shown in Figure 1.7, OFCs have been widely used in metrological applications [86]. We detail here a few of them related to the work presented in this thesis.

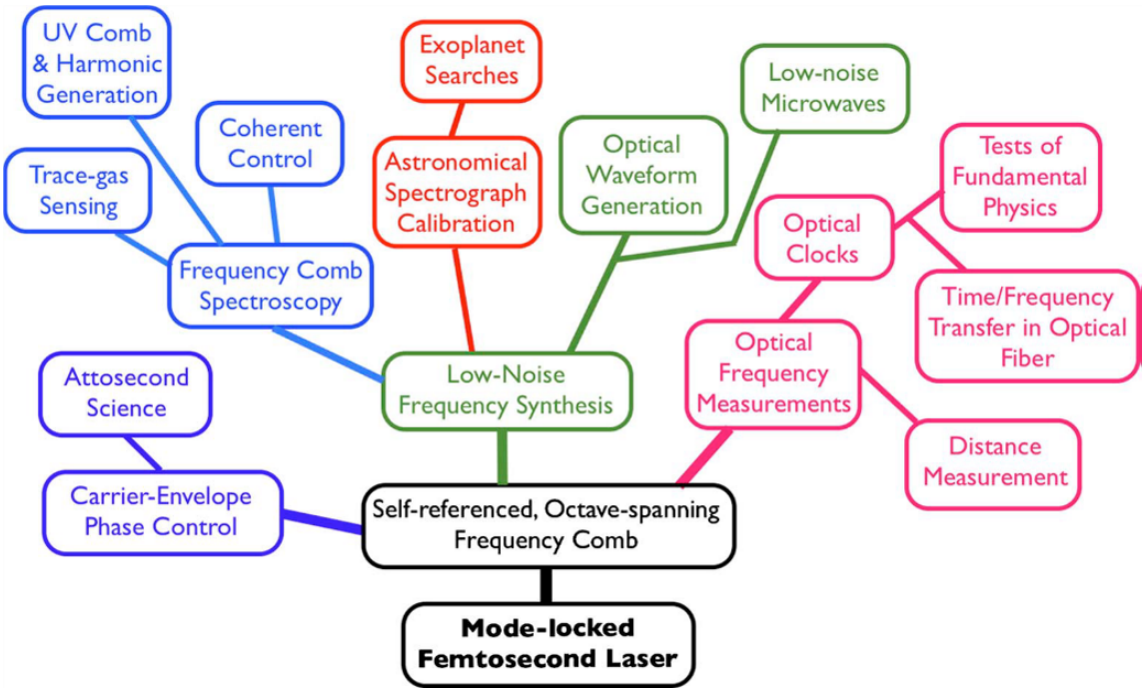

Figure 1.7 – Optical frequency comb application tree. Taken from [86].

The OFC enables to transfer frequency stability between laser sources working at distinct wavelengths. For instance, a slave laser is phase locked onto an OFC itself stabilized onto another laser that has a better stability. Therefore, the slave laser can copy the performance of the master one [90].

Furthermore, OFCs allow one to perform frequency measurement of an optical clock in terms of the SI second. To this end, both f_{rep} and f_{ceo} of the OFC are first stabilized to a radio-frequency signal generated from the primary standards. A beat-note signal of frequency $\Delta = f_c - f_n$ between the clock laser of frequency f_c and the closest mode of frequency $f_n = n \times f_{rep} + f_{ceo}$ of the OFC (n the integer of the comb mode) is then detected. Finally, the absolute frequency of the optical clock is then measured by counting the beat-note signal after having determined the integer n. In addition, it is possible to generate several outputs at different wavelengths from the same OFC, enabling to link optical clocks working at distinct wavelengths. As mentioned in subsection 1.2.1, the optical frequency ratios between optical clocks have been measured using OFCs with uncertainties much lower than those of direct frequency measurements against the microwave primary standard, showing the potential of optical clocks as candidates for the redefinition of the SI second unit. A collection of frequency ratios between optical clocks can also yield an invaluable resource in the search for a temporal variations of fundamental constants [4, 5, 91].

In addition, an OFC can be used to efficiently produce an ultra-stable signal in the microwave domain [92, 93] for applications in atomic frequency standards or high-

performance radar. In order to generate the crucial microwave signal, the comb should be locked onto a high spectral purity optical reference. The frequency stability of the reference is transferred to the repetition rate. Subsequently, the microwave signal is generated by photo-detecting the repetition rate or its higher harmonics.

Moreover, the teeth of an OFC can act as an optical ruler. OFCs are therefore known as very precise tools for spectroscopic measurements on atoms and molecules in different wavelength windows, in particular in the mid-IR region - a special window particularly relevant to this work, which hosts all rovibrational transitions of molecules. Locking a continuous-wave laser to an OFC referenced to a frequency reference allows molecular transitions to be measured with the highest uncertainties [45,46,71–75,94,95]. Moreover, the direct comb output can be used to probe the broadband atomic and molecular spectra using the dual frequency-comb spectroscopy technique [96–99].

Finally, a comb laser can also be used for the calibration of spectrometers in astronomy [100–105], for the generation of attosecond pulses or to explore the dynamics of ultrafast phenomena such as chemical reactions [106,107].

1.2.4 Optical frequency dissemination

At present, primary frequency standards and optical clocks provide the microwave and the optical signals, respectively, with the ultimate accuracies and stabilities (see subsection 1.2.1). However, not all laboratories can directly access these signals because of the complex and expensive setups. Moreover, frequency comparison of optical clocks between national metrological institutes to evaluate performances of these clocks is also an important challenge. The comparison can be performed via a transportable clock but transport of the clock is cumbersome and its performance is not as good as the laboratory clocks. Therefore, this creates the need for distributing reference signals between remotely located laboratories.

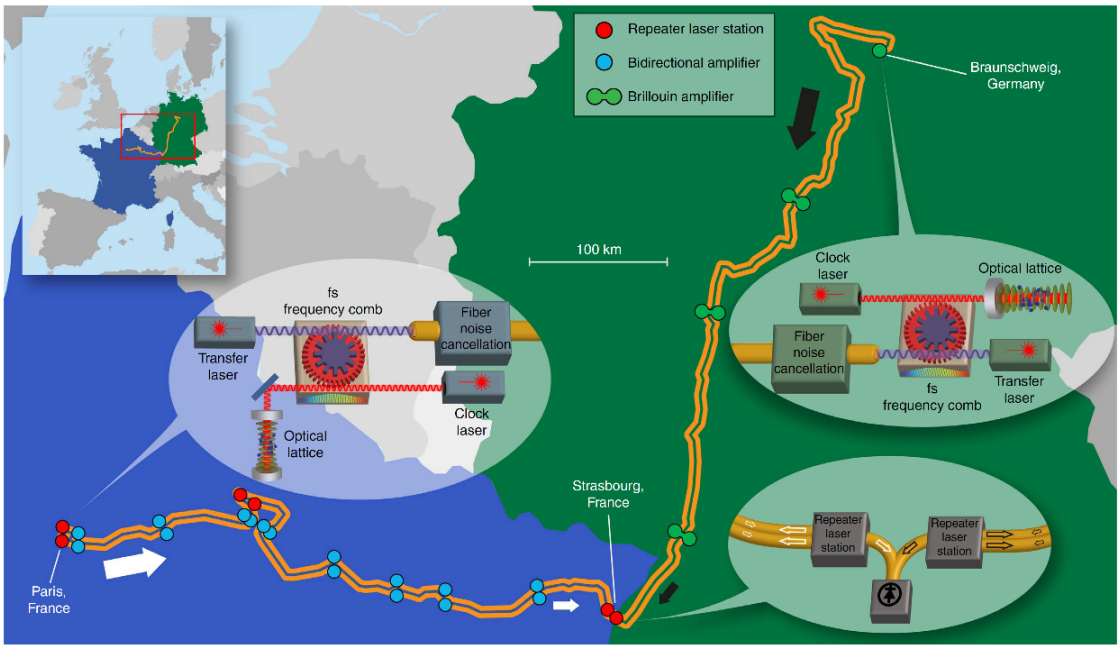

Figure 1.8 – Optical fiber link with 1415 km between LNE-SYRTE in Paris and PTB in Braunschweig for comparison between two optical clocks. Taken from [108].

The current conventional free-space technique for frequency comparison uses satellite-based dissemination and reaches a 10^{-15} fractional frequency stability after 1-day of averaging time [109,110] while primary frequency standards and optical clocks have accuracies at the 10^{-16} level and potential accuracies at the 10^{-18} level respectively, as mentioned in subsection 1.2.1. Satellite based techniques can thus not compare the ultra-stable and precise reference signals disciplined to these clocks without degrading their stability and performance. In the mean while, the transfer of the signals through optical fiber links have been reported with ultimate performances [50]. They have been implemented with ever-increasing performance and fiber length [111–113]. In this approach, an ultra-stable optical carrier at 1.54 μm (194.4 THz) is transferred over long distances. Active compensation of the phase noise added during propagation in the fiber is used to achieve low-noise optical frequency transfer (see chapter 2). The optical fiber link is thus the best candidate not only for the frequency comparison of remote optical clocks but also for distributing reference signals between laboratories (see below).

1.2.4.1 Distributing an ultra-stable and precise reference signal from a metrological institute to remote laboratories

We now consider the transfer of an ultra-stable and accurate [1] reference signal generated at a metrological institute to user laboratories where the references are needed for high precision measurements on atoms or molecules [34, 45, 94]. The principle of the transfer will be explained in more details in chapter 2. Here, we briefly show a few examples of transfers of reference signals between distant laboratories around the world.

Between LPL and LNE-SYRTE, a 43 km-long optical fiber link has been established [114]. The link allows a 1.54 μm ultra-stable reference signal generated at LNE-SYRTE to be transferred to LPL. Moreover, radio-frequency and microwave signals are also distributed via this link. Many details of this experimental setup will be presented in subsection 2.3.2.

In Germany, the Max Planck Institut für Quantenoptik (MPQ) in Garching is connected with the German metrological institute (PTB) via a pair of 920 km-long dedicated optical fiber links exhibiting a short-term frequency stability of 2×10^{-15} at 1 s averaging time [112]. In addition, a 146 km-long fiber has been established between PTB and Hanover for the optical frequency transfer with a fractional frequency instability of 3×10^{-15} at 1 s averaging time [115].

In Italy, a 642 km-long coherent optical fiber link, named Italian Link for Time and Frequency (LIFT), has been implemented with a short-term fractional instability of 1×10^{-14} at 1 s averaging time [116]. The link connects the Italian metrological institute (INRIM) to several scientific poles in Italy including a radio-telescope center [117] and the European laboratory for non-linear spectroscopy in Florence [118].

1.2.4.2 Comparison of two distant optical clocks

Phase-noise compensated fiber links enable high accuracy optical clocks separated by thousands of kilometers to be compared. In 2015, a 1415 km-long dedicated optical fiber link between France and Germany has been established for frequency comparison between optical clocks located at the respective national metrological institutes: LNE-SYRTE in

1. Here, for simplicity we design as accurate a signal whose frequency is precisely known (with an uncertainty typically smaller than 10^{-13}) thanks to a measurement to a primary standards.

Paris and Physikalisch-Technische Bundesanstalt (PTB) in Braunschweig [108]. The international link has two sections, one in France and another in Germany, as shown in Figure 1.8.

In France, the first section of this link is a 705 km-long cascaded optical link from Paris to Strasbourg using fibers of the French academic network with simultaneous internet data traffic. Repeater laser stations (see Figure 1.8) have been used to regenerate the optical phase of an ultra-stable laser at 194.4 THz (1.54 μm), referenced at LNE-SYRTE to an optical clock via an OFC. This allowed a cascaded link of two spans to be built: Paris − Reims and Reims − Strasbourg. Bi-directional erbium-doped fiber amplifiers (bi-EDFAs) were used to compensate the transmission loss of the ultra-stable laser. The integrity of the frequency dissemination is evaluated with the down link from Strasbourg to Paris [108]. In Germany, the other section of the international link is 710 km-long from Braunschweig to Strasbourg and uses fiber Brillouin amplifiers and a repeater laser station at Strasbourg to cascade this up-link with a parallel down-link from Strasbourg to Braunschweig for evaluation purposes [108, 111].

Frequency comparison between two remote strontium lattice optical clocks of LNE-SYRTE and PTB via the international link has been reported with an uncertainty of 5×10^{-17}. The remote comparison is only limited by the inaccuracy and instability of the clock themselves, with negligible contributions from the optical frequency transfer.

Moreover, another 812 km-long cascaded optical fiber link between LNE-SYRTE − LPL − NPL (National Physical Laboratory, the United Kingdom metrological institute) has been recently established for frequency comparison between remote strontium optical clocks, located at LNE-SYRTE and NPL [12]. This link has two spans, the first span of 769 km connecting NPL to LPL with the use of a repeater laser station at LPL and the second span of 43 km connecting LPL to LNE-SYRTE.

In short, the outstanding performances of the phase-compensated links lead to high-resolution remote comparisons between optical clocks. This is a powerful experimental tool in many applications, such as test of variations in time of fundamental constants [119], dark matter search [120–122] or test of special relativity [12].

1.3 Mid-infrared laser stabilization

1.3.1 The need for mid-infared laser stabilization

As mentioned in the thesis's introduction, molecules with their rich internal structures can play a decisive role in tests of fundamental physics. Most of these experiments can be cast as the measurement of absolute molecular frequencies and are often in the mid-IR spectral region. Free-running lasers with broad linewidths and frequency instability are not adequate for the measurements. Therefore, frequency stabilization of lasers in the mid-IR domain is really a challenge to obtain the narrow-linewidth lasers which are needed for many applications in high-precision spectroscopy.

1.3.2 Methods for the frequency stabilization of mid-infrared lasers

The frequency stabilization of a mid-IR lasers is performed by referencing its frequency to an ultra-stable reference signal. There are several types of reference signals, including atomic and molecular absorption lines, Fabry-Perot cavities, ultra-stable lasers, and OFCs.

1.3.2.1 Absorption line

The frequency noise of a laser can be reduced by locking its frequency to narrow atomic or molecular absorption lines. This provides not only a reduction of the laser short term frequency fluctuations but also stability and reproducibility in the long term. In the mid-IR domain, the $[F_2^{(2)}, P(2), \nu_3]$ rovibrational transition of CH_4 around 3.39 μm was recommended as a secondary frequency standard (see subsection 1.2.1) with a relative standard uncertainty of 3×10^{-12} [70]. He-Ne lasers locked to saturated absorption resonance of this transition of CH_4 have been demonstrated with a short-term frequency stability of 10^{-12} at 1 s averaging time [123, 124]. In the mean while, an absorption transition of OsO_4 around 10.3 μm in coincidence with the $R(10)$ line of CO_2 laser was recommended as a secondary frequency standard with a relative standard of 1.4×10^{-13}. CO_2 lasers locked to the saturated absorption resonance of this transition exhibit the best fractional frequency stability of 4×10^{-15} at 300 s averaging time and a long term reproducibility of ± 10 Hz [47]. Moreover, the frequency stability of a CO_2 laser locked to two-photon SF_6 line was found to be similar to the OsO_4-stabilized CO_2 laser [125]. However, the best long-term stabilities can be obtained only with a few intense and isolated molecular transitions.

1.3.2.2 Ultra-stable Fabry-Perot cavity

Frequency stabilization of a laser can be achieved by locking the laser to a high finesse cavity, for instance, using the Pound-Drever-Hall (PDH) technique [126, 127]. The frequency stability of the laser is then defined by the stability of the reference cavity length. The absolute frequency is however not known.

So far, the state-of-the-art stabilities for cavity-stabilized lasers with lowest frequency stabilities are found in the near-IR spectral domain where cavities can be fabricated with the best finesses. In the near-IR domain, the size of the spots on the mirrors is larger than in the visible, also results in a better averaging of the thermal noise. For instance, lasers at 1.5 μm locked to ultra-stable silicon cavities (finesse of $\sim$500 000) operating at 124 K [84] and 4 K [49, 85] have been demonstrated with fractional frequency stabilities below 1×10^{-16} for averaging times between 1 and 100 s, with promising direction to reach stability better than 1×10^{-17}.

In the mid-IR domain, attempts to lock lasers to stable cavities have been demonstrated [48, 128–130]. However, their stability performance is still far from those obtained in the ultra-stable near-IR region because it is not possible to build a cavity with finesse similar to that of the near-IR cavity due to the limitation of mirror's coating technology in the mid-IR spectral window.

1.3.2.3 Locking to a more stable laser

A noisy laser can easily copy the stability of a stable laser by processing the beat note between these lasers. For instance, a continuous wave QCL emitting around 9.2 μm was phase-locked to a free-running CO_2 laser [37]. The free-running emission spectrum in the megaHertz range of the QCL was strongly narrowed down to the kilohertz level. More recently, a coherent phase-locking of a continuous wave QCL emitting around 10.35 μm to a CO_2 laser locked to a saturated absorption line of OsO_4 has been demonstrated at LPL with a frequency stability of about 1 Hz at 1 s averaging time [40]. The obtained linewidth of the QCL is about 10 Hz, which is 4-5 orders of magnitude smaller than a

free running linewidth of the QCL. The absolute frequency uncertainty of this stabilized QCL is few tens of Hz, given by that of the OsO_4/CO_2 standard.

1.3.2.4 Locking to an optical frequency comb

An optical frequency comb can be used to transfer the stability of a radio-frequency or an optical frequency signal to a mid-IR laser. This is performed via two cascaded steps. First, the comb repetition rate is phase-locked to the reference signal. Then, the mid-IR laser is stabilized to the OFC.

Optical frequency comb locked to a radio-frequency or optical frequency reference

The repetition rate of an OFC can be stabilized to a precise ultra-low noise radio-frequency signal, for example, a 10 MHz signal generated by a commercial rubidium (Rb) standard with a short-term stability around 4×10^{-12} at 1 s and a accuracy in the order of 10^{-12} [60]. However, performances of the standard in the long-term is not as good as in the short-term. The signal from the Global Positioning System (GPS) exhibits a good long-term stability of 10^{-12} at 10^5 s [60]. Therefore, a better signal can be generated by referencing the Rb clock (or a radio-frequency signal generated by an thermal-stabilized quartz oscillator, see section 2.4) to the GPS signal. Typically, the GPS-disciplined rubidium oscillator has an uncertainty in the 10^{-11} level. This technique is typically used in many laboratories for laser frequency's stabilization in both the near- and mid-IR domain [39, 42–44, 131].

In addition, we can stabilize the comb repetition rate to an ultra-stable near-IR signal, that is generated by a laser at 1.54 μm locked to an ultra-stable cavity and that is calibrated against the primary standard, as mentioned in subsections 1.2.2. In consequence, the comb repetition rate is traceable to the primary standard and has the stability of the cavity-stabilized laser, potentially at the 10^{-16} level at 1 s averaging time if one uses the state-of-the-art ultra-stable laser described in section 1.3.2.2. The performances of the stabilized repetition rate are much better than when using the GPS-disciplined Rb clock (see section 2.6 for more details).

Mid-IR stabilized to the comb

The frequency of the mid-IR source is then locked to a high harmonic of the repetition rate of the OFC using a nonlinear frequency conversion, such as sum frequency generation (SFG) [45, 51, 132, 133] or different frequency generation (DFG) [42, 46, 134–137]. The stability and uncertainty of the mid-IR laser's frequency are thus given by those of the radio-frequency or near-IR reference.

1.4 Previous precise molecular spectroscopic measurement at LPL

The MMTF group of LPL, to which I belong, has a long-standing interest in performing spectroscopic precise measurements on molecules at extreme resolutions around 10 μm. In this section, we first briefly describe how to perform a precise spectroscopic measurements. After that, we present previous ultra-high resolution spectroscopic studies at LPL.

In precise spectroscopic measurements, most of the systematic errors are propor-

tional to the linewidth of the molecular absorption lines, that is mainly broadened by the wide range of Doppler shifts and collisions between molecules (see section 1.1 for more details). Therefore, the strategy to achieve precise spectroscopy is minimization of the broadening. To overcome the Doppler effect without cooling molecules, saturated absorption spectroscopy based on the traditional pump-probe configuration is typically used (see section 1.1.3). However the saturation spectroscopy signal comes only from a small number of molecules for which the projection of the speed on the laser beam axis is zero. By contrast, Doppler-free two-photon spectroscopy that also uses two counter-propagating beams allows one to probe absorption signals from all molecules whatever their speed, when twice the laser frequency exactly equals the molecular resonance. As seen in subsection 1.1.3, the linewidth is also limited by the inverse of the transit time through the laser beam. To improve the resolution, the method of separated fields introduced by Ramsey can be used in association with a molecular beam [138]. In this technique, the laser frequency is compared to the molecular transition via interactions between molecules and two separate laser beams. Sensitivity of this technique is limited by the time-of-flight of molecules between the two laser beams. Combining two-photon spectroscopy and the Ramsey technique enables to achieve the best resolution, which is about 100 Hz [34].

Ultra-high resolution spectroscopy and metrology require very stable laser sources with a high spectral purity. Several frequency standards have been developed by locking the frequency of a laser to absorption lines of several molecules in a wide spectral range from the visible to the infrared domain [70] (see subsection 1.2.1). Their absolute frequencies are well known by calibration against primary frequency standard. They exhibit accuracies in the range of few ten of Hz to a few kHz and relative stabilities in the range of 10^{-13} to 10^{-14}. At LPL, several frequency standards around 10 μm have been developed. They are based on CO_2 lasers locked onto saturated absorption lines of OsO_4 or two-photon absorption signals of SF_6.

Our group has accumulated many years of experience in conducting ultra-high resolution spectroscopic experiments, and obtained several world records in the 8-12 μm spectral window of the CO_2 lasers.

In 1994, ultra-high resolution sub-Doppler spectroscopy of slow OsO_4 molecules in an 18 m-long cell were demonstrated [139]. Because the laser beam waist can not easily be increased over ∼10 cm, finite transit time broadening was overcome by selecting slow OsO_4 molecules in saturated spectroscopy at a very low pressure (2×10^{-6} Torr) and low laser fields (30 nW). A linewidth of 80 Hz (HWHM) was obtained for an OsO_4 transition. Three year after, the first observation of slow molecules in a 1.6 m long Fabry-Perot cavity by using Doppler-free two-photon spectroscopy was reported [140]. A transition of SF_6 at 28.4 THz was obtained with a linewidth of 280 Hz (HWHM).

In 2008, the Doppler-free two-photon Ramsey interferometry of a supersonic beam of SF_6 was demonstrated with an unprecedented resolution of ∼100 Hz (3×10^{-12} in relative value) [34]. In this experiment, the CO_2 laser used to record two-photon Ramsey fringes of SF_6 was compared to an accurate radio-frequency reference via an optical frequency comb (OFC). This reference was generated at LNE-SYRTE (the French national metrology institute for time and frequency) by a combination of a H-maser and a cryogenic sapphire oscillator controlled with a Cs fountain (see section 2.2) and distributed to LPL via a 43 km-long fiber link (see section 2.3). The combination of the CO_2 laser source and the

two-photon Ramsey interferometry allowed the absolute frequency of an SF_6 transition to be measured to within 0.6 Hz (a record relative uncertainty of 2×10^{-14} in this frequency range). The potential of this apparatus for probing fundamental physics was demonstrated by placing an upper limit on the temporal variation of the proton-to-electron mass ratio [34].

Direct phase-locking of a CO_2 laser around 10 μm to a remote optical frequency reference signal at 1.54 μm using an OFC at LPL was demonstrated in 2013 [51, 141]. This optical reference is generated at LNE-SYRTE by an ultra-stable laser at 1.54 μm locked to a high finesse cavity. Its absolute frequency is continuously calibrated against LNE-SYRTE's primary references via an OFC at LNE-SYRTE (see section 2.2). It is transferred to LPL via a 43 km-long fiber link in which noises added by the link to the signal is cancelled. The laser was used to measure a rovibrational line of OsO_4 around 10 μm with an uncertainty of 24 Hz (8×10^{-13} in relative value).

The CO_2 lasers at LPL are strong metrological tools but their lacks of frequency tunability is a large constraint for high precise spectroscopic studies. Recently, they were replaced by quantum cascade lasers (QCLs) providing a much larger tunability and achievable wavelengths covering the whole mid-IR region (see chapter 3). More recently, the state-of-the art frequency stabilization of a QCL at 10.3 μm was reported at the sub-Hz level [45]. The QCL was phase-locked to the remote optical reference signal from LNE-SYRTE and exhibited a relative stability and an accuracy of 2×10^{-15} and 10^{-14} respectively (see sections 3.3 and 3.4). The stabilization setup can straightforwardly be extended to the entire 9-11 μm spectral range without any loss of performance by using QCLs of adjacent emission spectra. The ultra-stable and SI-traceable QCL was used to measure molecular absorption frequencies with state-of-the-art uncertainties, confirming its potential for ultra-high precision spectroscopy [45].

1.5 Parity violation observation

The field of parity violation (PV), a specific feature of the weak interaction, began from a brilliant analysis of T.D. Lee and C.N. Yang in 1956 when they proposed that parity is not conserved [142]. They concluded that there was at this time no experimental evidence to support or to refute parity conservation in weak interactions. The Nobel Prize in Physics 1957 was awarded jointly to them for this investigation. The bold proposal was subsequently confirmed by experiments in different energy regimes. The first PV observation in nuclear β-decay was discovered by C.S. Wu and her co-workers in 1957 [143]. After this discovery, PV has been extensively observed in high energy physics experiments. M.A. Bouchiat and C. Bouchiat realized that the PV is also amplified in heavy atoms [144, 145]. They pointed out that the PV effect scales with the nuclear charge with the third power Z^3. In 1978, the parity violating phenomena in atom was first investigated by L.M. Barkov and M.S. Zolotarev in Bi [146], then followed by the unambiguous observation of PV effects in Tl [147, 148] and in Cs [149, 150]. In molecular physics, weak nuclear interaction between the nucleons and electrons in molecules leads to a shift of vibrational states between the two enantiomers of a chiral molecule (see below). Although very tiny, relativistic quantum chemistry calculations indicate that the energy difference between the two enantiomers of well chosen species is above the target sensitivity of an ultra-high resolution IR spectroscopy experiment under development [21].

1.5.1 Parity violation in chiral molecules

Looking for parity violating effects induced by the weak nuclear force in molecules has been a long-standing quest. Many molecules are chiral, existing in left- and right-handed structures, known as enantiomers, which are mirror images of one another. Figure 1.9 illustrates the potential energy surface of a chiral molecule showing two minima that are separated by an interconversion barrier associated with the left- and right-handed enantiomers. Strikingly, chiral rovibrational states are not the eigenstates of the symmetric molecular electromagnetic Hamiltonian and nutation from one to the other can happen by quantum tunnelling through the potential barrier. However, interaction with the environment, or decoherence, tends to hold the molecule in the left- or right-handed enantiomer. When the interconversion barrier between enantiomers is very high, which is the case for the molecules considered here, the left- and right-handed states can then be considered to a good approximation as energy eigenstates. In addition to the electromagnetic interaction, the weak interaction, one of the three other fundamental forces, is also at play in molecular systems, notably in the interaction between electrons and nuclei.

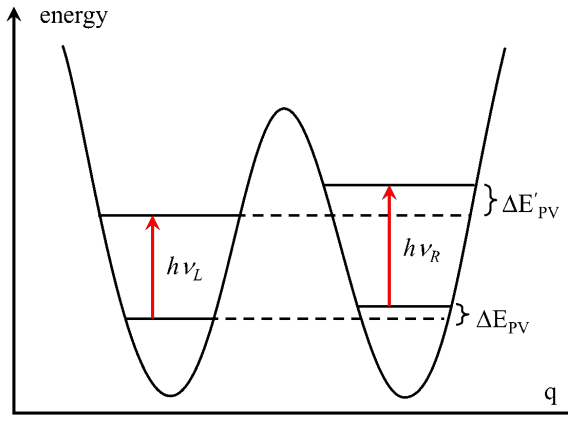

Figure 1.9 – The potential energy of a chiral molecule as a function of the inversion coordinate q. The weak interaction is responsible for a small PV energy difference ΔE_{PV} between the left "L" and right "R" enantiomers, and results in a difference between the rovibrational frequencies ν_L and ν_R of these enantiomers (h is the Planck constant). Adapted from [21].

In the presence of the weak force, a very small PV energy difference ΔE_{PV} occurs between these enantiomers, as shown in Figure 1.9. In this case, the left and right molecules are no longer the exact mirror images of each other [21]. The existence of energy differences between the left and right molecules have first been suggested by Y. Yamagata [151], D.W. Rein [152], and E. Gajzago and G. Marx [153].

Measuring differences in infrared absorption line frequencies was originally proposed by V.S. Letokhov in 1975 [154]. The nuclear weak interaction between nucleons and electrons in chiral molecule is responsible for small PV energy differences between the left- and right-handed enantiomers (ΔE_{PV} and $\Delta E'_{PV}$ in Figure 1.9 for two different vibrational states), and results in a difference between the rovibrational frequencies ν_L and ν_R of these enantiomers, as shown in Figure 1.9. Theoretical calculations indicate that this frequency difference is expected to be in the range of 10^{-12} to 10^{-18} depending

on the considered molecular transitions [21, 155–164].

Our group aims to make the first measurement of this symmetry-breaking energy differences. A successful first observation of PV in chiral would allow us to probe the Standard Model of particle physics and its limit [165] and might shed light on the question of biomolecular homochirality [166]. It will allow to benchmark quantum chemistry calculations that include the contribution of the weak interaction, which are the input to the mathematical models considering the origin of biological homochirality.

1.5.2 Proposed experimental approaches of the parity violation observation in chiral molecules

A number of techniques have been proposed for the observation of PV in chiral molecules, including rotational, rovibrational, electronic, Mössbauer and NMR spectroscopy, as well as crystallisation and solubility experiments, and optical activity measurements (see Refs. [21,165,167–169] and references therein). However, to our knowledge very few other groups currently pursue an experimental realisation. Dmitry Budker's group has recently proposed a measurement using NMR spectroscopy [170], and Martin Quack's group is currently pursuing a measurement based on the time evolution of parity in chiral species after a parity selection step [171]. The latter is an optical technique, but one quite different from our approach. It has distinct experimental challenges, and requires working with substantially different chiral species. This group has published a proof of principle using an achiral molecule [172] and has also proposed promising candidate species for this experiment [173].

Our approach is based on the 1975 suggestion by V.S. Letokhov [154] to search for a shift $\Delta\nu_{PV} = \nu_L - \nu_R$ in the frequencies ν_L and ν_R of the same rovibrational transition of left and right enantiomers [174], a signature of PV. In 1976, V.S. Letokhov group searched for such splittings by laser sub-Doppler absorption spectroscopy in the spectrum of racemic CHFClBr [175]. In 1977, Arimondo *et al* [176] compared rovibrational transitions in the separated enantiomers of camphor. They concluded that transition frequencies of the C-C*-CO bending mode of L- and D-camphor (C* denotes a chiral carbon) were founded to agree to within their experimental resolution of 10^{-8} in relative value. However, theoretical studies [159,177], carried out in 1999 and 2004 after the experiment, indicated that the parity violating effect is $\Delta\nu_{PV}/\nu \sim 10^{-19}$ in this molecule, 11 orders of magnitude smaller than their experimental sensitivity.

At LPL, an ultra-high resolution spectroscopic setup was also developed for PV observation in chiral molecules. The first measurement was carried out in 1999 in CHFClBr. This measurement was conducted on a rovibrational transition in the C-F vibrational band around 9.3 μm using saturated absorption spectroscopy in two separate 3 m-long Fabry-Perot cavities, as shown in Figure 1.10. These cavities were filled by enantiomers S-(+) and R-(–) of CHFClBr with enantiomeric excess (reflecting the degree to which a sample contains one enantiomer in larger amounts than the other) of 56.5% and 22%, respectively. Rovibrational spectrum of each enantiomer was simultaneously recorded in the two separate cavities by a CO_2 laser around 10 μm locked to an OsO_4 absorption line. The spectral linewidth is ~60 kHz. Over 10 days of measurements, a mean frequency difference $\Delta\nu_{PV}^{R(-)/S(+)} = \nu_{R(-)} - \nu_{S(+)}$ of 9.4 Hz between the two molecular samples was obtained with statistical and systematic uncertainties of 5.1 and 12.7 Hz respectively [178]. This gives an upper limit of $\Delta\nu_{PV}/\nu \sim 4 \times 10^{-13}$ for the PV effect. An improved

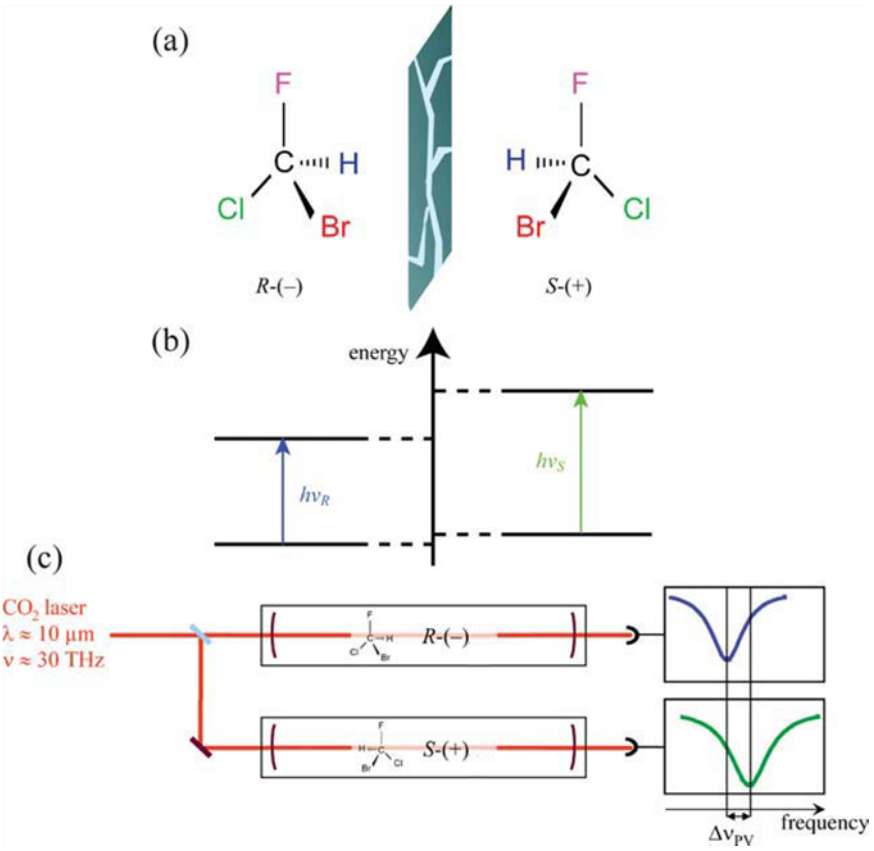

Figure 1.10 – Principle of the PV measurement on CHFClBr molecule. (a) CHFClBr enantiomers are not mirror images. (b) This leads to a difference between their rovibrational frequencies of $\Delta\nu_{PV} = \nu_L - \nu_R$. (c) The high-resolution spectra of these enantiomers are recorded simultaneously using two separated cavities. It should be noted that the frequency difference $\Delta\nu_{PV}$ is expected to be much smaller than the spectral linewidth. Taken from [21].

sensitivity $\Delta\nu_{PV}/\nu \sim 2.5 \times 10^{-13}$ was obtained when the experiment was repeated in 2002 [179] with new samples of higher enantiomeric excess: 72% for S-(+) and 56% for R-(–). This sensitivity was limited by uncontrollable residual impurities (resulting from the synthesis) present in the absorption cells (at a level below 5%) and responsible for uncompensated collisional shifts of the transition frequency. The nature and level of impurities were different in the $R(-)$ and $S(+)$ samples, resulting in an uncontrollable differential pressure shift. Theoretical studies, conducted in 2005 after the experiment was done, predicted that the PV effect for the C-F vibrational band of CHFClBr was −2.4 mHz, corresponding to $\Delta\nu_{PV}/\nu \sim -8 \times 10^{-17}$ [180].

To go beyond this limit, we are learning to work with molecules where the energy difference is expected to be far larger and we are building a more sensitive instrument.

1.5.3 Searching new chiral molecules

Parity violation in chiral molecules using ultra high-resolution spectroscopic measurements has not been observed so far, as mentioned above. An importance task in the observation of the PV effect is to find suitable chiral candidates (in particular with a bigger PV effect) for such measurements.

The MMTF team has launched collaborations with theoretical and experimental chemists to find the best chiral species. The search for suitable chiral molecules is guided by relativistic quantum chemistry calculations by T. Saue (Laboratoire de Chimie et Physique Quantique, Université Paul Sabatier), P. Schwerdtfeger (Centre for Theoretical Chemistry and Physics (CTCP), Massey University Auckland), and R. Bast (UiT The Arctic University of Norway). The synthesis of molecular candidates is directed by J. Crassous (Institut des sciences chimiques de Rennes, Université de Rennes 1).

The PV energy difference scales strongly with nuclear charge [144], so we consider molecules with heavy atoms near the chiral centre. We have already worked with theoretical and experimental chemists to find the best chiral species for measuring the PV energy difference. This led to the successful synthesis of solid oxorhenium organo-metallic compounds that have vibrational transitions around 30 THz and PV frequency shifts as large as ∼1 Hz (see [20, 21, 155, 157, 181] and references therein), up to 1000 times larger than in CHFClBr. Several other tracks are currently being followed and other molecules are being prepared. Our collaborators have recently found an uranium compound (N≡UHFI) with a record ∼20 Hz predicted PV frequency shift [156]. While synthesising and isolating such compounds has not been demonstrated so far, this could be possible in the future. Several criteria have been outlined for this search. The ideal candidate should:

— show a large PV vibrational frequency difference of a high intense fundamental rovibrational transition

— be available in large enantiomeric excess or, ideally, in enantiopure form, with two independent samples (one mainly containing left-handed molecules and the other enriched in the right-handed molecules)

— have high enough volatility or sublimate without decomposition to allow gas phase studies

— have a suitable 2-photon transition joining a state in the ground vibrational level $\nu = 0$ to one in $\nu = 2$, allowing to perform the Doppler-free two-photon Ramsey interferometry with the best resolution

— exhibit a structure as simple as possible so as to facilitate the spectroscopy and maintain a favourable partition function because the experimental sensitivity depends on the partition function, in particular avoid nuclei with a quadrupole moment to avoid large hyperfine structure

— have an intense band accessible to available mid-IR laser sources (QCL, CO_2 laser,...)

— be available at gram-scale

— be compatible to high-resolution spectroscopic measurements and thus not be subjected to internal relaxation processes such as internal vibrational relaxation (IVR).

1.5.4 New experimental setup under development

In this paragraph, we present the new experimental setup to test parity violation in cold chiral molecules.

In order to overcome the limit of the previous experiment (see 1.5.2), we propose to use a molecular beam, that allows to get rid off collisions and thus go beyond the collision limit. Molecules in gas phase can be cooled down to a few kelvins in a supersonic beam. However most of chiral molecules expected to exhibit large parity violation effect are

solid at room temperature [156], which constitutes a serious difficulty for high-resolution spectroscopy. In the mean while, buffer-gas beams of molecules, which are in gas phase or in solid state at room temperature, can be formed in a cryogenic cell - one of the latest molecular beam source technologies. They exhibit both low velocity and some of the highest beam fluxes to date [182], making them very attractive for precise spectroscopic measurements.

For probing the parity violation effect, the ideal configuration is to use Ramsey interferometer with molecular beam based on a mid-IR laser, that is so far the best method for ultra-high-resolution rovibrational molecular spectroscopy. At LPL, our group has a long-standing interest in performing spectroscopic precise measurements using CO_2 lasers. They emit at CO_2 molecular transitions. An emission transition is found every 30 to 50 GHz in the 9-11 wavelength range, and each line can be tuned over a few hundreds of MHz. This tuning range can be extended to a few GHz using electro-optic modulators (EOMs). However, there are many spectral regions not accessible with CO_2 lasers, which puts a strong constraint for PV observations. One solution is to use OFC-referenced continuous-wave [183, 184] or OFC mid-IR sources [89]. These are based on frequency mixing in nonlinear crystals and provide absolute frequency referencing and widely continuous frequency tunability, however they are very complex and often exhibit limited power. By comparison, QCLs offer broadband and continuous tuning over several hundred GHz and are available from 3 to 25 μm allowing the study of a considerable number of candidate species and thus providing invaluable flexibility.

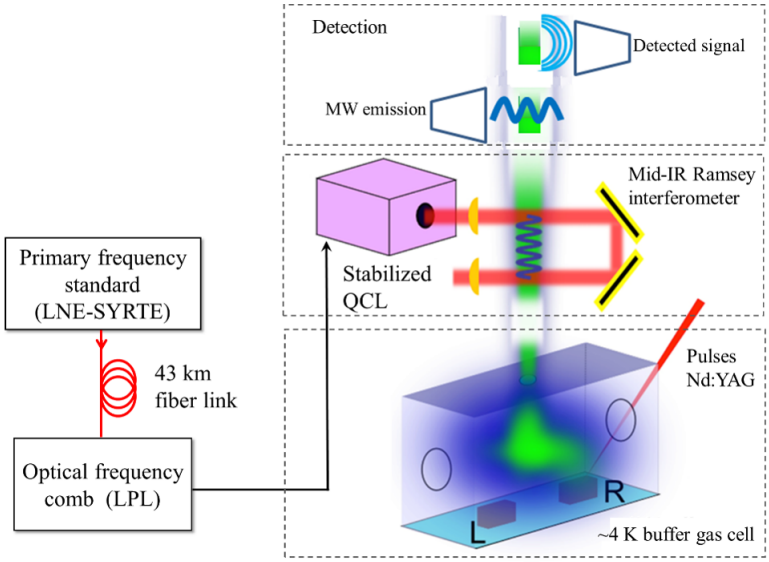

Figure 1.11 – The new experimental setup for observing PV effects in chiral molecules. In a 4 K cryogenic cell, buffer-gas molecular beams are formed using laser ablation (pulsed Nd:YAG) of solid-state molecules. Then, the molecular beam passes through a mid-IR Ramsey interferometer, where tiny changes in the rovibrational frequency of the left- and the right-molecules are measured. The SI-traceable Ramsey interferometer is based on a mid-IR QCL, that is phase-locked to the remote ultra-stable optical reference signal of LNE-SYRTE via an optical frequency. QCL: quantum cascade laser, MW: microwave.

The group is designing and constructing a state-of-the-art instrument for high-resolution vibrational spectroscopy of chiral molecules and for measuring PV. Figure 1.11 illustrates

the setup of this new experiment, composed of three main parts.

In the first part, a slow, cold molecular beam of the rhenium species of interest is made by producing the molecules in the gas phase by laser ablation inside a buffer-gas cell cooled to a few kelvins, and then extracting the cold molecules into a beam.

The molecules then pass through the second part, which is a Ramsey interferometer enough sensitive to measure tiny changes in the vibrational frequency of the molecules. To reach the required frequency, which is in the mid-IR spectral region, a QCL based Ramsey interferometer is used. To achieve the best frequency stability, the QCL is phase-locked to an OFC referenced to the remote optical reference signal calibrated to primary frequency standards (potentially optical clocks). This reference generated at LNE-SYRTE is distributed to our laboratory via the 43 km-long active noise compensated fiber link.

In the third part, molecules must then be detected with a high sensitivity. It is noted that the direct detection of laser absorption is not sensitive enough in the mid-IR region. We are currently investigating detectors based on cavity-enhanced schemes recording mid-IR absorption or the microwave field molecules emitted when they rotate.

To measure the PV vibrational frequency shift, the vibrational frequency of each enantiomer must be measured in this new apparatus. Because this is a differential measurement between the two enantiomers, most systematic frequency shifts will cancel out.

The ultimate precision of such a measurement is a key question. The statistical error is usually reduced as the square root of the accumulating time of the experiment, assuming white noise. It is difficult to provide a priori estimate of the systematic errors. However we can refer to the previous experiment using CHFClBr in cells. The differential pressure shifts which limited the previous experiment is not an issue in a molecular beam with no collisions. Furthermore, a large number of systematic effects will be identical for left- and right-handed molecules and will thus cancel out after our differential measurement. Finally, several systematic effects scale with the size of the measured spectral feature, which will be reduced from 100 kHz to 100 Hz. In conclusion, reducing the systematic errors to a few 0.01 Hz (10^{-15} in fractional value) is certainly realistic with this scheme [21].

Another source of comparison is the two-photon Ramsey experiment carried out on a supersonic beam of SF6, which showed a measurement precision of 0.6 Hz (10^{-14} in fractional value) [34]. This figure gives an order of magnitude estimate of the systematic errors on an absolute frequency measurement using the current technique. For a differential measurement like the one proposed in this project, we can reasonably expect a further order of magnitude increase in sensitivity. This confirms that measuring a frequency difference between enantiomers at a few hundredths of Hz level (10^{-15} in fractional value) is conceivable [20]. This figure will ultimately depend on the combination of the resolution chosen and the signal-to-noise ratio obtained for a specific molecule.

1.6 Concluding remarks

The work described in this thesis concentrates on developing a QCL based spectrometer around 10 μm that is suitable for applications in high-resolution spectroscopic studies and frequency metrology. First, we develop a QCL which combines (i) very low instability at a level better than a few 10^{-13}, in order to probe line shape of width of the order of 100

Hz, (ii) very high accuracy, with an uncertainty of the absolute frequency around 10^{-15}, and (iii) widely frequency tunability in order to probe rovibrational spectra. The stabilization set up is described in chapter 2 and 3. The widely-tunable frequency-controlled QCL has first been used to demonstrate high-resolution spectroscopy of a few molecules in a multipass cell, as shown in chapters 4 and 5. In the future it will be used for studying molecular spectra at the highest resolution, first in a Fabry-Perot cavity and ultimately in a slow and cold molecular beam, on the way to the first observation of parity non conservation in molecules.

CHAPTER 2

Tunable and SI-traceable optical frequency comb stabilized to a remote optical frequency reference signal

Contents

2.1 Introduction . . . 35
2.2 Reference signals from LNE-SYRTE . . . 36
2.2.1 Primary microwave reference signal . . . 36
2.2.2 Ultra-stable near-IR frequency reference from LNE-SYRTE . . . 38
2.2.3 Calibration of the US laser frequency to the primary standards 43
2.3 Transfer of a stabilized frequency reference between LNE-SYRTE and LPL . . . 44
2.3.1 Principle of fiber based optical frequency transfer . . . 44
2.3.2 Optical frequency transfer between LNE-SYRTE and LPL . . . 45
2.4 Local radio frequency references . . . 51
2.5 Widely tunable and ultra-stable optical local oscillator at 1.54 μm . . . 52
2.5.1 Experimental setup . . . 52
2.5.2 Low-phase noise microwave synthesizer without phase jumps . 54
2.6 The optical frequency comb at LPL . . . 55
2.6.1 The OFC at LPL: introduction and modules . . . 55
2.6.2 Free-running optical frequency comb . . . 61
2.7 Frequency stabilization of the OFC repetition rate onto the OLO . . . 63
2.7.1 Experimental setup . . . 63
2.7.2 Performances of the stabilization of the repetition rate of the OFC 65
2.7.3 Upgrading the experimental setup . . . 68
2.8 OFC repetition rate tuning performances . . . 70
2.9 Conclusion . . . 71

2.1 Introduction

We describe in this chapter the stabilization of an optical frequency comb to an ultra-stable (US) laser at 1.54 μm laser located at LNE-SYRTE, the French national

metrology institute for time and frequency. There, this ultra-stable laser is referenced to primary frequency standards, potentially Cs clocks that realizes the time-frequency standard within the International System of Units. The frequency reference is transferred over 43-km to LPL via an optical fiber link.

First, we introduce reference signals generated at LNE SYRTE, including an accurate microwave reference and an ultra-stable optical frequency reference. The former is generated from a combination of a cryogenic sapphire oscillator and a hydrogen maser. Its absolute frequency is measured against Cs clocks at LNE-SYRTE. The ultra-stable optical frequency reference is a laser at 1.54 μm phase-locked to a high-finesse cavity. Its absolute frequency is calibrated against the accurate microwave reference.

Second, we describe the experimental setup for transferring the spectral properties of the US optical reference signal over 43 km from LNE-SYRTE to LPL via an optical fiber link with active compensation of the phase noise added to the signal by the link during the propagation. After that, we report the development of a 1.54 μm optical local oscillator at LPL whose output frequency is referenced to the incoming optical signal and can be continuously tuned over 9 GHz using an electro-optic modulator driven by a home-built microwave synthesizer.

Finally, we describe the experimental setup for stabilization of the repetition rate of an optical frequency comb to this local oscillator. This setup allows the wide tuneability of the OLO to be transferred to the repetition rate.

2.2 Reference signals from LNE-SYRTE

2.2.1 Primary microwave reference signal

2.2.1.1 Atomic fountain clocks

At LNE-SYRTE, three atomic fountain clocks are used to provide an ultra-accurate microwave reference. The first clock F01 is a Cs fountain in operation since 1994. The second clock FO2 is a dual fountain operating simultaneously with Rb and Cs since 2009. The third clock FOM, developed in the context of the space clock PHARAO, is a transportable clock based on Cs. The atomic transitions between hyperfine sub-levels $F = 3 \rightarrow F = 4$ for Cs at 9.192 GHz and $F = 1 \rightarrow F = 2$ for Rb at 6.834 GHz are probed using Ramsey interferometry [185].

Typical accuracies of these fountains are 3.5×10^{-16} for FO1, 2.1×10^{-16} for FO2-Cs, 6.9×10^{-16} for FOM, and 3.3×10^{-16} for FO2-Rb [66]. The fractional frequency instability curve between the FO1 and FO2 clocks is shown in Figure 2.1 (blue triangles). It is below 1×10^{-14} at 100 s averaging time. This graph also plots the frequency instability of the FO1 clock (red circles) and the FO2 clock (black squares) that were measured against an accurate and ultra-stable microwave signal, produced by an cryogenic sapphire oscillator locked to a hydrogen maser (see below).

2.2.1.2 Accurate and ultra-stable microwave reference signal

All three fountain clocks of LNE-SYRTE share a common microwave signal that is generated by combination of a liquid-helium cooled cryogenic sapphire oscillator (CSO) and one of four hydrogen masers (H-masers). The CSO has been developed in collaboration between LNE-SYRTE and University of Western Australia [65]. The core of the

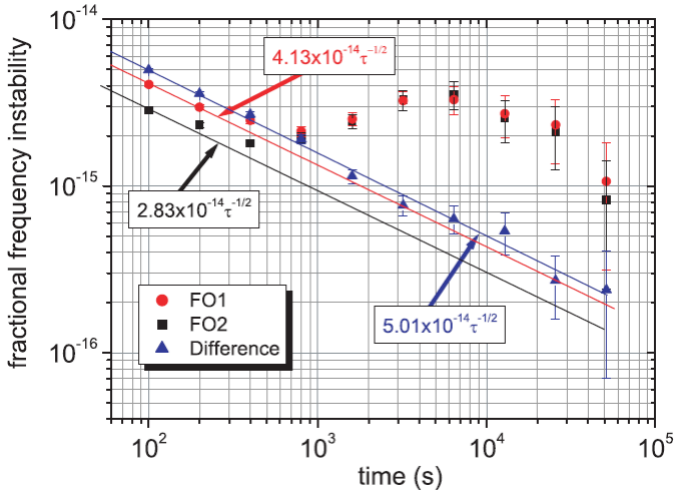

Figure 2.1 – Fractional frequency instability (Allan deviation) between the FO1 clock and the FO2 clock (blue triangles). After 50 000 s averaging time, the stability between these clocks is 2.2×10^{-16}. This graph also plots the fractional frequency instability of the FO1 clock (red circles) and the the FO2 clock (black squares) against a cryogenic sapphire oscillator locked a hydrogen maser (see text in subsection 2.2.1.2). Taken from [186].

CSO is a sapphire resonator surrounded by a cylindrical super-conductive niobium cavity. The oscillator uses a whispering gallery mode with an operational frequency of about 11.932 GHz. The crystal is maintained in a dewar at a temperature of 4 K. As shown in Figure 2.2, the frequency stability of the free-running CSO is estimated to be around $1 - 2 \times 10^{-15}$ between 1 s and 1000 s averaging time with a drift of about 1.5×10^{-13} per day, while the H-maser frequency stability is around 10^{-13} at 1 s averaging time and reaches a noise floor about 2×10^{-15} at 1000 s averaging time [65].

In order to compensate the CSO frequency drift, a microwave 11.98 GHz signal, demoted as the ultra-stable microwave reference (UMR) signal, is derived from the free-running CSO. This frequency is divided down to 100 MHz and locked to one of the four H-masers via a low-bandwidth phase-lock loop (PLL), as shown in Figure 2.3. In consequence, the 11.98 GHz signal has the phase noise properties of the CSO for time scales less than 1000 s and copies the mid- and long-term stability of the H-maser [185].

The 11.98 GHz signal is the high-performance reference. Microwave signals at 6.834 and 9.192 GHz, directly synthesized from the 11.98 GHz signal, are used for the FO2 clock that is located close to the CSO. In addition, short-length optical fiber links are used to transfer the UMR signal to other laboratories (see subsection 2.3.1 for more details). To this end, microwave signals at 8.985 and 1 GHz derived from the UMR signal are used to modulate the amplitudes of 1.54 μm laser diodes, that are injected in optical fiber links and transferred to other laboratories, i.e. atomic fountain laboratories (FO1 and FOM), optical clock laboratories or other purposes. At the end of each fiber link, a part of the incoming signal is sent back to the UMR lab where it is demodulated. The phase difference between the original signal and the demodulated signal, caused by the noises added during the propagation, is cancelled through a feedback to a fibre stretcher and to a fibre heater.

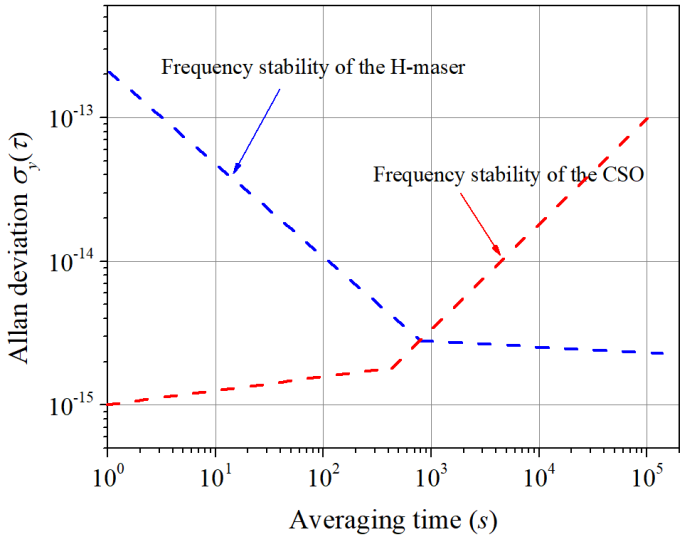

Figure 2.2 – Estimation of the fractional frequency stabilities (Allan deviations) of the CSO and the H-maser. The frequency stability of the CSO is around $1 - 2 \times 10^{-15}$ for averaging times between 1 s and 1000 s with a drift of about 1.5×10^{-13} per day. The H-maser frequency stability starts is 10^{-13} at 1 s to reach a floor of about 2×10^{-15} at 1000 s. Adapted from [65].

Furthermore, the 8.985 GHz signal is used not only to measure optical frequencies of ultra-stable lasers at LNE-SYRTE (see subsection 2.2.3) but also to compare the UMR signal with optical clocks signal through OFCs. In addition, a radio-frequency signal at 200 MHz (not shown in Figure 2.3) is also generated from the UMR signal and transferred to LPL where it will be used as a radio-frequency reference signal for our experiments at LPL (see subsection 2.3.2.3). Finally, accurate and ultra-stable microwave signals from the H-masers provide the connection to the international atomic time (TAI) and the local timescales, and to satellite time-transfer systems, such as global positioning system (GPS) and two-way satellite time and frequency transfer(TWSTFT), as shown on top of Figure 2.3.

2.2.2 Ultra-stable near-IR frequency reference from LNE-SYRTE

In our experiment, the optical frequency reference signal is produced by a laser emitting at 1.54μm phase-locked to an ultra-stable cavity. In this subsection, we introduce two different experimental setups of cavity-stabilized lasers that have been developed at LNE-SYRTE [114, 187]. Ultra-stable signals at 1.54 μm from both systems have been transferred to LPL through an optical fiber link, that will be described later.

2.2.2.1 First US laser stabilized to the "white" cavity

The first US laser (US laser #1) has been in operation since 2008 [188]. Its experimental setup is illustrated in Figure 2.4(a). A fiber laser at 1.54 μm with a free-running linewidth of about 1 kHz is phase-locked on a high finesse Fabry-Perot cavity (finesse ~800 000) using the Pound-Drever-Hall method [127].

The cavity is made of a 10-cm ultra-low expansion glass spacer and two highly reflecting mirrors with a 50 cm curvature radius. It is maintained in a vacuum chamber at a

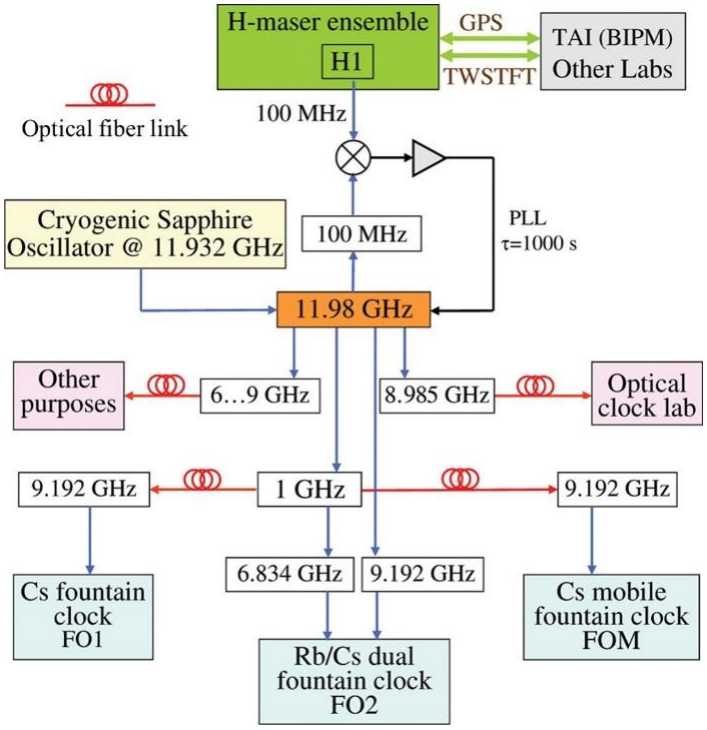

Figure 2.3 – LNE-SYRTE clock ensemble. At the ultra-stable microwave frequency reference laboratory, an ultra-low noise reference signal at 11.932 GHz is generated by the CSO. A 11.98 GHz signal generated from this CSO signal is slowly phase-locked to the output of the H-maser (H1) with an averaging time τ ∼1000 s. Microwave signals at 8.985 GHz and 1 GHz derived from the UMR signal are used to modulate the amplitudes of 1.54 μm laser diodes, that are injected in optical fiber links and transferred to other laboratories, i.e. atomic fountains lab (FO1 and FOM), optical clock lab. The noises added by the links are cancelled using the active noise compensation technique (see subsection 2.3.1 for more details). In addition, the microwave signal from one of four H-masers provides the connection to the international atomic time (TAI) and the local timescales, and to satellite time-transfer systems, such as the global positioning system (GPS) and two-way satellite time and frequency transfer (TWSTFT). BIPM: The International Bureau of Weights and Measures; FO1, FO2, and FOM: the atomic fountain clocks; PLL: phase-lock loop. Taken from [66].

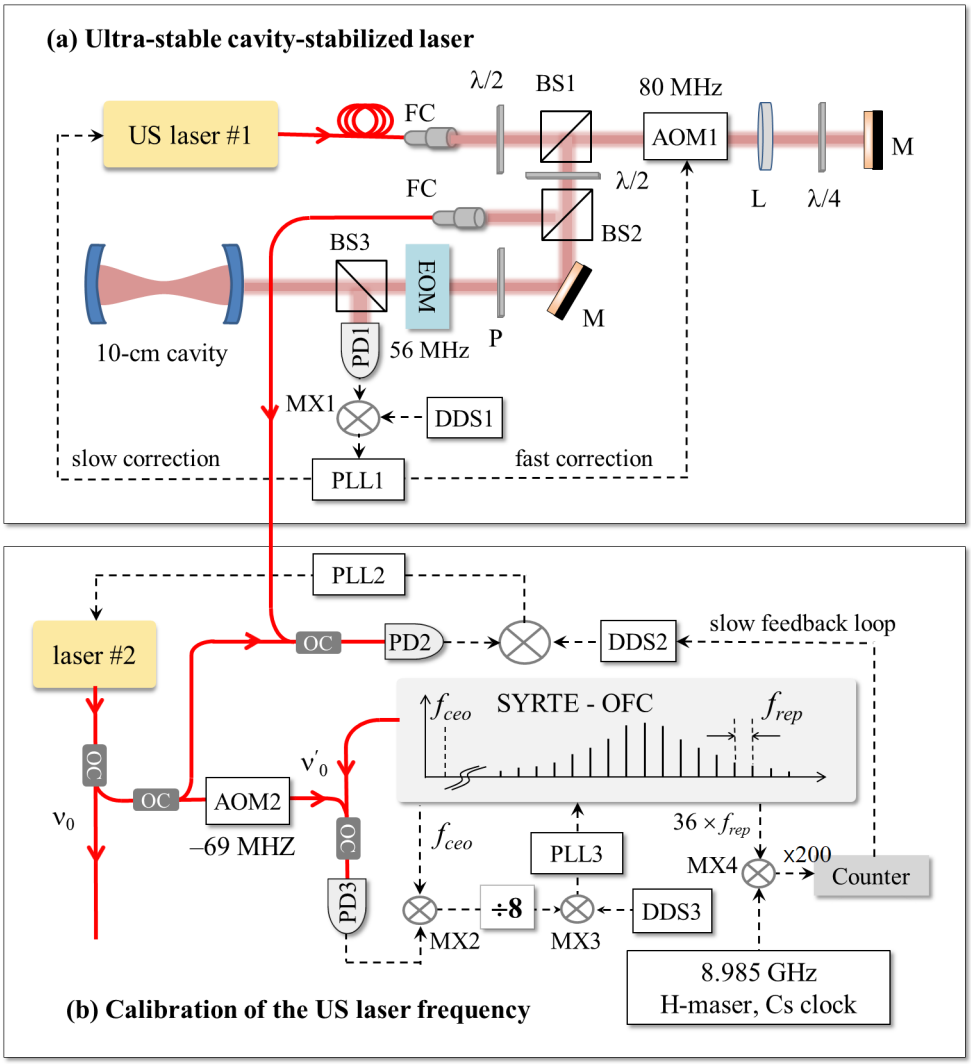

Figure 2.4 – (a) Scheme of the frequency stabilization setup of the 1.54 μm laser on the high finesse cavity, adapted from [188]. (b) Generation of an optical local oscillator at LNE-SYRTE: the laser #2 is phase-locked onto the US laser #1 and repetition rate (f_{rep}) of an optical frequency comb of LNE-SYRTE (SYRTE OFC) is phase-locked onto the laser #2 for the measurement of its absolute frequency and the cancellation of the frequency drift of the cavity. A frequency difference between the 36^{th} harmonic of f_{rep} and the 8.985 GHz signal is made equal to 275 kHz and then multiplied by 200 before being counted by a radio-frequency counter. US laser: ultra-stable laser, BS1-3: beam splitters, MX1-4: mixers, FC: fiber coupler, AOM: acousto-optic modulator, EOM: electro-optic modulator, L: lens, P: polarizer, M: mirror, PLL: phase lock loop, OFC: optical frequency comb, PD: photodiode, $\lambda/2$: half-wave plate, $\lambda/4$: quarter-wave plate, DDS: direct digital synthesizer.

pressure below 10^{-7} mbar and thermally isolated by one gold-coated aluminium thermal shield. The whole experimental system is mounted on a commercial vibration isolation platform and set in a "white" wooden box for acoustical damping [114].

After coupling to free space, most of the output power of the fiber laser passes through the beam splitter BS1 and towards an acousto-optic modulator (AOM1), as shown in Figure 2.4(a). After double-passing through the AOM1, the laser beam is frequency-shifted by 160 MHz and is then reflected by the first beam splitter BS1 toward a second beam splitter BS2, that splits the laser beam into two parts. The first part is directed to the US cavity for the frequency stabilization, while the other part is coupled in a fiber to be used as an US signal. For the stabilization, the laser is phase-modulated by an electro-optic modulator (EOM) and then fed to the cavity. A third beam splitter BS3 guides the cavity reflected laser beam to a photodiode (PD1, Figure 2.4(a)), where a beat-note signal between the optical carrier and two sidebands far detuned from the cavity resonance (PDH method) is detected. In the mixer MX1, this beat-note signal is demodulated by a signal only phase-shifted from the EOM modulation, in order to maximize the amplitude of the resulting error signal. At the mixer output, an error signal is generated and then converted into a fast- and a slow-correction signal by a phase-lock loop (PPL1, Figure 2.4(a)). Finally, the laser frequency is stabilized to the cavity by feeding the fast correction to the AOM and the slow correction to the internal piezo-electric actuator of the laser.

Performances of the first US laser

A beat-note signal between two similar cavity-stabilized lasers was generated to evaluate the performances of the first US laser (see [188] for more details). The frequency noise power spectrum desity (PSD) of the beat-note signal was analysed with a fast Fourier transform (FFT) spectrum analyzer. Results are plotted in Figure 2.5(a). In the range from 1 Hz to 10 kHz, it is well below 10^{-1} Hz^2/Hz. By dividing by a factor of 2, the frequency noise of each laser is 5×10^{-2} Hz^2/Hz, giving a laser linewidth below 1 Hz considering a white noise at this level [188].

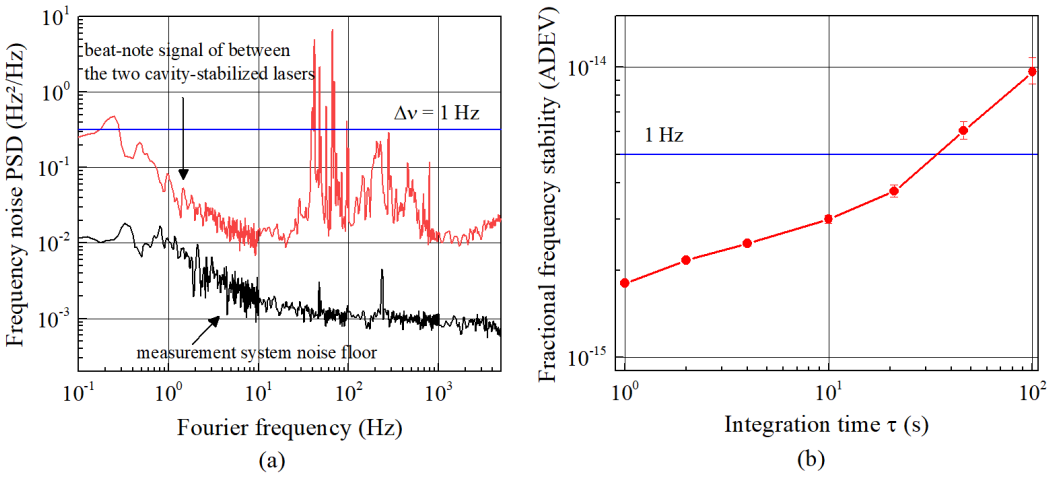

Figure 2.5 – (a) Frequency noise PSD and (b) fractional frequency stability of the beat-note signal between the two cavity-stabilized lasers located at LNE-SYRTE (a 0.3 Hz/s drift has been removed). Taken from [188].

The frequency stability of the beat-note signal was determined by calculating the overlapping Allan deviation (ADEV) of the beat-note signal frequency acquired with a Π-type counter (see Appendix A). Figure 2.5(b) shows the fractional frequency stability of the beat-note signal after a linear drift of about 0.3 Hz/s is removed. It is below 2×10^{-15} at 1 s averaging time. For measurement times smaller than 30 s, the frequency stability is below 1 Hz. The frequency stability of the cavity-stabilized lasers in the long-term is mainly limited by the thermal noise effects of the mirrors and the ambient temperature fluctuation [188].

2.2.2.2 Second US laser stabilized to the "CUS" cavity

Recently, another US laser has been setup at LNE-SYRTE. It is based on an extended cavity laser diode at 1.54 μm locked to another high finesse cavity, named "CUS" (see [187] for more details). The "CUS" cavity was realized and assembled by SODERN Space Company and then transported to LNE-SYRTE for tests. It is a 10-cm long cylinder that is rigidly held at its mid-plane by an engineered mechanical interface providing an efficient decoupling from thermal and vibration perturbations [187]. This US laser is the main optical frequency reference signal used for the studies presented in the manuscript.

Performances of the second US laser

The frequency noise PSD of the second US laser was evaluated using the beat-note signal between this laser and the first US laser. Figure 2.6(a) shows the frequency noise PSD of the beat-note signal. It is about 1×10^{-2} Hz^2/Hz for Fourier frequency between 10 Hz and 1000 Hz. It is dominated by the noise of the first US laser [187].

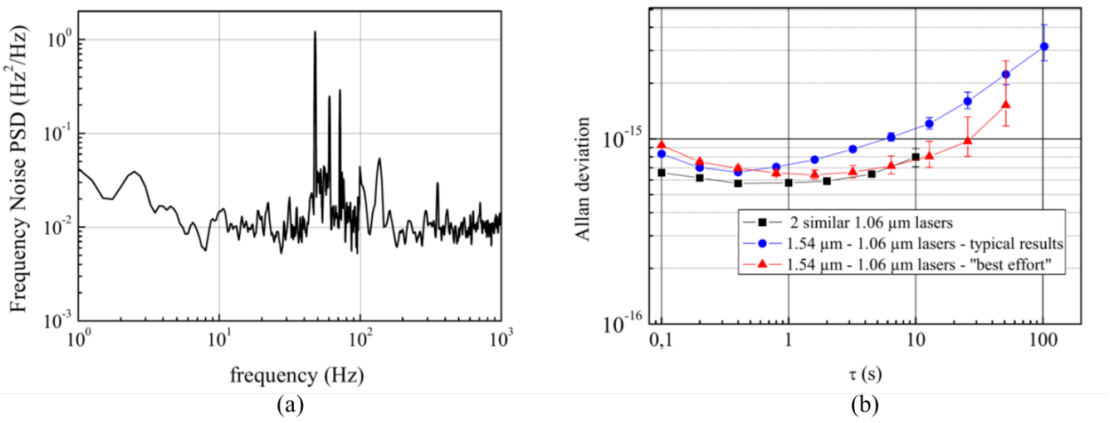

Figure 2.6 – (a) Frequency noise power spectrum density of the beat-note signal between the second "CUS" cavity-stabilized laser and the "white" cavity-stabilized laser (see text). (b) Fractional frequency stability (Allan deviation). Blue circles: typical stability of the beat-note signal between a 1.06 μm ultra-stable laser from [189] and the 1.54 μm "CUS" cavity-stabilized laser. Red triangle: best results (1 Hz/s linear drift removed). Black squares: frequency stability of the beat-note signal between two equivalent 1.06 μm lasers.

To further evaluate the fractional frequency stability of the second US laser, a 1.06 μm laser with frequency stability of around 4×10^{-16} at 1 s [189] was used as a reference. The gap between the second US laser and the reference laser was bridged by an OFC [187]. A beat-note signal between these lasers was generated. As shown in Figure 2.6(b),

the fractional frequency stability of this beat-note signal is lower than 1×10^{-15} for averaging times between 0.1 to 6 s after removing a linear drift of 2.5 Hz/s (blue curve) and is typically around 8×10^{-16} at 1 s (blue curve). It is more than two times better than the first US laser.

In short, the US signals at 1.54 μm, generated by the two cavity-stabilized lasers ("white" and "CUS" cavities), exhibit fractional frequency stabilities of about 10^{-15} at 1 s, corresponding to a sub-hertz laser linewidth. However, they drift in frequency in the long-term and we also have poor knowledge of their absolute frequency. For the optical frequency transfer between distant laboratories, their absolute frequencies should be continuously measured against the primary reference signal, and then should be de-drifted (i.e. their frequency drift should be cancelled), that is the main subject of the next subsection.

2.2.3 Calibration of the US laser frequency to the primary standards

We now present how the absolute frequency of an ultra-stable laser is calibrated against the primary standards via an optical frequency comb (OFC) at LNE-SYRTE. The calibration is performed by using the following steps, as shown in Figure 2.4(b).

First, a slave laser diode (laser #2) is stabilized to the US laser #1. To this end, these lasers are combined on the photodiode PD2, where a beat-note signal is generated. The stabilization is performed by phase-locking the beat-note signal to a radio-frequency signal (produced by the tunable synthesizer DDS2) via the phase-lock loop PLL2.

After that, the repetition rate (f_{rep} ~250 MHz) of an OFC is phase-locked to laser #2 in order to measure the absolute frequency of this laser. To this end, frequency ν_0 of the latter is shifted by -69 MHz in an acousto-optic modulator (AOM2, Figure 2.4(b)). On the photodiode PD3, a beat-note signal $\Delta = \nu_0' - (nf_{rep} + f_{ceo})$ between the $\nu_0' = \nu_0 - 69$ MHz signal and the nearest optical mode $nf_{rep} + f_{ceo}$ of the OFC ($n \sim 800\,000$ the comb mode number and f_{ceo} the comb frequency offset) is generated. After removing f_{ceo} by mixing the beat-note signal with f_{ceo}, detected elsewhere, in the mixer MX2 and frequency-dividing by a factor of 8, the obtained beat-note signal at frequency $(\nu_0' - nf_{rep})/8$ is compared to a radio-frequency signal (produced by the synthesizer DDS3) in the mixer MX3. The resulting error signal is then converted into a fast- and a slow-correction signal by the phase-lock loop PLL3. The repetition rate is then phase-locked onto the laser #2 by applying the fast correction to an intra-cavity electro-optic modulator (EOM) (bandwidth > 400 kHz) and the slow correction to a piezo-electric actuator controlling the cavity length of the OFC [190] (bandwidth of a few kilohertz).

Finally, the 36^{th} harmonic of f_{rep} is continuously measured with a 1 s measurement time against the microwave reference signal at 8.985 GHz (see subsection 2.2.1) by a radio-frequency counter. The difference between 8.985 GHz and $36 \times f_{rep}$ is made equal to 275 kHz, and then multiplied by 200 before being counted. This way, the detection noise is larger than the counter noise. A slow feedback loop, based on this measurement, is used to correct the drift of laser #2 by applying a correction signal to the direct digital synthesizer DDS2. By determining the integer n (see Ref. [190] for more details), the absolute frequency of the laser #2 at frequency ν_0 can be easily derived from the f_{rep} measurement. It is then traceable to the primary standards with a 4×10^{-14} total absolute uncertainty, limited by the Cs fountain stability at 1 s measurement time (the

Cs fountain being used to measure the H-Maser frequency). In the following, laser #2 will be denoted as the US reference laser. The spectral properties of the laser are then transferred to LPL through an optical fiber link that will be described in the next section. The frequency ν_0' measured once per second is saved in real time on a repository accessible via hyper-text transfer protocol (http).

2.3 Transfer of a stabilized frequency reference between LNE-SYRTE and LPL

In this section, we first present the basic principle of the optical frequency transfer via an optical fiber with active noise compensation, the noise added during the propagation being actively cancelled. We then describe the 43-km long optical fiber link that allows the US optical reference signal of LNE-SYRTE to be transferred to LPL without any degradation of its stability.

2.3.1 Principle of fiber based optical frequency transfer

The principle of the optical frequency transfer with active noise compensation fiber link is shown in Figure 2.7. The optical signal arises from an US laser and its electric field is given by

$$E_{local}(t) = A_1 \cos\left(\omega_0 t + \varphi_{local}\right), \tag{2.1}$$

where A_1, ω_0, and φ_{local} are respectively the amplitude, angular frequency, and phase of the signal at the "local" end. The US laser output is separated into two branches by an optical coupler that is used to set up a Michelson interferometer. The optical signal is frequency shifted in an acousto-optical modulator (AOM1, angular frequency ω_{AOM}) which will be used in a feedback loop for noise compensation (see below). After a light propagation delay τ, the signal arrives the "remote" end.

During propagation, the mechanical vibrations and the environmental temperature fluctuations change the physical fiber length and the speed of the signal propagation and, therefore degrade the signal. A part of the incoming signal is sent back to the "local" end in order to address this issue (see below). A second acousto-optic modulator (AOM2) is set as a "marker" AOM at the "remote" end to distinguish the return signal from parasitic reflections occurring along the link.

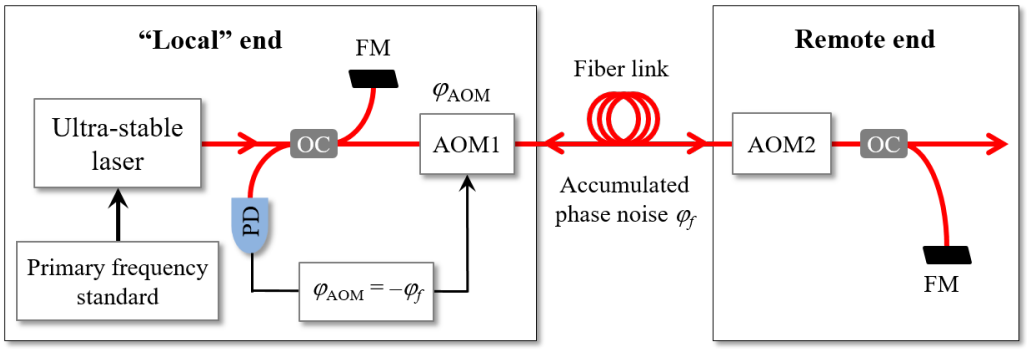

Figure 2.7 – Principle of the actively noise compensated link. AOM1 and AOM2: acousto-optic modulators, FM: Faraday mirror, PD: photodiode, OC: optical coupler.

At the "remote" end, the signal after a one-way transfer is thus given by

$$E_{remote}(t) = A_2 \cos\left[(\omega_0 + \omega_{AOM1} + \omega_{AOM2})\, t + \varphi_{local} + \varphi_{AOM} + \varphi_f\right], \tag{2.2}$$

in which A_2 denotes the amplitude of the signal at the "remote" end, φ_{AOM} refers to the phase shift produced by the acousto-optic modulator AOM1, and φ_f represents the added fiber phase noise, introduced through the fiber link.

We assume that the fiber phase noise due to the environment perturbations on the fiber link is equal in the forward- and backward-direction. In order to compensate the fiber phase noise, a part of the incoming signal is send back the "local" end. There, the electric field of the return signal after a round-trip is then given by

$$E_{rt}(t) = A_3 \cos\left[(\omega_0 + 2\omega_{AOM1} + 2\omega_{AOM2})\, t + \varphi_{local} + 2\varphi_{AOM} + 2\varphi_f\right]. \tag{2.3}$$

where A_3 denotes the amplitude of the signal at the "local" end after a round-trip. The phase difference between the input phase and the round-trip phase at the "local" end is given by $\Delta\phi = (2\omega_{AOM1} + 2\omega_{AOM2})\, t + 2\varphi_{AOM} + 2\varphi_f$. The resulting beat-note signal between the input signal and the return signal after a round-trip at frequency $2\omega_{AOM1} + 2\omega_{AOM2}$ is phase-locked to a radio-frequency reference signal using a phase-lock loop that generates a correction signal applied to AOM1 (see Figure 2.7). The phase difference $\varphi_{AOM} - \varphi_f$ is thus forced to be zero. Following equation 2.2, the electric field at the remote end after being compensated is given by

$$E_{remote}(t) = A_2 \cos\left[(\omega_0 + \omega_{AOM1} + \omega_{AOM2})\, t + \varphi_{local}\right], \tag{2.4}$$

in which the propagation-induced phase noise is cancelled. This setup allows the noise added by the fiber link during propagation to be compensated in real time.

2.3.2 Optical frequency transfer between LNE-SYRTE and LPL

In this subsection, we first present the experimental set-up for the dissemination of the US optical reference signal via a fiber link, connecting LNE-SYRTE with LPL. Then, we show the performance of this link. Finally, we briefly describe the transfer of an US accurate radio-frequency reference between the two laboratories through the same link.

2.3.2.1 Experimental setup

Figure 2.8 shows the experimental setup allowing us to distribute the US optical reference signal over 43 km from LNE-SYRTE to LPL via an active noise compensated link. This setup can be separated in two parts. The first part includes some short-length fiber links to transfer the US signal from the laser #2 to the input of the 43-km link to LPL. This part has slightly evolved during the last three years and we will describe below the configuration one used for the methanol absorption frequency measurement in June and October 2017, that will be described in chapter 4. The second part is the 43-km link consisting of two parallel optical fibers of 43 km.

The transfer of the ultra-stable laser to the link input end

The blue area of Figure 2.8 corresponds to a simplified sketch of the US laser described in Figure 2.4 and subsection 2.2.2. The US reference signal at frequency ν_0 ~1.54 μm from laser #2 is injected into a short length fiber of 30 m and transferred to another

experimental room where the setups dedicated to two long-haul optical fiber links (the 43-km link and another longer-length link) are operated. This short fiber link is a compensated link composed of two acousto-optic modulators (AOM2 and AOM3) and two Faraday mirrors (FM1 and FM2). The propagation-induced noise is cancelled by applying a correction signal to AOM2 using the phase-lock loop PPL2 (see section 2.2.1). The short link is followed by two repeater laser stations (RLS #1 and RLS #2) which are the starting points of the two long-haul links. Each link has two fibers, the first one to transfer the reference signal from LNE-SYRTE to other laboratories and the second to evaluate performances of the frequency transfer. The link starting from RLS#1 is the 4-span cascaded link of 2 × 705 km between LNE-SYRTE and University of Strasbourg mentioned in subsection 1.2.4. The link starting from RLS #2 is the 43 km-long optical fiber link to LPL.

In RLS #1, a 1.54 μm laser (laser #3) is phase-locked to laser #2 signal using PLL3, PD3, and DDS3. Details about links N and N+3 to Strasbourg can be found in Ref. [191]. An end-user output of RLS #1 is fed to RLS #2 via a short free-running fiber link of 5 m with an acousto-optic modulator (AOM5, 37 MHz). A Faraday mirror FM6 positioned in RLS #2 is used to reflect back the laser beam to the photodiode PD8 at the output of the RLS#1 station via a the Faraday mirror FM5. The round-trip delay fluctuation of this 5-m link is then detected at a frequency of 74 MHz on the photodiode PD8. The acquired data represent the free-running round-trip frequency noise of the link that can be compensated in post-processing [191].

Note that the two RLSs and the short 5-m fiber link were lately replaced by a single multi-branch station enabling to feed two or more fiber links.

The 43-km link with active noise compensation

In RLS #2, laser #4 is phase-locked to the laser #3 signal using PLL5, PD5, and DDS5. Laser #4 is split into two branches and fed into two fiber links to LPL, which constitute a so-called hybrid link [193]. The first fiber (F1) is used for the optical frequency transfer from LNE-SYRTE to LPL using the active noise compensation (ANC) method while evaluation of the performance of this ANC setup is carried out with the second fiber (F2) using the local two-way (LTW) method [192, 193] (see below).

Let us consider the optical transfer of the US laser from LNE-SYRTE to LPL on fiber F1. In RLS #2, the signal from laser #4 is frequency-shifted using AOM6, to which the feedback for noise compensation is applied. The light is then injected into fiber F1 and transferred to LPL. At the remote end of the link (LPL), to compensate the propagation-induced phase noise, part of the laser beam is reflected back to the local end (LNE-SYRTE) by a partial Faraday mirror (p-FM). The signal is also frequency-shifted in AOM7 in front of the p-FM in order to distinguish the reflected signal from spurious reflections.The transmission losses of around 20 dB of laser #4 signal are compensated using a bi-directional erbium-doped fiber amplifier (bi-EDFA) on the fiber F1.

At LNE-SYRTE, a beat-note signal between the round-trip signal and the local reference signal from the laser #4 reflected by the Faraday mirror FM7 is detected on photodiode PD6. The resulting beat-note signal is then phase locked onto a RF signal from the direct digital synthesizer (DDS6) using phase-lock loop PPL6. The results in compensating the propagation induced phase noise in fiber F1, the correction signal being driving frequency of the AOM6 by phase-lock loop PLL6.

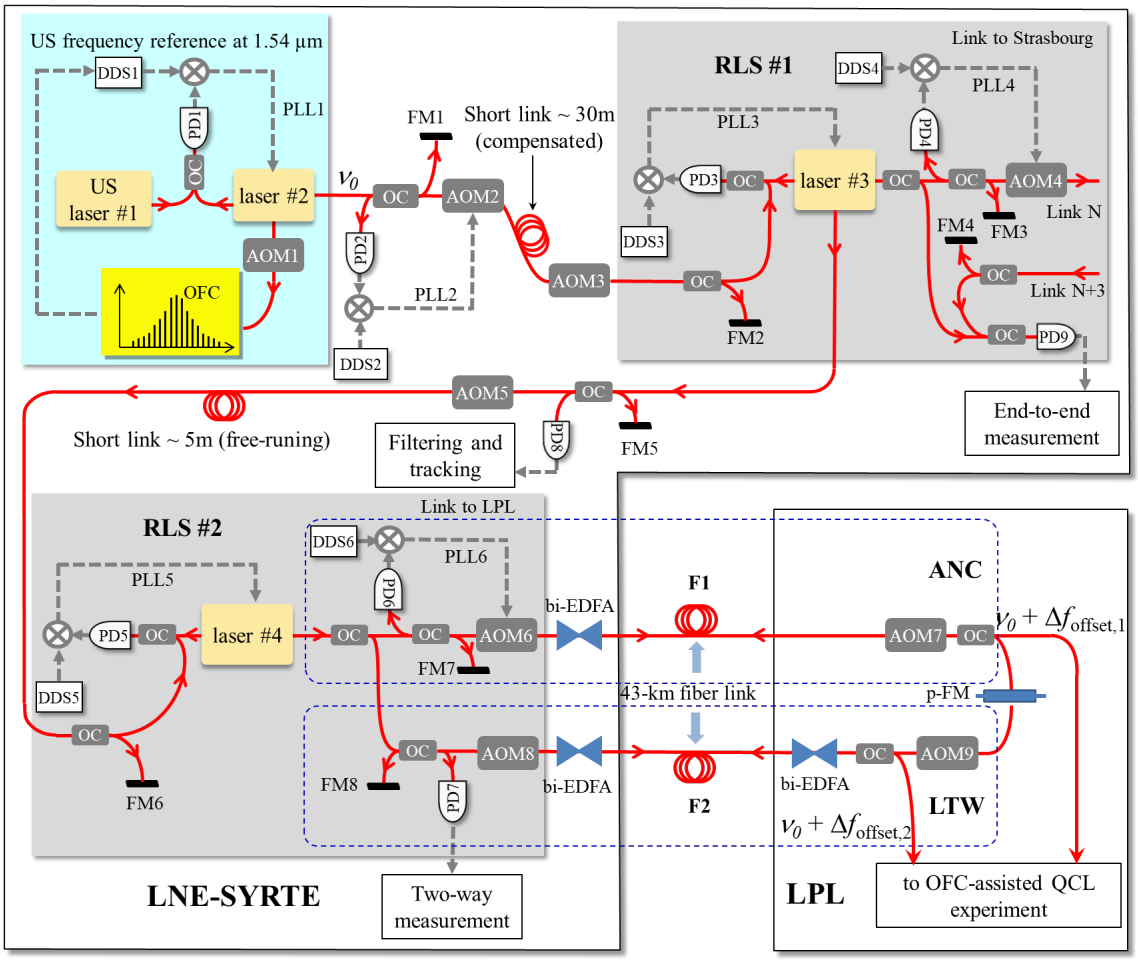

Figure 2.8 – Optical fiber links between LNE-SYRTE and LPL. A 1.54 μm ultra-stable (US) near-IR frequency reference signal calibrated to primary frequency standards is transferred from LNE-SYRTE to our lab via an upper fiber (F1) using active noise compensation (ANC). Frequency comparison between the two labs is performed with a lower fiber (F2) using the local two-way method (LTW). OFC: optical frequency comb, PLLs: phase lock loops, OCs: optical couplers, PDs: photodiodes, AOMs: acousto-optic modulators, RLSs: repeater laser stations, DDSs: direct digital synthesizers, F1: the first fiber, F2: the second fiber, bi-EDFAs: bi-directional erbium-doped fiber amplifiers, p-FM: partial Faraday mirror, and FMs: Faraday mirrors. Adapted from [191, 192].

The performances of the frequency transfer are evaluated using two-way frequency comparison in fiber F2 as detailed in the next section.

Two-way frequency comparison using fiber F2

This method is based on the frequency comparison of laser signals originating from both ends of the fiber link. It gives access to the sum of the residual propagation-induced phase noise in the fibers F1 and F2, thus giving an upper limit [1] of the residual propagation-induced phase noise for the signal transmitted from LNE-SYRTE to LPL. It was established to test the reciprocity of noise propagation on this link [192].

We now detail how the two-way phase noise is detected. The signal transferred to LPL through fiber F1, considered as a virtual ultra-stable laser (laser #5), is partly transmitted through a partial Faraday mirror (p-FM, Figure 2.8) to the fiber F2 and transferred back to LNE-SYRTE. At the LNE-SYRTE end, one detects a beat-note signal between this signal and laser #4 signal on photodiode PD7. This beat-note signal exhibits the following phase noise

$$\phi_{\mathrm{PD7_A}} = -\phi_{L4} + \phi_{L5} + \phi_{BN2}, \tag{2.5}$$

where ϕ_{L4} and ϕ_{L5} are the phases of laser #4 and the virtual laser #5, respectively and ϕ_{BN2} is the F2 phase noise arising from the backward propagation from LPL to LNE-SYRTE. The photodiode PD7 also detects a beat-note signal (at a different frequency) between laser #4 signal and the round-trip signal in fiber F2 from LNE-SYRTE to LPL and back which exhibits the following round-trip fiber noise

$$\phi_{\mathrm{PD7_B}} = \phi_{FN2} + \phi_{BN2}, \tag{2.6}$$

in which ϕ_{BN2} is the forward phase noise in the fiber F2. By combining both beat-note signals, the two-way phase noise ϕ_{TW} is given by:

$$\phi_{TW} = \phi_{\mathrm{PD7_A}} - \frac{1}{2}\phi_{\mathrm{PD7_B}} = (-\phi_{L4} + \phi_{L5}) - \frac{1}{2}\left(\phi_{FN2} - \phi_{BN2}\right), \tag{2.7}$$

where the first and second terms give the residual propagation noise in fibers F1 and F2, respectively.

Output signal at LPL

At LPL, two near-IR reference output signals are obtained at the link output and have been used as frequency references for the methanol frequency measurements presented in this work (see chapter 4). One signal of frequency $\nu_0 + \Delta_{offset,1}$ is extracted at the output of the compensated link (on fiber F1). The other one of frequency $\nu_0 + \Delta_{offset,2}$, is extracted from the free-running link using fiber F2. This latter signal exhibits the link frequency noise, which is negligible compared to our experimental sensitivity (see below). Here $\Delta_{offset,1}$ and $\Delta_{offset,2}$ are the constant offset frequencies between LNE-SYRTE and LPL, given by the values of the frequencies provided by DDS2, DDS3, and DDS5 and the frequencies driving AOM2, AOM3, AOM5, AOM6, AOM7, AOM8, and AOM9.

1. The residual propagation phase noise power spectrum density (PSD) in fiber F1 is expected to be between a half and a quarter of the two-way noise PSD due to high noise correlations between the two fibers [114].

2.3.2.2 Performances of the compensated link

Performances of the compensated link were evaluated by measuring its fractional frequency stability and frequency noise PSD [114, 192].

Fractional frequency stability

The frequency stability was evaluated by counting the beat-note signals detailed in the previous Section and measured on photodiode PD7 (Figure 2.8) either with a Π-type or a Λ-type counter and by processing the data to determine the frequency stability associated to ϕ_{TW} (see Equation 2.7). The frequency data were then processed using the overlapping Allan deviation (ADEV) and the modified Allan deviation (MDEV) (see subsection 1.2.1). Figure 2.9 (black dots) displays the free-running round-trip noise of the fiber F2. It is below 2×10^{-14} for averaging time between 1 s and 10^4 s and reaches a minimum value of 10^{-15} at around 400 s. The frequency stability of the hybrid fiber link of 86 km is displayed as red and blue dots on figure 2.9. ADEV and MDEV calculated from Π-type counter are around 6×10^{-16} at 1 s averaging time and then decrease with increasing averaging time with slopes of -1 and -3/2 (red curves) as expected for white phase noise, respectively. Stabilities calculated from the Λ-type are around 6×10^{-17} at 1 s. The corresponding MDEV decreases to a noise floor around 2×10^{-20} at 10^3 s (blue curves).

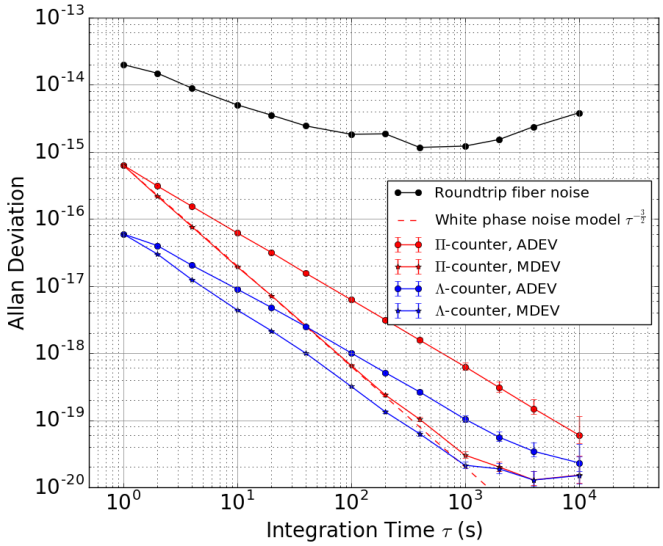

Figure 2.9 – Fractional frequency stability of the hybrid fiber link of 86 km in terms of the Allan deviation with a Π type counter and a Λ type counter. ADEV: the overlapping Allan deviation, MDEV the modified Allan deviation. Taken from [192].

Accuracy of the link

As demonstrated in [192], the accuracy of the hybrid link is estimated by calculating the mean offset frequency of the two-way signal. The mean value is $\sim 3 \times 10^{-20}$ with a statistical uncertainty of $\sim 3.9 \times 10^{-20}$ and $\sim 2.8 \times 10^{-20}$ given by both the long-term ADEV and MDEV at 40 000 s with Π-data and Λ-data respectively. The accuracy of link is limited by the statistical uncertainty contribution, at a conservative level of 4×10^{-20}.

Frequency noise power spectral density

In order to measure the frequency noise PSD, a 86-km compensated link was implemented by removing the partial Faraday mirror. Therefore, the local and remote ends are located at LNE-SYRTE as described in [114, 188, 194]. With phase noise compensation, the frequency noise PSD of a beat-note signal between the local laser beam and the beam transmitted through the 86-km length fiber was measured with a fast Fourier transform spectrum analyzer [193]. It is below 1×10^{-2} rad^2/Hz and shows a servo bump at 400 Hz. Figure 2.10 also displays the phase noise PSD of the free-running link (black curve) and of the US laser locked to the "CUS" cavity (see subsection 2.2.2). We can see that the noise of the compensated link is below the noise of this US laser.

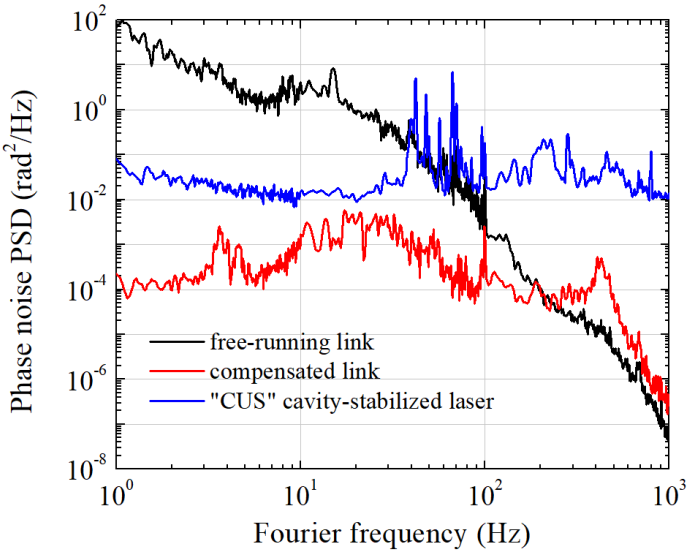

Figure 2.10 – Phase noise PSD of the 86-km free-running link (black curve), compensated fiber link (red curve), and the ultra-stable laser locked to the "CUS" cavity (blue curve, see subsection 2.2.2). Taken from [141, 188].

In short, the fractional frequency stability of the compensated link and the noise added by the link are below those of the US lasers. Therefore, the spectral purity properties of the US lasers are not degraded during the optical frequency transfer between LNE-SYRTE and LPL.

2.3.2.3 Transfer of radio frequency reference

We also use the two fibers between LPL and LNE-SYRTE to transfer a high precision ultra-stable 200 MHz signal. At LNE-SYRTE, a radio-frequency signal at frequency 200 MHz is synthesized from the microwave reference signal obtained using the CSO and the H-maser (see subsection 2.2.1). It is then used to modulate the intensity of an auxiliary laser diode at 1.54 μm [195]. The laser beam is then injected in the 43-km free-running fiber link and transferred to LPL. At LPL, the reference signal is detected by a fast photodiode.

As mentioned above, the frequency stability of the uncompensated link is below 2×10^{-14} between 1 s and 10 000 s, therefore the fractional uncertainty around 4×10^{-14} of the 200 MHz signal is not degraded during the transfer. At LPL, a 10 MHz signal

synthesized from the obtained 200 MHz signal is used as a local RF reference signal since 2018.

2.4 Local radio frequency references

A radio-frequency reference is typically a 10 MHz signal that is used for synchronization of all frequency counters and synthesizers in an experiment. In this section, we present the 10 MHz radio-frequency reference signal at LPL. It is an ultra-stable quartz oscillator disciplined to the global positioning system (GPS) signal. Moreover, we also show how the metrological characteristics of this signal were evaluated against the aforementioned 10 MHz signal synthesized from the radio-frequency reference signal provided by LNE-SYRTE.

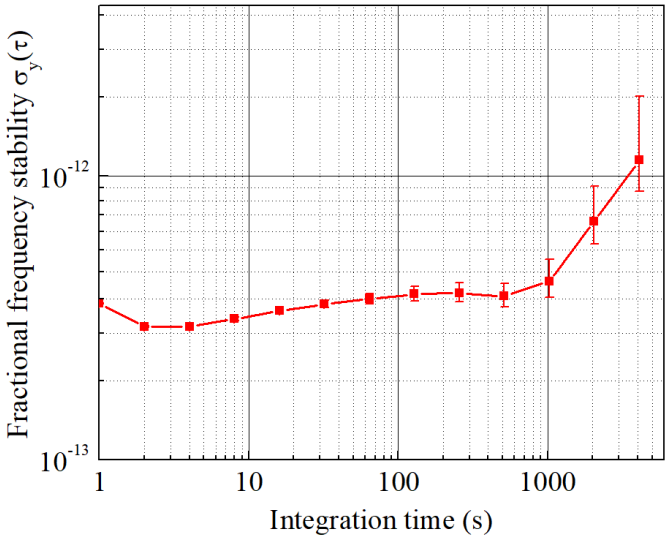

Figure 2.11 – Fractional frequency stability of the LPL ultra-stable quartz oscillator. It is measured using the beat-note signal between a remote near-IR signal transferred from LNE-SYRTE and a tooth of an OFC, the comb repetition rate and offset frequency of which are locked to the signal of quartz oscillator signal. Note that the 1-s stability is slightly degraded by the measurement floor which was not optimised. Taken from [141].

Figure 2.11 displays the frequency stability of our ultra-stable quartz oscillator. It was measured by locking the repetition rate and the frequency offset of a 1.54 μm fiber OFC at LPL (see section 2.6) to the 10 MHz quartz signal and by measuring the frequency fluctuations of the beat-note signal between an optical mode of the OFC and the remote US near-IR reference signal transferred from LNE-SYRTE (see subsection 2.2.2). The frequency stability of the oscillator is around 3×10^{-13} for averaging times between 1 s and 1000 s. However it is sensitive to thermal aging and other effects, leading to a frequency drift at mid- and long-term time scales (averaging time $\tau > 10$ s), as shown in Figure 2.11.

In order to control its frequency and remove the frequency drift, the quartz oscillator is disciplined on a GPS signal provided by a receiver (GPS E8-X, Quartzlock) using a servo loop with a bandwidth of 1000 s. In order to evaluate the frequency fluctuation of this GPS-disciplined quartz oscillator, its frequency is measured against the 200 MHz

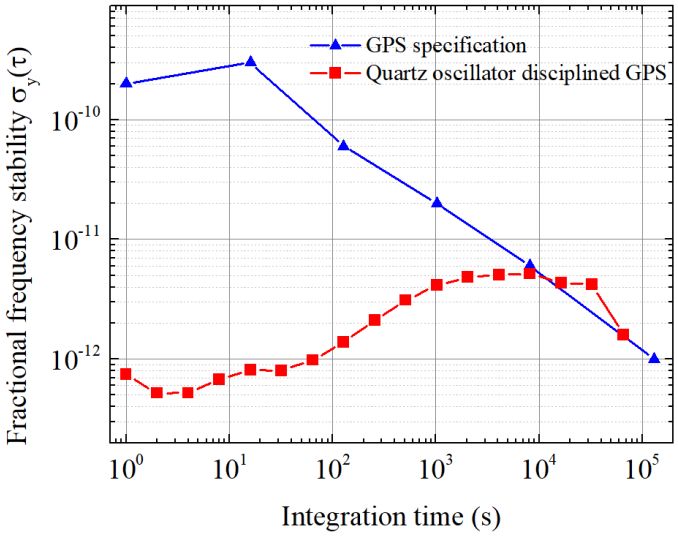

Figure 2.12 – Fractional frequency stabilities of the ultra-stable quartz oscillator disciplined on the GPS (red squares) and of the GPS signal delivered by our receiver (blue circles).

reference signal transferred from LNE-SYRTE (see subsection 2.3.2.3). Figure 2.12 shows the fractional frequency stability of the GPS-disciplined quartz oscillator. It is below the 10^{-11} level both at the short- and long-term time scales. This stability is good enough for our high-precision measurements at present and in the future.

It is noted that the GPS-disciplined quartz oscillator is not SI-traceable. Its accuracy is evaluated by comparing with the SI-traceable 200 MHz from LNE-SYRTE. Typically, we obtain an accuracy below 10^{-11}, as shown in Figure 2.12.

2.5 Widely tunable and ultra-stable optical local oscillator at 1.54 μm

Before my thesis, the remote US near-IR reference from LNE-SYRTE was used to phase-lock a local laser diode at 1.54 μm for signal regeneration. A QCL at around 10.3 μm was then stabilized to the repetition rate of an OFC, itself phase-locked to the local laser diode. Since the frequency of the local laser diode is fixed, the repetition rate of the OFC and in turn the QCL frequency are also fixed. Frequency tuning of the QCL was achieved by scanning the frequency of the radio-frequency oscillator used to phase-lock the QCL to the OFC. However, the QCL frequency cannot be tuned over more than 125 MHz (half the repetition rate of the OFC). We now report the development of an ultra-stable and tunable optical local oscillator (OLO) at 1.54 μm. This setup allows the OFC and the QCL to be continuously tuned on a wider range when they are phase-locked to the OLO (see section 2.7 and chapter 3).

2.5.1 Experimental setup

The OLO is based on a laser diode emitting at 1.54 μm. An electro-optic modulator (EOM) is used to generate sidebands around the laser diode's carrier frequency. As detailed below, one of these sidebands is then phase-locked to the incoming near-IR

reference signal from LNE-SYRTE. Thus its frequency has a fixed frequency offset respect to the remote reference signal. The laser diode carrier frequency can thus be tuned by scanning the frequency driving the EOM.

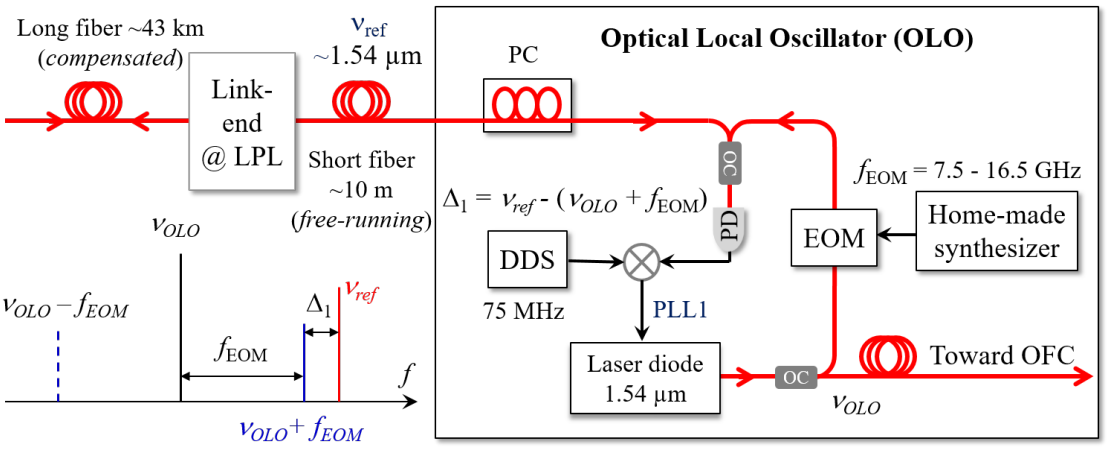

Figure 2.13 – Experimental setup for frequency stabilization of the optical local oscillator (OLO) upper sideband at 1.54 μm onto the near-IR reference from LNE-SYRTE. Frequency tuning of the OLO carrier results from tuning the frequency driving the EOM generating the sidebands. PC: polarization controller, PD: photodiode, PLL: phase lock loop, EOM: electro-optic modulator, DDS: direct digital synthesizer, OFC: optical frequency comb, OC: optical coupler.

Figure 2.13 shows the experimental setup of the OLO. The near-IR reference signal sent by LNE-SYRTE is transferred from the link end at LPL to the OLO setup via a short 10-m long uncompensated fiber link. The phase noise added by this link is negligible as detailed in subsection 3.4.2. Its polarization is adjusted by a fibered polarization controller. Some power of the local laser diode is sent to an EOM at 1.55 μm, generating two tunable sidebands of frequencies $\nu_{OLO} \pm f_{EOM}$ on both sides of the carrier frequency ν_{OLO}. Here, f_{EOM} is the EOM frequency precisely controlled by a home-made phase-jump-free microwave synthesizer based on a YIG (Yttrium Iron Garnet) oscillator, which has a tuning range of 9 GHz (see subsection 2.5.2 for more details).

We then detect a beat-note signal Δ_1 between the reference signal ν_{ref} and the upper sideband $\nu_{OLO} + f_{EOM}$ on a photodiode (PD1, Figure 2.13). The upper sideband is then phase-locked to ν_{ref} by referencing this beat-note signal to a fixed radio-frequency signal at $\Delta_1 = 75$ MHz, provided by a DDS, via a phase-lock loop (PLL1). This PLL uses a phase-frequency detector which imposes the sign of the beat-note signal $\nu_{ref} - (\nu_{OLO} + f_{EOM})$ to be positive and equal to Δ_1,

$$\Delta_1 = \nu_{ref} - (\nu_{OLO} + f_{EOM}). \tag{2.8}$$

Figure 2.14 shows the in-loop beat-note signal spectrum between the reference signal and the upper sideband of the OLO detected on a spectrum analyser when the phase-lock loop is closed. The bumps indicate that the servo bandwidth is around 120 kHz. It is high enough to transfer the coherence properties of the near-IR reference signal to the

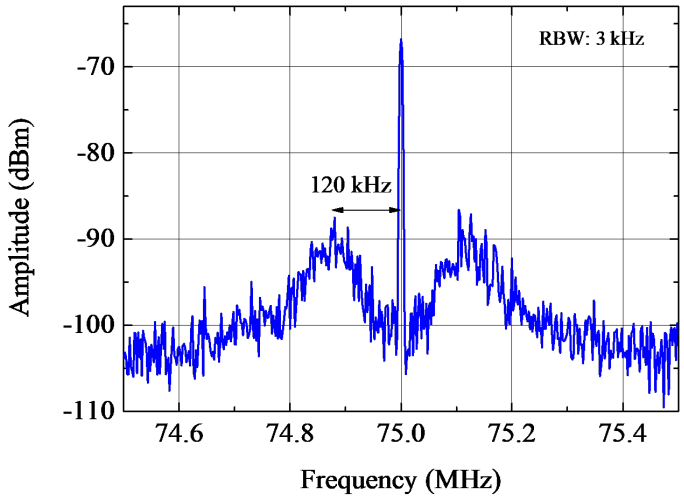

Figure 2.14 – Beat note at 75 MHz between the upper sideband of the OLO and the near-IR reference when the phase lock loop is closed. The bumps indicate that the servo bandwidth is around 120 kHz. RBW: resolution bandwidth.

OLO. The frequency of the OLO carrier is consequently given by

$$\nu_{OLO} = \nu_{ref} - f_{EOM} - \Delta_1. \tag{2.9}$$

Scanning the EOM frequency over 9 GHz leads to a widely tunable frequency stabilized OLO. We can sweep ν_{OLO} with a maximum rate of 500 MHz/s (limited by the bandwidth of a servo loop of the home-made microwave synthesizer, see below) and a minimum time-step of 1 ms.

2.5.2 Low-phase noise microwave synthesizer without phase jumps

As far as we know, phase-jump-free low-phase-noise synthesizers in the microwave domain, such as DDS, are not commercially available in the 8-18 GHz region. We thus developed a home-built low-phase-noise synthesizer based on an YIG oscillator which is tunable without phase jump from 7.5 to 16.5 GHz.

Figure 2.15 shows the electronic scheme of the home-made microwave synthesizer. A radio-frequency tracking oscillator, that is based on a voltage-controlled oscillator (VCO) referenced to the 10 MHz local reference signal, generates a clock signal of 1 GHz. A DDS uses this clock signal as a reference. Its frequency is tunable from 0 to ∼400 MHz. After dividing by 32 the YIG frequency, it is mixed with the doubled DDS frequency using a radio-frequency mixer. The resulting phase error signal is amplified and then converted into a fast- and a slow-correction signal via a servo loop. The YIG oscillator is then phase-locked to the DDS signal with a frequency ratio of 64 by applying a fast- and a slow-correction to the FM and TUNE port of the YIG oscillator, respectively.

In our setup, the radio-frequency tracking oscillator is referenced to the local 10 MHz generated by the US quartz oscillator disciplined on the GPS receiver, as discussed in section 2.4. Therefore, the resulting microwave signal has a fractional frequency stability below 10^{-12} between 1 s and 100 s and a frequency accuracy better than 10^{-11} (see

section 2.4). Figure 2.16 shows a photo of the microwave synthesizer rack including the YIG oscillator, the radio-frequency tracking oscillator, the DDS module, and the servo loop. Our custom-made microwave synthesizer is integrated in a rack-mounted packaging and is computer-controlled via a USB communication port. Adjusting the DDS frequency allows the synthesizer frequency, driving the EOM frequency f_{EOM}, to be continuously tuned without any phase jump over 9 GHz, limited by the YIG's span. It delivers a power of at least 15 dBm over its entire spectral window.

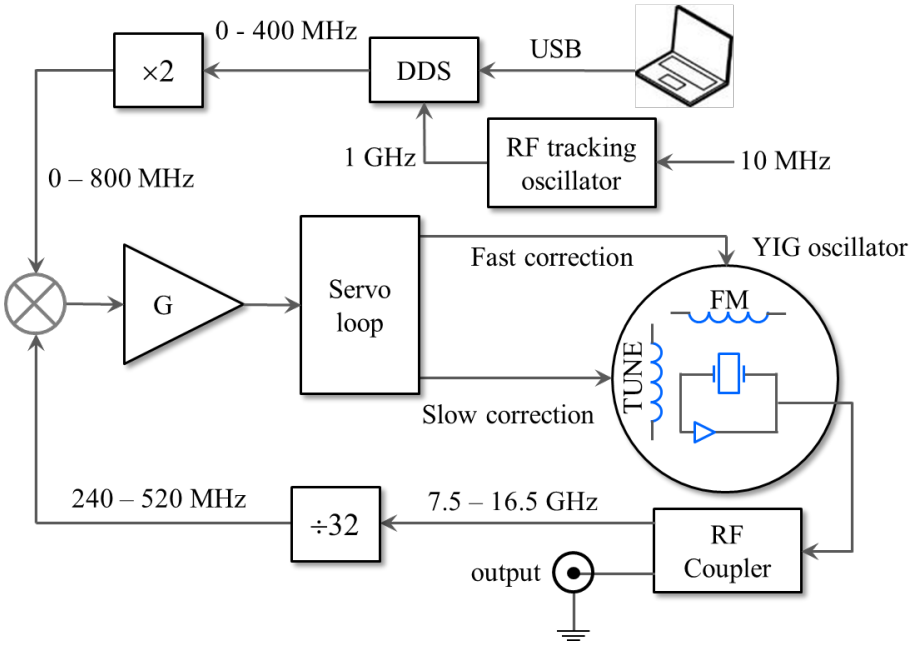

Figure 2.15 – The principle of the Yttrium Iron Garnet (YIG) oscillator based phase jump free microwave synthesizer. DDS: direct digital synthesizer, G: gain, RF: radio-frequency, FM and TUNE: YIG ports for fast and slow corrections.

2.6 The optical frequency comb at LPL

2.6.1 The OFC at LPL: introduction and modules

2.6.1.1 Introduction

At LPL, the OFC used in the present work is a Menlo Systems (FC 1500) Erbium (Er^{3+}) doped fiber laser. The OFC has a peak power wavelength centered at around 1.55 μm and a FWHM spectral bandwidth of 60 nm. The comb repetition rate is about 250 MHz and the ultra-short pulse duration is around 90 fs. The laser is specially designed for metrological applications and both its repetition rate and its carrier envelope offset frequency can be conveniently controlled (see below). Figure 2.17 shows a photograph of the OFC setup, that includes three modules: a femtosecond fiber laser module (M-Comb), a carrier envelope offset frequency detection module (P250-XPS), and a custom made module with an optical output centered at 1.85 μm (P250 HMP1850).

2.6.1.2 M-comb module

The M-comb module is a mode-locked fiber laser consisting of a ring fiber cavity providing the pulsed laser light, centered at around 1.55 μm. Figure 2.18 presents a

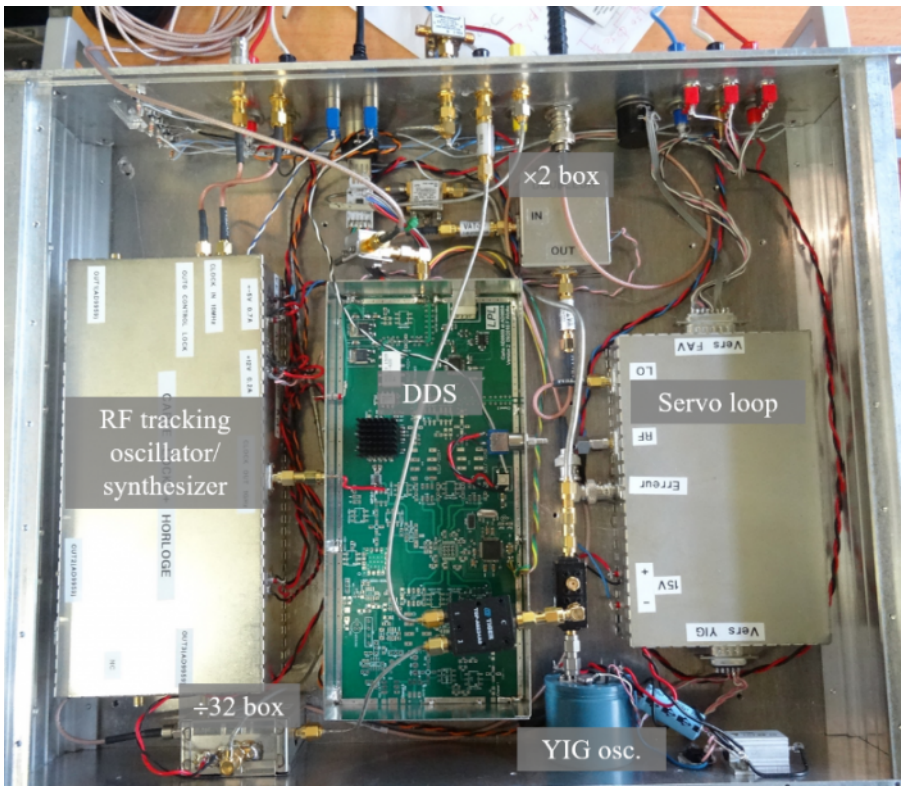

Figure 2.16 – Photograph of the YIG oscillator based microwave synthesizer rack with main components: the Yttrium Iron Garnet (YIG) oscillator (osc.), the RF tracking oscillator that generates the 1 GHz clock signal, the direct digital synthesizer (DDS), and the servo loop.

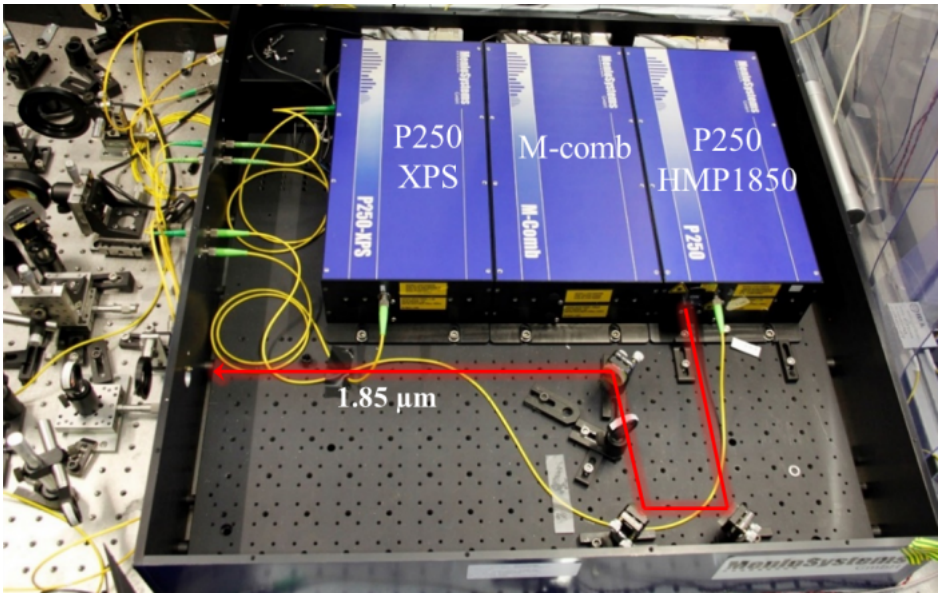

Figure 2.17 – Photograph of the Menlo System optical frequency comb at LPL. M-comb: femtosecond laser module, P250 XPS: carrier envelope offset generation module, and P250 HMP1850: 1.85 μm custom made module. The red beam represents the 1.85 μm free-space comb output and terminals connected to yellow fibers are 1.55 μm comb outputs.

scheme of the M-comb module. The ring cavity includes a fibered and a free-space section. The fibered section includes a 40-cm Erbium doped fiber pumped with two 980 nm pigtailed diode lasers while the free-space section includes the following elements: two pairs of wave plates (each pair includes a half-wave plate $\lambda/2$ and a quarter-wave plate $\lambda/4$) to control the mode-locking of the OFC; an electro-optic modulator (EOM) and a cavity mirror (M), mounted on a piezo-electric actuator, to control the cavity length, and in turn the repetition rate; another quarter-wave plate located between the beam splitter BS and the cavity mirror, a motorized wedge to control the comb offset frequency; an optical isolator (OI) to keep the ring cavity unidirectional; two beam splitters (BS); and two fiber collimators (FC). The generated spectrum of the laser is a frequency comb whose mode frequencies are given by

$$\nu_p = p \times f_{rep} + f_{ceo}, \tag{2.10}$$

where p is an integer and $p \sim$800 000, f_{rep} and f_{ceo} are the repetition rate and the carrier envelope offset frequency, respectively. The mirror (M) mounted on a piezo-electric (PZT) actuator allows the cavity length to be adjusted. Moreover, this retro-reflector can be also displaced using a step motor, enabling the cavity length to be varied over a wider range. The effective optical cavity length is around 1.2 m corresponding to the repetition rate of $\sim$250 MHz. An electro-optic modulator (EOM) of dimensions $2 \times 2 \times 7$ mm is also inserted in the cavity in order to adjust its length with a very high correction bandwidth. It is driven with a low voltage ranging from 0 to 20 V. As we will see, the combination of the low bandwidth piezo-electric actuator and the high bandwidth intra-cavity EOM allows f_{rep} to be stabilized to an US near-IR reference signal (see section 2.7).

Figure 2.19 shows the spectrum of the output of the OFC with a FWHM of about 33

nm. It was measured by an optical spectrum analyzer with a resolution of 6 GHz thus comb teeth can not be seen in the spectrum.

As mentioned above, the displacements of the piezo-electric actuator and the step motor of the retro-reflector (M) lead to the modification of the cavity length, and thus of the repetition rate of the OFC. The controller of the piezo-electric actuator has a voltage-amplifier with a ∼15 voltage gain and is driven by an input voltage ranging from 0 to 10 V. The output voltage of the controller thus varies from 0 to 150 V, allowing f_{rep} to be varied. The piezo-electric actuator originally installed in the OFC allowed f_{rep} to be tuned over a maximum range of ∼850 Hz, corresponding to a coefficient of about 4 Hz/V. We have recently replaced the piezo-electric actuator by a new one with a better tuning range of ∼3.5 kHz. This allows comb modes at 1.55 μm to be varied over a maximum tuning range of ∼3 GHz. In addition, the comb modes can be coarsely tuned via the step motor over a larger frequency range of more than 1 THz (corresponding to a ∼4 kHz tuning range of f_{rep} in steps of 10-80 Hz).

The comb output at 1.55 μm is split in five outputs by the fiber optic splitter (OS in Figure 2.18(a)). The first output is used for detecting the comb frequency offset. The second is fed to the HMP 1850M box to generate the additional pulsed source at 1.85 μm with the same f_{rep} of the original comb. The third output is used to stabilize the mid-IR sources as will be illustrated in chapter 3 and the two last ports are not used.

2.6.1.3 Carrier envelope offset frequency detection

The principle of the detection of the carrier evevelope offset frequency of the OFC is based on the f-$2f$ self-referencing interferometer [196], as shown in Figure 2.18(b). A part of the optical power from the femtosecond laser is coupled in a fiber and sent to a 1.54 μm high power Erbium-Doped Fiber Amplifier (EDFA) with three pump diodes at 980 nm. After amplification, the optical comb spectrum is broadened in a Highly Non Linear Fiber (HNLF) to an octave-spanning spectrum from 1000 to 2100 nm. The shape and the bandwidth of the spectrum are controlled by a polarization controller, named "Squeezer" (Figure 2.18(b)), located at the input of the amplifier and driven by three voltages. By tuning those voltages, the signal-to-noise ratio and intensity of f_{ceo} can be optimized. The laser beam is then sent to a Periodically Poled Lithium-Niobate (PPLN) waveguide crystal, where a part of the expanded comb at ∼2100 nm with comb mode frequencies $f_m = mf_{rep} + f_{ceo}$ (m the comb mode integer) is frequency-doubled. The comb modes of the frequency-doubled part at ∼1050 nm are given by $2f_m = 2mf_{rep} + 2f_{ceo}$. After reflection by a narrowband reflective fiber Bragg grating (FBG), designed at the specific wavelength of ∼1050 nm and acting as a filter, the high frequency part at 1050 nm of the initial comb, with comb mode frequencies $v_{2m} = 2mf_{rep} + f_{ceo}$, and the frequency doubled part around the same wavelength are mixed on a fast photodiode and a beat-note signal at frequency of $2v_m - v_{2m} = f_{ceo}$ is generated. This beat-note signal gives directly the offset frequency f_{ceo}. This offset frequency can be controlled by the translation of the step motor of the wedge and the current of the pump laser diodes shown in Figure 2.18(a). One step of the wedge's step motor leads to a shift of f_{ceo} of about 700 kHz with a maximum tuning range of 300 MHz while variation of the voltage of the pump laser diodes allows f_{ceo} to be varied with a sensitivity of ∼40 MHz/V.

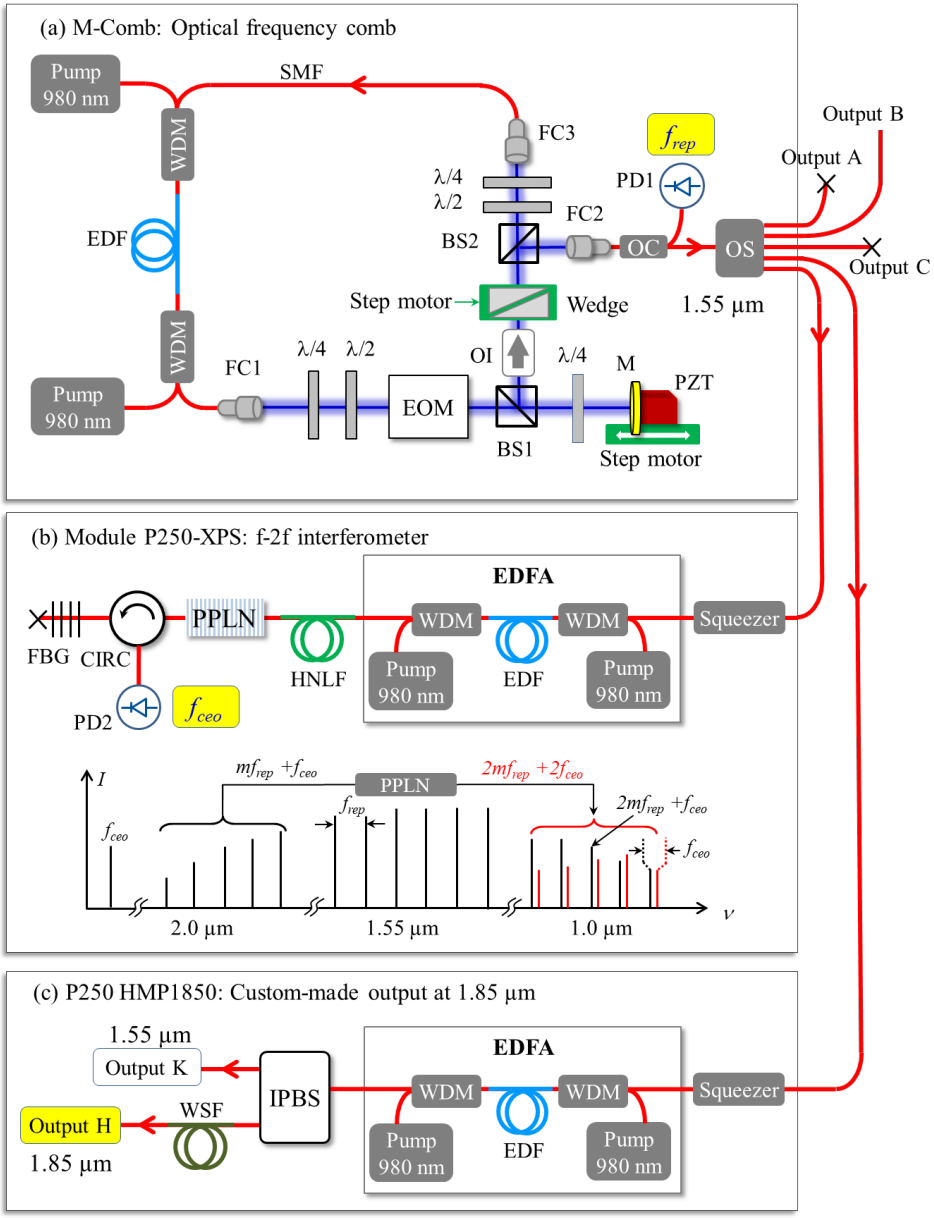

Figure 2.18 – (a) Cavity structure of the optical frequency comb. (b) Scheme of the P250XPS-WG module (top) and principle of the carrier envelope offset frequency measurement based on the f-$2f$ interferometer (bottom). (c) Scheme of the custom-made output at 1.85 μm. WDM: Wavelength-division multiplexing, EDF: Erbium doped fiber, FC: fiber collimator, OC: optical coupler, OS: optical splitter, $\lambda/4$: quarter-wave plate, $\lambda/2$: half-wave plate, OI: optical isolator, EOM: electro-optic modulator, M: mirror, PZT: piezo-electric actuator, PD: photodiode, HNLF: highly nonlinear fiber, PPLN: periodically poled lithium-niobate, CIRC: optical circulator, FBG: reflective fiber Bragg-grating, IPBS: inline polarization beam splitter, WSF: wavelength shifting fiber, SMF: single mode fiber, BS: beam splitter; EDFA: Erbium-Doped Fiber Amplifier.

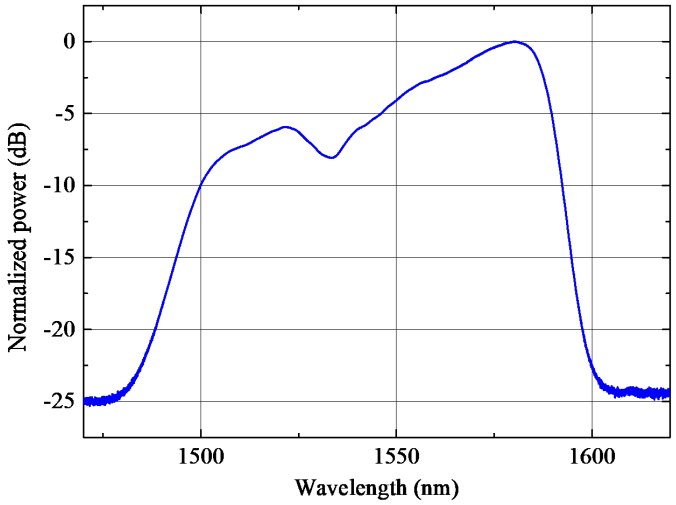

Figure 2.19 – The spectrum of the 1.55 μm output of the OFC as provided by the manufacturer.

2.6.1.4 Custom-made output at 1.85 μm

A custom-made output of the OFC at 1.85 μm (P250 HMP1850) is generated using a part of the OFC output (Figure 2.18(a)) at 1.55 μm. The principle of the custom-made comb generation is shown in Figure 2.18(c).

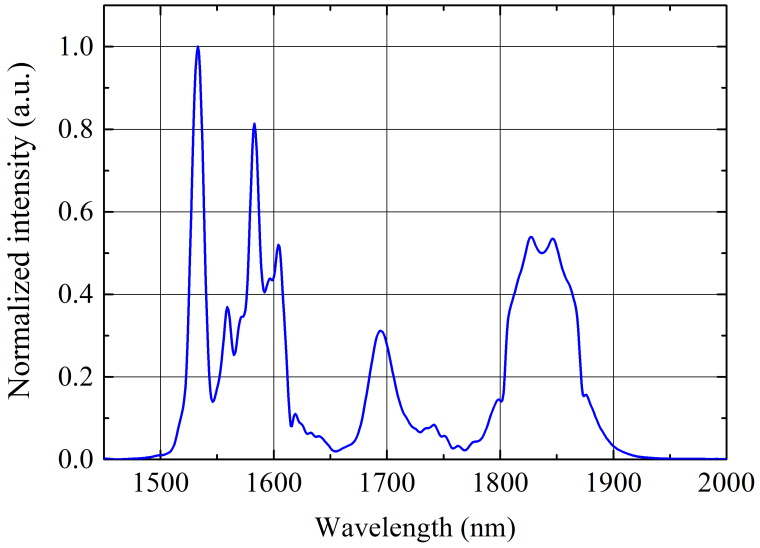

Figure 2.20 – Optical spectrum of the additional output comb H-HMP 1850 as provided by the manufacturer.

After controlling the polarization by changing the voltages of the squeezer, as shown in Figure 2.18(c), a part of the OFC at 1.55 μm is amplified by a pumped EDFA, followed by an inline polarization beam splitter (IPBS) separating the EDFA output into two branches. The first branch is an auxiliary output of the original comb at 1.55 μm, named

"Output K" that will be beaten against the OLO carrier frequency for locking f_{rep} to the OLO (see section 2.7). The other branch is fed into a non-linear fiber in which new comb modes of the comb are generated by an optical effect called the self-soliton Raman shift. The 1.55 μm wavelength of the original mode comb is shifted to higher wavelengths ranging from 1.52 to 1.9 μm nm due to the Raman effect in the non-linear fiber. The output power of the module is around 360 mW. Figure 2.20 shows the spectrum of the output of the custom-made module. The peak around 1.85 μm has a FWHM bandwidth of ∼44.5 nm .

2.6.1.5 Electronics and control

The OFC is controlled by a system developed by Menlo Systems. The system automatically finds the mode-lock. It controls the quality of the mode-locked laser and drives the two step motors (one for the retro-reflector and the other for the wedge, see Figure 2.18(a)) in order to tune f_{rep} and f_{ceo}. Moreover, the system includes also some electronics in order to lock these frequencies to a local radio frequency reference signal.

Both f_{rep} and f_{ceo} are measured with a integrated K+K counter. It includes four counters without dead time and with Π filter and is referenced to the local 10 MHz reference signal. The frequencies f_{rep} and f_{ceo} are typically measured with an uncertainty of 1 mHz and are continuously recorded using the Menlo Systems software.

2.6.2 Free-running optical frequency comb

2.6.2.1 Free-running repetition rate

Due to thermal and mechanical effects, the repetition rate of the OFC drifts. The frequency fluctuations of f_{rep} have been measured in the long-term [141]. In this measurement, the OFC repetition rate and its higher harmonics are detected by a fast photodiode (PD1, Figure 2.18(a)), located inside the M-Comb module. On this photodiode, a beat-note signal between the comb teeth is consequently generated. A high pass filter at 1 GHz was used to suppress the lower harmonics of f_{rep}. The resulting radio-frequency signal at the 4^{th} harmonic of f_{rep} is then mixed with a 980 MHz signal from an integrated synthesizer. At the output of the mixer, the obtained signal at ∼20 MHz is measured by the integrated K+K counter of the OFC system. Both accuracy and uncertainty of the frequency counter is ensured by the local 10 MHz reference signal used for the measurement. Absolute value of f_{rep} can be directly calculated from reading values of this counter using the following formula,

$$f_{rep} = \frac{f_{\text{counter}}}{4} + 245\,\text{MHz}. \tag{2.11}$$

Figure 2.21 shows the fluctuations of f_{rep}, measured during seven days. The amplitude of the fluctuation can reach 200 Hz/day.

2.6.2.2 Free-running comb offset frequency

The comb offset frequency f_{ceo} has a signal-to-noise ratio of about 30 dB at a resolution of 1 MHz. For this type of fiber laser, the comb offset frequency free-running noise is expected to be larger than that of a comb optical mode [197]. The typical linewidth is indeed about 400 kHz, which is approximaty two times larger than the comb mode

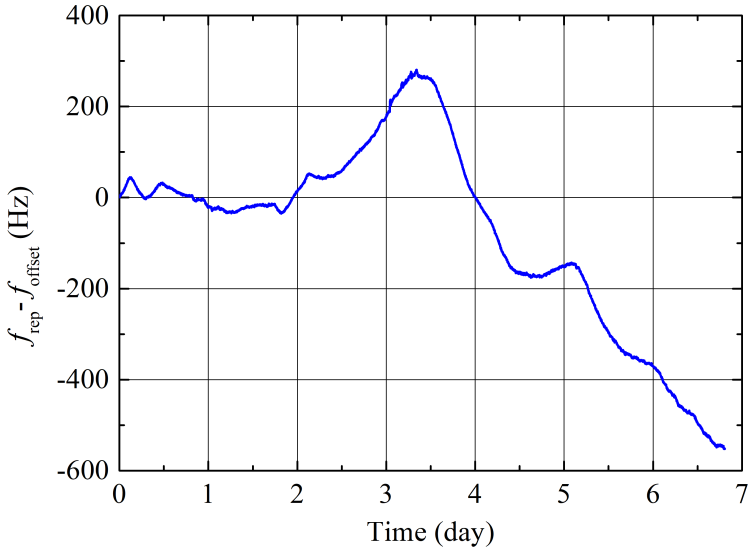

Figure 2.21 – Evolution of the free-running repetition rate of the OFC during a week. Taken from [141].

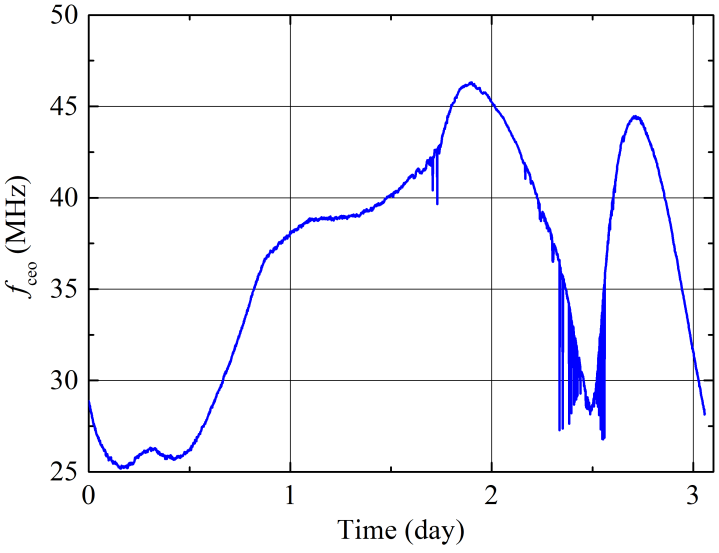

Figure 2.22 – Evolution of the free-running carrier envelope offset frequency of the OFC during several days. f_{offset} ~250 MHz is the value of f_{rep} at the beginning of the measurement. Taken from [141].

linewidth. Frequency fluctuations of the free-running f_{ceo} has also been recorded during several days [141]. This result is shown in Figure 2.22. The amplitude of these fluctuations can reach a few tens of MHz/day.

2.6.2.3 Phase-locking f_{rep} and f_{ceo} to the radio-frequency reference

The electronic control system of the OFC includes two integrated phase-lock loops allowing f_{rep} and f_{ceo} to be locked to a 20 MHz signal, synthesized from the local 10 MHz reference signal. The frequency f_{rep} is stabilized by feeding a correction signal to the piezo-electric actuator generated from the first phase-lock loop. A second phase-lock loop is used to stabilize f_{ceo} by applying a fast correction to the current of the pump laser diodes located in the M-comb module (Figure 2.18(a)) with a bandwidth of 20 kHz and a slow correction to the step motor of the wedge for corresponding long-term variations.

2.7 Frequency stabilization of the OFC repetition rate onto the OLO

The OFC can be used as a flywheel to transfer the spectral properties of the near-IR US laser to the mid-IR QCL laser. Since the QCL will be stabilized onto a high harmonic of the repetition rate (see chapter 3), only the repetition rate needs to be controlled with the near-IR US laser. Here, we first present in subsection 2.7.1 the experimental setup for stabilizing the repetition rate of the OFC to a sub-harmonic of the OLO carrier's frequency ν_{OLO}, whereas the offset frequency f_{ceo} of the OFC is left free-running. In subsection 2.7.2, we characterize the performances of the frequency stabilization of f_{rep} to ν_{OLO} by measuring the frequency noise PSD and frequency stability. It is noted that this setup has been used for our precision spectroscopic measurements, described in chapters 4 and 5, that have been performed before 2019. Recently, we have upgraded the setup to improve the tuning range of the repetition rate of the OFC. This will be described in subsection 2.7.3.

2.7.1 Experimental setup

The principle of the repetition rate stabilization is shown in Figure 2.23. We first detect the beat-note signal $\nu_{OLO} - (pf_{rep} + f_{ceo})$ between the OLO carrier frequency ν_{OLO} and the nearest tooth of the OFC at around 1.55 μm $\nu_p = pf_{rep} + f_{ceo}$ (p ~800 000 and f_{rep} ~250 MHz) on the photodiode PD. Then, we mix this signal with f_{ceo} in the mixer MX1 to suppress the f_{ceo} contribution. In consequence, we obtain the following beat signal

$$\nu_{OLO} - pf_{rep} = \pm\Delta_2, \tag{2.12}$$

which is then phase-locked to a radio-frequency reference signal synthesized by a DDS. As mentioned in subsection 2.6.1, f_{rep} can be coarsely tuned via a piezo-electric actuator or a step motor and finely tuned with an EOM. In this setup, we only use the piezo-electric actuator and the EOM to perform the stabilization.

Figure 2.23 shows the detailed scheme of the experimental setup. We use the 1.54 μm output of the custom-made 1.85 μm module (denoted "output K" of the module HMP 1850 in Figure 2.18(c) and Figure 2.23). After filtering and amplification, the beat-note signal at frequency $\nu_{OLO} - (pf_{rep} + f_{ceo})$ around 90 MHz is mixed with f_{ceo} (~60 MHz) in the mixer MX1. At the output of this mixer, a beat-note signal $\Delta_2 = \pm(\nu_{OLO} - pf_{rep})$ at ~150 MHz is obtained. It is then filtered by the band-pass filter (F4) and amplified with

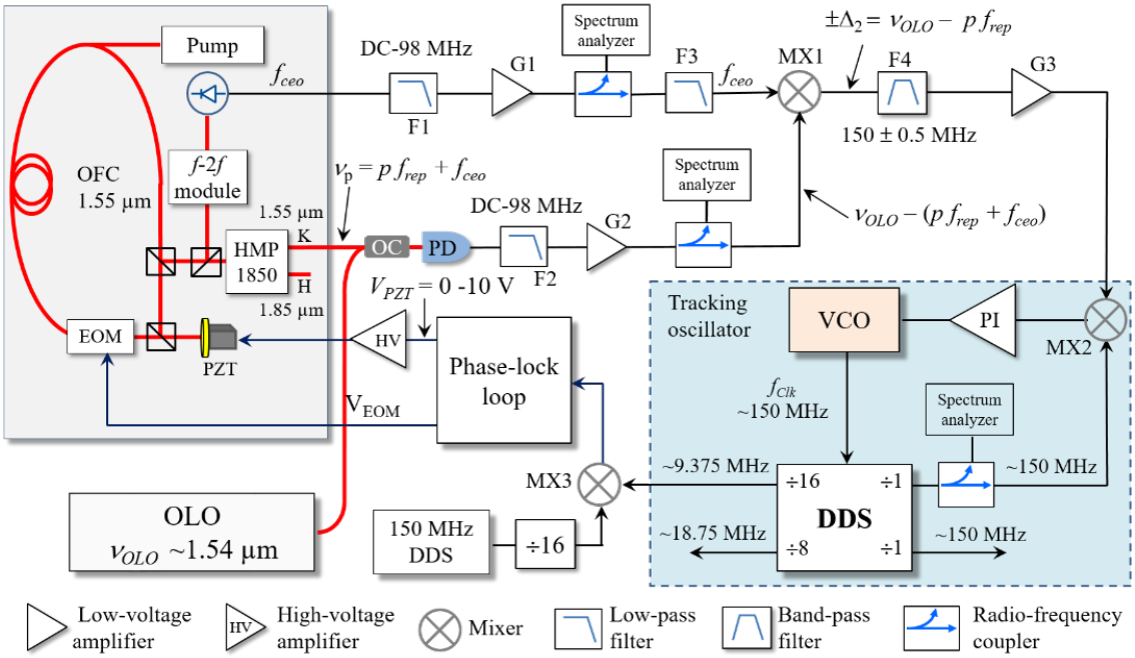

Figure 2.23 – The experimental setup for stabilizing f_{rep} of the OFC to the OLO carrier frequency. In the blue color area is a RF tracking oscillator. OFC: optical frequency comb, EOM: electro-optic modulator, OLO: optical local oscillator, PZT: piezo-electric actuator, VCO: voltage-controlled oscillator, MX: mixer, OC: optical coupler, F: filter, G: low-voltage amplifier, PI: proportional-integrator servo loop, and DDS: direct digital synthesizer.

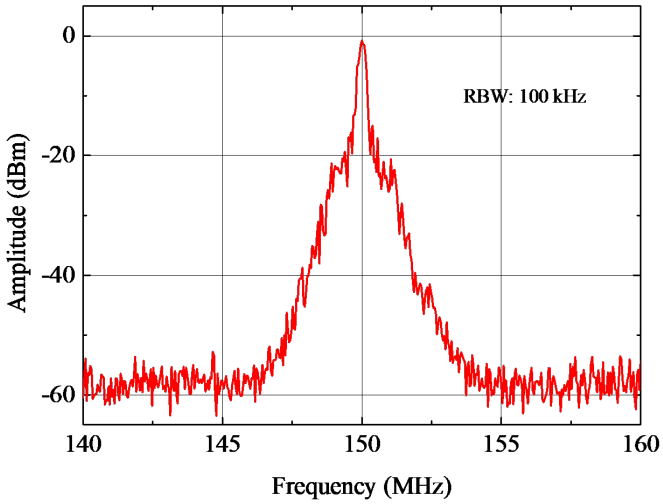

Figure 2.24 – Beat-note signal at 150 MHz between the OLO carrier and the nearest comb mode of the OFC after removing the comb offset frequency when the phase lock loop is closed. RBW: resolution bandwidth.

the amplifier G3. Inside a radio-frequency tracking oscillator (blue area), the beat-note signal is further amplified, filtered, and frequency-divided by 16. A tracking bandwidth of about ∼500 kHz is given by the proportional-integrator (PI) servo loop.

At the output of the tracking oscillator, we obtain a signal at a frequency of ∼9.375 MHz. This signal copies the f_{rep} noise at low Fourier frequencies below 500 kHz while the f_{rep} noise at higher Fourier frequencies is filtered by the PI servo loop of the tracking. In a mixer (MX3), the signal is then compared with a fixed 9.375 MHz reference, provided by a DDS synthesizer. At the mixer output, a phase error signal is generated and then converted into a fast- and a slow correction signal (V_{EOM} and V_{PZT}, Figure 2.23) by a phase-lock loop. Finally, f_{rep} is phase-locked to ν_{OLO} by feeding the fast-correction with a 0-20 V correction range to the intra-cavity EOM and the slow-correction to the high-voltage amplifier of the piezo-electric actuator where V_{PZT} is amplified 15 times and then fed to the actuator with a voltage range from 0 to 150 V (see subsection 2.6.1.2). Note that acting on the cavity length with the PZT actuator induces a small variation of the comb offset frequency. This variation can be minimized to 10 MHz over the whole PZT tuning range with a fine alignment of the cavity mirror. It is typically 20 to 30 MHz and is low enough to keep the beat-note signal $\nu_{OLO} - (pf_{rep} + f_{ceo})$ in the bandwidth of the low-pass filter placed after the photodiode PD in Figure 2.23. Therefore, frequency stabilization of f_{ceo} is not needed.

2.7.2 Performances of the stabilization of the repetition rate of the OFC

Performances of the f_{rep} stabilization were assessed by evaluating the frequency noise power spectrum density (PSD) and the stability of a beat-note signal between an optical mode of this comb ν_p and a second US laser $\nu_{ref,2}$ (optional US laser #2, Figure 2.25), located at LNE-SYRTE and transferred to LPL via the same optical fiber link as the first US laser. The optional US laser is a 1.54 μm laser locked to an US cavity, similar to the US laser #1 used to provide the near-IR reference signal. Frequencies of these

US lasers are very close, only 375 MHz apart [45]. They exhibit similar stabilities and phase noise PSDs since they are based on two very similar Fabry-Perot cavities and are transferred to LPL through the same fiber link.

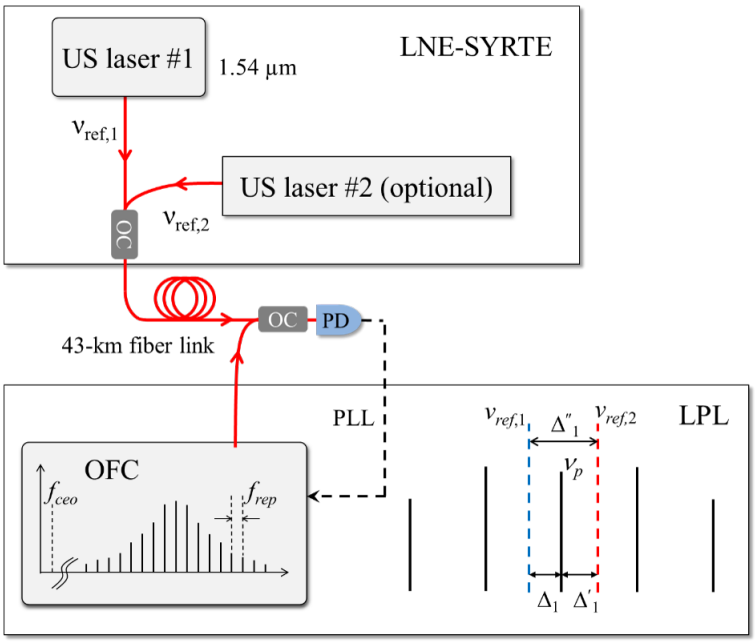

Figure 2.25 – The experimental setup for evaluating the spectral purity of the OFC. Note that the setups for the near-IR reference transfer between LNE-SYRTE and LPL are not presented in this figure. US: ultra-stable, OFC: optical frequency comb, OC: optical coupler, and PLL: phase-lock loop.

As illustrated in Figure 2.25, three beat-note signals were obtained on the photodiode PD (Figure 2.25): (i) the beat-note signal between an optical comb mode ν_p and the reference $\nu_{ref,1}$, denoted by Δ_1; (ii) the beat-note signal between this comb mode and the reference signal $\nu_{ref,2}$, denoted by Δ'_1; (iii) the beat-note signal between these reference signals, Δ"$_1$. The repetition rate is phase-locked onto the reference signal $\nu_{ref,1}$ of the US laser #1 after removing the comb offset frequency, as mentioned in subsection 2.7.1.

Frequency noise power spectral density

The frequency noise of the stabilized repetition rate was evaluated by analysing the noise PSD of the beat-note signal Δ'_1 with a fast Fourier transform spectrum analyzer. Since the phase noise accumulated along the fiber link during the near-IR reference transfer is approximately the same for both US lasers, any noise perturbations from the fiber link formed during the optical transfers are thus rejected to a very large extent. Therefore, it was not necessary to compensate the link noise for this measurement.

The measured frequency noise PSD of the beat-note signal is shown in Figure 2.26. It is below 5×10^4 Hz^2/Hz at 100 kHz Fourier frequency, limited by the ~500 kHz locking bandwidth. This noise exhibits a plateau at around 1 Hz^2/Hz between 1 and 100 Hz. It should be noted that the frequency noise PSD of the beat-note signal resulting from the combination of the stabilized f_{rep} and the US laser #2, does not contain the compensated link noise. The total OFC frequency noise is thus obtained by summing the frequency noises of the compensated link and of the OFC. Figure 2.26 also plots the frequency noise

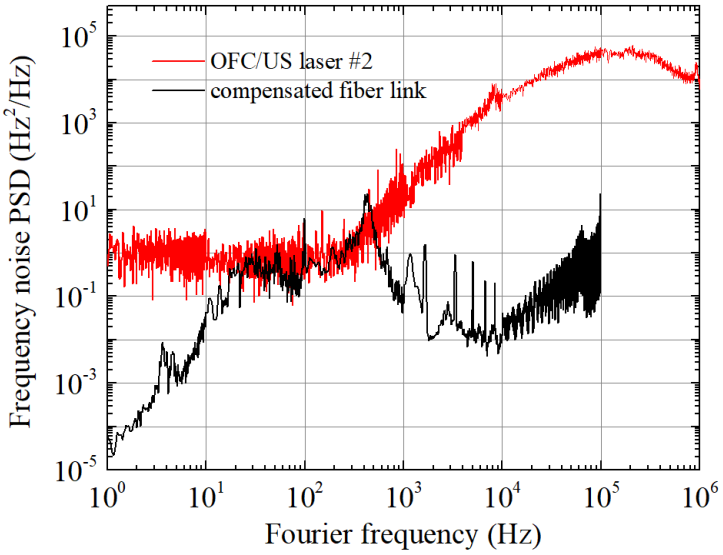

Figure 2.26 – Frequency noise power spectral density of the optical frequency comb and of the compensated link. Taken from [45].

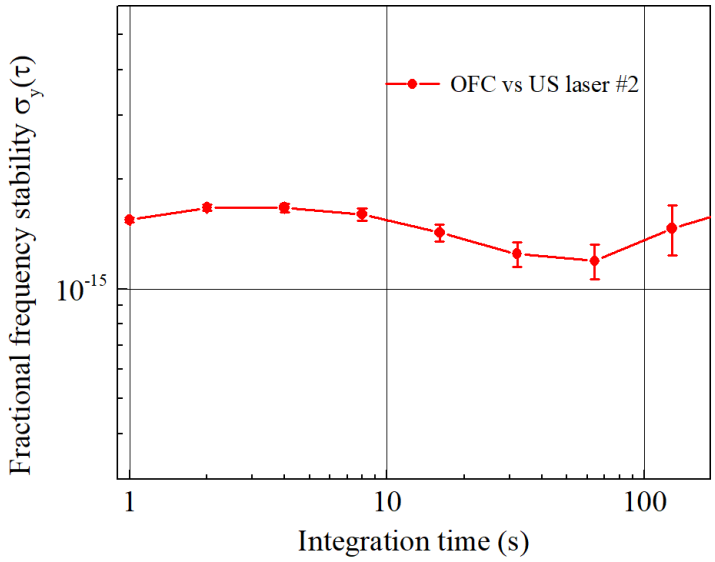

Figure 2.27 – Fractional frequency stabilities of the OFC. Overlapping Allan deviation processed from data measured using a Λ-type counter. Taken from [45].

PSD of the active noise compensated link. It is below or equal to the noise PSD of the beat-note signal. It means that the link adds a minor contribution to the comb noise.

Fractional frequency stability

The frequency stability of the stabilized f_{rep} was evaluated by counting the beat-note signal Δ_1' with a Λ-type counter with 1-s gate time. The fractional frequency stability of the OFC was then obtained by calculating the overlapping Allan deviation of the experimental data and dividing it by a factor of $\sqrt{2}$ (assuming an equal contribution for both US lasers). Figure 2.27 shows the fractional frequency stability of the OFC. It is below 2×10^{-15} for averaging times from 1 to 100 s after a linear drift of the cavities of about 0.3 Hz/s is removed. It is the same as the stability of the beatnote signal between the two US lasers. This shows that the noise of the phase-lock loops is negligible and thus the OFC frequency noise and stability are given by the US laser frequency noise and stability.

Uncertainty on the absolute frequency

Following Equations 2.9 and 2.12, f_{rep} is given by

$$f_{rep} = \frac{\nu_{OLO} \pm \Delta_2}{p} = \frac{\nu_{ref} - f_{EOM} + \Delta_1 \pm \Delta_2}{p}, \tag{2.13}$$

where the remote reference signal ν_{ref} is fixed, p ~800 000, and the beat-note signal frequencies Δ_1 and Δ_2 are constant. In practice, the sign of the beat-note signal Δ_2 is positive.

As detailed above, two phase-lock loops are used to lock the repetition rate of the OFC to the OLO and the OLO to the remote optical frequency reference signal that is transferred to LPL through an optical fiber link. The LNE-SYRTE ultra-stable signal is measured and controlled against the primary frequency standards of LNE-SYRTE. The phase-lock loops guarantee that there are no frequency errors and the formula 2.13 is exact. This ensures that the uncertainty on the absolute frequency of the repetition rate of the OFC is given by that of the LNE-SYRTE ultra-stable signal.

2.7.3 Upgrading the experimental setup

Our purpose is not only to stabilize the repetition rate of the OFC f_{rep} to the OLO carrier's frequency ν_{OLO} but also to allow f_{rep} to be widely tuned by scanning ν_{OLO}. The experimental setup described in subsection 2.7.1 only uses the EOM and the piezo-electric actuator for the stabilization of f_{rep}. Therefore, f_{rep} can be only tuned over 3.75 kHz, limited by the piezo-electric displacement (see subsection 2.6.1). As mentioned in subsection 2.6.1.2, the step motor also allows us to coarsely tune the cavity length, and thus the repetition rate of the OFC. However, it had not been used in the previous setup. It is possible to extend the tuning range of the stabilized repetition rate by using this step motor.

In order to improve the tuning range of f_{rep}, the EOM fine tuning, the continuous displacement of the piezo-electric actuator, and the large movements of the step motor have been combined since January 2019. Figure 2.28 illustrates the new experimental setup. The principle for locking f_{rep} is similar to the previous version. We detect a beat-note signal $\Delta_2 = \nu_{OLO} - p f_{rep}$ between ν_{OLO} and the nearest comb mode $p f_{rep} - f_{ceo}$ after

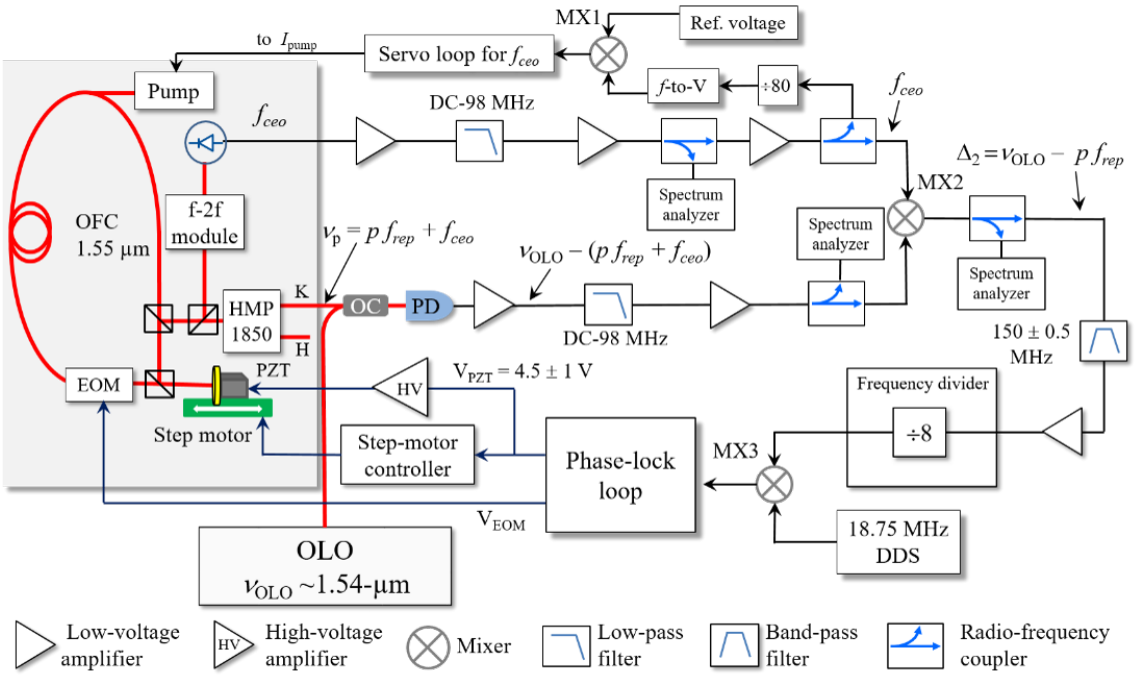

Figure 2.28 – The upgrading experimental setup for stabilizing f_{rep} of the OFC to the OLO carrier frequency. OFC: optical frequency comb, OLO: optical local oscillator, EOM: electro-optic modulator, PZT: piezo-electric actuator, OC: optical coupler, PD: photodiode, PLL: phase-lock loop, and DDS: direct digital synthesizer.

removal of the comb frequency offset f_{ceo}. This beat-note signal is then phase-locked to a radio-frequency signal. In addition, there are several upgrades to the previous setup.

As shown in Figure 2.26, the beat-note signals $\nu_{OLO} - (pf_{rep} + f_{ceo})$ at around 90 MHz and f_{ceo} are filtered with low-pass filters of 98 MHz bandwidth. In the previous setup, we checked that f_{ceo} can vary at most over 30 MHz when f_{rep} is tuned over 3.75 kHz. However, if the tuning range of f_{rep} is extended, variation of f_{ceo} could be such that it exceeds the filtering bandwidth. In the upgraded setup, we thus lock f_{ceo} at around 60 MHz by acting on the current of the pump lasers in Figure 2.18(a). Variation of f_{ceo} is converted into a voltage signal via a frequency-to-voltage converter (f-to-V, Figure 2.26). By comparing this signal with a given reference voltage, an error signal is generated and then used in a feedback loop to generate a servo signal which acts on the current of the pump lasers.

Furthermore, we have replaced the tracking oscillator of the previous setup (blue area, Figure 2.23) by a new radio-frequency divider. In this component, the beat-note signal Δ_2 at around 150 MHz is frequency-divided by a factor of 8. The obtained signal is then compared with a reference signal at 18.75 MHz (provided by a DDS referenced to the 10 MHz local reference signal) using the mixer MX3. An error signal is generated at the output of the mixer MX3, and then converted into a fast- and a slow-correction signal via a phase-lock loop. Finally, f_{rep} is phase-locked to ν_{OLO} by feeding the fast-correction signal (V_{EOM}) to the EOM and the slow-correction signal V_{PZT} to the piezo-electric actuator with an high-voltage amplifier (gain 15, see subsection 2.6.1.2). The electronics of the phase-lock loop has been upgraded and the dynamic of the EOM correction doubled with a ±20 V correction range (instead of 0-20 V previously).

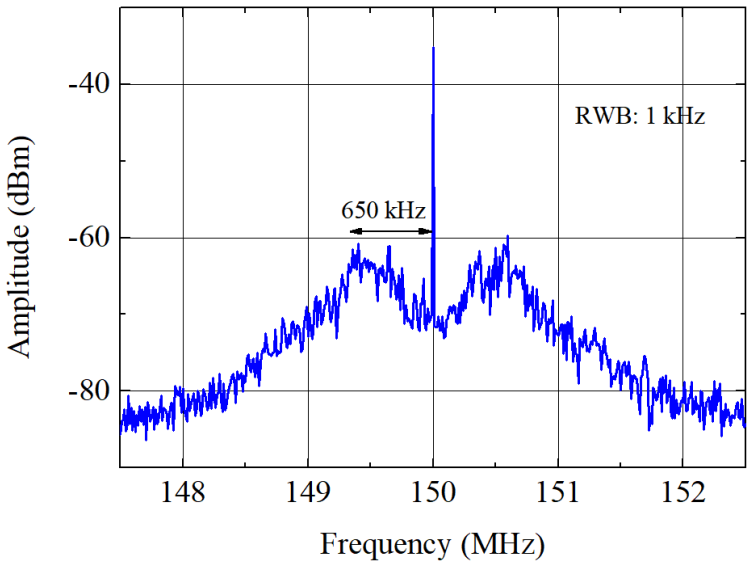

Figure 2.29 – Beat-note signal at 150 MHz between the OLO carrier and the nearest comb mode of the OFC after removing the comb offset frequency when the phase lock loop is closed. The bumps indicate that the servo bandwidth is around 650 kHz. RBW: resolution bandwidth.

Figure 2.29 displays the beat-note signal Δ_2 between the OLO and the nearest comb tooth for the upgraded setup. The bandwidth of the f_{rep} lock loop is about 650 kHz, as indicated by the bump of this beat-note signal. This bandwidth is high enough to enable a fast scan of the repetition rate of the OFC (see section 2.8). It is probably limited by the delay of the 150 MHz band-pass filter (Figure 2.28).

The tuning range of f_{rep} is increased by using the step motor to keep the driving voltage of the PZT actuator centered around 4.5 V. In order to control the step motor automatically, we use the "AutoControl" routine on the Fiber Comb Control software of the OFC, indicated as "step motor controller" in Figure 2.28. The routine allows us to control the step motor by keeping the voltage driving the step motor in a target voltage range. We use the correction voltage V_{PZT} to the piezo-electric actuator as the driving voltage of the step motor. The target voltage range is typically set to 3.5-5.5 V. Before closing the f_{rep} lock-loop, V_{PZT} is set around 4.5 V. During the frequency tuning, the "AutoControl" routine starts to move the step motor if V_{PZT} is below 3.5 V or above 5.5 V. This allows the locking of f_{rep} to be maintained over spans much broader than allowed by the piezo-electric actuator only.

In short, we have demonstrated an upgrade of the experimental-up that allows us to improve the tuning range of f_{rep} by using the combination of the EOM, the piezo-electric actuator, and the step motor.

2.8 OFC repetition rate tuning performances

We now present the OFC tuning performances when the frequency of the OLO carrier is scanned. Thanks to the setup described in Figure 2.28, scanning the OLO frequency allows the repetition rate of the OFC to be widely tuned while maintaining ultimate

stabilities of the remote optical reference signal.

Table 2.1 – Frequency tuning performances of a comb mode and the repetition rate of the OFC.

Actuators used	comb mode frequency (GHz)	f_{rep} (kHz)
PZT and EOM (before 2019)	3	3.75
PZT, EOM, and step motor (from 2019)	9	11.25
Potential with a new OLO	40	50

As mentioned in section 2.6, we can steeply tune ν_{OLO} up to 500 MHz/s with a minimum time-step of 1 ms. The maximum sampling rate of f_{rep} is thus equal to ∼625 Hz/s. Table 2.1 shows the tuning range of f_{rep} and ν_{OLO}. Before 2019, only the EOM and the piezo-electric actuator were used to phase-lock f_{rep} to ν_{OLO}, therefore f_{rep} could be only varied over 3.75 kHz (corresponding to a 3 GHz tuning range of a comb mode). It was limited by the course of the piezo-electric actuator used to act on the comb cavity length. Thanks to the combined use of the step motor, the EOM, and the PZT actuator, the tuning range of f_{rep} is now improved and can reach 11.25 kHz, corresponding to a 9 GHz tuning range of the comb mode. It is now limited by the 9 GHz tuning range of the OLO, given by the YIG span (see section 2.5.2). However, it could be possible to develop a new OLO with a larger tuning range of 40 GHz, corresponding to a tuning range of 50 kHz for f_{rep}, which is easily doable with the step motor.

As introduced at the beginning of section 2.7, we will stabilize a mid-IR QCL onto f_{rep}. Therefore, the wide tunability of f_{rep} will allow the QCL frequency to be continuously scanned over an unprecedented range (see chapter 3).

2.9 Conclusion

We have presented an US optical reference generated at LNE-SYRTE by a 1.54 μm laser locked to a high-finesse cavity. Its fractional frequency instability was measured to be lower than 8×10^{-16} at 1 s. Its absolute frequency is measured by an OFC at LNE-SYRTE once per second against the primary frequency standards of LNE-SYRTE with a fractional uncertainty of a few 10^{-14} at 1 s measurement time.

In addition, we have described an experimental setup for transferring an US optical reference signal together with a radio-frequency reference signal at 200 MHz from LNE-SYRTE to LPL. It uses a 43 km-long fiber link with compensation of the propagation induced phase noise. The residual phase noise instability added by the compensated link is below 10^{-15} at 1 s averaging time. This is below the stability of the US laser. The signal of the US reference is thus transferred to LPL without any degradation.

At LPL, an optical local oscillator at 1.54 μm has been developed with a wide frequency tunability covering 9 GHz. Furthermore, we have demonstrated an experimental setup for phase-locking the repetition rate of an OFC at LPL to this OLO carrier frequency. The OFC repetition rate thus copies the stability of the ultra-stable reference. The OFC frequency stability is found to be 2×10^{-15} between 1 and 500 s when the "white"

cavity-stabilized laser is used and is expected to have a stability lower than 1×10^{-15} when the "CUS" cavity-stabilized laser is used. Moreover, we have demonstrated the wide tuneability of the OFC repetition rate over 11.25 kHz by scanning the OLO carrier frequency which results in tuning the comb teeth frequency over ∼9 GHz.

CHAPTER 3

Development of a quantum cascade laser based widely tunable ultra-high resolution spectrometer

Contents

3.1 Introduction 73
3.2 Quantum cascade laser 75
3.2.1 What is a quantum cascade laser? 75
3.2.2 The LPL mid-infrared quantum cascade laser 77
3.3 Frequency stabilization of a quantum cascade laser to an optical frequency comb 84
3.3.1 Sum frequency generation 84
3.3.2 Locking the quantum cascade laser to the optical frequency comb 89
3.3.3 Performances of the QCL frequency stabilization 95
3.4 The QCL frequency control: summary and SI-traceability . . 99
3.4.1 Summary 99
3.4.2 SI-traceability of the QCL frequency 102
3.4.3 Determination of the QCL absolute frequency 103
3.5 Quantum cascade laser frequency tuning 105
3.5.1 Wide frequency tuning of the stabilized QCL using the step motor 105
3.5.2 Using neighbouring modes 109
3.5.3 Using a radio-frequency-stabilized OFC 109
3.5.4 Perspective 109
3.6 Conclusion 109

3.1 Introduction

With their rich internal structures, molecules can play a decisive role in many different fields, such as in high precision tests of physics (i.e. test of fundamental symmetries and measurement of fundamental constants and their possible variation in time), in physical chemistry (i.e. atmospheric physics, astro-chemistry) or in other applications (i.e. medical diagnosis, environment analysis), as mentioned in the thesis's introduction. Most of these experiments can be cast as high-precision spectroscopic measurements. They are often in the mid-IR domain where molecules exhibit intense and narrow rovibrational transitions. Thus, ultra-stable accurate sources in this region are highly desirable.

At LPL, custom built CO_2 lasers stabilized to OsO_4 saturated absorption lines, which are acting as secondary frequency standards, provide spectroscopic tools with a 1 Hz stability, a 10 Hz linewidth, and sub-100 Hz accuracy [198]. Recently, improving accuracies at the Hz level were achieved by referencing the CO_2 lasers to primary frequency standards in Paris via a 43 km-long fiber link [51]. Nevertheless, the limited frequency tunability of CO_2 lasers is a large constraint for the precise spectroscopic measurements. They emit at CO_2 molecular resonances. An emission line is found every 30-50 GHz in the 9-11 μm wavelength range, and each line is tunable over about 100 MHz. Although, as in our spectrometers, their spectra coverage can be extended a few hundreds of gigahertz using commercially available acousto-optic modulator (AOM) [181] and home-made electro-optic modulator (EOM) [198]. We are one of the few groups to have a rather complex 8-18 GHz EOM [199]. This is done at the expense of power (non-resonant EOMS at these wavelength have an efficiency of 10^{-4}). Moreover, the CO_2 laser is heavy, bulky and requires a low noise high voltage source for operation. Power decrease over time due to leaks, outgassing or CO_2 gas mixture degradation is also a drawback of this type of gas lasers. Quantum cascade lasers (QCLs) [200] with compact size are thus promising sources. Their principle of operation is based on optical transitions between quantized states resulting from spatial confinement in semiconductor multi-quantum wells. QCLs are available in the 3-25 μm mid-IR range with broadband continuous frequency tuning (i.e. over several hundreds of gigahertz for distributed feedback (DFB) QCLs or even more for external cavity (EC) QCLs, see subsection 3.2.1) at milliwatt to watt-level powers. However, their free-running linewidth of tens to thousands of kilohertz makes their frequency stabilization challenging.

For the most precise frequency measurements considered at LPL, we have to address both frequency stabilization and traceability of the QCL to a frequency standard. As mentioned in chapter 1, this can be achieved by phase-locking to secondary standards. Around 10 μm, although other combination of CO_2 emission lines and OsO_4 transitions may be used, only the R(10) CO_2 laser line locked to the saturated absorption of OsO_4 molecule is recommenced as a frequency standard by BIPM (Bureau International des Poids et Mesures) with an uncertainty of 20 Hz (6.9×10^{-13} in relative value) and a stability in the level of 10^{-15} [70, 201]. However, its accuracy is a few orders of magnitude worse than atomic references (i.e. 10^{-16} for the primary standard and potentially 10^{-18} for optical clocks, as mentioned in subsection 1.2.1). In addition, the frequency stability of the CO_2/OsO_4 secondary standard is also a few orders of magnitude worse than the state-of-the-art ultra-stable near-IR lasers ($< 10^{-16}$ at short averaging time, see Refs. [49, 84, 85]). The most stable and precise near-IR references are available in metrological institutes where they are produced by lasers stabilized to ultra-stable cavities and calibrated against primary frequency standards (see for instance in section 2.2, the 1.54 μm reference signal from LNE-SYRTE). Moreover, these references can be transferred to remote user laboratories via optical fiber links (see section 2.3). In order to take full advantage of the performances of these near-IR sources for molecular spectroscopy, it is essential to bridge the gap between the near-IR and mid-IR domains with an optical frequency comb. As mentioned in subsection 1.3.2, mid-IR lasers can be stabilized to a high harmonic of a comb repetition rate using sum-frequency generation (SFG) or difference frequency generation (DFG) processes in nonlinear crystals [42, 46, 134–137]. The first demonstration at LPL of the stabilization of a QCL to the remote near-IR reference from LNE-SYRTE has been recently reported in [45].

In this chapter, we first describe the QCL's operational principle and give general properties and spectral characteristics of the QCL emitting at 10.3 μm used at LPL. We then present the experimental setup for the frequency stabilization of the QCL to the repetition rate of the OFC using a SFG process in a $AgGaSe_2$ crystal and the resulting performances. Finally, we report the wide tunability of the QCL frequency at the precision of the near-IR reference of LNE-SYRTE.

3.2 Quantum cascade laser

In this section, we briefly introduce the operating principle of a QCL. We then present general properties of a QCL at 10.3 μm and how we measure the free-running frequency noise power spectral density (PSD) of this laser allowing us to estimate the QCL free-running linewidth and evaluate how much effort is needed for frequency stabilizing it.

3.2.1 What is a quantum cascade laser?

A quantum cascade laser (QCL) is a semiconductor laser whose active core is a multiple quantum-well structure. The first QCL was demonstrated in 1994 by J. Faist and co-workers at Bell-Labs laboratory [200]. Since then, many different types of QCLs have been reported.

In a conventional laser diode, light is generated by radiative recombinations of electrons and holes. The laser wavelength is essentially established by the semiconductor bandgap. Thus, different materials have to be chosen to get different laser wavelengths. It is difficult to make a laser diode with a low bandgap energy $E_g < 0.3$ eV corresponding to wavelength $\lambda > 3$ μm [202]. For QCLs, by contrast, only one type of charge carriers, electrons, is used for the photon emissions and optical transitions occur between quantized states in the conduction band. The latter are generated by spatial confinements in the quantum-well structure, as detailed below.

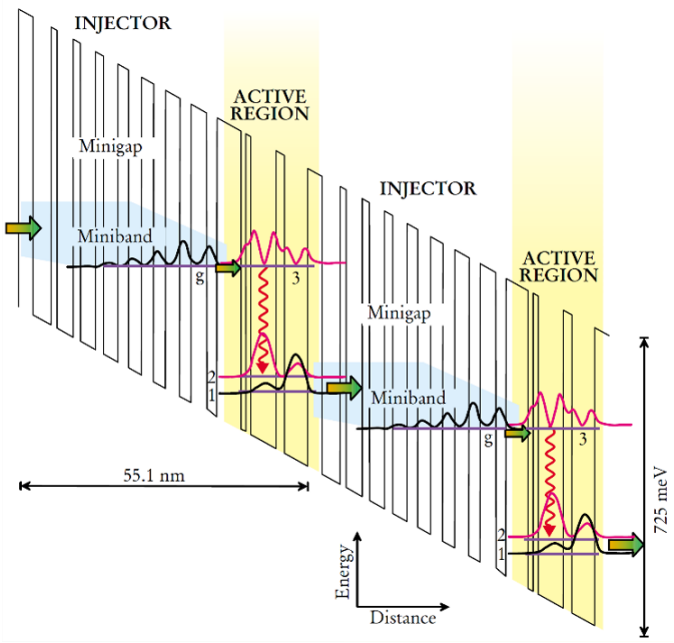

Figure 3.1 – Schematic energy diagram of a multiple quantum well active region QCL with two active regions and two electron injectors. Taken from [203].

A QCL is made of a series of identical stages (typically a few tens to over hundred stages). Each stage includes an electron injector and an active region. Figure 3.1 shows one of the simplest structure of a QCL with two injectors and two active regions [203]. Each injector is composed of many repeated quantum wells with thin barriers separating them. This is called a superlattice structure. When wave functions in the quantum wells are coupled together through the thin barriers, the electronic states of the superlattice structure form delocalised minibands, indicated by the blue shaded regions in this figure. Each active region contains a smaller number of repeated quantum wells with thicker barriers that prevent the coupling between these adjacent wells. This is called a multiple quantum well structure. Such a laser is called a multiple quantum well QCL. In the particular case of Figure 3.1, it is composed of three quantum wells with three quantized states, denoted state 1, 2, and 3. An external electric field is applied to inject electrons from a miniband (state g) in the injector to an upper state (state 3) in the active region via resonant tunnelling. A photon is generated via the optical transition from state 3 to state 2 (below state 3), symbolized by the red arrows in the active region. The lifetime of state 3 is designed to be much longer than state 2 to achieve a large population inversion between these states. For this purpose, the lowest state (state 1) is approximately positioned an optical phonon energy below state 2, which allows electrons from this level to quickly scatter to state 1 via non-radiative transitions. The electrons rapidly move into the next injector via a miniband and are then reinjected into the next active region where the optical transitions are repeated. Unlike in a laser diode, in a QCL, many photons can be generated by the same electron. The QCL wavelength is determined by the energy difference between state 3 and state 2 in the active region, that can be tailored by changing the thickness of the quantum wells and is no longer limited by the gap of the semiconductor material. Multiple quantum well QCLs are typically built to emit at wavelengths up to about 11 μm [203].

There exist another type of QCLs, the superlattice quantum cascade lasers, which can emit at wavelengths longer than about 10 μm [203]. Their active regions are made of multiple quantum wells coupled together thin barrier, and are called superlattice active regions. As in the case of the superlattice injector above, electronics states form minibands separated by minigaps. In a superlattice QCL, light is generated by optical transitions between the upper and lower minibands (state *1* and state *2* in Figure 3.2). The laser wavelength is therefore defined by the minigap of the superlattice structure, which depends on the thickness of the layers making up the superlattice [203].

QCLs cover a wide range of wavelengths ranging from the far-IR to the mid-IR regions. They are generally classified according to their resonators. There are three common resonator configurations for QCLs: Fabry-Perot (FP) QCL, distributed feedback (DFB) QCL, and external cavity (EC) QCL. A FP-QCL consists of the bare QCL chip with high reflection coatings on the end facets of the laser ridge. Emission of this type of QCL is typically multimode and unsuitable for the many applications requiring a single frequency and narrow-linewidth source, such as high resolution spectroscopy or metrology. In a DFB-QCL, a Bragg grating integrated into the laser waveguide along the light propagation direction allows the laser to emit the light at very specific wavelength given by the grating periodicity. The tuning range of a DFB-QCL can be reach 10 cm^{-1} and is covered by changing the injection current and/or the operating temperature, leading to variation of the laser cavity length and in turn the wavelength. The DFB-QCLs have a good spectral purity and are thus the most commonly used for high resolution

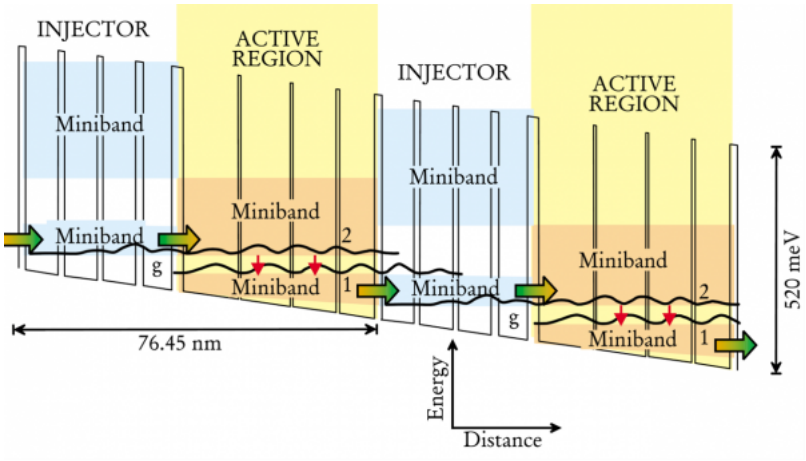

Figure 3.2 – Schematic energy diagram of a superlattice QCL with two superlattice active regions. Taken from [203].

spectroscopy. The EC-QCLs use an external diffraction grating to select a monomode emission. Changing the angle of the diffraction grating allows the emitting wavelength of the EC-QCLs to be tuned up to 120 cm^{-1} without mode-hop and above 500 cm^{-1} overall. The EC-QCLs have also good spectral purity and are suitable for broadband molecular absorption spectroscopy.

3.2.2 The LPL mid-infrared quantum cascade laser

3.2.2.1 General properties

We use a commercial DFB QCL provided by Alpes Lasers. The QCL chip is a ridge of InGaAs and AlInAs grown on InP. The QCL is delivered in the LLH (Laboratory Laser Housing) package. This package is a housing unit including a Peltier module and a QCL chip as shown in Figure 3.3. The temperature of the QCL is measured by a PT-100 temperature sensor. Cooling of the QCL is provided by a combination of a water chiller and a Peltier module driven by a commercial temperature controller (Alpes Lasers, TC-3). The QCL chip can be cooled down to 243 K. The un-collimated output beam goes through an anti-reflective coated ZnSe window (3-12 μm).

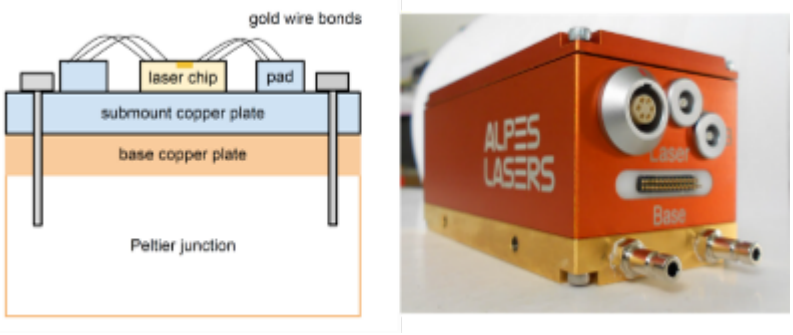

Figure 3.3 – (a) The QCL chip is mounted on a submount copper plate itself mounted on a base copper plate which lies on a Peltier junction for the cooling process. (b) Photograph of the QCL in its LLH housing.

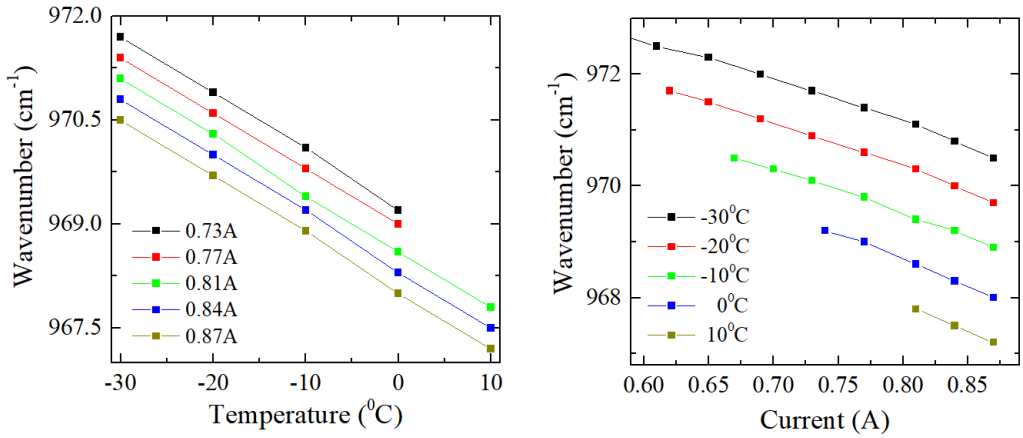

Figure 3.4 – QCL wavelength versus operating temperature (a) and versus injection current (b) as provided by the manufacturer.

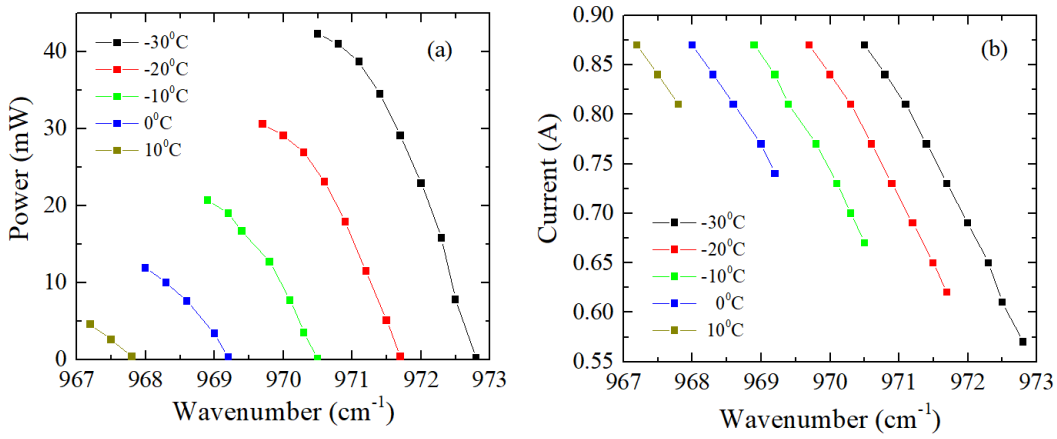

Figure 3.5 – (a) Output power as a function of the single mode emission frequency for different temperatures and (b) applied DC current as a function of the single mode frequency for different temperatures as provided by the manufacturer.

The QCL wavelength can be tuned from 967 to 973 cm^{-1} (corresponding to a tuning range of 60 nm or 180 GHz) by tuning the operating temperature (243 to 283 K) and/or the injection current. Figure 3.4 shows the temperature and current dependence of the QCL wavelength. From this, we extract typical temperature-to-frequency and current-to-frequency conversion factors of $\Delta\nu/\Delta T = -0.082 \pm 0.002$ cm^{-1}/K (corresponding to 2.46 ± 0.06 MHz/mK) and $\Delta\nu/\Delta I = -8.59 \pm 1.1$ cm^{-1}/A (corresponding to -257 ± 33 MHz/mA), respectively (error bars include here the range over which those factor vary over the full temperature and current range). Figure 3.5 displays output power (a) and applied DC current (b) of the QCL as a function of the single mode emission frequency for different temperatures. The QCL exhibits a maximum output power of 40 mW, as showed in Figure 3.5(a) and can be operated up to 870 mA for all temperatures, as showed in Figure 3.5(b).

3.2.2.2 Spectral characteristics of the free-running QCL

Frequency noise power spectral density measurement

In this part, we describe the frequency noise measurement of the free-running QCL allowing us to estimate a feedback bandwidth required to narrow its linewidth. There are two typical techniques used to measure the frequency noise power spectral density (PSD) of a free-running QCL.

The first technique uses the side of a rovibrational molecular absorption line as a frequency discriminator for the laser [40, 204, 205]. A cell is filled with a gas of molecules and the transmitted light is detected on a photodetector. The laser frequency is tuned to the side of the direct absorption signal at about half-maximum where the laser frequency fluctuations are converted in a detectable intensity variation. The frequency range over which the slope of the absorption signal is linear gives a constant intensity-to-frequency sensitivity for all corresponding Fourier frequencies. The QCL frequency noise PSD is obtained by converting the intensity fluctuation PSD using this intensity-to-frequency conversion factor.

In the second technique, a laser with frequency noise smaller than the free-running QCL is used as a reference source. The QCL frequency noise is then measured via the beat-note signal between these lasers. This technique has the advantage of being immune to intensity fluctuations of the lasers.

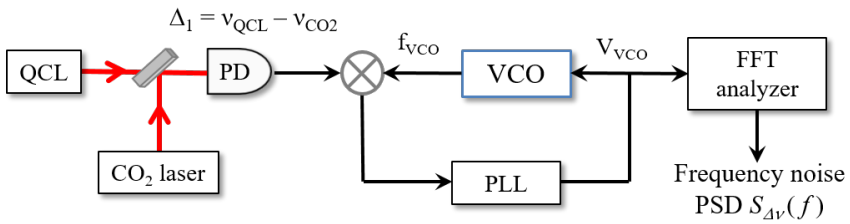

Figure 3.6 – Experimental setup for measuring the frequency noise power spectrum density (PSD) of the free-running QCL. PD: photodiode, VCO: voltage controlled oscillator, PLL: phase-lock loop, FFT: fast Fourier transform.

We have used the second technique to measure the frequency noise PSD of our DFB QCL. A free-running CO_2 laser with frequency noise of about 10^2 Hz^2/Hz^{-1} at 1 Hz Fourier frequency (see appendix C) was used as a reference source. Figure 3.6 illustrates the measurement principle. A beat-note signal at frequency $f_{beat}(t)$ ~150 MHz between the two lasers is detected on a liquid nitrogen cooled HgCdTe detector. A voltage-controlled oscillator (VCO) at frequency $f_{VCO}(t)$ ~150 MHz is phase-locked onto the beat-note signal via a phase-lock loop (PLL). The amplitude fluctuations of the PLL correction signal copy the beat-note signal's frequency noise and thus the QCL frequency noise. The frequency noise PSD of the QCL is thus derived by multiplying the PLL correction voltage noise PSD by a voltage-to-frequency conversion factor. Figure 3.7 shows the QCL frequency noise PSD. It is 10^{10} Hz^2/Hz at 1 Hz and shows $1/f$ slope at frequencies below 100 kHz, and a steeper slope at high Fourier frequencies.

Moreover, we also measure the frequency noise resulting from the current noise of the home-made low noise current source used to drive the QCL. To this end, two identical home-built current sources but of opposite polarity are connected according to Figure 3.8

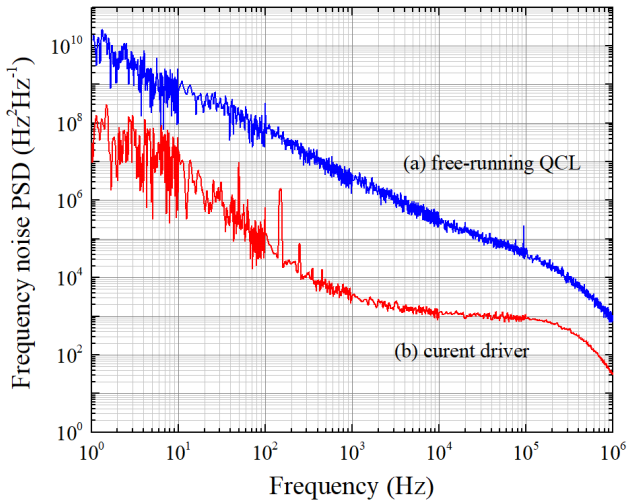

Figure 3.7 – (a) Frequency noise PSD of the free-running LPL QCL. (b) Frequency noise PSD resulting from the current noise of the home made low-noise current source used to drive the QCL.

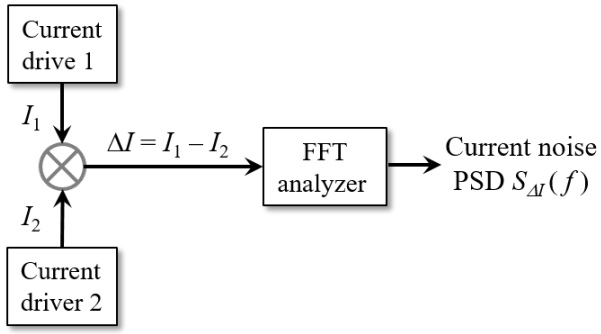

Figure 3.8 – Experimental setup to measure the current noise PSD $S_{\Delta I}(f)$ of the QCL current driver.

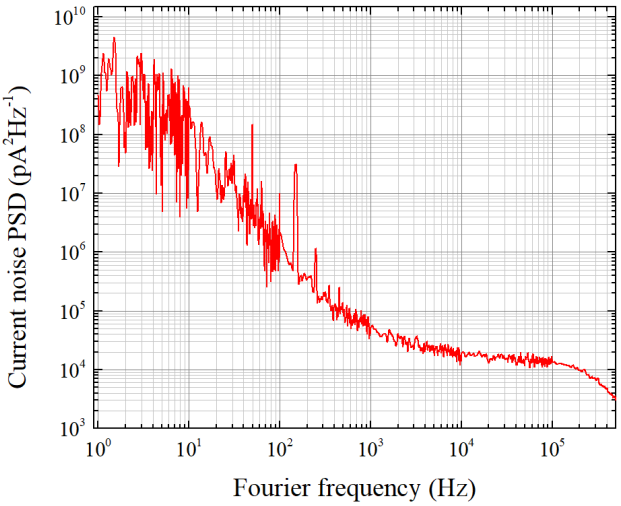

Figure 3.9 – Current noise PSD of the QCL current driver.

and set to deliver the same current. The residual AC current $\Delta I = I_1 - I_2$ has the noise contribution from both sources. Figure 3.9 shows the corresponding current noise PSD. It is about 10^9 pA^2.Hz^{-1} at 1 Hz Fourier frequency and then reduces to 10^4 pA^2.Hz^{-1} at 10^4 Hz. To estimate influence of the current noise to the QCL frequency noise, we convert this current noise spectrum to frequency noise PSD by multiplying with a laser DC current-to-frequency response of ∼257 MHz/mA (see above part 3.2.2.1). This result is shown in Figure 3.7 (line b). It is two orders of magnitude smaller than the free-running QCL noise. We conclude that the contribution of the current driver noise to the QCL frequency noise is negligible.

Frequency noise PSD and optical line shape

The frequency noise PSD contains all the information on the laser frequency noise. It is possible to calculate the laser line shape and thus the laser linewidth from the laser frequency noise PSD while the reverse process i.e., calculating the exact frequency noise spectrum from the laser line shape is not possible. This line shape and linewidth are useful for spectroscopic applications and modelling the molecular absorption line shape. Here, we briefly show the relation between the frequency noise PSD $S_{\delta\nu}(f)$ and the emission line shape $S_E(\nu)$ of the laser [206–208].

We assume that the laser light field is given by $E(t) = E_0 \exp[i(2\pi\nu_0 t + \phi(t))]$ with $\phi(t)$ a random phase noise in the time domain. The instantaneous laser frequency $\nu(t)$ and the frequency fluctuations $\delta\nu(t)$ are given by $\nu(t) = \nu_0 + \frac{1}{2\pi}\frac{\partial\phi(t)}{\partial t}$ and $\delta\nu(t) = \dfrac{1}{2\pi}\dfrac{\partial\phi(t)}{\partial t}$, respectively. The determination of the laser line shape from the frequency noise is done in two steps. First, the autocorrelation function $\Gamma_E(\tau)$ of the laser electric field $\Gamma_E(\tau) = \langle E(t+\tau)E^*(t)\rangle$ is calculated as an exponential of the integral of the frequency noise PSD $S_{\delta\nu}(f)$, filtered by a sinc function and takes the following form [208]

$$\Gamma_E(\tau) = E_0^2 e^{i2\pi\nu_0\tau} e^{-2\int_0^\infty S_{\delta\nu}(f)\frac{\sin^2(\pi f\tau)}{f^2}df}. \tag{3.1}$$

According to the Wiener-Khintchine theorem, the laser line shape $S_E(\nu - \nu_0)$ is the Fourier transform of this autocorrelation function [208]

$$\begin{aligned} S_E(\nu-\nu_0) &= 2\int_{-\infty}^{\infty} e^{-i2\pi\nu\tau}\Gamma_E(\tau)d\tau \\ &= 2E_0^2\int_{-\infty}^{\infty} e^{-i2\pi(\nu-\nu_0)\tau} e^{-2\int_0^\infty S_{\delta\nu}(f)\frac{\sin^2(\pi f\tau)}{f^2}df} d\tau \end{aligned} \tag{3.2}$$

Simple approximation for determination of the laser linewidth

Unfortunately, the previous formula most often cannot be analytically integrated. The laser linewidth can be obtained using a simple approximation method. An explanation of this method is presented in more details in Ref. [208]. As shown in Figure 3.10, a β-separation line separates the frequency noise PSD into two regions with a significantly different influence on the optical line shape: (i) the slow frequency modulation region, where the noise has a high modulation index $S_{\delta\nu}(f) > \frac{8\ln(2)f}{\pi^2}$, contributes to the laser

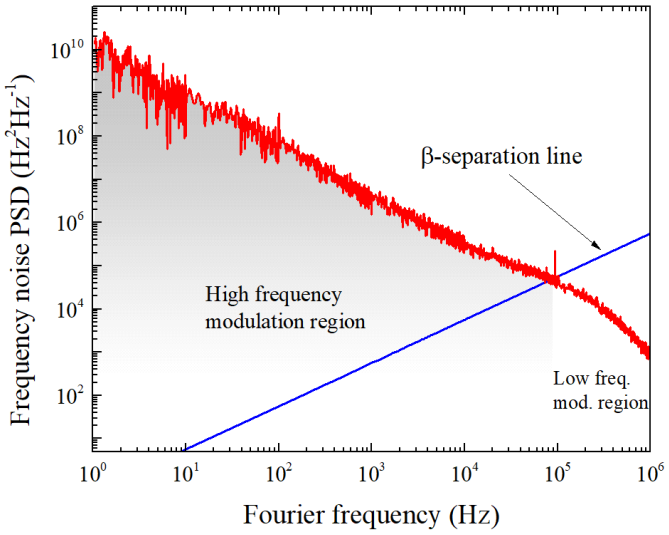

Figure 3.10 – The frequency noise PSD of our QCL is separated into two portions by the β-separation line, the high modulation index and low modulation index regions.

line shape and (ii) the fast frequency modulation region where $S_{\delta\nu}(f) < \frac{8\ln(2)f}{\pi^2}$ and where the frequency fluctuations have a low modulation index, so that it only contributes to the wings of the line shape [209].

The β-separation line crosses the frequency noise PSD spectrum at a Fourier frequency of f_c (in our particular case, $f_c = 87.3$ kHz). The full width at half maximum (FWHM) linewidth of the laser is then given by a simple expression with a good accuracy better than 10% [208],

$$\mathrm{FWHM} = \sqrt{8\ln(2)A}, \tag{3.3}$$

where A is the surface under the PSD, in the high modulation index region, given by

$$A = \int_{1/T_0}^{\infty} H\left(S_{\delta\nu}(f) - \frac{8\ln(2)f}{\pi^2}\right) S_{\delta\nu}(f)df = \int_{1/T_0}^{f_c} S_{\delta\nu}(f)df, \tag{3.4}$$

where H is the Heaviside step function, $H(x) = 1$ if $x \geq 0$ and $H(x) = 0$ if $x < 0$. The cut-off frequency $1/T_0$ is the inverse of the observation time T_0 over which the laser line shape is measured. It corresponds to the resolution bandwidth of the measurement. Figure 3.11 shows the QCL linewidths as a function of the resolution bandwidth ($1/T_0$) that is calculated from the frequency noise PSD $S_{\delta\nu}(f)$ using the β-separation line method (red solid line). Narrower linewidths are achieved for shorter measuring times (i.e. FWHM = 640 kHz at 1 s, and FWHM = 300 kHz at 1 ms). However, the linewidth can not be narrower than typically the inverse of the observation time and at a very short measuring time (smaller than 10 μs in our case), the linewidth measured will be limited by the resolution bandwidth (red dashed line). In this regime, the exact value of the measured linewidth will depend on the details of the shape of the temporal measurement window, but the resolution bandwidth $1/T_0$ is a good estimate.

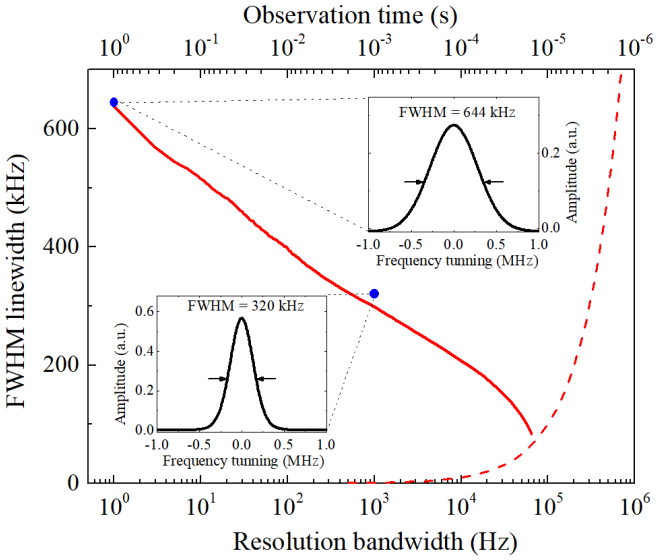

Figure 3.11 – Dependence of the free-running QCL linewidth on resolution bandwidth or observation time, calculated from the frequency noise PSD of Figure 3.7(a). The dashed line corresponds to the limit given by the resolution bandwidth. Two insets show the numerically calculated QCL line shapes at resolution bandwidths of 1 Hz and 1 kHz with corresponding linewidths of 644 kHz and 320 kHz.

Numerical calculation of the laser line shape and linewidth

As seen in the previous section, the line shape will depend on the observation time T_0. The relation between the laser line shape $S_E(f)$ and the frequency noise PSD $S_{\delta\nu}(f)$ is given by Equation 3.2. Only Fourier components of the phase noise spectrum for frequencies $f > 1/T_0$ contribute to the laser line shape (see supplementary of Ref. [210]). The lower bound of the integral in Equation 3.1 is thus replaced by $1/T_0$ (making the integral finite). Because of the finite observation time T_0, the laser electric field $E(t)$ is also windowed by a rectangular function $r(t)$ that equals to 1 between $t = 0$ and $t = T_0$ and 0 everywhere else. This leads the autocorrelation function $\Gamma_E(\tau)$ of $E(t)$ to be weighted by a triangular function: $(1 - |\tau|/T_0)$ between $-T_0$ and T_0 and 0 everywhere else. The autocorrelation function $\Gamma_E^{T_0}(\tau)$ of the field observed over a time T_0 is given by

$$\Gamma_E^{T_0}(\tau) = \langle E(t+\tau)r(t+\tau)E^*(t)r^*(t)\rangle. \tag{3.5}$$

$$\Gamma_E^{T_0}(\tau) \simeq \langle E(t+\tau)E^*(t)\rangle\langle r(t+\tau)(t)r^*(t)\rangle = \begin{cases} \left(1 - \frac{|\tau|}{T_0}\right)\Gamma_E(\tau) & \text{if} |\tau| \leq T_0 \\ 0 & \text{if} |\tau| > T_0. \end{cases} \tag{3.6}$$

The laser line shape observed over the finite observation time T_0 is derived as the Fourier transform of the modified autocorrelation function $\Gamma_E^{T_0}(\tau)$

$$\begin{aligned} S_E(\nu-\nu_0) &= 2\int_{-\infty}^{\infty} e^{-i2\pi\nu\tau}\Gamma_E^{T_0}(\tau)d\tau \\ &= 4E_0^2\int_0^{T_0}\left(1-\frac{|\tau|}{T_0}\right)\cos[2\pi(\nu-\nu_0)\tau]e^{-2\int_{1/T_0}^{\infty} S_{\delta\nu}(f)\frac{\sin^2(\pi f\tau)}{f^2}df}d\tau. \end{aligned} \tag{3.7}$$

Note that the minimum Fourier frequency at which has been measured the PSD (1 Hz in our case) gives an upper bound on the observation time T_0 at which the line shape can be calculated (1 s in our case).

Insets in Figure 3.11 show two numerically calculated line shapes of the free-running QCL at observation times of 1 s and 1 ms. Their FWHM linewidths are found to be 644 kHz and 320 kHz respectively and agree well with those determined from the approximate method using the β-separation line. The line shapes are almost Gaussians as expected from the $\sim 1/f$ dependence of the frequency noise PSD [211].

3.3 Frequency stabilization of a quantum cascade laser to an optical frequency comb

We describe in this section the experimental setup for the frequency stabilization of the QCL frequency onto the OFC using a sum-frequency generation process in a $AgGaSe_2$ crystal. We then report the resulting performances in terms of stability and frequency noise.

3.3.1 Sum frequency generation

3.3.1.1 Principle of sum-frequency generation

A sum-frequency generation process combines two radiations at different angular frequencies ω_1 and ω_2 in a nonlinear optical medium to generate a radiation at an angular frequency $\omega_{SFG} = \omega_1 + \omega_2$, as shown in Figure 3.12.

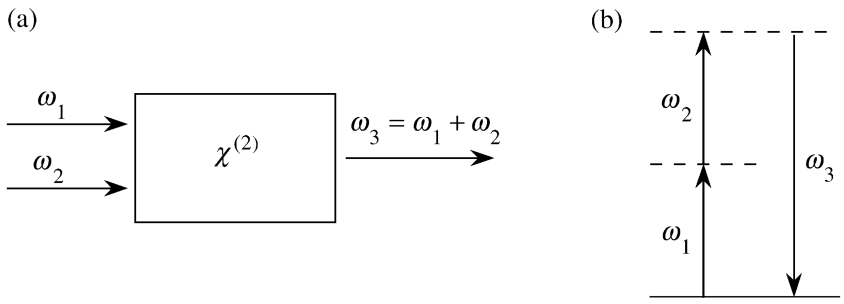

Figure 3.12 – Sum frequency generation: (a) Schematic of the SFG process and (b) energy levels of the three beams.

In nonlinear optics, the relationship between the polarization $P(t)$ of a medium and

the incoming electric field strength $E(t)$ of the light can be described by [212]

$$\begin{aligned} P(t) &= \varepsilon_0[\chi^{(1)}E(t) + \chi^{(2)}E^2(t) + \chi^{(3)}E^3(t) + ...] \\ &= P^{(1)}(t) + P^{(2)}(t) + P^{(3)}(t) + ..., \end{aligned} \tag{3.8}$$

where ε_0 is the free space permittivity, $\chi^{(1)}$ is known as the linear optical susceptibility, and $\chi^{(2)}$ and $\chi^{(3)}$ are known as second- and third- order nonlinear optical susceptibilities respectively.

The electric field in the nonlinear crystal is the sum of the two incident electric fields from the two lasers with corresponding frequencies ω_1 and ω_2, given by

$$E(t) = E_1 e^{i\omega_1 t} + E_2 e^{i\omega_2 t} + cc. \tag{3.9}$$

Let us consider only the second-order term of the polarization $P^{(2)}(t)$ which can be written as [212]:

$$\begin{aligned} P^{(2)}(t) = \varepsilon_0\chi^{(2)}E^2(t) = \varepsilon_0\chi^{(2)}[E_1^2 e^{2i\omega_1 t} + E_2^2 e^{2i\omega_2 t} + 2E_1E_2e^{i(\omega_1+\omega_2)t} \\ + 2E_1E_2^* e^{i(\omega_1-\omega_2)t} + c.c.] + 2\varepsilon_0\chi^{(2)}[E_1E_1^* + E_2E_2^*]. \end{aligned} \tag{3.10}$$

The propagation of the two lasers with angular frequencies ω_1 and ω_2 in a second order nonlinear crystal gives rise to a new light wave at frequency $\omega_3 = \omega_1 + \omega_2$, corresponding to sum frequency generation. The SFG process is frequently used for up-conversion of long-wave light to shorter-wave light (i.e. mid-IR radiation to near-IR radiation). Moreover, according to Equation 3.10, light at other frequencies is also observed (i.e. second harmonic generations (SHG) at frequencies $2\omega_1$ and $2\omega_2$ and difference frequency generation (DFG) at frequency $\omega_1 - \omega_2$).

Phase matching

Here, we only consider the SFG process in the nonlinear crystal. Under usual conditions, the SFG light wave is very weak because of phase mismatch between the interacting waves ω_1 and ω_2 along the propagation direction. This phase mismatch is given by

$$\Delta\vec{k} = \vec{k_1} + \vec{k_2} - \vec{k_3}, \tag{3.11}$$

where $\vec{k_i}$ are the wave vectors of the waves with frequencies ω_i (i= 1, 2, 3), $|\vec{k_i}| = \omega_i n_i/c$ with n_i the refection index at the frequency ω_i, and c the speed of light. The SFG wave can be observed under the phase-matching condition: $\Delta\vec{k} = 0$ or $n_3\omega_3 = n_1\omega_1 + n_2\omega_2$.

We now consider an uniaxial crystal for which we can define the optic axis (z axis) as the direction for which the index is the same whatever the polarization. As shown in Figure 3.13(a), a light beam polarized perpendicular to the principle plane $(\vec{k}, \vec{z})$ containing the z axis and the wave vector light $\vec{k}$ is called ordinary (o) beam (or ray) and experiences the refractive index n_o, which is the ordinary refractive index of the crystal. On the contrary, a light beam polarized in the principle plane is called extraordinary (e) beam (or ray). Such light experiences a refractive index $n_e(\theta)$ which depends on the angle θ (the angle between the z axis and the wave vector $\vec{k}$),

$$n_e^\theta(\theta) = \frac{n_o n_e}{(n_e^2 cos^2\theta + n_o^2 sin^2\theta)^{1/2}}, \tag{3.12}$$

where n_e is the extraordinary refractive index of the crystal. The phase-matching can be thus achieved by adjusting the angle θ to obtain the value of $n_e(\theta)$ for which the phase matching condition $\Delta k = 0$. Moreover, the refractive index is strongly temperature-dependent for some birefringent crystal. Therefore, the phase matching can be also obtained by holding the θ angle and varying the crystal temperature.

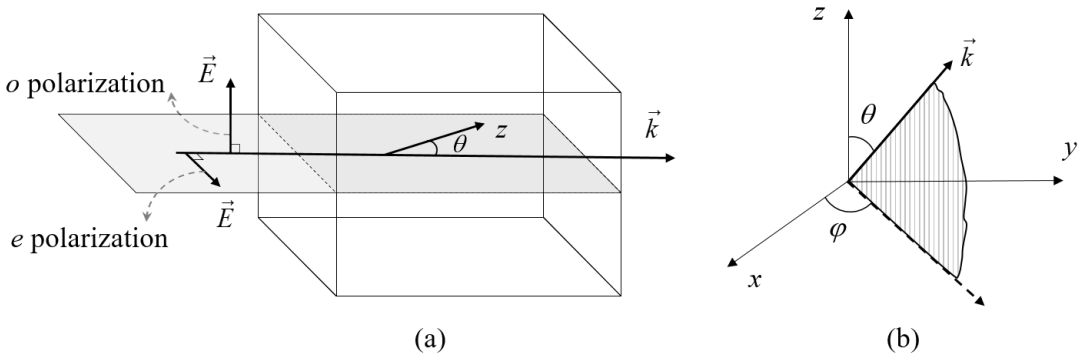

Figure 3.13 – (a) The polarization (i.e. direction of the electric field vector $\vec{E}$) of an ordinary (o) beam is perpendicular to the principle plane containing the optic z axis and the wave vector $\vec{k}$, an extraordinary (e) beam is polarized in the principle plane, and θ is the angle between the z axis and the vector $\vec{k}$. (b) Polar coordinate system for the description of the uniaxial crystal's refraction properties: φ is the angle between the projection of the vector $\vec{k}$ on the plane (x, y) and the x axis. Adapted from [213].

Types of phase matching

In principle, uniaxial crystals can be used with two types of phase matching. Type I phase matching corresponds to the case where the two incident waves have the same polarization (i.e. both o beams or both e beams) and the SFG wave's polarization is perpendicular to the incident waves, (e beam or o beam respectively). This results in two phase matching configurations: "*ooe*" and "*eeo*". On the contrary, type II phase matching means that the two interacting waves have orthogonal polarizations (i.e., one is an o beam and the other one is an e beam) and the SFG wave is polarized parallel to one of the incident beams. The second type has two phase matching configurations: "*eoe*" and "*oeo*".

3.3.1.2 Sum frequency generation in a $AgGaSe_2$ crystal

In our experiment, we have chosen a silver gallium selenite ($AgGaSe_2$) crystal to perform a SFG process between the QCL beam at wavelength $\lambda_1 = 10.3$ μm and the custom comb output at wavelength $\lambda_2 = 1.85$ μm. The resulting SFG beam has a wavelength of $\lambda_3 = 1.55$ μm, as shown in Figure 3.14. This crystal has dimensions 5 x 5 mm in width and height and a length of 10 mm. It has a large transparency ranging from 0.71 to 19 μm [213]. Anti-reflection layers are deposited on both facets. The residual facet reflection is ~0.7% for the 10.3 μm beam and ~0.2% for the 1.85 μm beam.

We use a type I phase matching with "*ooe*" configuration. Both the QCL and the 1.85 μm beams are polarized along the o ray of the crystal, as indicated in Figure 3.14. At the crystal output, the resulting SFG beam at $\lambda_3 = 1.55$ μm has a polarization perpendicular to the incident beams. The walk-off angle ρ between the Poynting vector $\vec{s}$ of the SFG

beam and the wave vector $\vec{k}$ is about 0.61^0, resulting in a distance δ separating the $\vec{k}$ axis and the SFG beam of about ~ 0.11 mm [212] (see Figure 3.14).

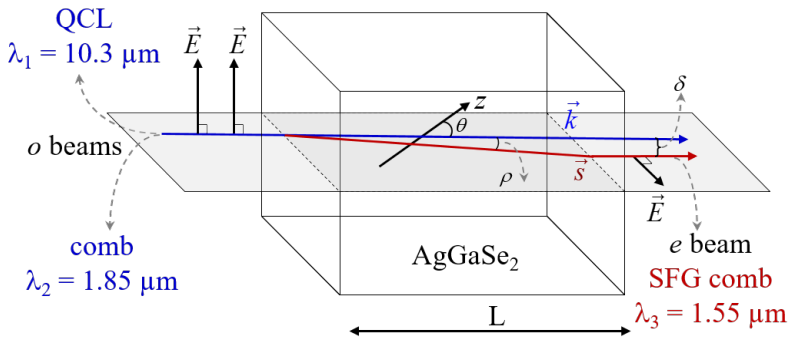

Figure 3.14 – The SFG beam with extraordinary (e) polarization is generated in the $AgGaSe_2$ crystal from the combination of the 10.3 μm and 1.85 μm beams with ordinary (o) polarizations. θ: phase matching angle, ρ:walk-off angle, $\vec{s}$: Poynting vector, $\vec{k}$: wave vector, and *delta*: distance separating between $\vec{k}$ and $\vec{s}$.

As mentioned above, we only obtain the SFG beam when the phase-mismatch is controlled to be zero. The SFG crystal is thus rotated as close as possible to the relevant phase-matching angle (for type I phase-matching), given by the following equation

$$\theta = \arctan\left(\sqrt{\frac{1-U}{W-1}}\right) \tag{3.13}$$

with $U = \left(\frac{A+B}{C}\right)^2$, $W = \left(\frac{A+B}{F}\right)^2$, $A = \frac{n_{o1}}{\lambda_1}$, $B = \frac{n_{o2}}{\lambda_2}$, $C = \frac{n_{o3}}{\lambda_3}$,and $F = \frac{n_{e3}}{\lambda_3}$, in which λ_i $(i = 1, 2, 3)$ are respectively the wavelengths of the QCL beam, the custom comb beam, and the SFG comb beam [213], n_{oi} are the wavelength-dependent ordinary refractive indices of the ordinary interacting beams at wavelengths λ_i, and n_{e3} is the wavelength-dependent extraordinary reflective index of the SFG beam at wavelength λ_3. The refractive indices are determined by the following equation,

$$n^2 = A + \frac{B}{(\lambda^a - C)} + \frac{F}{(\lambda^b - G)} + \frac{D}{\left(1 - \frac{E}{\lambda^c}\right)}, \tag{3.14}$$

where A to G parameters and a to c parameters can be found in Ref. [214] for both the ordinary and the extraordinary index. For mid-IR beam at 10.3 μm, phase matching is thus obtained with $\theta \sim 51°$.

Power conversion efficiency

Following V.G. Dmitriev et al [213], an approximate power conversion efficiency of the SFG is given by

$$\Gamma_{SFG} = \frac{P_3}{P_1 P_2} = \frac{2^3 \pi^2 d_{\text{eff}}^2 L^2}{\varepsilon_0 c n_{o1} n_{o2} n_{e3} \lambda_3^2 w_0^2} \left(\frac{\sin\left(\Delta k \frac{L}{2}\right)}{\Delta k \frac{L}{2}}\right)^2, \tag{3.15}$$

where P_1 and P_2 are the powers of the two interacting beams, P_3 is the SFG beam's power at wavelength λ_3, L refers to the crystal length, Δk is the wave mismatch, w_0 represents the waists of the incident lasers (assuming that both incident lasers have the same waist), n_{o1} and n_{o2} are the ordinary refractive indices given by Equation 3.14, n_{e3} is the extraordinary index given by Equation 3.12, and d_{eff} refers to the effective nonlinearity of crystal. For the $AgGaSe_2$ crystal, the latter is given by $d_{\text{eff}} = d_{36} \sin\theta \sin 2\varphi$ [213], where $d_{36} = 33$ pm/V is an element of the tensor and φ is the angle between the projection of the $\vec{k}$ vector on the (x, y) plane and the x axis, as shown in Figure 3.13(b). The effective nonlinearity is found to be $d_{\text{eff}} = 25.65$ pm/V with $\varphi = 45°$. When $\Delta k = 0.886\pi/L$, the conversion efficient is reduced by a factor two.

Following Equation 3.15, the theoretical conversion efficiency is 2.35 mW/W^2 for a waist of $w_0 = 100\mu$m and phase mismatch of $\Delta k = 0$. Note that this is just an approximate calculation in the case of equal waists. In order to optimize the conversion efficiency of the crystal, a more refined calculation should be performed taking into account the walk-off angle and the different waists of the two beams. This was done by Jean-Jacques Zondy [215,216]. The conversion efficiency is found to be maximum for the following waists $w_{0,10.6\mu\text{m}} = 51$ μm and $w_{0,1.84\mu\text{m}} = 39.4$ μm, and is 2.223 mW/W^2.

Spectral acceptance

Let us calculate the spectral acceptance of SFG when λ_2 (the wavelength of the 1.85 μm beam in our case) is varied. This is the spectral window over which the efficiency of SFG stays higher than half of the maximum efficiency even if Δk is not zero any more. We can then compare it to the spectral bandwidth of the 1.85 comb. From [213], the calculated FWHM spectral acceptance (FWHM of Γ_{SFG} in Equation 3.15 when λ_2 is varied) of the "*ooe*" crystal type is given by

$$\Delta\nu_2 = \frac{0.886}{L}\left| n_{o2} - n_{e3} - \lambda_2 \frac{\partial n_{o2}}{\partial \lambda_2} + \lambda_3 \frac{\partial n_3^e(\theta)}{\partial \lambda_3} \right|^{-1}, \tag{3.16}$$

where $n_3^e(\theta)$ is the refractive index of the extraordinary SFG beam depending on the θ angle. The resulting calculated FWHM spectral acceptance of the crystal for the 1.85 μm beam is ~14 nm (~1.22 THz), corresponding to ~4 900 comb teeth.

As shown in Figure 2.20, the custom output centered at 1.84 μm has a FWHM spectral bandwidth of ~65 nm (~5.8 THz), corresponding to 23 200 comb teeth. The 1.85 μm comb output is filtered by an optical bandpass filter (F1850, Figure 2.22) that has a center wavelength of 1.84 nm and a FWHM bandwidth of 89 nm. Therefore, all teeth of the custom comb are sent to the $AgGaSe_2$ crystal for SFG with the QCL beam.

We can see that the SFG spectral acceptance limits the SFG process to only one-fourth of the 1.85 μm comb's teeth. It thus reduces the above SFG theoretical efficiency by a factor 4. In that case, the calculated efficiency of the SFG is ~ 0.6 mW/W^2. Finally, the spectral bandwidth of the 1.55 μm SFG comb is expected to be ~11.7 nm (~1.02 THz), corresponding to 4100 comb teeth.

Mid-IR spectral coverage

We now consider the SFG of the mid-IR QCL of wavelength λ_1 with a comb mode around 1.85 μm at wavelength λ_2. We obtain a SFG laser of wavelength λ_3 ($\lambda_3 = (1/\lambda_1 + 1/\lambda_2)^{-1}$). As mentioned in section 2.6, the original comb output at 1.55 μm and

the custom comb output at 1.85 μm have FWHM spectral band widths of 33 nm (λ_2 wavelength ranging from 1.555 to 1.588 μm) and 65 nm (λ_3 wavelength ranging from 1.805 to 1.870 μm), respectively. These spectral ranges give a constraint on the mid-IR QCL wavelength we can use, in order that the SFG laser beam falls in the accessible range of our 1.55 μm comb.

Figure 3.15 shows the range of mid-IR wavelengths λ_1 that can be used for SFG with the 1.85 μm comb output, for the spectral bandwidths indicated above. Figure 3.16 displays the corresponding range of calculated (using Equation 3.13) phase-matching angle θ as a function of (λ_2, λ_3). It varies from 48° to 54°, which can easily be accommodated in our optical system by controlling the tilt of the crystal.

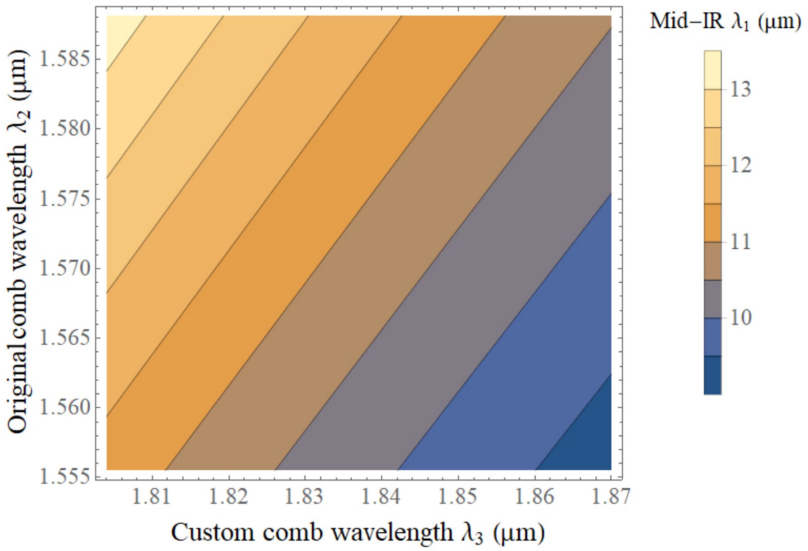

Figure 3.15 – Mid-IR wavelength range λ_1 that can be used for SFG: the original comb spans from 1.555 to 1.588 μm (corresponding to the FWHM bandwith of the comb spectrum in Figure 2.19) and the custom comb spans from 1.805 nm to 1.870 μm (corresponding to the FWHM bandwith of the comb spectrum in Figure 2.20).

Note that other mid-IR frequency wavelengths are potentially reachable by replacing the custom comb module by other commercially available ones spanning different spectral windows. Using a longer-wavelength custom output would allow to carry out SFG with shorter mid-IR wavelengths and vice versa. Using another appropriate non-linear crystal may then be required.

3.3.2 Locking the quantum cascade laser to the optical frequency comb

3.3.2.1 Overview

The principle for the stabilization of the QCL at 10.3 μm to the OFC is to use up-frequency conversion in the $AgGaSe_2$ crystal. A custom output of the comb at 1.85 μm is overlapped with the 10.3 μm QCL beam in the non-linear crystal. The resulting shifted comb, centered at 1.55 μm, is then combined with the 1.55 μm main comb output, yielding a beat-note signal between the QCL frequency and the OFC. The QCL is then locked to the OFC via phase-locking this beat-note signal to a fixed frequency signal and by applying a correction signal to the QCL current.

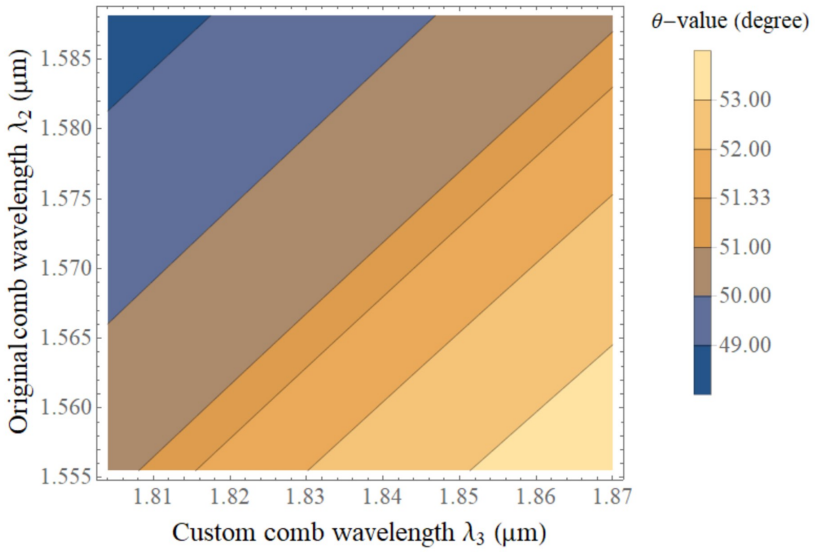

Figure 3.16 – Calculated phase-matching angle θ (using Equation Equation 3.13) for carrying out SFG $(1/\lambda_1 + 1/\lambda_2)^{-1} = \lambda_3$ as a function of (λ_2, λ_3). Corresponding values of the mid-IR wavelength λ_1 are displayed in Figure 3.15. λ_2 is the 1.55 μm main comb wavelength and λ_3 is the 1.85 μm custom comb wavelength.

3.3.2.2 Experimental setup details

The whole experimental setup for the frequency stabilization of the QCL is shown in Figure 3.17. A technical protocol for the SFG setup alignment is presented in Appendix B.

Optical alignment for the SFG process

In order to generate the SFG signal, the two laser beams at 10.3 μm and 1.85 μm are overlapped in the $AgGaSe_2$ crystal. We use an optical isolator (InnPho, FIO-5-10.3-EW) working in the 10 μm region to protect the QCL from back reflections (OI in Figures 3.17 and 3.19). The diverging QCL beam is focused in this optical isolator by the lens L_1 (Thorlabs, C036TME-F, $f = 4$ mm) for minimizing power loss that could result from the beam clipping by the small aperture of the isolator of about 4 mm. At the isolator output, the QCL beam is approximately collimated by a long focal lens L_2 and then separated into two parts by a beam splitter (BS_1, Figure 3.17). The first part (20% of total power) is directed toward a spectroscopy setup that will be described in chapter 4 while the second part (80% of total power) is directed toward another optical table where the OFC is located. The QCL polarization is adjusted to be parallel with that of the 1.85 μm beam using a half wave-plate ($\lambda/2$, Figure 3.17).

We now consider the custom 1.85 μm beam with comb mode frequencies $q \times f_{rep} + f_{ceo}$ (q ~680 000). A band-pass interference filter (CVI, F1850) centered at 1.85 μm with a bandwidth of 89 nm FWHM is set at the custom comb output to filter out radiations at wavelengths between 1.5 to 1.8 μm (see Figure 2.20). The resulting beam is then filtered by a polarizer (P_1) with an extinction ratio over 10000:1.

The QCL and the 1.85 μm beams with typical powers of around 5.5 mW and 21 mW respectively are superimposed using a dichroic beam splitter (BS_2) (see Figure 3.17).

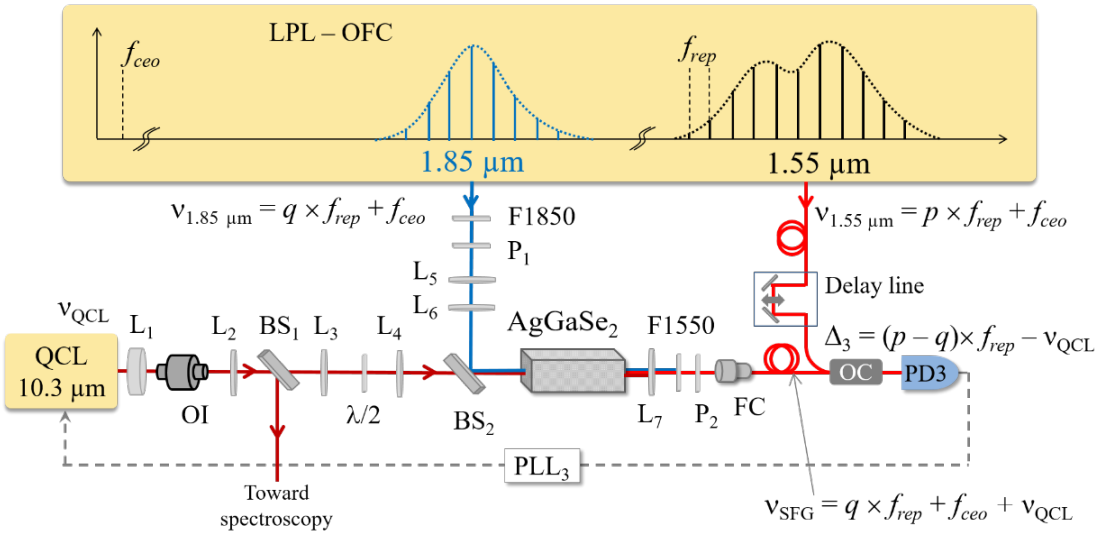

Figure 3.17 – Experimental setup for the stabilization of the QCL frequency onto the optical frequency comb (see also Figure 3.19). The 1.85 μm custom comb output is overlapped with the 10.3 μm QCL beam in the $AgGaSe_2$ crystal for the sum-frequency generation. A resulting shifted comb at 1.55 μm is then combined with the 1.55 μm main comb, yielding a beat-note signal on the photodiode PD_3 between the QCL frequency and a high harmonic of the comb repetition rate (see equation 3.20). Finally, this beat-note signal is used to lock the QCL frequency to the OFC via a phase-lock loop (PLL3). OFC: optical frequency comb, P_i: polarizers, L_i: lenses, F1550: optical filter at 1.550 μm, F1850: optical filter at 1.850 μm, OI: optical isolator, PD_i: photodetectors, BS: beam splitter, OC: optical coupler, FC: fiber coupler.

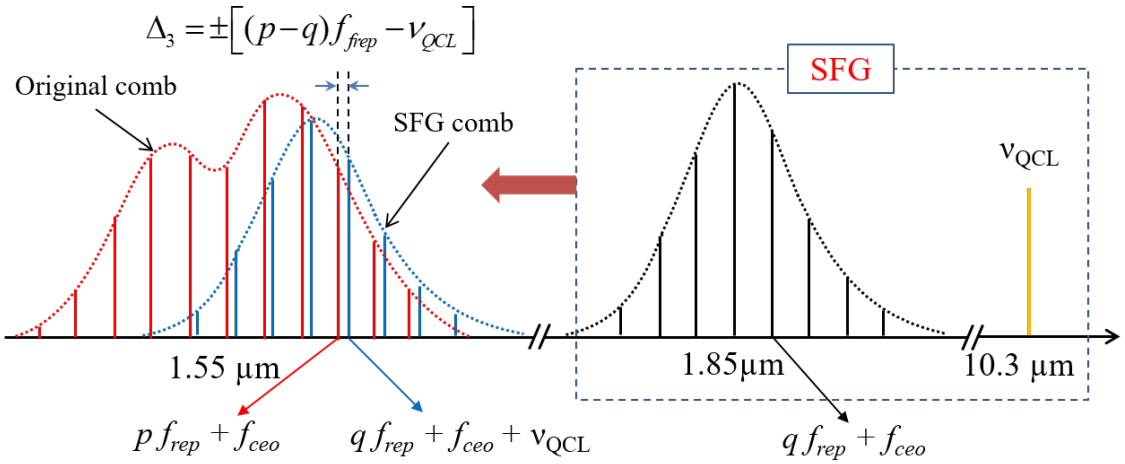

Figure 3.18 – Sum frequency generation between a custom comb output at 1.85 μm (black comb), of mode frequencies $q \times f_{rep} + f_{ceo}$ with q an integer, and a QCL beam of frequency ν_{QCL} results in a SFG comb (red comb) at around 1.55 μm of mode frequency $qf_{rep} + f_{ceo} + \nu_{QCL}$. The beat-note signal of the SFG comb with the original comb centered at 1.55 μm (blue comb) of mode frequency $p \times f_{rep} + f_{ceo}$ with p an integer is at a frequency $\Delta_3 = \pm\left[(p-q)f_{rep} - \nu_{QCL}\right]$. SFG: sum-frequency generation.

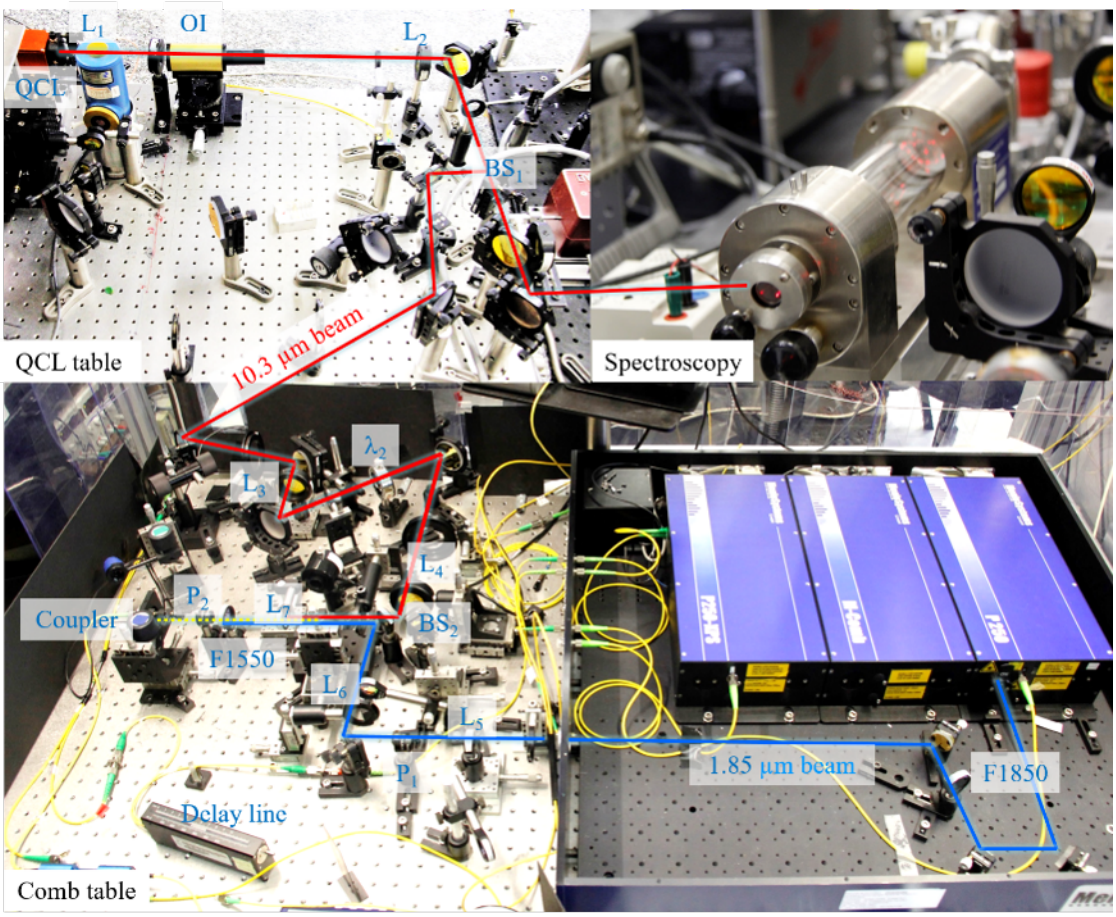

Figure 3.19 – Photograph of the experimental setup that occupies two optical tables. One table contains the optical frequency comb and the sum-frequency generation setup. The other one hosts the QCL and the saturated absorption spectroscopy setup that includes a multi-pass absorption cell.

Around 75% power of the 1.85 μm comb's power (∼16 mW) is reflected on the BS_2 and around 75% power of the QCL (∼ 4.5 mW) is transmitted through this beam splitter. These beams are focused at the center of the crystal by two telescopes: the first one composed of lenses L_3 ($f_3 = 254$ mm) and L_4 ($f_4 = 100$ mm) for the QCL beam and the second one composed of lenses L_5 ($f_5 = 75$ mm) and L_6 ($f_6 = 75$ mm) for the 1.85 μm beam. The setup has been designed in such a way to approach the theoretical optima given in subsection 3.3.1.2. At the crystal output, we obtain a resulting shifted comb (SFG comb) centered at 1.55 μm with comb mode frequencies

$$\nu_{\mathrm{SFG}} = q \times f_{rep} + f_{ceo} + \nu_{\mathrm{QCL}}, \tag{3.17}$$

as illustrated in Figure 3.18. In addition, the 1.85 μm and the QCL beams are also present at the crystal output.

Coupling SFG beam into an optical fiber

The free-space SFG beam is coupled into an optical fiber and then combined with the fibered original comb output to generate a beat-note signal that is required to lock the

QCL to the OFC, as mentioned in the overview part. To this end, firstly, the SFG beam is shaped by the lens L_7 (f_7 = 40mm, see Figures 3.17 and 3.19) to be approximately collimated. The QCL beam transmitted through the crystal is blocked by this lens which does not transmit mid-IR radiations. Secondly, an optical filter (CVI, F1550) is installed after the lens to cancel the remaining part of the 1.85 μm beam. The latter is also filtered out by the polarizer P_2 whose transmission axis is set parallel to the extraordinary polarization axis of the SFG beam and thus perpendicular to the 1.85 μm polarization (see subsection 3.3.1.2). Finally, the SFG beam is injected into an optical fiber using a collimator (Thorlabs, PAF-X-5C). Since it is not fully matched to the SFG beam's geometry, only ~50% of the SFG beam power is coupled into the fiber.

In order to evaluate the power conversion efficiency of the SFG process, the SFG beam's power at the output of the crystal has to be determined. However, it is not possible to perform this measurement because of much stronger residual powers of both 10.3 μm and 1.85 μm. In practice, the SFG beam power is measured at the entrance of the optical coupler where these residual beams are completely filtered out. It is about 18 nW. The transmissions of the filter F1550 and the polarizer P_2 are about 50% and 85% respectively. The SFG power at the crystal output is thus expected to be ~42 nW, corresponding to a power conversion efficiency of $\Gamma_{SFG} = 0.6$ mW/W^2, agreeing well with the calculated efficiency (see subsection 3.3.1.2). This is also similar to measurement previously performed with the same 1.85 μm comb but at a higher power of ~25 mW and a CO_2 laser of power 200 mW [51]. In this experiment, the SFG power was found to be 2 μW, corresponding to a power conversion efficiency of 0.4 mW/W^2.

Generating a beat-note signal between the QCL and the OFC

Around 90% of the SFG beam power and around 10% of the original comb power at the same wavelength 1.55 μm are combined together via a 90/10 fiber coupler (see Figure 3.17). Note that these combs are matched in the time domain by a manually controlled variable optical delay line (General Photonics, VDL-001) in order to maximise the beat-note signal. In addition, the polarization of the SFG beam can be adjusted via an optical fiber controller (OZOptics, PFPC-11-1300-1550). These combs are then sent to a photodiode (PD3, Figure 3.17), yielding a beat-note signal at frequency

$$\Delta_3 = \pm\left[(p-q)f_{rep} - \nu_{\mathrm{QCL}}\right] = \pm\left[n\, f_{rep} - \nu_{\mathrm{QCL}}\right], \tag{3.18}$$

where $p-q = n$ is an integer of the order of 120 000. This beat-note signal is independent of the carrier envelope offset of the OFC. It depends only on the repetition rate through the n^{th} harmonic of repetition rate of the OFC. Frequency fluctuations of the beat-note signal are mainly caused by the QCL free-running noise.

Locking the QCL frequency to the repetition rate of the OFC

In order to phase-lock the QCL frequency to the n^{th} harmonic of the repetition rate of the OFC, we use a special home-made phase-lock loop (PLL3 in Figure 3.17), that is based on a phase-frequency detector (ON Semiconductor, MCH12140) instead of a phase detector as in usual phase-lock loop and that is displayed in Figure 3.20. The beat-note signal of frequency Δ_3 is first amplified and two low-bandpass filters allows us to filter out the parasitic beat-notes arising at f_{rep} and its harmonics and $\pm\Delta_3 \pm n f_{fep}$. The resulting signal is further filtered with a short band-pass filter (9.5-11.5 MHz) and amplified again.

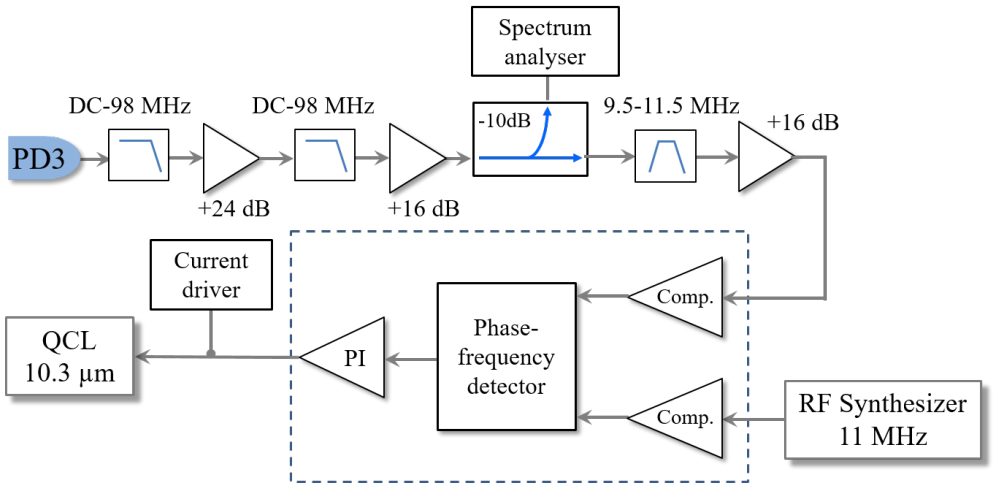

Figure 3.20 – Schematic for locking the QCL onto the OFC using a home-made phase-lock loop based on a quency detector. PD: photodiode, RF: radio frequency, Comp: high speed PECL/LVPECL fast comparator, PI: proportional-integral controller.

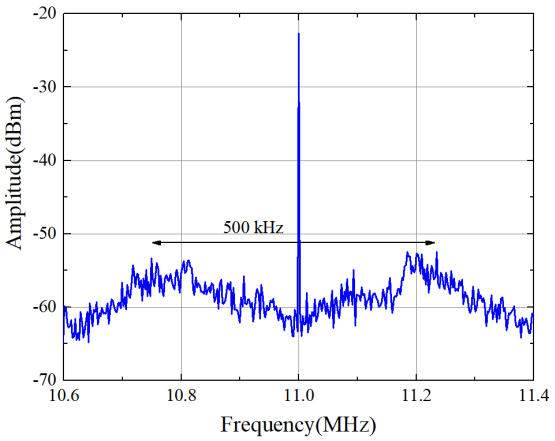

Figure 3.21 – In-loop beat-note signal between the QCL and a high harmonic of the OFC repetition rate recorded with a resolution bandwidth of 1 kHz. The bump of the beat-note signal indicates the locking bandwidth of 250 kHz.

In this phase-lock loop, both the phase and the frequency of the beat-note signal Δ_3 are compared with those of a fixed frequency signal at 11 MHz, provided by a DDS synthesizer, using the phase-frequency detector. An error signal is generated and then processed and converted into a correction signal via a proportional-integral (PI) circuit. The QCL frequency is then locked by feeding this correction to the QCL current. One obtains

$$\Delta_3 = nf_{rep} - \nu_{QCL}, \tag{3.19}$$

where the positive sign (compared to Equation 3.18) is imposed by the phase-frequency detector.

Figure 3.21 shows an in-loop beat-note signal at 11 MHz between the main comb output at 1.55 μm and the SFG comb exhibiting a signal-to-noise ratio (SNR) of about 25-30 dB in a resolution bandwidth of 100 kHz. The bump of the beat-note signal indicates a locking bandwidth of ∼250 kHz. We think that the beat-note signal's signal-to-noise ratio could be limited by a broadband noise in the 1.85 μm output, which results from the amplified spontaneous emission in the amplifier used to generate this 1.85 μm output.

3.3.3 Performances of the QCL frequency stabilization

3.3.3.1 Comparison between the stabilized QCL and a CO_2 laser stabilized to an OsO_4 saturated absorption line

In order to evaluate the performances of the frequency stabilization of the QCL to the optical frequency reference, a CO_2 laser whose frequency is locked to a saturated absorption OsO_4 line (CO_2/OsO_4 laser) [47, 198, 201] was used as a mid-IR reference. Its fractional frequency stability is 4×10^{-14} at 1s and can reach 10^{-14} after 100 s of integration. It then increases at longer time due to the frequency drift resulting from the systematic shift affecting the OsO_4 transition (see appendix C). Figure 3.22 shows an experimental setup to compare the frequency stability and the frequency noise level of the stabilized QCL and the CO_2/OsO_4 laser.

The signal at frequency Δ_4 on the photodiode PD_4 corresponds to the beat-note signal between the stabilized QCL and the CO_2/OsO_4 laser while the signal at frequency $\Delta_3^{'}$ on the photodiode PD_3 corresponds to the beat-note signal between a multiple of the repetition rate of the OFC ($n \times f_{rep}$) and the CO_2/OsO_4 laser. Frequencies of these signals were measured using Π-type frequency counters. Their fractional frequency stabilities were then obtained by calculating the overlapping Allan deviation of the experimental data. Figure 3.23 shows the frequency stabilities of the beat-note signal Δ_4 (line a, red) and of the beat-note signal $\Delta_3^{'}$ (line b, blue). Both these frequency stabilities are almost identical. They are equal to 4×10^{-14} at 1 s and decrease with $1/\tau^{-1/2}$ slope between 1 s to 100 s of averaging time. This results is found to be similar to previous measurement of the stability of the CO_2/OsO_4 laser [51]. These measurements are limited by the CO_2/OsO_4 laser's noise level. Therefore, they cannot provide the true stability level of the stabilized QCL. For comparison, we also plot in Figure 3.24 the OFC fractional frequency stability (line c, green) measured in subsection 2.7.2.

Figure 3.24 displays the frequency noise PSDs of beat-note signals Δ_4 (red line, a) and $\Delta_3^{'}$ (blue line, b). Those were obtained using a fast Fourier transform spectrum analyzer [45]. Here again, the frequency noise PSD of the OFC repetition rate stabilized to the

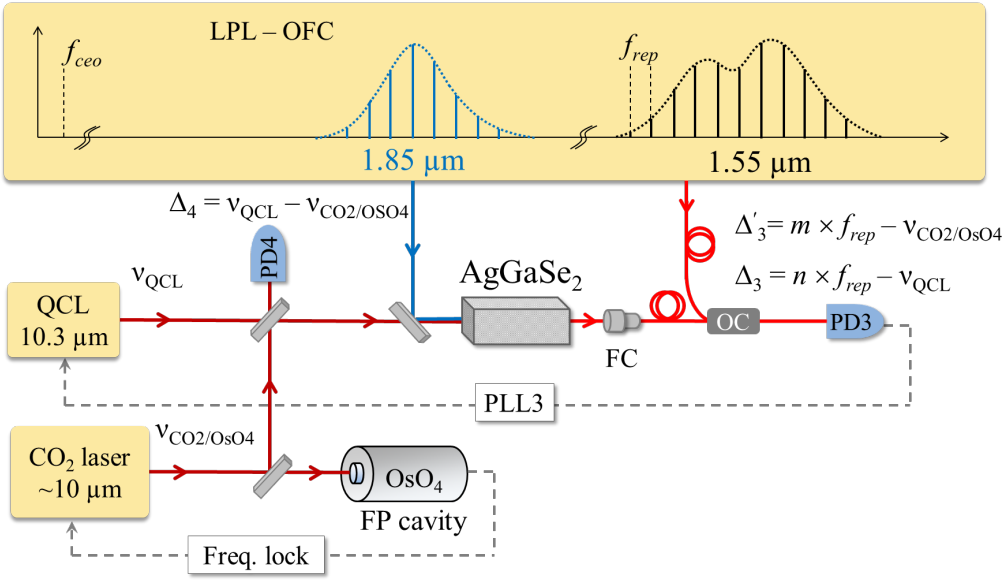

Figure 3.22 – Experimental setup for comparing the stability and the frequency noise between the stabilized QCL and the CO_2/OsO_4 laser. Two beat-note signals are detected on the photodiode PD_3: Δ_3 between the QCL and the comb, Δ'_3 between the CO_2/OsO_4 laser and the comb. The beat-note signal Δ_4 between the QCL and the CO_2/OsO_4 laser is detected on the photodiode PD_4. OFC: optical frequency comb, PD3 and PD4: photodetectors, BS: beam splitter, OC: optical coupler, FC: fiber coupler, FP cavity: Fabry-Perot cavity, PLL3: phase-lock loop, Freq. lock: servo loop for locking the CO_2 laser to an $OsOs_4$ saturated absorption line.

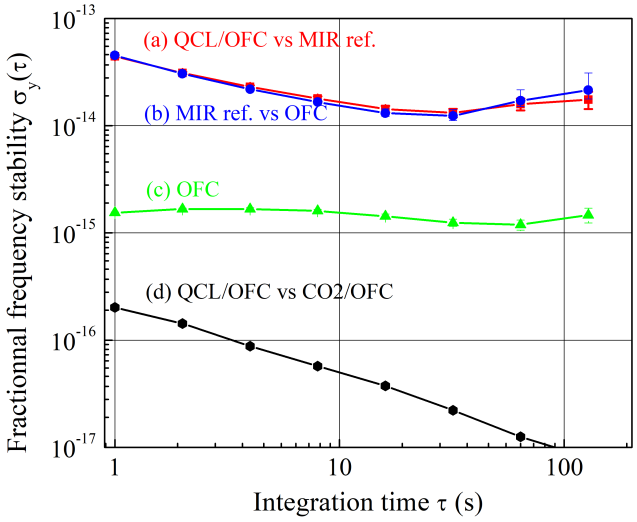

Figure 3.23 – Fractional frequency stabilities of the beat-note signals (a) between the QCL locked onto the OFC and the CO_2 locked to OsO_4, (b) between the CO_2 locked to OsO_4 and the OFC repetition rate, (c) the OFC (see subsection 2.7.2), (d) the beat-note signal between the QCL and the CO_2 both locked to the OFC repetition rate. Taken from [45].

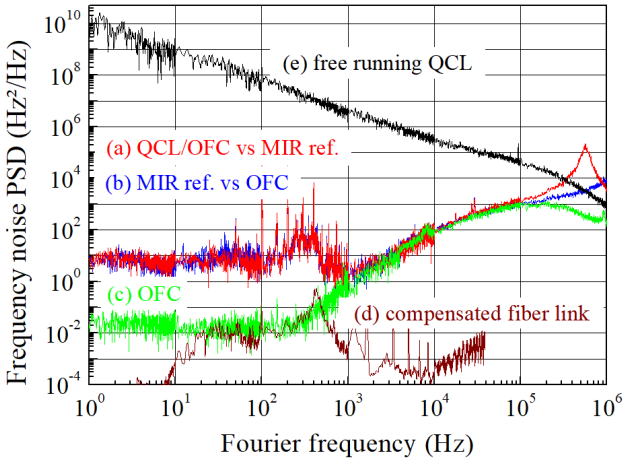

Figure 3.24 – Frequency noise power spectral densities of the beat-note signals (a) between the QCL locked onto the OFC and the CO_2 locked to saturated absorption of OsO_4, (b) between the CO_2 locked to saturated absorption of OsO_4 and the OFC repetition rate, (c) the OFC (see subsection 2.7.2), (d) the compensated link (see subsection 2.3.2), and (e) the free-running QCL (see subsection 3.2.2). Taken from [45].

OLO carrier frequency (line c, green) shown in section 2.7.2 is plotted for comparison, together with the 43-km long noise compensated link (line d, brown) already shown in subsection 2.7.2, too. Note that, to facilitate the comparison between curves, all curves display noise levels scaled to 29.1 THz which corresponds to the mid-IR frequency (10.3 μm). The frequency noise PSDs of the beat-note signals Δ_4 and Δ_3' are nearly at the level 10 Hz^2/Hz from 1 Hz to 1 kHz and increase up to 10^3 Hz^2/Hz at 100 kHz. These results are similar to our previous measurement of the frequency noise of the CO_2/OsO_4 laser [51]. Note that these measurements, limited by the noise of the CO_2/OsO_4 laser, can not give the true frequency noise PSD of the OFC-stabilized QCL. The bump around 400 Hz comes from the bandwidth of the CO_2 frequency lock to the OsO_4 saturation line [217]. Above 1 kHz where the CO_2 laser is free-running and exhibits very low noise, the noise of the two beat-note signals properly overlap with the OFC noise.

In short, due to the noise of the CO_2/OsO_4 laser, the stabilities and the frequency noises of the CO_2/QCL beat-note signal (Δ_4) can not fully provide the performances of the QCL frequency's stabilization to the OFC and OLO. Therefore, another experiment was carried out to demonstrate that the QCL is indeed copying the OFC stability and in turn the optical reference stability. It is detailed in the next section.

3.3.3.2 Experimental setup for the QCL stabilization's assessment

We expect that the frequency stability of the QCL is given by that of the repetition rate of the OFC. However, some noise can be added to the QCL frequency by the servo loop used to lock the QCL to the comb repetition rate and by the electronics. For that purpose, the experimental setup was modified to lock both the QCL and the CO_2 laser on the comb repetition rate, as illustrated in Figure 3.25. This allows us to estimate the noise contribution of the servo loop and the electronics via the beat-note signal Δ_4' between these stabilized mid-IR lasers on photodiode PD_4. To this end, both the QCL

and the CO_2 laser were combined with the custom comb ouput at 1.85 μm for SFG in the $AgGaSe_2$ crystal. Two beat-note signals were detected on photodiode PD_3 (Figure 3.25): Δ_3 between the QCL and the OFC and Δ_3' between the CO_2 laser and the OFC. These beat-note signals were then phase-locked to corresponding fixed radio frequency signals using two phase-lock loops PPL_3 and PPL_3'. Both lasers were thus stabilized on to the n^{th} harmonic of the comb repetition rate. The frequency of the beat-note signal Δ_4' between the QCL and the CO_2 laser was then counted using a Π-type counter. Finally, the frequency stability of this beat-note signal was obtained by calculating the overlapping Allan deviation of the acquired data.

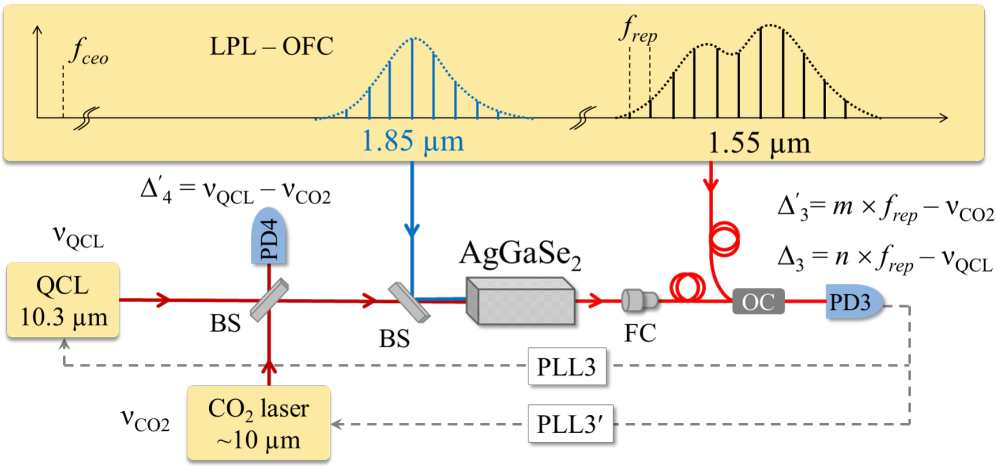

Figure 3.25 – Experimental setup for evaluating the QCL frequency noise. The QCL and the CO_2 laser are phase-locked onto the n^{th} and m^{th} harmonics of the repetition rate of the OFC, respectively, using two beat-note signals detected on photodiode PD3: Δ_3 between the QCL and the comb, Δ_3' between the CO_2 laser and the comb. A third beat-note signal Δ_4 between the QCL and the CO_2 laser is detected on photodiode PD4. OFC: optical frequency comb, BS: beam splitter, OC: optical coupler, FC: fiber coupler, PLL3 and PLL3′: phase-lock loops.

Figure 3.23 shows the frequency stability of the beat-note signal Δ_4' (line d, black). It is below 2×10^{-16} at 1 s, one order of magnitude smaller than the OFC frequency stability (line c, green), and below 10^{-17} after 100 s of averaging time. This demonstrates that the QCL and the CO_2 laser frequency fluctuations are identical at a level well below the OFC frequency stability. Thus both lasers copy the OFC spectral properties. The frequency fluctuation contribution of the phase-lock loop and the electronics is therefore negligible compared to that of the OFC. From this result, we conclude that the QCL stability is given by the frequency stability of the OFC (green line, c). The fractional frequency stability of the QCL is thus about 2×10^{-15} from 1 to 100 s, corresponding to a stability lower than 0.06 Hz at these time scales.

Similarly, we conclude that the stabilized QCL frequency noise PSD is given by the OFC PSD (green line, c) in Figure 3.24. This figure 3.24 also displays the free-running QCL PSD (black line, e) (see subsection 3.2.2.2) highlighting a 12 orders of magnitude reductions in the QCL frequency noise at 1 Hz.

Line shape of the stabilized QCL

The stabilized QCL's line shape can be calculated from the PSD frequency noise via the numerical calculation method described in subsection 3.2.2. To this end, the QCL frequency noise PSD at Fourier frequencies lower than 1 Hz, which can not easily been measured, is derived from the fractional frequency stability of the stabilized QCL/OFC (green line (c) in Figure 3.23) and combined with the measured QCL/OFC frequency noise PSD at Fourier frequencies larger than 1 Hz (green line (c) Figure 3.24). The QCL emission line shape is calculated using Equation 3.7 for different resolution bandwidths, RBW = 0.244, 1, 10, and 100 mHz, corresponding to observation times of $\sim$ 4100, 1000, 100, and 10 s, respectively (see subsection 3.2.2.2). Results are displayed in Figure 3.26(a-d), together with a Gaussian fit to the line shape. Figure 3.26(e) shows the dependence on the FWHM linewidth with the RBW and with the observation time. A minimum FWHM linewidth is found to be < 0.1 Hz at a resolution bandwidth of 100 mHz, corresponding to 10 s of integration time. The blue dashed curve corresponds to the limit given by the resolution bandwidth which dominates for integration time shorter than 10 s (see subsection 3.2.2.2).

3.4 The QCL frequency control: summary and SI-traceability

3.4.1 Summary

Here, we summarize the frequency stabilization of the QCL onto the remote near-IR reference signal from LNE-SYRTE via using an optical frequency comb and a SFG process in $AgGaSe_2$ crystal. The whole experimental setup is shown in Figure 3.27. The QCL is phase-locked to the remote optical reference via three cascade steps.

In the first step, a 1.54 μm laser diode is used as an optical local oscillator (OLO). Two sidebands of frequencies $\nu_{OLO} \pm f_{EOM}$ are generated around the OLO carrier frequency ν_{OLO} by mean of an EOM driven by a wide-tunable accurate home-made microwave synthesizer (see section 2.5). A beat-note signal of frequency Δ_1 between the incoming near-IR reference signal ν_{ref} transferred from LNE-SYRTE to LPL via the 43 km-long active noise compensated fiber link and the upper OLO sidebands ($\nu_{OLO} + f_{EOM}$) is generated on photodiode PD_1,

$$\Delta_1 = \nu_{ref} - (\nu_{OLO} + f_{EOM})\,. \tag{3.20}$$

The stability of the optical reference is then transferred to the OLO sideband's frequency by referencing the beat-note signal Δ_1 to a radio-frequency signal at 75 MHz provided by a DDS synthesizer via the first phase-lock loop (PLL_1, Figure 3.27). The OLO carrier frequency is then given by

$$\nu_{OLO} = \nu_{ref} - f_{EOM} - \Delta_1. \tag{3.21}$$

In the second step, the repetition rate of the OFC is phase-locked onto a subharmonic of the OLO carrier frequency ν_{OLO}, as described in section 2.8. A beat-note signal between the p^{th} comb mode $p \times f_{rep} + f_{ceo}$ and the OLO carrier frequency ν_{OLO} is generated on photodiode PD_2. After removing the carrier envelop offset frequency (f_{ceo})

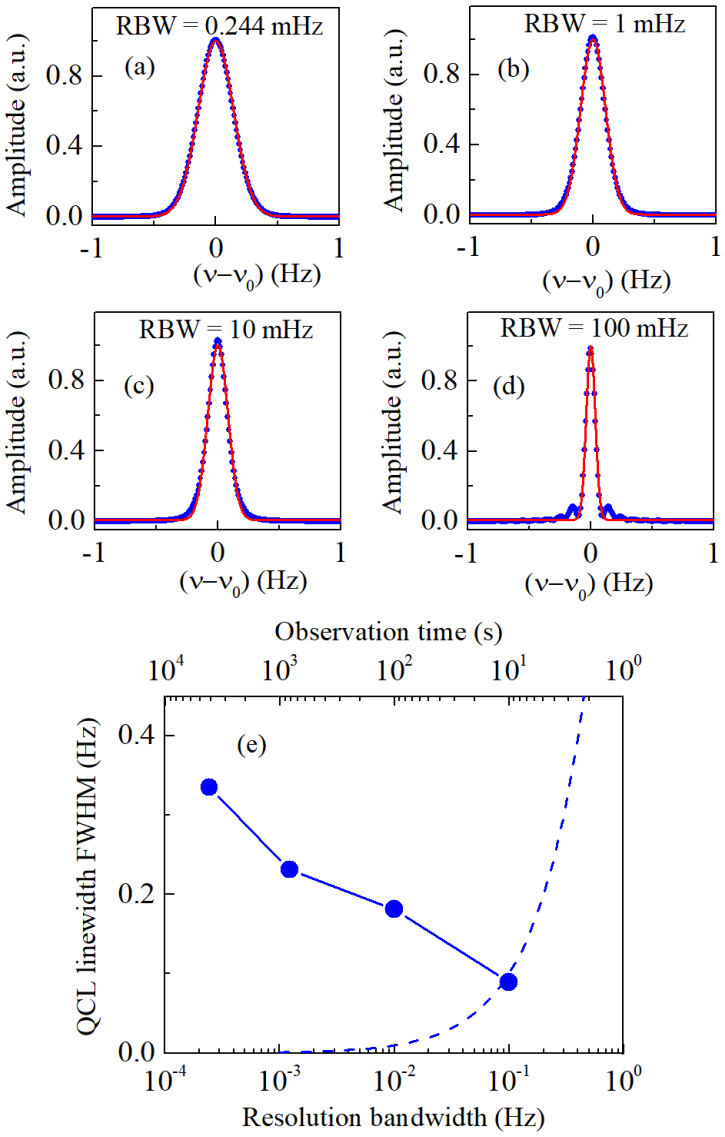

Figure 3.26 – (a-d) Calculated line shapes of the stabilized QCL at different resolution bandwidths, RBW = 0.244, 1, 10, and 100 mHz, corresponding to observation times of ∼ 4100, 1000, 100, and 10 s. (e) The stabilized QCL's linewidth as a function of resolution bandwidth (lower scale) and observation time (upper scale). The blue dashed line is the resolution bandwidth limited linewidth (see subsection 3.2.2.2) which dominates for observation times shorter than 10 s.

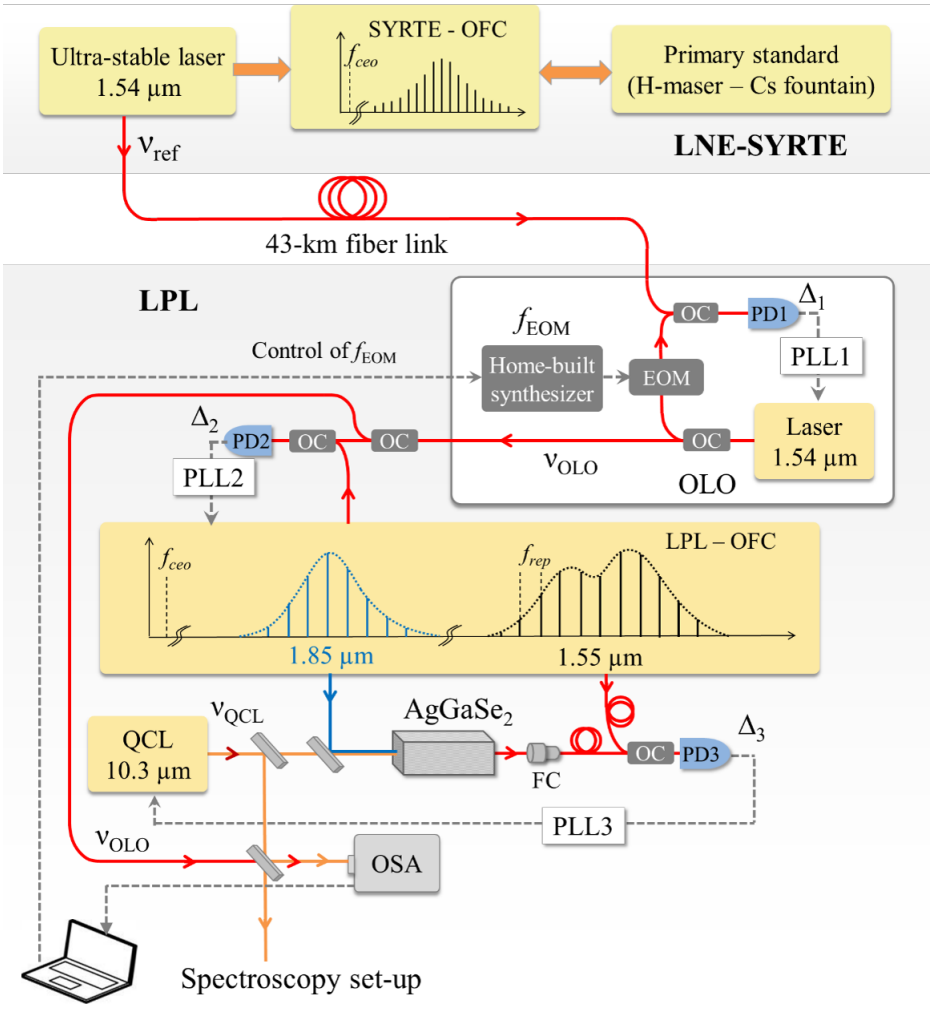

Figure 3.27 – Experimental setup of the widely tunable stabilized QCL. The near-IR reference signal is developed at LNE-SYRTE and transferred to LPL via the 43 km-long noise compensated fiber link. At LPL, sidebands of the OLO are generated by an EOM driven by a phase-jump-free synthesizer. One of the sidebands is phase-locked to the reference using PLL1. This allows the OLO carrier to be used as a tunable accurate and ultra-stable oscillator. Then, the repetition rate of the OFC is phase-locked to this OLO carrier frequency using PLL2. The QCL frequency is finally stabilized to a high harmonic of the repetition rate by performing the SFG in a $AgGaSe_2$ crystal and by processing the beat-note signal between the SFG comb and the main comb (using PPL3). Tuneability is thus transferred from the OLO to the OFC and finally the QCL. EOM: electro-optic modulator, PD: photodetector, PLL: phase-lock loop, OC: optical coupler, FC: fiber coupler, OSA: optical spectrum analyzer.

of the OFC, we obtain the resulting beat-note signal of frequency Δ_2, given by

$$\pm\,\Delta_2 = \nu_{OLO} - p f_{rep}. \tag{3.22}$$

The repetition rate of the OFC is stabilized to the OLO carrier frequency by phase-locking the positive beat-note signal Δ_2 to a radio-frequency signal at 150 MHz provided by another DDS synthesizer. The repetition rate of the OFC is then given by

$$f_{rep} = \frac{\nu_{OLO} - \Delta_2}{p}. \tag{3.23}$$

In the last step, the QCL frequency is phase-locked to the n^{th} harmonic of f_{rep}. To this end, the QCL beam at 10.3 μm and the custom comb output at 1.85 μm are focused in the $AgGaSe_2$ crystal to generate a shifted comb at a sum-frequency corresponding to 1.55 μm. A beat-note signal between the SFG comb and the original comb at 1.55 μm is generated on photodiode PD_3, free of f_{ceo} (as mentioned in subsection 3.3.2),

$$\Delta_3 = n f_{rep} - \nu_{QCL}. \tag{3.24}$$

The QCL frequency is finally stabilized to f_{rep} by phase-locking the beat-note signal Δ_3 to a fixed radio frequency signal at 11 MHz. Combining Equations 3.22, 3.24, and 3.25, the QCL frequency is given by

$$\nu_{QCL} = \frac{n}{p}\left(\nu_{ref} - f_{EOM} - \Delta_1 - \Delta_2\right) - \Delta_3, \tag{3.25}$$

with n/p ~0.15. The frequency f_{EOM} is precisely controlled by the home-made microwave synthesizer (see subsection 2.5.2). The frequencies Δ_1, Δ_2, and Δ_3 are produced by synthesizers that are used for the phase-lock loops PLL1, PLL2, and PLL3. These synthesizers use the 10 MHz local radio-frequency signal as a reference. The QCL frequency is thus directly linked to the remote optical reference signal ν_{ref} when the integers p and n are well defined (see subsection 3.4.3).

3.4.2 SI-traceability of the QCL frequency

As described above, we have established the direct link between the QCL frequency and the remote near-IR reference. Following Equation 3.25, the uncertainty of the QCL frequency scale is limited by this near-IR reference, the EOM frequency, and the beat-note signal frequencies.

As mentioned in section 2.2, the ultra-stable optical reference is provided by a 1.54 μm laser locked to a high-finesse cavity. Its absolute frequency is monitored every second against primary frequency standards by an optical frequency comb at LNE-SYRTE with an uncertainty of 4×10^{-14} at 1 s averaging time [66].

The reference signal is transferred to LPL through a 43-km long active noise-compensated fiber link (see subsection 2.3.2). The instabilities added by the link is below 10^{-15} at 1 s averaging time and the residual frequency bias is at a level of 4×10^{-20} [192, 193]. The reference signal is thus distributed to LPL without any degradation of its stability and uncertainty.

The reference frequency is sampled every second at LNE-SYRTE. The synchronization between the LNE-SYRTE and LPL measurement times is obtained using an NTP

(Network Time Protocol) connection to the LNE-SYRTE server. The uncertainty on the synchronization is estimated to be below 100 ms. The 1-10 Hz/s mean drift of the ultra-stable laser being removed (see subsection 2.2.3), the residual frequency drift lies below 10^{-2} Hz/s. The imperfect synchronization between the two laboratories leads to a frequency shift of 1 mHz at most and has thus no impact on the frequency uncertainty.

At LPL, the incoming near-IR reference signal is locally disseminated to the experimental setup using a 10 m-long optical fiber without any passive or active noise compensation. Taking into account air conditioning-induced ∼1-K peak-to-peak temperature fluctuations, we estimate the resulting free-running fiber phase noise to lead to a frequency instability below 10^{-15} at 1 s and decreasing at longer averaging times with a bump at $\sim 10^{-15}$ for a measurement time of a few hundreds of seconds corresponding to the air conditioning half cycling period [218].

The three cascaded phase-lock loops for the OLO frequency, the repetition rate of the OFC, and the QCL frequency (see section 3.4) ensure the traceability of the QCL's frequency to the LNE-SYRTE reference signal and in turn to LNE-SYRTE primary standards. All involved counters and DDS synthesizers used for the YIG oscillator frequency control and for the phase-lock loops are referenced to the same local radio frequency oscillator. This local reference signal has a stability better than 10^{-12} between 1 and 100 s, a long-term frequency stability better than 10^{-11} and its absolute frequency is determined with an uncertainty better than 10^{-11} (see section 2.4). This results in an uncertainty on the OLO carrier frequency and, in turn, on the mid-IR frequency scale, at the level of 8×10^{-16}, limited by the YIG oscillator's frequency uncertainty (uncertainty on f_{EOM} see Equation 3.25). The contribution from Δ_1, Δ_2, and Δ_3 is negligible at this level.

The uncertainty on the mid-IR frequency scale is thus dominated by the frequency uncertainty of 4×10^{-14} of the LNE-SYRTE ultra-stable reference. This has a negligible effect on our molecular resonance frequency measurements (see chapters 4 and 5).

3.4.3 Determination of the QCL absolute frequency

3.4.3.1 "Optical" protocol

We have developed a protocol to determine the QCL absolute frequency using the absolute optical frequency of the near-IR reference ν_{ref}, called "Optical" protocol. Values of the EOM frequency f_{EOM} and of the three beat-note signals at frequencies Δ_1, Δ_2, and Δ_3 in Equation 3.25 are precisely given by the home-built microwave synthesizer and DDS synthesizers. Values of ν_{ref}, n, and p need to be determined.

At LNE-SYRTE, the reference absolute frequency ν_0 (see subsection 2.3.2) measured once per second is saved in real time on a repository accessible via hyper-text transfer protocol (http). During the optical frequency transfer from LNE-SYRTE to LPL via the 43 km-long fiber link, this reference is frequency-shifted by a constant value Δ_{offset} resulting from the presence of acousto-optic modulators and phase-lock loops (see subsection 3.2.2). At LPL, the incoming reference absolute frequency ν_{ref} is thus given by $\nu_0 + \Delta f_{\text{offset}}$.

Let us denote f^0_{EOM}, f^0_{rep}, ν^0_{OLO}, and ν^0_{QCL} the EOM frequency, the repetition rate of the OFC, the OLO carrier frequency, and the QCL frequency at the start of a scan. The repetition rate f^0_{rep} is measured by a frequency counter. The QCL frequency ν^0_{QCL} is

monitored with an accuracy of ∼30 MHz (better than half the repetition rate) by mean of a ±1 ppm accuracy optical spectrum analyzer (OSA) with an operating wavelength range between 1 μm to 12 μm (Bristol Instruments, 771-B). The integers p and n are thus unequivocally determined using Equation 3.22 and 3.24 and rounding to the nearest integer (square brackets):

$$p = \left[\frac{\nu^0_{OLO} - \Delta_2}{f^0_{rep}} \right], \tag{3.26}$$

with $\nu^0_{OLO} = \nu_{ref} - f^0_{EOM} - \Delta_1$ and p ∼800 000,

$$n = \left[\frac{\nu^0_{QCL} + \Delta_3}{f^0_{rep}} \right] \tag{3.27}$$

with n ∼120 000. Absolute frequency of the stabilized QCL is then calculated using again Equation 3.25.

3.4.3.2 "Radio-frequency" protocol

We have also developed an alternative protocol for retrieving the absolute frequency scale which does not require to know the absolute frequency of the remote reference ν_{ref} but uses a local radio-frequency reference which is calibrated to primary frequency standard. Thus, this second method is called "radio-frequency" protocol. Here, n is again univocally determined using Equation 3.27. The QCL absolute frequency is then deduced using the following equation

$$\nu_{QCL} = n f_{rep} - \Delta_3, \tag{3.28}$$

where f_{rep} is measured by a frequency counter. The relative uncertainty on the measurement of f_{rep} is at the level of 10^{-11}, limited by the uncertainty of the local radio-frequency reference (see section 2.4). So this alternative method results in an uncertainty on the mid-IR frequency scale below 0.3 kHz.

Moreover, the recorded repetition rate values are not perfectly synchronized with the EOM frequency steps (scan frequency steps). Therefore, we replace them by

$$f'_{rep} = f_{rep0} - k \frac{\delta f_{EOM}}{p^*} \tag{3.29}$$

with

$$p^* = \left[\frac{\nu^{0*}_{OLO} - \Delta_2}{f_{rep0}} \right], \tag{3.30}$$

where δf_{EOM} is the EOM frequency step during scan and k is an integer corresponding to the scan frequency step number. The EOM instantaneous frequency is $f^0_{EOM} + k\delta f_{EOM}$ and the repetition rate step is $\delta f_{rep} = \frac{\delta f_{EOM}}{p*}$. The absolute frequency of the OLO carrier frequency at the start of a scan ν^0_{OLO} is measured using the optical spectrum analyzer with an accuracy of about 200 MHz (±1 ppm), larger than half the repetition rate, resulting in an uncertainty of ±1 on the comb mode number p^*. The resulting uncertainty on δf_{rep} leads to a frequency uncertainty for the QCL which increases during the scan and reaches a maximum that depends on the EOM frequency tuning range B.

This maximum uncertainty at the end of the scan is given by:

$$\delta\nu_{QCL} = nB\left(\frac{1}{p^*-1} - \frac{1}{p^*+1}\right) \simeq \frac{n2B}{p^{*2}}, \tag{3.31}$$

in which, B is the EOM tuning range. As an example, a scan with B=100 MHz results in an uncertainty of ∼40 Hz on the QCL frequency at the scan end. This uncertainty on δf_{rep} is thus negligible compared to the 0.3 kHz uncertainty on the measurement of f_{rep0}, which is thus the dominating contribution to the frequency scale uncertainty when the radio-frequency protocol is used.

3.5 Quantum cascade laser frequency tuning

In this section, we demonstrate how the QCL frequency can be widely tuned at the precision of the optical reference signal.

3.5.1 Wide frequency tuning of the stabilized QCL using the step motor

A widely tunable optical local oscillator (OLO) based on a 1.54 μm laser diode has been developed in order to be able to widely tune the QCL frequency, as mentioned in section 2.5. The OLO carrier frequency can be tuned over 9 GHz by scanning the EOM frequency given by the home-made microwave synthesizer (see subsection 2.5.2).

As described in section 2.5, the two phase-lock loops PLL_2 and PLL_3 (Figure 3.27) allow us to phase-lock the repetition rate f_{rep} of the OFC to the OLO carrier frequency and to stabilize the QCL frequency onto f_{rep}. When the PLL_2 is closed, sweeping the OLO carrier frequency leads f_{rep} to be varied by changing the cavity length by the piezo-electric actuator and/or the step motor of the intra-cavity mirror (see section 2.8). At the same time, the tunability of f_{rep} is transferred to the QCL frequency through the phase-lock loop PLL_3 while maintaining ultimate accuracies and stabilities.

3.5.1.1 Compensation of the delay between the SFG comb and the original comb

One has to be careful that tuning may be limited by the time delay adjustment between the SFG comb and the original comb on photodiode PD3 (Figure 3.17). Even if the delay line is well adjusted, there can be a delay of $T = m\tau$ between the two beams with $\tau = 1/f_{rep}$ the time spacing between two adjacent pulses and m an integer. Then, the pulse $\#k$ of the SFG comb overlaps with the pulse $\#(k+m)$ of the original comb. When f_{rep} is varied, this delay is also tuned, which degrades the pulses overlap and in turn the signal-to-noise ratio of the beat-note signal Δ_3. The variation ΔT of T when f_{rep} changes by Δf_{rep} is given by

$$\Delta T \simeq m\frac{\Delta f_{rep}}{f_{rep0}^2}. \tag{3.32}$$

If ΔT is larger than the pulse widths, the beat-note signal Δ_3 will be lost. ΔT thus has to be smaller than the pulse width of the two comb beams which is at least 100 fs and increases with propagation inside fibers (around 0.5 ps/m). For adjacent pulses ($m = 1$), the tuning range of f_{rep} is limited to $\Delta f_{rep} = 62.5$ kHz (assuming a pulse width of 1 ps). In order to overcome the problem, we need to adjust the delay in such a way that the pulses originating from the same laser pulses overlap ($m = 0$). In that case, T does not

vary when f_{rep} is tuned. For that purpose, we have set up an experiment to measure the delay between the two combs.

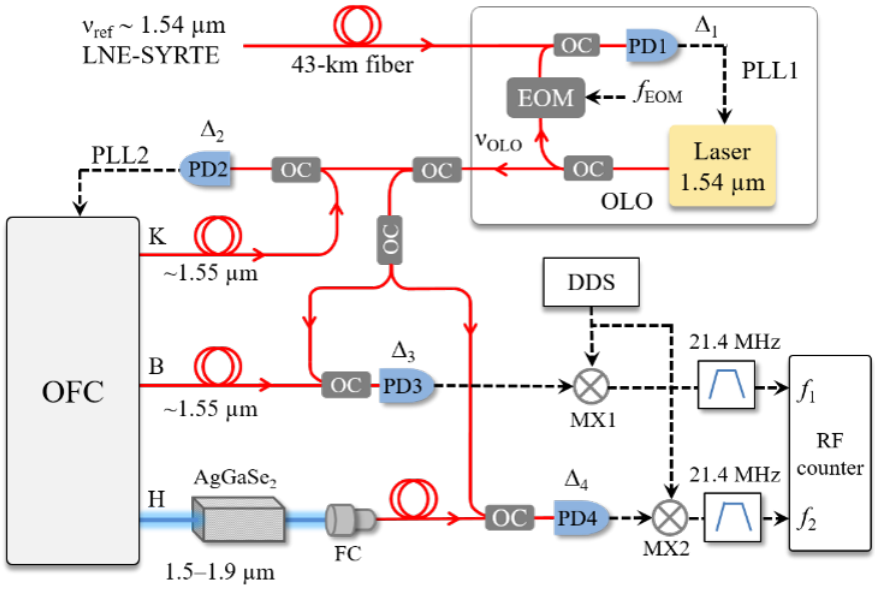

Figure 3.28 – Experimental setup for measuring the delay between the SFG comb beam (output H) and the original comb beam (output B). The comb repetition rate is phase-locked onto the OLO frequency via phase-lock loop PLL2. The latter is, in turn, stabilized to the remote optical reference signal from LNE-SYRTE using phase-lock loop PLL1. Two beat-note signals at around 70 MHz are detected: Δ_3 between the original comb and the OLO on photodiode PD3 and Δ_4 between the H output comb and the OLO on photodiode PD4. Their frequencies are converted to ~21.4 MHz by mixing with a radio-frequency signal at 91.4 MHz and counted by a counter. OFC: optical requency comb, OLO: optical local oscillator, EOM: electro-optic modulator, PD: photodetector, PLL: phase-lock loop, OC: optical coupler, RF: radio-frequency, DDS: direct digital synthesizer, MX: mixer, FC: fiber coupler.

Figure 3.28 shows the experimental setup for the measurement. This is based on the setup described in Figure 3.17. In order to measure the delay between the SFG and original comb beams, for simplicity, we take advantage that the wavelength of the custom comb output (H beam), used for the SFG, ranges from 1.5 to 1.9 μm (see Figure 2.20) and we use the part at ~1.55 μm of this custom output, instead of the SFG comb. That way, we benefit from the much higher power of the 1.55 μm beam (H beam). We thus remove the two filters F1850 and F1550 and set the transmission axis of the polarizer P2 (Figure 3.17) parallel to the ordinary polarization axis of the comb custom output's beam (H beam). We use the two beams just before the optical coupler used to generate the beat-note signal Δ_3 in Figure 3.27 and detect their beat-note signals with the OLO.

Then, two beat-note signals Δ_3 and Δ_4 at around 70 MHz between the H-beam and the OLO and between the B-beam and the OLO are detected on photodiodes PD3 and PD4, respectively as displayed in Figure 3.28. Their frequencies are given by

$$\Delta_3(t) = p f_{rep}(t - \tau_1) + f_{ceo} - \nu_{OLO}, \tag{3.33}$$

and

$$\Delta_4(t) = p f_{rep}(t - \tau_2) + f_{ceo} - \nu_{OLO}, \tag{3.34}$$

where $p \sim$800 000, $f_{rep}(t)$ is the value of f_{rep} at time t, f_{ceo} is the carrier envelope offset of the comb, τ_1 and τ_2 are the propagation delay between the fs-laser oscillator and PD3 and between fs-laser oscillator and PD4, respectively, and ν_{OLO} is the OLO frequency. $T = \tau_1 - \tau_2$ is thus the delay between the two comb beams. Note that f_{ceo} is also slightly depending on time, due to the coupling between the two comb parameters f_{ceo} and f_{rep}. However this dependence is negligible compared to that of f_{rep} thus, for simplicity, we assume that f_{ceo} is constant. When the comb is not tuned, f_{rep} is constant and thus $\Delta_3 = \Delta_4$.

In this setup, we first lock f_{rep} to the OLO by using the phase-lock loop PLL2. The OLO frequency is, in turn, stabilized to the remote optical frequency reference signal from LNE-SYRTE using phase-lock loop PLL1, as shown in Figure 3.28. The beat-notes are converted down to 21.4 MHz by mixing with a fixed radio-frequency signal provided by a direct digital synthesizer (DDS, Figure 3.28). The resulting signals at frequencies f_1 and f_2 are further filtered with two band-pass filters at 21.4 MHz.

We have performed a 9 GHz OLO frequency scan by tuning the home-made microwave synthesizer driving the EOM frequency, allowing f_{rep} to be varied with a range of $\Delta f_{rep} \sim$11.25 kHz (see subsection 3.4.1). The OLO is scanned with a frequency step of 300 kHz and a time step of 3 ms. We process the frequency difference $f_{12} = \Delta_4 - \Delta_3 = f_2 - f_1$ between these beat-note signals counted by a Π-type frequency counter with a gate time of 1 ms, as shown in Figure 3.28. We obtain the following signal

$$f_{12} = p\left[f_{rep}(t - \tau_2) - f_{rep}(t - \tau_1)\right]. \tag{3.35}$$

Suppose that f_{rep} varies as

$$f_{rep} = f_{rep0} + \alpha t, \tag{3.36}$$

then

$$f_{12} = p\alpha(t - \tau_2) - p\alpha(t - \tau_1) = p\alpha(\tau_1 - \tau_2) = p\alpha T. \tag{3.37}$$

The delay between the original and SFG comb beams is given by $T = \tau_1 - \tau_2 = n\Delta L/c$ with n the refractive index, ΔL the difference in propagation length between the two beams, and c the speed of light. The phase difference between the two beams is thus $f_{12}t$, inducing a variation ΔT of the delay T,

$$\begin{aligned} \Delta T &= \frac{f_{12}t}{p f_{rep}} = \frac{\alpha t n \Delta L}{f_{rep} c} \\ &= \frac{\Delta f_{rep}}{f_{rep}} \frac{n\Delta L}{c} \\ &= \frac{\Delta \nu_{OLO}}{\nu_{OLO}} \frac{n\Delta L}{c} \end{aligned} \tag{3.38}$$

in which Δf_{rep} and $\Delta \nu_{OLO}$ are the tuning range of the repetition rate and OLO, respectively. The variation of the delay is thus 25 fs/m/GHz.

Figure 3.29(a) shows the variation ΔT of the delay T between the original and the SFG comb beam without adjustment of the fiber length. We can see that the delay varies of $\sim$2.25 ps during a 9 GHz frequency tuning of ν_{OLO}. We thus deduce $\Delta L \simeq 10$ m.

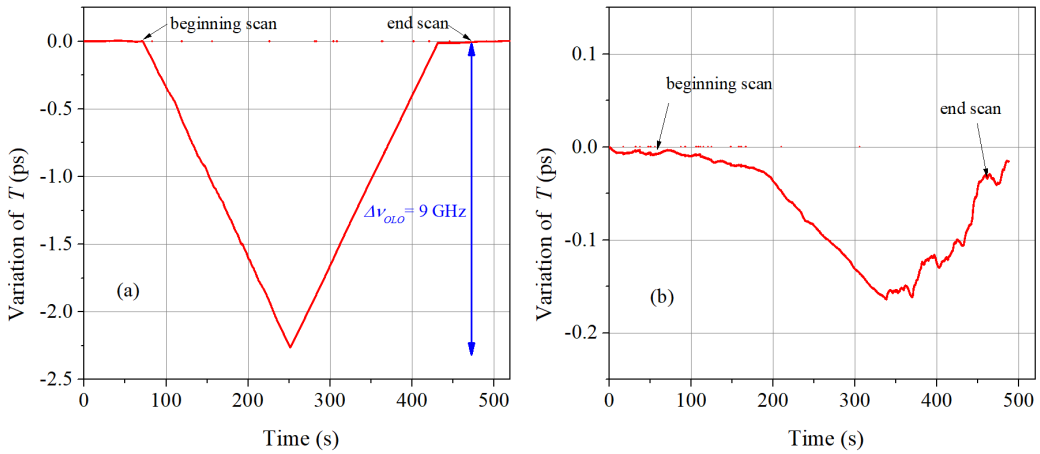

Figure 3.29 – Variations of the delay T between the original comb and the SFG comb during a 9 GHz frequency tuning of the OLO frequency: (a) before and (b) after adding 10 m-long fiber to the output of the original comb.

In order to compensate the delay between the two comb beams, we have added a 10 m-long fiber to the original comb beam (output B, see Figure 3.28). Then, we repeat the measurement to measure the delay between the comb beams after the adjustment. This result is shown in Figure 3.29(b). The delay between the two comb beams is a few tens of fs during the frequency tuning of ν_{OLO}, which is smaller than the pulse width of the SFG comb. These delay fluctuations most probably arise from temperature fluctuations which are not homogeneous for the two comb beams. One expects indeed a delay fluctuation of 37 fs/K/m in a fiber.

To conclude, after the delay adjustment we observe no significant delay variation when the comb repetition rate is scanned.

3.5.1.2 Results

The OLO carrier frequency can be continuously tuned over 9 GHz (see section 2.5), enabling the OFC repetition rate to be scanned over 11.65 kHz. Table 3.1 shows the frequency tuning ranges of the OLO frequency, the repetition rate, and the QCL frequency in two different cases.

(i) When only the PZT actuator is used to scan the comb cavity length, the frequency tuning range of the stabilized QCL is around 450 MHz, corresponding to a 3.89 kHz tuning range of f_{rep} (limited by the displacement of the PZT actuator) and to a 3 GHz tuning range of ν_{OLO}.

(ii) It is possible to increase the tuning range of ν_{QCL} by using the step motor or controlling the comb temperature, as mentioned in section 2.8. Under the current experimental condition, the step motor of the OFC intra-cavity mirror has been used and allows the QCL frequency to be tuned over 1.35 GHz, corresponding to a 11.65 kHz tuning range of f_{rep}. It is limited by the current 9 GHz tuning range of the OLO. Using a higher frequency EOM, it could be increased by a factor of 2 or 3. This widely-tunable, precise, and ultra-stable QCL will be used in chapters 4 and 5 to carry out high precision spectroscopic measurements.

Table 3.1 – Frequency tuning ranges of the OLO carrier frequency, the OFC repetition rate, and the QCL frequency.

	ν_{OLO} (GHz)	f_{rep} (kHz)	ν_{QCL} (MHz)
Reached with only PZT tuning	3	3.89	450
Reached with both PZT and stepper motor tuning	9	11.65	1 350

3.5.2 Using neighbouring modes

Additionally, it is possible to lock the QCL frequency to a neighboring harmonic of the OFC repetition rate and cascade 250 MHz continuous frequency scan of the QCL. Wider mid-IR frequency tuning has been obtained by performing such cascaded frequency scans. This will be illustrated in chapter 5 where ∼2.8 GHz long scans have been recorded.

3.5.3 Using a radio-frequency-stabilized OFC

Alternatively, we can also lock the comb directly to our local radio-frequency reference (and not to the optical frequency reference from LNE-SYRTE). In that case, we can achieve a total tuning range of f_{rep} of 1.25 MHz by moving the comb cavity length using the stepper motor. This allows us to make full advantage of the maximum continuous tuning range of the QCL frequency of about 180 GHz. However, in these current conditions, the QCL frequency noise is only partially reduced and the uncertainty of the QCL frequency is limited to around 10^{-11}, i.e. ∼300 Hz. These performances are much worse than those obtained with the LNE-SYRTE optical frequency reference, but they are still very appealing compared to the performance of traditional high-resolution molecular spectroscopy techniques.

3.5.4 Perspective

In order to obtain a wider continuous tuning range of ν_{QCL} without phase-locking the QCL frequency to a neighboring comb mode and still keeping the best stability absolute frequency control, the OLO should be upgraded. The three main components causing the limitation of the OLO's tuning range are: (i) the YIG microwave oscillator with tuning range of 9 GHz, (ii) the EOM tuning range of 10 GHz, and (iii) the laser diode tuning range of 10 GHz. They all should be replaced by new devices allowing wider frequency tuning. It may be possible to setup a new OLO with three-time wider tuning range using a 40 GHz EOM (commercially available). Such device would allow us to scan the stabilized QCL over 6 GHz. This is comparable to the tuning range of another QCL available at LPL that is locked to a CO_2 laser stabilized on a saturated absorption line of OsO_4 [40] but the system would exhibit a better stability, and a much better accuracy and spectral coverage.

3.6 Conclusion

We have stabilized the frequency of a 10.3 μm QCL to a high harmonic of comb repetition rate, itself controlled onto a widely-tunable and ultra-stable OLO referenced to a remote near-IR reference signal that is generated at LNE-SYRTE and transferred to LPL via a 43 km-long active noise compensated fiber link.

By scanning the frequency of the OLO, the QCL frequency can be continuously tuned up to 1.4 GHz at the precision of the primary frequency reference. It is possible to improve the QCL's frequency tuning range by a factor of three by setting up a new OLO. Moreover, we cover all the full spectral window of our QCL by locking the QCL frequency to various teeth of the OFC (see chapter 4). Additionally, by using appropriate non-linear crystals and module shaping the frequency comb spectrum, our stabilization method currently limited to the 9-13 μm window is extendable to the entire 5-20 μm molecular fingerprint region. Our work is also part of a global effort towards ever more precise ro-vibrational spectroscopic measurements in different frequency regions using nonlinear processes to control the frequency of laser sources (see for instance the recent studies, e.g. SFG [39, 41, 45, 219], DFG [44, 46, 135])

Our experimental setup allows the stability of the remote optical reference to be transferred to the QCL. The QCL absolute frequency is measured with an uncertainty at the sub-hertz level, thanks to the traceability to the primary frequency standards developed at LNE-SYRTE [66]. The performance are much better than non-SI traceable frequency reference. This is for instance a factor of 250 better than GPS-disciplined radio-frequency reference based measurements [39, 41–44, 131] and an improvement of more than six orders of magnitude compared to using traditional frequency synthesizers. The QCL's frequency stability is at the level of the reference, below 10^{-15} for averaging times from 0.1 to 10 s. To our knowledge, the level of stability and accuracy obtained using this method is better than any other reported in the mid-IR region. The QCL linewidth is found to be $\sim$0.1 Hz [45]. This level of spectral purity is important for pushing back the limits in ultra-high resolution molecular spectroscopy.

CHAPTER 4

High-precision mid-infrared spectrometer: application to the spectroscopy of methanol

Contents

4.1 The high-precision widely tunable SI-tracable QCL-based mid-infrared spectrometer . . . 112
4.1.1 Optical setup . . . 112
4.1.2 Vacuum setup . . . 116
4.1.3 Frequency modulation setup for saturated absorption spectroscopy 116
4.2 Rovibrational spectrum of methanol: an overview . . . 119
4.2.1 Methanol: a molecule with a variety of interests . . . 119
4.2.2 Structure of rovibrational energy levels and notation . . . 120
4.2.3 K-doublet . . . 123
4.2.4 High resolution spectroscopy of methanol in the literature . . . 124
4.3 Doppler-limited spectroscopy . . . 124
4.3.1 Spectrum acquisition . . . 124
4.3.2 Data processing and results . . . 125
4.4 Precise spectroscopy of methanol . . . 128
4.4.1 Spectrum acquisition . . . 128
4.4.2 Analysis of experimental data . . . 132
4.5 Spectroscopic measurements . . . 138
4.5.1 Power-induced frequency shift . . . 138
4.5.2 Pressure-induced frequency shift . . . 139
4.5.3 Power- and pressure-induced broadening effects . . . 140
4.5.4 Estimation of the transition dipole moment . . . 143
4.6 Absolute frequency measurement of rovibrational transitions of methanol . . . 143
4.6.1 Absolute frequency measurement of the $P(E,\mathrm{co},0,2,33)$ methanol transition . . . 143
4.6.2 Absolute frequency determination of other methanol transitions 151
4.6.3 Summary . . . 160
4.7 Asymmetry K-doublets for A-symmetry transitions . . . 162
4.7.1 Resolved K-doublets . . . 163
4.7.2 Un-resolved K-doublet . . . 169
4.7.3 Summary . . . 169

4.8 Tunability and spectral coverage 172
4.8.1 Wide tunability 172
4.8.2 Spectral coverage 177
4.9 Conclusion 178

4.1 The high-precision widely tunable SI-tracable QCL-based mid-infrared spectrometer

We now report on a versatile mid-IR high-precision spectrometer that is based on the ultra-stable and widely-tunable QCL described in chapter 3. Our purpose is to probe a variety of species and rovibrational transitions, including the weakest lines. We thus need a high sensitivity at the low pressure required for carrying out high resolution spectroscopy.

The conventional method to obtain a high sensitivity is to increase the optical path length, using for instance a Fabry-Perot cavity or a multipass absorption cell. A Fabry-Perot cavity, with typical length of 1 m and finesse over 100, provides an equivalent optical path length several tens of metre and allows us to keep pressure at sub-Pa level, thus minimizing collision shift and broadening. Moreover, it provides a high control of the optical spatial mode, thus allowing a very good control of systematic effects related to the beam geometry. However, the cavity length has to be locked to the laser frequency, limiting the frequency tuning to around 100 MHz due to the lack of tunability of the cavity length. In comparison, a multi-pass absorption cell also provides a large effective path length in a small volume and allows one to perform wide continuous frequency scans covering several molecular transitions. In this work, we develop a high-precision widely tunable spectrometer around 10 μm based on a multi-pass absorption cell and the SI-traceable QCL.

4.1.1 Optical setup

Figure 4.1 shows the experimental setup of the QCL based spectrometer that allows both direct and saturated absorption spectra to be acquired. It is based on a Herriot astigmatic multipass absorption cell (Aerodyne Research, model AMAC-36) [220]. With a 20-cm long distance between the mirrors and 182 paths, the multipass cell provides an effective absorption length of 36.4 m and allows us to perform spectroscopic measurements at low pressures. It has two astigmatic concave mirrors of ∼20 cm radius of curvature facing each other. The reflectivity of these mirrors is ∼99.2% for wavelengths ranging from 3 to 10 μm. The QCL beam can enter and exit the cell through a hole of diameter 4.3 mm in one of those mirrors and reflect back and forth between them.

As illustrated in panel (a) of Figure 4.1, the QCL beam goes through a Faraday isolator (IO) and is split into two beams using an 80/20 beam splitter (BS1). The most powerful beam (∼10 mW) is directed to the sum frequency generation (SFG) setup for locking the QCL frequency to a high harmonic of the repetition rate of the optical frequency comb (OFC), as presented in section 3.3.

Panel (b) of Figure 4.1 shows the spectroscopic setup using ∼20% of the QCL power (∼2.6 mW). For carrying out saturated absorption spectroscopy (see principle in subsection 1.1.3), the QCL beam is split into two parts by beam splitter BS3. A small part of the QCL power (∼0.3 mW), reflected by BS3, is directed to the optical spectrum analyzer

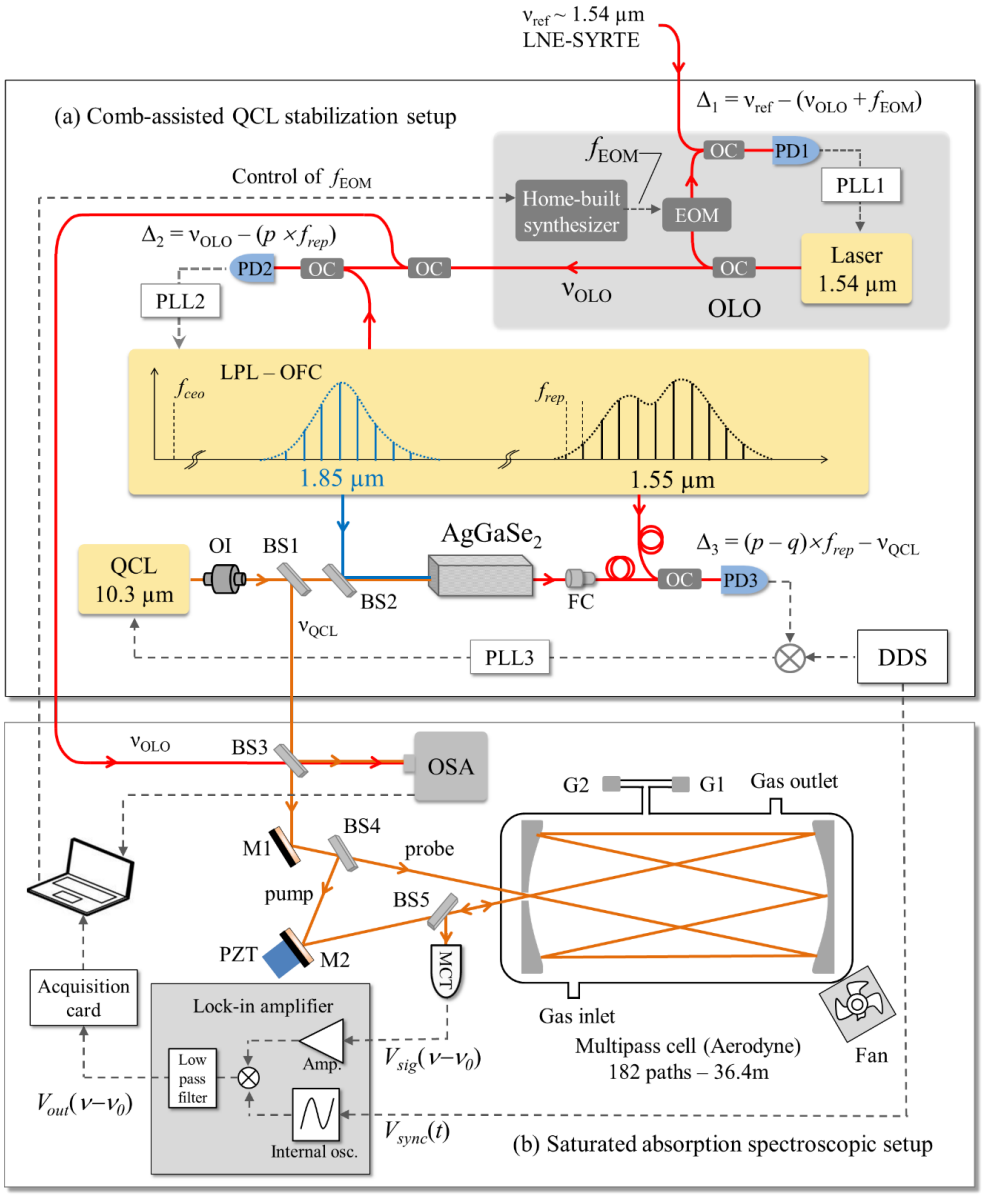

Figure 4.1 – (a) Experimental setup for locking the QCL frequency to the remote optical frequency reference ν_{ref} via an optical frequency comb (OFC), as described in section 3.4. (b) Experimental setup for recording saturated absorption spectra of molecules in a multi-pass absorption cell using the stabilized QCL and frequency modulation. The QCL beam is separated into pump and probe beam using the beam splitter BS4, which are then coupled into the multi-pass cell to perform saturated (or linear) absorption spectroscopy. The probe beam is directed to the mercury-cadmium-telluride (MCT) photodetector in which the sub-Doppler spectrum is probed. The QCL frequency is modulated via the direct digital synthesizer (DDS) of PLL3 (see text). The detected signal from the MCT photodetector is demodulated using the lock-in amplifier and then acquired by an acquisition card. This setup also allows us to record direct absorption spectrum using the free-running QCL (in which case the pump beam is blocked, see section 4.3 for more details). PD1-3: photodiodes, BS1-5: beam splitters, M1 and M2: mirrors, PLL1-3: phase-lock loops, EOM: electro-optic modulator, OLO: optical local oscillator, DDS: direct digital synthesizer, OSA: optical spectrum analyzer, PZT: piezo-electric actuator, FC: fiber coupler, RF: radio frequency, G1 and G2: pressure gauges, Amp.: amplifier, MX: mixer, OC: optical coupler.

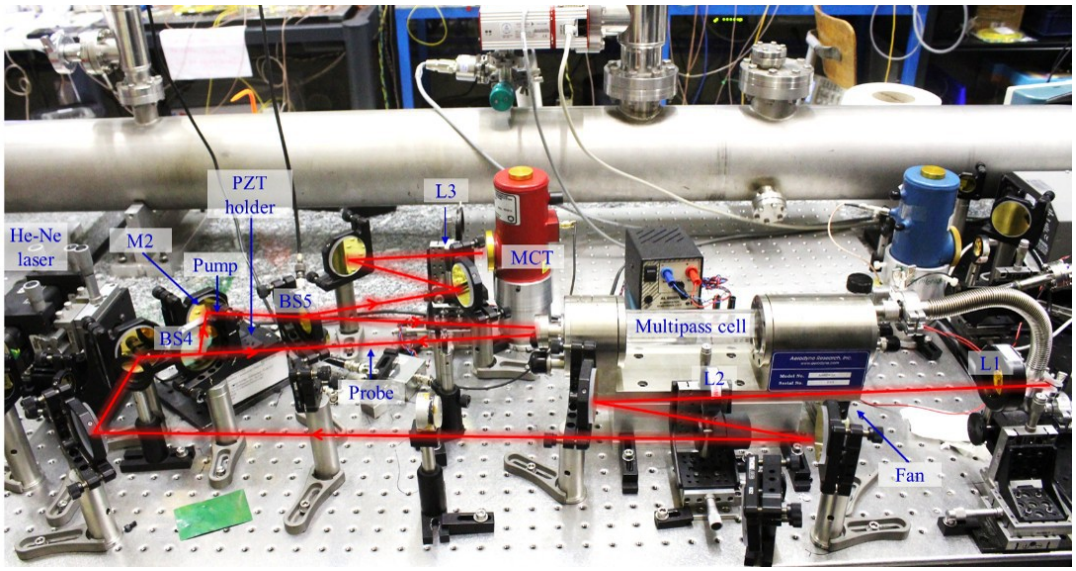

Figure 4.2 – Photograph of the experimental setup for carrying out linear and saturated absorption spectroscopy using a multi-pass absorption cell. MCT: mercury-cadmium-telluride photodetector, PZT: piezo-electric, BS: beam splitter, M: mirror.

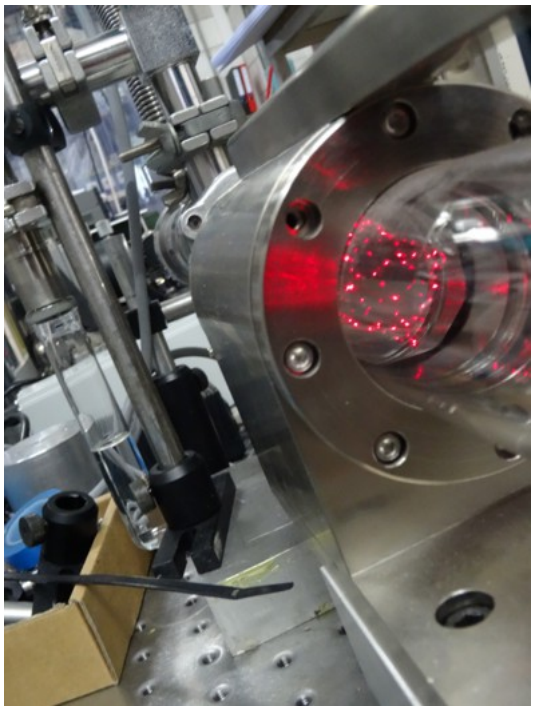

Figure 4.3 – Lissajous pattern traced out by a He-Ne laser beam on the astigmatic mirror within the AMAC-36 Herriot multi-pass cell.

(Bristol Instruments, MIR-771B) to monitor the QCL frequency (see subsection 3.4.3). The remaining part of the QCL power (∼2.3 mW), transmitted through BS3, is split in a pump and a probe beam using beam splitter BS4, as shown in Figures 4.1 and 4.2. The two beams are then coupled into the multipass cell with an incident power of the order of 1.3 mW and 0.7 mW, respectively. The optical alignment of the pump-probe configuration is realized using a visible He-Ne laser, as shown in Figure 4.3. The QCL beam is focused into the cell with a telescope made of a pair of lenses (L1 and L2, Figure 4.2) with respective focal lengths 63 mm and 200 mm. After exiting the cell, the probe beam is reflected on the beam splitter BS5 and then focused by a short focal length (f = 50 mm, L3 in Figure 4.2) on a liquid-nitrogen-cooled mercury-cadmium-telluride photodetector (MCT, Figures 4.1 and Figures 4.2). A transimpedance amplifier is used to convert the current of the photodetector into a voltage signal.

Unfortunately, undesirable interference fringes from the multipass cell limit the signal-to-noise ratio of our spectra. They are typically observed with multipass cell and relate to scattering of light on the mirror surfaces that can cause some light to exit the multipass cell early or late and interferes with light following the main path [220]. Various methods can be used to reduce optical fringes [221], among them, vibrating the multi-pass cell's mirrors [222, 223]. In our system, during data acquisition the mirror (M2) directing the pump beam toward the cell is vibrated by a piezo-electric transducer (PZT) driven by a high-voltage amplifier while the multipass cell is shaken by a fan with a broken blade (see Figures 4.1 and 4.2). The mirror vibration and the fan rotation are at frequencies around a few hundreds of Hz. This is fast enough to average out interference fringes during a typical measurement averaging time of 100 ms or even for averaging time at least longer than 1 ms. In consequence, the signal-to-noise ratio of spectra recorded in the presence of the vibrational forces is a few times higher than in the absence.

Additionally, Figure 4.1 also shows the frequency modulation/demodulation setup with lock-in amplifier used for high sensitivity detection (see below).

To optimize the coupling into the cell, we have measured the waist of the QCL beam w_0 in the multipass cell. This also happens to be useful to determine saturation intensity and estimate transit time γ_t in our spectroscopic measurement (see section 4.4). It is not easy to directly measure the propagation of the QCL beam inside the cell. In practice, we deflect the beam at the entrance of the cell with a mirror and measure its profile outside the cell. The knife-edge technique is used to measure the profile of the QCL beam at different longitudinal locations [224]. We first measure the radii at $1/e$ of the beam $w_{x/y}(z)$ at several positions z along the beam in both x- and y-axis (x-axis vertical, y-axis horizontal). Figure 4.4 displays the results, showing that the beam profile of the QCL is elliptical. Then, we fit to the data the theoretical beam profile $w(z)$ given by the following equation

$$w(z) = w_0 \sqrt{1 + \left(\frac{M^2 z}{z_R}\right)} \tag{4.1}$$

in which M^2 is the M-square parameter of the laser beam and $z_R = \pi w_0^2/\lambda$ is the Rayleigh length. The QCL beam approximately focuses at the center of the multipass cell along the x-axis and ∼1.5 cm away from the cell center along the y-axis (see Figure 4.4). The QCL beam waists at $1/e$-intensity are roughly found to be w_{0x} = 0.78 (0.02) mm with M_x^2 = 1.08 (0.02) for the x-axis and w_{0y} = 1.19 mm with M_y^2 = 1.61(0.09) for the y-axis.

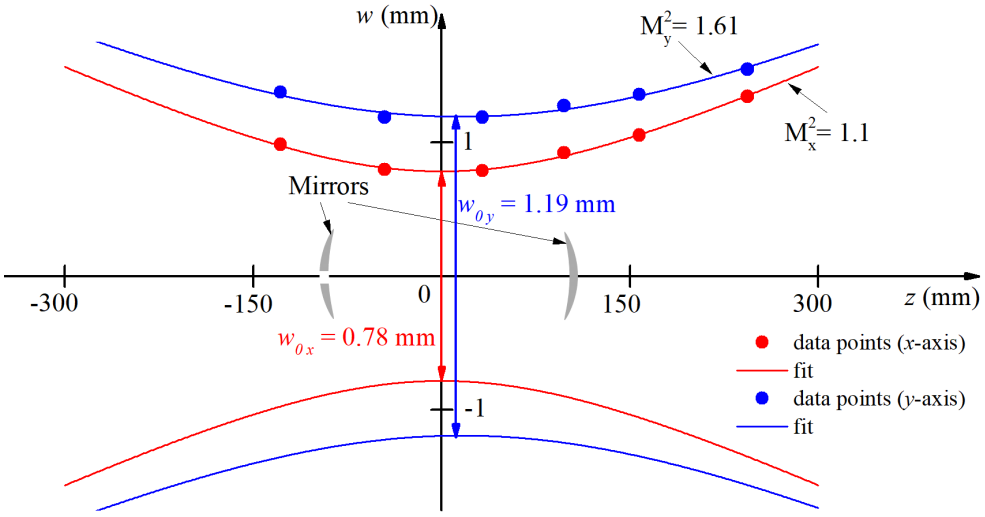

Figure 4.4 – Propagation of the QCL beam in the multipass cell. z is the direction of propagation. Red (respectively blue) points: $1/e$ radii along the x vertical (respectively y horizontal) axis. The data is measured using the knife-edge method. The red and blue solid line are fits to the data. The positions of the two vertical arrows feature the positions of the vertical and horizontal beam waist.

The cell is supposed to be quasi confocal [225], leading to a calculated waist of ∼0.57 mm (given by $w_0 = \left(\frac{\lambda d}{2\pi}\right)^2$ for the confocal case with λ ∼10.3 μm and $d = 20$ cm the distance between the two astigmatic mirrors [226]). The discrepancy between the theory and measurement is attributed to an underestimation of our measurement uncertainty and to the ellipticity of the beam and the deviation from an ideal Gaussian beam. We will consider w_0 to lie between 0.6 and 1.2 mm for the calculation of transit time and transition dipole moments later (see section 4.4).

4.1.2 Vacuum setup

Gas pressure in the mutipass cell is controlled using two pressure gauges, G1 (CMR 365 Pfeiffer Vacuum) and G2 (698A-01TRD MKS Baratron). The cell is evacuated to 10^{-5} Pa with a compact turbo-molecular pump station (HiCube80, Pfeiffer Vacuum GmbH). Gas samples can be leaked into the multi-pass cell through a leak valve. The leak rate/surface outgassing of the cell is found to be around 0.1 Pa/h.

4.1.3 Frequency modulation setup for saturated absorption spectroscopy

The experimental setup allows us to acquire both Doppler-limited spectra using only the probe beam (see section 4.3) and saturated absorption spectrum using the pump-probe configuration (see section 4.4). The sensitivity of saturated absorption spectroscopy is limited by various sources (e.g. amplitude of the Doppler-free dip, background noise of the detector, interference fringes, mechanical vibration leading to beam-pointing-induced noise,...). In order to overcome these limitations, we use the frequency modulation technique that allows the signal-to-noise ratio to be improved. Here, we present the frequency modulation spectroscopy setup: the QCL frequency is modulated at a frequency of typically 20 kHz and the signal detected by the MCT photodetector is fed to

a lock-in amplifier (SR830, Stanford Research Systems) for demodulation.

Modulation of the QCL frequency

As illustrated in Figure 4.1, the QCL at frequency ν_{QCL} is stabilized to the n^{th} harmonic of the repetition rate f_{rep} of the OFC by phase-locking the beat-note signal at frequency $nf_{rep} - \nu_{QCL}$ to a radio frequency reference signal at a fixed frequency Δ_3 (see subsection 3.3.2). Following Equation 3.24, the QCL frequency can be written as

$$\nu_{QCL} = nf_{rep} - \Delta_3, \tag{4.2}$$

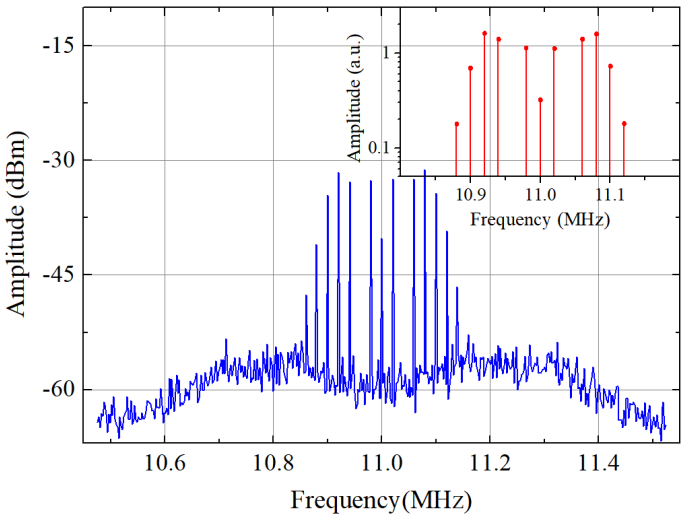

Figure 4.5 – In-loop beat-note signal at 11 MHz between the QCL and the OFC in the presence of the frequency modulation: $f_m = 20$ kHz, $\Delta\nu_m = 100$ kHz, and $f_{RF} = 11$ MHz. The beat-note signal includes one carrier at 11 MHz and seven sidebands on each side. Intensities of the sidebands follow the Bessel function. The inset shows the simulating intensity of the beatnote.

The QCL frequency can be modulated by modulating the radio-frequency reference Δ_3 at a modulation frequency f_m smaller than the PLL bandwidth with a frequency excursion $\Delta\nu_m$. Since the modulation frequency is smaller than the phase-lock loop bandwidth, the frequency modulation is copied to the QCL and the instantaneous QCL frequency can be written as

$$\nu_{QCL}(t) = \nu_c + \Delta\nu_m \cos(2\pi f_m t), \tag{4.3}$$

in which ν_c is the carrier frequency of the QCL, $\nu_c = nf_{rep} - \Delta_3$. Figure 4.5 shows a beat-note signal between the QCL and the n^{th} harmonic of the repetition rate of the OFC centered at a frequency of 11 MHz when the phase-lock loop PPL3 (Figure 4.1) is closed. The modulation frequency f_m is 20 kHz and the frequency excursion $\Delta\nu_m$ is 100 kHz, giving a modulation index $\Delta\nu_m/f_m$ of 5. The beat-note signal includes a carrier at 11 MHz and seven sidebands on each side. Comparison with theory (see inset in Figure 4.5) shows that their intensities are weighted by the Bessel function, as expected. This means that the modulation of the radio-frequency reference signal of PLL3 is properly

transferred to the QCL frequency.

Detection of the frequency modulated signal

After propagation in the multipass absorption cell containing the gas-phase molecular sample, the transmitted power of the probe beam is detected by a MCT photodetector (see Figure 4.1). In the vicinity of an absorption molecular transition with a center frequency of ν_0, the saturated absorption signal is very coarsely approximated using the Beer-Lambert law [1],

$$V_{sig}\left(\nu-\nu_0\right) \propto I_0 \exp\left[-\alpha\left(\nu-\nu_0\right)\right], \tag{4.4}$$

where I_0 is the incident power of the probe beam and $\alpha(\nu-\nu_0)$ is the absorbance with ν the instantaneous frequency of the QCL (see subsection 1.1.2).

In order to demodulate, the signal $V_{sig}(\nu-\nu_0)$ is fed to the input of the lock-in amplifier (see Figure 4.1). There, it is amplified and then multiplied by a radio-frequency reference signal. This reference is generated by an internal oscillator of the lock-in amplifier, that is phase-locked to the signal from the direct digital synthesizer (DDS, Figure 4.1) that produces the frequency modulation, and that is used as an external reference for the lock-in amplifier. The resulting signal is filtered in the lock-in amplifier by a low-pass filter. The output signal of the lock-in amplifier is finally acquired by an acquisition card (USB-6060, National Instruments).

The lock-in amplifier allows us to detect the demodulated signal at different harmonic frequencies, typically first-, second-, and third harmonic. When the frequency excursion $\Delta\nu_m$ is much smaller than the linewidth of the considered molecular transition, the detected signals $S_{1f}(\nu-\nu_0)$, $S_{2f}(\nu-\nu_0)$, and $S_{3f}(\nu-\nu_0)$ at these harmonics are approximately proportional to the first, second-, and third-derivative of the signal $V_{sig}(\nu-\nu_0)$ respectively

$$S_{1f}(\nu-\nu_0) \propto \frac{1}{2}\Delta\nu_m V_{ref} V'_{sig}(\nu-\nu_0), \tag{4.5}$$

$$S_{2f}(\nu-\nu_0) \propto \frac{1}{8}\Delta\nu_m^2 V_{ref} V''_{sig}(\nu-\nu_0), \tag{4.6}$$

and

$$S_{3f}(\nu-\nu_0) \propto \frac{1}{48}\Delta\nu_m^3 V_{ref} V'''_{sig}(\nu-\nu_0) \tag{4.7}$$

where V_{ref} is the amplitude of the lock-in reference signal. When the frequency excursion $\Delta\nu_m$ is close to or higher than the resonance linewidth, the detected signal will be distorted. Its line shape becomes more complicated. This will be in part described in chapter 5.

Shape of the detected signals

In saturated absorption spectroscopy, the absorbance $\alpha(\nu-\nu_0)$ can be coarsely approximated as the combination of a narrow Lorentzian resonance peak at the frequency ν_0 on a background Gaussian line shape,

$$\alpha(\nu-\nu_0) = A\Phi_D\left(\nu-\nu_0\right)\left[1-\chi\Phi_L\left(\nu-\nu_0\right)\right] \tag{4.8}$$

1. The Beer-Lambert low is however in principle not valid when saturation becomes significant. There exists an analytical generalization of the Beer-Lamber law, that takes into account the saturation [25].

with A is the absorbance factor, $\Phi_D(\nu)$ the Doppler-broadened Gaussian absorption line shape, $\Phi_L(\nu)$ the Lorentzian saturated absorption line shape, and χ is a factor related to the contrast of the saturated absorption feature. These line shapes are normalized (integral equals 1) and given by

$$\Phi_D(\nu - \nu_0) = \sqrt{\frac{2}{\pi}} \frac{1}{\Delta\nu_D} e^{-\ln 2\left(\frac{\nu-\nu_0}{\Delta\nu_D}\right)^2}, \tag{4.9}$$

and

$$\Phi_L(\nu - \nu_0) = \frac{1}{\pi} \frac{\nu_L}{(\nu - \nu_0)^2 + \gamma^2}, \tag{4.10}$$

where $\Delta\nu_D$ and γ are the HWHM widths of the Gaussian and Lorentzian normalized line shapes, respectively (see subsection 1.1.2). Panel (a) of Figure 4.6 displays a calculated saturated absorption signal $V_{sig}(\nu - \nu_0)$. The first-, second-, and third-harmonic detection signals are shows in panels (b-d) of Figure 4.6.

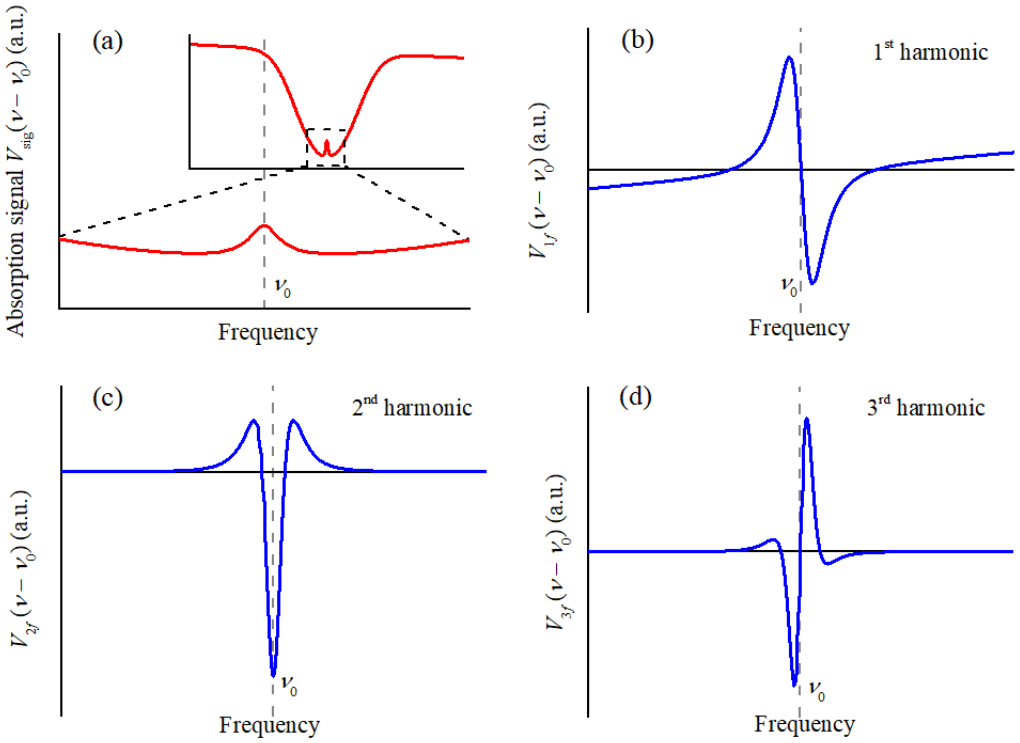

Figure 4.6 – (a) Direct saturated absorption signal with a linear baseline, (b) first-, (c) second-, and (d) third-harmonic detection signals of the saturated absorption signal. The spectra are calculated using Equations 4.4-4.10 with simulation parameters: $\Delta\nu_D = 5$ MHz, $\gamma = 0.2$ MHz, $\chi = 0.01$, and a baseline slope of -0.002 a.u./MHz.

4.2 Rovibrational spectrum of methanol: an overview

4.2.1 Methanol: a molecule with a variety of interests

We consider methanol, a slightly asymmetric top molecule with a strong fundamental vibrational band at around 10 μm, as a test molecule in order to assess the performances of our spectrometer. This molecule is one of the most abundant interstellar and proto-

stellar molecules and is found throughout the universe in a wide variety of astronomical sources [227]. It is thus an excellent probe of the physical conditions and history of interstellar clouds, but its intrinsically dense spectrum contributes significantly to the "grass" in any interstellar radio astronomy observation and needs to be accurately removed during searches for lines of new molecules. Methanol is important for interstellar chemistry too, because its formation provides a pathway to more complex molecules that are necessary for life. Closer to us, methanol is the second most abundant organic molecules in the Earth's atmosphere after methane [228] and has a significant impact on air quality and is implicated in the production of tropospheric ozone [229]. Retrieving methanol concentration in air from remote-sensing observations is thus a real challenge for environmental and human health issues, and requires accurate laboratory spectroscopic measurements [53]. Although one of the simplest asymmetric-top with a hindered internal rotor, methanol has a rather intricate rotation-torsion-vibration energy structure and is as such also a very important molecule for fundamental infrared and microwave spectroscopy [230–232], metrological applications and frequency calibration [233, 234], the realization of optically-pumped far-infrared gas lasers [235] or fundamental physics tests. It has for instance been identified as a very good candidate for probing the limits of the Standard Model because it is one of the most sensitive molecules for a search of a varying proton-to-electron mass ratio [236].

4.2.2 Structure of rovibrational energy levels and notation

The molecule consists of an OH group attached to a methyl (CH_3) group. With six nuclei, it has 12 normal vibrational modes assigned from ν_1 to ν_{12}, as shown in Figure 4.7.

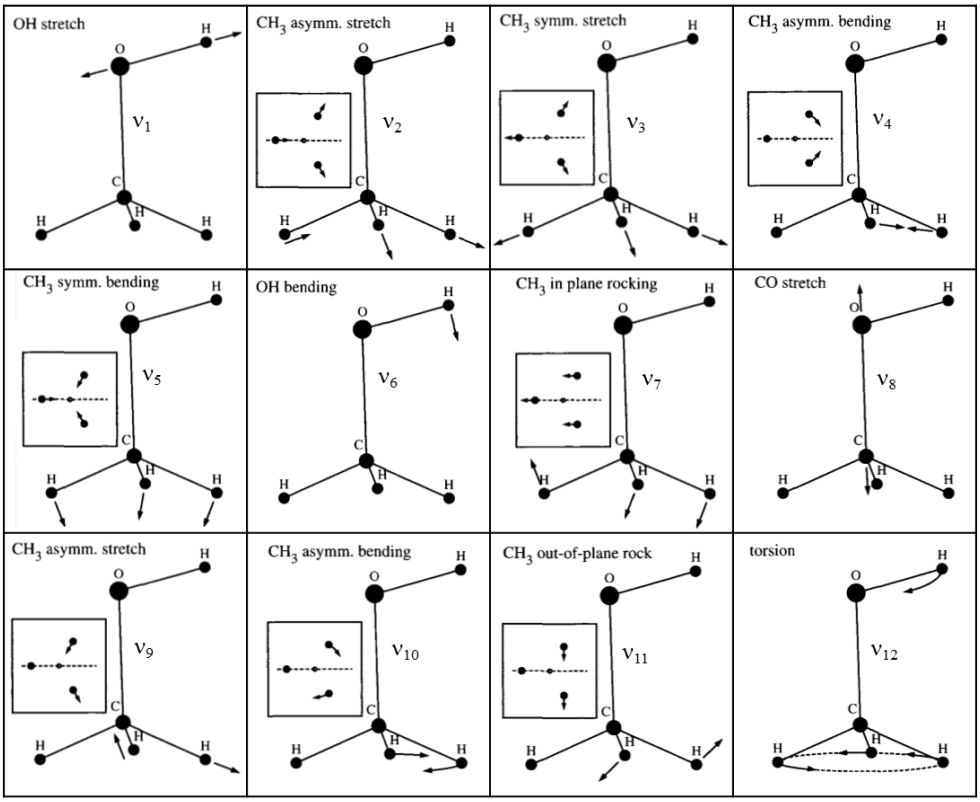

Figure 4.7 – The 12 vibrational modes of the methanol molecule. Taken from [237].

The overall rotation is described by three moments of inertia I_a, I_b, and I_c along the three principle axes of the molecules (the a axis along the CH_3 top axis, the c axis perpendicular to the COH plan, and the b axis perpendicular to the a and c axes [237]). The total angular momentum of the molecule and its projection onto the a axis are given by quantum numbers J and K respectively.

Note that the ν_{12} torsional mode corresponds to the hindered internal rotation of the OH group with respect to the methyl group. This hindered internal rotation occurs in a threefold barrier because of the interaction between the OH and methyl groups, as shown on left-hand side of Figure 4.8. As tunnelling between the three wells through the barrier is possible, each rovibrational level of methanol is split into three torsional sub-levels of respective torsional symmetry $E1$, $E2$, and A (see Figure 4.8). Levels of $E1$ and $E2$ symmetry for $K = 0$ cannot be distinguished and are labelled as E. In addition, energy levels of A-symmetries with $K \neq 0$ are further split by the slight asymmetry of the molecule (K-doubling). Such internal rotation is commonly found out in polyatomic molecules.

The torsion-vibration-rotation energy levels of the molecule are labelled as (σ, ν, t, K, J), where σ denotes the torsional symmetry (A or E), ν refers to the vibrational mode, t indicates the torsional mode (ν_{12}) quantum number, and $J \geq K$ [238]. The vibrational modes of v are denoted as *gr*, *co*, *ri*, *ro*, *oh*, *sb* and *ab* for the ground, ν_8 C-O stretching, ν_7 in-plane and ν_{11} out-of-plane CH3 rocking, ν_6 OH-bending, ν_5 symmetric and ν_4 asymmetric CH3-bending mode, respectively [239]. For E-symmetry levels, K is a signed quantum number with positive and negative values corresponding to levels labelled E_1, respectively E_2. For A-symmetry level, a superscript $+/-$ is added on K to distinguish the $A+$ and $A-$ components.

Neglecting higher-order torsional barrier terms and the effects of centrifugal distortion and torsion-vibration-rotation interactions, the torsion-vibration-rotation energy is basically expressed as [240]

$$E(\sigma, t, K, J) = E_\nu + B_{eff} J(J+1) + (A - B_{\text{eff}}) K^2 + F \left\langle P_\gamma^2 \right\rangle + \frac{1}{2} V_3 \left\langle 1 - \cos 3\gamma \right\rangle , \quad (4.11)$$

where the first term corresponds to the molecular vibration. The second and the third terms refer to the molecular rotation with A the rotational constant while the effective value B_{eff} is a function of the moments of inertia I_b and I_c and the product of inertia I_{ab}. The two last terms describe the internal rotation around the a axis in which F is the reduced torsional constant, P_γ is the torsional angular momentum, V_3 is the tunnel barrier parameter, γ is the internal torsional angle between the OH and methyl groups, and $\langle\ \rangle$ indicates the mean over the considered eigenstates.

Simple $\Delta K = 0$ and $\Delta t = 0$ rovibrational transitions are labelled by $P(\sigma, \nu, t, K, J)$, $Q(\sigma, \nu, t, K, J)$ and $R(\sigma, \nu, t, K, J)$ with σ, K, and J, the torsional symmetry and rotational quantum numbers of the lower state, and with P, Q, and R referring to $\Delta J = -1$, 0, and $+1$ transitions, respectively. $\Delta K = -1$ (respectively $+1$) transitions with $\Delta t = 0$ are labelled ${}^{P}P(\sigma, \nu, t, K, J)$, ${}^{P}Q(\sigma, \nu, t, K, J)$, and ${}^{P}R(\sigma, \nu, t, K, J)$ – respectively ${}^{R}P(\sigma, \nu, t, K, J)$, ${}^{R}Q(\sigma, \nu, t, K, J)$, and ${}^{R}R(\sigma, \nu, t, K, J)$. Other transitions are labelled with their upper and lower states $(\sigma', \nu', t', K', J') \leftarrow (\sigma'', \nu'', t'', K'', J'')$.

Most of the transitions of this molecule occur with the C-O stretch vibrational mode whose center is around 1033.5 cm^{-1}. Figure 4.9 displays stick spectra of the A-symmetry

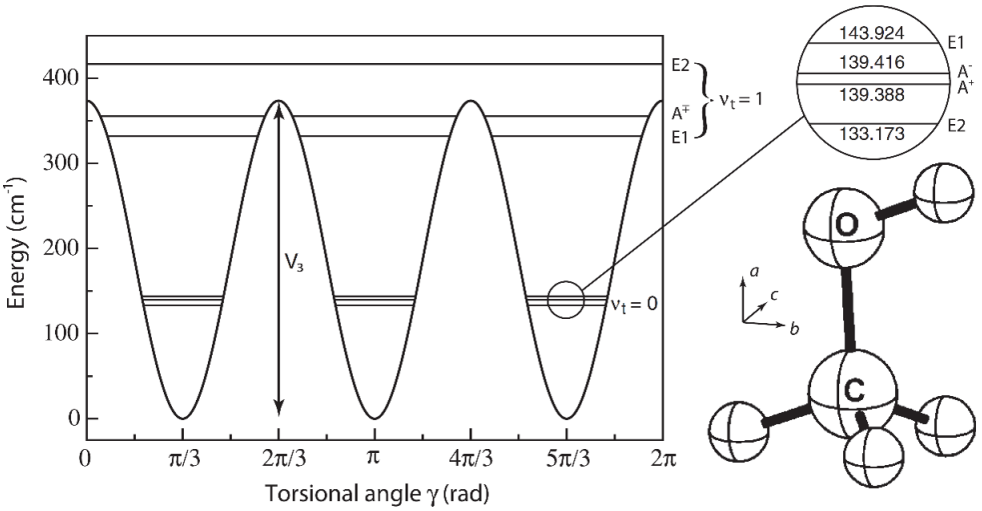

Figure 4.8 – Torsional potential as a function of internal rotation angle of the OH group with respect to the methyl group. The tunneling through the potential barriers leads to the splitting of K levels into three levels of respective symmetry A, $E1$, and $E2$. Moreover, the A-symmetry levels are split into + and - sublevels due to the asymmetry of methanol. Taken from [241].

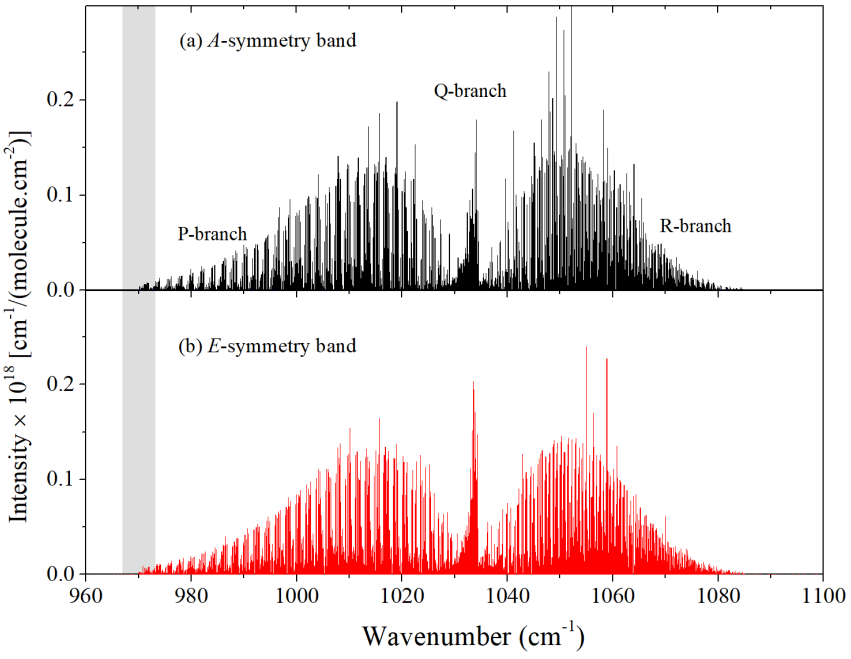

Figure 4.9 – Stick spectra of the A-symmetry band (top) and of the E-symmetry band (bottom) of the methanol, taken from the HITRAN data [54]. Gray area on the left refers the spectral coverage of our QCL (from 968 cm^{-1} to 973 cm^{-1}). P, Q, and R branches correspond to rovibrational transitions with $\Delta J = -1$, 0, +1, respectively.

band (top) and the E symmetry band (bottom) of this C-O stretching vibrational mode of the methanol, obtained from the HITRAN database [54]. Dark area in the figure corresponds to the frequency tunability of our QCL.

4.2.3 K-doublet

As mentioned in subsection 4.2.2, the energy level of each A-symmetry state is split into sublevels $A+$ and $A-$ due to the asymmetry of methanol. The energy difference between these sublevels can be calculated by perturbation theory using the matrix elements of an asymmetric Hamiltonian (see in [237] for more details). It is usually expressed as [242]

$$\Delta E_{\mathrm{A}+/-}(\nu, t, K, J) = \frac{(J+K)!}{(J-K)!}\left[S\left(\nu, t, K\right) + J(J+1)T\left(\nu, t, K\right)\right], \tag{4.12}$$

where $S(\nu, t, K)$ and $T(\nu, t, K)$ are known as the asymmetry splitting parameters.

"Normal" K-doublet

We now consider A-symmetry rovibrational transitions between the ground state and the first excited C-O stretching vibrational state ($\nu_8 = 1$) of methanol. For the transitions considered here, the symmetry A^+/A^- is conserved when the molecule interacts with light, giving rise to two transitions, one between A^+ levels, the other one between A^- levels. The energy shift between the $A+$ and $A-$ levels is slightly different between the ground state and the $\nu_8 = 1$ vibrational state. This leads to a frequency difference between the two optical transitions and thus to a so-called K-doublet. As shown in Figure 4.10(a), black- and blue-curve give the J-dependences of the frequency splitting of K-doublets $P(A, co, 0, 2^{+/-}, J)$ and $P(A, co, 0, 3^{+/-}, J)$, respectively, in the P branch of the methanol. The data are extracted from the HITRAN database [54]. The frequency splitting of K-doublets for $J < 15$ are set to zero as they were not resolved in the Fourier transform spectra, that were used to built this database. We can see that for $K = 2$ and 3, the frequency difference between two components of a K-doublet increases with J at a given K value but decreases rapidly with K at a given J value.

"Singular" K-doublet

Let us consider "singular" K-doublets which results from the mixing between near-degenerate levels in two different vibrational modes. For instance, Figure 4.10(b) shows the J-reduced energy levels (energy to which 0.8 $J(J+1)$ has been substracted, see caption) of vibrationally excited $(A, co, 0, 4^{+/-}, J)$ and $(A, ri, 0, 1^{-}, J)$ substate J-series of $A+/-$ symmetry belonging to the ν_8 and ν_7 vibrational modes, respectively [239]. The data shown in Figure 4.10(b) are extracted from the calculation of R.M. Lees and his co-workers, reported in the supplementary of Ref. [239]. Following R.M.Lees et al [239], crossing of energy levels between two such substate J-series of two different vibrational modes gives rise to J-localized perturbations, thus locally mixing the levels of the two series which leads to local energy shifts. In particular, this will lead to a modification of the energy splitting between $A+$ and $A-$ sublevels with respect to the expected behaviour given by Equation 4.12. This in turn results in singularities in the frequency splitting of associated K-doublets that connect those perturbed vibrationally excited $A+/-$ levels to their counterpart in the ground state. Figure 4.10(b) shows that a perturbation is expected in the vibrationally excited $(A, co, 0, 4^{+/-}, J)$ J-series for values of J around 29 or 30. As a result of this, a clear perturbation in the associated K-

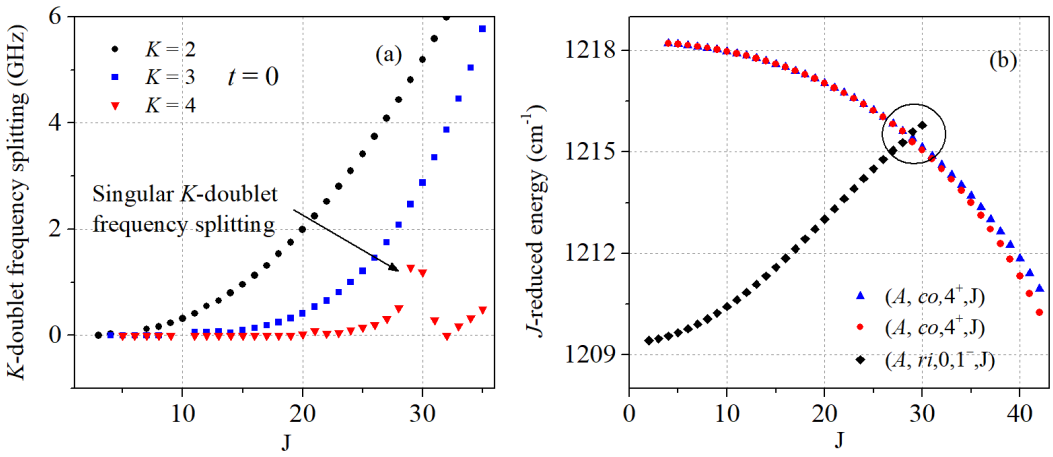

Figure 4.10 – (a) J-dependences of the frequency splitting between K-doublets $P(A, co, 0, K^+, J)$ and $P(A, co, 0, K^-, J)$ in torsional mode $t = 0$, for $K = 2$, 3, and 4. (b) J-reduced energy of some relevant upper-state levels of A-torsional symmetry for methanol. The J-reduced energy is the state energy to which $0.8J(J + 1)$ has been subtracted, where 0.8 cm^{-1} corresponds to a representative B-value [239].

doublet frequency splittings between the $K = 4$ $P(A, co, 0, 4^+, J)$ and $P(A, co, 0, 4^-, J)$ transitions is observed in Figure 4.10(a) for values of J around 29 or 30.

4.2.4 High resolution spectroscopy of methanol in the literature

Here, we briefly review previous high resolution spectroscopic measurements in the C-O stretching vibrational band of methanol exhibiting high intense lines around 10 μm. Infrared Fourier transform spectroscopy of this mode has been extensively studied [237, 243–246]. However, the resolution of the Fourier transform spectroscopy is limited. The highest-resolution instruments can achieve an instrumental resolution of around 30 MHz, of the order of the Doppler-broadening in room temperature gas samples which results in line center frequency uncertainties of several MHz typically. Many blended features including A-symmetry K-doublets were not resolved by this spectroscopic technique. Around 2000, Z.D. Sun and co-workers reported absolute frequencies of almost 700 transitions that were measured from 1016 to 1063 cm^{-1} with an accuracy of the order of 100 kHz using a CO_2-laser-microwave-sideband spectrometer [234, 242, 247, 248]. Most of those are however intense lines belonging to the Q and R branches, with a small fraction only of low J lines in the P branch (see Figure 4.9). In comparison, as illustrated in Figure 4.9, we have studied weak transitions at relatively high J in the P-branch. In addition, the absolute frequency of a weak absorption line around 947.7 cm^{-1} has been measured with an uncertainty of 2.4 kHz using a heterodyne CO_2 laser spectrometer [233].

4.3 Doppler-limited spectroscopy

4.3.1 Spectrum acquisition

We now describe how direct absorption spectroscopy of methanol is carried out using the experimental setup illustrated in the panel (b) of Figure 4.1. The pump beam is blocked for these experiments. The multipass absorption cell is filled with a vapor of

methanol using a leak valve. The free-running QCL is cooled at 243-K and is driven using the home-built low-noise current driver (see subsection 3.2.2) at a DC current i_0. A sawtooth voltage ramp with a peak-to-peak voltage of 20 V at a frequency of 100 Hz provided by a function generator is converted to an approximately linear current ramp using a $R = 1k\Omega$ resistor (see Figure 4.11) and is combined with the DC current i_0 and then sent to the QCL. As mentioned in subsection 3.2.2, the QCL has a current-to-frequency conversion factor of about 257 MHz/mA, thus each spectrum is recorded over a frequency span of about 5 GHz.

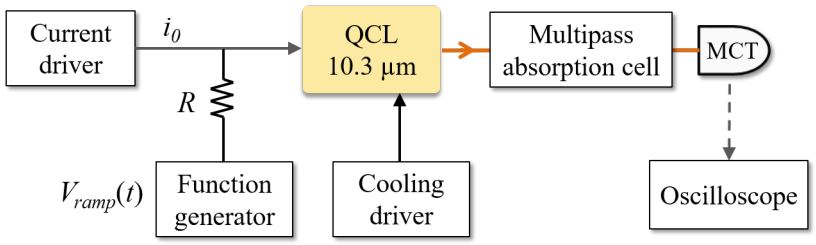

Figure 4.11 – Experimental setup for scanning the free-runing QCL frequency. A voltage ramp signal $V_{ramp}(t)$ is produced by a function generator and is converted into a current ramp via a $R = 1$ kΩ resistor. This current ramp is combined with the current i_0, provided by the DC current driver of the QCL and sent to the QCL.

After propagation in the multipass absorption cell, the probe beam is detected by the MCT photodetector (see Figure 4.1). The signal is recorded using a high-speed oscilloscope. We have obtained several spectra covering various spectral windows by changing the DC current driving the QCL. During the measurements, the multipass cell is shaken using a broken fan to average out undesirable interference fringes caused by the beam superposition inside the multipass cell, as mentioned in subsection 4.1.1. The fringes present even in the absence of molecules in the multipass cell. The signal-to-noise ratio of the average spectra is five times higher when using the fan.

4.3.2 Data processing and results

We now consider how the absolute frequency axis of a direct absorption spectrum is obtained. First, a list of central positions of the absorption lines is obtained by fitting the raw data to a set of Gaussian line shapes. Those are obtained in some arbitrary units corresponding to the oscilloscope time base. The frequencies of some of these lines are reported in the HITRAN database [54], and we fit a polynomial to this list of absolute frequencies as a function of the corresponding experimental raw frequencies. In each recorded spectrum, the order of the polynomial is taken equal to the number of methanol lines from the HITRAN database used as references. This polynomial function is then used to convert the raw data horizontal scale into an absolute frequency scale. The HITRAN frequencies used for this reconstruction are obtained from frequency positions recorded with a ∼15 MHz uncertainty. We take this as a good estimate of the uncertainty of the reconstructed frequency scale.

Figure 4.12(bottom, black curve) shows a Doppler-limited spectrum of methanol in the P-branch in the range from 971.687 to 971.803 cm^{-1} after reconstructing the frequency axis. It is recorded at a pressure of ∼7 Pa and a temperature of ∼295 K. The red curve is a fit to the data corresponding to a sum of 17 Gaussian line shapes. The

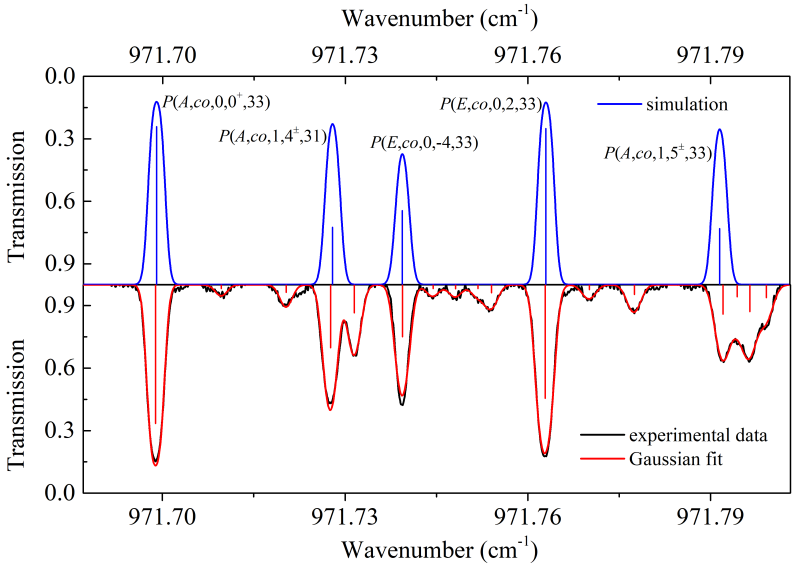

Figure 4.12 – Doppler-limited absorption spectrum from 971.687 to 971.803 cm^{-1} of methanol in the multipass cell (bottom, black curve). It is recorded at a pressure of ∼7 Pa using the free-running QCL. The red curve is a fit to the data, corresponding to a sum of 17 Gaussian line shapes. The resulting line-center frequencies are indicated by red sticks. The blue curve is the simulated spectrum using the HITRAN database. Blue sticks indicate the line-center frequencies of methanol lines reported in the HITRAN database.

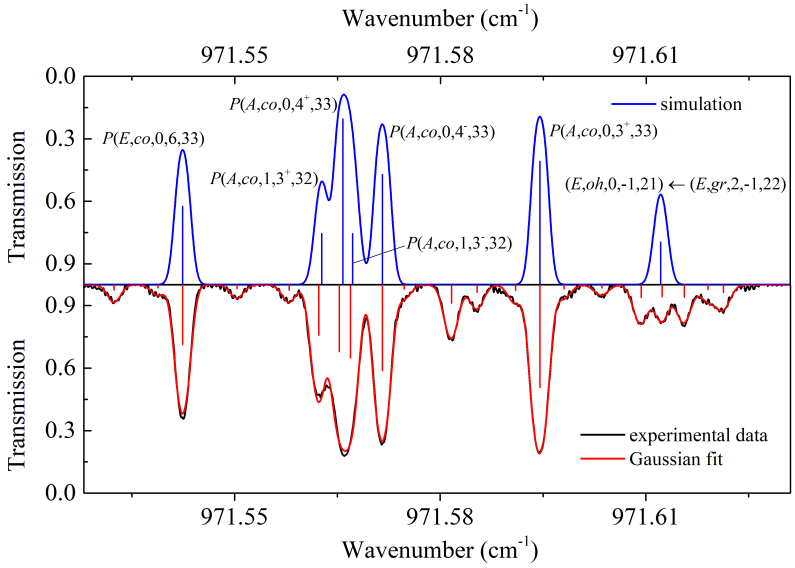

Figure 4.13 – Doppler-limited absorption spectrum from 971.528 to 971.631 cm^{-1} of methanol in the multipass cell (bottom, black curve). It is recorded at a pressure of ∼7 Pa using the free-running QCL. The red curve is a fit to the data, corresponding to a sum of 20 Gaussian line shapes. The resulting line-center frequencies are indicated by red sticks. The blue curve is the simulated spectrum using the HITRAN database. Blue sticks indicate the line-center frequencies of methanol lines reported in the HITRAN database.

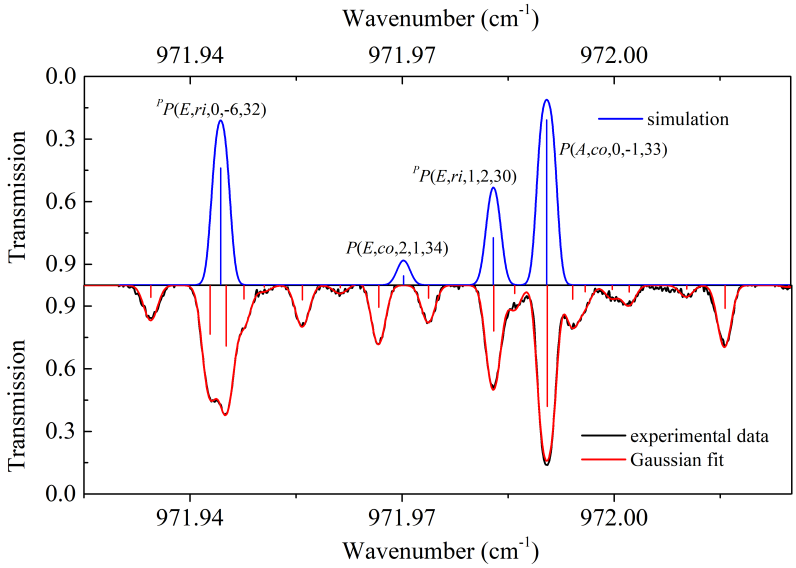

Figure 4.14 – Doppler-limited absorption spectrum from 971.925 to 972.025 cm^{-1} of methanol in the multipass cell (bottom, black curve). It is recorded at a pressure of ∼7 Pa using the free-running QCL. The red curve is a fit to the data, corresponding to a sum of 17 Gaussian line shapes. The resulting line-center frequencies are indicated by red sticks. The blue curve is the simulated spectrum using the HITRAN database. Blue sticks indicate the line-center frequencies of methanol lines reported in the HITRAN database.

resulting FWHM linewidth is found to be ∼64 MHz, agreeing well with expected Doppler broadening of ∼64.6 MHz. Line-center positions and relative intensities of the 17 rovibrational transitions identified in the spectrum of Figure 4.12 are indicated by red sticks. Figure 4.12 (top, blue curve) shows a calculated spectrum using the HITRAN database [54] simulated with same experimental conditions (pressure of 7 Pa, temperature of 295 K, absorption length 36.4 m). We can observe relatively important discrepancies between the experiment and the theory both in the line intensities and positions of absorption lines between these spectra. For instance, around 971.73 cm^{-1} an unresolved $P(A, co, 1, 4^{\pm}, 31)$ K-doublet is predicted in the HITRAN database at a frequency of 971.72791 cm^{-1} while the experimental spectrum exhibits two partially resolved lines, corresponding most probably to the $P(A, co, 1, 4^{\pm}, 31)$ K-doublet and another weak transition on the low frequency side, not reported so far. Around 971.792 cm^{-1} again, an unresolved $P(A, co, 1, 5^{\pm}, 33)$ K-doublet is predicted in the HITRAN database. At the same position, the data shows four partially resolved transitions of methanol, the intensities of which are at least two times smaller than the predicted K-doublet. Moreover, our experimental data exhibit many low intensity lines not reported in the HITRAN database, that most probably belong to hot bands corresponding to a torsional excitation $t = 2$ or more.

Figures 4.13 and 4.14 display Doppler-limited spectra of methanol (black curves) from 971.528 to 971.631 cm^{-1} and from 971.925 to 972.025 cm^{-1} together with the resulting Gaussian fits (red curves) and spectra calculated using the HITRAN database (top, blue curves). The experimental conditions are similar to the previous spectrum. We can see that in Figure 4.13 our spectrum shows a triplet around 971.61211 cm^{-1} while only the $(E, oh, 0, -1, 21) \leftarrow (E, gr, 2, -1, 22)$ rovibrational transition of the ν_6 OH-

bending vibrational mode is present in the HITRAN database. In Figure 4.14, we resolve three rovibrational methanol lines around 971.944 cm^{-1} while only the $P(E, ri, 0, -6, 32)$ transition of the ν_7 in-plane CH3 rocking vibrational mode is reported in the HITRAN database at 971.94430 cm^{-1}. In addition, our experimental data shown in Figures 4.13 and 4.14 again exhibit many low intensity lines not reported in the HITRAN database, that most probably belong to hot bands corresponding to a torsional excitation $t = 2$ or more.

The absolute line-center frequencies of the observed rovibrational transitions of methanol shown in Figures 4.12-4.14 and observed in additional spectra, not shown here, are listed in Appendix E together when possible with (sometimes tentative) assignments deduced from the HITRAN database. We estimate a conservative uncertainty on the line positions to be 30 MHz, limited by the quality of the frequency scale reconstruction.

4.4 Precise spectroscopy of methanol

In this section, we focus on saturated absorption spectroscopy of methanol around 29.1 THz (between 970 cm^{-1} and 973 cm^{-1}). We first describe how we acquire a saturated absorption spectrum using the stabilized QCL and the frequency modulation setup. Then, we present the analysis of the recorded spectrum.

4.4.1 Spectrum acquisition

4.4.1.1 Sub-Doppler spectroscopy using the free-running QCL

In order to better understand why the stabilized QCL and the frequency modulation technique are needed to measure a saturated absorption spectrum, we plot in Figure 4.15(a) a sub-Doppler spectrum of the $P(A, co, 0, 1^+, 33)$ rovibrational transition of methanol using the free-running QCL. It is recorded at ∼2 Pa using the experimental setup described in subsection 4.3.2 after having obviously unblocked the pump beam. The spectrum exhibits a saturated absorption peak on a Doppler-broadened profile with a contrast of ∼9%. Although both the mirror M2 and multipass cell (Figure 4.1) are shaken during acquisition, residual interference fringes are clearly observed in the spectrum, limiting the signal-to-noise ratio of the spectrum. The FWHM linewidth of the saturated absorption feature is found to be ∼2 MHz, mainly due to the QCL free-running frequency fluctuations and other effects, such as transit time, power broadening, and collisional effect. As will be shown in the following, both the resolution and the signal-to-noise ratio can be much improved using the comb-stabilized QCL and the frequency modulation technique.

4.4.1.2 Spectrum acquisition with the stabilized QCL and frequency modulation technique

In this paragraph, we present how a saturated absorption spectrum is acquired using the ultra-stable and widely-tunable QCL and the frequency modulation technique. Typically, each spectrum is acquired by tuning the home-made microwave synthesizer driving the EOM frequency (see section 3.5). The OLO carrier frequency, the OFC repetition rate and QCL frequency are thus scanned in a series of discrete steps. The signal of the lock-in amplifier is recorded using a data acquisition computer card. The same home-built C# program controls the microwave synthesizer's frequency and the acquisition card.

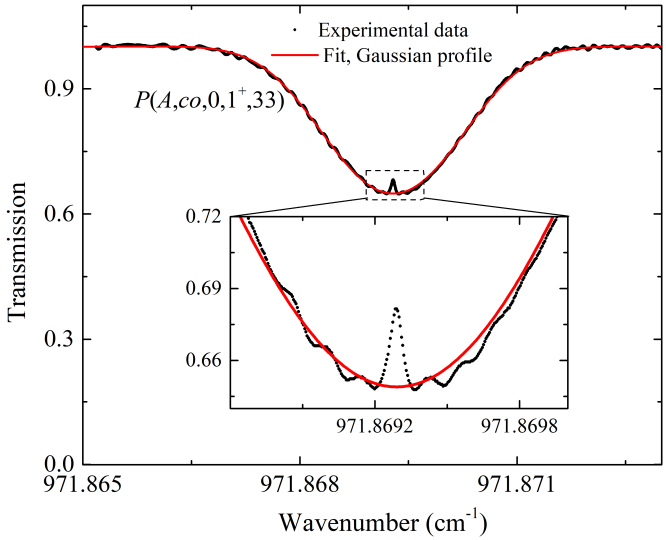

Figure 4.15 – Saturated absorption spectroscopy of $P(A, co, 0, 1^+, 33)$ transition near 971.869 cm^{-1} recorded at 2 Pa with the free-running QCL. The inset shows a zoom of the saturated absorption feature.

Interface of the acquisition software

Figure 4.16 shows the interface of this program based on the Internet Explorer software. On the top, the "Console" panel indicates the status of the program. The left panels allow the user to set the parameters of the microwave synthesizer (e.g. scan type - up, down, or up and down-, number of scans, start frequency, stop frequency, frequency step, and time step) and the panel at the right displays the current spectrum and the average spectrum. The interface's bottom area, the "Save Export" panel, allows the user to export acquired data in various formats (e.g. CSV, JSON,...). Files saved in the JSON format, that is a data format derived from the JavaScript format, not only save the measured data but also save all the settings of the microwave synthesizer and the acquisition card. Files saved in the CSV format only save the acquired spectrum.

Saturated absorption without frequency modulation

Figure 4.17 shows a direct saturated absorption spectrum of the $P(E, co, 0, 2, 33)$ rovibrational transition of the ν_8 C-O stretching vibrational mode of methanol recorded without using frequency modulation. The contrast between the sub-Doppler feature and the Doppler-broadened absorption is ∼9%. The frequency axis is reconstructed using the radio-frequency protocol described in subsection 3.5.1. This spectrum is recorded at 1.5 Pa with a frequency step of about ∼45 kHz and averaged after 88 pairs of up and down scans. The saturated absorption feature has a signal-to-noise ratio of ∼16 and a FWHM linewidth of ∼700 kHz −three times narrower than when using the free-running QCL.

Saturated absorption with frequency modulation

As described in subsection 4.1.3, the frequency modulation technique is used to improve the signal-to-noise ratio of sub-Doppler spectroscopy. We apply a frequency modulation on both the pump and probe beams at a frequency of $f_m = 20$ kHz via the radio-frequency reference of the phase-lock loop (PLL3, Figure 4.1) used to lock the

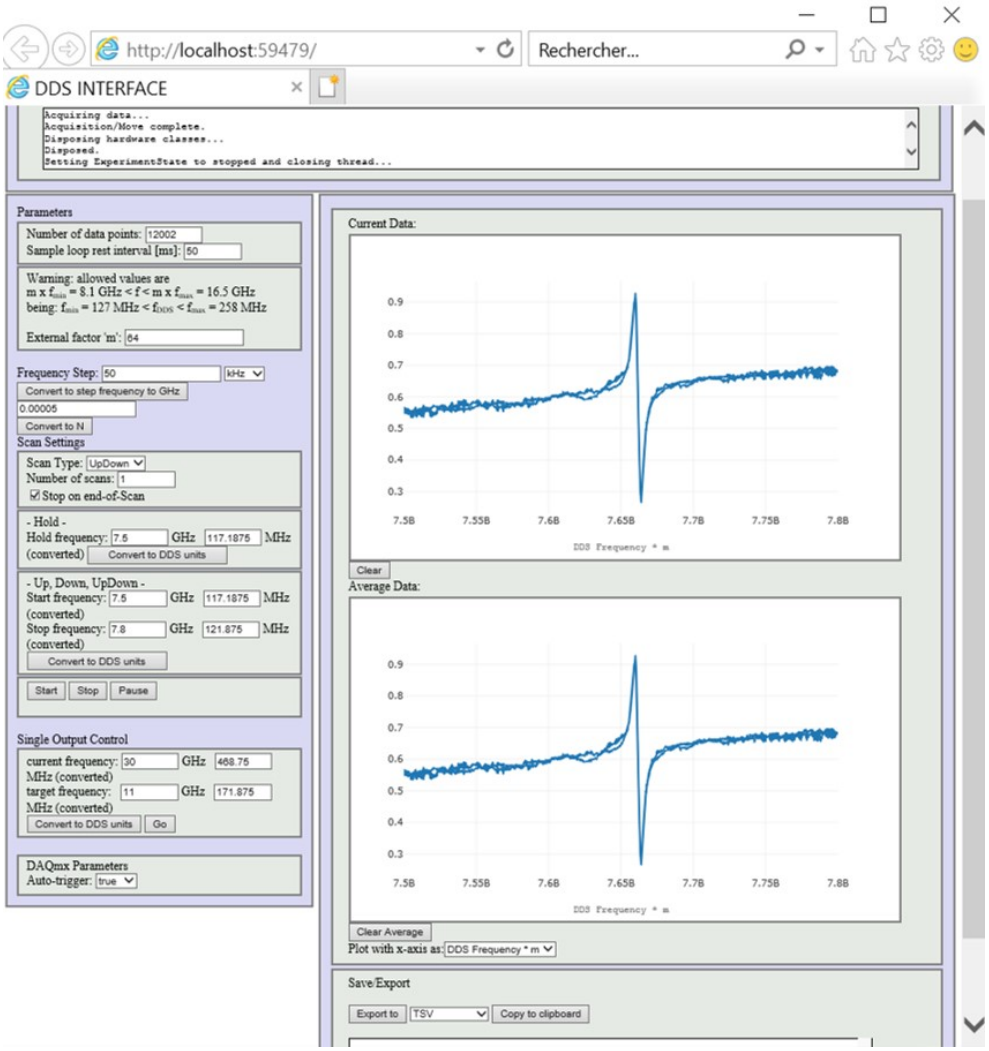

Figure 4.16 – Interface of the C# acquisition software. At the top, the console information indicates the status of the program. Parameters of the microwave synthesizer (e.g. scan type -up, down, or up and down-, start frequency, stop frequency, frequency step, and time step) are set at in the left panels while the current and averaged spectra are plotted on the right panels. At the bottom, the "Save Export" panel allows the user to export measured data in various formats (e.g. CSV, JSON,...).

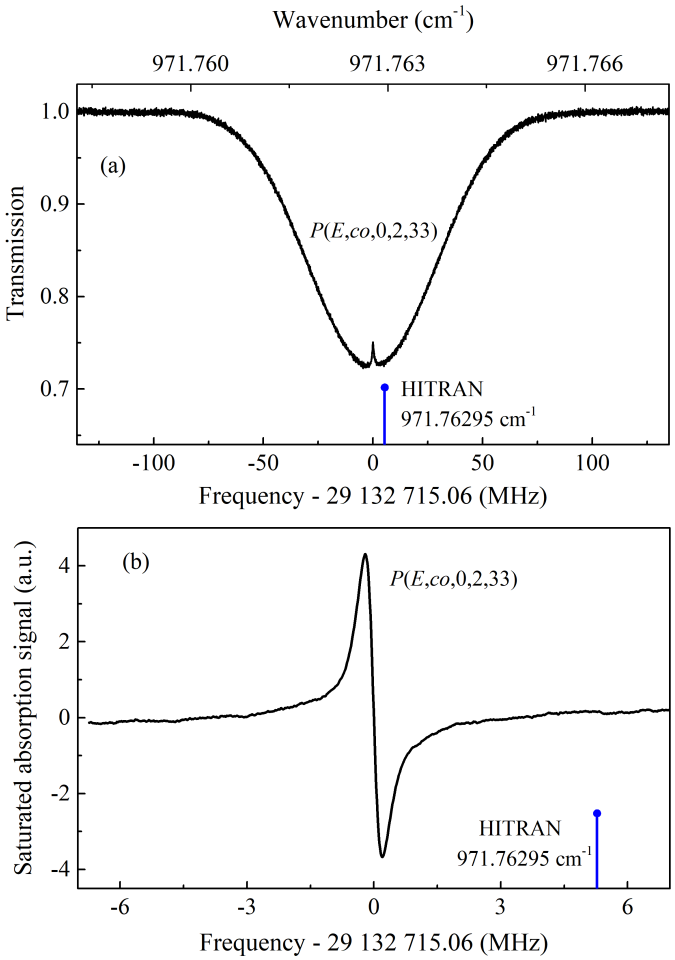

Figure 4.17 – (a) Saturated absorption spectroscopy of the $P(E, co, 0, 2, 33)$ rovibrational transition of methanol with the stabilized QCL. This transition is reported in the HITRAN database [54] at 971.76295 cm^{-1}, as shown by the blue sticks. Experimental parameters: pressure, 1.5 Pa; frequency step, ∼45 kHz; average of 88 pairs of up and down scans; total measurement time per point, 0.528 s; whole spectrum measurement time, 3170 s. (b) Saturated absorption spectrum of the $P(E, co, 0, 2, 33)$ rovibrational line of methanol recorded using frequency modulation and first-harmonic detection. Experimental conditions: pressure, 1 Pa; modulation frequency, 20 kHz; frequency modulation excursion, 50 kHz; frequency step, ∼15 kHz; average of 5 pairs of scans of opposite frequency sweep direction; total integration time per point, 1 s; whole spectrum measurement time, 917 s.

QCL frequency onto the repetition rate of the OFC (see subsection 4.1.3). Mainly first-, but also second- and third-harmonic detection of the lock-in amplifier will be used to obtain the modulation spectroscopy. Increasing the frequency modulation excursion allows the signal-to-noise ratio to be improved but this leads to broadening of the molecular absorption transition. Therefore, the choice of modulation parameters will result from a trade-off between the signal-to-noise ratio increase and the broadening. In this work, frequency excursion will range from 50 to 400 kHz, to be compared with a typical 700 kHz transition linewidth.

We carry out frequency scans in both frequency sweep directions, with increasing and decreasing frequencies and consider only averages of a pair of such up and down scans. In this way, frequency shifts induced by the limited detection bandwidth of the lock-in amplifier are eliminated [249,250]. Spectra are typically recorded with an EOM frequency step (and thus an OLO carrier frequency step) $\Delta f_{EOM} = 100$ kHz and a step duration of 100 ms. This results in steps of ∼125 mHz and ∼15 kHz for f_{rep} and ν_{QCL}, respectively. Note that the time constant of the lock-in amplifier used to demodulate the absorption signal is also chosen to be 100 ms which allows us to obtain ample signal-to-noise ratio in a single scan. During the scan, the comb repetition rate f_{rep} is also recorded in real time.

Figure 4.17 shows a saturated absorption spectrum of the $P(E, co, 0, 2, 33)$ rovibrational transition averaged over five pairs of up and down scans, after retrieval of the absolute frequency scale using the optical protocol presented in subsection 3.4.3. It exhibits a signal-to-noise ratio of ∼650 and a peak-to-peak linewidth of about ∼400 kHz (corresponding to ∼700 kHz FWHM of the saturated absorption spectrum), which is a combination of the pressure broadening (∼200 kHz/Pa FWHM, see below), transit time broadening (∼120 kHz FWHM, see below) and power broadening (see below). Using the frequency modulation technique thus results in a huge increase of signal-to-noise ratio.

4.4.2 Analysis of experimental data

In this subsection, we first describe our line shape model used to fit the saturated absorption spectrum of methanol. Then, we present the procedure for analysing the data and determining resonance center frequency and its uncertainty.

4.4.2.1 Line shape's issue

Compared to a single cell, the saturated absorption line shape of molecular spectrum recorded in the multipass cell is expected to be rather intricate. The mirrors's reflectivity results in a 15% to 20% transmission after 182 passes. The pump and probe powers thus inversely vary by almost an order of magnitude through the cell: the pump power decreases from 1.7 to 0.22 mW and the probe power increases from 0.12 to 0.9 (see Figure 4.18). This leads to a pump-to-probe power ratio ranging from ∼15 to ∼0.3, a ∼50% total power variation depending on the pass number, and in turn to marked fluctuations of the saturation parameter. The resulting line shape is thus likely to deviate from the Lorentzian profile typically used in the pressure broadened regime of our experiments.

Here, we use one saturated absorption spectrum of the $P(E, co, 0, 2, 33)$ rovibrational transition of methanol to find the model of the saturated absorption line shape, that best matches our data. As shown in Figure 4.19(a), the spectrum is recorded at 1 Pa and averaged after one up and one down scan (corresponding to one of the 5 pairs contributing

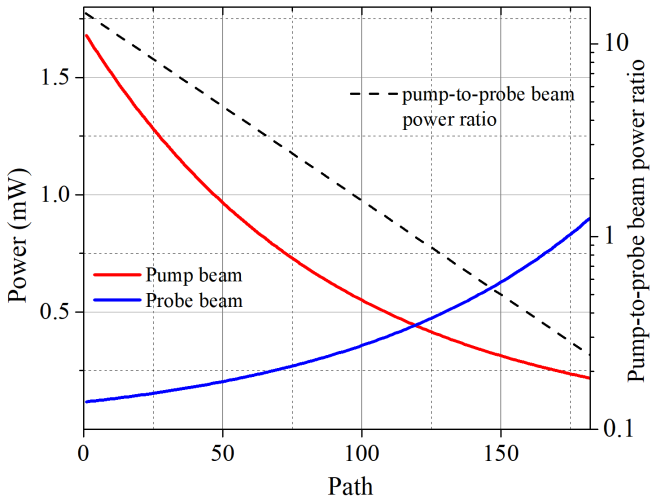

Figure 4.18 – Variation of the pump and probe beam powers as a function of the pass number in the multipass absorption cell. Dash line describes power ratio between the pump and probe beams.

to Figure 4.17). It exhibits a signal-to-noise ratio of 315. A simple line shape including the sum of a first-derivative of a Lorentzian and a linear baseline is fitted to the data. The resulting residuals bring to light the asymmetry of the observed spectrum line shape. We note that this asymmetry does not depend on the scan direction. Several effects associated with line broadening can contribute to the line shape asymmetry, amongst which following effects are likely causes:

– The residual amplitude modulation associated with frequency modulation.

– The power variation over a frequency scan that can result from (i) the gain curve, (ii) the underlying Doppler envelop that can be non-trivial in case of neighbouring lines that are not resolved in the Doppler regime, (iii) local etaloning effects due to the multipass cell.

Those line shape issues will ultimately limit the determination of the center frequency, as will be seen in section 4.6.

We adopt a phenomenological approach to deal with our lack of knowledge of the right model for the line shape by fitting the recorded spectrum (Figure 4.19) to different profiles which are composed of two terms, the first one modelling the saturated absorption feature and the second one accounting for the baseline.

Regarding the saturated absorption feature, we have tried to fit to the data many different profiles:

(i) Various sums of derivatives of increasing order (both odd and even) of a Lorentzian.

(ii) A sum of a Lorentzian and a dispersive-like profile (here we multiply the Lorentzian by a term $[B(\nu - \nu_0) + 1]$ which models the asymmetry).

(ii) Various sums of derivatives of increasing order (both odd and even) of a Voigt profile.

(iii) We have tried all this considering or not the Beer-Lambert law.

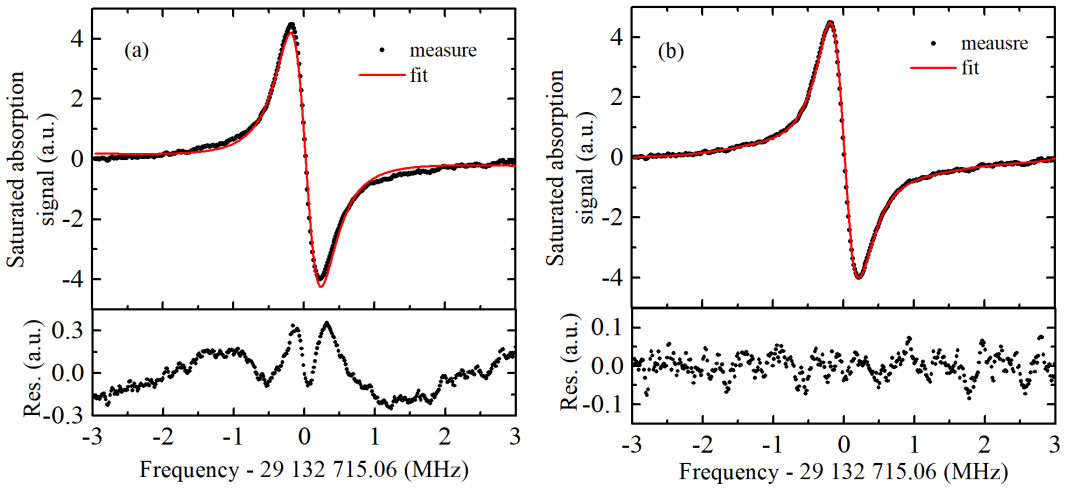

Figure 4.19 – Saturated absorption spectrum of the $P(E, co, 0, 2, 33)$ ν_8 rovibrational transition of methanol with fit and residuals. The data (black dots) are recorded using frequency modulation and first-harmonic detection. The red solid line in panel (a) is a fit to the data using a simple line shape including the sum of a first-derivative of a Lorentzian and a linear baseline, resulting in a reduced chi-squared of ∼20. The red solid line in panel (b) is a fit to the data of a line shape given by Equation 4.13, resulting in a reduced chi-squared of 1.27. Residuals of each fit are shown on the bottom graphs. Experimental conditions: pressure, 1 Pa; modulation frequency, 20 kHz; frequency modulation excursion, 50 kHz; frequency step, ∼15 kHz; average of one pair of up and down scans (corresponding to one of the five pairs contributing to Figure 4.17(b)); total integration time per point, 200 ms; whole spectrum measurement time, 80.2 s.

As shown in Figures 4.17 and 4.18, the baseline exhibits some remaining, non-stationary, interference fringes which we attribute to the limited efficiency of our strategy to scramble multipass cell-induced etaloning effects (see section 4.1). For this reason, a Gaussian profile or a low-order polynomial, that would model the underlying Doppler broadened feature, are not good enough to model the base line. We have tried to fit the residual fringes with a sum of periodic functions, but this did not work well enough. We have thus decided to model the baseline by a relatively high-order (order N) polynomial. We have tried various values of N to find an optimum. We also vary the spectral range over which the fit was performed from 15 MHz to 6 MHz.

To find the model that best matches our data, we use the following criteria: (i) the residuals should be smooth with no feature inside, (ii) the line-center frequencies obtained from data recorded using different harmonic detections should be similar, and (iii) the value of the minimum of χ^2 obtained from the fit should be reasonable (i.e. reduced chi-square χ^2_{red} around 1).

After making analyses with these different models, we notice that the dispersive term is really needed to fit our data and in particular to deal with the asymmetry. At the end, we find that the line shape, that best-matches with the saturated absorption feature, is a Lorentzian multiplied by an amplitude that varies linearly or equivalently the sum of a Lorentzian and a dispersive-like shape (see Equation 4.14). Finally, the model used for

fitting n^{th}-harmonic detection data is given by

$$\frac{\partial^n}{\partial^n \nu} g(\nu) + \sum_{i=0}^{N} s_i (\nu - \nu_0)^i \tag{4.13}$$

with

$$g(\nu) = A[B(\nu - \nu_0) + 1]L(\nu) \tag{4.14}$$

and

$$L(\nu) = \frac{1}{\pi} \frac{\gamma}{(\nu - \nu_0)^2 + \gamma^2}, \tag{4.15}$$

where A, γ, and ν_0 represent the area, the HWHM and the center of the Lorentzian curve $L(\nu)$, B is the asymmetry factor, and $\sum_{i=0}^{N} s_i(\nu - \nu_0)^i$ is a polynomial of order N modelling the baseline.

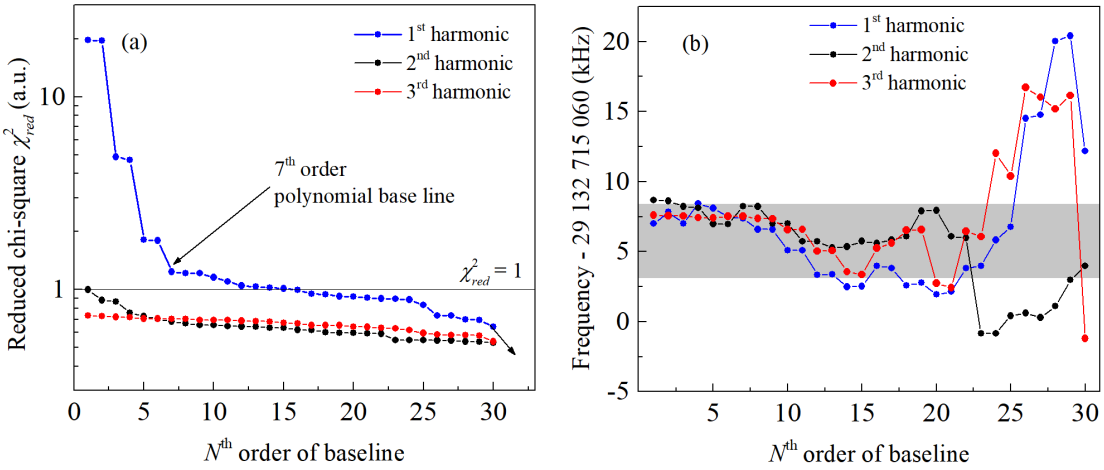

Figure 4.20 – (a) Minimized reduced chi-square value χ^2_{red} of the fit as a function of the order N of the baseline and (b) Fitted absolute frequency of the spectrum (see Figure 4.19) as a function of the order N of the baseline.

In order to find the best order N of the polynomial, we fit the line shape given by Equation 4.13 with $n = 1$ (first-harmonic detection) to the saturated absorption spectrum of the $P(E, co, 0, 2, 33)$ line of methanol over a span of 6 MHz (Figure 4.18(a)) with N varying from 1 to 30. Then, we look at the minimized reduced chi-square χ^2_{red} (see Appendix D for its definition) of the fits. Figure 4.20(a) (blue curve) shows the minimized χ^2_{red} value of each fit. It is around 20 with $N = 1$ and then rapidly decreases with N. We can see that χ^2_{red} is close to 1 for values of N between 7 and 20 and then decreases further. We also plot in Figure 4.20(b) (blue curve) the line-center frequency of the $P(E, co, 0, 2, 33)$ transition of methanol obtained from the 30 fits as a function of N. It varies within 5 kHz for $1 \leq N \leq 20$. For $N > 20$, the line-center frequency exhibits pronounced variations. We conclude for Figure 4.20(b) that $N > 20$ is too much and that the baseline start to fit the saturated absorption feature itself. We decide to choose $N = 7$ for analyzing our data, as it is the smallest N that give reasonable results for both the value of minimized χ^2_{red} and the line-center frequency. Note that even with $N = 7$, the baseline may well catch some non-Lorentzian contribution to the experimental profile.

Figure 4.19(b) shows the fit of the saturated absorption spectrum of the $P(E, co, 0, 2, 33)$ rovibrational of methanol, same data as Figure 4.18(a), using the line shape given by Equation 4.13 with $N = 7$, and its residuals. The minimized reduced chi-square value of the fit is ∼1.27. The line shape model with a seventh polynomial baseline is well-matched when fitting to the data over a span of 6 MHz. We have done similar studies when fitting the data over longer range. We then need to increase the order of the polynomial to correctly fit the data.

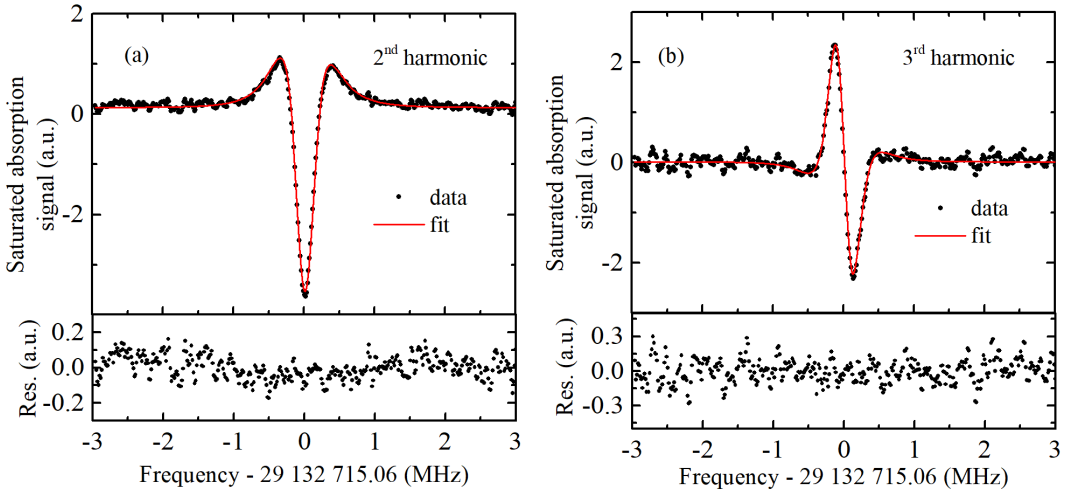

Figure 4.21 – Two saturated absorption spectrum of the $P(E, co, 0, 2, 33)$ rovibrational line of methanol, with their fits and residuals. The data (black dots) are recorded using frequency modulation and (a) second-harmonic detection and (b) third-harmonic detection. The red solid lines are fits to the data resulting in reduced chi-squared of 1.04 for the second-derivative spectrum and 0.8 for for the third-derivative spectrum. Residuals of each fit are shown on the bottom of each graphs. Experimental conditions: pressure, 1 Pa; modulation frequency, 20 kHz; frequency modulation excursion, 100 kHz for the second-harmonic detection and 150 kHz for the third-harmonic detection; frequency step, ∼15 kHz; average of one pair of up and down scans; total integration time per point, 200 ms; whole spectrum measurement time, 80.2 s.

In order to ensure that our line shape model also well-matches data recorded using higher harmonic detection (second criterion above), we have carried out saturated absorption spectra of the $P(E, co, 0, 2, 33)$ rovibrational of methanol using second- and third-harmonic detection. The experimental conditions are the following: pressure of 1 Pa, frequency modulation of 20 kHz, frequency excursions of 100 kHz for second-harmonic detection and 150 kHz for third-harmonic detection. The data correspond to an average of one pair of up and down scans. The results are shown in panels (a) and (b) of Figure 4.21. They exhibit signal-to-noise ratios of 75 (second harmonic) and 40 (third harmonic).

We fit to the saturated absorption data shown in Figure 4.21 (a) and (b) the model of Equation 4.13 with $n = 2$ and 3 and with N ranging from 1 to 30. The value of the minimized χ^2_{red} obtained from each fit is shown in Figure 4.20 (black curve for second-harmonic and red curve for third-harmonic). It is ∼1 at $N = 1$ and then slowly goes down, showing that the polynomial baseline is not needed for the fits. This is expected

because the residual fringes have a typical width different from the saturation feature and are thus naturally filtered out by the lock-in detection. Therefore, line shapes of saturated absorption spectra can be fitted using

$$\frac{\partial^2}{\partial^2 \nu} g(\nu) + s_0 \tag{4.16}$$

for the second-harmonic detection signal and

$$\frac{\partial^3}{\partial^3 \nu} g(\nu) + s_0 \tag{4.17}$$

for the third-harmonic detection signal, in which $g(\nu)$ is given by Equation 4.14 and s_0 is an offset (polynomial of order zero). In addition, the fitted absolute frequencies of the $P(E, co, 0, 2, 33)$ line for the second- and third-harmonic detection spectra with N ranging from 1 to 30 are plotted in Figure 4.20(b) together with those obtained from the fits to the first-harmonic detection spectrum. We can see that the absolute frequencies of the spectra recorded by the first-, second-, and third-derivative detections are consistent within ∼5 kHz for values of $N \leq 17$. Figure 4.21 also shows the resulting fits to the data using the line shapes given by Equations 4.16 and 4.17, and their residuals. The minimized χ^2_{red} values of these fits are found to be 1.04 for the second-harmonic spectrum and 0.8 for the third-harmonic spectrum.

Finally, we have also fitted the variety of line shape profiles listed above to the second and third harmonic detection data. Amongst all the models considered, $g(\nu)$ is the simplest for which fitting to first-, second-, and third-harmonic detection data (using the corresponding derivatives of $g(\nu)$, see Equations 4.16 and 4.17) all converged to a transition center frequency to within 5 kHz. Most of the other profiles happen to be inconsistent at the few tens of kilohertz level, which gives $g(\nu)$ the necessary credit, further confirmed by the exemplary outcome of our least-squares procedure (chi-square values and residuals).

4.4.2.2 Data processing procedure

In order to determine the absolute frequency of a rovibrational transition of methanol, we typically record five pairs of back and forth spectra for each measurement. The absolute frequency scale is obtained by following one of the protocols described in subsection 3.4.3. Then, we perform "a pair by pair" analysis of the data. We first average each single pair to cancel frequency shifts induced by the limited detection bandwidth (see subsection 4.4.1) and assign the same error bar to all data points of such a single averaged spectrum. This experimental error bar is calculated as the standard deviation of the residuals obtained after fitting a second-order polynomial to a small portion of the spectrum far from resonance. The second order polynomial is chosen because it reproduces well the lineshape locally without interpolating the noise. For the data shown in Figure 4.19, it is ∼1% of the signal peak-to-peak amplitude.

Then, we fit the model to the average spectrum of each pair. We typically find that the dispersion of the five frequencies resulting from the analysis of the five pairs is a few times larger than the uncertainty resulting from the fit to a single pair. Figure 4.22 (blue points), for instance, shows the five frequencies and error bars resulting from the fits for the five pairs of the $P(E, co, 0, 2, 33)$ rovibrational transition of methanol, contributing

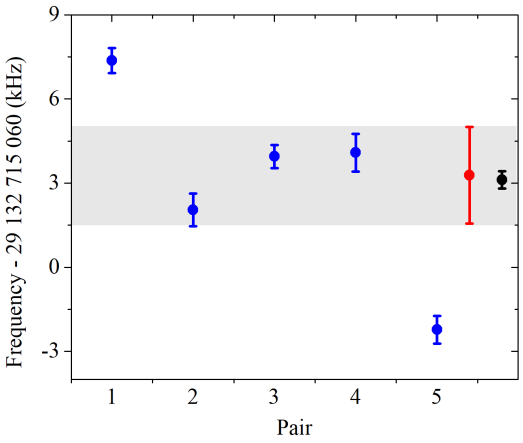

Figure 4.22 – Five absolute frequencies of the $P(E, co, 0, 2, 33)$ rovibrational transition obtained from the fits to a series of five averaged pairs of up and down spectra. The red point is the weighted mean with a weighted standard error shown as a grey area. The black point is the absolute frequency and corresponding uncertainty resulting from the fit of the averaged spectrum of five pairs (see text).

to Figure 4.17(b) (the average of the first pair is also displayed in Figure 4.19). The red point is the weighed mean of these five frequencies with an weighted standard error (see Appendix D for its definition) of 1.7 kHz. Error bars resulting from the fits are used as weights.

There exists another way to determine the resonance frequency in which we first take the average of the five pairs (as shown in Figure 4.17(b)) and then fit the line shape to the averaged spectrum. The uncertainty resulting from the fit is then smaller than the dispersion of the resonance frequencies of the five pairs in the previous way (see black point in Figure 4.22). Therefore, to be conservative, we decide to use the "pair by pair" analysis to process data.

In the following, one measurement will typically consist of five pairs of up and down scans. In order to take into account the variation of the obtained absolute frequency from pair-to-pair, we will always carry out a "pair-by-pair" analysis and use the resulting weighted mean (see Appendix D for its definition) and weighted standard error to determine the absolute frequency and the uncertainty on this frequency for this measurement.

4.5 Spectroscopic measurements

In this section, we first present the experimental study of the power- and pressure-induced shifts of the $P(E, co, 0, 2, 33)$ rovibrational transition of methanol. Then, we discuss the power- and pressure-induced broadening effects to the linewidth of the transition.

4.5.1 Power-induced frequency shift

A significant shift of the line-center frequency is observed when varying the laser power. We have measured saturated absorption spectra of the $P(E, co, 0, 2, 33)$ rovibrational transition of methanol at different intra-cell laser powers ranging from 0.05 mW to 1.1 mW. We define the intra-cell average laser power as the total power from the

two counter-propagating beams averaged over the 182 paths inside the cell. We have performed twelve measurements at 1.1 mW, eight measurements at 0.82 mW, and three others at lower powers. Note that the twenty measurements recorded at 0.82 mW and 1.1 mW will be used in section 4.6 to determine the absolute frequency of the $P(E, co, 0, 2, 33)$ methanol line. For each measurement, we record five pairs of back and forth spectra at the same pressure of 1 Pa by using frequency modulation and first-harmonic detection. The absolute frequency of each measurement is determined by following the procedure detailed above. The results are shown in Figure 4.23. The line-center frequency decreases with increasing intra-cell averaged laser power. Note that, the shift actually varies from path-to-path due to power variations but that we only measure here the mean shift.

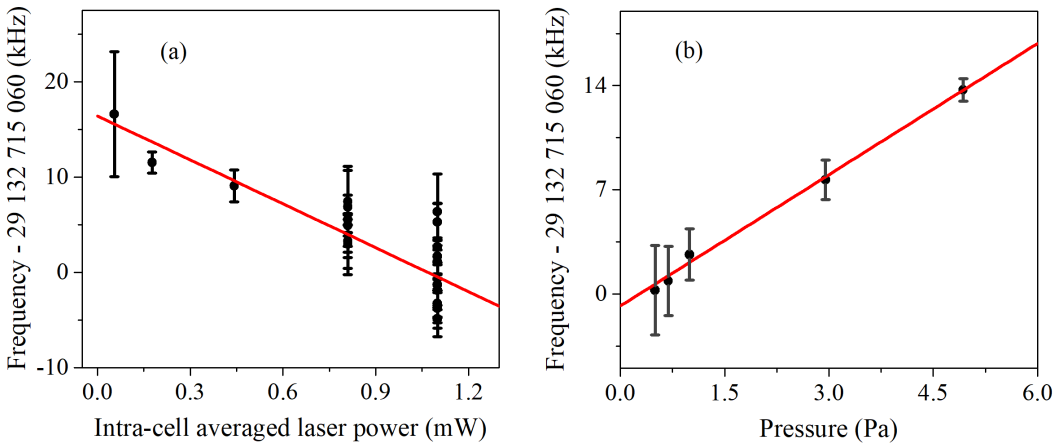

Figure 4.23 – The line-center frequency of the $P(E, co, 0, 2, 33)$ rovibrational transition of methanol as a function of (a) intra-cell average laser power and (b) pressure. The red solid lines are weighted linear fits to the data.

The red line in Figure 4.23(a) is a weighted linear fit in which we use the uncertainty of each measurement (determined using the procedure described in the previous section) as the weights. The fit allows a power-dependent shift coefficient of -15.4 (1.3) kHz/mW to be determined and a transition frequency of 29 132 715 076.4 (1.1) kHz to be extrapolated at zero-power. The 1-σ uncertainty quoted into parentheses correspond to the error bar of the weighted linear fit and does not include systematic effects.

4.5.2 Pressure-induced frequency shift

We have also measured the line-center frequency of the $P(E, co, 0, 2, 33)$ transition at different pressures in the range from 0.3 to 6 Pa. As described in subsection 4.4.2.1, saturated absorption spectrum is recorded at 1 Pa over a span of ∼15 MHz. The span is reduced to 6 MHz in order to be able to fit the data using a reasonable order $N = 7$ for the polynomial baseline. In these experimental conditions, the ratio between the frequency span and the FWHM linewidth of the spectra is $\Delta\nu_{QCL}/\gamma \sim 8$. At higher pressures, the linewidth is broadened due to collisional effects. The saturated absorption feature thus occupies a larger part of the 6 MHz spectral window. If the frequency span of the spectrum is not expanded, the seventh-order polynomial baseline start to fit the saturated absorption feature itself. For this pressure dependence analysis, we thus adapt the frequency range used for fitting the data to the pressure by keeping $\Delta\nu_{QCL}/\gamma$

constant and around 8.

Figure 4.23(b) shows the absolute frequency of the $P(E, co, 0, 2, 33)$ transition as a function of pressure. A pressure-dependent shift coefficient of +2.9(0.3) kHz/Pa is found by using a weighted linear fit of the observed central frequencies. It is of similar magnitude but opposite in sign compared to the only, to our knowledge, other mid-IR measurement available in the literature [233]. It can be used to deduce the collisionless transition frequency (see below).

4.5.3 Power- and pressure-induced broadening effects

We now present in this paragraph effects of power and pressure to the linewidth of the $P(E, co, 0, 2, 33)$ rovibrational transition of methanol. From the analysis of the saturated absorption spectra of the transition, we obtain two sets of spectral linewidths, as a function of intra-cell averaged power or pressure. It is noted that the linewidth of each measurement is a weighted mean (with its associated weighted standard error) of the five linewidths of the five averaged pairs of up and down spectra, following a procedure similar to that described in subsection 4.4.2.2 (we use again the uncertainty resulting from the fit of averaged pairs as the weights).

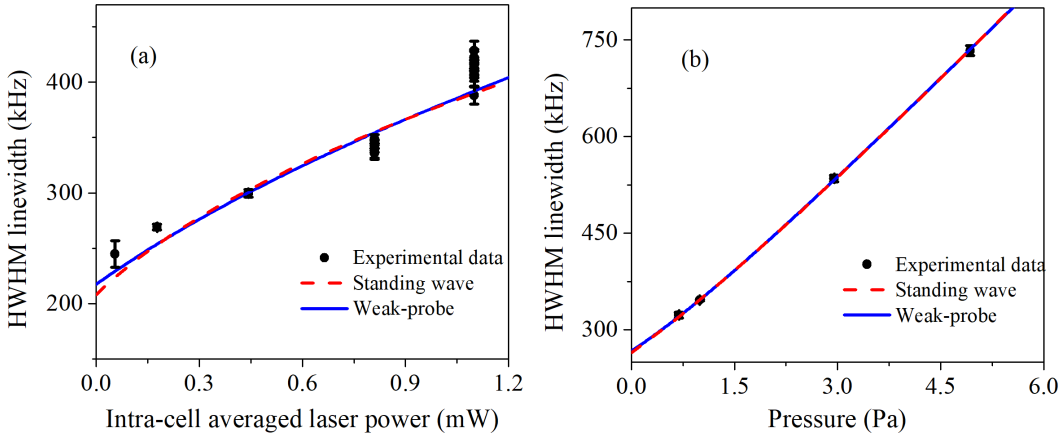

Figure 4.24 – Linewidth of the $P(E, co, 0, 2, 33)$ rovibrational transition of methanol as a function of (a) intra-cell averaged laser power and (b) pressure. The red dashed (blue solid) lines are weighted fits to the data for the standing wave (weak-probe) model.

Figure 4.24(a) shows the variation of the half-width at half-maximum (HWHM) of the $P(E, co, 0, 2, 33)$ transition of methanol as a function of power for a fixed pressure of 1 Pa. Note that to this broadening contributes the above mentioned inhomogeneous shift due to the power variation from path-to-path. However, we estimate this contribution to be smaller than 20 kHz (using the power shift data above), which is thus only a small contribution to the overall broadening. Figure 4.24(b) displays the HWHM linewidths of the $P(E, co, 0, 2, 33)$ rovibrational transition of methanol as a function of pressure for a fixed intra-cell averaged power of ∼0.8 mW.

As described in subsection 1.1.3, the power-broadened linewidth is given by Equation 1.23 when the absorption is saturated by a standing wave (pump and probe beams having the same power) and Equation 1.24 for a weak-probe beam. In our case, none of these models is adapted to the data because the pump-to-probe power ratio in the multipass

absorption cell varies over almost one order of magnitude from above to below unity (see Figure 4.18).

Additionally, the saturated absorption line shape is slightly distorted by the frequency modulation, and this has to be considered if we want to quantitatively analyze the pressure and power broaden data shown in Figure 4.24. We need to determine the influence of the frequency excursion used on the linewidth. To this end, we will simulate a set of first-harmonic detection signals for different values of $\Delta\nu_m$ and then fit them to the the first-derivative of a Lorentzian as we have done for the data. For the simulations, we use Arndt's model [251] that is based on a Lorentzian shape and that takes the frequency modulation into account and the resulting lineshape distortion. Note that we will use this model extensively in chapter 5 where it will be described in much details. We find that the linewidth obtained after fitting the simualted spectra is in practice, given by

$$\gamma_{\Delta\nu_m} = \sqrt{\gamma^2 + \Delta\nu_m^2}. \tag{4.18}$$

in which γ is the width (HWHM) of the simulated Lorentzian.

Thus, we decide to fit the experimental linewidth to the model given by Equation 4.18 where we replace γ by the power-broadened linewidth from either the standing wave model

$$\gamma = \gamma_0\sqrt{1 + \frac{P}{P_{sat}}}, \tag{4.19}$$

or weak probe case

$$\gamma = \frac{\gamma_0}{2}\left(1 + \sqrt{1 + \frac{P}{P_{sat}}}\right), \tag{4.20}$$

where γ_0 is the HWHM zero-power linewidth of the transition, P refers to the intra-cell average laser power, and P_{sat} represents the saturation power.

Let's assume a simple two-level system with relaxation mechanisms dominated by transit time and collisions [44, 59]. Let us denote $2\pi\gamma_\parallel$ and $2\pi\gamma_\perp$ (in units of angular frequency) the longitudinal (population) relaxation rate and transverse (transition dipole) relaxation rate, respectively, and $2\pi\gamma_1$ and $2\pi\gamma_2$ the population relaxation rates of the lower and upper states, respectively. Following V.S. Letokhov [59], in the absence of collision dephasing the transition dipole, a crude but reasonable assumption for a rovibrational transition, $\gamma_\parallel^{-1} = \left(\gamma_1^{-1} + \gamma_2^{-1}\right)/2$ and $\gamma_\perp = (\gamma_1 + \gamma_2)/2$.

If we assume $\gamma_1 = \gamma_2$, again a reasonable assumption for a rovibrational transition, we find $\gamma_\parallel = \gamma_\perp = \gamma_1 = \gamma_2$. We stress here that the transition dipole relaxation rate $\gamma_\perp$ corresponds to our the linewidth at zero-power γ_0 of our measured resonances. It can be written in the following way

$$\gamma_\perp = \gamma_0 = \gamma_e + B_p p \tag{4.21}$$

where γ_e is the zero-power and zero-pressure linewidth, expected to be dominated by the transit time effect and p is the gas pressure. The saturation parameter s is given by

$$s = \frac{P}{P_{sat}} = \frac{I}{I_{sat}} = \frac{\Omega_0^2}{4\pi^2\gamma_\parallel\gamma_\perp}, \tag{4.22}$$

where

$$I_{sat} = P_{sat}/(\pi w_0^2) \tag{4.23}$$

Table 4.1 – Spectroscopic parameters of the $P(E1, co, 0, 2, 33)$ rovibrational transition of methanol extracted from the analysis of the power and pressure dependences.

Parameters	Values
Saturation power, P_{sat} (mW) at 1 Pa	0.31 (0.15)
Zero-power linewidth, γ_0 (kHz)	207 (6)
Pressure broadening, B_P (kHz/Pa)	110 (8)
Zero-power and zero-pressure linewidth, γ_e (kHz)	161 (60)

is the saturation mean intensity of the transition with w_0 the laser beam waist and Ω_0 the Rabi frequency, given by

$$\Omega_0 = \mu_{12} E/\hbar \tag{4.24}$$

in which, $\hbar$ is the reduced Planck constant, E is the electric field, and μ_{12} is the transition dipole moment. Following our approximations mentioned above, the saturation parameter s has thus the following form:

$$s = \frac{P}{P_{sat}} = \frac{\Omega_0^2}{4\pi^2(\gamma_e + B_p p)^2}. \tag{4.25}$$

Injecting Equations 4.21 and 4.25 in the formulas 4.19 and 4.20 we obtain

$$\gamma = (\gamma_e + B_p p)\sqrt{1 + \frac{\Omega_0^2}{4\pi^2\left(\gamma_e + B_p p\right)^2}}, \tag{4.26}$$

for the standing-wave case and

$$\gamma = \frac{(\gamma_e + B_p p)}{2}\left(1 + \sqrt{1 + \frac{\Omega_0^2}{4\pi^2\left(\gamma_e + B_p p\right)^2}}\right), \tag{4.27}$$

for the weak probe case.

In the following, we use the formulas above to analyze our data. We first fit to the power dependence data the simple models given by injecting Equations 4.19 and 4.20 in Equation 4.18 (the pressure dependence of the width or saturation parameter do not need to be considered here). This results in a saturation power P_{sat} of 0.46 and 0.16 mW, corresponding to the standing wave case (red dashed line in Figure 4.24(a)) and weak-probe case (blue solid line), respectively. We deduce an averaged saturation power of P_{sat} = 0.31 (0.15) mW as listed in Table 4.1. This is a very crude estimation of an effective saturation mean power as the power varies by about an order of magnitude from path-to-path in the cell and because we use two different models that result from approximations which are relatively far from our experimental conditions. Similarly, we deduce a HWHM Lorentzian linewidth at zero-power of γ_0 =207 (6) kHz, expected to be mainly limited by transit time and collisional effect (see below). The uncertainties quoted into parentheses correspond to $1-\sigma$ uncertainties obtained from the two values resulting from the two fits.

We now consider the pressure-dependence data for which we have to use the models

given by Equations 4.26 and 4.27 which take into account the pressure dependence of both the width and the saturation parameter. We inject those models in Equation 4.18 and fit this to the data. The red dashed curve and the blue solid curve in Figure 4.24 (b) show the results from the fits. The HWHM pressure-broadening coefficient is found to be similar for both the standing wave and weak-probe cases with a mean value $B_p = 110$ (8) kHz/Pa. The mean Rabi frequency of the two models is $\frac{\Omega_0}{2\pi} = 220$ (70) kHz. In addition, the mean zero-power and zero-pressure linewidth is γ_e =161 (60) kHz. Here again, the uncertainties quoted into parentheses correspond to $1-\sigma$ uncertainties obtained from the two values resulting from the two fits. The pressure-broadening coefficient, and the zero-power and zero-pressure linewidth found are in relatively good agreement with the HWHM zero-power linewidth obtained from the power-dependence study above (206 kHz at 1 Pa). The HWHM transit time γ_t, calculated from Equation 1.22 with $w_0 = 0.6$ and 1.2 mm (see subsection 4.1.1), is ∼40 and 80 kHz, respectively, approximately two times smaller from the linewidth at zero-power and zero-pressure that we find here. This difference may be caused by the approximations made in our linewidth models, but also by the complicated distortion of the line shape that probably results from the use of a multipass cell (see subsection 4.4.2.1)

The results of our analyses of the pressure and power dependence of the linewidth are summarized in Table 4.1.

4.5.4 Estimation of the transition dipole moment

The saturation intensity I_{sat} can be written as

$$\begin{aligned} I_{sat} = I\frac{\gamma_\parallel\gamma_\perp}{\Omega_0^2} &= \frac{1}{2}\epsilon_0 cE^2\ \frac{\hbar^2\gamma_\parallel\gamma_\perp}{E^2\mu_{12}^2} \\ &= \frac{1}{2}\frac{\epsilon_0 c\hbar^2\gamma_\parallel\gamma_\perp}{\mu_{12}^2} \end{aligned} \tag{4.28}$$

in which c is the speed of light, ϵ_0 is the vacuum permittivity. By combining Equations 4.23 and 4.28, taking $\gamma_\parallel = \gamma_\perp = \gamma_0$ and using the values of γ_0 and P_{sat} given in Table 4.1, the transition dipole moment μ_{12} is estimated to be $\mu_{12} = 4$ (-1.5/ + 3) $\times 10^{-31}$ C.m = 0.12 (-0.04/+0.09) Debye. The uncertainties quoted into parentheses comes from the uncertainty on w_0 as detailed in Section 4.1.1.

4.6 Absolute frequency measurement of rovibrational transitions of methanol

We present in this section the absolute frequency measurement of several rovibrational transitions of methanol.

4.6.1 Absolute frequency measurement of the $P(E,co,0,2,33)$ methanol transition

In this subsection we determinate the absolute frequency of the $P(E, co, 0, 2, 33)$ rovibrational transition of methanol. First, we describe the measurement reproducibility of the central frequency of the transition from day to day in order to estimate the statistical uncertainty. Then, we discuss the results of the measurement and detail the uncertainty budget.

4.6.1.1 Reproducibility

We have carried out twenty measurements to determine the central frequency of the $P(E, co, 0, 2, 33)$ rovibrational transition of methanol, twelve measurements in June 2017 and eight measurements in October 2017. In June, we used a fiber link without any active noise compensation to transfer the optical reference from LNE-SYRTE to LPL, while in October we used the noise compensated fiber link, as mentioned in subsection 2.3.2. For each measurement, we performed five pairs of back and forth scans using frequency modulation and first-harmonic detection. The frequency scale of the spectra are determined using the optical protocol, as described in subsection 3.4.3. However, we also use the alternative radio-frequency protocol for a comparison between these protocols and to check the consistency of the analysis. Between June and October, the fan with a broken blade, used to shake the multipass cell, was replaced by another one leading to better fringe scrambling. This results in a signal-to-noise ratio increased by a factor of about 1.5 from June to October. All measurements were carried out at a pressure of 1 Pa, but the intra-cell average laser power used for spectroscopy was reduced by about 30%, from 1.1 mW in June to 0.8 mW in October. The recorded spectra were processed by following the data processing procedure detailed in subsection 4.4.2.

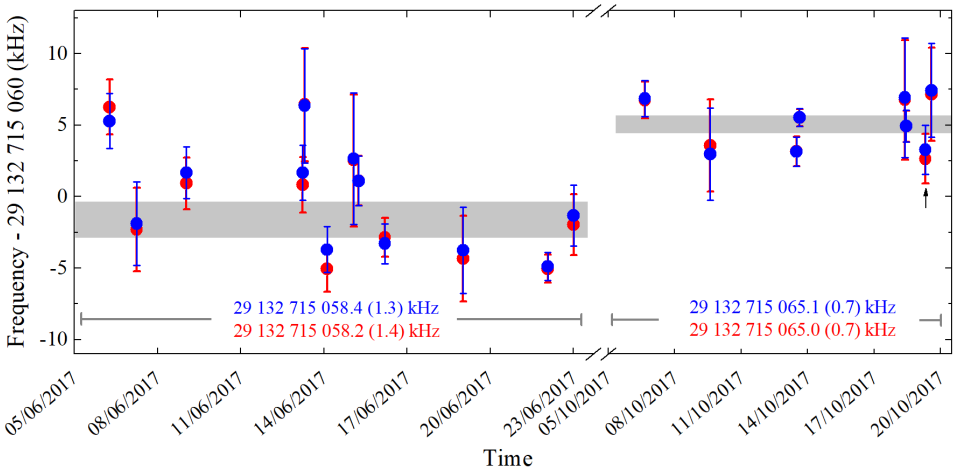

Figure 4.25 – Frequency measurements of the $P(E, co, 0, 2, 33)$ rovibrational methanol line. Twenty measurements were carried out in June and October 2017. The data obtained using the optical protocol are shown in blue, those obtained using the radio-frequency protocol in red. The transition frequency resulting from the weighted mean of all June (respectively October) data are indicated with the associated 1 σ weighted standard errors symbolized by the grey rectangles. The red asterisk pinpoints the measurement corresponding to Figures 4.17(b) an 4.21. The 6.7 (1.5) kHz difference between the two campaigns is attributed to a power-dependent shift (see text).

Figure 4.25 displays the transition frequencies and their uncertainty for the twenty measurements of the $P(E, co, 0, 2, 33)$ transition of methanol (previously shown in Figures 4.17(b) and 4.19). The data obtained from the optical protocol are shown in blue, while those obtained from the radio-frequency protocol are displayed in red. The frequencies difference between the two protocols are smaller than 1 kHz within the measurement uncertainty. As shown in Figure 4.25, the transition frequency resulting from the weighted mean of all June-respectively October data is 29 132 715 058.4 (1.3) kHz-

respectively 29 132 715 065.1 (0.7) kHz for the optical protocol and 29 132 715 058.2 (1.4) kHz-respectively 29 132 715 065.0 (0.7) kHz for the radio-frequency protocol. The uncertainties quoted into parentheses are the 1-σ weighted standard errors calculated using the uncertainties on each measurement as weights. It is our estimation of the statistical errors. We can see that these protocols give similar results within 0.2 kHz. The notable progress in measurement repeatability between June and October, shown by the decrease in weighted standard deviation (see Appendix D for its definition) from 3.5 kHz in June to 1.3 kHz in October, results from the improvement of the signal-to-noise ratio of spectra. A −6.7 (1.5) kHz difference between the data recorded in June and October is attributed to the variation of the QCL power from 1.1 mW in June to 0.8 mW in October (as mentioned above). It is in good agreement with the power-induced shift of −4.6 (0.4) kHz, given by the power-dependent shift coefficient of −15.4 (1.3) kHz/mW measured in subsection 4.5.1. Note that these twenty measurements have actually been used in the analysis of subsection 4.5.1 to determined the power-dependent shift.

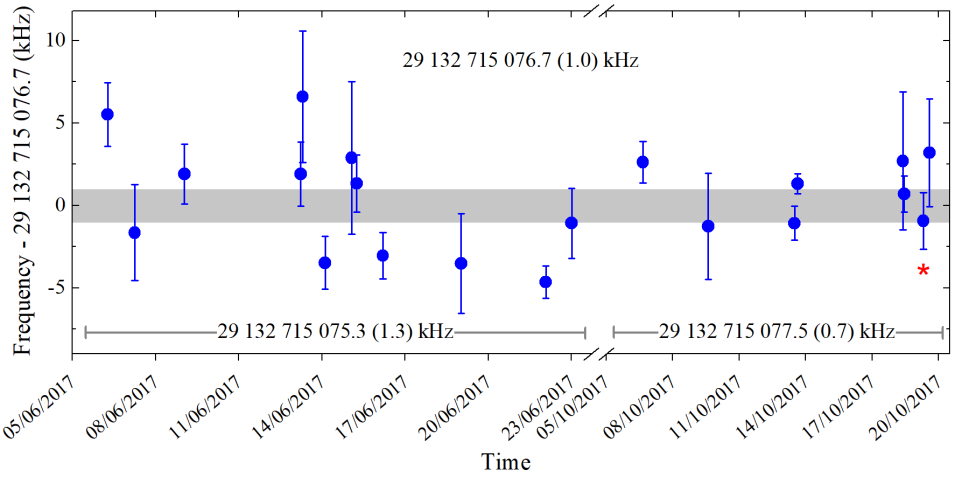

Figure 4.26 – Frequency measurements of the $P(E, co, 0, 2, 33)$ rovibrational methanol line extrapolated to zero-power. Twenty measurements were carried out in June and October 2017. The transition frequency resulting from the weighted mean of all June (respectively October) data are indicated with the associated 1-σ weighted standard errors. The transition frequency resulting from the weighted mean of all data is also indicated at the top with the associated 1-σ weighted standard error also symbolized by the grey rectangle. The red asterisk pinpoints the measurement corresponding to Figure 4.17(b).

Considering the data obtained from the optical protocol, the transition frequencies of the twenty measurements of the $P(E, co, 0, 2, 33)$ transition of methanol are extrapolated at zero-power by using the power-dependent shift coefficient of -15.4 kHz/mW. The results are plotted in Figure 4.26. The error bars of resonance frequencies in Figure 4.25 are the same than those in Figure 4.26. The transition frequency resulting from the weighted mean of all data extrapolated at zero-power is 29 132 715 076.7 (1.0) kHz. The transition frequency resulting from the weighted mean of all June - respectively October - data extrapolated at zero-power shown in Figure 4.26 is 29 132 715 075.3 (1.3) kHz - respectively 29 132 715 077.5 (0.7) kHz. The 1-σ weighted standard errors quoted into parentheses correspond to our statistical uncertainties. The 2.2 kHz difference between

the data recorded in June and October is compatible with the combination of the 1.4 kHz uncertainty resulting from the power-dependence shift correction (see below) and the statistical uncertainty.

4.6.1.2 Uncertainty budget

In this section, we give the uncertainty budget of the $P(E, co, 0, 2, 33)$ absorption frequency measurement, which includes statistical and systematic uncertainties. The final budget is summarized in Table 4.2.

a) Frequency scale

As discussed in subsection 3.4.2, the uncertainty on the QCL frequency is limited by the remote optical reference distributed from LNE-SYRTE to LPL via the 43 km-long fiber link. The frequency of the remote reference signal is measured at LNE-SYRTE against an H-maser itself monitored against primary standards (see subsection 2.2.3). Its absolute frequency is measured every second and known with an uncertainty better than 4×10^{-14}. The uncertainty associated to the transfer link is better than 10^{-19} when the phase noise added by the link is actively compensated (see subsection 2.3.2.2). When the link is free-running, the link mean frequency offset is below 10^{-14} and so is the link instability for averaging times longer than a few seconds.

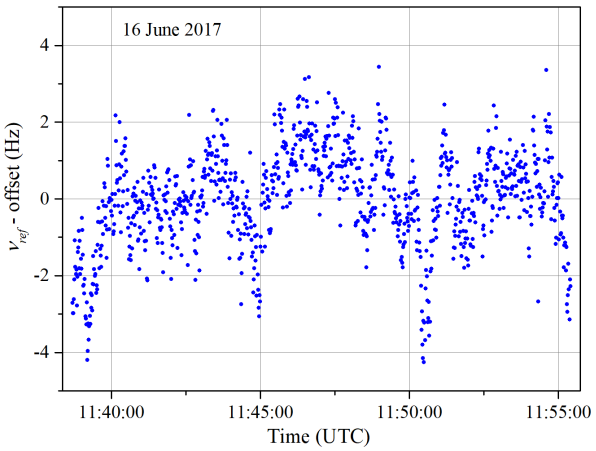

Figure 4.27 – Variation of the remote optical frequency reference ν_{ref} during the saturated absorption measurement of the $P(E, co, 0, 2, 33)$ rovibrational methanol line on 16 June 2017. Offset: mean of the all data.

In addition, the QCL frequency uncertainty could also be limited by the method used to reconstruct the frequency axis of each recorded spectrum. The QCL frequency scale is reconstructed using Equation 3.26, in which the frequency ν_{ref} of the remote reference signal is measured once per second at LNE-SYRTE and saved on a repository accessible via hyper-text transfer protocol (http) website, as mentioned in subsection 3.4.3. However, during a measurement of typically total time of 1000 s, the frequency fluctuations of the optical reference signal is a few Hz (∼1 Hz, see Figure 4.27 for instance), therefore we fix ν_{ref} in Equation 3.26 to the absolute frequency of the optical reference at the middle time of each measurement.

In short, for a typical measurement consisting of five pairs of up and down scans, the

uncertainty of the QCL frequency scale is thus dominated by the frequency uncertainty of 4×10^{-14} of the calibration to the H-maser/primary standards. This has a negligible effect on our molecular frequency measurements (see below).

b) Influences of laser power and collisions

As demonstrated in section 4.5, the power-induced frequency shift coefficient of the $P(E, co, 0, 2, 33)$ rovibrational transition of methanol is found to be -15.4 (1.3) kHz/mW. We have extrapolated the line-center frequency of the transition at zero-power, as mentioned above. Note that we estimate an upper bound in power fluctuations of 10% during a measurement and from one to another. This leads to frequency fluctuations of the order of 0.3 kHz which contribute to our statistical uncertainty. Note that the 5% specified accuracy of the power meter results in a systematic uncertainty of at most 0.75 kHz at our highest power of 1.1 mW, but doesn't affect our extrapolation to zero-power. The overall power shift correction uncertainty is 1.4 kHz.

Moreover, the pressure-induced frequency shift of the $P(E, co, 0, 2, 33)$ rovibrational transition of methanol (see section 4.5) can be used to deduce the collisionless transition frequency (see subsection 4.6.1.4). For the measurements in Figure 4.25 recorded at a pressure of 1 Pa, the uncertainty associated to this pressure shift correction is 0.3 kHz. Pressure fluctuations smaller than 0.02 Pa during a measurement and from one to another result in frequency fluctuations smaller than 0.1 kHz which contribute to our statistical uncertainty at a negligible level. By measuring pressures using different gauges of various technologies, we estimate an upper bound on the pressure measurement accuracy to be 0.02 Pa which translates into a 0.05 kHz frequency inaccuracy but doesn't affect our extrapolation to zero-power. The overall pressure shift correction uncertainty is thus 0.3 kHz.

c) Other spectroscopic effects

In addition, there are also other spectroscopic effects contributing to the uncertainty of the frequency measurement, such as wave-front curvature shift, gas-lens effect, the presence of a recoil doublet, second-order Doppler effect, and magnetic effects. Their contributions are included in Table 4.2 under "other spectroscopic effects".

Wave-front curvature induced frequency shift

As theoretically and experimentally studied by C.J. Bordé and his co-workers [58,252], the line-center frequency of a molecular rovibrational transition can be blue- or red-shifted if the wave-front of the laser beam is not flat. A detailed explanation of this effect can also be found in C. Chardonnet's thesis [253].

Let us consider a Gaussian beam propagating along the z axis, and a molecule crossing the beam perpendicularly at a speed v_r and (for simplification) passing through the centre of the beam. The instantaneous frequency "*seen*" by the molecule is given by the time derivative of the electric field phase, leading to:

$$\omega - k v_r \frac{r}{R(z)}, \tag{4.29}$$

with ω the angular frequency of the laser beam, r the transverse position of the molecule in the beam with respect to the centre of the beam, and $R(z)$ the wave-front radius of curvature at the longitudinal position z of the molecule. The non-zero wave-front

curvature of a Gaussian laser beam thus induces a first-order residual Doppler shift, that varies linearly with r, that is zero on average, and that actually results in the transit-time broadening.

Let us now consider a saturated absorption configuration with two perfectly matched counter-propagating beams of opposite radius of curvature $R(z)$ and $-R(z)$. We assume that the molecule interacts first with the pump beam of radius of curvature $R(z)$ and then with the probe beam of radius of curvature $-R(z)$. According to Equation 4.29, during the first interaction (respectively second), the frequency "*seen*" by the molecule is $\omega - kv_r r/R(z)$ (respectively $\omega + kv_r(r+\Delta r)/R(z)$, with Δr the distance between the two locations where the interactions happen). Importantly, the mean frequency "*seen*" by the molecule is $\omega + kv_r \Delta r/R(z)$, leading to a shift with respect to ω, positive or negative depending on the sign of the radius of curvature. The frequency of the molecular resonance is blue-shifted (respectively red-shifted) for converging (respectively diverging) pump beam.

Following C. Chardonnet [253], the frequency shift induced by the wave-front curvature for a finite length of absorbing sample located between the longitudinal position z_1 and z_2 with respect to the beams's waist is given by the following formula,

$$\delta_{\text{wfc}} = \frac{1}{2\pi}\frac{u}{w_0}\frac{2.5}{\eta}K_D \tag{4.30}$$

with

$$K_D = 2b^2\frac{z_2^2 - z_1^2}{(b^2+4z_1^2)(b^2+4z_2^2)}\left[\arctan\left(\frac{2z_2}{b}\right) - \arctan\left(\frac{2z_1}{b}\right)\right]^{-1}, \tag{4.31}$$

where $b = w_0^2 2\pi/\lambda$ is the confocal parameter with λ the laser wavelength and w_0 the beam waist in the cell, and $\eta \sim 3$ a parameter that depends on the dipole relaxation rate [253].

Note that if the pump and probe beams are one and the same beam retro-reflected on itself, both beams are playing the role of the pump and the probe with opposite radii of curvature. This leads to an averaged zero curvature-shift. Note also that in the case of a symmetric Fabry-Perot cavity for which the waist is in the middle of the cavity, we have $z_1 = -z_2$ and the curvature-induced shift is zero.

In our particular case, if the laser beam waist is perfectly centered in the multipass cell, for the same reason, no wavefront-curvature-induced residual Doppler shift is expected provided that the beam waist is well centered in the multipass cell. As detailed in section 4.1, this is, however, only achieved to within a few centimeters. Using Equation 4.30, this results in a potential systematic shift smaller than 10 kHz associated to each of the 182 individual paths of the cell. However, this curvature-induced shift can be negative or positive depending on which side of the cell center the beam waist is located. In our astigmatic Heriott multipass cell, from path to path, the beam waist will alternatively be displaced nearly symmetrically on one side of the cell center and the other. Moreover, no particular care was taken to match the focus of the two counter-propagating beams which are thus most probably not well matched and focus at slightly different positions. For these reasons, we expect the overall systematic shift resulting from the combination of the 182 path to average out to less than 1 kHz. Finally, due to regular realignments of the optical setup, the residual curvature-induced shift fluctuates from one measurement in

Figure 4.26 to the other in a range smaller than ±1 kHz, and therefore simply contributes to our statistical uncertainty.

Gas-lens effect

Gas-lens effects stem from the transverse dependence of the medium index of refraction that results from the interaction with a Gaussian transverse profile laser beam. The medium then behaves as a converging or diverging lens, depending on which side of the resonance the laser is tuned which leads to a beam diameter decrease or increase. Anything that clips the beam (any optics, pinhole, iris,...) will then lead to a frequency-dependent power variation of dispersive nature. This distorts the line shape [47, 254]. In our case, the central coupling hole of the multipass cell front mirror through which the beam also exits the cell is potentially clipping the beam. Following C. Chardonnet's thesis [253], the gas-lens effect induced frequency shift is given by [1]

$$\delta_{\mathrm{gl}} = \gamma \frac{2L}{b} \frac{\dfrac{R^2}{w^2}}{\exp\left(\dfrac{2R^2}{w^2}\right) - \left(1 - \dfrac{2R^2}{w^2}\right)} \tag{4.32}$$

where γ is the FWHM linewidth of the spectroscopic feature, L is the absorption length (length of the multipass cell), R is the radius of the clipping aperture (mirror hole of the multipass cell), and w is the spot size of the laser beam at the clipping aperture (at the mirror of the cell). We use Equation 4.32 to calculate the resulting shift. Because the vertical and horizontal waists of the beam in the cell are not located at the same position and because we have an uncertainty of their positions of a few cm (see section 4.1), we calculate the gas-lens induced shift for waist positions ranging from 0 to 5 cm respect to the multipass cell center. Taking also into account our uncertainty on the size of the waists (see section 4.1), we estimate a conservative upper bound of the resulting frequency shift to be +5 kHz. We stress here that formula 4.32 is valid for a perfectly centered clipping hole and that in this case, the shift is positive. In the case of an ill-centered clipping optics, it is also possible to numerically calculate the corresponding shift. It is then of the same order of magnitude but can either be positive or negative. We thus take our conservative estimate based on Equation 4.32 as our uncertainty on this systematic effect.

Recoil doublet

Saturation spectroscopy leads to a photon recoil doublet that is symmetric to the recoil-free transition center and does not produce any shift [257]. The frequency separation between the two doublets is given by [60],

$$\delta_{\mathrm{rc}} = \frac{h\nu_0^2}{mc^2}, \tag{4.33}$$

in which h is the Plank constant, m is the molecular mass, ν is the molecular line-center frequency, and c is the speed of light. For methanol at ∼972 cm^{-1}, the doublet splitting

1. Note that formula 4.32 has no explicit dependence on pressure, density or signal amplitude (apart from the fact that gamma can potentially depend on pressure in the collisionally limited case). This is because the correction induced by the gas lens effect to the symmetric line shape results in adding a dispersive like profile of amplitude proportional to (and of same width as) the original signal [253,255,256].

is ∼120 Hz.

Second-order Doppler effect

Frequency shift of the transition-center frequency due to the second-order Doppler effect is calculated from the following equation [60],

$$\delta_{\text{sde}} = \nu_0 \frac{u^2}{2c^2} \tag{4.34}$$

where u is the most probable methanol velocity. It is found to be ∼25 Hz at room temperature with negligible fluctuations given a conservative upper limit of 2-K temperature variation of our gas sample.

Magnetic frequency shift

In addition, the magnetic frequency shift due to the Zeeman effect is expected to be of the order of a few tens of Hz (resulting from the local Earth magnetic field magnitude of ∼ 0.5 Gauss), with variations 100 times smaller (our estimation is based on a study carried out on the OsO_4 molecule [258]). It is thus negligible.

Black-body radiation shift

The black-body radiation shift of rovibrational molecular lines has been calculated for a few simple molecules only [259] but it has never been observed. It is expected to be weak with negligible fluctuations within a 2 K temperature variation range.

4.6.1.3 Line fitting

As mentioned in subsection 4.4.2, by fitting derivatives of $g(\nu)$ to first, second and third harmonic detection data, all fits converged to a transition center frequency within 5 kHz. We therefore assign a conservative 5 kHz systematic uncertainty to the lack of knowledge of the correct model for the line shape. This covers the multipass cell-induced profile complication, the asymmetry issue and the difficulties resulting from interference fringes affecting the baseline.

The modulation frequency of 20 kHz and frequency excursion of 50 kHz used are both much smaller than the line width (∼700 kHz FWHM around 1 Pa). We thus expect negligible frequency modulation-induced distortion of the line shape. We have investigated this by recording spectra using different frequency excursions ranging from 25 kHz to 250 kHz and using first or third harmonic detection. The fitted center frequency did not show any evidence of dependence upon the frequency excursion within our statistical uncertainty.

Note that the asymmetry factor B is found to be ∼0.3 MHz^{-1} within ±0.1 MHz^{-1} when fitting a single pair of up and down scans. We stress here that values of B for all other lines of methanol studied in the following will fall in this range. This is of opposite sign to what would be expected if this asymmetry factor would result from the QCL gain curve. However, the power variation over a frequency scan also depends on local residual etaloning that could come from the multipass cell or on the Doppler envelop which may well also be distorted when using a multipass cell.

Table 4.2 – Uncertainty budget table for the frequency measurements of the $P(E, co, 0, 2, 33)$ rovibrational transition of methanol in June and October 2017, all recorded at 1 Pa and displayed in Figure 4.26.

Systematics	Correction (kHz)	Uncertainty (kHz)
Frequency calibration	0	0.001
Power shift −15.4 (1.3) kHz/mW	+16.94 kHz for June measurement +12.32 kHz for October measurement	1.4
Pressure shift 2.9 (0.3) kHz/Pa	-2.9	0.3
Other spectroscopic effects	not measured, estimated to be < 5 kHz	5.0
Line fitting	0	5.0
Total systematics	+14.04 for June measurements +9.42 for October measurements	7.3
Statistics	0	1.0
Total	+14.04 for June measurements +9.42 for October measurements	7.4

4.6.1.4 Budget table, final absolute frequency, and discussion

Table 4.2 gives the global uncertainty budget. It summarizes all listed systematic effects, the corresponding corrections to apply to the measured resonance frequency, the associated uncertainties, and the statistical uncertainty. Note that the uncertainty on the frequency calibration is 0.001 kHz because we have used the optical protocol to determine the absolute frequency. When using instead the alternative radio-frequency protocol, the frequency calibration uncertainty would be 0.3 kHz (see subsection 3.4.3).

We finally deduce a zero-power and zero-pressure transition frequency of 29 132 715 074.3 (7.4) kHz for the $P(E, co, 0, 2, 33)$ resonance frequency. The 3×10^{-10} uncertainty is a factor of 2000 improvement over previous measurements performed using Fourier transform infrared (FTIR) spectroscopy [238] which have led to the current edition of the HITRAN database [54]. Our measured $P(E, co, 0, 2, 33)$ resonance frequency is shifted by -5263.1 kHz with respect to this previous measurement carried out at a pressure of 13 Pa and reported in the HITRAN database (see also Figure 4.17 above). This shift is consistent with deviations observed between previously measured CH_3OH saturated absorption spectroscopy data [242, 247] and the FTIR data contributing to the HITRAN database [237, 238]. This discrepancy has been attributed to calibration imperfections of FTIR spectrometers as discussed in [234, 238, 260].

4.6.2 Absolute frequency determination of other methanol transitions

In this subsection, we demonstrate absolute frequency measurement of other rovibrational transitions of methanol. For those transitions, the saturated absorption spectra have been recorded several times per several days or months to estimate the statistical uncertainty on their absolute line-center frequencies. The QCL frequency is modulated at 20 kHz with a frequency excursion of 50 kHz. Each measurement consists in recording five pairs of up and down scans with a QCL frequency step of $\sim$ 15 kHz and a step duration of 100 ms. Spectra are recorded using frequency modulation with first-harmonic

Table 4.3 – Systematic uncertainties affecting the rovibrational transition frequencies of methanol that will be described in this subsection.

Systematics	Correction (kHz)	Uncertainty (kHz)
Frequency calibration	0	0.001
Power shift (P power in mW)	$15.4 \times P$	$1.3 \times P$
Pressure shift (p pressure in Pa)	$-2.9 \times p$	$0.3 \times p$
Other spectroscopic effects	0	5.0
Line fitting	0	5.0 for SNR[a] > 130
		10 for SNR[a] < 130

[a]The SNR here is the SNR for an average of five pairs of up and down scans.

detection and a lock-in amplifier time constant of 100 ms. The frequency scale of each spectrum is reconstructed using the optical protocol (see subsection 3.4.3). In order to determine the line-center frequency of the transitions, we average each pair of up and down scans and then perform a "pair by pair" analysis (see subsection 4.4.2).

Systematic effects associated to the line-center frequencies of those transitions are listed in Table 4.3. The uncertainty on the frequency calibration is 0.001 kHz because we have used the optical protocol to determine the absolute frequency. For those transitions, we have not studied the pressure and power dependences (except one, $P(A, co, 0, 0^+, 33)$, for which the power dependence has been measured). We have thus used the power-induced shift coefficient of $-15.4(1.3)$ kHz/mW and the pressure-induced shift coefficient of 2.9(0.3) kHz/Pa of the $P(E, co, 0, 2, 33)$ transition (see section 4.5) to obtain zero-power and zero-pressure frequencies and to estimate the associated uncertainties on the line-center frequency correction (except again for line $P(A, co, 0, 0^+, 33)$, for which the measured power dependence is used). The uncertainty associated to the "other spectroscopic effects" as appearing in Table 4.3 is estimated to be 5 kHz, the same as for the $P(E, co, 0, 2, 33)$ methanol line (see Table 4.2). In addition, we have not carried out an extensive study of the effect of the model chosen on the fitted frequency which may well depend on the signal-to-noise ratio (SNR). We thus adopt the following rule regarding the systematic uncertainty associated to the line fitting issue:

– For transitions exhibiting a reasonable SNR of at least 130 for an average of five pairs of up and down scans (corresponding to 1/5 of the SNR obtained with the $P(E, co, 0, 2, 33)$ methanol line), we take 5 kHz, the same as for line $P(E, co, 0, 2, 33)$.

– For transitions exhibiting a smaller SNR for an average of five pairs of up and down scans, we take 10 kHz for the uncertainty on the line fitting.

Table 4.5 gives a summary of our absolute frequency measurements of subsections 4.6.1 and 4.6.2 and the corresponding shifts to the HITRAN values. In this table, we give two frequencies for each line:

– The "observed" frequency which is the frequency measured at the power and pressure used for carrying out the experiment, thus with no correction for the power- and pressure-shift. For those, the uncertainty given in the table is our statistical uncertainty.

– The "corrected" frequency obtained after correcting the "observed" frequency for the power- and pressure-shift. The uncertainty on those is affected by the correction

listed in Table 4.3. The uncertainty is thus the total uncertainty.

4.6.2.1 $P(A,co,0,0^+,33)$

We have measured saturated absorption spectra of the $P(A, co, 0, 0^+, 33)$ rovibrational transition in the A-symmetry band of methanol. This transition has a similar intensity to that of the $P(E, co, 0, 2, 33)$ transition discussed previously. The saturated absorption spectra are measured at 1 Pa. The intra-cell average laser power was reduced from 1.15 mW in June to 0.85 mW in October 2017. Figure 4.28(a) shows a saturated absorption spectrum of the $P(A, co, 0, 0^+, 33)$ rovibrational transition averaged over five up and down scans. It exhibits a signal-to-noise ratio of ∼540 and a peak-to-peak linewidth of ∼400 kHz (∼700 kHz FWHM), similar to the $P(E, co, 0, 2, 33)$ transition.

In order to determine the line-center frequency of the $P(A, co, 0, 0^+, 33)$ rovibrational transition, we perform a "pair by pair" analysis, as mentioned above. Figure 4.28(b) shows one such averaged pair of up and down scans of the $P(A, co, 0, 0^+, 33)$ rovibrational transition of methanol, contributing to Figure 4.28(a). It exhibits a signal-to-noise ratio of ∼220. The red solid line is the fit of the saturated absorption line shape given by Equation 4.13 to the data with a reduced chi-square of ∼1.7.

As with the $P(E, co, 0, 2, 33)$ rovibrational transition, we have carried out fourteen absolute frequency measurements of the $P(A, co, 0, 0^+, 33)$ rovibrational transition of methanol in June and October 2017: eleven measurements in June using a free-running fiber link and only three measurements in October using the active noise compensated fiber link. Figure 4.29 displays the transition frequencies and their uncertainties for the fourteen measurements of the $P(A, co, 0, 0^+, 33)$ rovibrational methanol line.

The transition frequency resulting from the weighted mean of all June- respectively October- data is 29 130 799 512.2 (0.8) kHz- respectively 29 130 799 517.2 (1.6) kHz, as shown in Figure 4.29. The 1-σ weighted standard errors quoted into parentheses correspond to our statistical uncertainties. In order to determine a power-induced frequency shift coefficient of the $P(A, co, 0, 0^+, 33)$ transition, we perform a weighted linear fit to the data plotted as a function of power. The coefficient is found to be −16.8 (2.7) kHz/mW, that agrees well with the result of the $P(E, co, 0, 2, 33)$ transition (see section 4.5). We have extrapolated all line-center frequencies of the $P(A, co, 0, 0^+, 33)$ transition at zero-power using this power shift. The final line-center frequency of the transition resulting from the weighted mean of all data at zero-power is 29 130 799 531.6 (0.8) kHz.

The total uncertainty budget of the $P(A, co, 0, 0^+, 33)$ transition of methanol is shown in Table 4.4. It lists systematic effects, the corresponding corrections to apply to the measured resonance frequency, and the associated uncertainties and gives the statistical uncertainty. The uncertainty associated to the line fitting is estimated to be 5 kHz (see Table 4.3). Note that the pressure shift of the transition is corrected by using the pressure-induced shift coefficient of the $P(E, co, 0, 2, 33)$ transition (see Table 4.3). We finally deduce a zero-power and zero-pressure transition frequency of 29 130 799 528.7 (7.9) kHz for the $P(A, co, 0, 0^+, 33)$ methanol line. The uncertainty quoted into parentheses corresponds to the total 1-σ uncertainty. The $P(A, co, 0, 0^+, 33)$ resonance frequency of our measurement is shifted −3 935.1 kHz with respect to the previous measurement reported in the HITRAN database.

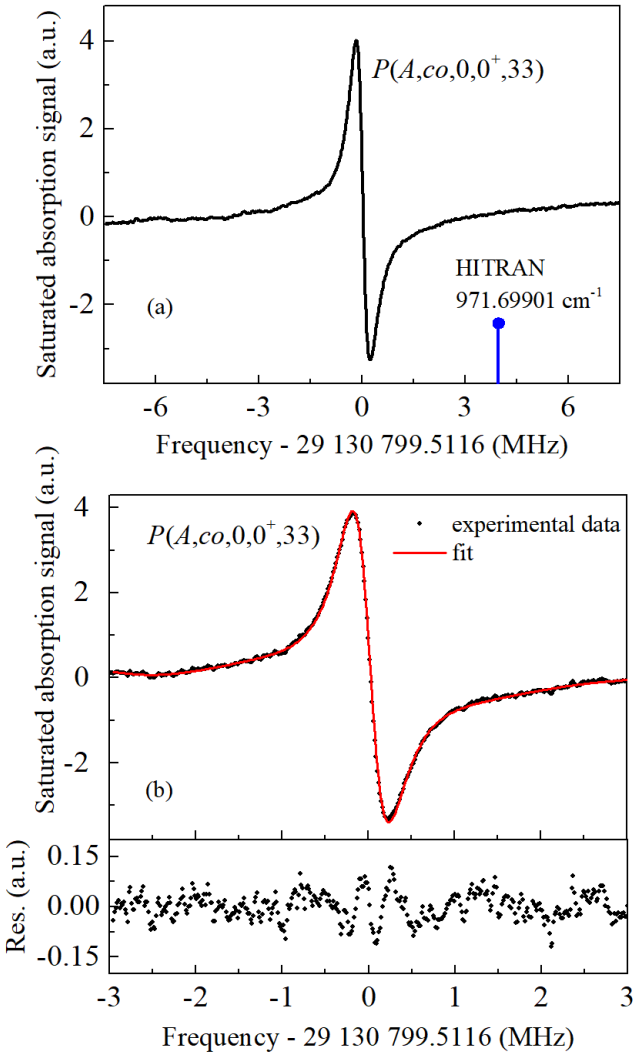

Figure 4.28 – (a) Saturated absorption spectrum of the $P(A, co, 0, 0^+, 33)$ rovibrational transition of methanol, recorded using frequency modulation and first-harmonic detection. This transition is reported in the HITRAN database [54] at 971.69901 cm^{-1}, as shown by the blue stick. Experimental conditions: pressure, 1 Pa; modulation frequency, 20 kHz; frequency modulation excursion, 50 kHz; frequency step, ∼15 kHz; average of five pairs of up and down scans; total integration time per point, 200 ms; whole spectrum measurement time, 1000 s. (b) Black dots: average of one pair of up and down spectra contributing to panel (a) of the figure, total integration time per point, 200 ms; whole spectrum measurement time, 80.2 s. The red solid line is a fit to the data of a line shape given by Equation 4.13, resulting in a reduced chi-squared of 1.71. The residuals of the fit are shown on the bottom graph.

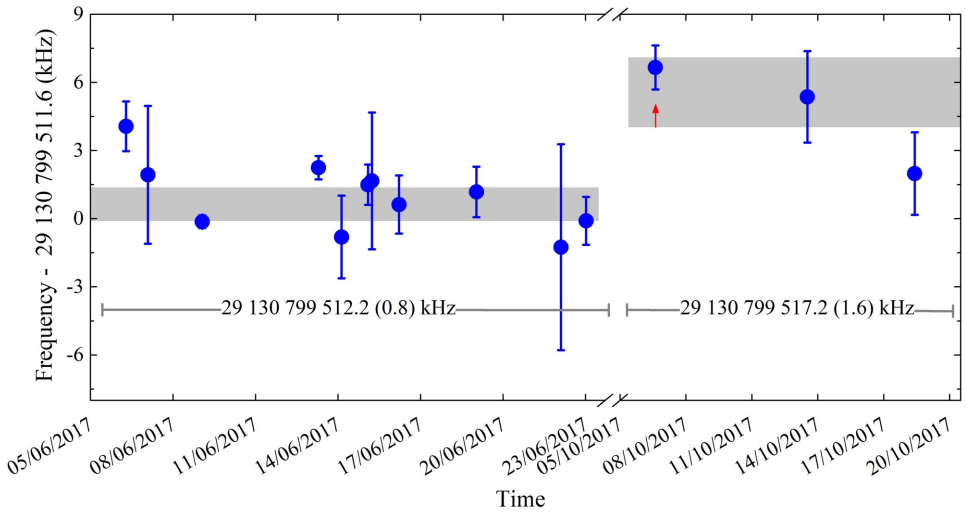

Figure 4.29 – Frequency measurements of the $P(A, co, 0, 0^+, 33)$ rovibrational methanol line. Fourteen measurements were carried out in June and October 2017. The transition frequency resulting from the weighted mean of all June (respectively October) data are indicated with the associated 1 σ weighted standard errors and symbolized by the grey rectangles. The 5.0 (1.8)kHz difference between the two measuring campaigns is attributed to a power-dependent shift. The red arrow pinpoints the measurement corresponding to Figure 4.28.

Table 4.4 – Uncertainty budget table for frequency measurements of the $P(A, co, 0, 0^+, 33)$ rovibrational transition of methanol in June and October 2017, all recorded at 1 Pa and displayed in Figure 4.29.

Systematics	Correction (kHz)	Uncertainty (kHz)
Frequency calibration	0	0.001
Power shift -16.8 (2.7) kHz/mW	+19.32 kHz for June measurement +14.28 kHz for October measurement	3.1
Pressure shift 2.9 (0.3) kHz/Pa[a]	-2.9	0.3
Other spectroscopic effects	not measured, estimated to be < 5 kHz	5.0
Line fitting	0	5.0[b]
Total systematics	+16.42 for June measurements +11.38 for October measurements	7.8
Statistics	0	0.8
Total	+16.42 for June measurements +11.38 for October measurements	7.9

[a] Taken to be equal to the pressure shift and associated uncertainty of $P(E, co, 0, 2, 33)$ methanol line.
[b] Following the rule given at the beginning of the subsection.

4.6.2.2 $^{P}P(A,ri,0,6^{-},33)$

We have measured the absolute frequency of the $^{P}P(A, ri, 0, 6^{-}, 33)$ rovibrational methanol line, a weak transition in the A-symmetry band of the ν_7 CH_3 in-plane rocking vibrational mode of methanol. Saturated absorption spectra of the transition were at a pressure of ∼2 Pa and a intra-cell average power of ∼1.1 mW. Figure 4.30(a) shows a saturated absorption spectrum of the $^{P}P(A, ri, 0, 6^{-}, 33)$ transition averaged after five pairs of up and down scans. It exhibits a signal-to-noise ratio of ∼73 and a peak-to-peak linewidth of ∼550 kHz (∼950 kHz FWHM).

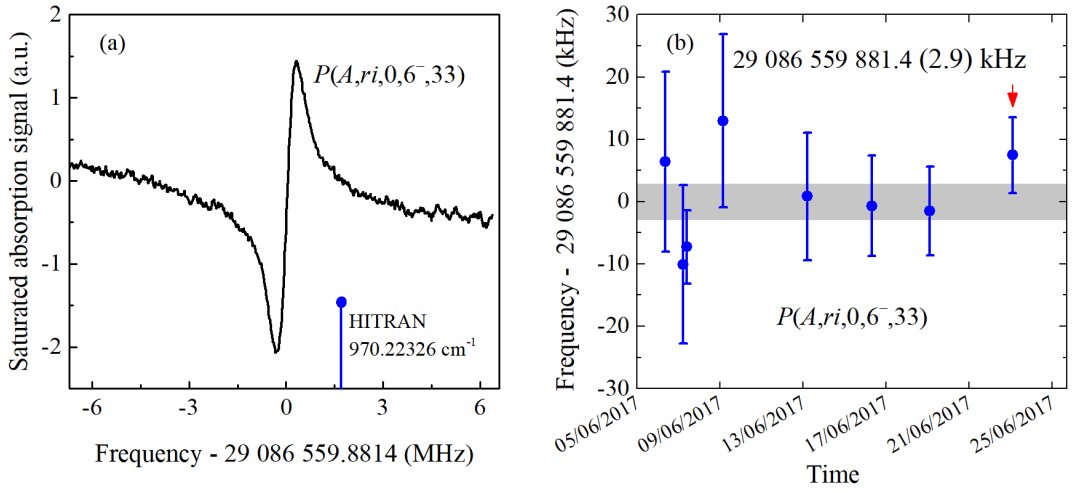

Figure 4.30 – (a) Saturated absorption spectrum of the $^{P}P(A, ri, 0, 6^{-}, 33)$ rovibrational transition of methanol, recorded using frequency modulation and first-harmonic detection. This transition is reported in the HITRAN database [54] at 970.22326 cm^{-1}, as shown by the blue stick. Experimental conditions: pressure, 2 Pa; modulation frequency, 20 kHz; frequency modulation excursion, 50 kHz; frequency step, ∼15 kHz; average of five pairs of up and down scans; total integration time per point, 1 s; whole spectrum measurement time, 875 s. (b) Frequency measurements of the $^{P}P(A, ri, 0, 6^{-}, 33)$ rovibrational methanol line. Eight measurements were carried out in June 2017. The transition frequency resulting from the weighted mean of all data is indicated with the associated 1-σ weighted standard error and symbolized by the grey rectangle. The red arrow pinpoints the measurement corresponding to panel (a) of the figure.

Figure 4.30(b) displays the transition frequencies and their uncertainty for eight measurements of the $^{P}P(A, ri, 0, 6^{-}, 33)$ rovibrational transition of methanol carried out in June 2017. The transition frequency resulting from the weighted mean of all data is 29 086 559 881.4 (2.9) kHz, as shown in Figure 4.30(b). The 1-σ weighted standard error quoted into parentheses correspond to our statistical uncertainty. Due to weaker line-intensity, the $^{P}P(A, ri, 0, 6^{-}, 33)$ transition has a statistical uncertainty three times larger than the two transitions described above.

Uncertainty of the line fitting is estimated conservatively to be 10 kHz (following the rule given at the beginning of this subsection). Following Table 4.3, the total systematic uncertainty of the $^{P}P(A, ri, 0, 6^{-}, 33)$ methanol line after power and pressure correction is estimated to be 11.3 kHz. The zero-power and zero-pressure line-center frequency of the $^{P}P(A, ri, 0, 6^{-}, 33)$ methanol line is calculated to be 29 086 559 889.5 (11.7) kHz. The uncertainty quoted into parentheses corresponds to the total uncertainty. Our mea-

sured ${}^{P}P(A, ri, 0, 6^{-}, 33)$ resonance frequency is shifted −1 699.9 kHz with respect to the previous measurement reported in the HITRAN database.

4.6.2.3 ${}^{P}P(E,ri,0,-5,32)$ and $P(A,co,0,13^{\pm},33)$

In this paragraph, we describe the line-center frequency measurements of a few other rovibrational transitions of methanol around 971.944 cm^{-1}. Figure 4.31(a) shows a portion of a direct absorption spectrum of methanol measured in the multipass absorption cell at ∼7 Pa with the free-running QCL (see section 4.3). A pair of transitions at ∼971.9428 and ∼971.9451 is partially resolved in this spectrum. However, only one transition, ${}^{P}P(E, ri, 0, -5, 32)$, is reported at 971.94430 cm^{-1} in the HITRAN database [54]. It is noted that this database of methanol is based on the study of L.H. Xu and her co-workers in 2004 [238]. Three years later, this group has reported another list of rovibrational transitions of methanol [239]. The new list now reports two degenerate transitions, the ${}^{P}P(E, ri, 0, -5, 32)$ (already present in the HITRAN database) and the $P(A, co, 0, 13^{\pm}, 33)$, at a frequency slightly different of 971.94418 cm^{-1} .

We have carried out saturated absorption spectroscopy of these blended lines at a pressure of ∼1 Pa and an intra-cell average power of ∼0.75 mW. One example of a saturated absorption spectrum is shown in Figure 4.31(b). It is composed of two spectra obtained from two successive measurements. Each spectrum is the average of five pairs of up and down scans. We can see that three rovibrational features of methanol are resolved, denoted as lines (1), (2), and (3). Their signal-to-noise ratios are 280, 30 and 220, respectively. We have carefully checked that there is no other absorption line between lines (2) and (3) by performing a wide scan spanning from 971.42 to 971.46 cm^{-1} (see subsection 4.8.1). It is unclear which one of the three resolved transitions are the ${}^{P}P(E, ri, 0, -5, 32)$ and $P(A, co, 0, 13^{\pm}, 33)$ transitions of methanol.

We have carried out line-center absolute frequency measurement of the three transitions eleven times: ten measurements in June and only one in October 2017. The transition frequencies and associated uncertainties of the eleven measurements of lines (1), (2), and (3) are displayed in panels (c-e) of Figure 4.31, respectively. For the ten measurements of June 2017 (we forget here the only measurement of October carried out at a different power), the transition frequency resulting from the weighted mean of all data at 1 Pa pressure and 0.75 mW intra-cell average power is 29 138 113 980.3 (2.4) kHz for line (1), 29 138 117 987.6 (9) (kHz) for line (2), and 29 138 179 774.5 (3.0) kHz) for line (3). The 1-σ weighted standard errors quoted into parentheses correspond to our statistical uncertainties. The frequency difference between lines (1) and (2) is found to be 4 007.3 (11.4) kHz. Between lines (1) and (3), it is 65 794.2 (6.4) kHz.

Uncertainty of the line fitting is estimated to be 5 kHz for lines (1) and (3) and 10 kHz for line (2) (following the rule given at the beginning of this subsection). Following Table 4.3, after power and pressure correction, the total systematic uncertainties of these transitions are estimated to be 7.2 kHz for lines (1) and (3) and 11.3 kHz for line (2). The absolute frequencies of the three lines (1)-(3) at zero-power and zero-pressure are calculated to be 29 138 113 989.0 (7.6) kHz, 29 138 117 996.3 (14.5) kHz, and 29 138 179 783.2 (7.8) kHz, respectively, and listed in Table 4.5. The errors quoted into parentheses correspond to the total uncertainties. Our measured absolute frequencies are shifted by −43 101.9, −39 103.4, and 22 692.3 kHz with respect to the ${}^{P}P(E, ri, 0, -5, 32)$ rovibrational transition reported in the HITRAN database. They are shifted by −39 487.1, −35 479.8,

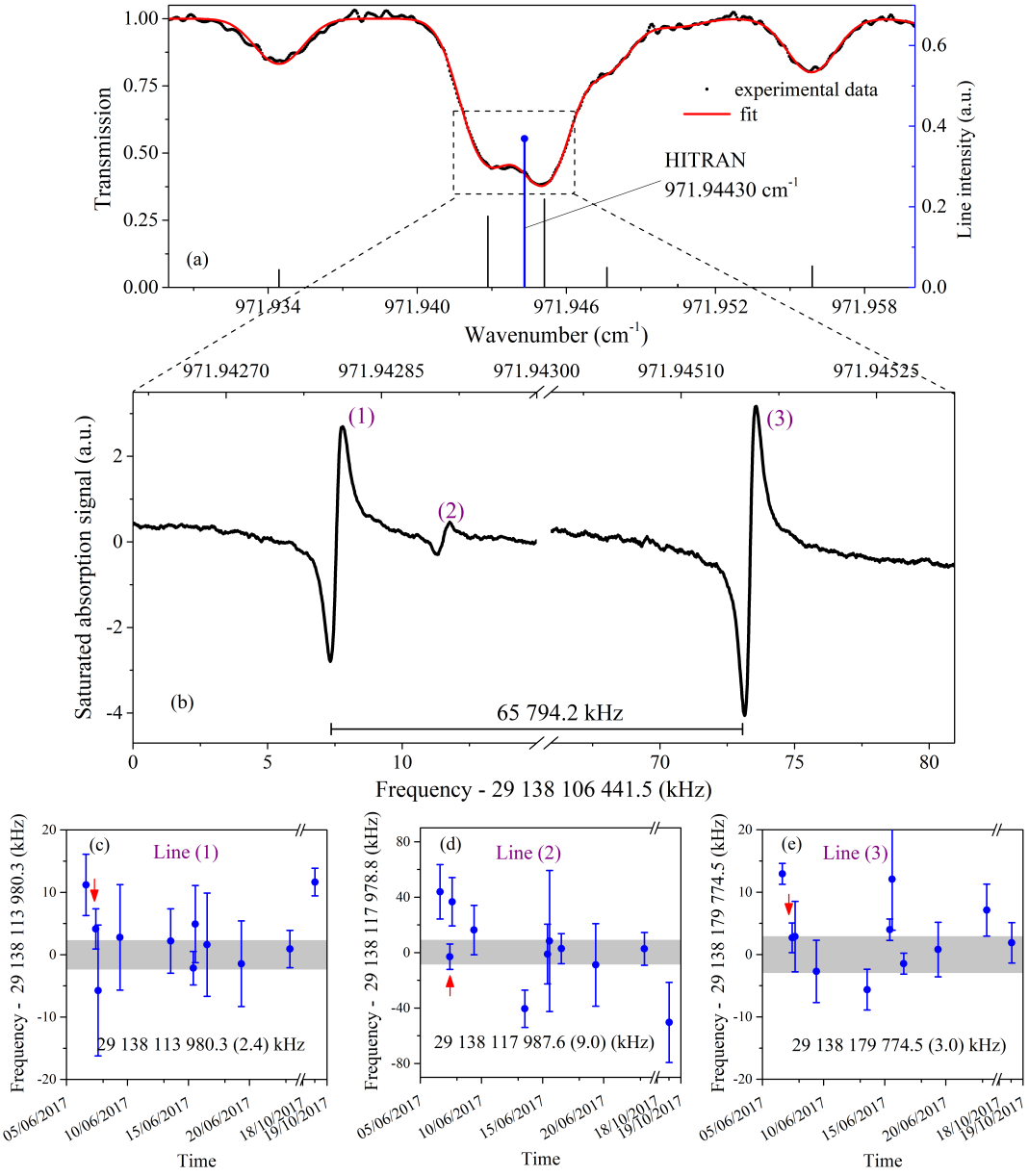

Figure 4.31 – (a) Direct absorption spectrum of methanol from 971.93 to 971.96 cm^{-1} (part of the spectrum in Figure 4.14. It is recorded at a pressure of ∼7 Pa using the free-running QCL. The red curve is a fit to the data. The $^{P}P(E, ri, 0, -5, 32)$ line frequency position reported in the HITRAN database [54] is also shown as a blue stick. (b) Saturated absorption spectrum showing three methanol transitions (1, 2, and 3) around 971.944 cm^{-1} recorded using frequency modulation and first-harmonic detection. Experimental conditions: pressure, 1 Pa; modulation frequency, 20 kHz; frequency modulation excursion, 50 kHz; frequency step, ∼15 kHz; average of 5 pairs of scans of opposite frequency sweep direction; total integration time per point, 1 s; whole spectrum measurement time, 2002 s. (c-e) Frequency measurements of the three rovibrational methanol lines (1), (2), and (3). Eleven measurements were carried out (ten measurements in June and one in October 2017). The transition frequency resulting from the weighted mean of data of June is indicated with the associated 1-σ weighted standard error and symbolized by the grey rectangular. The red arrow in each graph pinpoints the measurement corresponding to panel (b) of the figure.

and 26 307.1 kHz with respect to the ${}^{P}P(E, ri, 0, -5, 32)$ and $P(A, co, 0, 13^{\pm}, 33)$ transitions reported in Ref. [239]. Following Ref. [238, 239], as mentioned above, two of the three resolved lines might be the ${}^{P}P(E, ri, 0, -5, 32)$ and $P(A, co, 0, 13^{\pm}, 33)$ rovibrational transitions of methanol.

4.6.2.4 *P(E,co,1,-4,32)*

We now present the absolute frequency measurement of the $P(E, co, 1, -4, 32)$ rovibrational line of methanol, that is in the $E2$-symmetry band of the C-O stretching vibrational mode with torsion $t = 1$. We have carried out three measurements in June 2017 at a pressure of 2 Pa and an intra-cavity average power of 0.49 mW.

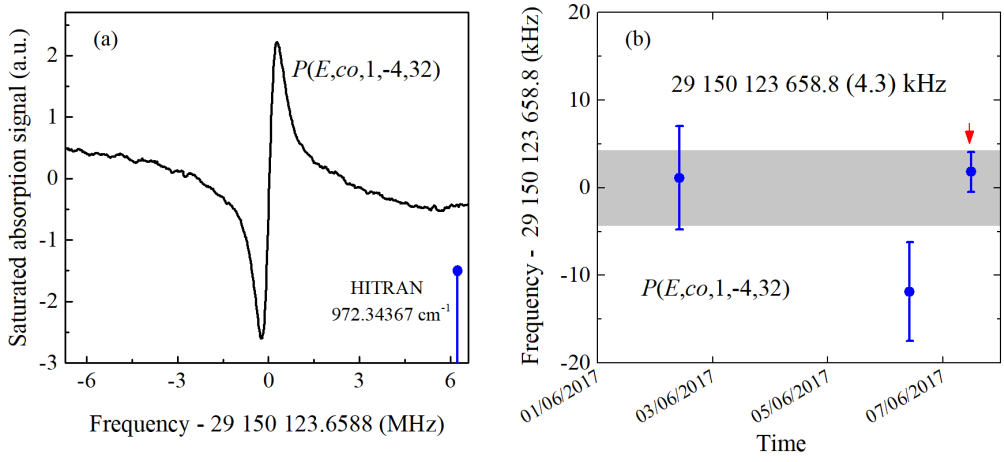

Figure 4.32 – (a) Saturated absorption spectrum of the $P(E, co, 1, -4, 32)$ rovibrational transition of methanol, recorded using frequency modulation and first-harmonic detection. This transition is reported in the HITRAN database [54] at 972.34367 cm^{-1}, as shown by the blue stick. Experimental conditions: pressure, 2 Pa; modulation frequency, 20 kHz; frequency modulation excursion, 50 kHz; frequency step, ∼15 kHz; average of five pairs of up and down scans; total integration time per point, 1 s; whole spectrum measurement time, 888 s. (b) Frequency measurements of the $P(E, co, 1, -4, 32)$ rovibrational methanol line. Three measurements were carried out in June 2017. The transition frequency resulting from the weighted mean of all data is indicated with the associated 1-σ weighted standard error and symbolized by the grey rectangular. The red arrow pinpoints the measurement corresponding to panel (a) of the figure.

Figure 4.32(a) shows a saturated absorption spectrum of the $P(E, co, 1, -4, 32)$ rovibrational transition of methanol, that is averaged over five pairs of up and down scans. It exhibits a signal-to-noise ratio of ∼198 and a peak-to-peak linewidth of ∼430 kHz (FWHM of ∼750 kHz). Figure 4.32(b) displays three absolute frequency measurements and their uncertainties of the $P(E, co, 1, -4, 32)$ line. It is noted that due to the lack of knowledge of the optical frequency reference ν_{ref}, the frequency axis of the measurement on 02 June 2019 is reconstructed using the radio-frequency protocol. The weighted mean of the frequencies is found to be 29 150 123 658.8 (4.3) kHz. The 1-σ weighted standard error quoted into parentheses correspond to our statistical uncertainty.

Uncertainty of the line fitting is estimated to be 5 kHz (see the rule given at the beginning of this subsection). Following Table 4.3, we have deduced a zero-power and zero-pressure transition frequency of 29 150 123 660.5 (8.4) kHz. The error quoted into

parentheses correspond to the total uncertainty. Our resonance frequency is shifted by −6 224.5 kHz with respect to frequency reported in the HITRAN database.

4.6.3 Summary

We list in Table 4.5 the line-center frequencies of rovibrational transitions of methanol determined above in subsection 4.6.1 and 4.6.2, including (i) observed line-center frequency, which is the frequency measured at the power and pressure used, with statistic uncertainty and (ii) corrected line-center frequency, that is extrapolated at zero-power and zero-pressure, with total uncertainty. Absolute frequencies (in cm^{-1}) of the transitions previously reported in the HITRAN and the difference between our measurements and this database are also shown in this table.

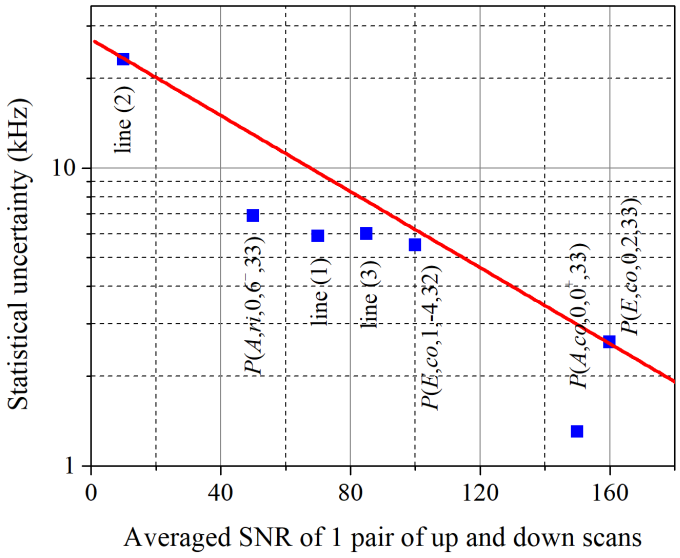

Figure 4.33 – Statistical uncertainty on the line center as a function of the signal-to-noise ratio of the signal-to-noise ratio (SNR) of the average of one pair of up and down spectra for the seven line studied previously. The red line is a conservative estimate of the dependence of the weighted standard deviation with the SNR.

In the following sections of this chapter, we will study other lines of methanol. In the next chapter, we will focus on other species. For most of those other studies, we have either carried out only one measurement consisting in recording five pairs of up and down spectra or even sometimes recorded one pair only of up and down spectra. As for all those, we have not repeated several measurements, we cannot determine the statistical uncertainty on the centre frequency. We have thus decided to estimate the statistical uncertainty based on the know-how gained in the previous extensive studies. Figure 4.33 displays the weighted standard deviation of all line-centre measurements as a function of the signal-to-noise ratio (SNR) of the average of one pair of up and down spectra for the seven lines studied previously (for example for line $P(E, co, 0, 2, 33)$, we take the weighted standard deviation of the 20 measurements displayed in Figure 4.26). The red line in Figure 4.33 is a conservative estimate of the dependence of the weighted standard deviation with the SNR. We now detail how we estimate a conservative statistical uncertainty on the line centre for the following measurements which have not

Table 4.5 – Measured line-center frequencies and associated uncertainty of methanol transitions studied in subsections 4.6.1 and 4.6.2 and corresponding values reported in the HITRAN database [54].

Line	HITRAN (cm^{-1})	This work (kHz)		Corrected − HITRAN (kHz)
		Observed (statistical uncertainty)	Corrected (total uncertainty)	
$P(E, co, 0, 2, 33)$	971.76295	29 132 715 058.4 (1.3)[b]	29 132 715 074.3 (7.4)	−5 263.1
		29 132 715 065.1 (0.7)[c]		
$P(A, co, 0, 0^+, 33)$	971.69901	29 130 799 512.2 (0.8)[d]	29 130 799 528.7 (7.9)	−3 935.7
		29 130 799 517.2 (1.6)[e]		
${}^PP(A, ri, 0, 6^-, 33)$	970.22326	29 086 559 881.4 (2.9)	29 086 559 892.5 (11.7)	−1 699.9
${}^PP(E, ri, 0, -5, 32)?$[a]	971.94430	29 138 113 980.3 (2.4)	29 138 113 989.0 (7.6)	−43 084.7
		29 138 117 987.6 (9.0)	29 138 117 996.3 (14.5)	−39 077.4
		29 138 179 774.5 (3.0)	29 138 179 783.2 (7.8)	22 709.5
$P(E, co, 1, -4, 32)$	972.34367	29 150 123 658.8 (4.3)	29 150 123 660.5 (8.4)	−6 224.5

[a] An alternative assignment is proposed in Ref. [239] where the ${}^PP(E, ri, 0, -5, 32)$ and $P(A, co, 0, 13^{\pm}, 33)$rovibrational transitions are reported at the same frequency of 971.94418 cm^{-1}.
[b] measured in June 2017 at a power of 1.1 mW (see subsection 4.6.1).
[c] measured in October 2017 at a power of 0.82 mW (see subsection 4.6.1).
[d] measured in June 2017 at a power of 1.15 mW (see subsection 4.6.2).
[e] measured in October 2017 at a power of 0.85 mW (see subsection 4.6.2).

Table 4.6 – Systematic uncertainties affecting the line-center frequencies of K-doublets of methanol that will be described in this subsection.

Systematics	Correction (kHz)	Uncertainty (kHz)
Frequency calibration	0	0.001 for "optical" protocol
		0.3 for "radio-frequency" protocol
Power shift (P power in mW)	$15.4 \times P$	$1.3 \times P$
Pressure shift (p pressure in Pa)	$-2.9 \times p$	$0.3 \times p$
Other spectroscopic effects	0	5.0
Line fitting	0	5.0 for SNR[a] > 130
		10 for SNR[a] < 130

[a]The SNR here is the SNR for an average of five pairs of up and down scans.

been repeated. We first determine the SNR of the average of one pair of up and down spectra. We then use Figure 4.33. For data for which we have recorded five pairs of up and down spectra, or only one, because we have not repeated the measurement, we assign a conservative statistical uncertainty on the line centre twice larger than that given by the red line of Figure 4.33 at the associated SNR. Finally, the SNR of some data is smaller than 10, the smaller SNR contributing to Figure 4.33. For all those data, the error bar given by the fit is large enough that it dominates the statistical uncertainty. However, because again, we have not repeated the measurement, we assign a statistical uncertainty to those measurements's line centre equal to twice the error bar given by the fit of one pair of up and down spectra.

4.7 Asymmetry *K*-doublets for *A*-symmetry transitions

As mentioned in subsection 4.2.4, due to the asymmetry of methanol, each A-symmetry energy level is split into $A+$ and $A-$ sublevels. Energy shifts between these sublevels is slightly different between the ground state and the vibrational state. This leads to frequency shifts and the existence of K-doublet (see subsection 4.2.3). In this work, we only consider K-doublets in the C-O stretching vibrational mode. For low values of K, the frequency difference between two components of a K-doublet is very large, ranging from few tens of MHz to a few GHz (see Figure 4.10(a)). At a given J, it rapidly decreases with K. Therefore, the frequency difference is expected to be small at high values of K. However, as described in subsection 4.2.3 there are some singular K-doublets that have larger frequency differences between $A+$ and $A-$ transitions than expected because of the local resonance between two series of substates of two different vibrational modes (see Figure 4.10).

For K values equal or above 7, we do not expect to resolve "normal" K-doublet splittings, even with our high resolution spectrometer. However, in this section, we demonstrate the first measurement of several singular K-doublets of methanol that can be detected with our spectrometer for K values of 7 and 10.

Most of K-doublets presented in this section have been carried out only one measurement consisting in recording five pairs of up and down spectra (except one, for which the line-center frequency measurement is repeated in several times). Again, the know-how gained in our metrological study of methanol allows us to establish a meaningful uncer-

tainty budgets for those K-doublets. Statistical uncertainty associated on the line-center frequency of those K-doublets are conservatively estimated to be twice the value given by the red line of Figure 4.33, as mentioned in subsection 4.6.3. In order to estimate systematic uncertainty associated to the line-center frequency and extrapolate the absolute frequency at zero-power and zero-pressure, we apply the same procedure that we have used in the previous section (see Table 4.3). However, some times the absolute frequency axis is given by the radio-frequency protocol, for which the "frequency calibration" uncertainty is given by 0.3 kHz (see subsection 3.4.3), as shown in Table 4.6.

4.7.1 Resolved *K*-doublets

4.7.1.1 *P*(*A*,*co*,0,10$^{\pm}$,34) and *P*(*A*,*co*,0,10$^{\pm}$,33)

P(*A*,*co*,0,10$^{\pm}$,34)

We have measured saturated absorption spectra of the $P(A, co, 0, 10^{\pm}, 34)$ K-doublet, previously reported as degenerate in the HITRAN database at a frequency of 970.01170 cm^{-1} with calculated line-intensities of 4.472×10^{-23} and 2.956×10^{-23} cm^{-1}/mol.cm^{-2}, respectively. Figure 4.34(a) shows a saturated absorption spectrum of the K-doublet that is an average over five pairs of up and down scans. The experimental conditions are the following: pressure of ∼1.7 Pa, intra-cell average power of ∼0.96 mW, second-harmonic detection. Modulation parameters are listed in the caption of Figure 4.34. The frequency axis of spectra is reconstructed using the radio-frequency protocol. The spectrum exhibits a FWHM linewidth of ∼1060 kHz and a signal-to-noise ratio of ∼80. The two absorption transitions with an interval of about 3.2 MHz have been resolved. Their intensities are nearly equal while they were reported to be different by ∼34% in the HITRAN database (see above). We find an unexpected dip which lies midway between the two "genuine" transitions. We attribute this to a collision-induced crossover. As explained in Section 4.2.4, the two "genuine" transitions do not share any common level. However, connection between these two transitions most probably happens as a result of a collisional transfer of molecules between levels, leading to the additional central dip [261].

We have only measured five pairs of up down spectra for the K-doublet. In order to determine the line-center frequencies of the $P(A, co, 0, 10^{\pm}, 34)$ K-doublet, we perform a "pair by pair" analysis, as described in subsection 4.4.2.2. In all such resolved K-doublets, the sum of three saturated absorption profiles given by Equation 4.16 with a zero-order polynomial baseline (in second-harmonic detection, only an offset is needed to model the baseline, see subsection 4.4.2), and the same linewidth and B asymmetry factor, but three different intensities are fitted to the data. The crossover's frequency is set equal to the mean of the A^+ and A^- transition frequencies. Figure 4.34(b) displays an averaged pair of up and down scans of the K-doublet, the resulting fit to the data, and its residuals. This fit has a reduced chi-squared of 1.32. Following this, the line-center frequency of each transition is given by the weighted mean of the five fitted frequencies in which weights are calculated from the fitted error bars. Finally, the line-center frequencies of the $P(A, co, 0, 10^{\pm}, 34)$ K-doublet are founded to be 29 080 214 506.6 kHz and 29 080 217 692.6 kHz.

Again, only five pairs of up and down spectra of the K-doublet have been recorded and the averaged SNR of one pair is found to be ∼30. Following the rule exposed in subsection 4.6.3, the statistical uncertainties of the two transitions of the K-doublet are

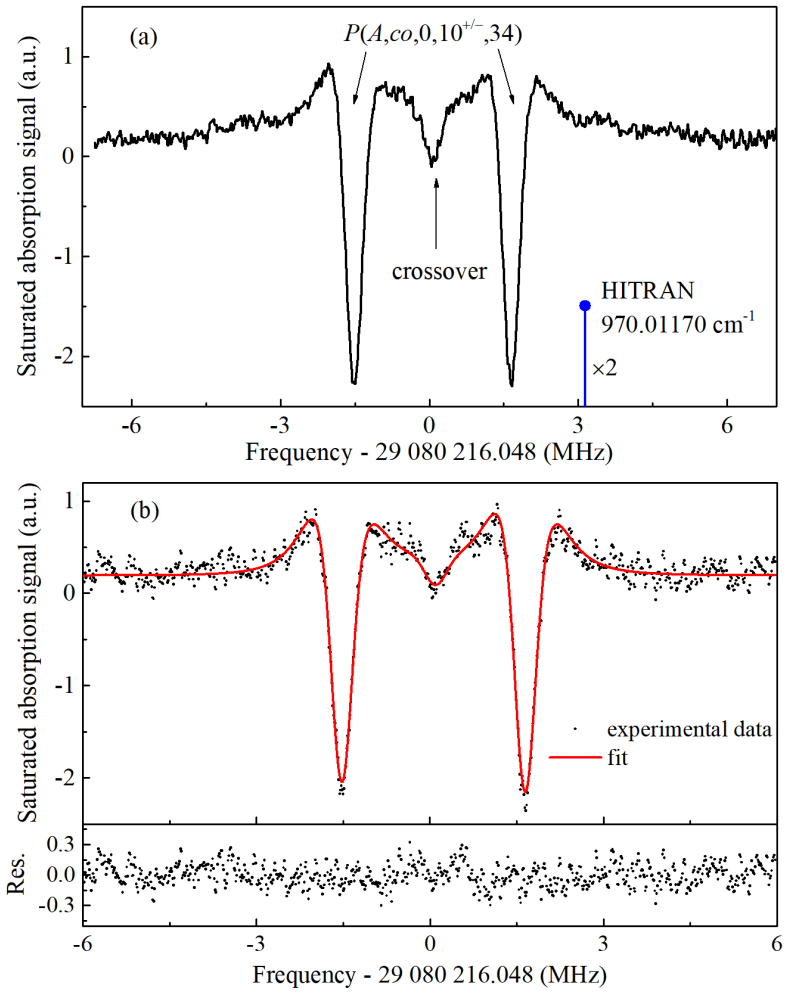

Figure 4.34 – (a) Saturated absorption spectrum of the $P(A, co, 0, 10^{\pm}, 34)$ K-doublet around 970.011 cm^{-1} recorded using frequency modulation and second-harmonic detection. Experimental conditions: pressure, 1.7 Pa; modulation frequency, 20 kHz; frequency modulation excursion, 180 kHz; frequency step, ∼15 kHz; average of five pairs of up and down scans; total integration time per point, 1 s; whole spectrum measurement time, 920 s. The $P(A, co, 0, 10^{\pm}, 34)$ degenerate (indicated by ×2) doublet position reported in the HITRAN database [54] is also shown as a blue stick. (b) One averaged pair of up and down scans contributing to the data of panel (a), the resulting fit to the data, and its residuals. The total integration time per point is 200 ms, whole spectrum measurement time: 160 s.

conservatively estimated to be 34.8 kHz. Using Table 4.6, the total systematic uncertainty on the absolute center frequencies of these two lines is estimated to be 11.3 kHz and the line-center frequencies of the $P(A, co, 0, 10^{\pm}, 34)$ K-doublet extrapolated at zero-power and zero-pressure are 29 080 214 516.5 (36.6) kHz and 29 080 217 702.5 (36.6) kHz. The uncertainties quoted into parentheses correspond to our total uncertainties. The lines are thus shifted by −4 666.7 kHz and −1 480.7 kHz with respect to the frequency reported in the HITRAN database.

$P(A, co, 0, 10^{\pm}, 33)$

We have also carried out one measurement of the $P(A, co, 0, 10^{\pm}, 33)$ K-doublet, previously reported as degenerate in the HITRAN database at a frequency of 972.19306 cm^{-1} with line-intensities of 1.395×10^{-22} $cm^{-1}/mol.cm^{-2}$ for the $P(A, co, 0, 10^{+}, 33)$ transition and 1.687×10^{-22} $cm^{-1}/mol.cm^{-2}$ for the $P(A, co, 0, 10^{-}, 33)$ transition. Figure 4.35 shows a saturated absorption spectrum of the K-doublet averaged over five pairs of back and forth scans. The experimental conditions are the following: pressure of 1.7 Pa, intra-cell average power of 0.87 mW, second-harmonic detection. Modulation parameters are listed in the caption of Figure 4.35. We use the radio-frequency protocol to reconstruct the frequency axis of the spectrum. In order to determine the line-center frequencies of the two components of the $P(A, co, 0, 10^{\pm}, 33)$ K-doublet, we perform an analysis similar to that of the $P(A, co, 0, 10^{\pm}, 34)$ K-doublet. The spectrum exhibits two transitions of the $P(A, co, 0, 10^{\pm}, 33)$ K-doublet (and a collision induced crossover in the middle) with a FWHM linewidth of ∼1020 kHz and a signal-to-noise ratio of ∼240. These transitions are similar in intensity as reported in the HITRAN database. Figure 4.34(b) displays one averaged pair of up and down scans of the K-doublet, the resulting fit to the data, and its residuals. This fit has a reduced chi-squared of 1.58. Line-center frequencies of the $P(A, co, 0, 10^{+}, 33)$ and $P(A, co, 0, 10^{-}, 33)$ rovibrational transitions are found to be 29 145 608 511.3 and 29 145 615 202.7 kHz.

We have only measure five pairs of up and down spectra. The averaged SNR of one pair is found to be ∼95. The statistical uncertainty of the two transitions of the K-doublet are thus conservatively estimated to be 13.4 kHz (see subsection 4.6.3). By using Table 4.6, the total systematic uncertainty on the absolute center frequencies of the K-doublet is estimated to be 7.2 kHz and the line-center frequencies extrapolated at zero-power and zero-pressure are 29 145 608 519.5 (15.2) kHz and 29 145 615 211.2 (15.2) kHz, listed in Table 4.7. The uncertainties quoted into parentheses correspond to our total uncertainties. Our measured resonance frequencies of the $P(A, co, 0, 10^{\pm}, 33)$ K-doublet are shifted by −6 191.3 kHz and 500.4 kHz with respect to the previous measurement reported in the HITRAN database.

From the measurements, we find that the frequency differences between two components of the $P(A, co, 0, 10^{\pm}, 34)$ and $P(A, co, 0, 10^{\pm}, 33)$ K-doublets are 3 186.0 (73.2) and 6 691.7 (30.4) kHz while those of other K-doublets with the same values of J (J = 33 and 34) but K = 8, 11, and 12 could not be observed with our spectrometer (see below). This demonstrates that the $P(A, co, 0, 10^{\pm}, 34)$ and $P(A, co, 0, 10^{\pm}, 33)$ rovibrational transitions of methanol are "singular" K-doublets, the shifts of which may be enhanced by coupling of the C-O stretching vibrational mode to another vibrational mode, as mentioned in subsection 4.2.4. Indeed, following calculations of R.M. Lees and his co-workers [239], the $(A, co, 0, 10, J)$ J-series of states of the ν_8 C-O stretching vibrational mode cross the $(A, oh, 0, 3^{\pm}, J)$ J-series of states of the ν_6 OH-bending vibrational

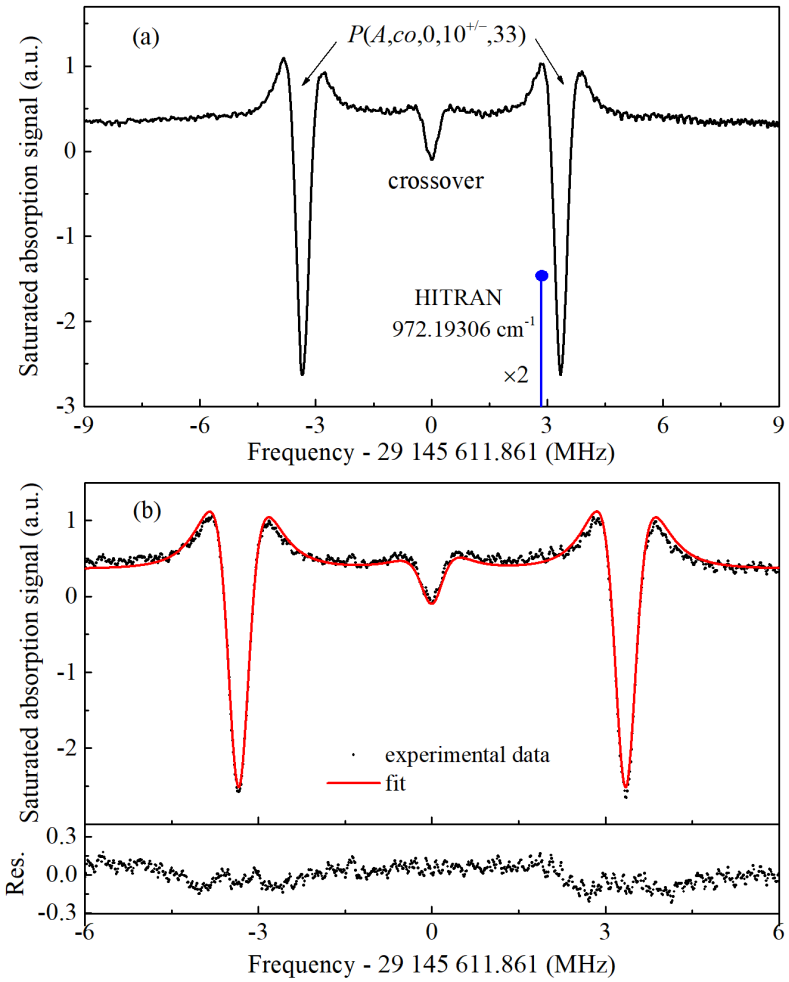

Figure 4.35 – (a) Saturated absorption spectrum of the $P(A, co, 0, 10^{\pm}, 33)$ K-doublet recorded using frequency modulation and second-harmonic detection. Experimental conditions: pressure, 1.7 Pa; modulation frequency, 20 kHz; frequency modulation excursion, 200 kHz; frequency step, ∼15 kHz; average of five pairs of up and down scans; total integration time per point, 1 s; whole spectrum measurement time, 1301 s. The $P(A, co, 0, 10^{\pm}, 33)$ degenerate (indicated by ×2) doublet position reported in the HITRAN database [54] is also shown as a blue stick. (b) One averaged pair of up and down scans contributing to the data of panel (a), the resulting fit to the data, its residuals. The total integration time per point is 200 ms, whole spectrum measurement time: 180 s.

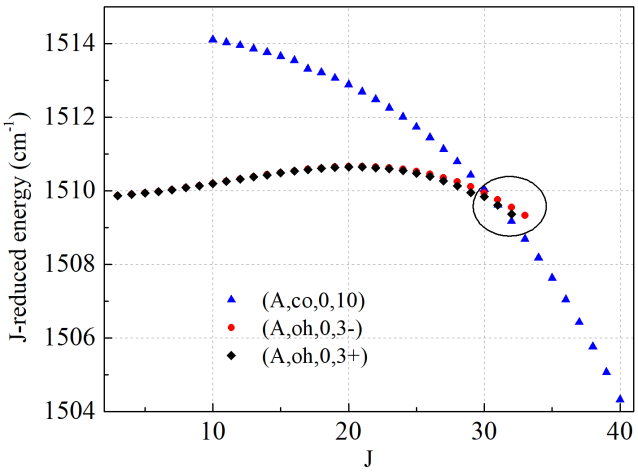

Figure 4.36 – J-reduced energy of the upper-state levels of A torsional symmetry for methanol. The J-reduced energy is the energy reduced by $0.8J(J+1)$, where 0.8 cm^{-1} corresponds to a representative B-value. The circle highlights a local resonance between the $(A, co, 0, 10, J)$ J-series of states of the ν_8 C-O stretching vibrational mode and the $(A, oh, 0, 3^{\pm}, J)$ J-series of states of the ν_6 OH-bending vibrational mode. Note that J-values in the graph correspond to the J quantum number of the energy levels in the vibrationally excited states while J-values in our notation of the rovibrational transitions correspond to the J quantum number of the lower state.

mode for values of J between 30 and 33, as shown in Figure 4.36. This crossing between substates is at the origin of the singular shifts we observe.

4.7.1.2 $P(A,co,1,7^{\pm},29)$

Another singular K-doublet in the torsional state $t = 1$ is $P(A, co, 1, 7^{\pm}, 29)$ of the ν_8 C-O stretching mode with $K = 7$ and $J = 29$. The $P(A, co, 1, 7^{\pm}, 29)$ K-doublet is reported as degenerate in the HITRAN database at a frequency of 972.431070 cm^{-1} with line intensities of 5.261×10^{-23} and 2.300×10^{-22} $cm^{-1}/mol.cm^{-2}$, respectively. Figure 4.37 displays a saturated absorption spectrum of the K-doublet that is recorded at a pressure of 1 Pa and an intra-cell average power of 0.65 mW using frequency modulation and first-harmonic detection. Parameters of the modulation are listed in the caption of Figure 4.37. It is an average over five pairs of up and down scans and its frequency axis is determined using the optical protocol. The spectrum exhibits two absorption features (and a collision-induced crossover in the middle) with a peak-to-peak linewidth of ∼400 kHz (FWHM 700 kHz), and a signal-to-noise ratio of ∼ 73.5. We can see that line-intensities of these transitions are approximately equal while those reported in the HITRAN database are different by a factor of about 4.3 times .

We have carried out five measurements of the line-center frequency of the K-doublet in June 2017. Each measurement consists in five pairs of back and forth spectra. We perform a "pair by pair" analysis. Figure 4.37(b) shows a saturated absorption spectrum of the $P(A, co, 1, 7^{\pm}, 29)$ K-doublet that is averaged after one up-down scan, the resulting fit to the data, and its residuals. Figures 4.37(c) and (d) display the transition frequencies and their uncertainties of the two rovibrational transitions of the $P(A, co, 1, 7^{\pm}, 29)$ K-

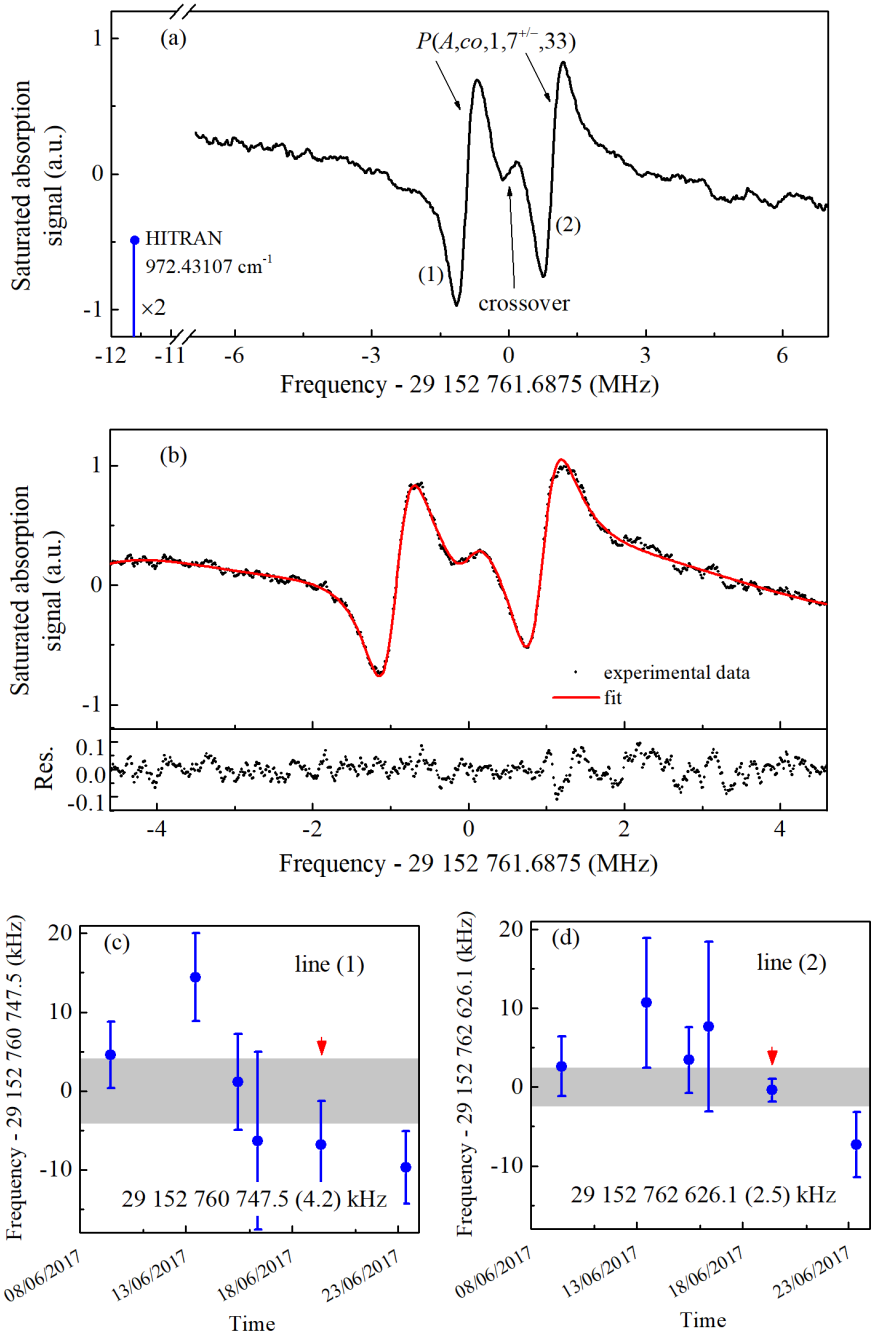

Figure 4.37 – (a) Saturated absorption spectrum of the $P(A, co, 1, 7^{\pm}, 29)$ K-doublet around 972.431 cm^{-1}, that is averaged over five pairs of up and down scans. The $P(A, co, 1, 7^{\pm}, 29)$ degenerate (indicated by $\times 2$) doublet position reported in the HITRAN database [54] is also shown as a blue stick. Experimental conditions: pressure, 1 Pa; modulation frequency, 20 kHz; frequency modulation excursion, 50 kHz; total integration time per point, 1 s; whole spectrum measurement time, 924 s. (b) An average of one up and down scans, the resulting fit to the data, and its residuals. (c) and (d) Frequency measurements of the $P(A, co, 1, 7^{\pm}, 29)$ K-doublet. The transition frequencies resulting from the weighted mean of all data are indicated with the associated 1-σ weighted standard errors and symbolized by the grey rectangulars. The red arrows pinpoint the measurement corresponding to panel (a) of the figure.

doublet for the five measurements. The transition frequencies resulting from the weighted means of all data for the two components of the K-doublet are 29 152 760 747.5 (4.2) kHz and 29 152 762 626.1 (2.5) kHz. The 1-σ weighted standard errors quoted into parentheses correspond to our statistical uncertainties. Contribution of the line-fitting to the systematic uncertainty is estimated to be 10 kHz (see Table 4.6). Following Table 4.6, the total systematic uncertainty of the two transitions of the K-doublet is estimated to be 11.3 kHz and the line-center frequencies of $P(A, co, 1, 7^{\pm}, 29)$ K-doublet extrapolated at zero-power and zero-pressure are found to be 29 152 760 754.6 (12.1) and 29 152 762 633.2 (11.6) kHz. The uncertainties quoted into parentheses correspond to the total uncertainties. Our measured resonance frequencies of the $P(A, co, 1, 7^{\pm}, 29)$ K-doublet are shifted by 10 683.5 and 12 562.1 kHz with respect to the degenerate frequency reported in the HITRAN database.

We suspect the enhancement of this K-doublet splitting to result from a J-localized perturbation between the $P(A, co, 1, 7^{\pm}, J)$ J-series of states of the ν_8 C-O stretching vibrational mode and the $P(A, sb, 0, 1^{+}, J)$ J-series of states of the ν_5 symmetric CH3-bending mode vibrational mode calculations carried out by R.M. Lees and his co-workers [239] for $J < 24$ are compatible with this hypothesis, but however no calculation at J around 29 are unfortunately reported.

4.7.2 Un-resolved K-doublet

Furthermore, we have measured the absolute frequencies of other K-doublets of the C-O stretching mode in the torsional mode $t = 0$ with $K = 8$, 11, and 12 for $J = 33$ and 34. The frequency difference between $A+$ and $A-$ rovibrational transitions are expected to be small, therefore those were not resolved by our spectrometer. All frequency measurements of the K-doublets are carried out at a pressure of ∼1.7 Pa in second-harmonic detection with a frequency modulation of 20 kHz and frequency modulation excursion ranging from 150 to 200 kHz. Saturated absorption spectra are typically acquired with only one measurement of five pairs of back and forth scans. Absolute line-center frequencies of these K-type doublets are determined by applying the "pair by pair" analysis. Details for each K-doublet including sub-Doppler spectrum, experimental conditions, uncertainty budget are shown in Appendix F. The resulting frequencies of the K-doublets extrapolated at zero-power and zero-pressure are listed in Table 4.8. The errors quoted into parentheses correspond to the total uncertainties in which the statistical uncertainty of each line is conservatively estimated by following the procedure described in subsection 4.6.3.

4.7.3 Summary

Tables 4.7 and 4.8 show the frequencies and shifts with respect to the HITRAN database of the six un-resolved and the three resolved K-doublets. They includes (i) observed line-center frequency, which is the frequency measured at the power and pressure used, with statistic uncertainty and (ii) corrected line-center frequency, that is extrapolated at zero-power and zero-pressure, with total uncertainty. They are on average red-shifted by a few MHz with respect to the HITRAN database.

Table 4.7 – Measured line-center frequencies of several singular K-doublet of methanol and corresponding values reported in the HITRAN database [54].

Line	HITRAN (cm^{-1})	This work (kHz)		Corrected − HITRAN (kHz)
		Observed (statistical uncertainty)	Corrected (total uncertainty)	
$P(A, co, 0, 10^{\pm}, 34)$	970.01170	29 080 214 506.6 (34.8)[a]	29 080 214 516.5 (36.6)	−4 666.7
		29 080 217 692.6 (34.8)[a]	29 080 217 702.5 (36.6)	−1 480.7
$P(A, co, 0, 10^{\pm}, 33)$	972.19306	29 145 608 511.0 (13.4)[b]	29 145 608 519.5 (15.3)	−6 191.3
		29 145 615 202.7 (13.4)[b]	29 145 615 211.2 (15.3)	500.4
$P(A, co, 1, 7^{\pm}, 33)$	972.43107	29 152 760 747.5 (4.2)[c]	29 152 760 754.6 (12.1)	10 683.5
		29 152 762 626.1 (2.5)[c]	29 152 762 633.2 (11.6)	12 562.1

[a,b]Statistical uncertainty is conservatively estimated from the know-how gained in our metrological study of methanol (see subsection 4.6.3).
[c]Statistical uncertainty is calculated from the repeated measurements.

Table 4.8 – Line-center frequencies of un-resolved K-doublets of methanol.

Line	HITRAN (cm^{-1})	This work (kHz)		Corrected − HITRAN (kHz)
		Observed (statistical uncertainty)	Corrected (total uncertainty)	
$P(A, co, 0, 12^{\pm}, 34)$	970.16604	29 084 844 350.8 (22.1)[a]	29 084 844 360.2 (23.2)	−1 819.8
$P(A, co, 0, 11^{\pm}, 34)$	970.56107	29 096 690 239.3 (6.4)[a]	29 096 690 248.4 (9.6)	1 367.0
$P(A, co, 0, 8^{\pm}, 34)$	970.75148	29 102 407 302.5 (18.5)[a]	29 102 407 313.0 (19.9)	10 083.4
$P(A, co, 0, 12^{\pm}, 33)$	972.35908	29 150 580 325.3 (19.0)[a]	29 150 580 330.1 (20.3)	−11 535.1
$P(A, co, 0, 11^{\pm}, 33)$	972.73971	29 161 997 474.9 (43.3)[a]	29 161 997 474.5 (44.7)	−5 391.0
$P(A, co, 0, 8^{\pm}, 33)$	972.86626	29 165 790 301.8 (29.6)[a]	29 165 790 302.9 (31.6)	−6 436.2

[a] Statistical uncertainty is conservatively estimated from the know-how gained in our metrological study of methanol (see subsection 4.6.3).

4.8 Tunability and spectral coverage

4.8.1 Wide tunability

In this subsection, we demonstrate the unprecedented tuning capability of the QCL resulting from the implementation of our widely-tunable accurate and ultra-stable OLO (see section 3.5). As described in section 2.7, the QCL frequency is phase-locked to the n^{th} harmonic of the repetition rate (f_{rep}) of the OFC, itself stabilized to the OLO carrier frequency. The home-made microwave synthesizer driving the EOM frequency of the OLO allows us to continuously tune the OLO carrier frequency over 9 GHz. The repetition rate and the QCL frequency are thus scanned. As mentioned in 3.5, the tuning range of the QCL frequency reached 0.45 or 1.35 GHz, depending which experimental setup is used for tuning the comb (see section 3.5).

As mentioned in section 2.7, before 2019 we only used the piezo-electric modulator (PZT, Figure 2.23) to tune f_{rep} of the OFC. The tuning range of the stabilized QCL was thus limited to around 450 MHz by the PZT acting on the OFC cavity length (see Table 3.1). Figure 4.38 shows a saturated absorption spectrum of methanol with a span of ∼400 MHz (from 971.559 to 971.573 cm^{-1}), that was recorded using this setup. It was recorded at 1 Pa and averaged after one up and down scan. The frequency modulation excursion is 50 kHz. The spectrum exhibits five neighbouring rovibrational transitions labelled with the notations given in subsection 4.2.2. Doppler-limited absorption of these transitions is shown in Figure 4.13. The oscillations in the baseline of Figure 4.38 result from the Doppler contribution to the line shape. Each absorption line is fitted with the first-derivative of a sum of a Lorentzian and a Gaussian to model the saturated absorption and the Doppler contribution, respectively. It is noted that this fit is not used to determine resonance frequency of the resolved transitions because it does not include the asymmetry and full model for the baseline (see below). It is just used here as a guide-to-the-eye. The Gaussian FWHM linewidth is found to be 63 (0.5) MHz, in good agreement with the expected Doppler broadening of 64.5 MHz.

In order to determine line-center frequencies, we first take a spectral range of ∼6 MHz around each transitions from the broadband spectrum. Then, we fit the saturated line shape given Equation 4.13 to the data using $N = 7$ (the spectrum is recorded using first-harmonic detection). Statistical uncertainties of the five measured transitions are estimated by following the rule given in subsection 4.6.3. We estimate systematic effects by using Table 4.6 but with the "frequency calibration" uncertainty of 0.5 kHz (see Equation 3.31). In Table 4.9, we list line-center frequencies and their uncertainties for the five transitions with two sets: (i) observed frequencies with estimated statistical uncertainties and (ii) corrected frequencies at zero-power and zero-pressure with total uncertainties.

Since 2019, the experimental setup of the f_{rep} lock has been upgraded. In this setup, the continuous displacement of the PZT actuator and the large movement of the stepper motor (Figure 2.28) have been combined to improve the tuning range of f_{rep} (see section 2.7 for more details). As demonstrated in section 3.5, the tunability of the OLO is fully transferred to f_{rep}, thus to the QCL frequency. The continuous tuning range of the QCL frequency is ∼1.35 GHz, limited by the YIG's span of the OLO.

Figure 4.39 shows a saturated absorption spectrum with a span of ∼1.35 GHz (from ∼971.312 to ∼971.357) recorded using the upgraded setup in the first-harmonic detection.

Table 4.9 – Line-center frequencies of rovibrational transitions of methanol shown in Figure 4.38 and corresponding values reported in the HITRAN database [54].

Line	HITRAN (cm^{-1})	This work (kHz)		Corrected − HITRAN (kHz)
		Observed (statistical uncertainty)	Corrected (total uncertainty)	
$P(A, co, 1, 3^-, 32)$	971.56269	29 126 697 255.0 (33.8)	29 126 697 264.4 (35.6)	−19 429.2
$(A, sb, 0, 1^-, 10)$ $\leftarrow (A, gr, 2, 1^-, 11)$	971.56335	29 126 743 944.9 (48.8)	29 126 743 954.3 (50.1)	7 474.4
$P(A, co, 0, 4^+, 33)$	971.56577	29 126 809 704.2 (19.6)	29 126 809 713.6 (20.9)	683.9
$P(A, co, 1, 3^-, 32)$	971.56717	29 126 848 497.2 (40.9)	29 126 848 506.6 (42.4)	−2 494.0
$P(A, co, 0, 4^-, 33)$	971.57152	29 126 978 060.9 (21.7)	29 126 978 070.3 (22.9)	−3 340.0

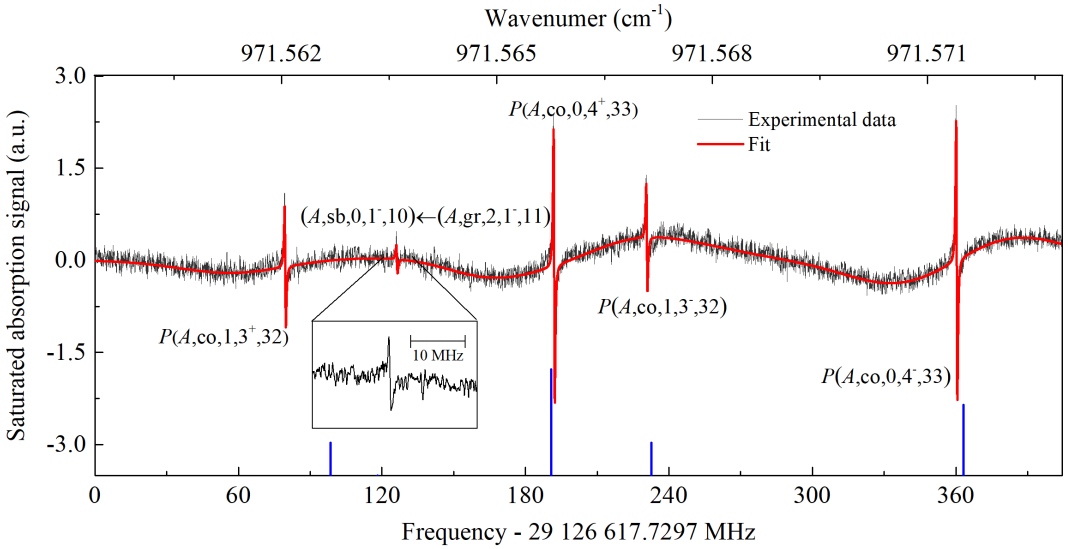

Figure 4.38 – Saturated absorption spectrum of methanol spanning 400 MHz recorded using frequency modulation and first-harmonic detection (black dots). Blue sticks indicate the line frequency positions reported in the HITRAN database [54]. Experimental conditions: pressure, 1 Pa; modulation frequency, 20 kHz; frequency modulation excursion, 50 kHz; frequency step, ∼15 kHz; average of 1 pair of scans of opposite frequency sweep direction; total integration time per point, 200 ms, whole spectrum measurement time, 5400 s. The oscillations in the baseline result from the Doppler contribution. The red solid line is a fit to the data (see text). The inset is a zoom on the small $(A, sb, 0, 1-, 10) \leftarrow (A, gr, 2, 1-, 11)$.

It is measured at 1.5 Pa and averaged over five pairs of up and down scans, after retrieval of the absolute frequency scale following the optical protocol. To improve the signal-to-noise ratio of the spectrum, a frequency excursion of 250 kHz has been used. The spectrum exhibits fourteen rovibrational transitions of methanol. The red solid line is a fit to the data. Each line is fitted with the first derivative of a sum of a Lorentzian and a Gaussian to model the saturated absorption and Doppler contribution, respectively. This fit just used as a guide-to-the-eye. The transitions reported in the HITRAN database in the spectral window covered are shown as blue sticks. The observed transitions, that we could not assign at all, are indicated with blue arrows.

In order to determine the line-center frequencies of the fourteen resolved rovibrational transitions, we take a spectral range of ∼6 MHz around each transitions, as mentioned above. In this case, we perform a "pair by pair" analysis. Figure 4.39(c) shows a saturated absorption spectrum of the $P(A, co, 0, 2^-, 33)$ rovibrational transition of methanol that is averaged after one pair of up and down scans. The red solid curve is the fit of the saturated absorption line shape model (given by Equation 4.13) to the data and its residuals. We can see that the residuals have some structures related to the distortion of the spectrum caused by the higher frequency excursion. Therefore, a model that takes into account the higher frequency excursion (such as the one used in chapter 5) could be considered in this case.

We follow the rule given in subsection 4.6.3 to estimate statistical uncertainties of the fourteen transitions while total systematic uncertainties of the transitions are determined

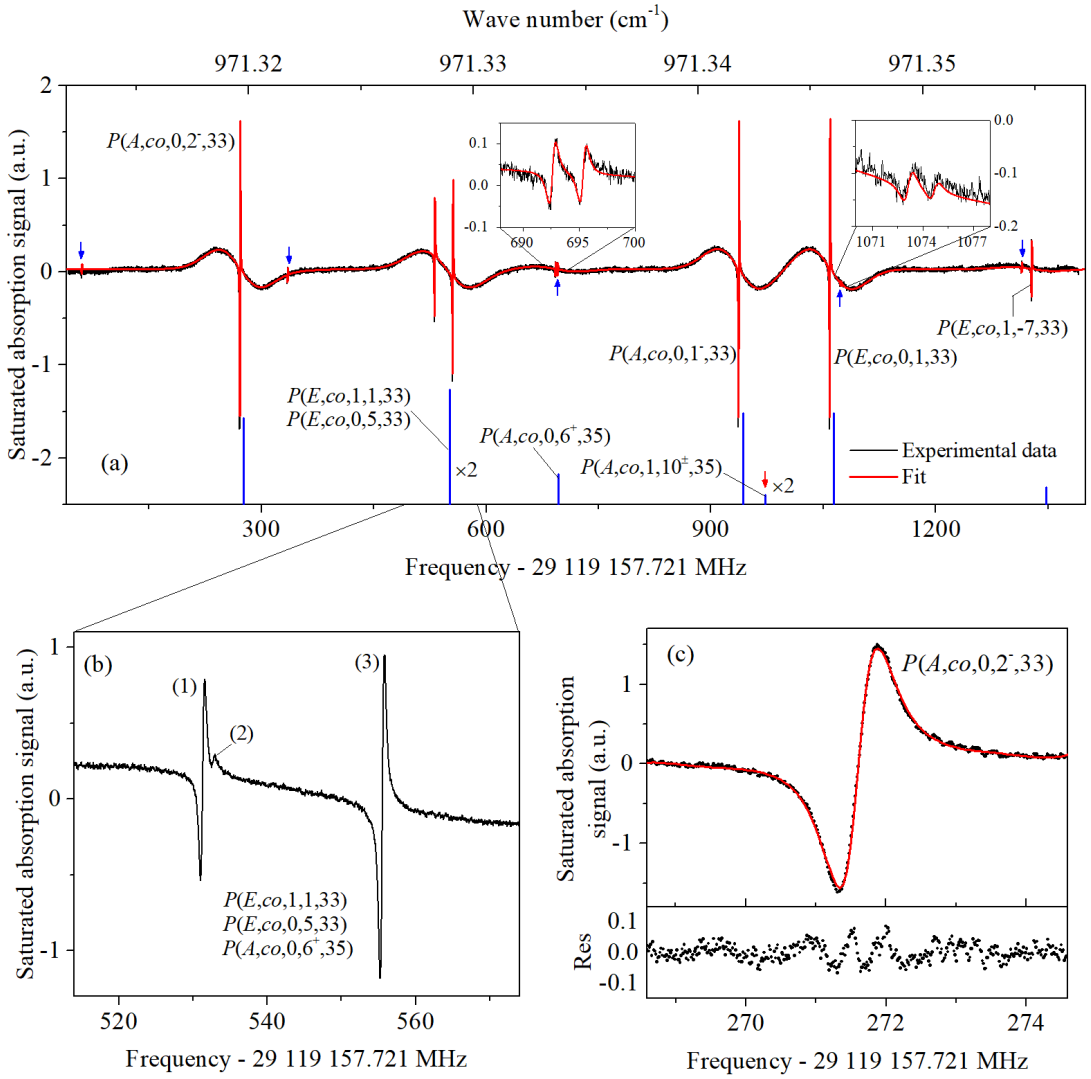

Figure 4.39 – (a) Saturated absorption spectrum of methanol spanning ∼1.35 GHz recorded using frequency modulation and first-harmonic detection (black curve). Blue sticks indicate the line frequency positions reported in the HITRAN database [54]. Experimental conditions: pressure, 1.5 Pa; modulation frequency, 20 kHz; frequency modulation excursion, 250 kHz; frequency step, ∼15 kHz; average of five pairs of scans of opposite frequency sweep direction; total integration time per point, 100 ms, whole spectrum measurement time, 9000 s. The oscillations in the baseline result from the Doppler contribution to the line shape. (b) A zoom of the saturated absorption spectrum at around 971.328 cm^{-1}. Lines (1-3) are tentatively assigned to the $P(E, co, 1, 1, 33)$, $P(E, co, 0, 5, 33)$, and $P(A, co, 0, 6^+, 35)$ rovibrational transitions without deciding which one is which. (c) Saturated absorption spectrum of the $P(A, co, 0, 2^-, 33)$ rovibrational transition of methanol averaged after one up and down scan. The red solid curve is the fit of the saturated absorption line shape model (given by Equation 4.13) to the data. The residuals are shown on the bottom graph.

Table 4.10 – Line-center frequencies of rovibrational transitions of methanol shown in Figure 4.39 and corresponding values reported in the HITRAN database when a match is possible [54]. The uncertainties of the transitions are conservatively estimated from the know-how gained in our metrological study of methanol (see Table 4.6 and subsection 4.6.3).

Line	HITRAN (cm^{-1})	This work (kHz)		Corrected − HITRAN (kHz)
		Observed (statistical uncertainty)	Corrected (total uncertainty)	
-	-	29 119 218 282.8 (150.0)	29 119 218 290.9 (150.2)	-
$P(A, co, 0, 2^-, 33)$	971.31977	29 119 429 314.0 (6.8)	29 119 429 322.1 (9.9)	−4 813.1
-	-	29 119 492 875.6 (47.3)	29 119 492 883.7 (47.9)	-
$P(E, co, 1, 1, 33)$	971.32894	29 119 689 030.2 (21.7)	29 119 689 038.3 (22.9)	
$P(E, co, 0, 5, 33)$		29 119 690 650.9 (200.0)	29 119 690 659.0 (200.4)	
$P(A, co, 0, 6^+, 35)$?	971.33377	29 119 713 236.5 (10.4)	29 119 713 244.6 (12.7)	
$P(A, co, 1, 10^\pm, 35)$?	971.34300	29 119 850 345.0 (150)	29 119 850 353.1 (150.5)	
		29 119 853 058.2 (150)	29 119 853 066.3 (150.5)	
$P(A, co, 0, 1^-, 33)$	971.34199	29 120 094 738.6 (5.2)	29 120 094 746.7 (8.9)	−5 527.3
$P(E, co, 0, 1, 33)$	971.34604	29 120 216 331.8 (6.5)	29 120 216 339.9 (9.7)	−5 350.1
$P(A, co, 1, 10^\pm, 35)$?	971.34300	29 120 230 841.1 (200)	29 120 230 849.2 (200.4)	
		29 120 232 434.4 (200)	29 120 232 442.5 (200.4)	
-	-	29 120 472 378.8 (150)	29 120 472 386.9 (150.2)	-
$P(E, co, 1, -7, 33)$	971.35548	29 120 485 592.4 (34.3)	29 120 485 600.5 (35.1)	−19 093.6

?: tentative assignments.

using Table 4.6. We list in Table 4.10 the line-center frequencies of the transitions and their uncertainties, including: (i) observed frequencies (without power and pressure corrections) with estimated uncertainties and (ii) corrected frequencies at zero-power and zero-pressure with total uncertainties.

Of particular interest, two low-intensity doublets can be resolved around 971.334 and 971.346 cm^{-1} in our spectrum (see insets of Figure 4.39(a)). The frequency difference between the two transitions of the doublets are 2.66 (0.07) and 1.70 (0.16) MHz, respectively. This demonstrates the high sensitivity of our high-resolution spectrometer. As indicated by the red arrow, the K-doublet $P(A, co, 1, 10^{\pm}, 35)$ of methanol is reported as degenerate in the HITRAN database at 971.34300 cm^{-1} with the same line intensities of 3.5×10^{-23} $cm^{-1}/mol.cm^{-2}$ for the two components of the doublet. However, no rovibrational transition of methanol is observed in this area. One of the resolved doublets around 971.334 and 971.346 cm^{-1} might be this $P(A, co, 1, 10^{\pm}, 35)$ K-doublet.

Moving to the spectral window around 971.328 cm^{-1}, three rovibrational transitions of methanol (two intense and one very weak) are resolved in our spectrum and labelled as lines (1), (2), and (3) (see Figure 4.39(b)). Absolute frequencies of these lines are listed in Table 4.9. Without being able to decide which one is which, we tentatively assign them to the three lines indicated in Figure 4.39(b). In Ref. [239], three transitions $P(E, co, 1, 1, 33)$, $P(E, co, 0, 5, 33)$, and $P(A, co, 0, 6^{+}, 35)$ are listed at the same degenerate frequency of 971.32880 cm^{-1}. In comparison, in the HITRAN database, the $P(E, co, 1, 1, 33)$ and $P(E, co, 0, 5, 33)$ transitions are reported at a degenerate frequency of 971.328940 cm^{-1} with corresponding line-intensities of 4.977×10^{-22} and 3.234×10^{-23} $cm^{-1}/mol.cm^{-2}$, and the $P(A, co, 0, 6^{+}, 35)$ transition is reported at 971.33377 cm^{-1} with a line-intensity of 2.199×10^{-23} $cm^{-1}/mol.cm^{-2}$. As shown in Figure 4.39(a), the position of the $P(A, co, 0, 6^{+}, 35)$ rovibrational transition of methanol reported in the HITRAN database could correspond to observed doublet transitions at ~971.334 cm^{-1} rather than to one of the three lines (1-3) in Figure 4.39(b), but the intensity does not match. In Table 4.9, we report the line-center frequencies of transitions (1), (2), and (3) and we assign this triplet to the three lines discussed here without deciding which one is which.

4.8.2 Spectral coverage

The tuning capability is also achievable anywhere in the entire QCL spectral range allowing to take full advantage of the QCL's tunability. Figure 4.40 shows 38 rovibrational transitions of methanol, that have been recorded in a spectral window covering about 90 GHz, i.e. anywhere where sufficient power is available for locking the QCL to the OFC. In particular, this allows us to access regions inaccessible to frequency-stabilized CO_2 lasers typically used so far by us and others for precise spectroscopic measurements in this region (red and green bars in Figure 4.40).

The combination of broad spectral coverage and high-resolution allowed us not only to detect many molecular resonances of methanol but also to resolve K-type doublets of the molecule to our knowledge resolved for the first time.

Note also that the spectral coverage of our setup can be extended to the entire 8-13 μm range without any modification of the comb or non-linear crystal but using a series of QCLs of adjacent emission spectrum (see section 3.3.1).

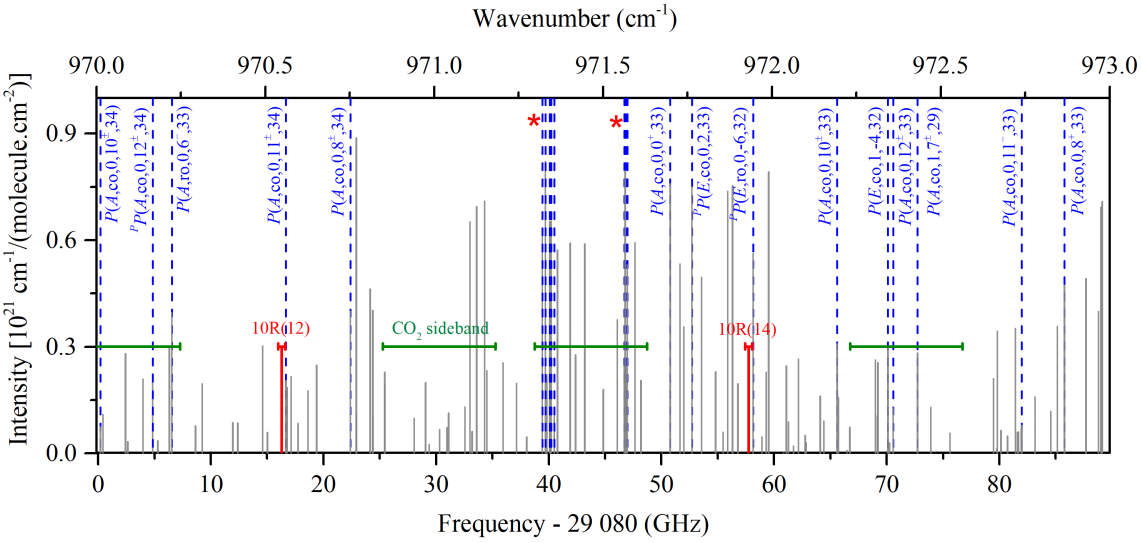

Figure 4.40 – Spectral range coverage. Black solid sticks: spectrum of methanol simulated using the HITRAN data [54]. Blue dashed sticks: methanol lines whose absolute frequencies have been measured by us (see sections 4.6 and 4.7 and subsection 4.8.1). The spectral range covered is of ∼90 GHz. The red asterisks pinpoint the data shown in Figure 4.17 (around 971.75 cm^{-1}) and Figure 4.38 (around 971.56 cm^{-1}). The red sticks: CO_2 laser's lines. Red bars and greens bars are the spectral tuning ranges reachable with CO_2 lasers at LPL, using acousto-optic modulator (red bars) or a custom-made microwave electro-optical modulator (green bars) [199] available in the laboratory.

4.9 Conclusion

In this chapter, we described the development of a high resolution mid-IR spectrometer based on the comb-assisted QCL. The use of the multipass cell provides high detection sensitivity allowing relatively high-J (around 30) rovibrational lines to be probed at the low pressures required for ultra-high resolution measurements. This unique spectrometer provides an unprecedented combination of resolution, tunability, and frequency and detection sensitivity around 10 μm.

We have demonstrated Doppler-limited spectroscopy of methanol in the P-branch of the C-O stretching mode using a free-running QCL. Many low-intensity rovibrational transitions of the molecule, that are not reported so far, have been observed and subtle structures have been resolved most probably for the first time.

We have reported the experimental setup for acquiring saturated absorption spectroscopy of methanol in the multipass cell using the SI-traceable QCL and the frequency-modulation technique. We used the novel experiment to carry out saturated absorption spectroscopy of rovibrational lines of methanol in a spectral window between 970 and 973 cm^{-1} (∼90 GHz), corresponding to ∼50% of the QCL's tuning range. This allows some methanol rovibrational frequencies to be determined with a ∼1 kHz statistical uncertainty and a sub-10 kHz global uncertainty. This corresponds to a relative uncertainty of a few 10^{-10}, which is a factor of 2000 improvement over previous measurements performed using Fourier transform infrared (FTIR) spectroscopy [238] which have led to the current edition of the HITRAN database [54]. These uncertainties are mainly limited by two systematic effects:

– The "line fitting" systematic effect which results from to the lack of knowledge of the correct model for the line shape and covers the multipass cell-induced profile complication, the asymmetry issue and the difficulties resulting from interference fringes affecting the baseline. The associated uncertainty is estimated to be between 5 kHz and 10 kHz depending on the signal-to-noise ratio.

– The gas-lens effect associated to the clipping of the QCL beam at the mirror hole of the cell (see subsection 4.6.1.2) resulting in an uncertainty at the level of 5 kHz.

Furthermore, the developed setup allowed us to probe several singular K-doublets of methanol for $K = 7$ and 10 related to J-localized perturbation between two J-series of states of two different vibrational modes of methanol. To our knowledge, they are resolved for the first time.

We demonstrated continuous tunability over a span of 1.35 GHz, a 10-fold improvement compared to previous measurements at such ultra-high levels of spectral purity [45]. It is a major advance allowing us to continuously scan the QCL frequency at the precision of the ultra-stable near-IR reference with traceability to the primary standards. In the latter, the QCL frequency was swept by scanning the frequency of a radio-frequency reference signal of a PLL used to phase-lock the QCL onto the OFC, and so the scanning window was limited to about half of the comb repetition rate, i.e. about 100 MHz. The continuous span range could be further increased by a factor three by improving the tuning capabilities of our OLO setup.

Our experimental data can be used for calibrating spectra of other experiments. They also may be used to refine the modelling of the methanol molecule.

Other saturated absorption spectroscopy measurements in the C-O stretch vibrational mode of methanol are found in the literature. The frequencies of almost 700 transitions have, for instance, been measured from 1016 to 1063 cm^{-1} with an accuracy of the order of 100 kHz using a CO2-laser-microwave-sideband spectrometer [234, 242, 247, 248]. Most of those, however, belong to the Q and R branches, with a small fraction only of low J lines in the P branch. There is, to our knowledge, only one other frequency measurement of a weak absorption line around 947.7 cm^1 with an uncertainty of 2.4 kHz comparable to ours.

At the exception of the three transitions around 971.944 cm^{-1}, which is a very peculiar case (we resolve lines that were unresolved before, see subsection 4.6.2.3), we find that the line-center frequencies are typically shifted by a few MHz to the red of the frequencies reported in the HITRAN database (see Tables 4.5,4.8, and 4.7). This shift is much higher than any systematic effects. It is consistent with deviations observed between previously measured CH_3OH saturated absorption spectroscopy data [242, 247, 248] and the FTIR data contributing to the HITRAN database [237, 238]. This discrepancy has been attributed to calibration imperfections of FTIR spectrometers as discussed in [234, 238, 260].

Finally, the know-how gained in our metrological study of methanol allows us to establish meaningful uncertainty budgets for the resonance frequencies of methanol and other molecules (see chapter 5).

CHAPTER 5

High-resolution spectroscopy of trioxane and ammonia

Contents

5.1 Introduction 181
5.2 High-precision spectroscopy of trioxane 182
5.2.1 Introduction 182
5.2.2 Direct absorption spectrum of the ν_5 vibrational mode of trioxane 184
5.2.3 Saturated absorption spectroscopy in the ν_5 vibrational mode of trioxane 185
5.2.4 Broadband saturated absorption spectra of trioxane 190
5.2.5 Spectroscopic constants of trioxane 198
5.2.6 Summary 200
5.3 Hyperfine structure in ammonia 200
5.3.1 Introduction 200
5.3.2 The hyperfine structure in ammonia 200
5.3.3 Saturated absorption spectroscopy of the ν_2 vibrational mode $as R(1,1)$ ammonia transition 205
5.3.4 Hyperfine structure analysis and spectroscopic parameters . . . 205
5.3.5 Summary 209

5.1 Introduction

In this chapter, we demonstrate the potential of the instrumentation developed in the previous chapters for carrying out precise and broadband spectroscopic measurements of various molecules in the spectral window accessible with the QCL. We focus here on the study of trioxane and ammonia, which absorb in the spectral window of our QCL. The know-how gained in our metrological study of methanol (see previous chapter) allows us to establish meaningful uncertainty budgets for the resonance frequencies of trioxane and ammonia. Trioxane, with 12 atoms, is probably one of the largest molecule, if not the largest, for which saturated absorption spectroscopy is demonstrated and shows potential for frequency metrology and frequency calibration as it could provide an almost continuous set of precise references in the 10 μm region. We also unravel the hyperfine structure of an ammonia transition previously inaccessible with standard ultra-stable lasers such as frequency stabilized CO_2 lasers.

5.2 High-precision spectroscopy of trioxane

5.2.1 Introduction

Trioxane $(CH_2O)_3$, shown in the inset of Figure 5.1(a), is a three-unit cyclic polymer of formaldehyde. It is one of the smallest members of a class of molecules called polyoxymethylene (POM) $(CH_2O)_n$. Trioxane and other various forms of POM have been proposed as extended sources of formaldehyde in cometary comae, making them important molecules in studies of prebiotic chemistry [262, 263]. Although they have been studied in laboratory simulations of cometary conditions [262], they have not been unambiguously detected yet in real cometary. Trioxane is also an important molecule for the realization of optically-pumped far-infrared gas lasers [264], in particular now that QCLs, which are widely available in the mid-IR region, can be used as pump lasers [265, 266]. As will be shown here, it might also be used in frequency metrology and frequency calibration given the almost continuous set of transitions that can be potentially used as precise frequency references in the 850-1100 cm^{-1} spectral window

Trioxane is an oblate symmetric molecule belonging to the C_{3v} symmetry group. The 17 rovibrational fundamental modes of the molecule were first assigned by A.T. Stair and J. Rud Nielsen [267]. The microwave spectrum of this molecule is well known. In 1964, the rotational constants of trioxane for the ground state and low-lying excited states was measured by T. Oka et al [268]. J.M. Colmont and co-workers then restudied the ground state [269, 270] and analyzed the excited vibrational states below 850 cm^{-1}: ν_7, ν_{19}, ν_{20}, $2\nu_{20}$, $\nu_7 + \nu_{20}$, $\nu_{19} + \nu_{20}$, reporting a set of rotational parameters for these [269, 271, 272]. In 1989 J. Gadhi et al [270] and then in 1996, H. Klein [273] measured rotational spectrum of trioxane with high resolution up to 947 GHz, enabling to determine accurate constants for the ground state. In 1992, the molecular parameters of the ν_{17} mode centered around 1072 cm^{-1} were measured by J.F. Henninot *et al* [274] using linear absorption spectroscopy with a CO_2 laser. More recently, B.M. Gibson et al [275] have determined the spectroscopic parameters of the ν_{16} mode centered around 1177 cm^{-1} by using Doppler-limited absorption spectroscopy with a QCL. For the ν_5 CO stretching mode, D. Dangoisse measured the absolute frequency of six trioxane rovibrational transitions (three transitions in the P branch, two in the Q branch, and only one in R branch) with an uncertainty of about 40 MHz using a CO_2 laser [264]. Molecular parameters of the $\nu_5 = 1$ first excited vibrational mode were also determined at relatively low precision.

In the 1000 cm^{-1} region, three intense vibrational modes are active in the infrared region. The first one is the ν_{18} mode centered around 944 cm^{-1}, that corresponds to the rocking vibration of the methyl group (CH_2). The others are the ν_5 and ν_{17} vibrational modes, which correspond to the symmetric and antisymmetric stretching vibrations of the C-O bond. They are centered around 977 and 1070 cm^{-1}, respectively. In this work, we focus on the high-resolution spectrum of the ν_5 vibrational mode of the molecule.

Figure 5.1 shows a Fourier transform infrared (FTIR) spectrum at room temperature of the ν_5 vibrational mode of trioxane. This spectrum was recorded at MONARIS by P. Asselin and co-workers using a Bruker IFS 120 HR interferometer at a resolution of 0.0025 cm^{-1} in a White-type 16-path cell resulting in a 5 m absorption length [276]. It consists of the Q branch in the center, the P branch (at low frequency side), and the R branch (at high frequency side). Hot bands are also visible in this spectrum. Each branch is

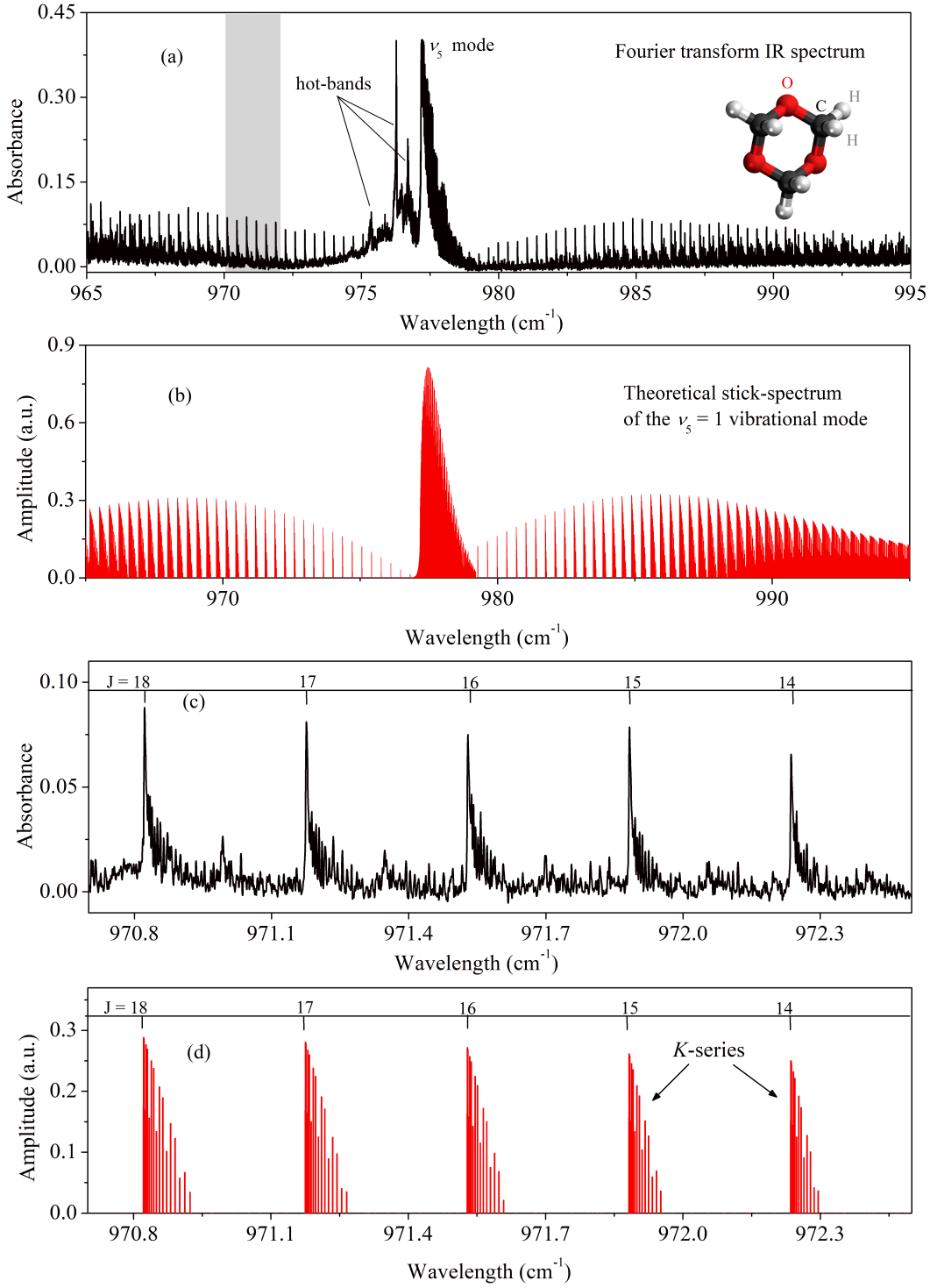

Figure 5.1 – (a) Cell-FTIR room-temperature spectrum of the 965-995 cm^{-1} region of trioxane recorded with a resolution of 0.0025 cm^{-1} recorded at MONARIS by P. Asselin et al [276]. The grey area on the left refers the spectral coverage of our QCL (from 968 cm^{-1} to 973 cm^{-1}). (b) Theoretical stick-spectrum of the $\nu_5 = 1$ vibrational mode of trioxane from 945 to 1010 cm^{-1} (see text for description). (c) and (d) Zooms of the FTIR spectrum and the theoretical stick-spectrum, respectively, from 970.7 to 972.5 cm^{-1} exhibiting five sub-branches (J ranging from 14 to 18).

composed of sub-branches for which J (the total rotational angular momentum quantum number) is fixed. Each sub-branch is composed of transitions which are unresolved in the spectrum shown, each corresponding to a different value of K (the quantum number for the projection of the total rotational angular momentum on the molecular symmetry axis), see Figure 5.1. Figure 5.1(b) displays a theoretical stick-spectrum (red sticks), that is calculated from a preliminary theoretical model under construction by P. Asselin and B. Darquié (see subsection 5.2.1). This model, that will not be detailed here, results from the assignment of the MONARIS FTIR spectrum and of about 100 saturated absorption transitions of trioxane belonging to the P and Q branches recorded at LPL in a 58-cm long cell using an ultra-stable CO_2 laser (see Appendix C). It simulates the position of the lines with a sub-MHz uncertainty. Figure 5.1(c) and (d) show zooms of the FTIR spectrum and the theoretical stick-spectrum of trioxane, respectively, with J ranging from 14 to 18.

Rovibrational transitions between the ground and the first excited state are designated by $P(J,K)$, $Q(J,K)$, and $R(J,K)$. The main capital letter P, Q, and R correspond to $\Delta J = -1$, 0, and 1, respectively, where J and K are the ground state rotational quantum numbers. The ν_5 mode is a parallel band for which rovibrational transitions obey $\Delta K = 0$.

In this section, we present Doppler-limited and saturated absorption spectra of rovibrational transitions of trioxane belonging to the ν_5 vibrational mode at room temperature, observed in the multipass absorption cell. Then, we report line-center frequencies of about 300 rovibrational transitions of trioxane around 10 μm. Some of these transitions will be used to determine the spectroscopic rotational constants in the first excited state $\nu_5 = 1$ of trioxane and the band center frequency.

5.2.2 Direct absorption spectrum of the ν_5 vibrational mode of trioxane

We use the experimental setup described in section 4.3 to measure the direct absorption spectrum of trioxane. The crystalline trioxane sample is contained in a glass tube. Its vapour pressure at room temperature is about 750 Pa. A controlled pressure of trioxane is injected into the multipass absorption cell via a leak-valve. The frequency of the free-running QCL is tuned through several rovibrational transition of trioxane following the same procedure as that used for recording Doppler broadened spectra of methanol (see section 4.3). The direct absorption spectrum of the molecule is acquired using an oscilloscope.

In order to determine the frequency scale of the spectrum, we follow the same procedure as used for methanol (see section 4.3). First, a list of central positions of trioxane transitions is obtained by fitting the recorded spectrum with Gaussian spectral lineshape. After that, the frequency scale is retrieved by making an interpolation of this list with a set of corresponding absolute frequencies, that is obtained from the saturated absorption measurements described in the next section.

We have used the multipass cell to record one direct absorption spectrum in the sub-branch $P(J = 16, K)$ of room temperature trioxane in the multipass absorption cell around 971.55 cm^{-1}. The pressure of trioxane is about 3 Pa. Figure 5.2(a) shows the spectrum after retrieval of the absolute frequency scale together with the corresponding cell-FTIR spectrum. Our frequency scale's uncertainty is expected to be below 3 MHz, that is mainly limited by the fitting errors (i.e. errors of the fitted central positions and

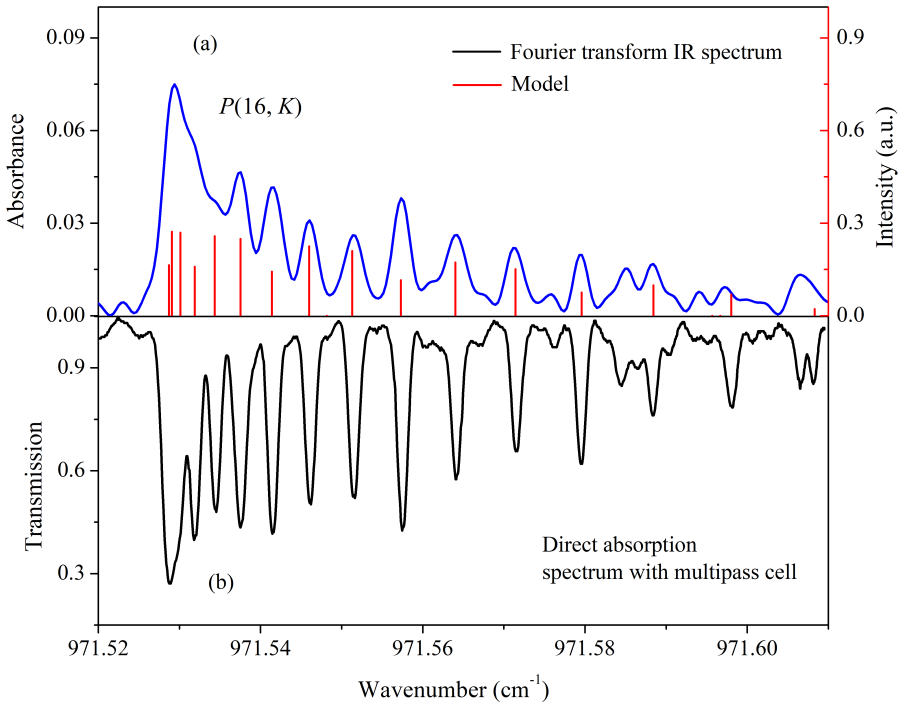

Figure 5.2 – (a) Fourier transform room-temperature spectrum of the ν_5 band of trioxane (zoom of the spectrum shown in Figure 5.1, see details in subsection 5.2.1) together with a calculated stick-spectrum (red sticks, see subsection 5.2.1) ranging from 971.52 to 971.61 cm^{-1}. (b) Direct absorption spectroscopy of room temperature trioxane recorded in the multipass cell with the free-running QCL.

of the interpolation). The Gaussian FWHM linewidth of the spectrum is found to be ∼44 MHz, in agreement with the expected value.

5.2.3 Saturated absorption spectroscopy in the ν_5 vibrational mode of trioxane

5.2.3.1 Spectrum acquisition

We have performed saturated absorption spectroscopy of trioxane by using our high-precision widely-tunable SI-traceable QCL spectrometer (see description in section 4.1). The 10.3 μm QCL is phase-locked to the n^{th} harmonic of the comb repetition rate, itself stabilized to the ultra-stable optical local oscillator (OLO). By scanning the OLO frequency, the QCL frequency can be tuned through several absorption lines of trioxane (see section 3.5 for more details).

As mentioned in subsection 3.5.1, before 2019 the frequency tuning range of the comb-assisted QCL was limited to 450 MHz due to the piezo-electric actuator used to act on the comb's cavity length. Since 2019 continuous tuning over 1.35 GHz is possible when both the piezo-electric actuator and the stepper motor are used (see subsection 3.5). It is noted that the saturated absorption spectra of trioxane presented in this work were recorded before the upgrade.

Saturated absorption spectra of trioxane have been recorded at room temperature in the multipass absorption cell at a typical pressure ∼1.5 Pa using frequency modulation

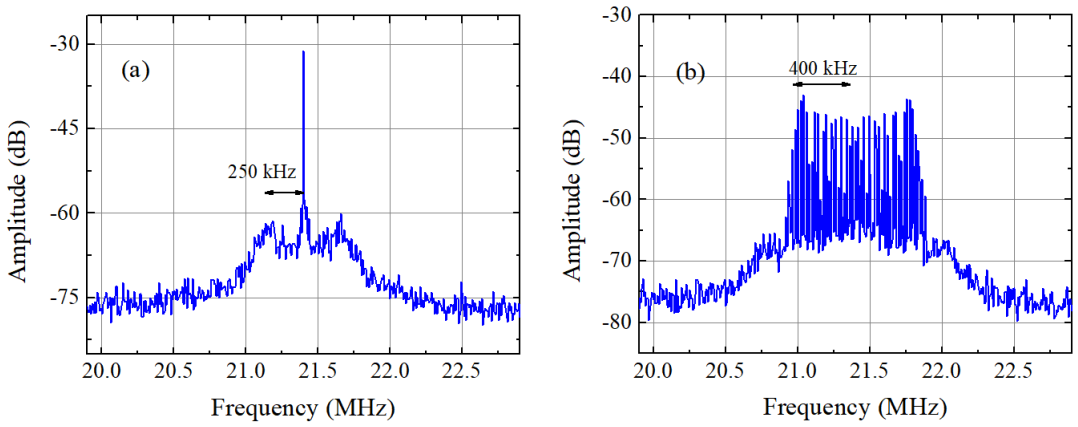

Figure 5.3 – In-loop beat-note signals at 21.4 MHz between the QCL and the OFC (a) in the absence of the frequency modulation and (b) in the presence of the frequency modulation: $f_m = 20$ kHz, $\Delta\nu_m = 400$ kHz (see subsection 4.1.3 for the definition of those parameters).

and third-harmonic detection (see subsection 4.1.3 for the description of the frequency modulation procedure). Figure 5.3 shows beat-note signals between the QCL and the n^{th} harmonic of the repetition rate of the OFC centered at a frequency of 21.4 MHz when the phase-lock loop PPL3 (see Figure 4.1) is closed. As shown in panel (b) of the figure, a high frequency modulation excursion of 400 kHz has been used in order to improve the signal-to-noise ratio (SNR) of the spectra. Each sub-Doppler spectrum is acquired by tuning the QCL frequency over ∼300 MHz (corresponding to ∼1.73 GHz of the OLO). We carry out frequency scans in both sweep directions, with increasing and decreasing frequencies and consider only the average of such a pair of up and down scans. The absolute frequency scale is obtained by using the radio-frequency protocol, as described in subsection 3.4.3.

Figure 5.4(a) (black points) shows an example of a saturated absorption spectrum of trioxane recorded with a span of 255 MHz, ranging from 971.527 to 971.536 cm^{-1}. It shows five high-intensity rovibrational transitions of the P-branch ($J = 16$ sub-branch) of the ν_5 vibrational mode with K ranging from 0 to 4. Moreover, five low-intensity rovibrational transitions are also visible. They are likely rovibrational transitions belonging to hot bands (transitions starting from vibrationally excited states of low frequency modes, such as ν_{19} (305 cm^{-1}), ν_7 (467 cm^{-1}), or ν_{18} (525 cm^{-1}) [276]). Figure 5.4(b) shows a saturated absorption spectrum of a low-intensity non-assigned rovibrational transition around 971.53036 cm^{-1}. Figure 5.4(c) shows a saturated absorption spectrum of the high-intensity $P(16, 4)$ rovibrational transition around 971.53766 cm^{-1}. The red lines are fits to the data. In Figure 5.4, each transition is fitted with a model, that is similar to the one used in the previous chapter for the analysis of methanol (Equation 4.17) except that here, the small asymmetric contribution is absent as it is not essential for the following discussion. The transitions exhibit a peak-to-peak linewidth of ∼410 kHz (FWHM Lorentzian linewidth ∼740 kHz). Considering the $P(16, 4)$ rovibrational transition shown in Figure 5.4(c), it is obvious that the spectrum is distorted because of the high frequency excursion used for the QCL frequency modulation. We thus had to use a model that takes into account this distortion for a proper analysis of those data. A

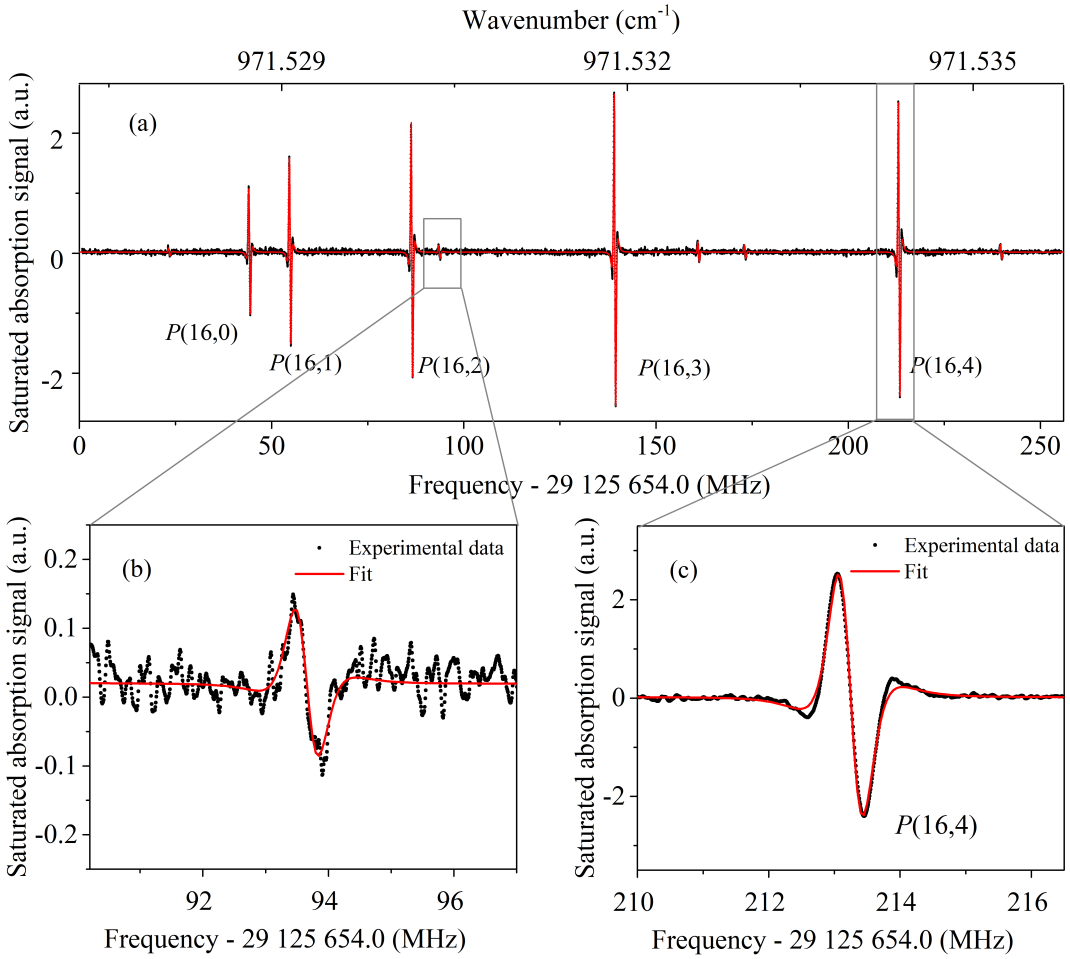

Figure 5.4 – (a) Saturated absorption spectrum of trioxane spanning ∼255 MHz recorded using frequency modulation and third-harmonic detection (black dots). The red solid line is a fit to the data. Each line is fitted with a theoretical profile combining a zeroth-order polynomial function and the third derivative of a Lorentzian. Experimental conditions: pressure, 1.5 Pa; modulation frequency, 20 kHz; frequency modulation excursion, 400 kHz; frequency step, ∼7.77 kHz; average of a pair of up and down scans; total integration time per point, 10 ms; whole spectrum measurement time, 340 s. (b) Zoom on a non-assigned low-intensity transition around 971.53036 cm^{-1}. (c) Zoom on the $P(16, 4)$ transition of trioxane around 971.53766 cm^{-1}.

complete theoretical line shape model that involves the modulation-induced distortion is described in the next section.

5.2.3.2 Line shape

As mentioned above, a high frequency modulation excursion allows us to improve the SNR of the sub-Doppler spectrum. However, it distorts the spectrum and the determination of the line-center frequency of the rovibrational transitions of trioxane may suffer from systematic shifts if the line shape model does not include this distortion. The signal $S_{nf}(\Delta\nu_m, \nu)$ detected at n^{th} harmonic detection of lock-in amplifier, is given by

$$S_{nf}(\Delta\nu_m, \nu) = b(\nu) + s_{nf}(\Delta\nu_m, \nu), \tag{5.1}$$

in which the first term describes the baseline, the second term describes the saturated absorption line shape, and $\Delta\nu_m$ is the frequency modulation excursion. As seen in subsection 4.4.2.1, for the first-harmonic detection ($1f$), a high-order polynomial baseline was required in order to fit the Gaussian profile and the residual interference fringes. For second- ($2f$), third- ($3f$), and higher-harmonic detections, the baseline is simplified to an offset s_0 (see for instance Figure 4.21 for methanol and Figure 5.4(c) for trioxane). The detected signal $S_{nf}(\Delta\nu_m, \nu)$ for $n > 1$ thus reduces to

$$S_{nf}(\Delta\nu_m, \nu) = s_0 + s_{nf}(\Delta\nu_m, \nu). \tag{5.2}$$

Theoretical models for frequency modulation spectroscopy have been studied by several authors, such as R. Arndt [251], J. Reid and D. Labrie [277], and J. M. Supplee and co-worker [278]. However, these investigations did not take into account the intensity modulation that results from the frequency modulation of the laser and that most probably is the source of the asymmetry observed in our methanol data (see subsection 4.4.2.1). Based on Arndt's model which considers a pure frequency modulation, a rigorous theoretical description of the line shape obtained in frequency modulation spectroscopy taking into account the combined frequency modulation and intensity modulation was developed by S. Schilt et al [279]. This description was developed to model direct absorption spectroscopic measurements at high pressure and thus considers a Lorentzian line shape and takes into account the Beer-Lambert law. We have made straight forward modifications to adapt it to our case of a Lorentzian line shape with no contribution from the Beer-Lambert law. We write the detected signal $s(\nu)$ in the following form

$$\begin{aligned} s(\nu) = {} & A\left[B_1\nu_c - B_2\Delta\nu_m\cos(2\pi f_m t) - \nu_0 + 1\right] \\ & \times \frac{1}{\pi}\frac{\gamma}{\left[\nu_c - \Delta\nu_m\cos(2\pi f_m t + \Psi) - \nu_0\right]^2 + \gamma^2}, \end{aligned} \tag{5.3}$$

in which A are the height of the signal, f_m is the frequency modulation, $\Delta\nu_m$ is the frequency modulation excursion, γ is the HWHM linewidth, B_1 and B_2 are the asymmetry factors related to intensity modulation for quasistatic frequency and for the modulation frequency, respectively (see below) and Ψ is the phase shift between the intensity modulation and frequency modulation.

We have basically included the frequency modulation of Equation 4.3 in the line shape model already used for methanol (Equation 4.14, that has the linearly varying amplitude to take into account effects such as the linear variation of the incident optical power as

a function of the frequency). We have however introduced three subtleties:

– We have introduced a phase shift Ψ between the intensity modulation and the frequency modulation. Note that this phase shift was often introduced in the intensity modulation but we prefer to introduce it in the frequency modulation as it is probably closer to the experimental conditions. Indeed, when the laser injection current is modulated, the light intensity is simultaneously modulated whereas the modulation of the light frequency is phase shifted. In our model, the phase 0 thus corresponds to the current modulation phase.

– Unlike Equation 4.3 a negative sign is chosen in front of $\Delta\nu_m$ to obtain a zero phase shift (instead of π) at low modulation frequencies (the frequency of the QCL decreases when the current increases).

– We have introduced two different slopes B_1 and B_2 to describes the laser power variation as a function of the optical frequency, because the efficiency of the intensity modulation depends on the modulation frequency and so that the B coefficient takes a different value at the modulation frequency f_m or at the low-frequency of the ramp used to scan the laser line through the absorption feature. Note that taking $B_1 = B_2$ would correspond to exactly combine Equation 4.3 and 4.14 (apart from the sign and phase issues discussed above).

Let us denote $x = (\nu - \nu_0)/\gamma$ the normalized frequency. Following a procedure similar to those proposed by R. Arndt in his model for pure frequency modulation, the expansion of the signal into a Fourier series gives [279]:

$$s(x) = A\left[\sum_{n=0}^{\infty} s_{np}(x)\cos n2\pi f_m t - \sum_{n=0}^{\infty} s_{nq}(x)\sin n2\pi f_m t\right]. \tag{5.4}$$

Following S. Schilt et al [279], the amplitude of in-phase and quadrature terms at the n^{th} harmonic-detection are respectively given by

$$\begin{aligned} s_{np}(x) = {} & (\gamma B_1 x + 1)\cos n\Psi s_n(x) - \gamma B_1 \frac{m}{2}\left(\frac{\epsilon_n}{2} - \epsilon_n + 1\right) s_{n+1}(x) \\ & - \gamma B_2 \frac{m}{2}\left\{\frac{2}{\epsilon_{n-1}}\cos\left[(n-1)\Psi\right] s_{n-1}(x) + (\epsilon_n - 1)\cos\left[(n+1)\Psi\right] s_{n+1}(x)\right\} \end{aligned} \tag{5.5}$$

$$\begin{aligned} s_{nq}(x) = {} & (\gamma B_1 x + 1)\sin n\Psi s_n(x) - \gamma B_1 \frac{m}{2}\left(\frac{\epsilon_n}{2} - \epsilon_n + 1\right) s_{n+1}(x) \\ & - \gamma B_2 \frac{m}{2}\left\{\frac{2}{\epsilon_{n-1}}\sin\left[(n-1)\Psi\right] s_{n-1}(x) + (\epsilon_n - 1)\sin\left[(n+1)\Psi\right] s_{n+1}(x)\right\} \end{aligned} \tag{5.6}$$

in which $m = \Delta\nu_m/\gamma$, $\epsilon_0 = 1$, $\epsilon_n = 2$ for $n \geq 1$, terms $s_{n-1}(x)$, $s_n(x)$, and $s_{n+1}(x)$ are the components of the signal $s(x)$ at the n^{th} harmonic detection, that do not take into account the distortion induced by the intensity modulation (pure frequency modulation) and are given from Arndt's model [251],

$$s_n(x) = \frac{1}{2} i^n \epsilon_n \frac{\left[\sqrt{(1-ix)^2 + m^2} - (1-ix)\right]^n}{m^n \sqrt{(1-ix)^2 + m^2}} + c.c. \tag{5.7}$$

where *c.c.* is the complex conjugate. The lock-in amplifier allows us not only to detect

the in-phase and quadrature signals but also the signal $s_{n,\phi}(x)$ at any detection phase Φ_n, with respect to the phase of the intensity modulation

$$s_{nf,\Phi}(x) = [s_{np}(x)\cos\Phi_n + s_{nq}(x)\sin\Phi_n] \tag{5.8}$$

Following S. Schilt et al [279], at n^{th} harmonic detection, a signal $s_{n,\Phi}(x)$ of maximum amplitude is reached for the detection phase

$$\Phi_{n,max} = n\Psi + k\pi, \tag{5.9}$$

where k is an integer. By introducing Equation 5.9 into Equation 5.8, we obtain the signal of maximum amplitude that can be detected

$$\begin{aligned} s_{n,\Phi_{max}}(x) = (\gamma B_1 x + 1)s_n(x) - \gamma B_1 \frac{m}{2}\left(\frac{\epsilon_n}{2} - \epsilon_n + 1\right) s_{n+1}(x) \\ - \gamma B_2 \frac{m}{2}\cos\Psi\left[\frac{2}{\epsilon_{n-1}} s_{n-1}(x) + (\epsilon_n - 1)s_{n+1}(x)\right]. \end{aligned} \tag{5.10}$$

For the third-harmonic detection which is used in this section, our experimental procedure consisting in choosing the phase that maximises the signal, this formula corresponds to our experimental line shape. Such a signal can be written as

$$s_{3f,\Phi_{max}}(x) = (\gamma B_1 x + 1)s_3(x) - \gamma B_2 \frac{m}{2}\cos\Psi\left[2s_2(x) + s_4(x)\right]. \tag{5.11}$$

in which the $s_2(x)$, $s_3(x)$, and $s_4(x)$ terms are given by Equation 5.7. Note that if $B_1 = B_2 = B$, and when the frequency modulation excursion $\Delta\nu_m$ is much smaller than the spectral linewidth γ ($\Delta\nu_m \ll \gamma$), the signal $s_{nf}(\nu)$ reduces to the n^{th} derivative of the spectral line shape $s(\nu) = g(\nu) = A\left[B(\nu - \nu_0) + 1\right]L(\nu)$ with ν_0 that we have used for fitting the methanol data recorded at low index of modulation (see Equations 4.17). The saturated absorption line shape is finally given by

$$S_{3f}(x) = s_0 + s_{3f,\Phi_{max}}(x). \tag{5.12}$$

In the next section, we will fit this line shape to saturated absorption spectra of trioxane to determine absolute line-center frequencies of rovibrational transitions and other parameters.

5.2.4 Broadband saturated absorption spectra of trioxane

In this subsection, we present how wide saturated absorption spectra of trioxane spanning over few GHz are recorded. We report line-center frequencies of 314 rovibrational transition of trioxane.

5.2.4.1 Experimental procedure for recording broadband sub-Doppler spectra

As mentioned above, saturated absorption spectra presented in this chapter have been recorded before 2019. At this time, each spectrum could only be measured with a maximum continuous tuning range of ∼450 MHz. In order to extend the spectral range of saturated absorption spectrum of trioxane, we record adjacent spectra spanning typically 300 MHz, with a little bit of overlap (around few tens MHz) from one to another. After

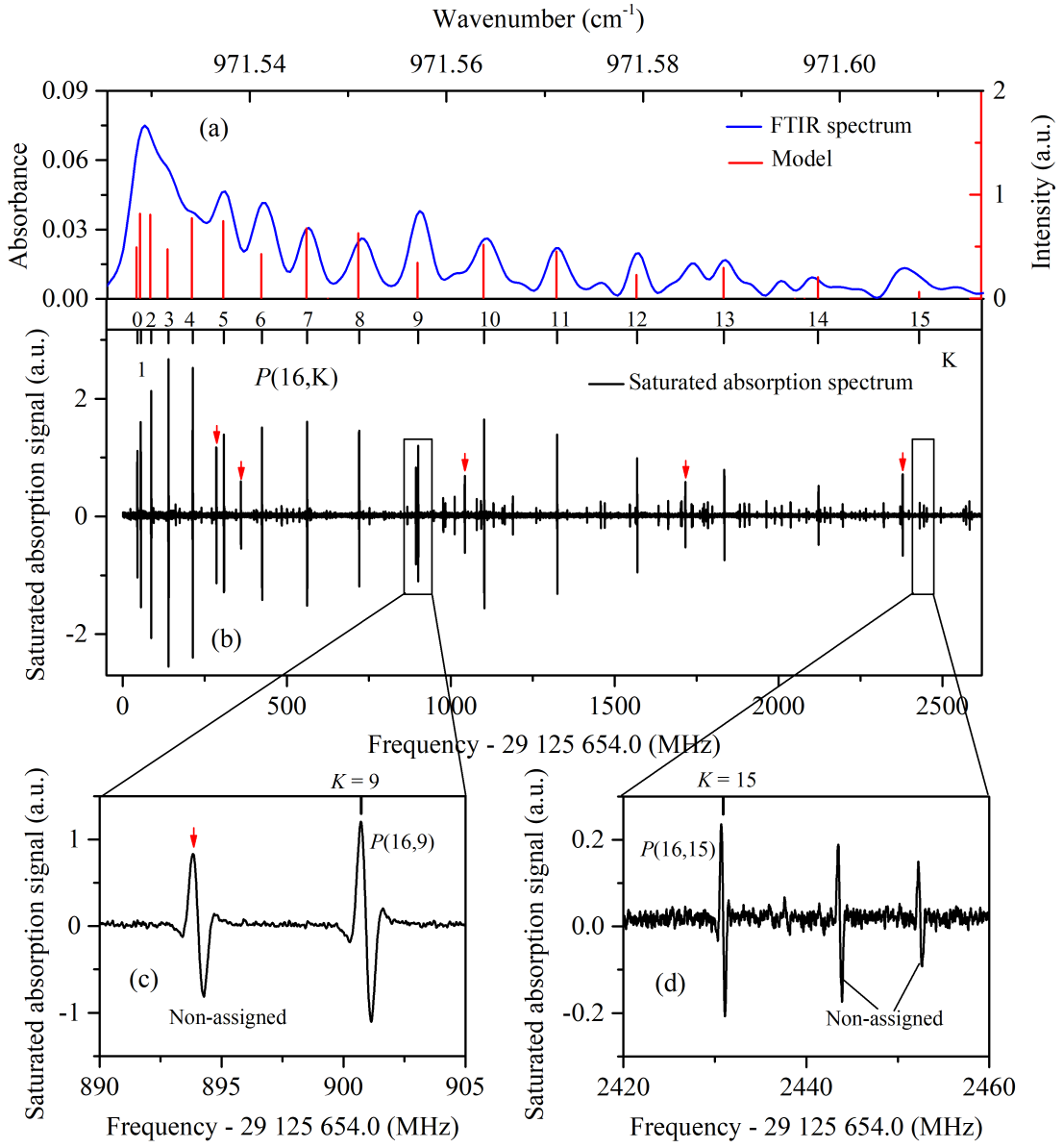

Figure 5.5 – (a) Fourier transform room temperature spectrum of the ν_5 band of trioxane (zoom of the spectrum shown in Figure 5.1, see details in subsection 5.2.1) together with a calculated stick-spectrum (red sticks, see subsection 5.2.1) ranging from 971.525 to 971.615 cm^{-1}. (b) Saturated absorption spectrum of trioxane spanning ∼2.6 GHz. High-intensity lines but not in the model are indicated with red arrows. Experimental conditions: pressure, 1.5 Pa; modulation frequency, 20 kHz; frequency modulation excursion, 400 kHz; frequency step, ∼7.77 kHz; lock-in amplifier time constant, 10 ms; step duration, 5 ms; average of a pair of up and down scans; whole spectrum measurement time, ∼3500 s. Black sticks indicate the positions of the assigned transitions from the $P(16, K)$ sub-branch and are labelled by the K quantum number. (c) A zoom showing the saturated absorption spectrum of the $P(16, 9)$ lying next to a non-assigned rovibrational transition of trioxane. (d) A zoom showing the saturated absorption spectrum of the $P(16, 15)$ lying next to two non-assigned weak rovibrational transitions of trioxane.

each measurement, we thus unlock the QCL frequency while the phase-lock loops PLL1 and PPL2 (see Figure 4.1) for locking the OLO sideband to the remote reference signal and the comb repetition rate to the OLO carrier, respectively, are kept closed. Then, we adjust the QCL current to shift the QCL frequency by about 250 MHz and lock the QCL frequency to the next harmonic of the comb repetition rate. The QCL frequency is also monitored using the optical spectrum analyser (OSA, Figure 4.2) to make sure that we phase-lock it to the neighboured harmonic of f_{rep}. This setup allows the tunability to be drastically extended. Saturated absorption spectra, obtained after such several cascaded measurements, are combined together to provide a broadband spectrum over a few GHz and even more. We however have to unlock and relock the QCL frequency between each portion of the spectrum requiring manual intervention and taking quite some time.

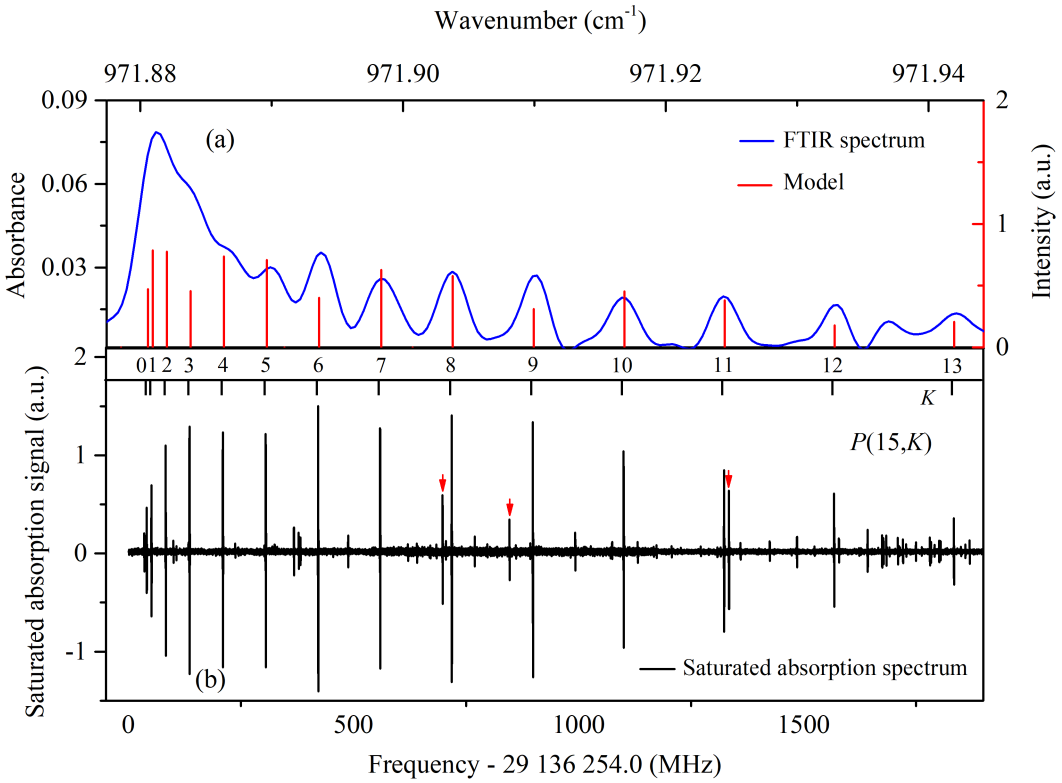

Figure 5.6 – (a) Fourier transform room temperature spectrum of the ν_5 band of trioxane (zoom of the spectrum shown in Figure 5.1, see details in subsection 5.2.1) together with a calculated stick-spectrum (red sticks, see subsection 5.2.1) ranging from 971.877 to 971.944 cm^{-1}. High-intensity lines but not in the model are indicated with red arrows. (b) Saturated absorption spectrum of trioxane spanning of ∼1.9 GHz. Experimental conditions: pressure, 1.5 Pa; modulation frequency, 20 kHz; frequency modulation excursion, 400 kHz; frequency step, ∼7.77 kHz; lock-in amplifier time constant, 10 ms; step duration, 5 ms; average of a pair of up and down scans; whole spectrum measurement time, ∼2560 s. Black sticks indicate the positions of the assigned transitions from the $P(15, K)$ sub-branch and are labelled by the K quantum number.

Figure 5.5(b) shows a saturated absorption spectrum of the sub-branch $P(J = 16, K)$ of trioxane (blue curve) spanning ∼2.7 GHz, ranging from 971.526 to 971.615 cm^{-1}. It is composed of 12 cascaded measurements. Each portion of the spectrum is recorded

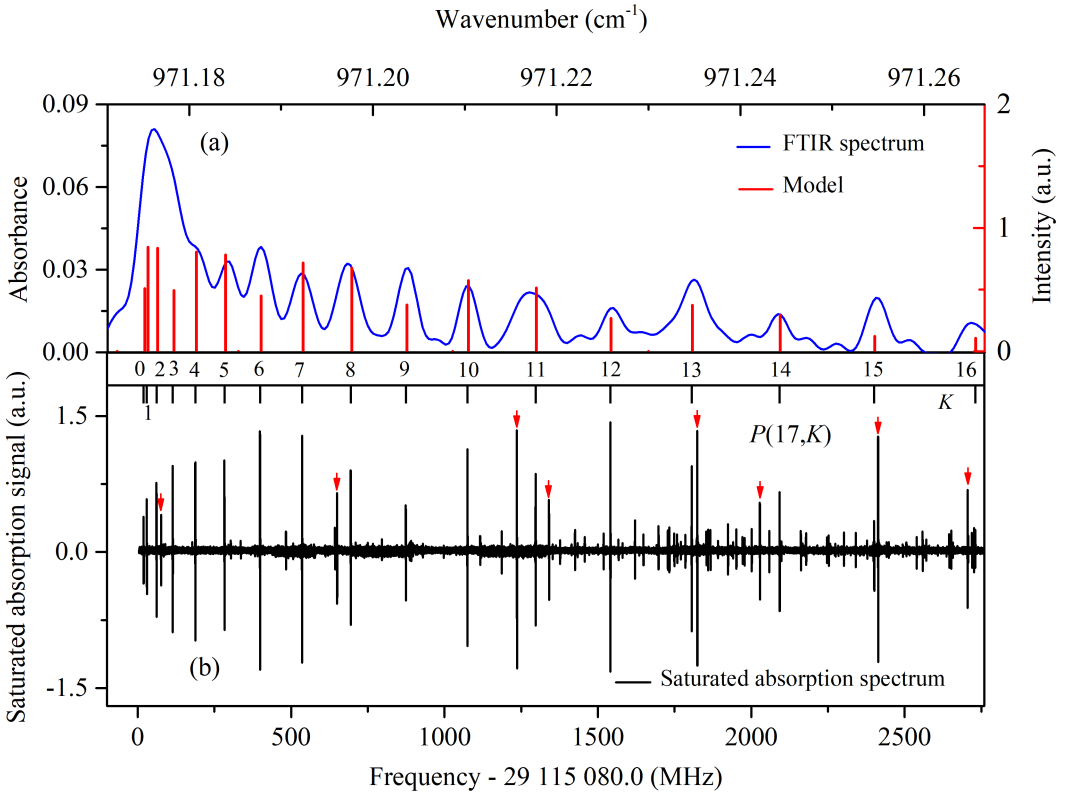

Figure 5.7 – (a) Fourier transform room temperature spectrum of the ν_5 band of trioxane (zoom of the spectrum shown in Figure 5.1, see details in subsection 5.2.1) together with a calculated stick-spectrum (red sticks, see subsection 5.2.1) ranging from 971.171 to 971.267 cm^{-1}. (b) Saturated absorption spectrum of trioxane with a span of ∼2.7 GHz. High-intensity lines but not in the model are indicated with red arrows. Experimental conditions: pressure, 1.5 Pa; modulation frequency, 20 kHz; frequency modulation excursion, 400 kHz; frequency step, ∼7.77 kHz; lock-in amplifier time constant, 10 ms; step duration, 5 ms; average of a pair of up and down scans; whole spectrum measurement time, ∼3680 s. Black sticks indicate the positions of the assigned transitions from the $P(15, K)$ sub-branch and are labelled by the K quantum number.

using frequency modulation and third-harmonic detection. It is the average of a pair of up and down scans. The experimental conditions are following: pressure of 1.5 Pa, frequency modulation of 20 kHz, frequency excursion of 400 kHz. The frequency axis of the spectrum is reconstructed using the radio-frequency protocol (see subsection 3.4.3). This spectrum exhibits 142 rovibrational trioxane lines of various strength (SNR ranging from 10 to 300). Among those, $P(16, K)$ K-series transitions of the ν_5 vibrational mode with K ranging from 0 to 15 are clearly visible. For comparison, we plot in Figure 5.5(a) the FTIR spectrum recorded at MONARIS by P. Asselin and his co-worker (black curve, zoom of the spectrum shown in Figure 5.1, see details in section 5.2.1) and a theoretical stick-spectrum (red lines), that is calculated from the preliminary theoretical model under construction (see subsection 5.2.1). The theory includes only the fundamental of the ν_5 vibrational mode. It nicely reproduces the K series of the $P(16, K)$ sub-branch, with K ranging from 0 to 16.

Most of the low-intensity lines in the spectrum are attributed to hot bands which

are not included in the theory. Most of the high-intensity lines belong to the $P(16, K)$ sub-branch, but our spectrum also exhibits relatively high-intensity lines that are not in the model. They are labelled with red arrows on Figure 5.5(b). It is not clear at that stage whether those lines belong to hot bands or result from the presence of impurities. Note that the presence of those relatively high-intensity lines is also clear in the FTIR spectrum shown in Figure 5.5(a), even if they are not resolved, and the FTIR spectrum was recorded a few years before the current QCL spectrum with a different batch of trioxane. Despite the presence of those additional relatively high-intensity lines and of many weak lines, the accuracy of the model (sub-MHz uncertainty on line positions) allows us to assign 16 lines of the $P(16, K)$ sub-branch with no ambiguity.

The positions of the assigned transitions from the $P(16, K)$ sub-branch, labelled by their K quantum number, are featured by the black sticks on the upper axis of Figure 5.5(b). We see that they coincide very well with the red sticks of the model displayed at the bottom of Figure 5.5(a). The positions of the experimental transitions of trioxane are in perfect agreement with the preliminary model. It enables us to clearly distinguish between the lines belonging to the $P(16, K)$ sub-branch and other lines, as illustrated with the two insets (c) and (d) of Figure 5.5. Inset (c) of Figure 5.5 zooms on an area where a relatively high-intensity additional line is found close to the also relatively intense $P(16, 3)$ transition, and inset (d) zooms on an area where a few weak lines are found close to the weak $P(16, 5)$ transition.

We have also carried out two other broadband saturated spectra of trioxane in the ν_5 vibrational mode, that were recorded in the same experimental conditions as those of the previous spectrum. Figures 5.6(b) shows a saturated absorption spectrum of trioxane (black curve) on a spanning range of ∼1.9 GHz (from 971.877 to 971.944 cm^{-1}) covering a part of the $P(15, K)$ sub-branch. As in Figure 5.5, Figure 5.6 compares the saturated absorption data to the FTIR data recorded at MONARIS (blue curve in Figure 5.6(a)) and theoretical model (red sticks in Figure 5.6(b)). The saturated absorption spectrum exhibits 69 rovibrational transitions of various intensities (SNR ranging from 10 to 350) with again many weak lines most probably belonging to hot bands and a few relatively high intensity lines not predicted by the model. The positions of the 14 assigned transitions from the $P(15, K)$ sub-branch, labelled by their K quantum number, are featured by the black sticks on the upper axis of Figure 5.6. The positions of these assigned transitions of trioxane are in perfect agreement with the preliminary model.

Figure 5.7 shows a similar study of the $P(17, K)$ sub-branch with saturated absorption spectrum spanning ∼2.7 GHz, ranging from 971.171 to 971.267 cm^{-1}. This spectrum exhibits 104 rovibrational transitions of trioxane (SNR ranging from 10 to 170). Among those, 17 transitions are assigned to the $P(17, K)$ sub-branch, as indicated by the black sticks on the upper axis of Figure 5.7.

5.2.4.2 Determination of line-center frequencies

In this part, we determine the absolute frequencies and linewidths of the ∼320 rovibrational transitions of trioxane shown above. They include 47 transitions assigned to the three sub-branches $P(15, J)$, $P(16, J)$, and $P(17, J)$, all other transitions being not assigned.

In order to determine line-center frequencies of each rovibrational transition of trioxane, we select a spectral range of ∼6 MHz around each transition and we fit to the data

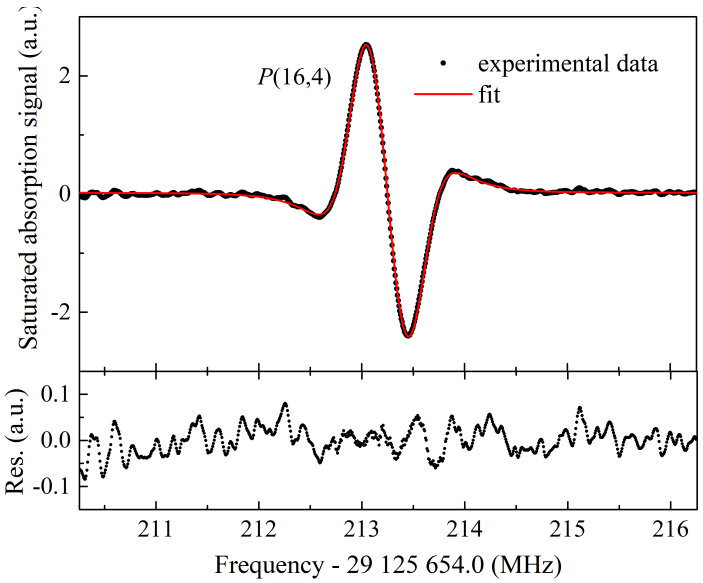

Figure 5.8 – Saturated absorption spectrum of the $P(16,4)$ rovibrational transition of trioxane, with fit and residuals. The data (black dots) are recorded using frequency modulation and third-harmonic detection. The red line is a fit to the data resulting a reduced chi-squared of 1.1. Residuals are shown on the bottom graph. Experimental conditions: pressure, 1.5 Pa; modulation frequency, 20 kHz; frequency modulation excursion, 400 kHz; frequency step, ∼7.77 kHz; average of a pair of up and down scans; total integration time per point, 10 ms; whole spectrum measurement time, ∼8 s. The red solid line is a fit to the data.

the line shape model given by Equation 5.12. We consider the average of a pair of up and down scans in order to cancel out the frequency shift induced by the limited detection bandwidth [249, 250] (see subsection 4.4.1). We assign the same error bar to all data points of the averaged spectrum. In a similar fashion to what was done in subsection 4.4.2 for methanol, this experimental error bar is calculated as the standard deviation of the residuals obtained after fitting a zeroth-order polynomial to a small portion of the spectrum far from the resonance. This error bar is roughly the same for all spectra and, depending on the line intensity, ranges from 0.28% to 10% of the peak-to-peak amplitude, corresponding SNRs ranging from 10 to 350.

For the set of 320 transitions, the reduced chi-squared obtained are ranging from 1 to 2, which confirms that our model matches well the data. As an example, Figure 5.8 shows the saturated absorption spectrum of the $P(16,4)$ rovibrational transition of trioxane, the resulting fit, and its residuals. The fit has a reduced chi-squared of ∼1.1. The fitted frequency excursion of the QCL frequency modulation is found to be 410 kHz within ±20 kHz. This is in good agreement with 400 kHz, the value we set in the direct digital synthesizer used to generate the frequency modulation (see Figures 4.5 and 5.3). This also gives confidence in the model used.

The three parameters B_1, B_2, and Ψ that account for the asymmetry of the line-shape and the residual intensity modulation can in fact not be fitted independently. Equation 5.10 shows that these are two independent parameters, namely B_1 and $B_2 \cos\Psi$. To determine a conservative error bar associated to the lack of knowledge of the correct model for the line shape that results in particular from the asymmetry and the multipass

cell induced profile complication (see section 4.4.2.1), we fit the recorded spectra using Equation 5.10 in three different ways:

1. We fix $B_1 = B_2 \cos\Psi = 0$ which corresponds to neglecting the line shape asymmetry.

2. We take $B_1 = B_2 \cos\Psi$ and leave this parameter free to be adjusted. This is compatible with having only one intensity modulation parameter, with the following physical interpretation: the intensity modulation and the frequency modulation are in phase (Ψ=0) and the efficiency of the intensity modulation is the same at the modulation frequency f_m and at the low-frequency of the ramp ($B_1 = B_2$).

3. Both B_1 and $B - 2\cos\Psi$ are independently adjusted which is compatible with the following physical interpretations: (i) the intensity modulation and the frequency modulation are in phase ($\Psi = 0$) and the efficiency of the intensity modulation is different at the modulation frequency f_m and at the low-frequency of the ramp ($B_1 \neq B_2$); (ii) their exist a non-zero dephasing Ψ between the intensity modulation and the frequency modulation but the efficiency of the intensity modulation is the same at the modulation frequency f_m and at the low-frequency of the ramp ($B_1 = B_2$); (iii) $\Psi \neq 0$ and ($B_1 \neq B_2$), which is the general case, but again, the experiment does not allow us to independently estimate these three parameters.

Table 5.1 – Uncertainty budget table for the absolute line-center frequency measurements of trioxane.

Systematics	Uncertainty (kHz)
Frequency calibration	0.4
Line fitting	2
Pressure and power	not considered
Other spectroscopic effects	5
Total systematics	5.4
Estimated statistic	twice the value given by the red line in Figure 4.33

The result of this procedure is that all fits converged to the same transition centre frequency within 2 kHz. We therefore assign a conservative 2 kHz systematic uncertainty to the lack of knowledge of the correct model for the line shape. Note that typical values for B_1 and $B_2 \cos\Psi$ range from -0.1 to -0.3 MHz^{-1}, whatever fit is carried out. This is of the same order of magnitude but of opposite sign compared to the value of the asymmetry parameter B found when fitting methanol data in the previous chapter. If attributed to the intensity modulation that results from frequency modulation, this quantity will depend on the underlying Doppler envelop which is different between methanol and trioxane. For the latter molecule indeed, transitions are not fully resolved in the Doppler broadened regime. It may well also be further influenced by a multipass-cell-induced Doppler profile complication.

The other systematic effects affecting the line centre include the frequency calibration, the uncertainty of which is 0.4 kHz when using the radio-frequency protocol (see subsection 3.4.3) and the 5 kHz uncertainty arising from the other spectroscopic effects

Table 5.2 – Absolute line-center frequencies and total uncertainties of rovibrational transitions assigned to the $P(15, K)$, $P(16, K)$, and $P(17, K)$ sub-branches of trioxane.

Transition	Absolute frequency (kHz)	Transition	Absolute frequency (kHz)	Transition	Absolute frequency (kHz)
	$J = 15$		$J = 16$		$J = 17$
$P(15, 0)$	29 136 294 385.8 (5.5)	$P(16, 0)$	29 125 698 263.5 (10.7)	$P(17, 0,)$	29 115 099 123.6 (28.7)
$P(15, 1)$	29 136 304 956.6 (5.9)	$P(16, 1)$	29 125 708 819.2 (6.0)	$P(17, 1)$	29 115 109 661.9 (22.2)
$P(15, 2)$	29 136 336 697.4 (5.4)	$P(16, 2)$	29 125 740 500.8 (5.6)	$P(17, 2)$	29 115 141 273.2 (12.6)
$P(15, 3)$	29 136 389 610.3 (5.4)	$P(16, 3)$	29 125 793 308.2 (5.4)	$P(17, 3)$	29 115 193 959.8 (9.9)
$P(15, 4)$	29 136 463 704.6 (5.4)	$P(16, 4)$	29 125 867 253.1 (5.9)	$P(17, 4)$	29 115 267 746.2 (10.6)
$P(15, 5)$	29 136 559 001.6 (5.4)	$P(16, 5)$	29 125 962 362.4 (6.1)	$P(17, 5)$	29 115 362 656.8 (8.3)
$P(15, 6)$	29 136 675 522.8 (5.4)	$P(16, 6)$	29 126 078 650.6 (6.9)	$P(17, 6)$	29 115 478 697.7 (8.1)
$P(15, 7)$	29 136 813 299.1 (5.6)	$P(16, 7)$	29 126 216 152.8 (5.6)	$P(17, 7)$	29 115 615 916.0 (10.1)
$P(15, 8)$	29 136 972 362.8 (7.1)	$P(16, 8)$	29 126 374 898.7 (6.5)	$P(17, 8)$	29 115 774 323.2 (21.5)
$P(15, 9)$	29 137 152 755.1 (6.5)	$P(16, 9)$	29 126 554 924.1 (6.1)	$P(17, 9)$	29 115 953 973.4 (29.6)
$P(15, 10)$	29 137 354 517.8 (5.6)	$P(16, 10)$	29 126 756 286.2 (6.2)	$P(17, 10)$	29 116 154 904.0 (15.8)
$P(15, 11)$	29 137 577 698.0 (6.4)	$P(16, 11)$	29 126 979 024.3 (7.8)	$P(17, 11)$	29 116 377 182.3 (13.9)
$P(15, 12)$	29 137 822 354.5 (9.1)	$P(16, 12)$	29 127 223 191.0 (6.4)	$P(17, 12)$	29 116 620 844.1 (6.4)
$P(15, 13)$	29 138 088 539.4 (23.6)	$P(16, 13)$	29 127 488 856.3 (6.4)	$P(17, 13)$	29 116 885 949.4 (7.5)
		$P(16, 14)$	29 127 776 070.0 (10.6)	$P(17, 14)$	29 117 172 572.2 (13.1)
		$P(16, 15)$	29 128 084 906.5 (25.5)	$P(17, 15)$	29 117 480 748.9 (25.2)
				$P(17, 16)$	29 117 810 609.6 (29.5)

listed in subsection 4.6.1.2. Here, power and pressure-induced frequency shifts have not been measured and we thus give absolute frequencies at the measured pressures and powers, and there is thus no associated contribution to the error budget.

We have only recorded one pair of up and down scans for most of the lines. We have thus not recorded enough data to calculate the statistical uncertainty associated to each transition frequency. We can only give an estimation of the statistical uncertainty based on the know-how gained with our extensive work on methanol (see subsection 4.6.3). Several transitions of trioxane have been measured twice. The typical weighted standard deviation of two such frequencies is ∼5 kHz for high-intensity transitions having a SNR > 120 (averaged SNR of one pair of up and down scans only), ∼10 kHz for transitions exhibiting a SNR between 60 and 120, and 20 kHz for transition having a SNR between 20 and 60. These results are compatible with those we have obtained in the metrological studies on methanol, as described in subsection 4.6.3. We are thus confident that the statistical uncertainty of one measurement is comparable for methanol and trioxane for lines exhibiting a similar SNR. But, as we have not measured it, we apply the same rule that has been used in the previous chapter in similar conditions when only one pair of up and down scans was recorded: we assign to trioxane absolute frequencies a conservative statistical uncertainty twice the value given by the red line in Figure 4.33 at the same one-pair signal-to-noise ratio (see subsection 4.6.3).

Table 5.1 summarizes the total uncertainty budget for lines of trioxane. Table 5.2 lists the line-centre absolute frequencies and total uncertainties of the 47 rovibrational transitions assigned to the three $P(15,K)$, $P(16,K)$, and $P(17,K)$ sub-branches of trioxane. The line-centre absolute frequencies and total uncertainties of the 268 non-assigned rovibrational transitions of trioxane are given in Appendix G.

5.2.5 Spectroscopic constants of trioxane

In this section, we want to exploit the line-centre frequency measurements of the previous section to determine the rotational parameters of trioxane in the $\nu_5 = 1$ vibrationally excited state and the mode centre frequency.

Trioxane is an oblate symmetric rovibrator. The energy terms for the ground state (gr) are given by the following expression

$$\begin{aligned} E_{gr}(J,K) = {} & BJ(J+1) + (C-B)K^2 \\ & - D_J J^2(J+1)^2 - D_{JK} J(J+1)K^2 - D_K K^4 \\ & + H_J J^3(J+1)^3 + H_{JK} J^2(J+1)^2 K^2 + H_{KJ} J(J+1)K^4 + H_K K^6. \end{aligned} \tag{5.13}$$

with B and C the rotational constants, D_J, D_{JK}, and D_K the quartic centrifugal distortion constants, H_J, H_{JK}, H_{KJ}, and H_K the sextic constants.

In the ground state, the spectroscopic constants (B, D_J, D_{JK}, H_J, H_{JK}, and H_{KJ}) have been determined from the pure rotational spectrum of trioxane recorded with high resolution in the frequency range between 326 and 947 GHz [273]. The rotational constant C has been derived by J.M. Colmont from the microwave study of the isotopic asymmetric form of the molecule [280] and the last quartic centrifugal distortion constant D_K is supposed to have in the ground state a value very close to the small one of the distortion constant derived again by J.M. Colmont from the microwave study of the isotopic asymmetric form of the molecule [264, 280].

The rovibrational energy terms in the first excited state of the ν_5 vibrational state are given by

$$\begin{aligned} E_{\nu_5}(J,K) = \nu_5 &+ B'J(J+1) + (C'-B')K^2 \\ &- D'_J J^2(J+1)^2 - D'_{JK}J(J+1)K^2 - D'_K K^4 \\ &+ H'_J J^3(J+1)^3 + H'_{JK}J^2(J+1)^2K^2 + H'_{KJ}J(J+1)K^4 + H'_K K^6, \end{aligned} \tag{5.14}$$

where ν_5 represents the central frequency of the ν_5 vibrational mode. The ν_5 mode is a parallel mode for which transitions satisfy $\Delta K = 0$. In the P branch to which belong all of the transitions we have measured, the frequency of a rovibrational transition between the ground state and the first vibrationally excited $\nu_5 = 1$ state may thus be written as

$$\nu = E_{\nu_5}(J-1,K) - E_{gr}(J,K). \tag{5.15}$$

The last sextic centrifugal distortion constants H_K and H'_K are not included in the fitting model, because they are too small to be determined in our experiment.

Table 5.3 – Spectroscopic constants of the ground state and the first excited $\nu_5 = 1$ vibrational state of trioxane. In this work, parameters H_J, H_{KJ}, and H_J of the $\nu_5 = 1$ state are fixed to those of the ground state. The uncertainties in parentheses correspond to one standard deviation.

Parameters	Ground state $\nu_5 = 0$	Excited state $\nu_5 = 1$	
		This work	Ref. [264]
ν_5 (cm^1)	-	977.1709721(45)	977.172(20)
B (MHz)	5273.257180(33)[a]	5271.4704(12)	5271.473(3)
C (MHz)	2933.95[b]	2942.9231(12)	2950.15[d]
D_J (kHz)	1.3438797(80)[a]	1.3344(25)	1.352(8)
D_{JK} (kHz)	-2.016295(17)[a]	-1.4462(10)	-2.09(2)
D_K (kHz)	-0.17[b]	-0.38722(40)	
H_J (Hz)	0.00049061(55)[a]	0.00049061[c]	
H_{JK} (Hz)	-0.0020978(15)[a]	-0.0020978[c]	
H_{KJ} (Hz)	0.0027408(34)[a]	0.0027408[c]	

[a]Data taken from H. Klein et al. [273] and [b]data taken from J.M. Colmont [280] and D. Dangoisse et al [264].
[c]Fixed and taken equal to the ground state values.
[d]This value is calculated from $\delta C = C' - C = 16.2 \pm 1.5$ MHz of Ref. [264].

In order to determine the molecular constants of trioxane in the first vibrationally excited $\nu_5 = 1$ state, we fix the ground state parameters to those found in the literature (see above). Those are listed in Table 5.3.

We then fit the model given in Equation 5.15 to the 47 line-center frequencies and associated uncertainties of the three $P(15,K)$, $P(16,K)$, and $P(17,K)$ sub-branches of trioxane given in Table 5.2. The number of line positions measured in the previous section is not enough to allow us to fit all centrifugal distortion constants up to the sextic order and we thus fix the sextic centrifugal distortion constants to their ground state value.

The obtained spectroscopic constants of the first excited $\nu_5 = 1$ vibrational state of trioxane are listed in Table 5.3. The band center ν_5 is found to be 977.1709721 cm^{-1} (29 294 848 761.2 kHz) with a uncertainty of 4.5×10^{-6} cm^{-1} (145 kHz). Our results are in good agreement with a previous study [264] but they show better uncertainties on all parameters, in particular a three-order-of-magnitude or more improvement on the determination of ν_5 and C', a factor of 15 improvement on D_{JK} and the determination of a new constant, D'_K.

5.2.6 Summary

We have presented direct absorption and saturated absorption spectra of trioxane. More than 300 rovibrational transitions of trioxane were measured and 47 were fitted to determine the set of spectroscopic parameters of the first excited $\nu_5 = 1$ vibrational state of the molecule. To our knowledge, trioxane with 12 atoms is the largest molecule whose saturated absorption spectroscopy has been demonstrated. Furthermore, these data could be suitable for astronomical observation of trioxane in cometary comae as a tracer for polyoxymethylene [275].

5.3 Hyperfine structure in ammonia

5.3.1 Introduction

Ammonia ($^{14}NH_3$), consisting of one nitrogen (N) atom and three hydrogen (H) atoms, is a good textbook example of a non-rigid molecule with a well-known double minimum potential energy surface exhibiting an inversional splitting of energy levels, as shown in Figure 5.9. The umbrella angle between the vertical axis crossing through the N atom and one of the three N-H axes is denoted by ρ. The potential energy is smallest at around 68° and 112° corresponding to two positions of the N atom on each side of the plan of the three-hydrogen atoms. The ν_2 umbrella fundamental band, the strongest absorption band of ammonia, is associated to rovibrational transitions around 10 μm corresponding to the motion of the N atom perpendicular to the hydrogen plane. Its spectrum is displayed in Figure 5.10. Due to the tunnelling effect resulting from the finite barrier height of about 2023 cm^{-1}, each vibrational level is split into a symmetric level (s) and an asymmetric level (a).

The hyperfine Hamiltonian of ammonia is very well known [282–284]. The hyperfine structure was recorded with a molecular beam in the microwave domain, providing excellent information about the hyperfine constants in the ground state [284–286]. In the infrared domain, our group has already measured saturated absorption spectra of the $asR(5,0)$, $asQ(8,7)$, and $saQ(6,3)$ lines of $^{14}NH_3$ and also the $asR(2,0)$ line of $^{15}NH_3$ [287–290].

In this section, we report the first measurement of the hyperfine structure of the ν_2 vibrational mode $asR(1,1)$ transition of ammonia. It has never been measured so far because it was not easily accessible with ultra-stable CO_2 lasers typically used so far in this spectral region for precise spectroscopic measurements.

5.3.2 The hyperfine structure in ammonia

Hyperfine splitting of ammonia has five contributions:

- The interaction between the nuclear quadrupole moment of the nitrogen nucleus

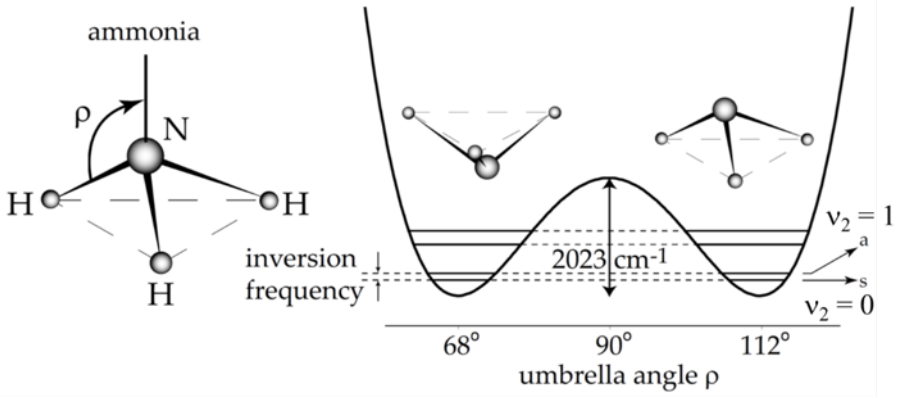

Figure 5.9 – Ammonia with one nitrogen atom and three hydrogen atoms (left). Potential energy of the ν_2 vibrational mode as a function of the umbrella angle ρ together with the ground level $\nu_2 = 0$ and first excited level $\nu_2 = 1$. Each level is split into two sublevels, denoted by s and a. Taken from [281].

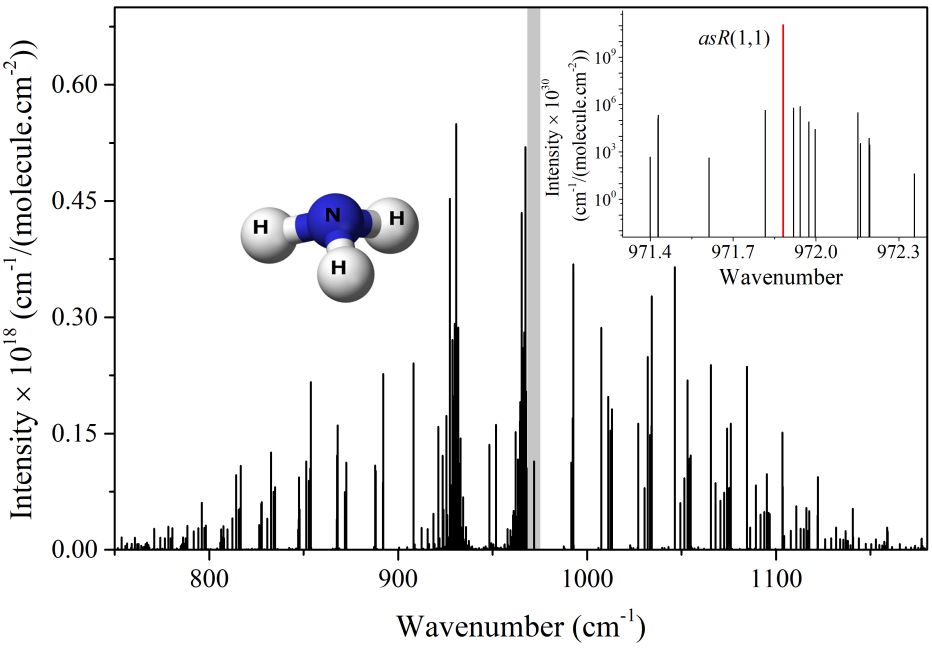

Figure 5.10 – Stick-spectrum of the ν_2 umbrella fundamental band of ammonia, reported in the HITRAN database [54]. The inset is a zoom of the spectrum (intensity in log scale) with wavelength ranging from 970 cm^{-1} to 973 cm^{-1} corresponding to the spectral coverage of our mid-IR spectrometer. It exhibits only one high-intensity line in the R-branch, the $asR(1,1)$ transition (red stick).

and the gradient of the electric field created by all other charges at the nucleus.

- The spin-rotation interactions between the magnetic field induced by the molecular rotation and the magnetic moment of the nitrogen (N).

- The spin-rotation interactions between the magnetic field induced by the molecular rotation and the magnetic moment of the hydrogen (H) nuclei.

- The spin-spin interaction between the nitrogen atom and the three hydrogen atoms.

- The spin-spin interaction between the hydrogen atoms themselves.

The hyperfine Hamiltonian can thus be written as

$$H = H_{eQq} + H_R + H_S + H_T + H_U, \tag{5.16}$$

in which, the first term describes the dominant electric-quadrupole coupling, the second and third correspond to the N spin-rotation coupling and the H spin-rotation coupling, and the two last terms represent the N-H spin-spin interaction, and the H-H spin-spin interaction. As detailed in the following, the five interactions are strength-characterized by five coupling parameters, usually denoted by eQq, R, S, T, and U respectively according to notations first introduced by Kukolich [285]. A detail explanation about the hyperfine structure in ammonia is also presented in Cyril Lemarchand's thesis [291]. The hyperfine structure is dominated by the nitrogen nucleus electric quadrupole interaction which results in energy splittings at the level of a few megahertz. The spin-rotation and spin-spin interactions are much smaller (shifts and splittings at the 10 kHz level at most) and can be neglected in this work.

Electric quadrupole interaction

Due to the nitrogen nuclear spin $I_N = 1$, each rovibrational level is split into three sub-levels, labelled by the quantum number F, where $\vec{F}$ is the sum of the rotational angular momentum $\vec{J}$ (rotation) and the spin of the nitrogen nucleus $\vec{I_N}$:

$$\vec{F} = \vec{J} + \vec{I_N}. \tag{5.17}$$

Following [292], for a symmetric top like NH_3, the first order energy shift due to the electric quadrupole interaction is

$$H^{\nu}_{eQq}(J,K,F) = eQq^{\nu}\left[3\frac{K^2}{J(J+1)} - 1\right] f(I,J,F), \tag{5.18}$$

We neglect here matrix elements of the electric quadrupole Hamiltonian off-diagonal in J. eQq^{ν} is the quadrupole coupling constant of vibrational state v and $f(I,J,F)$ is the Casimir's function, given by

$$f(I,J,F) = \frac{\frac{3}{4}C(C+1) - I(I+1)J(J+1)}{2I(2I-1)(2J-1)(2J+3)}, \tag{5.19}$$

where

$$C = F(F+1) - I(I+1) - J(J+1). \tag{5.20}$$

and I is the nitrogen spin and J is the rotational angular momentum.

Table 5.4 – Parameters in kHz for the determination of the quadrupole hyperfine constant eQq in the $\nu_2 = 0$ ground state [293] and the $\nu_2 = 1$ first excited vibrational state [294] of the ammonia molecule.

Parameters	Ground state $\nu_2 = 0$ [293]		Excited state $\nu_2 = 1$ [294]	
	s levels	a levels	s levels	a levels
$eQq_0^{\nu*}$	−4091.27	−4087.46	−4433.39	-4275.54
eQq_{dist}^{ν}	−1.048	−1.048	−1.048	-1.048
δQ_J^{ν}	1.081	1.062	1.497	1.049
δQ_K^{ν}	−0.486	−0.473	−0.762	-0.457
$\delta Q_{JJ}^{\nu} \times 10^4$	−1.016	−0.668	−2.892	0.903
$\delta Q_{JK}^{\nu} \times 10^4$	3.153	2.001	9.551	−3.402
$\delta Q_{JJ}^{\nu} \times 10^4$	−1.460	−0.544	−6.210	4.145

The numerous studies of the hyperfine structure in the ground vibrational levels [282–286, 293, 295] allow us to accurately fix the value of the hyperfine constant eQq^0 of the ground state. Following [293], the J,K dependence of the ground state quadrupole coupling constant is given by the following equation,

$$\begin{aligned} eQq^{\nu} =& eQq_0^{\nu*} + eQq_{dist}^{\nu} Z(J,K) + \delta Q_J^{\nu}\left[J(J+1) - K^2\right] + \delta Q_K^{\nu} K^2 \\ &+ \delta Q_{JJ}^{\nu} J^2(J+1)^2 + \delta Q_{JK}^{\nu} J(J+1)K^2 + \delta Q_{KK}^{\nu} K^4, \end{aligned} \tag{5.21}$$

with

$$Z(J,K) = \frac{K^2(4K^2-1)}{3K^2 - J(J+1)} - 2K^2, \tag{5.22}$$

the parameter $eQq_0^{\nu*}$ is the effective quadrupole constant in the absence of the molecular rotation, and the remaining parameters (eQq_{dist}^{ν}, Q_J^{ν}, Q_K^{ν}, Q_{JJ}^{ν}, Q_{JK}^{ν}, and Q_K^{ν}) are constants modelling the effects resulting from the centrifugal distortion of the ammonia molecule. The values of these parameters for the $\nu_2 = 0$ ground state are summarized in Table 5.4. Equation 5.21 allows the ground-state eQq^0 values to be reproduced with an uncertainty of 1 kHz [293, 294]. Values for the $\nu_2 = 1$ vibrationally excited state have also been predicted theoretically [294] and are also listed in Table 5.4. The uncertainty on these theoretical values is however difficult to estimate.

Selection rule and intensity

The hyperfine transitions follow the selection rule

$$\Delta F = 0, \pm 1. \tag{5.23}$$

In linear absorption spectroscopy, their relative intensities, proportional to the square of the dipole moment matrix elements, are

$$(2F^1+1)(2F^0+1)\begin{Bmatrix} J^1 & F^1 & I_N \\ F^0 & J^0 & 1 \end{Bmatrix}^2 \tag{5.24}$$

where F^{ν} and J^{ν} are the quantum numbers in the low ($\nu = 0$) and upper ($\nu = 1$) states.

Description of hyperfine level structure of the *asR*(1,1) ammonia transition

As shown in inset of Figure 5.10, the $asR(1,1)$ rovibrational transition around 971.88 cm^{-1} is the only high-intensity transition in the spectral range of our QCL (970-973 cm^{-1}). This transition, for which $\Delta J = 1$ and $\Delta K = 0$, links the asymmetric ground vibrational state level $|J = 1, K = 1, a\rangle$ to the symmetric $\nu_2 = 1$ vibrationally excited vibrational level $|J = 2, K = 1, s\rangle$. Its hyperfine structure is displayed in Figure 5.11. Due to the nitrogen nuclear spin $I_N = 1$, the lower and upper levels are both split into three hyperfine sub-levels (labelled by the hyperfine quantum number F, see above) F_0 = 0, 1, and 2 and F_1 = 1, 2, 3, respectively.

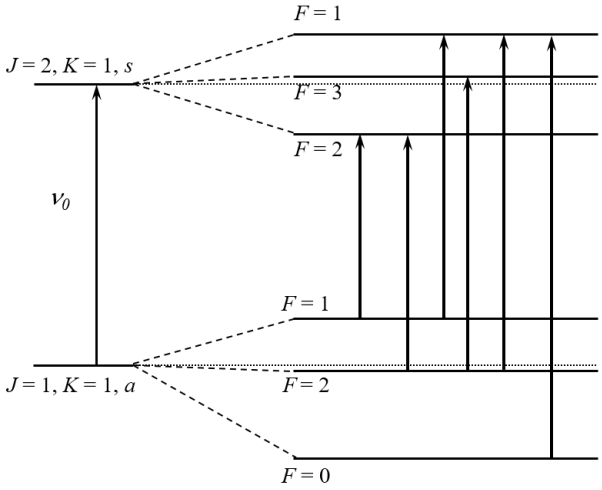

Figure 5.11 – Hyperfine energy levels of the $asR(1,1)$ rovibrational transition of the ν_2 vibrational mode. The arrows indicate the six hyperfine transitions.

Using Equations 5.21 and 5.22 and Table 5.4, we calculate the quadrupole coupling constants to be $eQq^0 = -4091.7$ (1.0) kHz in the a lower state and $eQq^1 = -4423.5$ kHz in the s upper state (without predicted uncertainty). Knowing these constants, we then calculate the resulting energy shifts $H_{eQq^0}(J^0, K^0, F^0)$ due to the electric quadrupole interaction using Equation 5.18 in the lower state:

$$\begin{aligned} H_{eQq^0}(1,1,0) &= \frac{eQq^0}{4}, \\ H_{eQq^0}(1,1,1) &= \frac{-eQq^0}{8}, \\ H_{eQq^0}(1,1,2) &= \frac{eQq^0}{40}, \end{aligned} \tag{5.25}$$

and $H_{eQq^1}(J^1, K^1, F^1)$ in the upper state:

$$\begin{aligned} H_{eQq^1}(2,1,1) &= \frac{-eQq^1}{8}, \\ H_{eQq^1}(2,1,2) &= \frac{eQq^1}{8}, \\ H_{eQq^1}(2,1,3) &= \frac{-eQq^1}{28}. \end{aligned} \tag{5.26}$$

According to the selection rules given above, this transition has six hyperfine components which are displayed in Figure 5.11.

5.3.3 Saturated absorption spectroscopy of the ν_2 vibrational mode $asR(1,1)$ ammonia transition

5.3.3.1 Data acquisition and experimental results

We have successfully recorded the hyperfine structure of the $asR(1,1)$ rovibrational transition by carrying out saturated absorption spectroscopy using our mid-IR spectrometer. The experimental conditions are optimized to narrow the linewidth as much as possible in order to reach the best possible resolution to allow the hyperfine structure to be resolved. In particular, the multipass absorption cell is filled with the minimum possible pressure of ammonia. The signal intensity is such that a very small amount of ammonia is required in the multipass cell to get a good signal-to-noise ratio. After injecting a little bit of ammonia, we actually keep on pumping on the cell while accumulating data. The pressure is around our gauges resolution and we can thus only give an upper bound of 50 mPa on the ammonia pressure. Frequency modulation at 20 kHz, with a frequency deviation of 150 kHz and third harmonic demodulation are used. Figure 5.12 displays a saturated absorption spectrum of the $asR(1,1)$ rovibrational transition of $^{14}NH_3$, that is averaged over 15 pairs of up and down scans. It exhibit a signal-to-noise ratio of ∼166. The frequency axis of the spectrum is reconstructed using the optical protocol (see subsection 3.4.3).

The spectrum is expected to exhibit six strong $\Delta F = 0, \pm 1$ hyperfine features, but also eight cross-over transitions, which are shown in Figure 5.13. Figure 5.13(a) displays all ∨-type cross-over transitions between transitions which share the same lower state, and Figure 5.13(b) displays all ∧-type cross-over transitions between transitions which share the same upper state. These crossover transitions are expected at a frequency equal to the mean of the involved transition frequencies.

5.3.4 Hyperfine structure analysis and spectroscopic parameters

The quadrupole coupling constant in the ground state $|J = 1, K = 1, a\rangle$ is determined with a 1 kHz uncertainty using Equation 5.21 and the parameters listed in Table 5.4. The quadrupole coupling constant in the $\nu_2 = 1$ $|J = 2, K = 1, s\rangle$ upper state can however not be determined with such a good uncertainty. It can be deduced from Equation 5.21 and the upper-state parameters listed in Table 5.4 without knowledge of uncertainty. In addition, it has also been determined from a rotational spectroscopy study of the ν_2 vibrationally excited state. In this study, the $(\nu_2, J, K)^{a/s} = (1, 2, 1)^s \leftarrow (1, 1, 1)^a$ microwave transition was recorded at Doppler-limited resolution [296], allowing eQq^1 to be measured, giving $eQq^1 = -4\,429\,(12)$ kHz.

In this section, we want to demonstrate that our saturated absorption data leads to a better estimate of eQq^1. In order to determine eQq^1, we fit the data displayed in Figure 5.12 with the sum of 14 transitions corresponding to the six $\Delta F = 0, \pm 1$ hyperfine features and the eight crossover transitions. In view of the relatively small index of modulation used in this study (line-width of 680 kHz FWHM, see below and frequency deviation of 150 kHz), we use for each of the 14 transitions the line shape given by Equation 4.17 and used in our methanol study. Using Equations 5.18 to 5.20, we determine the line-centre frequencies of the six hyperfine features $\nu_{F^1 \leftarrow F^0}$ between the lower (quantum number

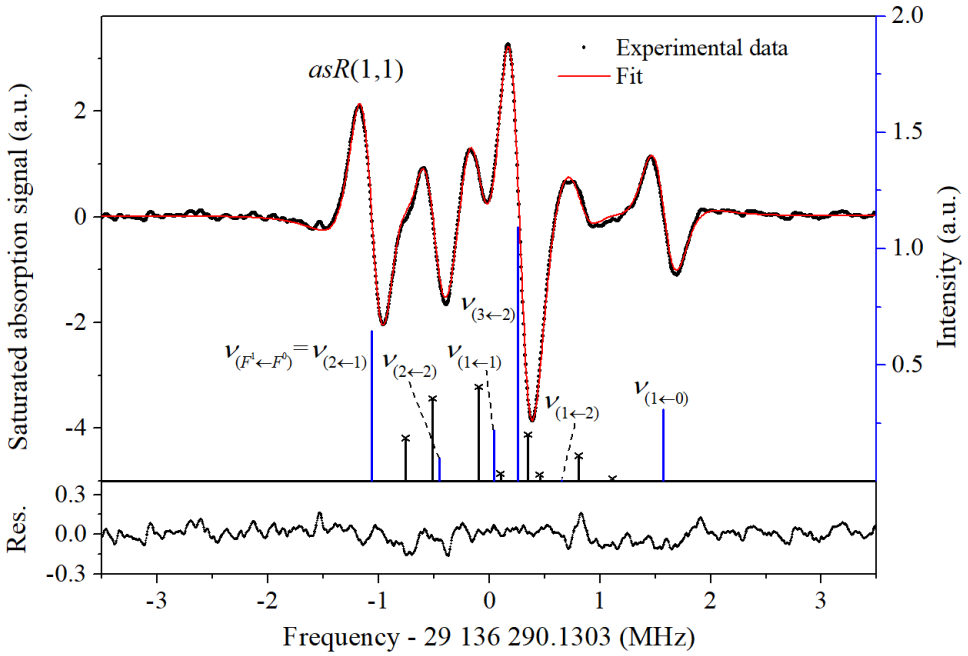

Figure 5.12 – Saturated absorption spectrum of the $asR(1,1)$ rovibrational transition of ammonia, the resulting fit to the data, and its residuals. Residuals are shown on the bottom graph. The fitted positions and intensities of the six principle hyperfine components are indicated by blue sticks. The fitted positions and intensities of the eight crossovers are indicated by black sticks. Experimental conditions: pressure, below 50 mPa; modulation frequency, 20 kHz; frequency modulation excursion, 150 kHz; frequency step, ∼15 kHz; average of over 15 pairs of up and down scans; total integration time per point, 0.9 s; whole spectrum measurement time, ∼1400 s.

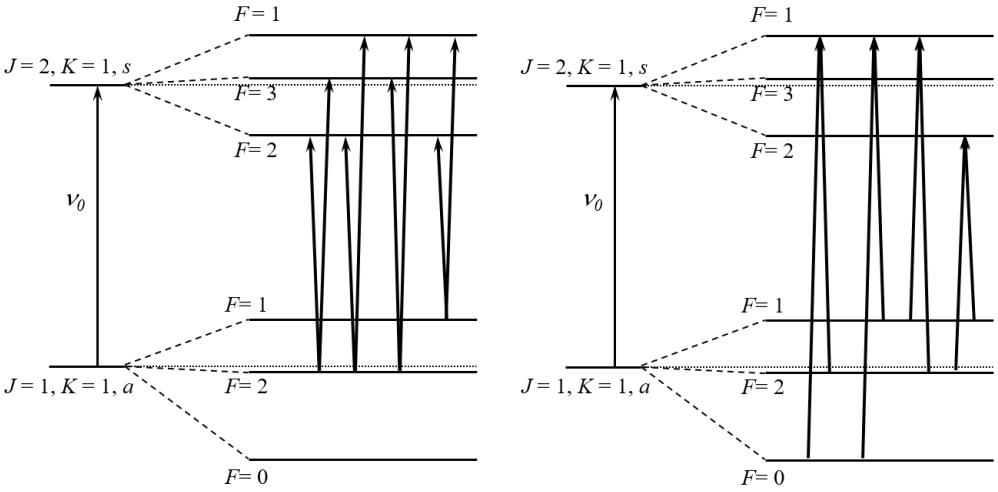

Figure 5.13 – The energy level diagram of ammonia for the eight crossovers. (a) Four ∨-type cross-over transitions between transitions which share the same lower state. (b) (a) Four ∧-type cross-over transitions between transitions which share the same upper state.

F^0) and the upper (quantum number F^1) levels of the $asR(1,1)$ rovibrational transition to be

$$\begin{cases} \nu_{2\leftarrow 1} = \nu_0 + \dfrac{eQq_0}{8} + \dfrac{eQq_1}{8} \\ \nu_{2\leftarrow 2} = \nu_0 - \dfrac{eQq_0}{40} + \dfrac{eQq_1}{8} \\ \nu_{1\leftarrow 1} = \nu_0 + \dfrac{eQq_0}{8} - \dfrac{eQq_1}{8} \\ \nu_{3\leftarrow 2} = \nu_0 - \dfrac{eQq_0}{40} - \dfrac{eQq_1}{28} \\ \nu_{1\leftarrow 2} = \nu_0 - \dfrac{eQq_0}{40} - \dfrac{eQq_1}{8} \\ \nu_{1\leftarrow 0} = \nu_0 - \dfrac{eQq_0}{4} - \dfrac{eQq_1}{8} \end{cases} \tag{5.27}$$

in which ν_0 is the line-center frequency of the $asR(1,1)$ transition in the absence of hyperfine structure.

We can also determine easily the positions $\nu_{(F^1,F^{1\prime})\leftarrow F^0}$ of the four ∨-type cross-overs transitions (between transitions which share the same lower level of quantum number F^0, but couple to different upper levels of quantum number F^1 and $F^{1\prime}$) and $\nu_{F^1\leftarrow(F^0,F^{0\prime})}$ of the four ∧-type cross-overs transitions (between transitions which share the same upper level of quantum number F^1, but couple to different lower levels of quantum number F^0

and $F^{0'}$) to be:

$$\begin{cases} \nu_{2\leftarrow(1,2)} = \frac{1}{2}\left(\nu_{2\leftarrow1} + \nu_{2\leftarrow2}\right) = \nu_0 + \frac{eQq_0}{20} + \frac{eQq_1}{8} \\ \nu_{(1,2)\leftarrow1} = \frac{1}{2}\left(\nu_{2\leftarrow1} + \nu_{1\leftarrow1}\right) = \nu_0 + \frac{eQq_0}{8} \\ \nu_{(2,3)\leftarrow2} = \frac{1}{2}\left(\nu_{2\leftarrow2} + \nu_{3\leftarrow2}\right) = \nu_0 - \frac{eQq_0}{40} + \frac{5eQq_1}{112} \\ \nu_{(1,2)\leftarrow2} = \frac{1}{2}\left(\nu_{2\leftarrow2} + \nu_{1\leftarrow2}\right) = \nu_0 - \frac{eQq_0}{40} \\ \nu_{1\leftarrow(1,2)} = \frac{1}{2}\left(\nu_{1\leftarrow1} + \nu_{1\leftarrow2}\right) = \nu_0 + \frac{eQq_0}{20} - \frac{eQq_1}{8} \\ \nu_{1\leftarrow(0,1)} = \frac{1}{2}\left(\nu_{1\leftarrow1} + \nu_{1\leftarrow0}\right) = \nu_0 - \frac{eQq_0}{16} - \frac{eQq_1}{8} \\ \nu_{(1,3)\leftarrow2} = \frac{1}{2}\left(\nu_{3\leftarrow3} + \nu_{1\leftarrow2}\right) = \nu_0 - \frac{eQq_0}{40} - \frac{9eQq_1}{112} \\ \nu_{1\leftarrow(0,2)} = \frac{1}{2}\left(\nu_{1\leftarrow2} + \nu_{1\leftarrow0}\right) = \nu_0 - \frac{11eQq_0}{40} - \frac{eQq_1}{8} \end{cases} \tag{5.28}$$

In order to determine eQq^1, in our fitting process, we fix the value of eQq^0 to −4 091.7 kHz, the value determined using Equation 5.21 and the parameters listed in Table 5.4 (see above). As can be seen from the previous formulas, once eQq^0 is fixed, the frequency positions of the 14 hyperfine components depend on only two parameters, the hyperfine-structure-less centre frequency ν_0 of the transition, and eQq^1, which determine the relative positions of the 14 hyperfine components.

Figure 5.12 displays the result of the fit to the data (red solid line) together with its residuals. The blue and black sticks in the figure feature the positions and intensities of the fitted $\Delta F = 0, \pm1$ hyperfine components and of the crossover transitions, respectively. The quadrupole coupling constant in the upper state eQq^1 is fitted to be −4 419 kHz within ±2 kHz. In order to evaluate the effect of the line shape model on this parameter, we have also fitted data with simple third derivatives of Lorentzian, instead of the asymmetric line shape of Equation 4.17. The resulting values of eQq^1 agree within 1 kHz, showing that the details of the model have a minor effect on this parameter. Thus, we take 3 kHz as an conservative uncertainty of eQq^1. As shown in Table 5.5, the value of eQq^1 found for the $asR(1,1)$ rovibrational transition is in perfect agreement with the previous microwave study [296] (see above). We however have an uncertainty on the value of eQq^1 four times better than the previous study. Moreover, our $eQq1$ value is shifted by 4.3 kHz with respect to the theoretical prediction of Ref. [294] that can be determined from Equation 5.21 and Table 5.4.

Table 5.5 – The measured quadrupole hyperfine constant eQq^1 (in kHz) of the $(\nu_2, J, K)^{a/s} = (1,2,1)^s$ rovibrational level of ammonia together with the predicted value calculated from Equation 5.21 and the previous value measured using microwave Doppler-limited spectroscopy [296].

This work	Ref. [296]	Predicted [294]
−4 419.2 (3.0)	−4 429 (12.0)	−4 424

In addition, the line-center frequency ν_0 of this transition is determined to be 29 136 290 130.3 kHz. Again, we use the know-how gained in our metrological study of methanol (see subsection 4.6.3) to establish a conservative uncertainty budget for the $asR(1,1)$ rovibrational transition of ammonia. Although we have recorded 15 pairs of up and down spectra, those were recorded in a raw, and was not repeated from day to day. We again apply the rule that has been used previously when a limited number of scans was recorded: we assign to the ammonia absolute frequency a conservative statistical uncertainty of 30 kHz, corresponding to twice the value given by the red line in Figure 4.33 at an SNR of 45, the averaged SNR of one pair of up and down scans for our ammonia data (see subsection 4.6.3).

The statistical uncertainty is thus conservatively estimated to be ∼30 kHz. Following the rule given at the beginning of subsection 4.6.2, uncertainty associated to the line fitting is estimated to be 5 kHz (SNR of the averaged spectrum in Figure 5.12 is ∼166 mentioned above). Contributions of power and pressure effects are not considered. Uncertainty due to other spectroscopic effects is estimated to be ∼5 kHz (see subsection 4.6.1.2). The total uncertainty is finally found to be 30.8 kHz. Our resonance frequency of the $asR(1,1)$ rovibrational transition of ammonia is shifted 75.7 kHz with respect to the previous measurement reported in the HITRAN database [54].

Note that the linewidth is taken as equal for all 14 hyperfine components in the fit of the saturated absorption spectrum. We determine a FWHM linewidth to be ∼680 kHz with a 2 kHz uncertainty (given by the fit), which is an unknown combination of pressure broadening, transit-time broadening, power broadening and frequency modulation-induced distortion. The FWHM transit time is estimated to be in the range 110 to 220 kHz (using Equation 1.22 with the beam waist w_0 ranging from 0.6 to 1.2 mm, see section 4.1). Following the HITRAN database [54], the $asR(1,1)$ rovibrational transition has a FWHM self-pressure broadening of ∼260 kHz/Pa, thus the collisional broadening is estimated to be < 13 kHz (pressure < 50 mPa, see above). Contribution of the frequency modulation to the linewidth is estimated to be ∼20 kHz (see Equation 4.18). We expect that the remaining contribution is due to the power broadening, that is not fully studied in this work.

5.3.5 Summary

We have recorded saturated absorption spectroscopy of the $asR(1,1)$ rovibrational ammonia line and resolved for the first time the quadrupole hyperfine structure of this transition. From the analysis of the spectrum, we have determined the quadrupole hyperfine constant $eQq_1 = -4\,419.2\ (3)$ kHz with uncertainty four times better than the previous study in the microwave domain.

General conclusion and perspectives

We have developed an apparatus for the ultra-stable, precise, and widely tunable frequency control of QCLs in the mid-IR spectral window. A QCL working at ∼10.3 μm is phase-locked onto an OFC at 1.55 μm, itself stabilized to an optical local oscillator (OLO). The latter is based on a laser diode working at 1.54 μm. One sideband of the laser diode, generated by an EOM, is phase-locked onto an ultra-stable optical frequency reference signal, remotely transferred from LNE-SYRTE via a 43-km long fiber link, with traceability to primary frequency standards. The OLO carrier frequency can be precisely scanned over 9 GHz using a home-made microwave synthesizer. This allows the QCL frequency to be continuously tuned over a span of ∼1.4 GHz, which is more than an order of magnitude improvement compared to previous measurements [45, 46]. The QCL frequency is SI-traceable with an uncertainty on its absolute frequency at the Hz level, thanks to the reference to the optical frequency reference signal of LNE-SYRTE [66]. This is a factor of ∼250 better than GPS-disciplined radio-frequency reference based measurements [39, 41–44, 131, 297] and an improvement of more than six orders of magnitude compared to using traditional frequency synthesizers. These two methods in addition are not SI-traceable. Moreover, our method results in a QCL frequency stability below 10^{-15} at for averaging times longer than 0.1 s, given by the remote ultra-stable optical reference. This level of spectral purity is important for pushing back the limits in ultra-high resolution molecular spectroscopy.

We have demonstrated a mid-IR spectrometer based on the ultra-stable and widely-tunable QCL and a multipass absorption cell. We have used this spectrometer to carry out saturated absorption spectroscopy of rovibrational transitions of methanol in the P branch of the C-O stretching vibrational mode in a spectral window of ∼100 GHz, corresponding to ∼50% of the QCL's tuning range. Combining the multipass cell and a frequency modulation method for saturated absorption spectroscopy provides high detection sensitivity allowing relatively high-J (around 30) rovibrational lines to be probed at the low pressures required for ultra-high resolution measurements. This unique spectrometer provides an unprecedented combination of resolution, tunability, and frequency and detection sensitivity around 10 μm. Line-center frequencies of 38 rovibrational transitions of methanol have been measured. Among those, absolute frequencies of high-intensity transitions are determined with a ∼1 kHz statistical uncertainty and sub-10 kHz total uncertainty. This corresponds to a relative uncertainty of a few 10^{-10}, which is an improvement of ∼2000 over previous measurements. Moreover, the setup allowed us to probe several singular K-doublets, weak lines, and weak doublets of methanol for the first time.

The know-how gained in our metrological study of some methanol lines allows us to establish meaningful uncertainty budgets for the resonance frequencies of other methanol

lines as well as other molecules, namely trioxane and ammonia in this work.

Beside metrological measurements, our high-resolution and precise mid-IR spectrometer has been used for molecular studies, for instance for determining accurate spectroscopic parameters of trioxane or for studding subtle internal dynamics of ammonia (hyperfine structure). We have recorded broadband saturated absorption spectra of trioxane over spectral ranges of several GHz. Such data were impossible to record with CO_2 lasers so far. Line-center frequencies of more than 300 rovibrational transitions of trioxane have been measured in which 47 transitions were used to determine the rotational constants of the first excited $\nu_5 = 1$ of the molecule. These measurements make trioxane with 12 atoms one of the largest molecule to have been probed by saturated absorption spectroscopy. Moreover, we have probed the quadrupole hyperfine structure of the $asR(1,1)$ rovibrational transition of ammonia for the first time, which has not previously been studied because it was not accessible with ultra-stable CO_2 lasers used so far in this spectral region for precise spectroscopic measurements. Our experimental data can be used for calibrating other experiments or refining the model of the molecules.

Moreover, our experimental setup can also be operated with the free-runing QCL to record Doppler-limited absorption spectra. We have used it to probe the P branchs of the ν_8 vibrational mode of methanol and of the ν_5 vibrational mode of trioxane. Many weak rovibrational transitions of methanol, that are not reported so far, have been observed and subtle structures have been resolved most probably for the first time.

The continuous span range of our SI-traceable and ultra-stable QCL is currently limited at 1.4 GHz due to the OLO. It could be further improved by a factor of three or four by setting up a new OLO using a higher frequency EOM and an upgraded synthesizer. In addition, our stabilization method is currently limited to the 9-13 μm spectral window. It can be extendable to the entire 5-20 μm molecular fingerprint region using appropriate non-linear crystals and modules that shape the frequency comb spectrum. Our work is also part of a global effort towards ever more precise rovibrational spectroscopic measurements in different frequency regions using nonlinear processes to control the frequency of mid-IR laser sources (see for instance the recent studies, e.g. 3 μm [297]; 4.3 μm [42]; 5.4 μm [41, 298]; 5.8 μm [46]; 7.8 μm [43]; 8.6 μm [44]; 9 μm [39], $\sim$10 μm [45, 51]).

Ramsey interferometry is the highest-resolution method demonstrated for rovibrational molecular spectroscopy [34]. Buffer-gas-cooling, one of the recently demonstrated cold molecular source technologies [299–303], provides slow-moving molecular beams with typical velocities of $\sim$100 m/s, one order of magnitude lower than conventional supersonic counterparts ($\sim$1000 m/s). This results in the increase in interrogation time for the Ramsey interferometry experiment. Combining the SI-traceable, widely-tunable, and ultra-stable QCL in a Ramsey interferometer with the buffer-gas-beams would give record-breaking tens of hertz or smaller fringe spacings, more than an order of magnitude improvement over the previous record obtained at LPL [34]. Such experiments could potentially lead to molecular frequency measurements at uncertainties reaching the 2×10^{-16} ultimate accuracy of the Cs fountains [66], or even better by controlling the frequency of the remote near-IR reference with new generation optical clocks [297, 304].

Although the results reported in this thesis are not at these extreme levels, they are at a degree of resolution requiring us to evaluate subtle systematic effects such as the wavefront-curvature and gas-lens-effect-induced frequency shift usually ignored. Note that these are magnified when using a multipass cell, which in addition leads to etaloning

effects and the resulting difficulties in the line shape modelling. The two main contributions to the uncertainty budget, the wavefront-curvature effect and "line fitting", can thus be reduced by replacing the multipass cell with a Fabry-Perot cavity a few meters long, which also results in an improved resolution [45]. With such a cavity, the transit time broadening can be narrower at least one order of magnitude by increasing the beam waist over several millimetres, and the optical path length is larger than the multipass cell, we can thus work at lower pressure, at least ten time compared to the multipass cell, allowing the collisional broadening to be reduced. In addition, for a given incident power, the cavity provides averaging power, "*seen*" by molecules, much higher than in the multipass cell. In consequence, uncertainty on the line-center frequency of molecular resonances as low as a few tens of hertz are reachable [45]. However, we need to lock the cavity length to the laser frequency, limiting the frequency tuning due to the limited tunability of the cavity length (∼100 MHz). The multipass cell configuration is thus particularly appropriate for broadband studies at relatively high levels of resolution, while the Fabry-Perot cavity is needed for the most precise measurements.

The ultra-high-resolution and precise spectrometer will allow us to probe more and more complex molecules of interest for fundamental spectroscopy, atmospheric physics, astrophysics, and fundamental physics. Increasing the size of quantum objects that can be probed using saturated absorption technique is not straight forward. Those are more difficult to saturate, have weaker line, and/or can suffer from internal vibrational relaxation (IVR). At LPL, we are currently trying to probe sub-Doppler spectroscopy of dimethyl sulfide CH_3SCH_3 (DMS). This molecule is a species of interest for atmospheric studies because it is the most abundant sulphur compounds of biogenic source emitted in the atmosphere [305]. Moreover, DMS has potential astrophysical interest since it is the sulphur analog of dimethyl ether, a relatively abundant molecule in interstellar medium [306, 307].

Combination of broadband tunability, high sensitivity, and resolution demonstrated in this thesis will participate in driving the next generation spectroscopic technology. It could in particular help for future precise spectroscopic measurement for testing fundamental physics such as stringent tests of quantum electrodynamics [32], precise measurements of the electron-to-proton mass ratio m_e/m_p [29, 31, 32], searching for physics beyond the standard model by measuring possible variations of m_e/m_p [34, 308, 309], and looking for fifth forces or extra dimensions at the molecular scale [29, 32]. In particular, the measurement of possible variation of m_e/m_p could be done by combining Ramsey interferometry (in a beam, in a trap, or in a fountain) with ultra-stable QCLs and ultra-cold molecules, for instance ammonia fountain at 10 μm [302] or ultra-cold trapped CaF, a molecule that our group is starting to study around 17 μm in collaboration with the Center for Cold Matter, Imperial College London.

Another important topic in fundamental physics is the measurement of the frequency difference between two enantiomers of a chiral molecule induced by the parity violation inherent in the weak interaction [20, 299]. At LPL, we are developing a new instrument to pursue our experimental investigations of the effect. This instrument will benefit from the extension of the spectral coverage demonstrated in this thesis, allowing to considerably increase the number of potential candidate species for parity violation observation. Combination of Ramsey interferometry with a new cold molecules source under development will enable us to reach the highest resolution and precision possible with our QCL.

A third development is currently performed in order to enhance the detection sensitivity of the mid-IR frequency tiny signal. All this work is expected to lead to the first observation of parity violation in molecules, one of the most intriguing challenges in molecular physics.

APPENDIX A

K+K counter

A K+K counter is a multichannel high resolution phase and frequency counter that measures the phase of up to 4 channels without dead time [310, 311]. It is synchronized to an external reference signal at 10 MHz. For each channel, the phase is measured with a resolution of 12.2 ps every $\tau_0 = 1$ ms. It is possible to select a measurement on different gate times τ, up to 30 s. Inside the counter, the microprocessor achieves averaging of 1 ms measurements corresponding to the chosen gate time, and transmits the final result expressed in phase or in frequency to the FXE software.

We assume that a radio-frequency signal whose frequency is needed to be measured has the form

$$V(t) = A\sin(2\pi\nu(t)t), \tag{A.1}$$

where $\nu(t)$ is the instantaneous fractional frequency of the signal.

A single counter measurement over a gate time τ can be written as following

$$f_{meas,k} = \int_{-\infty}^{\infty} \nu(t)\omega(t - t_k; \tau)dt, \tag{A.2}$$

where $\omega(t;\tau)$ is the estimating function.

As shown in subsection 2.3.2.2, two types of measurements are possible, which lead to slightly different estimates of the Allan deviation. For the Π-type counter, it is given by

$$\omega_\Pi(t;\tau) = \begin{cases} 1/\tau & 0 < t < \tau \\ 0 & \text{elsewhere.} \end{cases} \tag{A.3}$$

For the Λ-type counter, it can be approximated, when $\tau \gg \tau_0$, by

$$\omega_\Lambda(t;\tau) = \begin{cases} t/\tau & 0 < t < \tau \\ 2 - t/\tau & \tau < t < 2\tau \\ 0 & \text{elsewhere.} \end{cases} \tag{A.4}$$

APPENDIX B

Technical protocol for the sum frequency generation process

To produce the sum frequency generation (SFG) signal, we follow two sections:

B.1 Creating a free space SFG signal

Both the 10.3 μm QCL beam and 1.85 μm beam are overlapped at the center of the SFG crystal by using telescope on each beam. To ensure that both beams are overlapped, a removable mirror is positioned at the output of the crystal. These laser beams are centered in two irises and then directed to a power meter. This allow us to make sure that the beams are actually superimposed together.

After emerging from the SFG crystal, the QCL beam is absorbed by the lens L_7 (see Figure 3.17) while the emissions of the 1.85 μm comb and SFG comb are collimated by the lens. Both beams are then directed to an optical filter at 1.55 μm (CVI, F1550). Here, the 1.85 μm beam is strongly attenuated.

In our experiment conditions, the AgGaSe2 crystal has type I *ooe* phase matching. The 10 μm and 1.85 μm beams (ordinary (o) beams) have perpendicular polarizations while the SFG beam at 1.55 μm (extraordinary (e) beam) has parallel polarization. The polarization axis of polarizer P2 is set parallel to the polarization of the SFG beam. The residual 1.85 μm beam transmitted by the F1550 can then be completely filtered out.

The SFG comb power is measured by a high-sensitivity power meter (Coherent, LaserMate-Q, wavelength from 800 to 1800 nm). To this end, the QCL beam is first blocked using a beam blocker and the background power P_0 is measured. The QCL beam is then unblocked and the power meter typically indicates a value around P_0 + 30 nW. The added 30 nW power come from the SFG process.

B.2 Coupling SFG signal in a fiber

A fiber coupler (Thorlabs, PAF2-5C) is mounted on a threaded kinematic mount with two adjusters. The mount is placed on a three-dimension translation stage. The fiber coupler contains a short focus lens magnetically attached to a tilt plate that can be adjusted directly on the vertical and horizontal directions. In addition, the lens can be tilted perpendicular to the optical axis by three incremental adjusters.

The walk-off angle between the SFG beam and the 1.85 μm comb is small and the

beams are very close. Directly coupling of the SFG beam into the optical fiber is quite difficult because its power is very low. First, we try to couple the 1.85 μm beam instead of the SFG beam into the optical fiber. To do that, we remove the optical filter at 1.55 μm and the polarization axis of the polarizer P2 is aligned parallel to the 1.85 μm beam polarization axis. We adjust the kinematic mount and the translation stage to optimize the power of the 1.85μm beam into the fiber.

To couple the SFG beam into the optical fiber, the polarization of the P2 is set back parallel to the SFG comb polarization axis. Because the 1.55μm SFG beam is very close to the 1.85 μm beam, a weak power from the SFG beam can be detected using the fibered power meter (less 1 nW). Alignment of the mount and the translation stage is made to maximize the detected power of the SFG.

Finally, we fine tune the longitudinal position of the lens in the coupler by adjusting the three z-axis adjusters to optimize the coupling efficiency. In our experiment, the coupling efficiency is at 50% and could be improved by using a fiber coupler better matched to the beam geometry.

APPENDIX C

OsO_4-stabilized CO_2 laser

C.1 Introduction

The carbone dioxide (CO_2) laser is a mid-IR high-power source whose wavelength can cover from 8 μm to 12 μm. At LPL, three CO_2 lasers have been used for 25 years for very high precision measurement using molecules. A LPL CO_2 laser includes a 1.2-m long Pyrex triple tube filled by typically 10 mTorr of a gas mixture containing ~2% of CO_2 molecules. A diffraction grating and a 92% reflection mirror located at the ends of the tube realize a laser cavity. The grating can be rotated using a micro-translation stage to choose the CO_2 emission lines. In addition, the mirror is glued onto a piezo-electric actuator which allows the cavity length to be tuned. The laser inversion population is obtained using a high continuous voltage discharge of 15 kV with a current of 15 mA. The laser emits a rovibrational transition of vibrationally excited CO_2 molecules. A free-running CO_2 laser has a linewidth around 700 Hz which can be reduced to the 10 Hz level by frequency locking of the laser to the rovibrational transition of molecules, such as saturated absorption lines of OsO_4 [47, 48, 201] or two-photon transition of SF_6 [125].

C.2 Operating principle

Let us consider the frequency stabilization of the CO_2 laser onto a saturated absorption line of the OsO_4 molecule. There are two main reasons to choose transitions of this molecule as a reference standard. The first one is the absence of a magnetic hyperfine structure. The molecule has thus the small fundamental frequency shifts and its absorption lines have high intensities and narrow linewidths. Another reason is that many transitions of this molecule can be found in the 10 μm range [312]. The principle of the frequency stabilization is presented in Figure C.1. A 1.5-m long Fabry-Perot cavity with a finesse of about 100 is filled with a gas phase of OsO_4. A broadband (~10 GHz) CdTe EOM generates two sidebands. One of these sidebands is brought into resonance with the OsO_4 line. The EOM frequency ν_{EOM} is modulated at two different frequencies, f_1 and f_2 using a RF synthesizer. To detect the molecular line, the cavity length is frequency locked to the sideband frequency with a first servo-loop which has a bandwidth of ~500 Hz. A second servo-loop including a fast- and slow-correction locks the sideband of the laser to the OsO_4 saturated absorption molecular line.

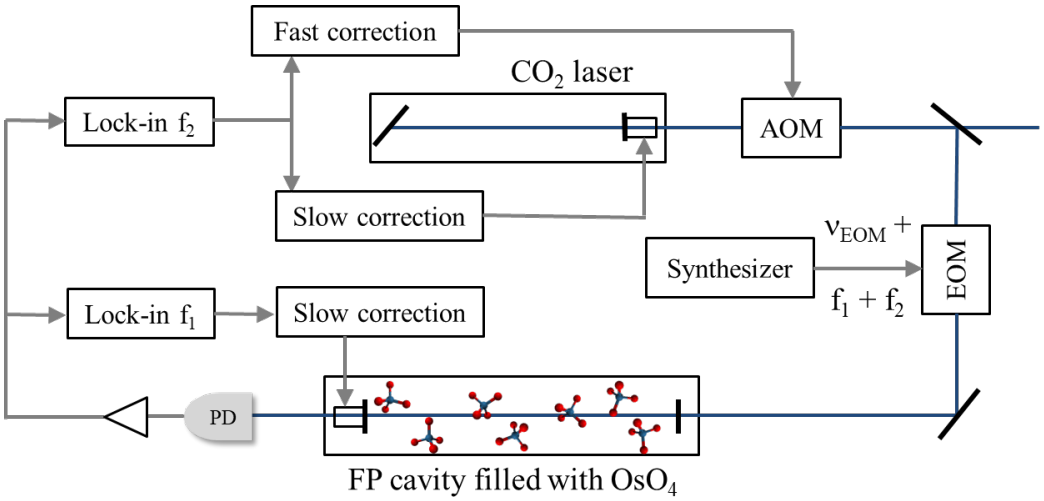

Figure C.1 – Schematic for locking the CO_2 laser on the saturated absorption transition of the OsO_4 molecule. AOM: acousto-optic modulator, EOM: electro-optic modulator, PD: photodiode.

C.3 Performances

By stabilizing two CO_2 lasers onto the same strong OsO_4 saturated absorption line, we can obtain the frequency noise PSD and the fractional frequency stability using a beat note between these stabilized lasers. The performances of the frequency stabilization of the CO_2 laser have been presented in Vincent Bernard's thesis [217].

Figure C.2 shows the frequency noise PSD of a free-running and a OSO_4 stabilized CO_2 laser. Below 100 Hz, the frequency noise of the stabilized CO_2 laser is smaller than the free-running laser by one order of magnitude. The bump around 400 Hz corresponds to the locking bandwidth of the servo-loop. Typically, the CO_2 laser stabilized to the OsO_4 line has a narrow linewidth of 10 Hz.

Figure C.3 illustrates the fractional frequency stability of the P(14) CO_2 laser line stabilized to the P(46) OsO_4 line which was obtained in 1997 from the beat note between two independent stabilized CO_2 lasers. The frequency stability is $3 \times 10^{-14}\,\tau^{-1/2}$ for integration times between 1 and 100 s corresponding to less than 1 Hz level.

Moreover, the frequency stability of the stabilized laser can be obtained by beating it with the LPL femtosecond laser locked to the optical frequency reference transferred from LNE-SYRTE to LPL via the optical fiber link. Figure C.4 shows the frequency stability of the CO_2 laser when stabilized to the P(55) line or R(67) line of OsO_4.

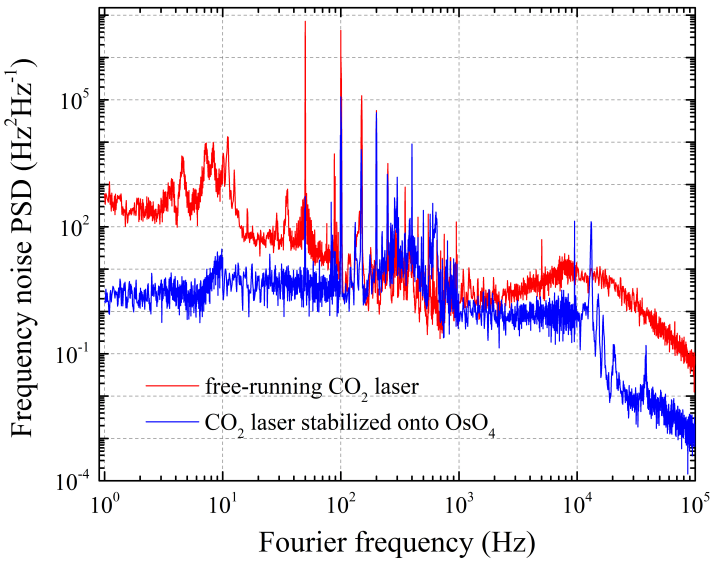

Figure C.2 – The frequency noise PSD of the free running CO_2 laser and the CO_2 laser stabilized on a OsO_4 saturated absorption line.

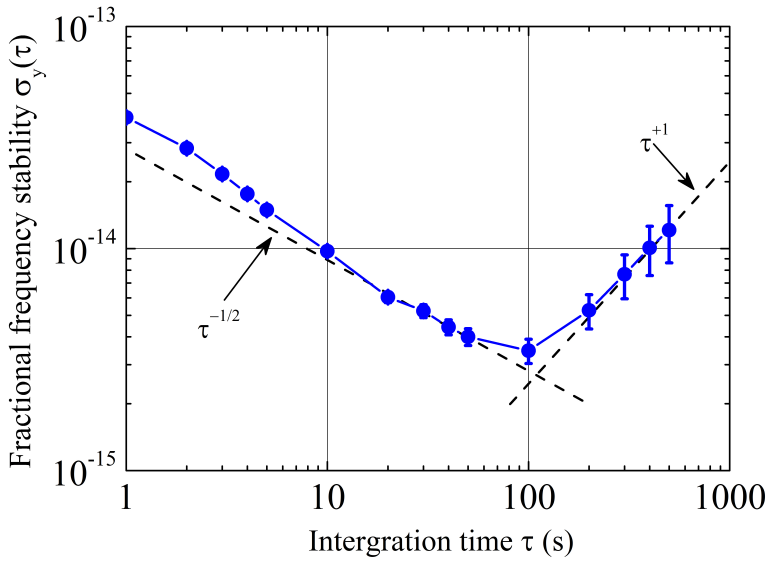

Figure C.3 – The fractional frequency stability of the P(14) CO_2 laser line stabilized to the P(46) OsO_4 line. The two dash lines show the $\tau^{-1/2}$ and τ^{+1} slopes.

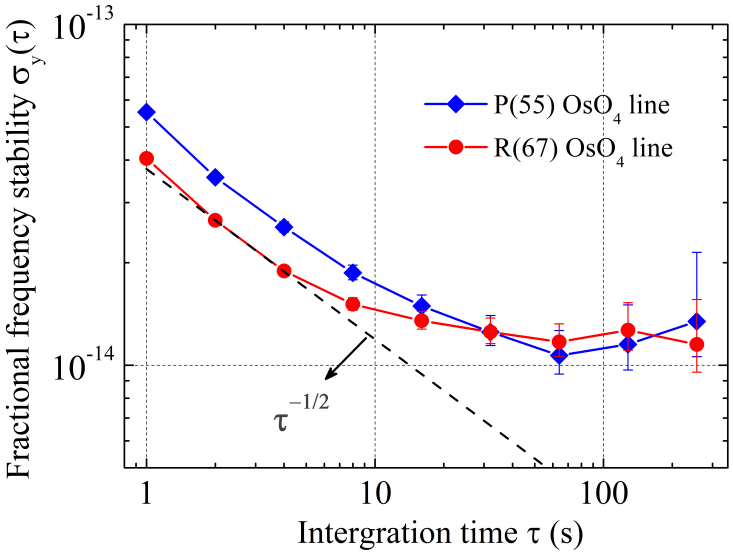

Figure C.4 – The fractional frequency stability of the CO_2 laser line stabilized to the P(46) and R(67) OsO_4 lines. The dash line shows the $\tau^{-1/2}$ slope, measured by beating the CO_2 laser with the optical frequency comb locked to the ultra-stable reference from LNE-SYRTE.

APPENDIX D

Means and errors of the frequency measurement

In this appendix, we list formulas of various types of means and errors which have been used to determine molecular parameters and then uncertainty, and in particular the absolute frequencies of molecular resonances. In addition, we also give the formulas of chi-squared and reduced chi-squared.

The standard formula of the unweighted mean $\bar{f}$ is

$$\bar{f} = \frac{\sum_{i=1}^{N} f_i}{N}, \tag{D.1}$$

where f_i is the value of the i^{th} measurement and N is the number of the measurements.

The formula of the best estimator of the standard deviation is

$$s = \sqrt{\frac{\sum_{i=1}^{N}(f_i - \bar{f})^2}{N-1}}. \tag{D.2}$$

The weight w_i of the i^{th} measurement exhibiting an experimental error bar e_i is given

$$w_i = \frac{1}{e_i^2} \frac{1}{\sum_{i=1}^{N} \frac{1}{e_i^2}}. \tag{D.3}$$

The formula of the weighted mean is

$$\bar{f}_w = \sum_{i=1}^{N} w_i f_i. \tag{D.4}$$

The formula of the weighted standard deviation is

$$sd_w = \sqrt{\frac{N'}{N'-1} \sum_{i=1}^{N} w_i (f_i - \bar{f}_w)^2}. \tag{D.5}$$

where N' is the number of non-zero weights.

The formula of the weighted standard error is

$$se_w = sd_w \sqrt{\sum_{i=1}^{N} w_i^2} \tag{D.6}$$

The formula of the chi-squared used to evaluate the fit of a spectrum is

$$\chi^2 = \sum_{i=1}^{N} \frac{(O_i - C_i)^2}{\sigma_i^2}, \tag{D.7}$$

where O_i is the i^{th} value of the measured data, C_i is the i^{th} value of the fitted data, and σ_i is the experimental error.

The formula of the reduced chi-squared is

$$\chi^2_{red} = \frac{\chi^2}{d}, \tag{D.8}$$

in which d is the degree of freedom, that equals to the number of experimental data N minus the number of fitted parameters n.

APPENDIX E

List of line-center frequencies of methanol recorded by direct absorption spectra

In this appendix, we first shows direct absorption spectra of methanol that have not been presented in chapter 4. Figures E.1-E.4 display Doppler-limited spectra of methanol (black curves) with different spectral ranges together with the resulting Gaussian fits (red curves) and spectra calculated using the HITRAN database (top, blue curves). The are recorded at a pressure of ∼7 Pa and a room temperature of ∼295 K using the experimental setup illustrated in Figure 4.11. The frequency axes are reconstructed using rovibrational transitions of methanol reported in HITRAN database as references (see section 4.3 for details).

We list in Table E.1 line-center frequencies of rovibrational transitions of methanol recorded with the free-running QCL together when possible with (sometimes tentative) assignments deduced from the HITRAN database. As mentioned in section 4.3, we estimate a conservative uncertainty on the line positions to be 30 MHz, limited by the quality of the frequency scale reconstruction.

Table E.1: Line-center frequencies of rovibrational transitions of methanol recorded by Doppler-limited absorption spectra together when possible with assignments deduced from the HITRAN database. Line-center position in cm^{-1}, intensity in cm^{-1}/molecule.cm^{-2}.

Fig.	HITRAN			This work		Note
	Transition	Position	Intensity	Position	Intensity	
Figure 4.13	-	-	-	971.53241	1.95×10^{-23}	3
	-	-	-	971.53878	1.19×10^{-23}	3
	$P(E, co, 0, 6, 33)$	971.54240	3.76×10^{-22}	971.54240	2.16×10^{-22}	1
	-	-	-	971.55033	1.47×10^{-23}	3
	-	-	-	971.55793	1.97×10^{-23}	3
	$P(A, co, 1, 3^+, 32)$	971.56269	2.45×10^{-22}	971.56225	1.82×10^{-22}	2
	$P(A, co, 1, 3^+, 32)$	971.56335	1.75×10^{-25}			4
	$(A, sb, 0, 1^-, 10)$	971.56577	7.95×10^{-22}	971.56522	2.41×10^{-22}	2
	$\leftarrow (A, gr, 2, 1^-, 11)$					
	$P(A, co, 1, 3^-, 32)$	971.56717	2.45×10^{-22}	971.56686	2.64×10^{-22}	2

	$P(A, co, 0, 4^-, 33)$	971.57152	5.30×10^{-22}	971.57152	3.09×10^{-22}	1
	-	-	-	971.57471	1.55×10^{-23}	3
	-	-	-	971.58159	6.66×10^{-23}	3
	-	-	-	971.58532	2.76×10^{-23}	3
	-	-	-	971.59095	2.09×10^{-23}	3
	$P(A, co, 0, 3^+, 33)$	971.59449	5.92×10^{-22}	971.59449	3.7×10^{-22}	1
	-	-	-	971.59799	1.55×10^{-23}	3
	-	-	-	971.60350	1.16×10^{-23}	3
	-	-	-	971.60922	4.63×10^{-23}	3
	$(E, oh, 0, -1, 21)$ $\leftarrow (E, gr, 2, -1, 22)$	971.61211	2.05×10^{-22}	971.61229	4.32×10^{-23}	1
	-	-	-	971.61553	4.50×10^{-23}	3
	-	-	-	971.61898	1.73×10^{-23}	3
	-	-	-	971.62123	2.8×10^{-23}	3
Figure 4.12	$P(A, co, 0, 0^+, 33)$	971.69901	7.59×10^{-22}	971.69888	4.99×10^{-22}	1
	-	-	-	971.70966	1.35×10^{-23}	3
	-	-	-	971.72030	2.78×10^{-23}	3
	$P(A, co, 0, 0^+, 33)$	971.72791	2.75×10^{-22}	971.72756	2.27×10^{-22}	3
	$P(A, co, 0, 0^-, 33)$	971.72791	2.58×10^{-22}			
	-	-	-	971.73147	1.02×10^{-22}	2
	$P(E, co, 0, -4, 33)$	971.73937	3.56×10^{-22}	971.73937	1.87×10^{-22}	1
	-	-	-	971.74438	1.41×10^{-23}	3
	-	-	-	971.74806	1.49×10^{-23}	3
	-	-	-	971.75174	1.41×10^{-23}	3
	-	-	-	971.75396	2.94×10^{-22}	3
	$P(E, co, 0, 42, 33)$	971.76295	7.49×10^{-22}	971.76277	4.08×10^{-22}	1
	-	-	-	971.77003	1.74×10^{-23}	3
	-	-	-	971.77740	3.48×10^{-23}	3
	$P(A, co, 1, 5^+, 33)$ $P(A, co, 1, 5^-, 33)$	971.79149	2.25×10^{-22} 2.70×10^{-22}	971.79194	1.06×10^{-22}	2
	$P(A, co, 0, 5^\pm, 33)$?	-	-	971.79427	4.35×10^{-23}	2
	-	-	-	971.79635	9.68×10^{-23}	3
	-	-	-	971.79902	4.69×10^{-23}	3
	-	-	-	971.74632	1.67×10^{-23}	3
	-	-	-	971.75072	1.63×10^{-23}	3
	-	-	-	971.75328	3.16×10^{-23}	3
	$P(E, co, 0, 42, 33)$	971.76295	7.49×10^{-22}	971.76277	4.50×10^{-22}	1
	-	-	-	971.77020	1.66×10^{-23}	3
	-	-	-	971.77755	3.42×10^{-23}	3
Figure E.1	$P(A, co, 1, 5^+, 33)$? $P(A, co, 1, 5^-, 33)$?	971.79149	2.25×10^{-22} 2.70×10^{-22}	971.79155	1.07×10^{-22}	2
	-	-	-	971.79372	4.50×10^{-23}	2
	$P(A, co, 0, 5^\pm, 33)$?	-	-	971.79569	9.8×10^{-23}	3
	-	-	-	971.79815	4.67×10^{-23}	3
	-	-	-	971.80536	2.81×10^{-23}	3
	-	-	-	971.81917	2.27×10^{-23}	3
	$P(E, co, 0, 8, 33)$	971.83309	2.30×10^{-22}	971.83309	1.48×10^{-22}	1
	$P(A, co, 0, 1^+, 33)$	971.86929	7.37×10^{-22}	971.86929	5.08×10^{-22}	1
	-	-	-	971.87277	1.33×10^{-23}	3

Figure E.2	-	-	-	971.88161	8.57×10^{-23}	3
	$P(E, co, 0, 0, 33)$	971.88335	7.53×10^{-22}	971.88443	4.78×10^{-22}	2
	$P(E, co, 1, -5, 30)$	971.89903	1.96×10^{-22}	971.89902	1.38×10^{-22}	1
	-	-	-	971.90234	2.09×10^{-23}	3
	-	-	-	971.91487	3.69×10^{-23}	3
	-	-	-	971.91731	2.12×10^{-23}	3
	-	-	-	971.92066	1.72×10^{-23}	3
	-	-	-	971.92697	3.67×10^{-23}	3
	-	-	-	971.93097	9.62×10^{-24}	3
	-	-	-	971.93556	4.08×10^{-23}	3
	-	-	-	971.94293	1.61×10^{-22}	1,4
	${}^{P}P(E, ri, 0, -5, 32)$	971.94430	5.62×10^{-22}	971.94500	1.94×10^{-22}	1
	-	-	-	971.94757	4.12×10^{-23}	3
	-	-	-	971.95053	7.19×10^{-24}	3
	-	-	-	971.95553	5.24×10^{-23}	3
	-	-	-	971.96087	1.18×10^{-23}	3
Figure 4.14	-	-	-	971.93443	4.36×10^{-23}	3
	-	-	-	971.94283	1.76×10^{-22}	1,4
	${}^{P}P(E, ri, 0, -5, 32)$	971.94430	5.62×10^{-22}	971.94510	2.19×10^{-22}	1
	-	-	-	971.94761	4.96×10^{-23}	3
	-	-	-	971.95046	7.24×10^{-24}	3
	-	-	-	971.95587	5.26×10^{-23}	3
	-	-	-	971.96454	3.12×10^{-24}	3
	-	-	-	971.96122	9.58×10^{-24}	3
	-	-	-	971.96664	7.91×10^{-23}	3
	$P(E, co, 2, 1, 34)$	971.97019	4.54×10^{-23}	971.97369	4.67×10^{-23}	2
	${}^{P}P(E, ri, 1, 2, 30)$	971.98291	2.28×10^{-22}	971.98290	1.64×10^{-22}	1
	-	-	-	971.98587	2.95×10^{-23}	3
	-	-	-	971.99047	4.36×10^{-22}	3
	-	-	-	971.99404	5.06×10^{-23}	3
	-	-	-	971.99582	2.38×10^{-23}	3
	-	-	-	971.99964	1.54×10^{-23}	3
	$P(E, co, 0, -1, 33)$	971.99046	7.92×10^{-22}	972.00204	2.42×10^{-23}	1
	-	-	-	972.01018	1.36×10^{-23}	3
	-	-	-	972.01558	8.32×10^{-23}	3
	-	-	-	972.02459	2.10×10^{-24}	3
Figure E.3	-	-	-	972.29197	1.70×10^{-23}	3
	-	-	-	972.29405	3.41×10^{-23}	3
	${}^{P}P(A, ri, 0, 6^{+}, 32)$	972.30634	2.62×10^{-22}	972.30634	2.41×10^{-22}	1
	$P(E, co, 0, 10, 33)$	972.31199	1.05×10^{-22}			4
	${}^{P}P(A, ri, 0, 6^{-}, 32)$	972.31410	2.55×10^{-22}	972.31427	2.47×10^{-22}	2
	-	-	-	972.31874	1.16×10^{-23}	3
	-	-	-	972.32440	1.64×10^{-23}	3
	-	-	-	972.34044	2.04×10^{-23}	3
	$P(E, co, 1, -4, 32)$	972.34367	3.02×10^{-22}	972.34362	1.52×10^{-22}	1
	$(E, gr, 3, -5, 34)$ $\leftarrow (E, gr, 0, -5, 35)$	972.34824	2.90×10^{-23}	972.34830	3.07×10^{-23}	1
	-	-	-	972.35202	1.00×10^{-23}	3
	$P(A, co, 0, 12^{-}, 33)$ $P(A, co, 0, 12^{+}, 33)$	972.35908	7.09×10^{-23} 5.62×10^{-23}	972.35906	8.72×10^{-23}	1
	-	-	-	972.36141	2.13×10^{-23}	3

	-	-	-	972.36653	7.58×10^{-23}	3
	-	-	-	972.36880	2.37×10^{-23}	3
	-	-	-	972.37316	1.24×10^{-23}	3
Figure E.4	-	-	-	972.41286	1.17×10^{-23}	3
	-	-	-	972.41998	2.81×10^{-23}	3
	$P(A, co, 1, 7^-, 29)$ $P(A, co, 1, 7^+, 29)$	972.35908	5.26×10^{-23} 2.30×10^{-22}	972.43107	1.95×10^{-22}	1
	-	-	-	972.43878	2.28×10^{-23}	3
	-	-	-	972.46449	1.19×10^{-23}	3
	$P(A, co, 0, 9, 33)$	972.47046	1.29×10^{-22}	972.47046	1.11×10^{-22}	1
	-	-	-	972.47905	3.12×10^{-23}	3
	-	-	-	972.48895	7.53×10^{-23}	3

1: Absolute frequency from the HITRAN database used for calibration.
2: Absolute frequency from the HITRAN database not used for calibration.
3: Potential new transition.
4: Rovibrational transition reported in the HITRAN database apparently not observed in our data.
?: tentative assignments by us.

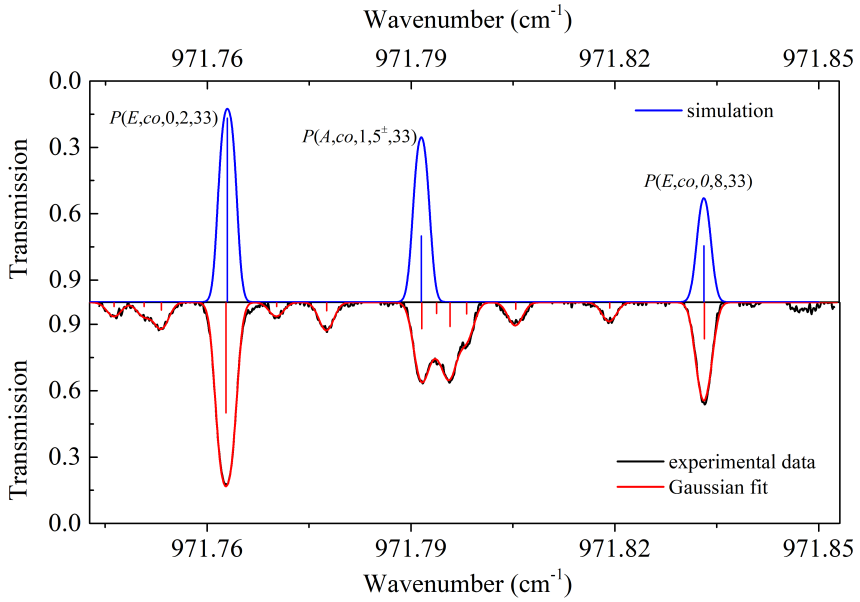

Figure E.1 – Doppler-limited absorption spectrum from 971.743 to 971.853 cm^{-1} of methanol in the multipass cell (bottom, black curve). It is recorded at a pressure of ∼7 Pa using the free-running QCL. The red curve is a fit to the data, corresponding to a sum of 13 Gaussian line shapes. The resulting line-center frequencies are indicated by red sticks. The blue curve is the simulated spectrum using the HITRAN database. Blue sticks indicate the line-center frequencies of methanol lines reported in the HITRAN database.

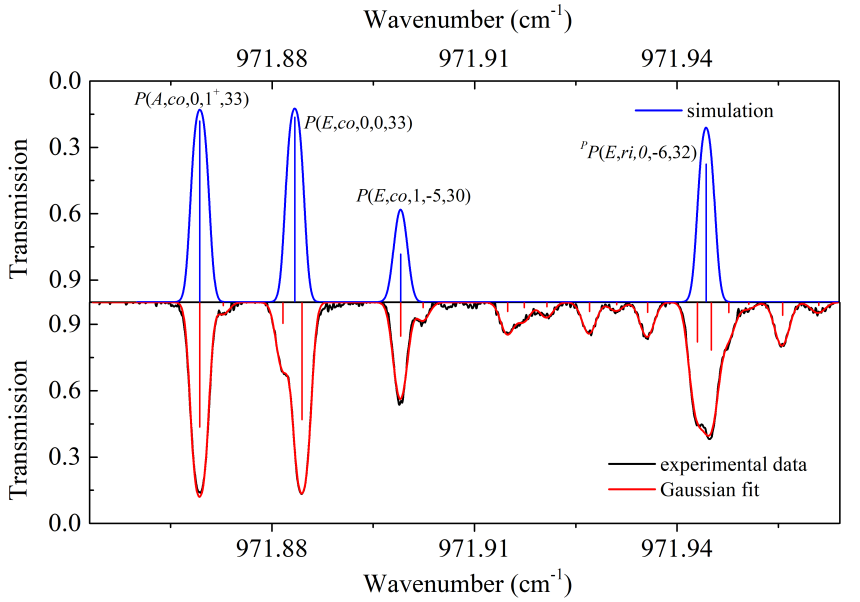

Figure E.2 – Doppler-limited absorption spectrum from 971.853 to 971.964 cm^{-1} of methanol in the multipass cell (bottom, black curve). It is recorded at a pressure of ∼7 Pa using the free-running QCL. The red curve is a fit to the data, corresponding to a sum of 18 Gaussian line shapes. The resulting line-center frequencies are indicated by red sticks. The blue curve is the simulated spectrum using the HITRAN database. Blue sticks indicate the line-center frequencies of methanol lines reported in the HITRAN database.

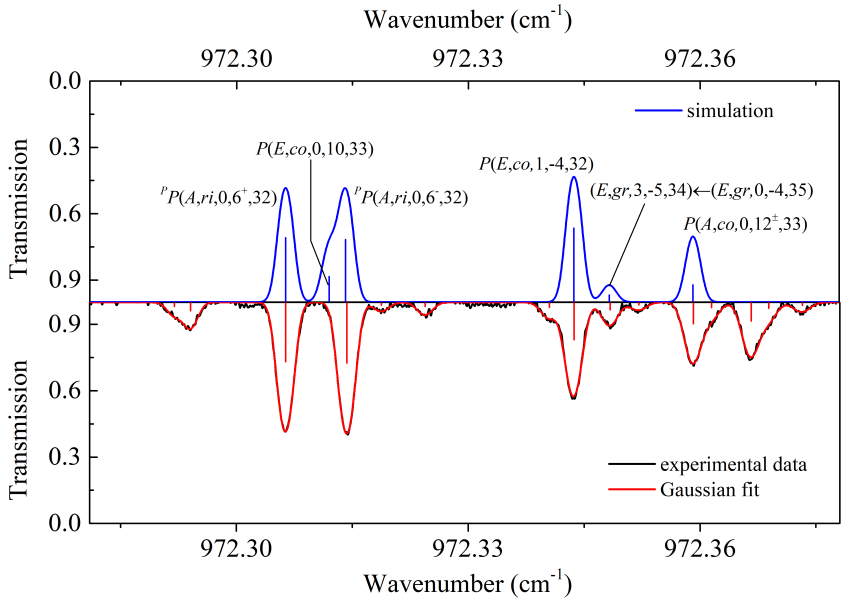

Figure E.3 – Doppler-limited absorption spectrum from 972.281 to 972.378 cm^{-1} of methanol in the multipass cell (bottom, black curve). It is recorded at a pressure of ∼7 Pa using the free-running QCL. The red curve is a fit to the data, corresponding to a sum of 15 Gaussian line shapes. The resulting line-center frequencies are indicated by red sticks. The blue curve is the simulated spectrum using the HITRAN database. Blue sticks indicate the line-center frequencies of methanol lines reported in the HITRAN database.

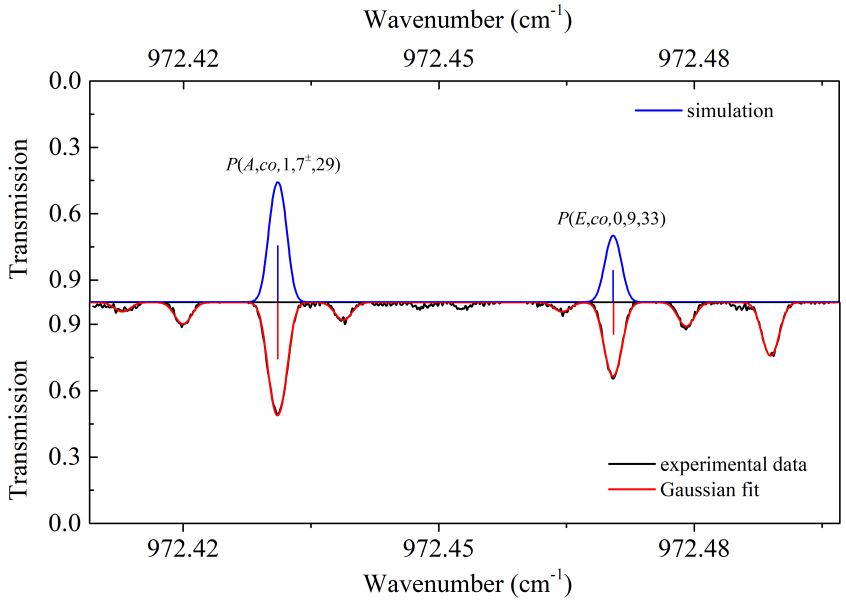

Figure E.4 – Doppler-limited absorption spectrum from 972.409 to 972.497 cm^{-1} of methanol in the multipass cell (bottom, black curve). It is recorded at a pressure of ∼7 Pa using the free-running QCL. The red curve is a fit to the data, corresponding to a sum of 8 Gaussian line shapes. The resulting line-center frequencies are indicated by red sticks. The blue curve is the simulated spectrum using the HITRAN database. Blue sticks indicate the line-center frequencies of methanol lines reported in the HITRAN database.

APPENDIX F

Saturated absorption spectra of non-resolved K-doublets

In this appendix, we show saturated absorption spectra of several non-resolved K-doublets of methanol with $K = 8$, 11, 12 and $J = 33$ and 34. As mentioned in subsection **??**, for each non-resolved K-doublet, we have only carried out only one measurement consisting in recording five pairs of up and down spectra. Figures F.1-F.6 show saturated absorption of the six non-resolved K-doublets: $P(A, co, 0, 12^{\pm}, 34)$, $P(A, co, 0, 11^{\pm}, 34)$, $P(A, co, 0, 8^{\pm}, 34)$,$P(A, co, 0, 12^{\pm}, 33)$, $P(A, co, 0, 11^{\pm}, 33)$, and $P(A, co, 0, 8^{\pm}, 33)$, respectively. Modulation parameters are listed in the captions of the figures. The frequency axes are reconstructed using the radio-frequency protocol. Line-center frequencies of these K-doublets are determined by applying the "pair by pair" analysis and listed in Table 4.8. Statistical uncertainty of each transition is estimated using the rule described in subsection 4.6.3 while systematic uncertainty is determined by following Table 4.6.

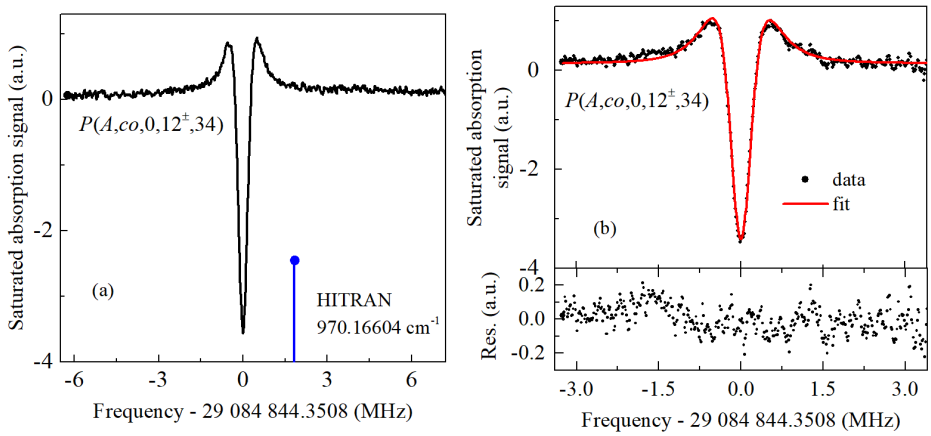

Figure F.1 – (a) Saturated absorption spectrum of the $P(A, co, 0, 12^{\pm}, 34)$ K-doublet around 970.166 cm^{-1} recorded using frequency modulation and second-harmonic detection. Experimental conditions: pressure, 1.7 Pa; intra-cell average laser power, ∼0.8 mW; modulation frequency, 20 kHz; frequency modulation excursion, 180 kHz; frequency step, ∼15 kHz; average of five pairs of up and down scans; total integration time per point, 1 s; whole spectrum measurement time, 901 s. The $P(A, co, 0, 12^{\pm}, 34)$ degenerate (indicated by ×2) doublet position reported in the HITRAN database [54] is also shown as a blue stick. (b) One averaged pair of up and down scans contributing to the data of panel (a), the resulting fit to the data, and its residuals. The total integration time per point is 200 ms, whole spectrum measurement time: 89 s.

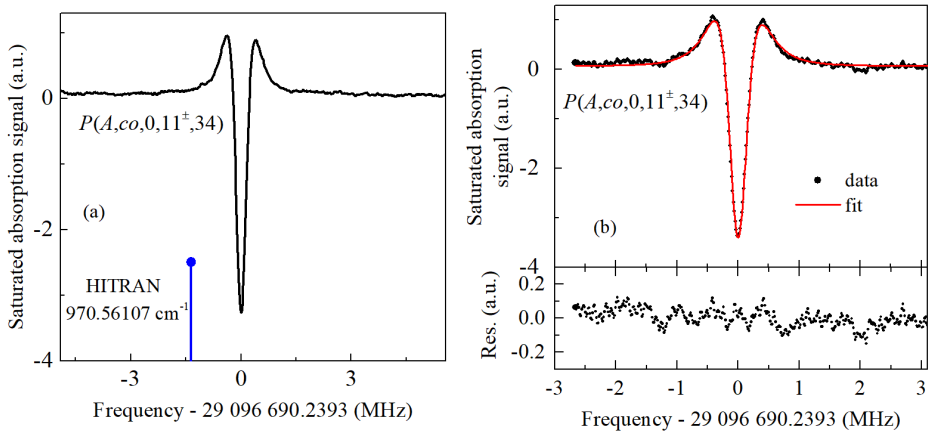

Figure F.2 – (a) Saturated absorption spectrum of the $P(A, co, 0, 11^{\pm}, 34)$ K-doublet around 970.516 cm^{-1} recorded using frequency modulation and second-harmonic detection. Experimental conditions: pressure, ∼1.7 Pa; intra-cell average laser power, ∼0.78 mW; modulation frequency, 20 kHz; frequency modulation excursion, 150 kHz; frequency step, ∼15 kHz; average of five pairs of up and down scans; total integration time per point, 1 s; whole spectrum measurement time, 701 s. The $P(A, co, 0, 11^{\pm}, 34)$ degenerate (indicated by ×2) doublet position reported in the HITRAN database [54] is also shown as a blue stick. (b) One averaged pair of up and down scans contributing to the data of panel (a), the resulting fit to the data, and its residuals. The total integration time per point is 200 ms, whole spectrum measurement time: 77 s.

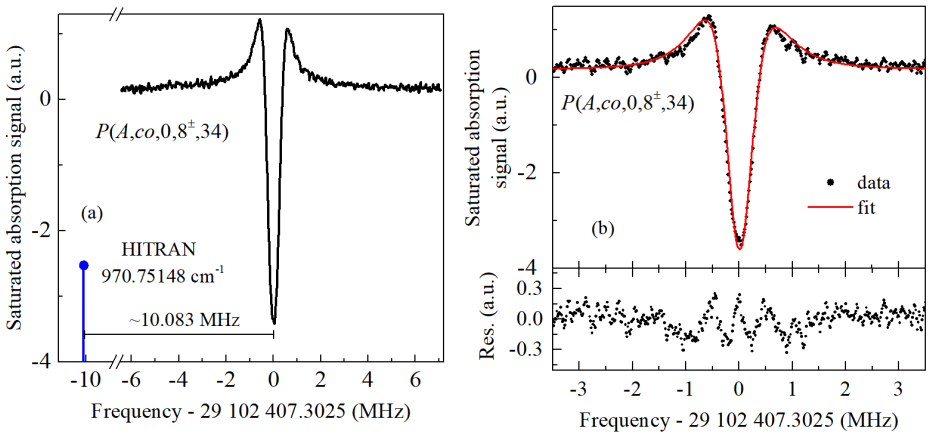

Figure F.3 – (a) Saturated absorption spectrum of the $P(A, co, 0, 8^{\pm}, 34)$ K-doublet around 970.751 cm^{-1} recorded using frequency modulation and second-harmonic detection. Experimental conditions: pressure, 1.7 Pa; intra-cell average laser power, ∼0.87 mW; modulation frequency, 20 kHz; frequency modulation excursion, 180 kHz; frequency step, ∼15 kHz; average of five pairs of up and down scans; total integration time per point, 1 s; whole spectrum measurement time, 901 s. The $P(A, co, 0, 8^{\pm}, 33)$ degenerate (indicated by ×2) doublet position reported in the HITRAN database [54] is also shown as a blue stick. (b) One averaged pair of up and down scans contributing to the data of panel (a), the resulting fit to the data, and its residuals. The total integration time per point is 200 ms, whole spectrum measurement time: 94 s.

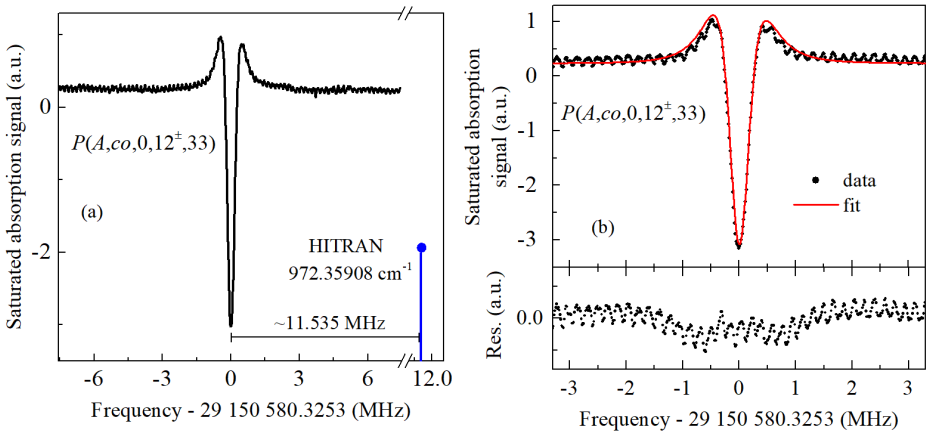

Figure F.4 – (a) Saturated absorption spectrum of the $P(A, co, 0, 12^{\pm}, 33)$ K-doublet around 972.359 cm^{-1} recorded using frequency modulation and second-harmonic detection. Experimental conditions: pressure, 1.7 Pa; intra-cell average laser power, ∼0.87 mW; modulation frequency, 20 kHz; frequency modulation excursion, 200 kHz; frequency step, ∼15 kHz; average of five pairs of up and down scans; total integration time per point, 1 s; whole spectrum measurement time, 1001 s. The $P(A, co, 0, 12^{\pm}, 33)$ degenerate (indicated by ×2) doublet position reported in the HITRAN database [54] is also shown as a blue stick. (b) One averaged pair of up and down scans contributing to the data of panel (a), the resulting fit to the data, and its residuals. The total integration time per point is 200 ms, whole spectrum measurement time: 88 s.

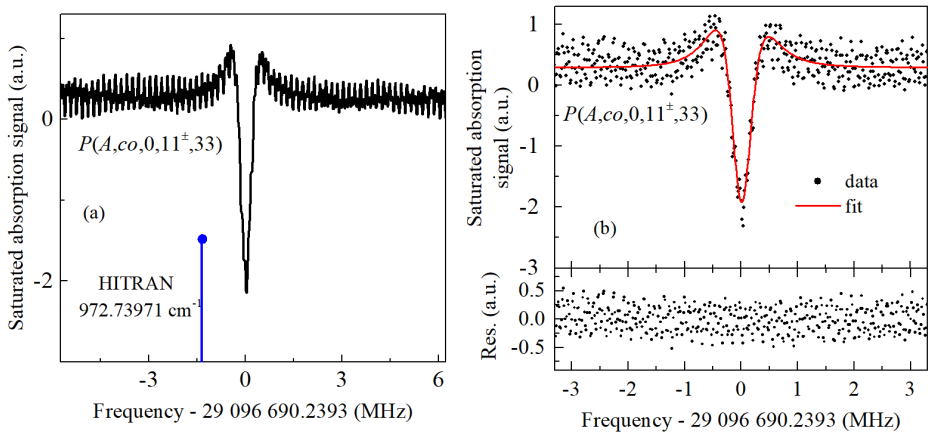

Figure F.5 – (a) Saturated absorption spectrum of the $P(A, co, 0, 11^{\pm}, 33)$ K-doublet around 970.011 cm^{-1} recorded using frequency modulation and second-harmonic detection. Experimental conditions: pressure, 1.7 Pa; intra-cell average laser power, ∼0.16 mW; modulation frequency, 20 kHz; frequency modulation excursion, 180 kHz; frequency step, ∼15 kHz; average of five pairs of up and down scans; total integration time per point, 1 s; whole spectrum measurement time, 801 s. The $P(A, co, 0, 11^{\pm}, 33)$ degenerate (indicated by ×2) doublet position reported in the HITRAN database [54] is also shown as a blue stick. (b) One averaged pair of up and down scans contributing to the data of panel (a), the resulting fit to the data, and its residuals. The total integration time per point is 200 ms, whole spectrum measurement time: 88 s.

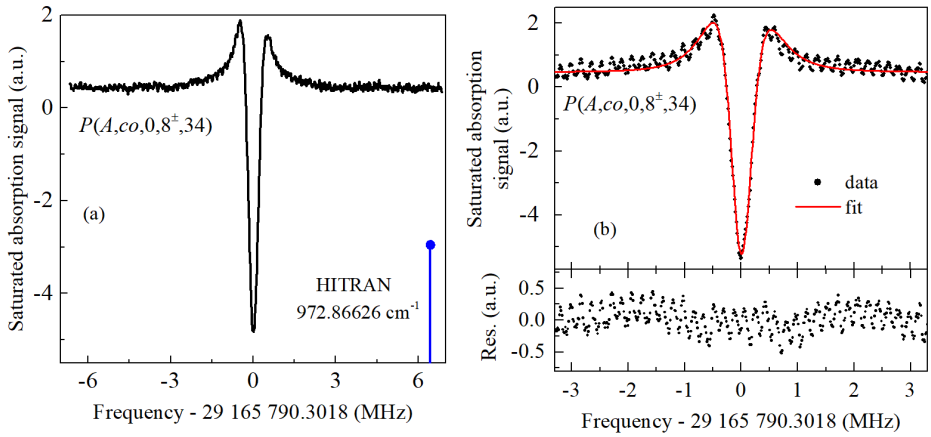

Figure F.6 – (a) Saturated absorption spectrum of the $P(A, co, 0, 8^{\pm}, 34)$ K-doublet around 970.011 cm^{-1} recorded using frequency modulation and second-harmonic detection. Experimental conditions: pressure, 1.7 Pa; intra-cell average laser power, ∼0.26 mW; modulation frequency, 20 kHz; frequency modulation excursion, 180 kHz; frequency step, ∼15 kHz; average of five pairs of up and down scans; total integration time per point, 1 s; whole spectrum measurement time, 901 s. The $P(A, co, 0, 8^{\pm}, 34)$ degenerate (indicated by ×2) doublet position reported in the HITRAN database [54] is also shown as a blue stick. (b) One averaged pair of up and down scans contributing to the data of panel (a), the resulting fit to the data, and its residuals. The total integration time per point is 200 ms, whole spectrum measurement time: 84 s.

APPENDIX G

Line-center frequencies and uncertainties of rovibrational lines of trioxane

Table G.1: Line-center frequencies and total uncertainties of non-assigned rovibrational transitions of trioxane.

$J = 15$	$J = 16$	$J = 17$
29 136 289 063.5 (22.4)	29 125 677 376.3 (49.6)	29 115 099 123.6 (28.7)
29 136 294 385.8 (5.5)	29 125 698 263.5 (10.7)	29 115 109 661.9 (22.2)
29 136 304 956.6 (5.9)	29 125 708 819.2 (6.0)	29 115 141 273.2 (12.6)
29 136 336 697.4 (5.4)	29 125 740 500.8 (5.6)	29 115 156 219.3 (26.1)
29 136 353 791.1 (35.3)	29 125 747 659.0 (43.6)	29 115 164 436.0 (50)
29 136 360 523.2 (40.5)	29 125 793 308.2 (5.4)	29 115 170 278.5 (42)
29 136 387 500.3 (38.1)	29 125 815 061.6 (42.4)	29 115 193 959.8 (9.9)
29 136 389 610.3 (5.4)	29 125 827 160.1 (45.3)	29 115 258 103.8 (45.4)
29 136 463 704.6 (5.4)	29 125 867 253.1 (5.9)	29 115 267 746.2 (10.6)
29 136 491 165.5 (40.7)	29 125 893 776.6 (45.9)	29 115 362 656.8 (8.3)
29 136 559 001.6 (5.4)	29 125 925 439.4 (40.1)	29 115 383 577.4 (44.3)
29 136 621 747.1 (23.7)	29 125 939 359.4 (9.6)	29 115 415 855.0 (44.8)
29 136 632 346.5 (29.1)	29 125 962 362.4 (6.1)	29 115 462 374.1 (49.2)
29 136 636 163.6 (33)	29 125 964 323.6 (45.5)	29 115 478 697.7 (8.1)
29 136 675 522.8 (5.4)	29 125 999 534.3 (46.5)	29 115 563 304.0 (42.5)
29 136 742 214.7 (31.2)	29 126 014 210.1 (21.1)	29 115 586 818.1 (48.5)
29 136 813 299.1 (5.6)	29 126 053 314.7 (45.7)	29 115 615 916.0 (10.1)
29 136 874 960.5 (49)	29 126 060 500.3 (47.8)	29 115 654 534.7 (50.9)
29 136 895 043.3 (43.9)	29 126 063 484.3 (44.7)	29 115 691 394.5 (49.2)
29 136 952 104.3 (21.4)	29 126 078 650.6 (6.9)	29 115 723 039.4 (40.1)
29 136 959 468.9 (44.3)	29 126 091 064.1 (44.5)	29 115 729 976.5 (24.4)
29 136 972 362.8 (7.1)	29 126 102 964.9 (50.5)	29 115 774 323.2 (21.5)
29 137 023 561.9 (36.8)	29 126 106 675.3 (51.9)	29 115 876 220.9 (50.2)
29 137 100 857.9 (28.4)	29 126 122 779.8 (43.8)	29 115 953 973.4 (29.6)
29 137 115 144.7 (45.6)	29 126 138 212.7 (39.9)	29 116 009 523.0 (50.7)
29 137 146 891.7 (48.6)	29 126 139 343.9 (45.2)	29 116 077 348.8 (51.4)
29 137 152 755.1 (6.5)	29 126 155 121.1 (42.6)	29 116 153 143.9 (51.2)
29 137 246 918.9 (33.9)	29 126 173 835.4 (42.1)	29 116 154 904.0 (15.8)
29 137 328 973.7 (45.4)	29 126 192 390.9 (41)	29 116 196 311.9 (44.5)
29 137 354 517.8 (5.6)	29 126 210 045.3 (48.6)	29 116 266 701.2 (41.4)

29 137 385 650.7 (37.4)
29 137 387 376.0 (48.4)
29 137 427 759.3 (42.1)
29 137 461 268.3 (41)
29 137 526 066.8 (44.8)
29 137 562 856.0 (46.4)
29 137 577 698.0 (6.4)
29 137 588 495.0 (8.5)
29 137 614 218.3 (39.9)
29 137 679 360.5 (39.2)
29 137 738 957.6 (46.1)
29 137 739 929.4 (30.5)
29 137 778 819.5 (44.5)
29 137 822 354.5 (9.1)
29 137 833 172.7 (37.7)
29 137 877 990.5 (47.6)
29 137 896 760.2 (27.3)
29 137 906 153.4 (50.2)
29 137 928 951.8 (37)
29 137 932 087.7 (40.2)
29 137 938 434.2 (38)
29 137 945 410.0 (50.9)
29 137 964 071.1 (39.1)
29 137 966 882.7 (49.3)
29 137 968 626.5 (49.9)
29 137 975 265.8 (41.3)
29 137 982 475.5 (47.6)
29 138 004 220.8 (41.8)
29 138 017 157.9 (49.7)
29 138 035 127.7 (38.4)
29 138 037 737.8 (42.3)
29 138 045 551.6 (48.7)
29 138 055 687.9 (41.9)
29 138 058 907.1 (43.8)
29 138 088 539.4 (23.6)
29 138 104 275.4 (49.6)
29 138 113 984.8 (46.9)
29 138 123 545.0 (42.6)
29 138 156 603.6 (40.9)

29 126 216 152.8 (5.6)
29 126 224 518.0 (43)
29 126 228 837.5 (47.3)
29 126 275 616.2 (47.7)
29 126 352 193.0 (50.2)
29 126 374 898.7 (6.5)
29 126 388 117.9 (45.5)
29 126 404 761.2 (49.3)
29 126 406 238.6 (40.1)
29 126 420 723.0 (46.7)
29 126 448 883.2 (49)
29 126 451 007.1 (50.3)
29 126 455 715.4 (50)
29 126 466 148.9 (49.2)
29 126 474 707.1 (48.6)
29 126 481 379.7 (51.7)
29 126 501 105.7 (49)
29 126 521 862.4 (43.2)
29 126 548 046.7 (10.7)
29 126 554 924.1 (6.1)
29 126 591 642.4 (48.9)
29 126 602 743.0 (46)
29 126 631 269.1 (28.8)
29 126 637 687.7 (35.6)
29 126 638 842.8 (47.1)
29 126 666 125.2 (30.2)
29 126 697 167.3 (15)
29 126 707 008.1 (49.9)
29 126 733 434.4 (33.5)
29 126 746 780.3 (36.9)
29 126 756 286.2 (6.2)
29 126 784 865.2 (40.8)
29 126 811 464.8 (46.4)
29 126 818 678.6 (44.6)
29 126 843 647.7 (29.8)
29 126 915 173.2 (44.3)
29 126 926 742.7 (49.2)
29 126 979 024.3 (7.8)
29 127 009 834.5 (47)
29 127 069 845.5 (45.8)
29 127 070 793.6 (51.6)
29 127 106 817.3 (51.1)
29 127 111 936.0 (35.8)
29 127 124 103.9 (37.5)
29 127 141 891.3 (50.1)
29 127 165 517.0 (51.5)
29 127 200 894.2 (35.6)
29 127 218 110.2 (39.7)
29 127 223 191.0 (6.4)
29 127 247 896.0 (47.5)
29 127 288 256.5 (34.1)
29 127 317 510.8 (30.5)
29 127 356 251.6 (35)
29 127 358 798.4 (33.1)

29 116 316 172.9 (10.9)
29 116 377 182.3 (13.9)
29 116 420 818.9 (25.6)
29 116 432 667.9 (48.3)
29 116 457 002.9 (47.4)
29 116 494 021.6 (50.7)
29 116 505 568.0 (44.1)
29 116 514 258.9 (49.7)
29 116 536 991.7 (46.1)
29 116 598 703.9 (37)
29 116 620 844.1 (6.4)
29 116 647 252.5 (42.5)
29 116 660 341.8 (45.4)
29 116 701 056.2 (25.8)
29 116 728 621.8 (35.2)
29 116 777 697.6 (29.2)
29 116 778 298.2 (32.1)
29 116 808 068.9 (33.6)
29 116 810 370.9 (32.4)
29 116 813 199.4 (30.9)
29 116 829 029.2 (35.8)
29 116 833 083.2 (47.7)
29 116 838 611.3 (40)
29 116 841 389.8 (49.3)
29 116 850 635.4 (41.3)
29 116 865 389.2 (36.4)
29 116 885 949.4 (7.5)
29 116 902 572.4 (45.2)
29 116 904 136.9 (8.6)
29 116 933 638.3 (37.8)
29 116 939 163.5 (36.5)
29 116 947 124.2 (35.8)
29 116 970 165.6 (51.1)
29 116 971 831.9 (47)
29 117 004 288.3 (33.4)
29 117 020 828.3 (48.2)
29 117 031 548.7 (36.4)
29 117 051 830.2 (41.6)
29 117 058 466.8 (39.9)
29 117 081 561.8 (36.2)
29 117 108 210.3 (24.2)
29 117 138 755.1 (35.1)
29 117 172 572.2 (13.1)
29 117 178 662.0 (45.3)
29 117 241 868.0 (37.9)
29 117 258 352.5 (43.4)
29 117 259 193.1 (41.3)
29 117 327 158.1 (42.6)
29 117 332 600.9 (41.5)
29 117 354 609.3 (47.6)
29 117 363 850.7 (49.6)
29 117 382 171.5 (36.1)
29 117 420 983.8 (39.6)
29 117 457 964.3 (46.7)

29 127 369 951.9 (13)
29 127 389 082.8 (35)
29 127 392 392.3 (36.6)
29 127 414 611.9 (44.8)
29 127 422 977.9 (39.1)
29 127 426 696.9 (34.9)
29 127 433 300.2 (40.5)
29 127 438 730.0 (31.9)
29 127 452 352.6 (35.5)
29 127 488 856.3 (6.4)
29 127 502 344.7 (37.4)
29 127 525 878.6 (50)
29 127 530 548.4 (47.1)
29 127 532 363.1 (45.6)
29 127 536 217.3 (31.9)
29 127 550 360.9 (32.4)
29 127 553 401.5 (49.8)
29 127 564 807.7 (29.4)
29 127 589 000.4 (48.7)
29 127 617 132.7 (30)
29 127 642 668.3 (36.8)
29 127 664 040.0 (35.1)
29 127 691 011.8 (27.3)
29 127 71 6838.7 (41.1)
29 127 739 184.1 (34.6)
29 127 746 601.6 (42.2)
29 127 771 019.1 (40.7)
29 127 776 070.0 (10.6)
29 127 781 666.0 (39.7)
29 127 794 755.8 (35.4)
29 127 801 876.6 (48.6)
29 127 812 375.0 (35.9)
29 127 845 221.5 (46.8)
29 127 850 044.6 (31.5)
29 127 877 140.1 (44.5)
29 127 888 637.0 (49.1)
29 127 902 389.2 (37.1)
29 127 914 036.6 (46.4)
29 127 920 844.9 (39.1)
29 127 921 458.6 (45.8)
29 127 947 586.3 (45.6)
29 127 974 877.8 (28.2)
29 127 977 939.9 (46)
29 128 025 468.5 (35.1)
29 128 028 220.1 (35.7)
29 128 032 092.9 (35.3)
29 128 032 784.5 (12.3)
29 128 051 454.4 (45.3)
29 128 084 906.5 (25.5)
29 128 091 865.6 (50)
29 128 097 672.8 (31.2)
29 128 106 459.4 (37.5)
29 128 149 070.1 (33.1)
29 128 218 296.4 (38.2)
29 117 478 630.4 (44.4)
29 117 479 462.3 (47.5)
29 117 480 748.9 (25.2)
29 117 493 689.4 (6.8)
29 117 496 997.2 (46.6)
29 117 520 977.1 (46.5)
29 117 528 486.9 (44.8)
29 117 573 759.7 (48.9)
29 117 585 676.8 (44.3)
29 117 619 457.0 (36)
29 117 638 737.2 (29.6)
29 117 650 755.5 (40.6)
29 117 725 380.1 (35.5)
29 117 732 156.5 (30.6)
29 117 737 167.0 (46.4)
29 117 785 381.5 (18.7)
29 117 787 578.8 (42.1)
29 117 799 533.2 (33.5)
29 117 806 206.4 (27.8)
29 117 810 609.6 (29.5)

29 128 226 017.8 (32.4)
29 128 234 827.4 (47.6)
29 128 236 653.8 (26.9)
29 128 243 439.5 (38.7)

Bibliography

[1] T. Udem, R. Holzwarth, and T. W. Hänsch, "Optical frequency metrology," Nature **416**, 233 (2002).

[2] A. Peters, K. Y. Chung, and S. Chu, "Measurement of gravitational acceleration by dropping atoms," Nature **400**, 849 (1999).

[3] R. Bouchendira, P. Cladé, S. Guellati-Khélifa, F. Nez, and F. Biraben, "New determination of the fine structure constant and test of the quantum electrodynamics," Physical Review Letters **106**, 080801 (2011).

[4] N. Huntemann, B. Lipphardt, C. Tamm, V. Gerginov, S. Weyers, and E. Peik, "Improved limit on a temporal variation of m_p/m_e from comparisons of Yb^+ and Cs atomic clocks," Physical Review Letters **113**, 210802 (2014).

[5] R. Godun, P. Nisbet-Jones, J. Jones, S. King, L. Johnson, H. Margolis, K. Szymaniec, S. Lea, K. Bongs, and P. Gill, "Frequency ratio of two optical clock transitions in $^{171}Yb^+$ and constraints on the time variation of fundamental constants," Physical Review Letters **113**, 210801 (2014).

[6] S. Blatt, A. D. Ludlow, G. K. Campbell, J. W. Thomsen, T. Zelevinsky, M. M. Boyd, J. Ye, X. Baillard, M. Fouché, R. Le Targat, A. Brusch, P. Lemonde, M. Takamoto, F.-L. Hong, H. Katori, and V. V. Flambaum, "New limits on coupling of fundamental constants to gravity using ^{87}Sr optical lattice clocks," Phys. Rev. Lett. **100**, 140801 (2008).

[7] T. M. Fortier, N. Ashby, J. C. Bergquist, M. J. Delaney, S. A. Diddams, T. P. Heavner, L. Hollberg, W. M. Itano, S. R. Jefferts, K. Kim, F. Levi, L. Lorini, W. H. Oskay, T. E. Parker, J. Shirley, and J. E. Stalnaker, "Precision atomic spectroscopy for improved limits on variation of the fine structure constant and local position invariance," Phys. Rev. Lett. **98**, 070801 (2007).

[8] J. Guéna, M. Abgrall, D. Rovera, P. Rosenbusch, M. E. Tobar, P. Laurent, A. Clairon, and S. Bize, "Improved tests of local position invariance using ^{87}Rb and ^{133}Cs fountains," Phys. Rev. Lett. **109**, 080801 (2012).

[9] M. Abgrall, B. Chupin, L. De Sarlo, J. Guéna, P. Laurent, Y. Le Coq, R. Le Targat, J. Lodewyck, M. Lours, P. Rosenbusch, G. D. Rovera, and S. Bize, "Atomic fountains and optical clocks at SYRTE: Status and perspectives," Comptes Rendus Physique **16**, 461–470 (2015).

[10] B. Bloom, T. Nicholson, J. Williams, S. Campbell, M. Bishof, X. Zhang, W. Zhang, S. Bromley, and J. Ye, "An optical lattice clock with accuracy and stability at the 10^{-18} level," Nature **506**, 71 (2014).

[11] N. Nemitz, T. Ohkubo, M. Takamoto, I. Ushijima, M. Das, N. Ohmae, and H. Katori, "Frequency ratio of Yb and Sr clocks with 5×10^{-17} uncertainty at 150 seconds averaging time," Nature Photonics **10**, 258 (2016).

[12] P. Delva, J. Lodewyck, S. Bilicki, E. Bookjans, G. Vallet, R. Le Targat, P.-E. Pottie, C. Guerlin, F. Meynadier, C. Le Poncin-Lafitte, O. Lopez, A. Amy-Klein, W.-K. Lee, N. Quintin, C. Lisdat, A. Al-Masoudi, S. Dörscher, C. Grebing, G. Grosche, A. Kuhl, S. Raupach, U. Sterr, I. R. Hill, R. Hobson, W. Bowden, J. Kronjäger, G. Marra, A. Rolland, F. N. Baynes, H. S. Margolis, and P. Gill, "Test of special relativity using a fiber network of optical clocks," Phys. Rev. Lett. **118**, 221102 (2017).

[13] J. J. Harrison, P. F. Bernath, and G. Kirchengast, "Spectroscopic requirements for ACCURATE, a microwave and infrared-laser occultation satellite mission," Journal of Quantitative Spectroscopy and Radiative Transfer **112**, 2347–2354 (2011).

[14] M. Guinet, D. Mondelain, C. Janssen, and C. Camy-Peyret, "Laser spectroscopic study of ozone in the 100 ← 000 band for the SWIFT instrument," Journal of Quantitative Spectroscopy and Radiative Transfer **111**, 961–972 (2010).

[15] E. Herbst and E. F. Van Dishoeck, "Complex organic interstellar molecules," Annual Review of Astronomy and Astrophysics **47**, 427–480 (2009).

[16] E. Hinds, "Testing time reversal symmetry using molecules," Physica Scripta **1997**, 34 (1997).

[17] J. J. Hudson, D. M. Kara, I. Smallman, B. E. Sauer, M. R. Tarbutt, and E. A. Hinds, "Improved measurement of the shape of the electron," Nature **473**, 493 (2011).

[18] V. Andreev and N. Hutzler, "Improved limit on the electric dipole moment of the electron," Nature **562**, 355–360 (2018).

[19] W. B. Cairncross, D. N. Gresh, M. Grau, K. C. Cossel, T. S. Roussy, Y. Ni, Y. Zhou, J. Ye, and E. A. Cornell, "Precision measurement of the electron's electric dipole moment using trapped molecular ions," Physical Review Letters **119**, 153001 (2017).

[20] S. K. Tokunaga, C. Stoeffler, F. Auguste, A. Shelkovnikov, C. Daussy, A. Amy-Klein, C. Chardonnet, and B. Darquié, "Probing weak force-induced parity violation by high-resolution mid-infrared molecular spectroscopy," Molecular Physics **111**, 2363–2373 (2013).

[21] B. Darquié, C. Stoeffler, A. Shelkovnikov, C. Daussy, A. Amy-Klein, C. Chardonnet, S. Zrig, L. Guy, J. Crassous, P. Soulard, P. Asselin, T. R. Huet, P. Schwerdtfeger, R. Bast, and T. Saue, "Progress toward the first observation of parity violation in chiral molecules by high-resolution laser spectroscopy," Chirality **22**, 870–884 (2010).

[22] M. Quack and J. Stohner, "Influence of parity violating weak nuclear potentials on vibrational and rotational frequencies in chiral molecules," Physical Review Letters **84**, 3807 (2000).

[23] A. Cournol, M. Manceau, M. Pierens, L. Lecordier, D. B. A. Tran, R. Santagata, B. Argence, A. Goncharov, O. Lopez, M. Abgrall, Y. L. Coq, R. L. Targat, H. A. Martinez, W. K. Lee, D. Xu, P. E. Pottie, R. J. Hendricks, T. E. Wall, J. M. Bieniewska, B. E. Sauer, M. R. Tarbutt, A. Amy-Klein, S. K. Tokunaga, and

B. Darquié, "A new experiment to test parity symmetry in cold chiral molecules using vibrational spectroscopy," Quantum Electronics **49**, 288 (2019).

[24] L. Moretti, A. Castrillo, E. Fasci, M. D. De Vizia, G. Casa, G. Galzerano, A. Merlone, P. Laporta, and L. Gianfrani, "Determination of the Boltzmann constant by means of precision measurements of $H_2^{18}O$ line shapes at 1.39 μm," Phys. Rev. Lett. **111**, 060803 (2013).

[25] S. Mejri, P. Sow, O. Kozlova, C. Ayari, S. Tokunaga, C. Chardonnet, S. Briaudeau, B. Darquié, F. Rohart, and C. Daussy, "Measuring the Boltzmann constant by mid-infrared laser spectroscopy of ammonia," Metrologia **52**, S314 (2015).

[26] J. Fischer, B. Fellmuth, C. Gaiser, T. Zandt, L. Pitre, F. Sparasci, M. D. Plimmer, M. de Podesta, R. Underwood, G. Sutton, G. Machin, R. M. Gavioso, D. M. Ripa, P. P. M. Steur, J. Qu, X. J. Feng, J. Zhang, M. R. Moldover, S. P. Benz, D. R. White, L. Gianfrani, A. Castrillo, L. Moretti, B. Darquié, E. Moufarej, C. Daussy, S. Briaudeau, O. Kozlova, L. Risegari, J. J. Segovia, M. C. Martín, and D. del Campo, "The Boltzmann project," Metrologia **55**, R1 (2018).

[27] C. Daussy, M. Guinet, A. Amy-Klein, K. Djerroud, Y. Hermier, S. Briaudeau, C. J. Bordé, and C. Chardonnet, "Direct determination of the Boltzmann constant by an optical method," Physical Review Letters **98**, 250801 (2007).

[28] V. Q. Tran, J.-P. Karr, A. Douillet, J. C. Koelemeij, and L. Hilico, "Two-photon spectroscopy of trapped HD^+ ions in the lamb-dicke regime," Physical Review A **88**, 033421 (2013).

[29] J. Biesheuvel, J.-P. Karr, L. Hilico, K. Eikema, W. Ubachs, and J. Koelemeij, "Probing QED and fundamental constants through laser spectroscopy of vibrational transitions in HD^+," Nature communications **7**, 10385 (2016).

[30] J.-P. Karr, S. Patra, J. C. J. Koelemeij, J. Heinrich, N. Sillitoe, A. Douillet, and L. Hilico, "Hydrogen molecular ions: new schemes for metrology and fundamental physics tests," Journal of Physics: Conference Series **723**, 012048 (2016).

[31] J. Koelemeij, B. Roth, A. Wicht, I. Ernsting, and S. Schiller, "Vibrational spectroscopy of HD^+ with 2-ppb accuracy," Physical Review Letters **98**, 173002 (2007).

[32] F. Cozijn, P. Dupré, E. Salumbides, K. Eikema, and W. Ubachs, "Sub-doppler frequency metrology in HD for tests of fundamental physics," Physical Review Letters **120**, 153002 (2018).

[33] B. P. Schmidt, "Nobel lecture: Accelerating expansion of the universe through observations of distant supernovae," Reviews of Modern Physics **84**, 1151 (2012).

[34] A. Shelkovnikov, R. J. Butcher, C. Chardonnet, and A. Amy-Klein, "Stability of the proton-to-electron mass ratio," Physical Review Letters **100**, 150801 (2008).

[35] J. Bagdonaite, W. Ubachs, M. Murphy, and J. Whitmore, "Constraint on a varying proton-electron mass ratio 1.5 billion years after the big bang," Physical Review Letters **114**, 071301 (2015).

[36] J. Bagdonaite, P. Jansen, C. Henkel, H. L. Bethlem, K. M. Menten, and W. Ubachs, "A stringent limit on a drifting proton-to-electron mass ratio from alcohol in the early universe," Science **339**, 46–48 (2013).

[37] F. Bielsa, A. Douillet, T. Valenzuela, J.-P. Karr, and L. Hilico, "Narrow-line phase-locked quantum cascade laser in the 9.2 μm range," Optics letters **32**, 1641–1643 (2007).

[38] F. Cappelli, I. Galli, S. Borri, G. Giusfredi, P. Cancio, D. Mazzotti, A. Montori, N. Akikusa, M. Yamanishi, S. Bartalini, and P. D. Natale, "Subkilohertz linewidth room-temperature mid-infrared quantum cascade laser using a molecular sub-Doppler reference," Opt. Lett. **37**, 4811–4813 (2012).

[39] A. A. Mills, D. Gatti, J. Jiang, C. Mohr, W. Mefford, L. Gianfrani, M. Fermann, I. Hartl, and M. Marangoni, "Coherent phase lock of a 9 μm quantum cascade laser to a 2 μm thulium optical frequency comb," Optics letters **37**, 4083–4085 (2012).

[40] P. L. T. Sow, S. Mejri, S. K. Tokunaga, O. Lopez, A. Goncharov, B. Argence, C. Chardonnet, A. Amy-Klein, C. Daussy, and B. Darquié, "A widely tunable 10-μm quantum cascade laser phase-locked to a state-of-the-art mid-infrared reference for precision molecular spectroscopy," Applied Physics Letters **104**, 264101 (2014).

[41] M. G. Hansen, E. Magoulakis, Q.-F. Chen, I. Ernsting, and S. Schiller, "Quantum cascade laser-based mid-IR frequency metrology system with ultra-narrow linewidth and 1×10^{-13}-level frequency instability," Optics letters **40**, 2289–2292 (2015).

[42] I. Galli, M. Siciliani de Cumis, F. Cappelli, S. Bartalini, D. Mazzotti, S. Borri, A. Montori, N. Akikusa, M. Yamanishi, G. Giusfredi, P. Cancio, and P. De Natale, "Comb-assisted subkilohertz linewidth quantum cascade laser for high-precision mid-infrared spectroscopy," Applied Physics Letters **102**, 121117 (2013).

[43] M. Lamperti, B. AlSaif, D. Gatti, M. Fermann, P. Laporta, A. Farooq, and M. Marangoni, "Absolute spectroscopy near 7.8 μm with a comb-locked extended-cavity quantum-cascade-laser," Scientific reports **8**, 1292 (2018).

[44] E. Vicentini, A. Gambetta, N. Coluccelli, E. Fasci, A. Castrillo, L. Gianfrani, V. D. Sarno, P. Maddaloni, A. Ceausu-Velcescu, P. D. Natale, Y. Wang, T. T. Fernandez, P. Laporta, and G. Galzerano, "Rovibrational fine structure and transition dipole moment of CF_3H by frequency-comb-assisted saturated spectroscopy at 8.6 μm," Journal of Quantitative Spectroscopy and Radiative Transfer (2018).

[45] B. Argence, B. Chanteau, O. Lopez, D. Nicolodi, M. Abgrall, C. Chardonnet, C. Daussy, B. Darquié, Y. Le Coq, and A. Amy-Klein, "Quantum cascade laser frequency stabilization at the sub-Hz level," Nature Photonics **9**, 456 (2015).

[46] G. Insero, S. Borri, D. Calonico, P. C. Pastor, C. Clivati, D. D'ambrosio, P. Natale, M. Inguscio, F. Levi, and G. Santambrogio, "Measuring molecular frequencies in the 1-10 μm range at 11-digits accuracy," Scientific reports **7**, 12780 (2017).

[47] O. Acef, "CO_2/OsO_4 lasers as frequency standards in the 29 THz range," IEEE transactions on instrumentation and measurement **46**, 162–165 (1997).

[48] V. Bernard, P. Durand, T. George, H. Nicolaisen, A. Amy-Klein, and C. Chardonnet, "Spectral purity and long-term stability of CO_2 lasers at the Hertz level," IEEE journal of quantum electronics **31**, 1913–1918 (1995).

[49] W. Zhang, J. M. Robinson, L. Sonderhouse, E. Oelker, C. Benko, J. L. Hall, T. Legero, D. G. Matei, F. Riehle, U. Sterr, and J. Ye, "Ultrastable silicon cavity in a continuously operating closed-cycle cryostat at 4 K," Physical Review Letters **119**, 243601 (2017).

[50] O. Lopez, F. Kéfélian, H. Jiang, A. Haboucha, A. Bercy, F. Stefani, B. Chanteau, A. Kanj, D. Rovera, J. Achkar, C. Chardonnet, P.-E. Pottie, A. Amy-Klein, and G. Santarelli, "Frequency and time transfer for metrology and beyond using telecommunication network fibres," Comptes Rendus Physique **16**, 531–539 (2015).

[51] B. Chanteau, O. Lopez, W. Zhang, D. Nicolodi, B. Argence, F. Auguste, M. Abgrall, C. Chardonnet, G. Santarelli, B. Darquié, Y. L. Coq, and A. Amy-Klein, "Mid-infrared laser phase-locking to a remote near-infrared frequency reference for high-precision molecular spectroscopy," New Journal of Physics **15**, 073003 (2013).

[52] J. L. McHale, *Molecular spectroscopy* (CRC Press, 2017).

[53] J. J. Harrison, N. D. Allen, and P. F. Bernath, "Infrared absorption cross sections for methanol," Journal of Quantitative Spectroscopy and Radiative Transfer **113**, 2189–2196 (2012).

[54] I. Gordon, L. Rothman, C. Hill, R. Kochanov, Y. Tan, P. Bernath, M. Birk, V. Boudon, A. Campargue, K. Chance, B. Drouin, J.-M. Flaud, R. Gamache, J. Hodges, D. Jacquemart, V. Perevalov, A. Perrin, K. Shine, M.-A. Smith, J. Tennyson, G. Toon, H. Tran, V. Tyuterev, A. Barbe, A. Császár, V. Devi, T. Furtenbacher, J. Harrison, J.-M. Hartmann, A. Jolly, T. Johnson, T. Karman, I. Kleiner, A. Kyuberis, J. Loos, O. Lyulin, S. Massie, S. Mikhailenko, N. Moazzen-Ahmadi, H. Müller, O. Naumenko, A. Nikitin, O. Polyansky, M. Rey, M. Rotger, S. Sharpe, K. Sung, E. Starikova, S. Tashkun, J. V. Auwera, G. Wagner, J. Wilzewski, P. Wcislo, S. Yu, and E. Zak, "The HITRAN2016 molecular spectroscopic database," Journal of Quantitative Spectroscopy and Radiative Transfer **203**, 3–69 (2017).

[55] I. V. Hertel and C.-P. Schulz, *Atoms, Molecules and Optical Physics 1: Atoms and Spectroscopy* (Springer, 2015).

[56] C. J. Foot, *Atomic physics*, vol. 7 (Oxford University Press, 2005).

[57] C. J. Bordé, "On the theory of linear absorption line shapes in gases," Comptes Rendus Physique **10**, 866–882 (2009).

[58] C. J. Bordé, J. Hall, C. Kunasz, and D. Hummer, "Saturated absorption line shape: Calculation of the transit-time broadening by a perturbation approach," Physical Review A **14**, 236 (1976).

[59] V. Letokhov, "Saturation spectroscopy," in "High-Resolution Laser Spectroscopy," (Springer, 1976), pp. 95–171.

[60] F. Riehle, *Frequency standards: basics and applications* (John Wiley & Sons, 2006).

[61] J. Rutman and F. Walls, "Characterization of frequency stability in precision frequency sources," Proceedings of the IEEE **79**, 952–960 (1991).

[62] E. Rubiola, *Phase noise and frequency stability in oscillators* (Cambridge University Press, 2009).

[63] W. J. Riley, "Handbook of frequency stability analysis," (2008).

[64] A. Clairon, S. Ghezali, G. Santarelli, L. S. Laurent Ph, M. Bahoura, E. Simon, S. Weyers, and K. Szymaniec, "Preliminary accuracy evaluation of a cesium fountain frequency standard," (1996).

[65] D. Chambon, S. Bize, M. Lours, F. Narbonneau, H. Marion, A. Clairon, G. Santarelli, A. Luiten, and M. Tobar, "Design and realization of a flywheel oscillator for advanced time and frequency metrology," Review of Scientific Instruments **76**, 094704 (2005).

[66] J. Guena, M. Abgrall, D. Rovera, P. Laurent, B. Chupin, M. Lours, G. Santarelli, P. Rosenbusch, M. E. Tobar, R. Li, K. Gibble, A. Clairon, and S. Bize, "Progress

in atomic fountains at LNE-SYRTE," IEEE Transactions on Ultrasonics, Ferroelectrics, and Frequency Control **59**, 391–409 (2012).

[67] S. Bize, Y. Sortais, M. Santos, C. Mandache, A. Clairon, and C. Salomon, "High-accuracy measurement of the ^{87}Rb ground-state hyperfine splitting in an atomic fountain," EPL (Europhysics Letters) **45**, 558 (1999).

[68] C. Fertig and K. Gibble, "Measurement and cancellation of the cold collision frequency shift in an ^{87}Rb fountain clock," Physical Review Letters **85**, 1622 (2000).

[69] Y. Ovchinnikov and G. Marra, "Accurate rubidium atomic fountain frequency standard," Metrologia **48**, 87 (2011).

[70] https://www.bipm.org/en/publications/mises-en-pratique/standard frequencies.html .

[71] A. Goncharov, A. Amy-Klein, O. Lopez, F. Du Burck, and C. Chardonnet, "Absolute frequency measurement of the iodine-stabilized Ar^+ laser at 514.6 nm using a femtosecond optical frequency comb," Applied Physics B **78**, 725–731 (2004).

[72] T. Kobayashi, D. Akamatsu, K. Hosaka, H. Inaba, S. Okubo, T. Tanabe, M. Yasuda, A. Onae, and F.-L. Hong, "Compact iodine-stabilized laser operating at 531 nm with stability at the 10^{-12} level and using a coin-sized laser module," Optics express **23**, 20749–20759 (2015).

[73] J. Ye, L. S. Ma, and J. L. Hall, "Molecular iodine clock," Physical Review Letters **87**, 270801 (2001).

[74] J. Jiang, A. Onae, H. Matsumoto, and F.-L. Hong, "Frequency measurement of acetylene-stabilized lasers using a femtosecond optical comb without carrier-envelope offset frequency control," Optics express **13**, 1958–1965 (2005).

[75] A. Amy-Klein, A. Goncharov, C. Daussy, C. Grain, O. Lopez, G. Santarelli, and C. Chardonnet, "Absolute frequency measurement in the 28-THz spectral region with a femtosecond laser comb and a long-distance optical link to a primary standard," Applied Physics B **78**, 25–30 (2004).

[76] M. Takamoto, F.-L. Hong, R. Higashi, and H. Katori, "An optical lattice clock," Nature **435**, 321 (2005).

[77] N. Huntemann, C. Sanner, B. Lipphardt, C. Tamm, and E. Peik, "Single-ion atomic clock with 3×10^{-18} systematic uncertainty," Physical Review Letters **116**, 063001 (2016).

[78] I. Ushijima, M. Takamoto, M. Das, T. Ohkubo, and H. Katori, "Cryogenic optical lattice clocks," Nature Photonics **9**, 185 (2015).

[79] T. Nicholson, S. Campbell, R. Hutson, G. Marti, B. Bloom, R. McNally, W. Zhang, M. Barrett, M. Safronova, G. Strouse *et al.*, "Systematic evaluation of an atomic clock at 2×10^{-18} total uncertainty," Nature communications **6**, 6896 (2015).

[80] K. Matsubara, H. Hachisu, Y. Li, S. Nagano, C. Locke, A. Nogami, M. Kajita, K. Hayasaka, T. Ido, and M. Hosokawa, "Direct comparison of a Ca^+ single-ion clock against a Sr lattice clock to verify the absolute frequency measurement," Optics express **20**, 22034–22041 (2012).

[81] K. Yamanaka, N. Ohmae, I. Ushijima, M. Takamoto, and H. Katori, "Frequency ratio of ^{199}Hg and ^{87}Sr optical lattice clocks beyond the SI limit," Physical Review Letters **114**, 230801 (2015).

[82] R. Tyumenev, M. Favier, S. Bilicki, E. Bookjans, R. Le Targat, J. Lodewyck, D. Nicolodi, Y. Le Coq, M. Abgrall, J. Guéna *et al.*, "Comparing a mercury optical lattice clock with microwave and optical frequency standards," New Journal of Physics **18**, 113002 (2016).

[83] D. Akamatsu, M. Yasuda, H. Inaba, K. Hosaka, T. Tanabe, A. Onae, and F.-L. Hong, "Frequency ratio measurement of ^{171}Yb and ^{87}Sr optical lattice clocks," Optics express **22**, 7898–7905 (2014).

[84] D. G. Matei, T. Legero, S. Häfner, C. Grebing, R. Weyrich, W. Zhang, L. Sonderhouse, J. M. Robinson, J. Ye, F. Riehle, and U. Sterr, "1.5 μm lasers with sub-10 mHz linewidth," Phys. Rev. Lett. **118**, 263202 (2017).

[85] J. M. Robinson, E. Oelker, W. R. Milner, W. Zhang, T. Legero, D. G. Matei, F. Riehle, U. Sterr, and J. Ye, "Crystalline optical cavity at 4 K with thermal-noise-limited instability and ultralow drift," Optica **6**, 240–243 (2019).

[86] S. A. Diddams, "The evolving optical frequency comb," J. Opt. Soc. Am. B **27**, B51–B62 (2010).

[87] R. Holzwarth, T. Udem, T. W. Hänsch, J. Knight, W. Wadsworth, and P. S. J. Russell, "Optical frequency synthesizer for precision spectroscopy," Physical Review Letters **85**, 2264 (2000).

[88] J. Ye and S. T. Cundiff, *Femtosecond optical frequency comb: principle, operation and applications* (Springer Science & Business Media, 2005).

[89] A. Schliesser, N. Picqué, and T. W. Hänsch, "Mid-infrared frequency combs," Nature Photonics **6**, 440 (2012).

[90] S. T. Cundiff, J. Ye, and J. L. Hall, "Optical frequency synthesis based on mode-locked lasers," Review of Scientific Instruments **72**, 3749 (2001).

[91] T. Rosenband, D. B. Hume, P. O. Schmidt, C. W. Chou, A. Brusch, L. Lorini, W. H. Oskay, R. E. Drullinger, T. M. Fortier, J. E. Stalnaker, S. A. Diddams, W. C. Swann, N. R. Newbury, W. M. Itano, D. J. Wineland, and J. C. Bergquist, "Frequency ratio of Al^+ and Hg^+ single-ion optical clocks; metrology at the 17th decimal place," Science **319**, 1808–1812 (2008).

[92] J. Millo, R. Boudot, M. Lours, P. Bourgeois, A. Luiten, Y. Le Coq, Y. Kersalé, and G. Santarelli, "Ultra-low-noise microwave extraction from fiber-based optical frequency comb," Optics letters **34**, 3707–3709 (2009).

[93] W. Zhang, S. Seidelin, A. Joshi, S. Datta, G. Santarelli, and Y. Le Coq, "Dual photo-detector system for low phase noise microwave generation with femtosecond lasers," Optics letters **39**, 1204–1207 (2014).

[94] A. Matveev, C. G. Parthey, K. Predehl, J. Alnis, A. Beyer, R. Holzwarth, T. Udem, T. Wilken, N. Kolachevsky, M. Abgrall, D. Rovera, C. Salomon, P. Laurent, G. Grosche, O. Terra, T. Legero, H. Schnatz, S. Weyers, B. Altschul, and T. W. Hänsch, "Precision measurement of the hydrogen 1S-2S frequency via a 920-km fiber link," Physical Review Letters **110**, 230801 (2013).

[95] D. Mondelain, T. Sala, S. Kassi, D. Romanini, M. Marangoni, and A. Campargue, "Broadband and highly sensitive comb-assisted cavity ring down spectroscopy of CO near 1.57 μm with sub-MHz frequency accuracy," Journal of Quantitative Spectroscopy and Radiative Transfer **154**, 35–43 (2015).

[96] J. Mandon, G. Guelachvili, and N. Picqué, "Fourier transform spectroscopy with a laser frequency comb," Nature Photonics **3**, 99 (2009).

[97] B. Bernhardt, A. Ozawa, P. Jacquet, M. Jacquey, Y. Kobayashi, T. Udem, R. Holzwarth, G. Guelachvili, T. W. Hänsch, and N. Picqué, "Cavity-enhanced dual-comb spectroscopy," Nature Photonics **4**, 55 (2010).

[98] I. Coddington, N. Newbury, and W. Swann, "Dual-comb spectroscopy," Optica **3**, 414–426 (2016).

[99] Z. Chen, M. Yan, T. W. Hänsch, and N. Picqué, "A phase-stable dual-comb interferometer," Nature communications **9**, 3035 (2018).

[100] G. G. Ycas, F. Quinlan, S. Osterman, G. Nave, and S. A. Diddams, "An optical frequency comb for infrared spectrograph calibration," in "Ground-based and Airborne Instrumentation for Astronomy III," , vol. 7735 (International Society for Optics and Photonics, 2010), vol. 7735, p. 77352R.

[101] X. Yi, K. Vahala, J. Li, S. Diddams, G. Ycas, P. Plavchan, S. Leifer, J. Sandhu, G. Vasisht, P. Chen, P. Gao, J. Gagne, E. Furlan, M. Bottom, E. Martin, M. Fitzgerald, G. Doppmann, and C. Beichman, "Demonstration of a near-IR line-referenced electro-optical laser frequency comb for precision radial velocity measurements in astronomy," Nature communications **7**, 10436 (2016).

[102] R. A. McCracken, J. M. Charsley, and D. T. Reid, "A decade of astrocombs: recent advances in frequency combs for astronomy," Optics express **25**, 15058–15078 (2017).

[103] R. A. McCracken, É. Depagne, R. B. Kuhn, N. Erasmus, L. A. Crause, and D. T. Reid, "Wavelength calibration of a high resolution spectrograph with a partially stabilized 15-GHz astrocomb from 550 to 890 nm," Optics Express **25**, 6450–6460 (2017).

[104] E. Obrzud, M. Rainer, A. Harutyunyan, B. Chazelas, M. Cecconi, A. Ghedina, E. Molinari, S. Kundermann, S. Lecomte, F. Pepe, F. Wildi, F. Bouchy, and T. Herr, "Broadband near-infrared astronomical spectrometer calibration and on-sky validation with an electro-optic laser frequency comb," Optics express **26**, 34830–34841 (2018).

[105] M. T. Murphy, T. Udem, R. Holzwarth, A. Sizmann, L. Pasquini, C. Araujo-Hauck, H. Dekker, S. D'Odorico, M. Fischer, T. Hänsch, and A. Manescau, "High-precision wavelength calibration of astronomical spectrographs with laser frequency combs," Monthly Notices of the Royal Astronomical Society **380**, 839–847 (2007).

[106] T. Q. Bui, B. J. Bjork, P. B. Changala, O. H. Heckl, B. Spaun, and J. Ye, "OD + CO ← D + CO_2 branching kinetics probed with time-resolved frequency comb spectroscopy," Chemical Physics Letters **683**, 91–95 (2017).

[107] T. Q. Bui, B. J. Bjork, P. B. Changala, T. L. Nguyen, J. F. Stanton, M. Okumura, and J. Ye, "Direct measurements of DOCO isomers in the kinetics of OD + CO," Science advances **4**, eaao4777 (2018).

[108] C. Lisdat, G. Grosche, N. Quintin, C. Shi, S. Raupach, C. Grebing, D. Nicolodi, F. Stefani, A. Al-Masoudi, S. Dörscher, S. HÃ¤fner, J.-L. Robyr, N. Chiodo, S. Bilicki, E. Bookjans, A. Koczwara, S. Koke, A. Kuhl, F. Wiotte, F. Meynadier, E. Camisard, M. Abgrall, M. Lours, T. Legero, H. Schnatz, U. Sterr, H. Denker, C. Chardonnet, Y. Le Coq, G. Santarelli, A. Amy-Klein, R. Le Targat, J. Lodewyck,

O. Lopez, and P.-E. Pottie, "A clock network for geodesy and fundamental science," Nature communications **7**, 12443 (2016).

[109] A. Bauch, J. Achkar, S. Bize, D. Calonico, R. Dach, R. Hlavać, L. Lorini, T. Parker, G. Petit, D. Piester, K. Szymaniec, and P. Uhrich, "Comparison between frequency standards in Europe and the USA at the 10^{-15} uncertainty level," Metrologia **43**, 109 (2005).

[110] M. Fujieda, D. Piester, T. Gotoh, J. Becker, M. Aida, and A. Bauch, "Carrier-phase two-way satellite frequency transfer over a very long baseline," Metrologia **51**, 253 (2014).

[111] N. Chiodo, N. Quintin, F. Stefani, F. Wiotte, E. Camisard, C. Chardonnet, G. Santarelli, A. Amy-Klein, P.-E. Pottie, and O. Lopez, "Cascaded optical fiber link using the internet network for remote clocks comparison," Optics Express **23**, 33927–33937 (2015).

[112] S. M. Raupach, A. Koczwara, and G. Grosche, "Brillouin amplification supports 1×10^{-20} uncertainty in optical frequency transfer over 1400 km of underground fiber," Physical Review A **92**, 021801 (2015).

[113] S. Droste, F. Ozimek, T. Udem, K. Predehl, T. Hänsch, H. Schnatz, G. Grosche, and R. Holzwarth, "Optical-frequency transfer over a single-span 1840 km fiber link," Physical Review Letters **111**, 110801 (2013).

[114] H. Jiang, F. Kéfélian, S. Crane, O. Lopez, M. Lours, J. Millo, D. Holleville, P. Lemonde, C. Chardonnet, A. Amy-Klein, and G. Santarelli, "Long-distance frequency transfer over an urban fiber link using optical phase stabilization," J. Opt. Soc. Am. B **25**, 2029–2035 (2008).

[115] G. Grosche, O. Terra, K. Predehl, R. Holzwarth, B. Lipphardt, F. Vogt, U. Sterr, and H. Schnatz, "Optical frequency transfer via 146 km fiber link with 10^{-19} relative accuracy," Optics letters **34**, 2270–2272 (2009).

[116] D. Calonico, E. K. Bertacco, C. E. Calosso, C. Clivati, G. A. Costanzo, M. Frittelli, A. Godone, A. Mura, N. Poli, D. V. Sutyrin, G. Tino, M. E. Zucco, and F. Levi, "High-accuracy coherent optical frequency transfer over a doubled 642-km fiber link," Applied Physics B **117**, 979–986 (2014).

[117] C. Clivati, G. A. Costanzo, M. Frittelli, F. Levi, A. Mura, M. Zucco, R. Ambrosini, C. Bortolotti, F. Perini, M. Roma, and D. Calonico, "A coherent fiber link for very long baseline interferometry," IEEE transactions on ultrasonics, ferroelectrics, and frequency control **62**, 1907–1912 (2015).

[118] C. Clivati, G. Cappellini, L. F. Livi, F. Poggiali, M. S. de Cumis, M. Mancini, G. Pagano, M. Frittelli, A. Mura, G. A. Costanzo, F. Levi, D. Calonico, L. Fallani, J. Catani, and M. Inguscio, "Measuring absolute frequencies beyond the GPS limit via long-haul optical frequency dissemination," Optics express **24**, 11865–11875 (2016).

[119] A. Yamaguchi, N. Shiga, S. Nagano, Y. Li, H. Ishijima, H. Hachisu, M. Kumagai, and T. Ido, "Stability transfer between two clock lasers operating at different wavelengths for absolute frequency measurement of clock transition in ^{87}Sr," Applied Physics Express **5**, 022701 (2012).

[120] W. Yang, D. Li, S. Zhang, and J. Zhao, "Hunting for dark matter with ultra-stable fibre as frequency delay system," Scientific reports **5**, 11469 (2015).

[121] L. M. Krauss, "Axions and atomic clocks," arXiv preprint arXiv:1905.10014 (2019).

[122] B. M. Roberts, P. Delva, A. Al-Masoudi, A. Amy-Klein, C. Bærentsen, C. F. A. Baynham, E. Benkler, S. Bilicki, S. Bize, W. Bowden, J. Calvert, V. Cambier, E. Cantin, E. A. Curtis, S. Dörscher, M. Favier, F. Frank, P. Gill, R. M. Godun, G. Grosche, C. Guo, A. Hees, I. R. Hill, R. Hobson, N. Huntemann, J. Kronjäger, S. Koke, A. Kuhl, R. Lange, T. Legero, B. Lipphardt, C. Lisdat, J. Lodewyck, O. Lopez, H. S. Margolis, H. Álvarez-Martínez, F. Meynadier, F. Ozimek, E. Peik, P. E. Pottie, N. Quintin, C. Sanner, L. D. Sarlo, M. Schioppo, R. Schwarz, A. Silva, U. Sterr, C. Tamm, R. L. Targat, P. Tuckey, G. Vallet, T. Waterholter, D. Xu, and P. Wolf, "Search for transient variations of the fine structure constant and dark matter using fiber-linked optical atomic clocks," (2019).

[123] S. M. Foreman, A. Marian, J. Ye, E. A. Petrukhin, M. A. Gubin, O. D. Mücke, F. N. Wong, E. P. Ippen, and F. X. Kärtner, "Demonstration of a HeNe/CH_4-based optical molecular clock," Optics Letters **30**, 570–572 (2005).

[124] M. Gubin, A. Kireev, A. Konyashchenko, P. Kryukov, A. Shelkovnikov, A. Tausenev, and D. Tyurikov, "Femtosecond fiber laser based methane optical clock," Applied Physics B **95**, 661–666 (2009).

[125] A. Amy-Klein, A. Goncharov, M. Guinet, C. Daussy, O. Lopez, A. Shelkovnikov, and C. Chardonnet, "Absolute frequency measurement of a SF_6 two-photon line by use of a femtosecond optical comb and sum-frequency generation," Optics letters **30**, 3320–3322 (2005).

[126] R. Drever, J. L. Hall, F. Kowalski, J. Hough, G. Ford, A. Munley, and H. Ward, "Laser phase and frequency stabilization using an optical resonator," Applied Physics B **31**, 97–105 (1983).

[127] E. D. Black, "An introduction to Pound-Drever-Hall laser frequency stabilization," American journal of physics **69**, 79–87 (2001).

[128] M. S. Taubman, T. L. Myers, B. D. Cannon, R. M. Williams, F. Capasso, C. Gmachl, D. L. Sivco, and A. Y. Cho, "Frequency stabilization of quantum-cascade lasers by use of optical cavities," Optics letters **27**, 2164–2166 (2002).

[129] E. Fasci, N. Coluccelli, M. Cassinerio, A. Gambetta, L. Hilico, L. Gianfrani, P. Laporta, A. Castrillo, and G. Galzerano, "Narrow-linewidth quantum cascade laser at 8.6 μm," Optics letters **39**, 4946–4949 (2014).

[130] M. Siciliani de Cumis, S. Borri, G. Insero, I. Galli, A. Savchenkov, D. Eliyahu, V. Ilchenko, N. Akikusa, A. Matsko, L. Maleki, and P. De Natale, "Microcavity-stabilized quantum cascade laser," Laser & Photonics Reviews **10**, 153–157 (2016).

[131] S. Kassi, T. Stoltmann, M. Casado, M. Daëron, and A. Campargue, "Lamb dip CRDS of highly saturated transitions of water near 1.4 μm," The Journal of chemical physics **148**, 054201 (2018).

[132] D. Gatti, A. Gambetta, A. Castrillo, G. Galzerano, P. Laporta, L. Gianfrani, and M. Marangoni, "High-precision molecular interrogation by direct referencing of a quantum-cascade-laser to a near-infrared frequency comb," Optics express **19**, 17520–17527 (2011).

[133] R. Santagata, D. B. A. Tran, B. Argence, O. Lopez, S. K. Tokunaga, F. Wiotte, H. Mouhamad, A. Goncharov, M. Abgrall, Y. L. Coq, H. Alvarez-Martinez, R. L.

Targat, W. K. Lee, D. Xu, P.-E. Pottie, B. Darquié, and A. Amy-Klein, "High-precision methanol spectroscopy with a widely tunable SI-traceable frequency-comb-based mid-infrared QCL," Optica **6**, 411–423 (2019).

[134] I. Galli, S. Bartalini, P. Cancio, G. Giusfredi, D. Mazzotti, and P. De Natale, "Ultra-stable, widely tunable and absolutely linked mid-IR coherent source," Optics Express **17**, 9582–9587 (2009).

[135] A. Gambetta, E. Vicentini, N. Coluccelli, Y. Wang, T. T. Fernandez, P. Maddaloni, P. De Natale, A. Castrillo, L. Gianfrani, P. Laporta, and G. Galzerano, "Versatile mid-infrared frequency-comb referenced sub-Doppler spectrometer," APL Photonics **3**, 046103 (2018).

[136] S. Borri, G. Insero, G. Santambrogio, D. Mazzotti, F. Cappelli, I. Galli, G. Galzerano, M. Marangoni, P. Laporta, V. Di Sarno, L. Santamaria, P. Maddaloni, and P. De Natale, "High-precision molecular spectroscopy in the mid-infrared using quantum cascade lasers," Applied Physics B **125**, 18 (2019).

[137] L. Consolino, F. Cappelli, M. S. de Cumis, and P. De Natale, "QCL-based frequency metrology from the mid-infrared to the THz range: a review," Nanophotonics **8**, 181–204 (2018).

[138] N. F. Ramsey, "A molecular beam resonance method with separated oscillating fields," Physical Review **78**, 695 (1950).

[139] C. Chardonnet, F. Guernet, G. Charton, and C. J. Bordé, "Ultrahigh-resolution saturation spectroscopy using slow molecules in an external cell," Applied Physics B **59**, 333–343 (1994).

[140] P. Durand, G. Nogues, V. Bernard, A. Amy-Klein, and C. Chardonnet, "Slow-molecule detection in Doppler-free two-photon spectroscopy," EPL (Europhysics Letters) **37**, 103 (1997).

[141] B. Chanteau, "Transfert à très haute résolution d'une référence de réquence ultra-stable par lien optique et application à la stabilisation d'un laser moyen-infrarouge," Ph.D. thesis, Université Paris-Nord-Paris XIII (2013).

[142] T.-D. Lee and C.-N. Yang, "Question of parity conservation in weak interactions," Physical Review **104**, 254 (1956).

[143] C.-S. Wu, E. Ambler, R. Hayward, D. Hoppes, and R. P. Hudson, "Experimental test of parity conservation in beta decay," Physical review **105**, 1413 (1957).

[144] M. Bouchiat and C. Bouchiat, "I. Parity violation induced by weak neutral currents in atomic physics," Journal de Physique **35**, 899–927 (1974).

[145] M. Bouchiat and C. Bouchiat, "Parity violation induced by weak neutral currents in atomic physics. Part II," Journal de Physique **36**, 493–509 (1975).

[146] L. Barkov and M. Zolotorev, "Measurement of optical activity of bismuth vapor," JETP Letters **28**, 50–3 (1978).

[147] R. Conti, P. Bucksbaum, S. Chu, E. Commins, and L. Hunter, "Preliminary observation of parity nonconservation in atomic thallium," Physical Review Letters **42**, 343 (1979).

[148] P. Bucksbaum, E. Commins, and L. Hunter, "Observations of parity nonconservation in atomic thallium," Physical Review D **24**, 1134 (1981).

[149] M. Bouchiat, J. Guena, L. Hunter, and L. Pottier, "Observation of a parity violation in cesium," Physics Letters B **117**, 358–364 (1982).

[150] C. Wood, S. Bennett, D. Cho, B. Masterson, J. Roberts, C. Tanner, and C. E. Wieman, "Measurement of parity nonconservation and an anapole moment in cesium," Science **275**, 1759–1763 (1997).

[151] Y. Yamagata, "A hypothesis for the asymmetric appearance of biomolecules on earth," Journal of Theoretical Biology **11**, 495–498 (1966).

[152] D. Rein, "Some remarks on parity violating effects of intramolecular interactions," Journal of molecular evolution **4**, 15–22 (1974).

[153] E. Gajzago and G. Marx, "Energy difference of mirror molecules," ATOMKI (At. Kut. Intez.) Kozlem., Suppl., v. 16, no. 2, pp. 177-184 (1974).

[154] V. S. Letokhov, "On difference of energy levels of left and right molecules due to weak interactions," Physics Letters A **53**, 275–276 (1975).

[155] N. Saleh, S. Zrig, T. Roisnel, L. Guy, R. Bast, T. Saue, B. Darquié, and J. Crassous, "A chiral rhenium complex with predicted high parity violation effects: synthesis, stereochemical characterization by VCD spectroscopy and quantum chemical calculations," Physical Chemistry Chemical Physics **15**, 10952–10959 (2013).

[156] M. Wormit, M. Olejniczak, A.-L. Deppenmeier, A. Borschevsky, T. Saue, and P. Schwerdtfeger, "Strong enhancement of parity violation effects in chiral uranium compounds," Physical Chemistry Chemical Physics **16**, 17043–17051 (2014).

[157] N. Saleh, R. Bast, N. Vanthuyne, C. Roussel, T. Saue, B. Darquié, and J. Crassous, "An oxorhenium complex bearing a chiral cyclohexane-1-olato-2-thiolato ligand: Synthesis, stereochemistry, and theoretical study of parity violation vibrational frequency shifts," Chirality **30**, 147–156 (2018).

[158] F. De Montigny, R. Bast, A. S. P. Gomes, G. Pilet, N. Vanthuyne, C. Roussel, L. Guy, P. Schwerdtfeger, T. Saue, and J. Crassous, "Chiral oxorhenium (V) complexes as candidates for the experimental observation of molecular parity violation: a structural, synthetic and theoretical study," Physical Chemistry Chemical Physics **12**, 8792–8803 (2010).

[159] P. Schwerdtfeger, A. Kühn, R. Bast, J. K. Laerdahl, F. Faglioni, and P. Lazzeretti, "The vibrational spectrum of camphor from ab initio and density functional theory and parity violation in the C-C*-CO bending mode," Chemical physics letters **383**, 496–501 (2004).

[160] R. Bast and P. Schwerdtfeger, "Parity-violation effects in the CF stretching mode of heavy-atom methyl fluorides," Physical Review Letters **91**, 023001 (2003).

[161] S. Nahrwold, R. Berger, and P. Schwerdtfeger, "Parity violation in nuclear magnetic resonance frequencies of chiral tetrahedral tungsten complexes NWXYZ (X, Y, Z= H, F, Cl, Br or I)," The Journal of chemical physics **140**, 024305 (2014).

[162] R. Berger, M. Quack, and J. Stohner, "Parity violation in fluorooxirane," Angewandte Chemie International Edition **40**, 1667–1670 (2001).

[163] P. Schwerdtfeger, J. K. Laerdahl, and C. Chardonnet, "Calculation of parity-violation effects for the cf stretching mode of chiral methyl fluorides," Physical Review A **65**, 042508 (2002).

[164] R. G. Viglione, R. Zanasi, P. Lazzeretti, and A. Ligabue, "Theoretical determination of parity-violating vibrational frequency differences between the enantiomers of the CHFClBr molecule," Physical Review A **62**, 052516 (2000).

[165] M. Quack, J. Stohner, and M. Willeke, "High-resolution spectroscopic studies and theory of parity violation in chiral molecules," Annu. Rev. Phys. Chem. **59**, 741–769 (2008).

[166] A. MacDermott, T. Fu, G. Hyde, R. Nakatsuka, and A. Coleman, "Electroweak parity-violating energy shifts of amino acids: The "Conformation problem"," Origins of Life and Evolution of Biospheres **39**, 407–437 (2009).

[167] I. Gonzalo, P. Bargueño, R. P. de Tudela, and S. Miret-Artés, "Towards the detection of parity symmetry breaking in chiral molecules," Chemical Physics Letters **489**, 127–129 (2010).

[168] C. Medcraft, R. Wolf, and M. Schnell, "High-resolution spectroscopy of the chiral metal complex [CpRe(CH_3)(CO)(NO)]: a potential candidate for probing parity violation," Angewandte Chemie International Edition **53**, 11656–11659 (2014).

[169] S. Eibenberger, J. Doyle, and D. Patterson, "Enantiomer-specific state transfer of chiral molecules," Physical Review Letters **118**, 123002 (2017).

[170] J. Eills, J. W. Blanchard, L. Bougas, M. G. Kozlov, A. Pines, and D. Budker, "Measuring molecular parity nonconservation using nuclear-magnetic-resonance spectroscopy," Physical Review A **96**, 042119 (2017).

[171] M. Quack, "On the measurement of the parity violating energy difference between enantiomers," Chemical physics letters **132**, 147–153 (1986).

[172] P. Dietiker, E. Miloglyadov, M. Quack, A. Schneider, and G. Seyfang, "Infrared laser induced population transfer and parity selection in $^{14}NH_3$: A proof of principle experiment towards detecting parity violation in chiral molecules," The Journal of chemical physics **143**, 244305 (2015).

[173] C. Fábri, L. Horný, and M. Quack, "Tunneling and parity violation in trisulfane (HSSSH): an almost ideal molecule for detecting parity violation in chiral molecules," ChemPhysChem **16**, 3584–3589 (2015).

[174] D. Antypas, A. Fabricant, L. Bougas, K. Tsigutkin, and D. Budker, "Towards improved measurements of parity violation in atomic ytterbium," Hyperfine Interactions **238**, 21 (2017).

[175] O. Kompanets, A. Kukudzhanov, V. Letokhov, and L. Gervits, "Narrow resonances of saturated absorption of the asymmetrical molecule CHFClBr and the possibility of weak current detection in molecular physics," Optics Communications **19**, 414–416 (1976).

[176] E. Arimondo, P. Glorieux, and T. Oka, "Observation of inverted infrared lamb dips in separated optical isomers," Optics Communications **23**, 369–372 (1977).

[177] P. Lazzeretti, R. Zanasi, and F. Faglioni, "Energetic stabilization of d-camphor via weak neutral currents," Physical Review E **60**, 871 (1999).

[178] C. Daussy, T. Marrel, A. Amy-Klein, C. Nguyen, C. J. Bordé, and C. Chardonnet, "Limit on the parity nonconserving energy difference between the enantiomers of a chiral molecule by laser spectroscopy," Physical Review Letters **83**, 1554 (1999).

[179] M. Ziskind, C. Daussy, T. Marrel, and C. Chardonnet, "Improved sensitivity in the search for a parity-violating energy difference in the vibrational spectrum of the enantiomers of CHFClBr," The European Physical Journal D-Atomic, Molecular, Optical and Plasma Physics **20**, 219–225 (2002).

[180] P. Schwerdtfeger, T. Saue, J. N. van Stralen, and L. Visscher, "Relativistic second-order many-body and density-functional theory for the parity-violation contribution to the C-F stretching mode in CHFClBr," Physical Review A **71**, 012103 (2005).

[181] C. Stoeffler, B. Darquié, A. Shelkovnikov, C. Daussy, A. Amy-Klein, C. Chardonnet, L. Guy, J. Crassous, T. R. Huet, P. Soulard, and P. Asselin, "High resolution spectroscopy of methyltrioxorhenium: towards the observation of parity violation in chiral molecules," Physical Chemistry Chemical Physics **13**, 854–863 (2011).

[182] N. R. Hutzler, H.-I. Lu, and J. M. Doyle, "The buffer gas beam: An intense, cold, and slow source for atoms and molecules," Chemical reviews **112**, 4803–4827 (2012).

[183] I. Galli, S. Bartalini, S. Borri, P. Cancio, D. Mazzotti, P. De Natale, and G. Giusfredi, "Molecular gas sensing below parts per trillion: radiocarbon-dioxide optical detection," Physical Review Letters **107**, 270802 (2011).

[184] I. Ricciardi, E. De Tommasi, P. Maddaloni, S. Mosca, A. Rocco, J.-J. Zondy, M. De Rosa, and P. De Natale, "Frequency-comb-referenced singly-resonant OPO for sub-Doppler spectroscopy," Optics express **20**, 9178–9186 (2012).

[185] J. Guena, P. Rosenbusch, P. Laurent, M. Abgrall, D. Rovera, G. Santarelli, M. E. Tobar, S. Bize, and A. Clairon, "Demonstration of a dual alkali Rb/Cs fountain clock," IEEE transactions on ultrasonics, ferroelectrics, and frequency control **57**, 647–653 (2010).

[186] S. Bize, P. Laurent, M. Abgrall, H. Marion, I. Maksimovic, L. Cacciapuoti, J. GrÃ¼nert, C. Vian, F. P. dos Santos, P. Rosenbusch, P. Lemonde, G. Santarelli, P. Wolf, A. Clairon, A. Luiten, M. Tobar, and C. Salomon, "Cold atom clocks and applications," Journal of Physics B: Atomic, molecular and optical physics **38**, S449 (2005).

[187] B. Argence, E. Prevost, T. Lévèque, R. Le Goff, S. Bize, P. Lemonde, and G. Santarelli, "Prototype of an ultra-stable optical cavity for space applications," Optics express **20**, 25409–25420 (2012).

[188] H. Jiang, "Development of ultra-stable laser sources and long-distance optical link via telecommunication networks," Ph.D. thesis, Université Paris-Nord-Paris XIII (2010).

[189] J. McFerran, D. Magalhaes, C. Mandache, J. Millo, W. Zhang, Y. Le Coq, G. Santarelli, and S. Bize, "Laser locking to the ^{199}Hg^{1}S$_0$-^{3}P$_0$ clock transition with $5.4 \times 10^{-15}/\sqrt{\tau}$ fractional frequency instability," Optics letters **37**, 3477–3479 (2012).

[190] Y. Le Coq, *Optical frequency combs and optical frequency measurements* (HDR thesis, Université Pierre et Marie Curie-Paris VI, 2014).

[191] D. Xu, E. Cantin, F. Frank, N. Quintin, F. Meynadier, P. Tuckey, A. Amy-Klein, O. Lopez, and P.-E. Pottie, "Two-branch fiber link for international clock networks," IEEE Transactions on Instrumentation and Measurement (2019).

[192] D. Xu, W.-K. Lee, F. Stefani, O. Lopez, A. Amy-Klein, and P.-E. Pottie, "Studying the fundamental limit of optical fiber links to the 10^{-21} level," Optics express **26**, 9515–9527 (2018).

[193] W.-K. Lee, F. Stefani, A. Bercy, O. Lopez, A. Amy-Klein, and P.-E. Pottie, "Hybrid fiber links for accurate optical frequency comparison," Applied Physics B **123**, 161 (2017).

[194] F. Kéfélian, O. Lopez, H. Jiang, C. Chardonnet, A. Amy-Klein, and G. Santarelli, "High-resolution optical frequency dissemination on a telecommunications network with data traffic," Optics letters **34**, 1573–1575 (2009).

[195] F. Narbonneau, M. Lours, S. Bize, A. Clairon, G. Santarelli, O. Lopez, C. Daussy, A. Amy-Klein, and C. Chardonnet, "High resolution frequency standard dissemination via optical fiber metropolitan network," Review of Scientific Instruments **77**, 064701 (2006).

[196] D. J. Jones, S. A. Diddams, J. K. Ranka, A. Stentz, R. S. Windeler, J. L. Hall, and S. T. Cundiff, "Carrier-envelope phase control of femtosecond mode-locked lasers and direct optical frequency synthesis," Science **288**, 635–639 (2000).

[197] M. Collombon, "Résonance noire à trois photons sur un nuage d'ions calcium confinés," Ph.D. thesis, Université d'Aix-Marseille (2019).

[198] V. Bernard, C. Daussy, G. Nogues, L. Constantin, P. Durand, A. Amy-Klein, A. Van Lerberghe, and C. Chardonnet, "CO_2 laser stabilization to 0.1-Hz level using external electrooptic modulation," IEEE Journal of Quantum Electronics **33**, 1282–1287 (1997).

[199] O. Pfister, F. Guernet, G. Charton, C. Chardonnet, F. Herlemont, and J. Legrand, "CO_2-laser sideband spectroscopy at ultrahigh resolution," J. Opt. Soc. Am. B **10**, 1521–1525 (1993).

[200] J. Faist, F. Capasso, D. L. Sivco, C. Sirtori, A. L. Hutchinson, and A. Y. Cho, "Quantum cascade laser," Science **264**, 553–556 (1994).

[201] C. Daussy, F. Ducos, G. Rovera, and O. Acef, "Performances of OsO_4/stabilized CO_2 lasers as optical frequency standards near 29 THz," IEEE transactions on ultrasonics, ferroelectrics, and frequency control **47**, 518–521 (2000).

[202] M. Razeghi, *Technology of quantum devices* (Springer, 2010).

[203] F. Capasso, C. Gmachl, D. L. Sivco, and A. Y. Cho, "Quantum Cascade Lasers," Physics Today **55**, 34 (2007).

[204] L. Tombez, J. Di Francesco, S. Schilt, G. Di Domenico, J. Faist, P. Thomann, and D. Hofstetter, "Frequency noise of free-running 4.6 μm distributed feedback quantum cascade lasers near room temperature," Optics letters **36**, 3109–3111 (2011).

[205] S. Bartalini, S. Borri, P. Cancio, A. Castrillo, I. Galli, G. Giusfredi, D. Mazzotti, L. Gianfrani, and P. De Natale, "Observing the intrinsic linewidth of a quantum-cascade laser: beyond the schawlow-townes limit," Physical Review Letters **104**, 083904 (2010).

[206] L. B. Mercer, "$1/f$ frequency noise effects on self-heterodyne linewidth measurements," Journal of Lightwave Technology **9**, 485–493 (1991).

[207] J. Tourrenc, "Caractérisation et modélisation du bruit d'amplitude optique, du bruit de fréquence et de la largeur de raie de vcsels monomode," Ph.D. thesis, Ph. D. dissertation (Université de Montpellier II, 2005) (2005).

[208] G. Di Domenico, S. Schilt, and P. Thomann, "Simple approach to the relation between laser frequency noise and laser line shape," Applied optics **49**, 4801–4807 (2010).

[209] N. Bucalovic, V. Dolgovskiy, C. Schori, P. Thomann, G. Di Domenico, and S. Schilt, "Experimental validation of a simple approximation to determine the linewidth of a laser from its frequency noise spectrum," Applied Optics **51**, 4582–4588 (2012).

[210] M. Bishof, X. Zhang, M. J. Martin, and J. Ye, "Optical spectrum analyzer with quantum-limited noise floor," Physical Review Letters **111**, 093604 (2013).

[211] G. Stéphan, T. Tam, S. Blin, P. Besnard, and M. Têtu, "Laser line shape and spectral density of frequency noise," Physical Review A **71**, 043809 (2005).

[212] R. W. Boyd, *Nonlinear optics* (Elsevier, 2003).

[213] V. G. Dmitriev, G. G. Gurzadyan, and D. N. Nikogosyan, *Handbook of nonlinear optical crystals*, vol. 64 (Springer, 2013).

[214] D. A. Roberts, "Dispersion equations for nonlinear optical crystals: KDP, $AgGaSe_2$, and $AgGaS_2$," Applied optics **35**, 4677–4688 (1996).

[215] J.-J. Zondy, "Private communication," (2010).

[216] J.-J. Zondy, D. Touahri, and O. Acef, "Absolute value of the d_{36} nonlinear coefficient of $AgGaS_2$: prospect for a low-threshold doubly resonant oscillator-based 3:1 frequency divider," J. Opt. Soc. Am. B **14**, 2481–2497 (1997).

[217] B. Vincent, "Stabilisation en fréquence de lasers á CO_2 en dessous du Hertz: application à la métrologie des fréquences dans la région spectrale de 30 THz," Ph.D. thesis, Université Paris 13 (1997).

[218] F. Stefani, O. Lopez, A. Bercy, W.-K. Lee, C. Chardonnet, G. Santarelli, P.-E. Pottie, and A. Amy-Klein, "Tackling the limits of optical fiber links," J. Opt. Soc. Am. B **32**, 787–797 (2015).

[219] B. AlSaif, M. Lamperti, D. Gatti, P. Laporta, M. Fermann, A. Farooq, O. Lyulin, A. Campargue, and M. Marangoni, "High accuracy line positions of the ν_1 fundamental band of $^{14}N_2{}^{16}O$," Journal of Quantitative Spectroscopy and Radiative Transfer **211**, 172–178 (2018).

[220] J. McManus, P. Kebabian, and M. Zahniser, "Astigmatic mirror multipass absorption cells for long-path-length spectroscopy," Applied Optics **34**, 3336–3348 (1995).

[221] J. B. McManus, M. S. Zahniser, and D. D. Nelson, "Dual quantum cascade laser trace gas instrument with astigmatic herriott cell at high pass number," Applied Optics **50**, A74–A85 (2011).

[222] L. Menzel, A. Kosterev, R. Curl, F. Tittel, C. Gmachl, F. Capasso, D. Sivco, J. Baillargeon, A. Hutchinson, A. Cho, and W. Urban, "Spectroscopic detection of biological NO with a quantum cascade laser," Applied Physics B **72**, 859–863 (2001).

[223] S. Viciani, A. Montori, A. Chiarugi, and F. D'Amato, "A portable quantum cascade laser spectrometer for atmospheric measurements of carbon monoxide," Sensors **18**, 2380 (2018).

[224] M. A. de Araújo, R. Silva, E. de Lima, D. P. Pereira, and P. C. de Oliveira, "Measurement of gaussian laser beam radius using the knife-edge technique: improvement on data analysis," Applied optics **48**, 393–396 (2009).

[225] A. R. Inc, "Astigmatic multi-pass IR absorption cells, owner's manual models AMAC-36, AMAC-76, AMAC-100, AMAC-200," (2001).

[226] W. T. Silfvast, *Laser fundamentals* (Cambridge university press, 2004).

[227] W. Batrla, H. Matthews, K. Menten, and C. Walmsley, "Detection of strong methanol masers towards galactic H II regions," Nature **326**, 49 (1987).

[228] H. Singh, Y. Chen, A. Staudt, D. Jacob, D. Blake, B. Heikes, and J. Snow, "Evidence from the Pacific troposphere for large global sources of oxygenated organic compounds," Nature **410**, 1078 (2001).

[229] W. G. of the Intergovernmental Panel on Climate Change (IPCC), "AR4 climate change 2007: Synthesis report," (2007).

[230] J. C. Pearson, A. M. Daly, and R. M. Lees, "Unraveling torsional bath interactions with the CO stretching state in methanol," Journal of Molecular Spectroscopy **318**, 70–77 (2015).

[231] L. Coudert, C. Gutlé, T. Huet, J.-U. Grabow, and S. Levshakov, "Spin-torsion effects in the hyperfine structure of methanol," The Journal of chemical physics **143**, 044304 (2015).

[232] B. Lankhaar, G. C. Groenenboom, and A. van der Avoird, "Hyperfine interactions and internal rotation in methanol," The Journal of chemical physics **145**, 244301 (2016).

[233] S. Y. Tochitsky and R. Butcher, "Precise measurements of line broadening and line shifts in low-pressure gases using a heterodyne CO_2 laser spectrometer: applications to C_2H_4 and CH_3OH," J. Opt. Soc. Am. B **15**, 1392–1398 (1998).

[234] Z.-D. Sun, R. M. Lees, and L.-H. Xu, "Saturation-dip measurements for the ν_8 CO stretching band of CH_3OH with a CO_2-laser-microwave-sideband spectrometer," J. Opt. Soc. Am. B **23**, 2398–2417 (2006).

[235] Z. X. Jiu, D. L. Zuo, L. Miao, Z. H. Cheng, and C. C. Qi, "Pulsed CH_3OH terahertz laser emission pumped by a TEA CO_2 laser," Journal of Infrared, Millimeter, and Terahertz Waves **31**, 885–891 (2010).

[236] M. Daprà, C. Henkel, S. Levshakov, K. Menten, S. Muller, H. Bethlem, S. Leurini, A. Lapinov, and W. Ubachs, "Testing the variability of the proton-to-electron mass ratio from observations of methanol in the dark cloud core L1498," Monthly Notices of the Royal Astronomical Society **472**, 4434–4443 (2017).

[237] G. Moruzzi, *Microwave, Infrared, and Laser Transitions of Methanol Atlas of Assigned Lines from 0 to 1258 cm^{-1}: 0* (CRC Press, 2018).

[238] L.-H. Xu, R. Lees, P. Wang, L. Brown, I. Kleiner, and J. Johns, "New assignments, line intensities, and HITRAN database for CH_3OH at 10 μm," Journal of Molecular Spectroscopy **228**, 453–470 (2004).

[239] R. Lees, L.-H. Xu, J. Johns, B. Winnewisser, and M. Lock, "Rotation–torsion–vibration term-value mapping for CH_3OH: Torsion-mediated doorways and corridors for intermode population transfer," Journal of Molecular Spectroscopy **243**, 168–181 (2007).

[240] I. Mukhopadhyay, R. Lees, W. Lewis-Bevan, and J. Johns, "Fourier transform spectroscopy of the CO-stretching band of C-13 methanol in the torsional ground state," The Journal of chemical physics **102**, 6444–6455 (1995).

[241] P. Jansen, I. Kleiner, L.-H. Xu, W. Ubachs, and H. L. Bethlem, "Sensitivity of transitions in internal rotor molecules to a possible variation of the proton-to-electron mass ratio," Physical Review A **84**, 062505 (2011).

[242] Z.-D. Sun, F. Matsushima, S. Tsunekawa, and K. Takagi, "Sub-Doppler spectroscopy of the C-O stretching fundamental band of methanol by use of microwave sidebands of CO_2 laser lines," J. Opt. Soc. Am. B **17**, 2068–2080 (2000).

[243] G. Moruzzi and F. Strumia, "High-resolution FIR and IR spectroscopy of CH_3OH," Infrared Physics **24**, 257–260 (1984).

[244] R. Lees, I. Mukhopadhyay, and J. Johns, "Assignment of IR transitions and FIR laser lines from torsionally excited CH_3OH," Optics communications **55**, 127–130 (1985).

[245] G. Moruzzi, F. Strumia, P. Carnesecchi, R. Lees, I. Mukhopadhyay, and J. Johns, "Fourier spectrum of CH_3OH between 950 and 1100 cm^{-1}," Infrared Physics **29**, 583–606 (1989).

[246] I. Mukhopadhyay and R. Lees, "High-resolution spectroscopy of methanol: Coriolis resonance and far infrared laser identification," Optics communications **97**, 194–198 (1993).

[247] Z.-D. Sun, T. Mizuochi, M. Kaneko, Y. Moriwaki, F. Matsushima, and K. Takagi, "Sub-Doppler spectroscopy by use of microwave sidebands of CO_2 laser lines applied to the CO stretching fundamental band of methanol," Molecules **8**, 92–102 (2003).

[248] Z.-D. Sun, S. Ishikuro, Y. Moriwaki, F. Matsushima, S. Tsunekawa, and K. Takagi, "Sub-Doppler measurements of $\nu_{CO} = 1 \leftarrow 0$, K=0, A/E lines of methanol with microwave sidebands of CO_2 laser lines," Journal of Molecular Spectroscopy **211**, 162–166 (2002).

[249] F. Rohart, S. Mejri, P. L. T. Sow, S. K. Tokunaga, C. Chardonnet, B. Darquié, H. Dinesan, E. Fasci, A. Castrillo, L. Gianfrani, and C. Daussy, "Absorption-line-shape recovery beyond the detection-bandwidth limit: Application to the precision spectroscopic measurement of the boltzmann constant," Physical Review A **90**, 042506 (2014).

[250] F. Rohart, "Overcoming the detection bandwidth limit in precision spectroscopy: The analytical apparatus function for a stepped frequency scan," Journal of Quantitative Spectroscopy and Radiative Transfer **187**, 490–504 (2017).

[251] R. Arndt, "Analytical line shapes for lorentzian signals broadened by modulation," Journal of Applied Physics **36**, 2522–2524 (1965).

[252] J. Hall and C. J. Bordé, "Shift and broadening of saturated absorption resonances due to curvature of the laser wave fronts," Applied Physics Letters **29**, 788–790 (1976).

[253] C. Chardonnet, "Spectroscopie de saturation de haute précision et sensibilité en champ laser fort: applications aux molécules OsO_4, SF_6 et CO_2 et à la métrologie des fréquences," Ph.D. thesis, Université Paris 13 (1989).

[254] P. Cérez and R. Felder, "Gas-lens effect and cavity design of some frequency-stabilized He-Ne lasers: author's reply to comments," Applied optics **22**, 3313_1–3314 (1983).

[255] E. N. Bazarov, G. A. Gerasimov, V. P. Gubin, S. Y. Otrokhov, A. I. Sazonov, N. I. Starostin, and V. Fomin, "Frequency shifts of a narrow resonance of oso4 in an external interferometer due to self-focusing of radiation," Soviet Journal of Quantum Electronics **21**, 695 (1991).

[256] A. Clairon, O. Acef, C. Chardonnet, and C. J. Bordé, "State-of-the-art for high accuracy frequency standards in the 28 THz range using saturated absorption resonances of OsO_4 and CO_2," in "Frequency standards and Metrology," (Springer, 1989), pp. 212–221.

[257] J. Hall, C. J. Bordé, and K. Uehara, "Direct optical resolution of the recoil effect using saturated absorption spectroscopy," Physical Review Letters **37**, 1339 (1976).

[258] O. Acef, "Metrological properties of co2oso4 optical frequency standard," Optics Communications **134**, 479–486 (1997).

[259] N. Vanhaecke and O. Dulieu, "Precision measurements with polar molecules: the role of the black body radiation," Molecular Physics **105**, 1723–1731 (2007).

[260] R. Forber, J. Tenenbaum, and M. Feld, "Laser Stark saturation spectroscopy in methyl alcohol," International Journal of Infrared and Millimeter Waves **1**, 527–560 (1980).

[261] J. Johns, A. McKellar, T. Oka, and M. Römheld, "Collision-induced Lamb dips in laser Stark spectroscopy," The Journal of Chemical Physics **62**, 1488–1496 (1975).

[262] H. Cottin, M.-C. Gazeau, J.-F. Doussin, and F. Raulin, "An experimental study of the photodegradation of polyoxymethylene at 122, 147 and 193 nm," Journal of photochemistry and photobiology A: Chemistry **135**, 53–64 (2000).

[263] H. Cottin, Y. Bénilan, M.-C. Gazeau, and F. Raulin, "Origin of cometary extended sources from degradation of refractory organics on grains: polyoxymethylene as formaldehyde parent molecule," Icarus **167**, 397–416 (2004).

[264] D. Dangoisse, J. Wascat, and J. Colmont, "Assignment of laser lines in an optically pumped submillimeter and near millimeter laser:$(H_2CO)_3$," International Journal of Infrared and Millimeter Waves **2**, 1177–1191 (1981).

[265] A. Pagies, G. Ducournau, and J.-F. Lampin, "Low-threshold terahertz molecular laser optically pumped by a quantum cascade laser," Apl Photonics **1**, 031302 (2016).

[266] M. Mičica, S. Eliet, M. Vanwolleghem, R. Motiyenko, A. Pienkina, L. Margulès, K. Postava, J. Pištora, and J.-F. Lampin, "High-resolution THz gain measurements in optically pumped ammonia," Optics express **26**, 21242–21248 (2018).

[267] A. Stair Jr and J. R. Nielsen, "Vibrational spectra of sym-trioxane," The Journal of Chemical Physics **27**, 402–407 (1957).

[268] T. Oka, K. Tsuchiya, S. Iwata, and Y. Morino, "Microwave spectrum of s-trioxane," Bulletin of the Chemical Society of Japan **37**, 4–7 (1964).

[269] J. Bellet, J.-M. Colmont, and J. Lemaire, "Millimeter wave study of the ground state and several excited vibrational states of trioxane," Journal of Molecular Spectroscopy **34**, 190–205 (1970).

[270] J. Gadhi, G. Wlodarczak, D. Boucher, and J. Demaison, "The submillimeter-wave spectrum of trioxane," Journal of Molecular Spectroscopy **133**, 406–412 (1989).

[271] J.-M. Colmont, "Assignment method of the rotational spectrum of a slightly asymmetric molecule: application to the ^{13}C and ^{18}O species of the molecule of trioxane," Journal of Molecular Spectroscopy **80**, 166–177 (1980).

[272] J.-M. Colmont, "Assignment of the microwave spectrum of trioxane in the ν_{19}(E)=ν_{20}(E)=1 state," Journal of Molecular Structure **62**, 85–94 (1980).

[273] H. Klein, S. Belov, and G. Winnewisser, "Terahertz spectrum of trioxane," Zeitschrift für Naturforschung A **51**, 123–128 (1996).

[274] J. Henninot, H. Bolvin, J. Demaison, and B. Lemoine, "The infrared spectrum of trioxane in a supersonic slit jet," Journal of Molecular Spectroscopy **152**, 62–68 (1992).

[275] B. M. Gibson, N. C. Koeppen, and B. J. McCall, "Rotationally-resolved spectroscopy of the ν_{16} band of 1, 3, 5-trioxane," Journal of Molecular Spectroscopy **317**, 47–49 (2015).

[276] P. A. et al, "Private communication," .

[277] J. Reid and D. Labrie, "Second-harmonic detection with tunable diode lasers-comparison of experiment and theory," Applied Physics B **26**, 203–210 (1981).

[278] J. M. Supplee, E. A. Whittaker, and W. Lenth, "Theoretical description of frequency modulation and wavelength modulation spectroscopy," Applied Optics **33**, 6294–6302 (1994).

[279] S. Schilt, L. Thevenaz, and P. Robert, "Wavelength modulation spectroscopy: combined frequency and intensity laser modulation," Applied optics **42**, 6728–6738 (2003).

[280] J. Colmont, "Étude en ondes millimétriques des variétés isotopiques en ^{13}c et ^{18}o de la molécule de trioxane: Structure de la molécule," Journal of Molecular Structure **21**, 387–396 (1974).

[281] J. van Veldhoven, "AC trapping and high-resolution spectroscopy of ammonia molecules," Ph.D. thesis, Radboud University Nijmegen (2006).

[282] G. Gunther-Mohr, R. White, A. Schawlow, W. Good, and D. Coles, "Hyperfine structure in the spectrum of $^{14}NH_3$. I. Experimental results," Physical Review **94**, 1184 (1954).

[283] J. Gordon, "Hyperfine structure in the inversion spectrum of $^{14}NH_3$ by a new high-resolution microwave spectrometer," Physical Review **99**, 1253 (1955).

[284] J. T. Hougen, "Reinterpretation of molecular beam hyperfine data for $^{14}NH_3$ and $^{15}NH_3$," The Journal of Chemical Physics **57**, 4207–4217 (1972).

[285] S. G. Kukolich and S. Wofsy, "$^{14}NH_3$ hyperfine structure and quadrupole coupling," The Journal of Chemical Physics **52**, 5477–5481 (1970).

[286] D. J. Ruben and S. G. Kukolich, "Beam maser measurements of distortion effects on quadrupole coupling in $^{14}NH_3$," The Journal of Chemical Physics **61**, 3780–3784 (1974).

[287] M. Ouhayoun, C. J. Bordé, and J. Bordé, "Vibrational dependence of the hyperfine quadrupole constant in $^{14}NH_3$ observed by saturated absorption spectroscopy," Molecular Physics **33**, 597–600 (1977).

[288] C. Salomon, C. Chardonnet, A. Van Lerberghe, C. Bréant, and C. J. Bordé, "Première observation de la structure hyperfine magnétique dans le spectre infrarouge de l'ammoniac," Journal de Physique Lettres **45**, 1125–1129 (1984).

[289] C. J. Bordé, J. Bordé, C. Bréant, C. Chardonnet, A. Van Lerberghe, and C. Salomon, "Internal dynamics of simple molecules revealed by the superfine and hyperfine structures of their infrared spectra," in "Laser Spectroscopy VII," (Springer, 1985), pp. 108–114.

[290] C. Lemarchand, M. Triki, B. Darquié, C. J. Bordé, C. Chardonnet, and C. Daussy, "Progress towards an accurate determination of the boltzmann constant by Doppler spectroscopy," New Journal of Physics **13**, 073028 (2011).

[291] C. Lemarchand, "Mesure de la constante de Boltzmann par spectroscopie laser: vers une contribution au futur Système International d'unités," Ph.D. thesis, Université Paris-Nord-Paris XIII (2012).

[292] W. Gordy, *Microwave Spectroscopy* (Springer Berlin Heidelberg, Berlin, Heidelberg, 1957).

[293] W. Weber, "Hyperfine structure in excited vibrational states of $^{14}nh_3$ studied by laser-Stark spectroscopy," J. Opt. Soc. Am. B **2**, 829–836 (1985).

[294] V. Špirko, "The inversional dependence of hyperfine quadrupole coupling in $^{14}nh_3$," Molecular Physics **38**, 1761–1766 (1979).

[295] J. P. Gordon, H. J. Zeiger, and C. H. Townes, "Molecular microwave oscillator and new hyperfine structure in the microwave spectrum of NH_{3s}," Physical Review **95**, 282 (1954).

[296] W. Hüttner and W. Majer, "The $\nu_2 = 1$ inversional dependence of the quadrupole coupling in $^{14}NH_3$," Molecular Physics **52**, 631–636 (1984).

[297] J. Karhu, M. Vainio, M. Metsälä, and L. Halonen, "Frequency comb assisted two-photon vibrational spectroscopy," Optics Express **25**, 4688–4699 (2017).

[298] M. G. Hansen, I. Ernsting, S. V. Vasilyev, A. Grisard, E. Lallier, B. Gérard, and S. Schiller, "Robust, frequency-stable and accurate mid-ir laser spectrometer based on frequency comb metrology of quantum cascade lasers up-converted in orientation-patterned GaAs," Optics express **21**, 27043–27056 (2013).

[299] S. Tokunaga, R. Hendricks, M. Tarbutt, and B. Darquié, "High-resolution mid-infrared spectroscopy of buffer-gas-cooled methyltrioxorhenium molecules," New Journal of Physics **19**, 053006 (2017).

[300] S. Truppe, H. Williams, M. Hambach, L. Caldwell, N. Fitch, E. Hinds, B. Sauer, and M. Tarbutt, "Molecules cooled below the Doppler limit," Nature Physics **13**, 1173 (2017).

[301] I. Kozyryev, L. Baum, K. Matsuda, B. L. Augenbraun, L. Anderegg, A. P. Sedlack, and J. M. Doyle, "Sisyphus laser cooling of a polyatomic molecule," Physical Review Letters **118**, 173201 (2017).

[302] C. Cheng, A. P. Van Der Poel, P. Jansen, M. Quintero-Pérez, T. E. Wall, W. Ubachs, and H. L. Bethlem, "Molecular fountain," Physical Review Letters **117**, 253201 (2016).

[303] A. Prehn, M. Ibrügger, R. Glöckner, G. Rempe, and M. Zeppenfeld, "Optoelectrical cooling of polar molecules to submillikelvin temperatures," Physical Review Letters **116**, 063005 (2016).

[304] K. Bielska, S. Wójtewicz, P. Morzyński, P. Ablewski, A. Cygan, M. Bober, J. Domysławska, M. Zawada, R. Ciuryło, P. Masłowski, and D. Lisak, "Absolute frequency determination of molecular transition in the Doppler regime at kHz level of accuracy," Journal of Quantitative Spectroscopy and Radiative Transfer **201**, 156–160 (2017).

[305] D. Simpson, W. Winiwarter, G. Börjesson, S. Cinderby, A. Ferreiro, A. Guenther, C. N. Hewitt, R. Janson, M. A. K. Khalil, S. Owen, , T. E. Pierce, H. Puxbaum, M. Shearer, U. Skiba, R. Steinbrecher, L. Tarrasón, and M. G. Öquist, "Inventorying emissions from nature in europe," Journal of Geophysical Research: Atmospheres **104**, 8113–8152 (1999).

[306] Bisschop, S. E., Schilke, P., Wyrowski, F., Belloche, A., Brinch, C., Endres, C. P., Güsten, R., Hafok, H., Heyminck, S., Jørgensen, J. K., Müller, H. S. P., Menten, K. M., Rolffs, R., and Schlemmer, S., "Dimethyl ether in its ground state, $\nu = 0$, and lowest two torsionally excited states, $\nu_{11} = 1$ and $\nu_{15} = 1$, in the high-mass star-forming region G327. 3-0.6," Astronomy & Astrophysics **552**, A122 (2013).

[307] M. Koerber, S. E. Bisschop, C. Endres, M. Kleshcheva, R. Pohl, A. Klein, F. Lewen, and S. Schlemmer, "Laboratory rotational spectra of the dimethyl ether 13C-isotopologues up to 1.5 THz," Astronomy & Astrophysics **558**, A112 (2013).

[308] H. L. Bethlem, M. Kajita, B. Sartakov, G. Meijer, and W. Ubachs, "Prospects for precision measurements on ammonia molecules in a fountain," The European Physical Journal Special Topics **163**, 55–69 (2008).

[309] P. Jansen, H. L. Bethlem, and W. Ubachs, "Perspective: Tipping the scales: Search for drifting constants from molecular spectra," The Journal of chemical physics **140**, 010901 (2014).

[310] E. Rubiola, "On the measurement of frequency and of its sample variance with high-resolution counters," Review of scientific instruments **76**, 054703 (2005).

[311] S. T. Dawkins, J. J. McFerran, and A. N. Luiten, "Considerations on the measurement of the stability of oscillators with frequency counters," Ieee transactions on ultrasonics, ferroelectrics, and frequency control **54**, 918–925 (2007).

[312] E. N. Bazarov, G. A. Gerasimov, V. P. Gubin, A. I. Sazonov, N. I. Starostin, V. Strel'nikov, and V. Fomin, "Stabilized CO_2/OsO_4 laser with a frequency reproducibility of 10^{12}," Quantum Electronics **17**, 1421–1424 (1987).

Widely tunable and SI-traceable frequency-comb-stabilised mid-infrared quantum cascade laser : application to high precision spectroscopic measurements of polyatomic molecules

Abstract : The thesis consists in developing a high-resolution mid-infrared spectrometer traceable to primary frequency standards and providing a unique combination of resolution, tunability, detection sensitivity, and frequency control. A quantum cascade laser (QCL) emitting at 10.3 μm is phase locked to an optical frequency comb stabilized to a remote 1.55 μm ultra-stable reference developed at LNE-SYRTE, monitored against primary frequency standards and transferred to LPL via an active noise compensated fibre link. This results in a 0.1 Hz QCL linewidth, a stability below 10^{-15} at 1 s and an uncertainty on its absolute frequency below 4×10^{-14}. Moreover, the setup allows the QCL to be widely scanned over 1.4 GHz while maintaining the highest stabilities and precisions. This QCL was used to carry out saturated absorption spectroscopy of several molecules in a compact multipass cell. We demonstrated statistical uncertainty on line-center frequencies at the kHz level and sub-10 kHz systematic uncertainty. We have recorded several singular K-doublets and many rovibrational transitions of methanol, in particular weak transitions and weak doublets - unreported so far. Precise parameters modelling trioxane have been determined with only a few tens of rovibrational transitions recorded at unprecedented accuracy. The quadrupole hyperfine structure of an ammonia transition has been resolved for the first time. This setup constitutes a key element for the project aiming at the first observation of parity violation in molecules currently held at LPL, and, more generally, for various fields of physics, from atmospheric and interstellar physics to fundamental physics beyond the standard model.

Keywords : ultra-high resolution molecular spectroscopy, frequency metrology, mid-infrared, quantum cascade lasers, optical frequency comb, saturated absorption spectroscopy, ultra-stable lasers, laser stabilization, optical fibre links, frequency reference transfer, methanol, hyperfine structure

Laser à Cascade Quantique stabilisé sur peigne de fréquence, largement accordable et calibré au SI : application à la spectroscopie de très haute précision de molécules polyatomiques

Résumé : Ce manuscrit présente le développement d'un spectromètre dans le moyen infra-rouge qui combine très haute résolution, accordabilité, sensibilité de détection et contrôle de la fréquence absolue. Un laser à cascade quantique (QCL) émettant à 10.3 μm est asservi en phase sur un peigne de fréquences optique lui-même stabilisé sur un laser ultrastable à 1.55 μm transmis par lien optique fibré à partir du LNE-SYRTE, où cette référence de fréquence est contrôlée par rapport aux étalons primaires. On obtient ainsi un QCL de largeur $\sim$0.1 Hz, avec une stabilité meilleure que 10^{-15} à 1 s, et une incertitude de 4×10^{-14} sur sa fréquence absolue. De plus, le QCL peut être balayé largement sur 1.4 GHz sans dégradation de la stabilité et du contrôle absolu de la fréquence. Ce QCL a permis de sonder plusieurs molécules par absorption saturée dans une cellule multipassage. Nous avons démontré une incertitude statistique sur la mesure des fréquences d'absorption au niveau du kHz et une incertitude systématique inférieure à 10 kHz. Nous avons enregistré de nombreuses raies du méthanol, dont plusieurs doublets et des raies très peu intenses, dont certaines n'avaient jamais été observées. La mesure de quelques dizaines de raies du trioxane nous a permis d'en déterminer les paramètres spectroscopiques avec précision. Nous avons également enregistré la structure hyperfine d'une raie de l'ammoniac jusqu'ici non résolue. Ce dispositif est essentiel pour le projet en cours au LPL d'observer la violation de parité dans les molécules. Il permettra également de nombreuses applications de la physique atmosphérique ou interstellaire aux tests de physique fondamentale au-delà du modèle standard.

Mots clés : spectroscopie moléculaire à ultra-haute résolution, métrologie des fréquences, moyen-infrarouge, lasers à cascade quantique, peigne de fréquence optique, spectroscopie d'absorption saturée, lasers ultra-stables, stabilisation laser, liens optiques fibrés, transfert de références de fréquence, méthanol, structure hyperfine